Early Cambrian black shale and associated polymetallic Ni-Mo-PGE-Au mineralization, South China

Doctoral Thesis

(Dissertation)

to be awarded the degree of

Doctor rerum naturalium (Dr. rer. nat.)

submitted by

Xu Lingang

from Nei Mongol, China

approved by the Faculty of Energy and Management Science,

Technical University of Clausthal

Date of oral examination

(July 6, 2011)

Chairperson of the Board of Examiners: Prof. Dr.-Ing. Norbert Meyer

Chief Reviewer: Prof. Dr. Bernd Lehmann

Reviewer: Prof. Dr. Kurt Mengel

This dissertation was undertaken at the Mineral Resources Department of the Institute of Disposal Research of the Technical University of Clausthal.

This thesis is dedicated to my mother and
sisters in appreciation of their love.

ABSTRACT

The transgressive Early Cambrian black shale sequence of the Niutitang Formation (and equivalent strata) in South China with abundant fossils (e.g. sponge spicules, algaes, arthropods, phyto- and zooplankton, and bacterial colonies) occurs in an about 1600 km-long belt that extends in the Yunnan, Guizhou, Hunan, Jiangxi, Anhui and Jiangsu provinces across the Yangtze Platform, overlying dolomite of the Neoproterozoic Dengying Formation. The widespread Early Cambrian black shale deposition is a reflection of a global ocean anoxia event during the Precambrian/Cambrian transition, which is a critical interval in Earth history characterized by global environmental and biological events such as the "Cambrian explosion". i.e. development of complex multicellular life. The lowermost part of the Niutitang Formation black shale sequence hosts a synsedimentary organic carbon- and phosphorite-rich polymetallic sulfide layer with extreme metal enrichment, locally mined as Ni-Mo-PGE-Au sulfide ore. The polymetallic sulfide ore layer is only several centimeters thick, but it shows great metal enrichment with Ni + Mo reaching up to 14 wt.%, and platinum group element (PGE) + Au concentrations around 1 g/t, as well as Se, Re, Os, As, Hg and Sb more than 10000 times enriched compared to average continental crust.

This thesis investigates the Early Cambrian Dingtai profile and four polymetallic Ni-Mo-PGE-Au sulfide ore deposits (Dazhuliushui and Maluhe in Guizhou province, and Sancha and Cili in Hunan province, respectively) on the Yangtze Platform, and tries to identify the Early Cambrian paleoenvironment and the metallogenic mechanisms of the spectacular stratiform polymetallic sulfide mineralization.

A composite Re-Os isochron of the sulfide ore layer on 14 samples, from the Dazhuliushui, Maluhe and Sancha mine sites, several hundred kilometers apart, defines an age of 521 ± 5 Ma (2 σ). This age is ~20 Ma younger than in previous less comprehensive Re-Os studies, and is consistent both with the biostratigraphic Tommotian age, and with recent studies applying the Pb-Pb and SHRIMP U-Pb

methods on over- and underlying rock units. The fact that all samples from the widely spaced localities plot on one isochron suggests that the polymetallic sulfide layer represents one regionally distributed stratigraphic level formed by the same geological processes. The initial $^{187}Os/^{188}Os$ value of the sulfide ore is 0.87 ± 0.07, which is equal to the initial $^{187}Os/^{188}Os$ ratio of ~0.80 of the black shale host rock, consistent with the seawater origin of the metals under depositional conditions of very low clastic input.

The Dingtai profile covers a ~33 m thick black shale sequence, which can be classified into three intervals based on Mo isotope composition, iron speciation and redox-sensitive element ratios. Interval 1 (0-1 m) has extreme metal and TOC enrichment and heavy $\delta^{98/95}Mo$ values. This unit has all features of a euxinic environment, and is then followed by interval 2 (1-11 m) with variably $\delta^{98/95}Mo$ composition. Elevated redox-sensitive elements and their ratios, and relatively high Fe_{HR}/Fe_T indicate that black shales from the interval 2 are still precipitated under a euxinic condition. The overlying intervals 3 (11-30 m) shows suboxic condition with generally light $\delta^{98/95}Mo$ values at the lowermost part and fluctuant $\delta^{98/95}Mo$ values at the uppermost part, and relatively low redox-sensitive element contents and their ratios. We propose a model of a partly closed ocean basin with periodic replenishment for the remarkably variability of $\delta^{98/95}Mo$ values. Light $\delta^{98/95}Mo$ values indicate restricted seawater circulation dominated by continental input, periodically replenished by fresh seawater with heavy $\delta^{98/95}Mo$. The relatively light $\delta^{98/95}Mo$ values of the Early Cambrian black shales compared to those of modern euxinic sediments are indicative of much more widespread anoxic marine environments during the Early Cambrian than today.

The polymetallic sulfide ores have relatively consistent heavy $\delta^{98/95}Mo$ values (from 0.94 to 1.38‰, with average of 1.13 ± 0.14‰, 1σ, n = 11) while the host black shale and phosphorite has variable $\delta^{98/95}Mo$ values (0.81‰ to 1.70‰, with average of 1.28 ± 0.41‰, 1σ, n = 14), reflecting both variable paleoenvironmental conditions from suboxic to euxinic, and partly closed-system fractionation in protected sedimentary basins. Both the polymetallic sulfides and the host black shales show

PGE distribution patterns similar to present-day seawater, but different from hydrothermal fluids. The polymetallic sulfide bed has a generally consistent metal enrichment by a factor of 10^7 compared to present-day seawater, while the host black shales are largely controlled by terrigenous input. Ni- and Mo-based metal ratios reveal that the polymetallic sulfide ores have ratios similar to present-day seawater. Both the polymetallic sulfide ores and the host black shales have Ni- and Mo-based metal ratios much higher than the hydrothermal sulfide ores. REE + Y patterns of the polymetallic sulfide bed are characterized by a remarkably positive Y anomaly, consistent with an origin of the REE budget dominantly from an aqueous environment (likely seawater), and not from clastic input.

The Re-Os geochronology, Mo isotope, PGE, and trace and rare-earth element geochemistry suggest that the metals in the polymetallic Ni-Mo-PGE-Au sulfide ore layer were scavenged from Early Cambrian seawater in restricted basins with very low clastic dilution, by both in-situ precipitation and short distance re-deposition of sulfide clasts. The Mo isotope data indicate an ocean globally less oxidized than today, with more widespread euxinic to suboxic environments.

Keywords: Re-Os dating, Mo isotopes, PGE, Trace and rare-earth elements, Polymetallic Ni-Mo-PGE-Au sulfide, Black shale, Seawater scavenging, Paleoenvironment, Early Cambrian, South China

ACKNOWLEDGEMENTS

I am indebted to a number of people who have supported me both personally and academically during my graduate studies at the Technical University of Clausthal.

First and foremost, I would like to express my honest acknowledgements to my supervisors, Prof. Dr. Bernd Lehmann in Clausthal and Prof. Dr. Mao Jingwen in Beijing, for their enthusiastic supervision, academic advice and financial support over the years at TU Clausthal. During the writing of several papers, they reviewed all my manuscripts with amazing efficiency and rigor which helped to much improve both scientific content and English expression. Their kind, simple, clear and rigorous ways have much influenced my scientific career. Without their support and help I would not have been able to finish.

I also thank Prof. Kurt Mengel for accepting to be the reviewer of this thesis. His constructive comments improved my thesis greatly.

I am grateful to Dr. Eike Gierth for his valuable support during ore microscopy study. Fred Türck is thanked for his computer assistance and experimental guidance in the laboratory. Ulf Hemmerling is thanked for the professional preparation of thin sections and polished sections. I also wish to thank Ms. Elvira Schulze, our secretary, for her permanent assistance.

Sincere gratitude is due to Dr. Daniel Hennig and Stephanie Lohmeier for their help during my days in Clausthal and many constructive discussions on scientific interests.

I am grateful to Dr. Mohammed Nekouvaght, Dr. Farhad Torab, Dr. Etienne Assie, Dr. Akwinga Victor Assah, Dr. Alexandre Raphael Cabral, Jasmi Hafiz Abdul Aziz, Dr. Ingo Böttcher, Jian Wei, Dr. Wan Bo, Dr. Gao Jianjing, Dr. Liu Yifei, Dr. Zhang Hongrui, Dr. An Fang for their friendliness, interest, help and fruitful discussions. I will also not forget Yu Bo, Lu Yuliang, Gu Xiaoqian, Lu Yiyang, Zhang Qian, Li Xiaodong and Zheng Shengxia for bringing me so much happiness in daily life.

I would like to thank all the staff of the Institute of Mineralogy and Mineral Resources at the Technical University of Clausthal for friendliness and assistance. All colleagues under the supervision of Prof. Mao Jingwen from Chinese University of Geoscience and Chinese Academy of Geological Sciences (CAGS) in Beijing are thanked for constructive discussions and assistances.

I also wish to express my special thanks to Dr. Ye Huishou, who encouraged me to apply for the schloarship from Chinese Scholarship Council for study aboard.

Dr. Zhang Ying from Institute of Geochemistry, Chinese Academy of Sciences deserves special mention for his assistance during sample collection during the first field trip in 2007. Wang Shangyan, He Lingbang and Wang Suhua are thanked for offering of important geological documents and generous assistance during my field work.

Prof. Thomas F. Nägler and Dr. Nadja Neubert from University of Bern, Switzerland are gratefully acknowledged for arranging access to their Molybdenum isotope laboratory facilities and offering technical support. Prof. Michael E. Böttcher from MPI for Marine Microbiology in Bremen performed the iron geochemical measurements. I would also like to thank Prof. Qu Wenjun and Prof. Du Andao from CAGS for Rhenium-Osmium isotopic measurements. Han Huiming from National Research Center of Geoanalysis in Beijing is thanked for a large amount of bulk rock geochemistry analysis.

This project has been financially supported by the Chinese Geological Survey Program (No. 1212010634001), the National Basic Research Program of China (No. 2007CB411302 & No. 2007CB411405) and the Chinese Scholarship Council, as well as by Deutsche Forschungsgemeinschaft (LE578/32-1). The Institute of Mineralogy and Mineral Resources of TU Clausthal provides me with office space and free access to the laboratary and all other facilitates.

Lastly, I would like to thank my family for their unending support and encouragement during my rather lengthy collegiate career. Sincere thanks are due to my mother for her great and selfless love.

LIST OF ABBRIVIATIONS

Ap	Apatite
Bra	Bravoite
Brt	Barite
BSE	Backscattered electron
Cal	Calcite
C_{org}	Organic carbonaceous material
Cpy	Chalcopyrite
DOP	Degree of pyritization
Dol	Dolomite
DSDP	Deep sea drilling project
Fe_{HR}	Highly reactive iron
Fe_T	Total iron
Ga	Billion years
Ger	Gersdorffite
GOE	Great oxidation event
ICP-AES	Inductively coupled plasma-atomic emission spectrometry
IEC	Ion exchange chromatography
INAA	Instrumental neutron activation analysis
Ma	Million years
MC-ICP-MS	Multi collector-inductively coupled plasma mass spectrome
Mi	Millerite
MOMO	Mean ocean Mo
MSWD	Mean square of weighted deviates
ng	Nanogram
OAE	Oceanic anoxic event
OC	Organic carbon
OM	Organic matters
PC/C	Precambrian/Cambrian

pg	Picogram
PGE	Platinum group element
Ph	Phosphate
ppb	Part per billion
ppm	Part per million
Py	Pyrite
Qtz	Quartz
REE	Rare earth element
Sedex	Sedimentary exhalative
SHRIMP	Sensitive high-resolution ion microprobe
Sph	Sphalerite
Ti	Tillite
TOC	Total organic carbon
VMS	Volcanogenetic massive sulfide
wt.%	Weight percent
XRF	X-ray fluorescence

CONTENTS

LIST OF FIGURES

Chapter one:

Chapter two:

Chapter three:

Chapter four:

Chapter five:

Chapter six:

Chapter seven:

Chapter eight:

LIST OF TABLES

Chapter one:

Chapter two:

Chapter four:

Chapter five:

Chapter six:

Chapter seven:

CHAPTER ONE:

INTRODUCTION

Over the past century the term “black shale” has been applied to certain sedimentary facies, which are interpreted to represent quite variable depositional settings and paleoenvironments. Here, a definition in terms of sedimentologic and geochemical parameters by Neuendorf et al. (2005) in “Glossary of Geology” is cited:

A black shale is a dark, thinly laminated carbonaceous shale, exceptionally rich in organic matter (5% or more carbon content) and sulfide (esp. iron sulfide, usually pyrite), and more commonly containing unusual concentrations of certain trace elements (U, V, Cu, Ni).

The most important constituent that differentiates black shales from other sedimentary rocks (e.g. mudstone, claystone) is organic matter (OM) content, which is the main cause of the dark color in black shale facies. The color of shales is related to amount, type and maturity of organic carbon (OC). For example, shales containing only 1-2% thermally mature OC are commonly black. The black coloration of shales is also influenced by the presence of very fine grained iron monosulfide minerals, but these monosulfides are unstable over geologic periods of time and the black coloration of monosulfide-bearing sediments fades rapidly when exposed to oxygen (Arthur and Sageman, 1994).

Lamination is a fundamental distinguishing feature of black shales. Lamination in mudrocks is defined as a parallel arrangement of layers less than 10 mm thick resulting from a regular alternation in fabric, grain size and/or color (Lundegard and Samuels, 1980). The genesis of finely laminated structures has long been a topic of interest, which is either because original lamination was disturbed by bioturbation or by physical processes, for instance, winnowing and redeposition (Arthur and Sageman, 1994). A number of studies have suggested that such laminations result from seasonal phytoplankton blooms (Degens and Ross, 1974; Calvert, 1964; Ross et al., 1970; Thomsen, 1989; Hattin, 1975). Lamination occurs when season-dependent oxygen concentration inhibits benthic metazoan activity or sediment supply. However, Sageman (1991) found that a wide range of different types of laminae are macroscopically similar, and do not related to a seasonal depositional cycle, but possibly reflect low sedimentary rates. In that case light-colored laminae represent the amalgamation of numerous annual productivity events, separated by darker clay and organic-rich laminae reflecting more rapidly and intermittently deposited mud. Fine-scale lamination can show signs of macrofaunal disturbance requiring benthic oxygen. That means undisturbed sediments can reveal complex histories of plaeoceanic redox conditions. It should be noted that the animals known to burrow and disturb primary lamination probably did not appear until the latest Neoproterozoic about 560 Ma age (Droser et al., 2002). Thus, preserved lamination at any scale tells us nothing about oxygen in the bottom waters of the Proterozoic and Archean ocean.

Another feature is that black shales commonly are enriched in metals. Vine and Tourtelo (1970) investigated black shales from a wide variety of geological environments, and found that black shales from marine environments contain higher amounts of Mo, Ni, V, Cr, Cu and a number of other metals than any other sedimentary rock. The enrichment factor of such elements in black shales is 10^5 to 10^6-fold higher than the metal concentrations in average seawater. The high concentration of trace metals in black shales was interpreted as removal from seawater controlled by redox state and sedimentation rate (Holland, 1979).

1.1 Historical perspective on black shales

Organic carbon-rich, microlaminated black shales occur throughout the geological history. Black shales have long intrigued geologists for three reasons: 1) Black shales host many economically important ore deposits (e.g. Au, Zn, Pb, Mo, P, Mn etc.), and understanding their genesis and distribution characteristics is important for mineral deposit exploration; 2) Black shales contain a number of ecologically harmful heavy metals, and understanding their geochemical behavior is significant to environmental protection; 3) OM in black shales is a product of complex factors, including primary productivity, water column anoxia, rates of clastic and biogenic sedimentation, mineralogical controls of organic preservation, etc. thus black shales are ideal for reconstructing paleoenvironments and understanding the evolution history of Earth.

Studies on black shales started in the early last century. Clarke (1904) suggested that the formation of Paleozoic black shales was similar to that of modern Black Sea sediments, representing deep water restricted sedimentary environments. Grabau (1913) argued that widely distributed marine black shales were deposited in coastal lagoons or marginal epicontinental seas on extensive mud flats exposed at low tide. Subsequently, through investigating OM deposition in Norwegain fjords, Strom (1939) reinforced the concept of restricted basins, suggesting that organic-rich black shale is deposited in anoxic barred basins. Fleming and Revelle (1939) gained similar conclusions, they presented a thorough and insightful treatment of the role of physical oceanographic processes on dissolved oxygen distribution in the water column and emphasized the role of sill depth or basin thresholds in controlling the rate of renewal of bottom water, taking California borderland basins and the Black Sea as example where stable stratification and sill-limited exchange of bottom waters promotes oxygen deficiency. Through investigating Devonian black shales of the Applachian region, Ruedemann (1935) suggested “toxic” bottom water conditions and argued against the concept of small embayments or lagoons as primary sites for black shale deposition. Twenhofel (1939) suggested that black shales accumulated in less stagnant and more open water, but waters that did not have good circulation. Based on previous studies, Pettijohn (1957) recognized that the pyritic black shales were unquestionably deposited under anaerobic conditions. however, whether the basin of accumulation was shallow or deep and whether it was landlocked or freely connected with the sea or even a stagnant area in the open sea has been much debated.

Many studies emphasized that reducing environments were most important in producing OC-rich strata. However, many researchers have indicated that organic enrichment is affected by complex factors, in addition to anoxia, such as the rates of clastic and biogenic sedimentation (Henrichs and Reeburgh, 1987; Sageman and Lyons, 2003), the level of OM input from primary production (Pedersen and Calvert, 1990) and clay content that can impact organic preservation (Mayer, 1994; Hedges and Keil, 1995; Kennedy et al., 2002). The inputs of clastic and biogenic materials can both dilute concentrations of OM and enhance its preservation when the rates of clastic and biogenic sedimentation are high. Goldman (1924) advocated the significance of rate of supply of OM with or without oxygen depletion. He suggested that in shallow bays that have no threshold, but which are rich in vegetation and have only a feeble deep water circulation, the bottom deposits often consist of black muds high in hydrogen sulfide and containing no animal life. The water themselves, however, will usually contain dissolved oxygen. The moderate stagnation in these cases is due to the large supply of decomposable OM rather than the lack of water exchange. Although this concept has been echoed by many studies, more complete models for black shale deposition suggesting that both high primary productivity and oxygen depletion in deeper water masses played a role in producing relatively OC-rich strata have been outlined until more recently (Parrish, 1982; Parrish and Curtis, 1982; Waples, 1983). Based on the fact that sediments accumulating in the modern Black Sea, the type locality of a euxinic basin, are not particularly enriched in OM despite the presence of an anoxic water column, although a sapropel containing extremely high carbon concentrations was deposited during the Holocene at the time when the basin was oxic, Pedersen and Calvert (1990) suggested that high primary production provides the first-order control on the accumulation of OM-rich facies in the modern oceans.

The discovery of widespread Cretaceous black shales as a result of the Deep Sea Drilling Project (DSDP) evoked great scientific interest. The Cretaceous black shales were recovered in a number of DSDP sites in all ocean basins (Ryan and Cita, 1977; Thiede and van Andel, 1977). Schlanger and Jenkyns (1976) first defined the concept of Oceanic Anoxic Events (OAE) to explain global scale distributed organic-rich units and paleoenvironment evolution. Although Arthur and Sageman (1994) suggested that the concept of OAE may be misleading in the sense that it does not distinguish between events with long and those with short durations, it is generally agreeable that the formation of black shales characterizes certain geological environments; therefore black shales become natural laboratories to study paleoenvironment evolution. Interpretation of ancient black shale deposits has been strongly influenced by observations of modern environments where OC-rich muds presently accumulate. For example, the Black Sea and the Baltic Sea represent large landlocked or silled basins; Peru, Namibia, NW margin of the Indian Ocean, California borderland basins and the Gulf of California represent open ocean environments affected by impingement of the midwater oxygen-minimum zone.

The formation of black shales is mainly influenced by two environmental factors: productivity and preservation. High productivity supplies a large amount of OM into sedimentary basins. Anoxic water columns are favorable for OM preservation. Fan et al. (2004) summarized three popular accepted models of anoxic sedimentary environments, including 1) Seawater transgression model: Transgressions caused by glacier melting after the ice age triggering sea level rise. The anoxic water columns resulting by sea level rise are favorable for the formation and preservation of black shales. 2) Basin model: Salinity stratification and stagnation conditions provide a lack of interaction between seawater columns at different levels, such conditions conduce formation of anoxic sedimentary environments, for example, the modern Black Sea. 3) Low oxygen model: In low latitude regions, ocean currents bring masses of nutrients to the near-surface water column, which leads to high productivity. Digestion of organic materials consums a great deal of oxygen. As Fan et al. (2004) pointed out, diagenetic processes of black shales are complicated and there are far more than these three models. Many studies have indicated the complexity of black shale formation. For example, anoxic events may be related to middle-oceanic ridge activity, volcanisms, back arc extension and continental rifting.

Because organic richness and benthic ecologies fail to identify benthic oxygen conditions at the time of deposition, researchers have turned increasingly to geochemical methods for revealing paleoenvironment evolution processes. Lyons et al. (2009) summarized the geochemical methods used most widely in reconstructions of ancient marine oxygen conditions, including: 1) rare-earth elements, specifically the cerium anomaly (German and Elderfield, 1990; Shields and Stille, 2001); 2) relationships between OC and pyrite sulfur (Berner and Reiswell, 1983; Raiswell and Berner, 1985, 1986; Lyons and Berner, 1992); 3) a broad range of trace metal approaches (Calvert and Pedersen, 1993; Morford and Emerson, 1999; Algeo and Maynard, 2004; Brumsack, 2006; McManus et al., 2006; Tribovillard et al., 2006); 4) sulfur and carbon isotope relationships (Calvert et al., 1996; Lyons, 1997; Shen et al., 2002; Jiang et al., 2007); 5) organic biomarker approaches (Sinninghe Damsté et al., 1993; Koopmans et al., 1996; Sinninghe Damsté and Schouten 2006); 6) iron speciation, including the well-know degree of pyritization (Raiswell et al., 1988; Raiswell and Canfield, 1998; Shen et al., 2002; Anderson and Raiswell, 2004); and 7) new frontiers in metal isotope systems, such as Fe and Mo (Arnold et al., 2004; Rouxel et al., 2005; Neubert et al., 2008; Pearce et al., 2008; Severmann et al., 2008; Johnson et al., 2008; Gordon et al., 2009; Kendall et al., 2009).

1.2 Scientific significance of this study

Early Cambrian black shales occur widely across southern China, Lesser Himalaya, northern Pakistan, Iran, northern Oman, western and northern Europe, Russia, Mongolia, southern Australia and Canada, and are commonly rich in organic materials and certain metals, i.c. PGE, Cu, Ni, Mo, Au, U, V, Mn, Fe, Co, Bi, Cr, Se (Markey et al., 1998). As cause-effect relationship, the widely exposed early Cambrian black shales correlate with global Precambrian/Cambrian (PC/C) geological and biological events, for example, extinction and accelerated diversification of metazoans, global oceanic anoxia, and major plate tectonic reconfiguration and volcanism (Kaufman et al., 1993; Shu et al., 2001; Doblas et al., 2002; Schröder and Grotzinger, 2007). Black shales formed in quite variable depositional settings and paleoenvironments, which may relate to interaction between lithosphere, hydrosphere, biosphere and atmosphere. Therefore, some geochemical parameters of black shales can be used as tools to understand Earth evolution, for example, atmosphere/surface interactions. Some redox-sensitive metals, such as Mo, Ni, V, U and Re, are preferentially hosted in black shales. The geochemical behavior of these redox-sensitive metals has been well documented, allowing the application to reconstruct the paleoenvironments.

In South China, the transgressive Early Cambrian black shale sequence of the Niutitang Formation (and equivalent strata) occurs in an about 1600 km-long belt that extends over Yunnan, Guizhou, Hunan, Jiangxi, Anhui and Jiangsu provinces across the Yangtze platform, unconformably overlying dolomite of the Neoproterozoic Dengying Formation (Zhu et al., 2004). The widely exposed Early Cambrian black shale in south China attracts geological interest for two reasons: 1) economic importance of the black shale-hosted polymetallic Ni-Mo-PGE-Au sulfide ore; and 2), significance of international stratigraphic correlation and paleoenvironmental reconstruction. In South China, an unusual polymetallic Ni-Mo-PGE-Au sulfide ore layer is locally hosted in the Niutitang Formation black shales (and equivalent strata) close to the PC/C boundary (<10 m above the boundary), with most well known ore-grade occurrences located in the Hunan and Guizhou Provinces. Although the sulfide- and organic-rich ore layer is mostly only 3-5 cm thick, it shows extreme enrichment in metals, and contains Ni + Mo up to 14 wt. % with platinum group element (PGE) + Au concentrations of 1g/t, and > 10^4-fold enrichment in Se, Re, Os, As, Hg, and Sb compared to average upper continental crust (Fan et al., 1984; Coveney et al., 1994; this study).

Although the polymetallic Ni-Mo-PGE-Au sulfide mineralization has been discovered more than 30 years ago, the metal origin is still much debated. A number of models have been proposed, including extraterrestrial impact origin (Fan et al., 1984), submarine-hydrothermal exhalative origin (Coveney et al., 1992; Lott et al., 1999; Steiner et al., 2001; Coveney, 2003; Jiang et al., 2003, 2006, 2007, 2009), diagenetic fluid flow origin (Horan et al., 1994), and seawater scavenging origin (Mao et al., 2001, 2002; Lehmann et al., 2003; 2007). The mineralization age is also controversial. The sulfide ores were dated using the Re-Os method by Horan et al. (1994), Li et al. (2002) and Mao et al. (2002), and yield isochron ages of 560 ± 50 Ma, 542 ± 11 Ma and 541 ± 16 Ma, respectively. Pb-Pb dating of the host black shales and polymetallic Ni-Mo-PGE-Au sulfide ores from the Niutitang Formation yields isochron ages of 531 ± 24 Ma and 521 ± 54 Ma, respectively (Jiang et al., 2006). Recently, Jiang et al. (2009) reported a SHRIMP U-Pb zircon age of 532.3 ± 0.7 Ma for a volcanic ash bed beneath the sulfide ore layer, thus they argued that the mineralization age of the sulfide ore layer must be younger than 532.3 ± 0.7 Ma. The Pb-Pb and SHRIMP U-Pb ages are in agreement with the biostratigraphic age of the Niutitang Formation, which contains arthropods, sponges and small shelly fossils of Tommotian age (~530 Ma) (Steiner et al., 2001).

Besides the above mentioned studies, many studies focused on basinal analysis, lithological assemblage, sedimentary fabric, petrological and organic geochemistry (Pu et al., 1993; Wu, 1999; Feng et al., 2002; Wang, 2004; Chen, 2006; Goldberg et al., 2007; Pi, 2007), which have made great progresses in understanding Early Cambrian black shale formation. For example, Pu et al. (1993) and Feng et al. (2003) established general Early Cambrian lithofacies paleogeography. Wu (1999) investigated organics in the Early Cambrian black shales, and concluded that the origin of OM was algae and fungi. Through investigating black shale profiles, Pi (2007) established the detailed lithostratigraphic framework of the Niutitang Formation black shales at Zunyi, Guizhou province.

Although the “deep anoxic basin” model has been popular for many years, when we study black shales more closely we find that they can actually form in a wide range of depositional conditions. Previous studies lack investigations of the evolution history of black shales spanning the whole Early Cambrian, and therefore, are hard to correlate with other Early Cambrian black shale occurrences all over the world. Moreover, some key scientific questions of the sulfide polymetallic mineralization, such as metal enrichment mechanisms and mineralization age, are controversial. My thesis is aimed to add some arguments on those uncertainties and to establish a reasonable metallogenetic model. In summary, the study of Early Cambrian black shales has both scientific and economic relevance.

1.3 Objectives

The present research is a descriptive and experimental study aimed at understanding Early Cambrian seawater redox conditions, and providing geochronologic and geochemical data on the black shale-hosted polymetallic Ni-Mo-PGE deposits of South China. The study area is situated between latitude 26°00`N and 29°12`N, and longitude 103°36`E and 110°52`E, and includes one geological outcrop profile (Dingtai profile) and four polymetallic Ni-Mo-PGE-Au sulfide mine sites (Dazhuliushui and Maluhe in Guizhou province, and Sancha and Cili in Hunan province, respectively). Through investigating the black shale profile of Early Cambrian age and comparing four Ni-Mo-PGE deposits consisting of several centimeter thick sulfide- and organic-rich beds with extremely high polymetallic contents (Ni and Mo in percent range, PGE+Au ~ 1g/t), this work tries to achieve the following objectives:

- To obtain geochemical data (bulk rock geochemistry and PGE) of the Early Cambrian geological profile and four mine sites.
- To investigate the Early Cambrian seawater redox conditions by Mo isotope geochemistry and degree of pyritization (DOP) data.
- To constrain the age of the Ni-Mo-PGE polymetallic mineralization by

Re-Os dating on black shale hosted ore samples.

- To establish a metallogenetic model by the combined application of the above mentioned geochemical and geochronological conclusions.

- To interpret the depositional mechanism for polymetallic Ni-Mo-PGE sulfide mineralization and Early Cambrian seawater evolution history.

1.4 Methodology

In order to achieve the above motioned objectives, this research combined both field observation and lab experiments. Studied objects, applied methods and objectives are presented in Fig. 1-1. The applied methods are briefly described as follows:

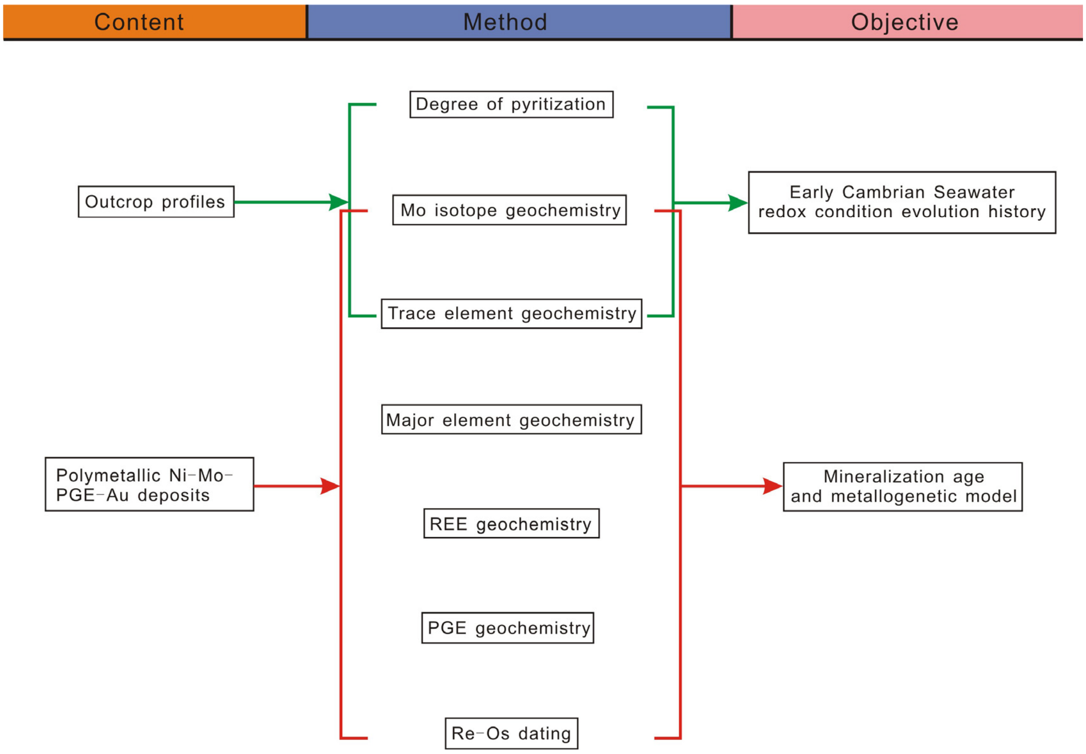

Fig. 1-1: Technical framework, methods and objectives of the thesis.

1.4.1 Field work and sample preparation

Under supervision of Prof. Bernd Lehmann and Prof. Mao Jingwen, two field work campaigns were carried out in 2007 and 2009, respectively. The study area is shown in Fig. 1-2. The first field work includes reconnaissance of one Early Cambrian Niutitang Formation black shale profile (Dingtai Profile) and three polymetallic Ni-Mo-PGE-Au sulfide mine sites (Dazhuliushui and Maluhe in Guizhou Province, and Sancha in Hunan Province). The second field work includes investigation of the Cili polymetallic Ni-Mo-PGE-Au sulfide deposit in Hunan province and complementary sample collection in the Sancha deposit. A total of ~300 rock samples were collected from outcrops, underground and drilling cores for petrographic, petrochemical and geochronologic studies. Sampling sites were located according to both GPS and geological map from 405 Geological Party in Jishou City, Hunan province. Sample preparation was done in Chinese University of Geosciences in Beijing. Some rock samples were powdered in Langfang Geochemical Laboratory, Hebei Province. More than 80 thin, polished and polished-thin sections were prepared in Clausthal for microscopic examination, which were performed at the Institute of Mineral Resources of Technical University of Clausthal (TUC), Germany (preparator: Ulf Hemmerling).

1.4.2 Whole rock geochemical analyses

About 200 powdered samples were analyzed for bulk geochemistry in order to investigate the chemical characteristics of the different rock units. Bulk geochemistry analyses were carried out in the National Research Center for Geoanalysis (NRCG), Chinese Academic of Geological Sciences in Beijing, the Federal Institute for Geosciences and Natural Resources (Bundesanstalt für Geowissenschaften und

Rohstoffe, BGR) in Hanover, and the commercial Acmelab in Canada (www.acmelab.com), respectively. In NRCG and Acmelab, major elements (SiO_2, TiO_2, Al_2O_3, Fe_2O_3, MnO, CaO, MgO, Na_2O, K_2O and P_2O_5) were determined by Inductively Coupled Plasma (ICP) atomic emission spectrometry. Trace and rare earth elements were analyzed using Inductively Coupled Plasma-Mass Spectrometry (ICP-MS) method. Total Organic Carbon (TOC) was analyzed by infrared C-S analyzer in NRCG, and Total Carbon (TC) and sulfur were determined by Leco in Acmelab. X-ray fluorescence spectrometry (XRF) method was applied in BGR Hannover for major and some trace elements. All bulk geochemistry data and analytical errors and detection limits are listed in Appendix. Detailed analytical techniques for the bulk geochemistry analysis are described as follows:

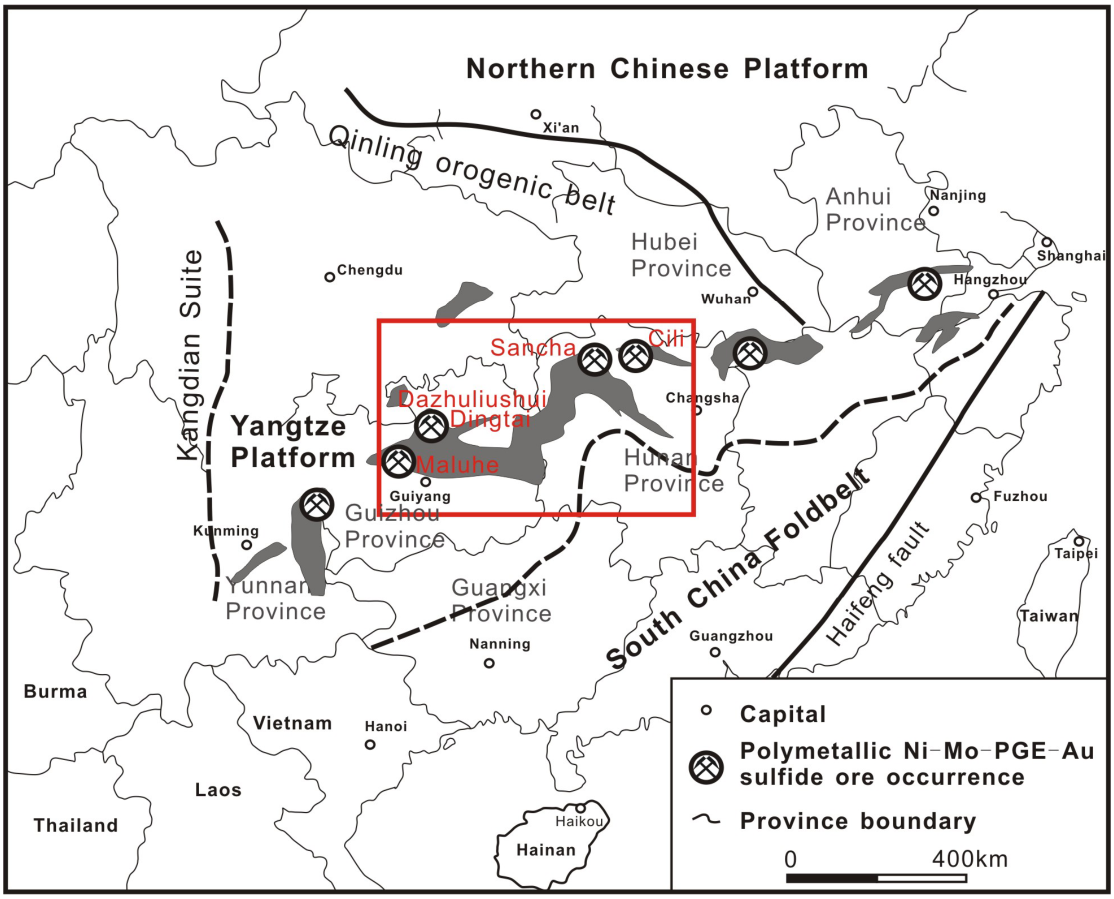

Fig. 1-2: Study area (red rectangle) and sample location (mining symbols in the red rectangle) in this work. Shaded area indicates Early Cambrian black shale occurrences in South China.

1.4.2.1 Inductively Coupled Plasma emission spectrometry (ICP)

Total abundances of the major oxides and several minor elements are reported on a 0.2 g sample analyzed by ICP-emission spectrometry following lithium metaborate/tetraborate fusion and diluted nitric acid digestion. Samples are prepared and analyzed in a batch system. Each batch contains a method reagent blank, certified reference material and certain sample replicates. Samples are mixed with a flux of lithium metaborate and lithium tetraborate and fused in an induction furnace. The molten melt is immediately poured into a solution of 5% nitric acid containing an internal standard, and mixed continuously until complete dissolution (~30 minutes). The sample solution is passed as aerosol from a nebulizer into an argon plasma. The inductively coupled plasma is a stream of argon atoms, heated by the inductive heating of a radio-frequency coil and ignited by a high-frequency Tesla spark, with a flame temperature in the range from 6000 to 10000 K. The sample dissociates in the argon plasma and a large number of atomic spectral lines are excited. The spectral lines are detected by a range of photomultipliers, they are compared with calibration lines, and their intensities are converted into concentrations. Calibration is performed using 7 prepared USGS and CANMET certified reference materials. One of the 7 standards is used during the analysis for every group of ten samples.

1.4.2.2 Inductively Coupled Plasma Mass Spectrometry (ICP-MS)

Total trace element analysis by ICP-MS in the AcmeLabs comprises two separate analyses. Rare earth and refractory elements are determined by ICP mass spectrometry following lithium metaborate/tetraborate fusion and nitric acid digestion of a 0.2 g sample. Sample decomposition procedure is same with that of the ICP analysis. In addition a separate 0.5 g split is digested in Aqua Regia and analyzed by ICP mass spectrometry to report the precious and base metals. This digestion can be used for Au, Ag, As, Bi, Cd, Cu, Hg, Mo Ni, Pb, Sb, Se, Tl and Zn.

1.4.2.3 X-Ray Fluorescence spectrometry (XRF)

The X-ray fluorescence technique is based on the excitation of a sample by X-ray and is applicable for major and some trace elements. The XRF technique is a physical method that suffers less from difficulties such as small sample size, incomplete dissolution, matrix effects and sample inhomogeneity found in “wet” methods. A primary X-ray beam excites secondary X-rays which have wavelengths characteristic of the elements present in the sample. The intensity of the secondary X-rays is used to determine the concentrations of the element compared to calibration standards. The XRF analysis of rock samples involves the preparation of the rock in two different forms, a pressed powder disc for trace element analysis and a glass bead made from the powdered sample fused with lithium metaborate or tetraborate for major element analysis. Relative uncertainties of the XRF analyses in the BGR Hannover are calculated according to the method of Rousseau (2001), with ≤ 3% for major elements and 10% to 30% for most trace elements.

1.4.3 Re-Os isotope analysis

Re-Os isotope analysis was conducted at the NRCG. Detailed sample preparation, chemical separation and analytical procedure have been described by Du et al. (1995, 2001, 2004). The enriched ^{190}Os and enriched ^{185}Re were obtained from Oak Ridge

National Laboratory (USA). In brief, a Carius tube (a thick-walled borosilicate glass ampoule) digestion was used for sample preparation and HCl-HNO_3 digestion was used for sample dissolution. The weighted sample (~100 mg) was loaded in a Carius tube through a long thin-necked funnel. Enriched ^{190}Os and ^{185}Re spike solution and 3 ml 10 M HCl + 5 ml 16 M HNO_3 were added while the bottom part of the tube was frozen at -50 to -80°C in an ethanol-liquid nitrogen slush. The top of the tube was sealed with an oxygen-propane torch. The tube was then placed in a stainless-steel jacket and heated for 24 h at 200°C. Upon cooling, the bottom part of the tube was kept frozen, the neck of the tube was broken, and the contents of the tube were poured into a distillation flask and the residue was washed out with 40 ml of deionized water.

Separation of osmium by distillation and separation of rhenium by extraction was performed following the analytical method of Du et al. (1995, 2001). OsO_4 was distilled at 105-110°C for 50 minutes and trapped in 10 ml of water, which was used for ICP-MS determination of the Os isotope ratio. The residual Re-baring solution was saved in a 150 ml Teflon beaker for Re separation and was evaporated to near-dryness. 1 ml of water was added and then evaporated to near-dryness twice to neutralize the residue. 10 ml 5M NaOH was added to the residue to change the solution into alkaline condition, followed by Re extraction with 10 ml of acetone in a 120 ml Teflon separation funnel. The Teflon beaker was librated for 5 minutes then the water phase was discarded. The acetone phase was washed with 2 ml 5M NaOH for 2 minutes. Then the acetone phase was transferred to a 150 ml Teflon beaker than contained 2 ml of water. The solution was heated at ~ 50°C to dryness to erase acetone. Several drops of concentrated HNO_3 and 30% H_2O_2 were added to eliminate residual Re and to dryness and then pick up in 2% HNO_3 that was used for ICP-MS determination of the Re isotope ratio. Cation-exchange resin was used to remove Na if the salinity of the Re-bearing solution was more than 1 mg/ml (Du et al., 2004).

A TJA X-series ICP-MS was used for Re and Os isotope determination. The analytical reliability was tested by analyses of the Certified Reference Material GBW04435 (HLP, Du et al., 2004). The molybdenite standard HLP is from a carbonatite vein-type Mo-Pb deposit in the Jinduicheng-Huanglongpu area of Shaanxi Province, China. The average Re-Os age for HLP is 219.5 ± 3.5 Ma (95% confidence), and is consistent with the certified value of 221 ± 5.6 Ma (Du et al., 2004). Average blanks for the Carius tube procedure are ~ 20 pg Re and ~ 1 pg Os. The decay constant used for ^{187}Re of 1.666×10^{-11}/year has an absolute uncertainy of ± 0.017 (1.0%) (Smoliar et al., 1996). Uncertainties for ^{187}Re/^{188}Os and ^{187}Os/^{188}Os are determined by error propagation of uncertainties in Re and Os mass spectrometer measurements, blank abundances and isotopic compositions, spike calibrations and reproducibility of standard Re and Os isotopic values. The Isoplot package of Ludwig (2005) was used to draw isochrones and the Re-Os age.

1.4.4 Mo isotope analysis

The sample preparation and measurement were done at the Isotope Geology Unit of the University of Bern, Switzerland (supervisor: Prof. Thomas Nägler). Between 4.5 and 5.0 g of powered sample was oxidized at 800°C for 12 hours to remove organic matter and about 0.1 g was employed for Mo isotope measurement for each sample. Mo was purified using the separation procedure described in Siebert et al. (2001), Wille et al. (2008) and Voegelin et al. (2009). A minor modification was done for the very Mo-rich ore samples. According to the previously determined Mo concentration, the approximate sample weight needed for measurement was calculated. The ore samples (with up to several wt.% Mo) were then pre-diluted to the ppm level to prevent lab contamination. To account for Mo isotope fractionation during column separation and to resolve instrumental mass bias, a calculated amount of ^{97}Mo-^{100}Mo double spike was added prior to dissolution and chemical purification. The ^{97}Mo-^{100}Mo double spike technique has several advantages: 1) low natural abundance of ^{97}Mo and ^{100}Mo, 2) no elemental isobaric interferences on ^{97}Mo, and ^{100}Mo is reducible from isobaric interferences of ^{100}Ru, and 3) highly enriched ^{97}Mo and ^{100}Mo can be obtained (Siebert et al., 2001).

The black shale sample with about 50 ng Mo was put in a Teflon beaker together with 6 M HCl to keep Mo in its highly soluble Mo^{6+} oxydation state, and then heated to ~100°C on a heating stage overnight. The sample material was dried and dissolved with concentrated HF and HNO_3 (4:1) at ~100°C. Subsequently, organic and detrital material was separated from solution by centrifugation. The solution was transferred into another Teflon beaker. In order to completely leach Mo, the residue was again heated in 6 M HCl at ~100°C overnight, and then added to the second beaker. The aliquots were combined and dried on a hot plate. After evaporation, the material was taken up in pre-prepared HCl + H_2O_2 solution (5 ml 4 M HCl and 0.3% H_2O_2) and loaded onto an anion exchange resin to wash out cations, followed by six-block stepwise loading onto anion exchange columns (Dowex^{TM} 1X8 resin, 200 - 400 mesh). Finally, the molybdate anion was eluted with 2 M HNO_3. For cleaning Fe and Zr from Mo solution, 6 ml 2 M HNO_3 is added to extract the Mo fraction, which is collected in a Teflon beaker and left to dry on a heating stage. A cation exchange column (Dowex 50WX8^{TM} resin, 200 - 400 mesh) was used to remove residual Fe. The dried Mo fraction is redissolved in 1 ml 0.5 M HCl and 0.1% H_2O_2 solution twice, and collected in a Teflon beaker. The remaining Mo is eluted with 4 ml 0.5 M HCl and 0.1% H_2O_2 solution and collected in the same beaker. Finally, the Mo-bearing solutions are dried and measured in 0.5 M HNO_3 solution on a Nu Instruments MC-ICP-MS connected to an ESI Apex nebulizer. A measurement usually consists of 4 blocks with 10 cycles each. One standard and three black shale samples were analyzed alternately so as to monitor for drift in instrument sensitivity.

Molybdenum isotope data are reported as defined by pervious studies as $\delta^{98/95}Mo_{sample}(‰) = [\ ^{98/95}Mo_{sample}/^{98/95}Mo_{standard}-1] \times 1000$. Throughout the text, sample Mo isotope data are reported as $\delta^{98/95}Mo$ relative to the Bern Laboratory standard solution (Johnson Matthews, 1000μg/ml (± 0.3%) ICP standard solution) as in McManus et al. (2002) and Siebert et al. (2003). The external standard reproducibility was 0.1 $\delta^{98/95}Mo$ (2σ).

1.4.5 DOP analysis

Degree of pyritization is used as an indicator of euxinic depositional conditions for ancient black shales (Berner, 1970; Canfield, 1989; Raiswell et al., 1994; Raiswell and Canfield, 1998; Shen et al., 2002; Anderson and Raiswell, 2004). In this study DOP is calculated as DOP = Fe_P/Fe_{HR}. The pool of highly reactive iron (Fe_{HR}) is defined as the sum of $Fe_P + Fe_D$, where Fe_P is the iron present as pyrite and Fe_D is the iron extracted with buffered Na dithionite solution (mainly iron oxides and small concentrations of iron-bearing silicates). Sulfur in Fe_P is extracted by hot acidic $CrCl_2$ solution and recalculated to Fe. Another redox indicator, Fe_{HR}/Fe_T ratio is applied in this study, where Fe_T represents the total iron in the sediment. The DOP analyses were done at the MPI for Marine Microbiology, Bremen, Germany (supervisor: Prof. Michael Böttcher).

1.4.6 PGE analysis

The PGE + Au concentrations of the polymetallic sulfide ores were analyzed in the National Research Center of Geoanalysis in Beijing using NiS-fire assay pre-concentration followed by ICP-MS measurement. A sample aliquot of 30 g powder was mixed with sodium carbonate, sodium borate, borax, glass powder, nickel powder, iron powder, sulfur and wheat flour. The mixture was transferred into a fire-clay crucible with an appropriate amount of ^{190}Os spike solution and covered with a thin $Na_2B_4O_7$ layer. The crucible was fused at 1150°C for 1 h and dried under an infrared lamp. After cooling, the crucible was broken and the Ni-Fe button removed into a glass beaker containing 60 ml H_2O for a minimum of 10 h. To better dissolve the button, ~30 ml HCl was added into the beaker and heated at ~110°C, until the solution became clear and little residue remained. The solution was then filtered by a milli-pore filter membrane (diameter 25 mm, 0.45 mm). The residue was collected and washed 5 times with ~15 ml water. Subsequently, the residue and the filter membrane were transferred into a 7 ml Telflon beaker, and sealed together with 1 ml HCl + 1 ml H_2O_2. The beaker was then heated at ~110°C for 1.5 h. After cooling to room temperature, the beaker was opened and the solution was transferred and diluted with H_2O to 10 ml for ICP-MS analysis. The detection limit is 0.02 ng/g for Ru, 0.001 ng/g for Rh, 0.06 ng/g for Pd, 0.007 ng/g for Os, 0.01 ng/g for Ir and 0.03 ng/g for Pt.

1.5 Thesis contents and work done

My thesis is jointly financially supported by Chinese National Basic Research Program (Project 2007CB411302), the Chinese Geological Survey Program (No. 1212010634001), and the Deutsche Forschungsgemeinschaft (LE578/32-1). My living expense and fees at the TU Clausthal is covered by a Chinese government research fellowship from China Scholarship Council (CSC) (from December 2007 to November 2010) and by Institute of Mineral Resources of Technical University of Clausthal (from December 2010 to June 2011).

My thesis consists of 8 chapters. Chapter 1 is a preface, aimed to briefly introduce the framework of my thesis, including study history, scientific significances, applied technical methods and perspectives. The following chapter explains the geographical situation, tectonic setting, paleogeographic evolution history and regional geology of the study area. Chapter 3 describes the geology of the four polymetallic Ni-Mo-PGE-Au sulfide ore deposits and the black shale profile of the Early Cambrian Niutitang Formation. Chapter 4 to 7 is the main part of this thesis. Re-Os dating of polymetallic Ni-Mo-PGE-Au sulfide mineralization in the Lower Cambrian Niutitang Formation black shales is presented in chapter 4. Chapters 5 and 6 are on Mo stable isotope geochemistry. Chapter 5 is a review of Mo and Mo stable isotope geochemistry, including its isotope system, analytical technical and applications to geology. Chapter 6 demonstrates our new findings by application of Mo isotope records of the Niutitang Formation black shale in order to constrain the problem of Early Cambrian seawater anoxia. Chapter 7 is a comparison of geochemical data (Mo isotope, PGE, trace- and rare-earth elements) among the polymetallic Ni-Mo-PGE-Au suffide ores, the host black shales, present-day seawater as well as selected typical hydrothermal massive sulfide deposits (VMS-, Sedex-type sulfides and modern black smoker mounds) to constrain the metal enrichment mechanism and processes. Finally, the last chapter (chapter 8) is allocated to the Early Cambrian seawater evolution and metallogenetic model.

The finished experiments associated with the thesis are listed in Table 1-1.

Table 1-1
List of field work and lab experiments associated with this thesis.

Content	Workload	Laboratory	Participant
Field work (sample collection)	Twice, Sep.-Nov.2007 and Dec.2010 (300 samples)		Xu Lingang, Zhang Ying, Bernd Lehmann
Field photoes	200		Xu Lingang
Microscopy observation	100	TU Clausthal	Xu Lingang
Bulk geochemistry analysis	180	NRCG,Geological Survey of Germany in Hannover,Acmelabs	Han Huiming, unknown staffs in Hannover and Acmelabs
Mo isotope	33	Isotope Group, Bern University, Switzerland	Xu Lingang, Nadia Neubert, Thomas Nägler
Degree of pyritization	26	Max-Planck-Institute for Marine Microbiology,Bremen	Michael Böttcher
Re-Os dating	32	NRCG	Qu Wenjun, Du Andao

1.6 References

Algeo, T.J., Maynard, J.B., 2004. Trace-element behavior and redox facies in core shales of Upper Pennsylvanian Kansas-type cyclothems. Chemical Geology 206, 289-318.

Anderson, T.F., Raiswell, R., 2004. Sources and mechanisms for the enrichment of highly reactive iron in euxinic Black sea sediments. American Journal of Sciences 304, 203-233.

Arnold, G.L., Anbar, A.D., Barling, J., Lyons, T.W., 2004. Molybdenum isotope evidence for widespread anoxia in mid-proterozoic oceans. Science 304, 87-90.

Arthur, M.A., Sageman, B.B., 1994. Marine black shales: Depositional mechanisms and environments of ancient deposits. Annual Review of Earth and Planetary Sciences 22, 499-551.

Berner, R.A., 1970. Sedimentary pyrite formation. American Journal of Science 268, 1-23.

Berner, R.A., Raiswell, R., 1983. Burial of organic-carbon and pyrite sulfur in sediments over Phanerozoic time: A new theory. Geochimica et Cosmochimica Acta 47, 855-862.

Brumsack, H.J., 2006. The trace metal content of recent organic carbon-rich sediments: Implications for Cretaceous black shale formation. Palaeogeography Palaeoclimatology Palaeoecology 232, 344-361.

Calvert, S.E., 1964. Factors affecting distribution of laminated diatomaceous sediments in Gulf of California. In Marine Geology of the Gulf of California. Van Andel, T.H., Shor, J.J., (eds.) Tulsa. American Association of Petroleum Geologists Bulletin, 311-330.

Calvert, S.E., Pedersen, T.F., 1993. Geochemistry of recent oxic and anoxic marine-sediments: Implications for the geological record. Marine Geology 113, 67-88.

Calvert, S.E., Thode, H.G., Yeung, D., Karlin, R.E., 1996. A stable isotope study of pyrite formation in the Late Pleistocene and Holocene sediments of the Black Sea. Geochimica et Cosmochimica Acta 60, 1261-1270.

Canfield, D.E., 1989. Reactive iron in marine sediments. Geochimica et Cosmochimia Acta 53, 619-632.

Chen, L., 2006. Sedimentology and geochemistry of the Early Cambrian black rock series in the Hunan-Guizhou area, China. Ph.D thesis, 1-103 (in Chinese with English abstract).

Clarke, J.M., 1904. Naples fauna in western New York, Part Ⅱ. New York State Museum Memories 6, 199-454.

Coveney Jr, R.M., Grauch, R.I., Murowchick, J.B., 1994. Metals, phosphate, and stone coal in the Proterozoic and Cambrian of China: The geolocial setting of precious metal-bearing Ni-Mo ore beds. Society of Economic Geologists Newsletter 18, 1 and 6-11.

Coveney Jr., R.M., 2003. Re-Os dating of polymetallic Ni-Mo-PGE-Au mineralization in Lower Cambrian black shales of South China and its geological significance — a discussion. Economic Geology 98, 661-662.

Coveney Jr., R.M., Murowchick, R.M., Grauch, J.B., Micheal, R.I., Glascock, D., Denison, D., 1992. Gold and platinum in shales with evidence against extraterrestrial sources of metals. Chemical Geology 99, 101-114.

Degens, E.T., Ross, D.A., (eds.) 1974. The Black Sea: Geology, chemistry, biology. American Association of Petroleum Geologists Memories 20, 183-199.

Doblas, M., Lopez-Ruiz, J., Cebria, J.M., Youbi, N., Degroote, E., 2002. Mantle insulation beneath the West African craton during the Precambrian-Cambrian transition. Geology 30, 839-842.

Droser, M.L., Jensen, S., Gehling, J.G., 2002. Trace fossils and substrates of the terminal Proterozoic-Cambrian transition: Implications for the record of early bilaterians and sediment mixing. Proceedings of the National Academy of Sciences of the United States of America 99, 12572-12576.

Du, A.D., He, H.L., Yin, N.W., 1995. A study of the rhenium-osmium geochronometry of molybdenites. Acta Geologica Sinica 8, 171-181 (in Chinese with English abstract).

Du, A.D., Wang, S.X., Sun, D.Z., Zhao, D.M., Liu, D.Y., 2001. Precise Re-Os dating of molybdenite using Carius tube, NTIMS and ICPMS, SGA-SEG Joint Biennial Meeting. Krakow, Poland, 405-407.

Du, A.D., Wu, S.Q., Sun, D.Z., Wang, S.X., Qu, W.J., Markey, R., Stain, H., Morgan, J., Malinovskiy, D., 2004. Preparation and certification of Re-Os dating reference materials: Molybdenites HLP and JDC. Geostandards and Geoanalytical Research 28, 41-52.

Fan, D., Yang, R.Y., Huang, Z.X., 1984. The Lower Cambrian black shales series and the iridium anomaly in south China. Developments in Geoscience, International Geological Congress, 27th. Moscow, Beijing Science Press 215-225.

Fan, D.L., Zhang, T., Ye, J., 2004. Black shales in China and related mineralization. Beijing: Sicence Publishing House 1-441 (in Chinese).

Feng, Z.Z., Peng, Y.M., Jin, Z.K., Bao, Z.D., 2002. Lithofacies paleogeography of the Early Cambrian in China. Journal of Palaeogeography 4, 1-12 (in Chinese with English abstract).

Fleming, R.H., Revelle, R., 1939. Physical processes in the ocean. In Recent Marine Sediments, Trask, P.D. (ed.) American Association of Petroleum Geologists Bulletin, 48-141.

German, C.R., Elderfield, H., 1990. Application of the Ce-anomaly as a paleoredox indicator: The ground rules. Paleoceanography 5, 823-833.

Goldberg, T., Strauss, H., Guo, Q.J., Liu, C.Q., 2007. Reconstructing marine redox conditions for the Early Cambrian Yangtze Platform: Evidence from biogenic sulphur and orgainic carbon isotopes. Palaeogeography, Palaeoclimatology, Palaeoecology 254, 175-193.

Goldman, M.I., 1924. "Black shale" formation in and about Chesapeake Bay. American Association of Petroleum Geologists Bulletin 8, 195-201.

Gordon, G.W., Lyons, T.W., Arnold, G.L., Roe, J., Sageman, B.B., Anbar, A.D., 2009. When do black shales tell molybdenum isotope tales? Geology 37, 535-538.

Grabau, A.W., 1913. Principles of stratigraphy. New York: Seiler, 1-1185.

Hattin, D.E., 1975. Petrology and origin of fecal pellets in Upper Cretaceous strata of Kansas and Saskatchewan. Journal of Sedimentary Petrology 45, 686-696.

Hedges, J.I., Keil, R.G., 1995. Sedimentary organic matter preservation: an assessment and speculative synthesis. Marine Chemistry 49, 81-115.

Henrichs, S.M., Reeburgh, W.S., 1987. Anaerobic mineralization of marine sediment organic matter: Rates and the role of anaerobic processes in the oceanic carbon economy. Geomicrobiology Journal 5, 191-237.

Holland, H.D., 1979. Metals in black shales: a reassessment. Economic Geology 74, 1676-1680.

Horan, M.F., Morgan, J.W., Grauch, R.I., Coveney, R.M., Murowchick, J.B., Hulbert, L.J., 1994. Rhenium and osmium isotopes in black shales and Ni-Mo-PGE-rich sulfide layers, Yukon-Territory, Canada, and Hunan and Guizhou provinces, China. Geochimica et Cosmochimica Acta 58, 257-265.

Jiang, G.Q., Kaufman, A.J., Christie-Blick, N., Zhang, S.H., Wu, H.C., 2007. Carbon isotope variability across the Ediacaran Yangtze platform in South China: Implication for a large surface-to-deep ocean $\delta^{13}C$ gradient. Earth and Planetary

Science Letters 261, 303-320.

Jiang, S.Y., Chen, Y.Q., Ling, H.F., Yang, J.H., Feng, H.Z., Ni, P., 2006. Trace- and rare-earth element geochemistry and Pb-Pb dating of black shales and intercalated Ni-Mo-PGE-Au sulfide ores in Lower Cambrian strata, Yangtze Platform, South China. Mineralium Deposita 41, 453-467.

Jiang, S.Y., Pi, D.H., Heubeck, C., Frimmel, H., Liu, Y.P., Deng, H.L., Ling, H.F., Yang, J.H., 2009. Early Cambrian ocean anoxia in South China. Nature 459, E5-E6.

Jiang, S.Y., Yang, J.H., Ling, H.F., Chen, Y.Q., Feng, H.Z., Zhao, K.D. Ni, P., 2007. Extreme enrichment of polymetallic Ni-Mo-PGE-Au in lower Cambrian black shales of South China: An Os isotope and PGE geochemical investigation. Palaeogeography, Palaeoclimatology, Palaeoecology 254, 217-228.

Jiang, S.Y., Yang, J.H., Ling, H.F., Feng, H.Z., Chen, Y.Q., Chen, J.H., 2003. Re-Os isotopes and PGE geochemistry of black shales and intercalated Ni-Mo polymetallic sulfide bed from the Lower Cambrian Niutitang Formation, South China. Progress in Natural Science 13, 788-794.

Johnson, C.M., Beard, B.L., Roden, E.E., 2008. The iron isotope fingerprints of redox and biogeochemical cycling in the modern and ancient Earth. Annual Review of Earth and Planetary Sciences 36, 457-493.

Kaufman, A.J., Jacobsen, S.B., Knoll, A.H., 1993. The vendian record of Sr and C isotopic variations in seawater: Implications for tectonics and paleoclimate. Earth and Planetary Science Letters 120, 409-430.

Kendall, B., Creaser, R.A., Gordon, G.W., Anbar, A.D., 2009. Re-Os and Mo isotope systematics of black shales from the Middle Proterozoic Velkerri and Wollogorang Formations, McArthur Basin, northern Australia. Geochimica et Cosmochimica Acta 73, 2534-2558.

Kennedy, M.J., Pevear, D.R., Hill, R.J., 2002. Mineral surface control of organic carbon in black shale. Science 295, 657-660.

Koopmans, M.P., Köster, J., van Kaam-Peters, H.M.E., Kenig, F., Schouten, S., Hartgers, W.A., de Leeuw, J.W., Damste, J.S.S., 1996. Diagenetic and catagenetic products of isorenieratene: Molecular indicators for photic zone anoxia. Geochimica et Cosmochimica Acta 60, 4467-4496.

Lehmann, B., Mao, J.W., Li, S.R., Zhang, G.D., Zeng, M.G., 2003. Re-Os dating of polymetallic Ni-Mo-PGE-Au mineralization in Lower Cambrian black shales of south China and its geological significance: A reply. Economic Geogolgy 98, 663-665.

Lehmann, B., Nägler, T.F., Holland, H.D., Wille, M., Mao, J.W., Pan, J.Y., Ma, D.S., Dulski, P., 2007. Highly metalliferous carbonaceous shale and Early Cambrian seawater. Geology 35, 403-406.

Li, S.Y., Xiao, Q.Y., Shen, J.F., Sun, L., Liu, B., Yan, B.K., 2002. Source of Lower Cambrian platinum group elements in black shales in Hunan and Guizhou provinces, China and the Re-Os isotope dating. Science China (Series D) 32, 568-575 (in Chinese with English abstract).

Lott, D.A., Coveney Jr., R.M., Murowchick, J.B., 1999. Sedimentary exhalative nickel-molybdenum ores in South China. Economic Geology 94, 1051-1066.

Ludwig, K., 2005. Isoplot/Ex version 3.23: a geochronogical toolkit for Microsoft Excel. Geochronology Center. Berkeley, California.

Lundegard, P.D., Samuels, N.D., 1980. Field classification of fine-grained sedimentary rocks. Journal of Sedimentary Petrology 50, 781-786.

Lyons, T.W., 1997. Sulfur isotopic trends and pathways of iron sulfide formation in upper Holocene sediments of the anoxic Black Sea. Geochimica et Cosmochimica Acta 61, 3367-3382.

Lyons, T.W., Anbar, A.D., Severmann, S., Scott, C., Gill, B.C., 2009. Tracking euxinia in the ancient ocean: A multiproxy perspective and proterozoic case study.

Annual Review of Earth and Planetary Sciences 37, 507-534.

Lyons, T.W., Berner, R.A., 1992. Carbon sulfur iron systematics of the uppermost deep-water sediments of the Black Sea. Chemical Geology 99, 1-27.

Mao, J.W., Lehmann, B., Du, A.D., Zhang, G.D., Ma, D.S., Wang, Y.T., Zeng, M.G., Kerrich, R., 2002. Re-Os dating of polymetallic Ni-Mo-PGE-Au mineralization in lower Cambrian black shales of south China and its geologic significance. Economic Geology 97, 1051-1061.

Mao, J.W., Zhang, G.D., Du, A.D., Wang, Y.T., Zeng, M.G., 2001. Geology, geochemistry, and Re-Os Isotopic dating of the Huangjiawan Ni-Mo-PGE deposit, Zunyi, Guizhou Province — with a discussion of the polymetallic mineralization of basal Cambrian black shales in South China. Acta Geologica Sinaca 75, 234-243 (in Chinese with English abstract).

Markey, R., Stein, H., Morgan, J., 1998. Highly precise Re-Os dating for molybdenite using alkaline fusion and NTIMS. Talanta 45, 935-946.

Mayer, L.M., 1994. Surface area control of organic carbon accumulation in continental shelf sediments. Geochimica et Cosmochimica Acta 58, 1271-1284.

McManus, J., Berelson, W.M., Severmann, S., Poulson, R.L., Hammond, D.E., Klinkhammer, G.P., Holm, C., 2006. Molybdenum and uranium geochemistry in continental margin sediments: Paleoproxy potential. Geochimica et Cosmochimica Acta 70, 4643-4662.

McManus, J., Nägler, T.F., Siebert, C., Wheat, C.G., Hammond, D.E., 2002. Oceanic molybdenum isotope fractionation: Diagenesis and hydrothermal ridge-flank alteration. Geochemistry, Geophysics, Geosystems 3, doi: 10.1029/2002GC000356.

Morford, J.L., Emerson, S., 1999. The geochemistry of redox sensitive trace metals in sediments. Geochimica et Cosmochimica Acta 63, 1735-1750.

Neubert, N., Nägler, T.F., Böttcher, M.E., 2008. Sulfidity controls molybdenum isotope fractionation into euxinic sediments: Evidence from the modern Black Sea. Geology 36, 775-778.

Neuendorf, K.K.E, Jackson, J.A., Mehl, J.P., 2005. Glossary of geology, 5th ed., American Geological Institute, Alexandria, Va.

Parrish, J.T., 1982. Upwelling and petroleum source beds, with reference to the Paleozoic. American Association of Petroleum Geologists Bulletin 66, 750-774.

Parrish, J.T., Curtis, R.L., 1982. Atmospheric circulation, upwelling, and organic-rich rocks in the Mesozoic and Cenozoic eras. Palaeogeography Palaeoclimatology Palaeoecology 40, 31-66.

Pearce, C.R., Cohen, A.S., Coe, A.L., Burton, K.W., 2008. Molybdenum isotope evidence for global ocean anoxia coupled with perturbations to the carbon cycle during the early Jurassic. Geology 36, 231-234.

Pedersen, T.F., Calvert, S.E., 1990. Anoxia vs productivity: What controls the formation of organic-carbon-rich sediments and sedimentary rocks. American Association of Petroleum Geologists Bulletin 74, 454-466.

Pettijohn, F., 1957. Sedimentary rock. New York: Harper, p. 1-718.

Pi, D.H., 2007. Geochemistry investigation of the Early Cambrian black shales in Zunyi, Guizhou provence. Ph.D thesis, 1-121 (in Chinese with English abstract).

Pu, X.C., Zhou, H.D., Wang, X.L., 1993. Cambrian lithofacies paleogeography and mineralization in south China, Beijing. Geological Publishing House, 191 (in Chinese).

Raiswell, R., Berner, R.A., 1985. Pyrite formation in euxinic and semi-euxinic sediments. American Journal of Science 285, 710-724.

Raiswell, R., Berner, R.A., 1986. Pyrite and organic matter in Phanerozoic normal marine shales. Geochimica et Cosmochimica Acta 50, 1967-1976.

Raiswell, R., Buckley, F., Berner, R.A., Anderson, T.F., 1988. Degree of pyritization of iron as a paleoenvironmental indicator of bottom water oxygenation. Journal of Sedimentary Petrology 58, 812-819.

Raiswell, R., Canfield, D.E., 1998. Sources of iron for pyrite formation in marine sediments. American Journal of Science 298, 219-245.

Raiswell, R., Canfield, D.E., Berner, R.A., 1994. A comparison of iron extraction methods for the determination of degree of pyritisation and the recognition of iron-limited pyrite formation. Chemical Geology 111, 101-110.

Ross, D.A., Degens, E.T., Macilvai.J, 1970. Black Sea: Recent sedimentary history. Science 170, 163-165.

Rousseau, R.M., 2001. Detection limit and estimate of uncertainty on analytical XRF results. The Rigaku Journal 18.

Rouxel, O.J., Bekker, A., Edwards, K.J., 2005. Iron isotope constraints on the Archean and Paleoproterozoic ocean redox state. Science 307, 1088-1091.

Ruedemann, R., 1935. Ecology of black mud shales of eastern New York. Journal of Paleontology 9, 79-91.

Ryan, W.B.F., Cita, M.B., 1977. Ignorance concerning episodes of ocean-wide stagnation. Marine Geology 23, 197-215.

Sageman, B.B., Lyons, T.W., 2003. Geochemistry of fine-grained sediments and sedimentary rocks. In Sediments, diagenesis, and sedimentary rocks. Treatise on Geochemistry, Mackenzie, F.T. ed., Amsterdam. Elsevier 7, 115-158.

Sagemm, B.B., 1991. High-resolution event stratigraphy, carbon geochemistry and paleobiology of the Upper Cenomanian Hartland Shale Member (Cretaceous), Greenhorn Formation, Western Interior. U.S. PhD Thesis. University of Colorado.

Schlanger, S.O., Jenkyns, H.C., 1976. Cretaceous oceanic anoxic events: causes and consequences. Geologie en mijnbouw 55, 179-184.

Schröder, S., Grotzinger, J.P., 2007. Evidence for anoxia at the Ediacaran-Cambrian boundary: the record of redox-sensitive trace elements and rare earth elements in Oman. Journal of the Geological Society 164, 175-187.

Severmann, S., Lyons, T.W., Anbar, A., McManus, J., Gordon, G., 2008. Modern iron isotope perspective on the benthic iron shuttle and the redox evolution of ancient oceans. Geology 36, 487-490.

Shen, Y.A., Canfield, D.E., Knoll, A.H., 2002. Middle Proterozoic ocean chemistry: evidence from the McArthur basin, Northern Australia. American Journal of Science 302, 81-109.

Shen, Y.A., 2002. C-isotope variations and paleoceanographic changes during the late Neoproterozoic on the Yangtze Platform, China. Precambrian Research 113, 121-133.

Shields, G., Stille, P., 2001. Diagenetic constraints on the use of cerium anomalies as palaeoseawater redox proxies: an isotopic and REE study of Cambrian phosphorites. Chemical Geology 175, 29-48.

Shu, D.G., Morris, S.C., Han, J., Chen, L., Zhang, X.L., Zhang, Z.F., Liu, H.Q., Li, Y., Liu, J.N., 2001. Primitive deuterostomes from the Chengjiang Lagerstatte (Lower Cambrian, China). Nature 414, 419-424.

Siebert, C., Nägler, T.F., Blanckenburg, F., Kramers, J.D., 2003. Molybdenum isotope records as a potential new proxy for paleoceanography. Earth and Planetary Science Letters 211, 159-171.

Siebert, C., Nägler, T.F., Kramers, J.D., 2001. Determination of molybdenum isotope fractionation by double-spike multicollector inductively coupled plasma mass spectrometry. Geochemistry, Geophysics, Geosystems 2, doi: 10.1029/2000GC000124.

Sinninghe Damsté, J.S., Schouten, S., 2006. Biological markers for anoxia in the photic zone of the water column. In Marine organic matter: Biomarkers, isotopes and DNA. The Handbook of Environmental Chemistry, Volkman, J.K., ed., Berlin. Springer 2N, 128-163.

Sinninghe Damsté, J.S., Wakeham, S.G., Kohnen, M.E.L., Hayes, J.M., Deleeuw, J.W., 1993. A 6,000-year sedimentary molecular record of chemocline excursions in the Black Sea. Nature 362, 827-829.

Smoliar, M.I., Walker, R.J., Morgan, J.W., 1996. Re-Os ages of group IIA, IIIA, IVA, and IVB iron meteorites. Science 271, 1099-1102.

Steiner, M., Wallis, E., Erdtmann, B.D., Zhao, Y.L., Yang, R.D., 2001. Submarine hydrothermal exhalative ore layers in black shales from South China and associated fossils: Insights into a Lower Cambrian facies and bio-evolution. Palaeogeography Palaeoclimatology Palaeoecology 169, 165-191.

Strom, K.M., 1939. Land-locked waters and the deposition of black muds. In Recent marine sediments, Trask, P.D., ed., American Association of Petroleum Geologists Bulletin, 356-372.

Thiede, J., Van Andel, T.H., 1977. The Paleoenvironment of anaerobic sediments in the Late Mesozoic South Atlantic Ocean. Earth and Planetary Science Letters 33, 301-309.

Thomsen, E., 1989. Seasonal variability in the production of Lower Cretaceous calcareous Nanoplankton. Geology 17, 715-717.

Tribovillard, N., Algeo, T.J., Lyons, T., Riboulleau, A., 2006. Trace metals as paleoredox and paleoproductivity proxies: An update. Chemical Geology 232, 12-32.

Twenhofel, W.H., 1939. Environments of origin of black shales. American Association of Petroleum Geologists Bulletin 23. 1178-1198.

Vine, J.D., Tourtelo, E.B., 1970. Geochemistry of black shale deposits: A summary report. Economic Geology 65, 253-272.

Voegelin, A.R., Nägler, T.F., Samankassou, E., Villa, I.M., 2009. Molybdenum isotopic composition of modern and Carboniferous carbonates. Chemical Geology 265, 488-498.

Wang, M., 2004. Geology, geochemistry and genesis of PGE-polymetallic deposits in the Lower Cambrian black rock series, Southern China. Ph.D thesis, 1-168 (in Chinese with English abstract).

Waples, D.W., 1983. Reappraisal of anoxia and organic richness, with emphasis on Cretaceous of North Atlantic. American Association of Petroleum Geologists Bulletin 67, 963-978.

Wille, M., Nägler, T.F., Lehmann, B., Schroder, S., Kramers, J.D., 2008. Hydrogen sulphide release to surface waters at the Precambrian/Cambrian boundary. Nature 453, 767-769.

Wu, C.D., Chen, Q.Y., Lei, J.J., 1999. The genesis factors and organic petrology of black shale series from the upper Sinian to the lower Cambrian, southwest of China. Acta Petrologica Sinica 15, 453-462 (in Chinese with English abstract).

Zhu, M.Y., Zhang, J.M., Steiner, M., Yang, A.H., Li, G.X., Erdtmann, B.D., 2004. Sinian-Cambrian stratigraphic framework for shallow- to deep-water environments of the Yangtze Platform: An integrated approach. Progress in Natural Science, 75-84.

CHAPTER TWO:

GEOGRAPHICAL SITUATION, TECTONIC SETTING, REGIONAL GEOLOGY AND PALEOGEOGRAPHIC EVOLUTION

2.1 Geographical setting

2.1.1 Location and accessibility of the study area

The study area is in Hunan and Guizhou provinces, where multi-nationality people (e.g. Han, Yao, Miao, Dong, Douyei and Tujia) live together. Geographical coordinates of the Dingtai profile, Dazhuliushui, Maluhe, Sancha and Cili polymetallic Ni-Mo-PGE-Au sulfide deposits are (27°42′ N and 106°39′ E), (27°43′ N and 106°39′ E), (26°45′ N and 105°37′ E), (29°04′ N and 110°35′ E) and (29°11′ N and 110°52′ E), respectively. Average elevation of the study area is 1100 m.

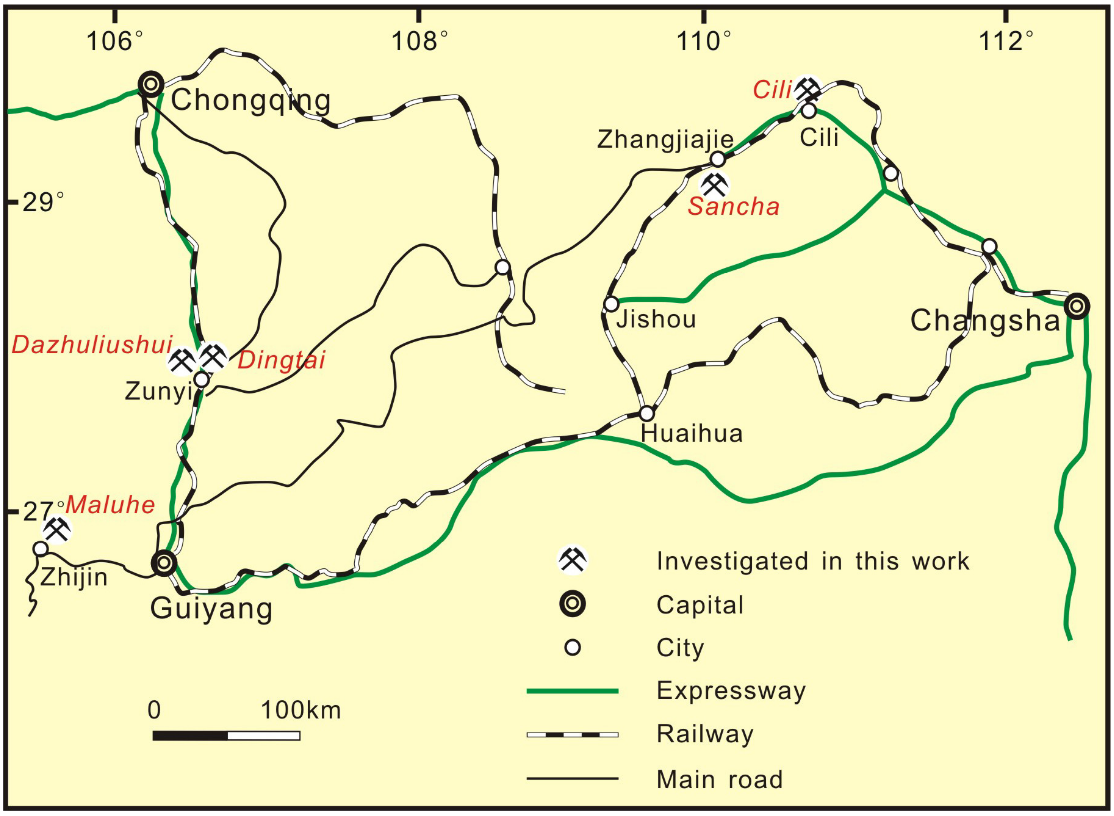

Fig. 2-1: Location and accessibility of the study area.

There are international airports near Guiyang, Changsha and Zhangjiajie, and frequent flights connect them to other cities. Expressway and railway networks are developed (Fig. 2-1). The studied mine sites including the Dazhuliushui near Zunyi, the Sancha near Zhangjiajie, and the Cili are easy to access, where country roads connect them to the main roads. However, the Maluhe mine site is located about 40 km north of Zhijin and traffic condition is very poor. Only narrow bumpy mountain roads are practicable to the Maluhe mine site.

2.1.2 Topography and hydrography

Guizhou province occupies the eastern part of the Yungui Plateau, rising between the Sichuan Basin and the Guangxi Basin. As a whole, the terrain of Guizhou gradually goes down eastwards. Guizhou has a rugged terrain, with numerous precipitous peaks and deep valleys, as well as extensive karsts formations, caves and underground rivers. Many date-shaped mini-basins scatter around the mountains. The Dalou Mountain in the northern part of the province forms the borderline of Guizhou. The Wuling Mountain in the north-eastern part of the province is abundant in biological resources and has been declared a key natural preserve of China. The Wumeng Mountain in the west borders Yunnan Province. The Miaoling Mountain in the central part of the province is the watershed between the Yangtze system and Pearl River system. Major rivers flowing through the province include the Wujiang River, the Chishuihe River, the Qingshui River, the Nanpan River and the Beipan River. These rivers have the common features of being narrow upstream but wide and open downstream (http://www.chinatoday.com/city/guizhou.htm).

Hunan Province is located on the south bank of the Yangtze River, and is surrounded by mountains and hills, such as the Wuling Mountains to the northwest, the Xuefeng Mountains to the west, the Nanling Mountains to the south, and the Luoxiao Mountains to the east. Mountains and hills occupy more than 80% of the area and plains comprise less than 20% of the whole province. Zhangjiajie in the Wuling Mountains is a world famous tourist attraction with great scenery in summer. The Xiangjiang, Zijiang, Yuanjiang and the Lishui Rivers converge to the Yangtze River at the Dongting Lake in the north Hunan. The Dongting Lake is the largest lake in the province and the second largest freshwater lake of China. Unfortunately, due to reclamation of land for agriculture, the Dongting Lake has been subdivided into many small lakes, and surrounding wetland habitats have been seriously damaged. Although local people and government have realized the significances of environmental protection, and part of reclamation has been stopped, more efforts to recover natural environment are still needed.

2.1.3 Climate and vegetation

The study area has a humid monsoon climate of the subtropical zone, with neither severe winter nor hot summer. Average temperature of January, the coldest month, is between 3-9ºC and that of July, the warmest month, is between 22-30ºC. The term “guiyang”, name of the capital of the Guizhou province, is used to describe that days of sunshine in this province are scarce. Annual average precipitation in Guizhou and Hunan is between 900-1700 mm. Most of the area in the two provinces has a long frost-free period, and two or three cropping systems are practiced.

2.2 Geological setting

2.2.1 Geological background

The investigated area is located in the Yangtze Platform. North and south sides of the Yangtze Platform are surrounded by the Northern Chinese Platform and the South China Foldbelt (Fig. 1-2). The NW-trending Qinling orogenic belt (also called Central orogenic belt) separates the Northern Chinese Platform and the Yangtze Platform. To the west, a series of ophiolite suites (e.g. the Kangdian suture, Ganze-Litang suture, Jinshajiang suture, Bangonghu-Nujiang suture and Indus river-Yalu-Zangbu suture) separate the Yangtze Platform and the Himalayan-Tibetan Plateau (Hou et al., 2007). The Yangtze Platform developed since Late Archean and formed a folded basement after the Jinning Movement (1.8 – 0.8 Ga). Thick Neoproterozoic to Triassic marine sediments and Jurassic to Cenozoic terrigenous sediments overlie the Yangtze basement. Paleomagnetic study reveals the Yangtze Platform was located in low-latitude area during Neoproterozoic, and shifted to the equator area in Late Permian (Seguin and Zhai, 1990). The Yangtze Platform collided first with the North China Craton during the Early Permian, and continued to collide while undergoing a clockwise rotation until the Early Cretaceous (Yokoyama et al., 2001).

2.2.2 Evolution history

In Chinese literature, geologists are accustomed using Chinese names of tectonic movements, which are, to some extent, not fully known internationally. Table 2-1 gives a correlation with the international scheme.

The paleogeographic evolution history of the investigated area since the Mesoproterozoic can be classified into three stages: Mesoproterozoic to Silurian stage, Devonian to Middle Triassic stage and Late Triassic to present day stage (Bureau of Geology and Mineral Exploration and Development of Guizhou Province, 1982; Liu et al., 1993). Characteristics of each stage are briefly summarized below:

Table 2-1

Tectonic movements in the Guizhou and Hunan provinces shown in Chinese and correlated international terminology (after Chen, 2006).

Geological age			Tectonic Period	Tetonic Movement	
Erathem Era	**System Period**	**Series Epoch**		**Guizhou**	**Hunan**
Cenozoic	Neogene	Holocene	Himalayanian	Himalayanian Movement	Himalayanian Movement (Late) (Taiwan Movement)
		Pleistocene			
		Pliocene			Himalayanian Movement (Late)
	Paleogene	Miocene			
		Oligocene			
		Eocene			
		Paleocene			
Mesozoic	Cretaceous	Upper	Yanshanian		
		Lower		Yanshan Movement	Ningzhen Movement Yanglukou Uplift
	Jurassic	Upper			
		Middle			Sandu Uplift
		Lower			Sanwan Uplift
	Triassic	Upper	Indosinian		
		Middle		Indo-China Movement (Anyuan Movement)	Anyuan Movement
		Lower			Guixi Movement
Paleozoic	Permian	Lopingian	Hercynian		
		Guadalupian		Hercynian Movement (Dongwu Movement)	
		Cisralian			Dongwu Uplift
	Carboniferous	Pennsylvanian			Qiangui Uplift
		Mississippian			Huainan Uplift
	Devonian	Upper			Liujiang Uplift
		Middle			
		Lower			
	Silurian	Pridoli	Caledonian	Caledonian Movement (Guangxi Movement)	Caledonian Movement
		Ludlow			
		Wenlock			
		Llandovery			
	Ordovician	Upper			Yichang Uplift
		Middle		Duyun Movement	
		Lower			
	Cambrian	Furongian			
		Series 3			
		Series 2			
		Terreneuvian			
	Neoproterozoic			Xuefeng Movement	Xuefeng Movement
	Mesoproterozoic			Wuling Movement	Wuling Movement

1) Mesoproterozoic to Silurian stage: The Mesoproterozoic Fanjingshan and Lengjiaxi Groups formed in marginal ocean basins, both of which consist of

meta-volcanic rocks at the bottom and terrestrial clastics at the upper part. During the Wuling Movement (Early Neoproterozoic), oceanic crust subducted beneath the continental crust northward, resulting in the formation of a new trench-arc-basin system. Banxi Group formed in this stage and consists dominantly of dark greenish mudstone and siltstone. During Early Neoproterozoic, the Yangtze platform was topographically characterized by high mountains and glaciers. Intensive erosion processes led to coarse-grained sedimentation, e.g. conglomerate, dominant in this stage. Since Late Neoproterozoic, a series of dramatic changes occurred in the Yangtze paleo-ocean. Dolomite with variable thickness of the Doushantuo Formation and the Dengying Formation precipitated during Late Neoproterozoic. A widely distributed black shale sequence of Early Cambrian age indicates that the oceanic anoxia may have existed widely. From Early Cambrian to Middle Ordovician, water depth of the marginal Yangtze paleo-ocean increased persistently. Meanwhile, the intra-plate carbonate platform to the west was uplifted.

2) Devonian to Middle Triassic stage: The paleogeographic evolution during this stage was controlled by back arc extension, which was related with Early Paleozoic orogenetic events. Littoral- and shallow-sea sediments, such as quartz sandstone and conglomerate, were dominant during the Devonian. From Early Carboniferous, transgression area extended gradually, which is reflected by classification of shallow water sediments of carbonate and sandstone, and deep water sediments of siliceous mudstone and carbonate. Seawater depth further increased to deep water sedimentation until Late Permian. Sediments of the Late Permian consist of sandstone, carbonate and mudstone.

3) Late Triassic to present day stage: The study area was uplifted and exposed after Late Triassic. Prevalent folds and faults indicate strong tectonic movements occurred during this stage. Pacific plate subduction produced formation of large scale basins with red bed sedimentation. A suite of coal-bearing strata deposited during Late Triassic. From Early Jurassic to Early Cretaceous, lithologies are dominated by dark reddish mudstone and sandstone, overlain by a suite of molasse sediments (e.g.

sandstone and conglomerate). Intermittent uplift occurred during Neogene, resulting in formation of lake sediments during Tertiary, and river sediments during Quaternary.

The Guizhou province is further divided into three tectonic units: the Yangtze Paraplatform, the Mesozoic Foldbelt and the Early Paleozoic Foldbelt (Fig. 2-2) (Bureau of Geology and Mineral Exploration and Development of Guizhou Province, 1982). From Mesoproterozoic, seven stages of tectonic movements including the Wuling Movement, the Xuefeng Movement, the Caledonian Movement, the Hercynian Movement, the Indosinian Movement, the Yanshanian Movement and the Himalayanian Movement affected the Guizhou Province (Table 2-1). The Yangtze Paraplatform and the Southeast Mesozoic Foldbelt have similar geological characteristics and evolution history during Mesoproterozoic and Neoproterozoic. The Wuling Movement formed the first folded basement, which is unconformably overlain by Neoproterozoic Banxi Group, Xiajiang Group and Danzhou Group. The lithology consists of meta-clastics and medium to felsic pyroclastic rocks. Uplift and metamorphism during the Xuefeng Movement formed the second folded basement during Neoproterozoic. The Yangtze Paraplatform is characterized by over-compensated sediments after the Neoproterozoic, contrary to the Southeast Mesozoic Foldbelt, which is characterized by starved basin sediments. The whole area was stable during the Caledonian, but followed by lithospheric uplift. NW-trending rifts developed after the lithospheric uplift, resulting in the formation of extensional oceanic basins and large scale eruption of basalt. However, intensive Indosinian movement stopped the further development of the extensional oceanic basins. During the Yanshanian to Himalayanian stage, the Yangtze platform was influenced by the subduction of the Pacific plate, leading to many inland basins developed during this stage. Even to present, the Guizhou province is still uplifting.

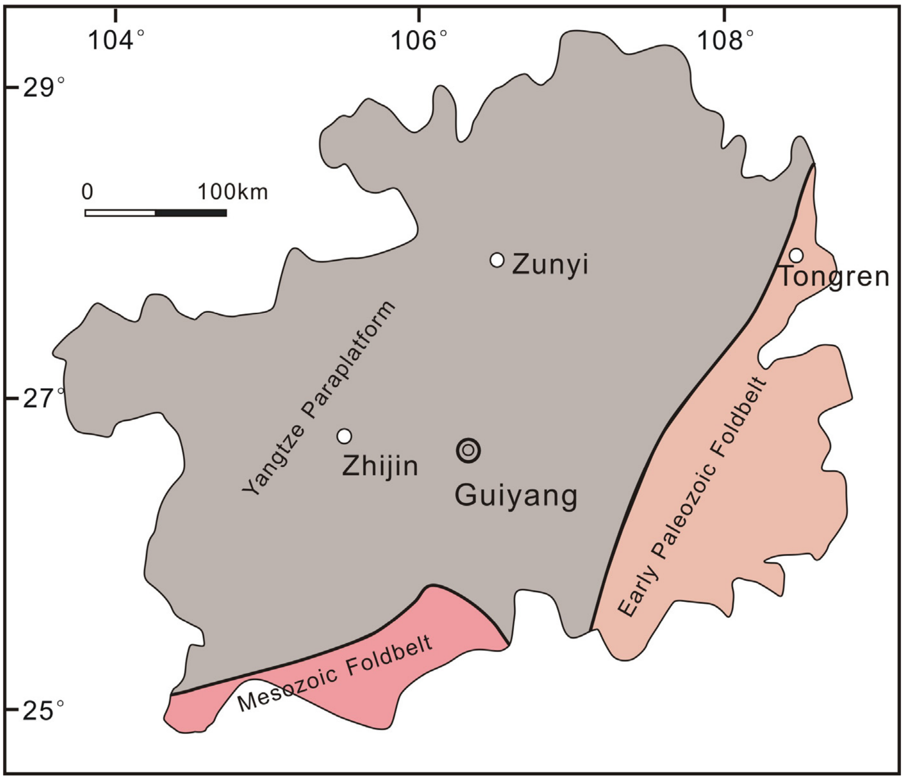

Fig. 2-2: Tectonic sketch map of Guizhou province (after Bureau of Geology and Mineral Exploration and Development of Guizhou Province, 1982).

In Hunan province, the continental crust underwent the Wuling Movement, the Xuefeng Movement, the Caledonian Movement, the Anyuan Movement, the Ningzhen Movement and the Himalayanian Movement (Table 2-1) (Bureau of Geology and Mineral Exploration and Development of Hunan Province, 1982). Intensive movements caused development of unconformities. Mesoproterozoic Wuling Movement is the earliest continental movement in Hunan province, which was characterized by intense orogenic movements. The Banxi Formation unconformably overlies the Lengjiaxi Formation. The Neoproterozoic Xuefeng Movement led to the formation of variable topography, which offered ideal sedimentary conditions for the large scale glacier formation. The continental crust movement during the Caledonian stage can be further classified into two steps: the Yichang uplift and the Caledonian Movement. The Yichang uplift occurred during the

Late Ordovician, resulting in large scale microcontinents formation. The Caledonian Movement is the most intensive orogenic phase in Hunan province, which formed the basic tectonic framework. After the Caledonian Movement, the area was relatively stable. The Hercynian Movement can be classified into three steps: the Liujiang uplift, the Huainan uplift and the Dongwu uplift. The Late Triassic is characterized by the Indosinian Movement, which consists of the Guixi Movement, the Anyuan Movement, the Sanwan uplift and the Sandu uplift. The Yanshanian Movement, consisting of Yanglukou uplift and Ningzhen Movement, is characterized by a large scale foldbelt, volcanic eruption and magmatic intrusion. Continental crust continuously uplifted during the Himalayian Movement, and formed a horseshoe-shaped basin in the Hunan province, which is characterized by high mountains to the east, west and south.

2.2.3 Regional stratigraphy

Mesoproterozoic to Quaternary strata are exposed in the study area. A brief summary of each stratigraphic unit in ascending order is shown as follows:

1). Mesoproterozoic:

The Fanjingshan Group and equivalent strata (Lengjiaxi Group in Hunan province) has an age of 1000 – 1400 Ma and is the oldest stratigraphic unit exposed in the study area (Bureau of Geology and Mineral Exploration and Development of Guizhou Province, 1982). Upwards, the Fanjingshan Group consists of Taojinhe Formation, Shejiagou Formation, Xiaojiahe Formation, Huixiangping Formation, Touchang Formation, Waxi Formation and Duyantang Formation. Lithology of the Fanjingshan Group gradually changed from metamorphic volcanic and terrigenous clastic rocks at lowermost part to meta-sandstone, metal-siltstone, slate, phyllite, schist and volcanic tuff at the uppermost unit.

2). Neoproterozoic:

The Banxi Group is unconformably underlain by the Fanjingshan Group and overlain by the Nantuo low grade metamorphic rocks. Two sedimentary cycles can be distinguished: the lower sedimentary cycle consists of low grade meta-sandstone, sandstone, layered tuff with interbedded carbonate rocks and carbonaceous slate, whereas the upper sedimentary cycle is locally intercalated with andesitic to felsic volcanic rocks.

The Nantuo Formation, Doushantuo Formation and Dengying Formation are exposed in ascending order above the Banxi Group. Lithology of the Nantuo Formation is mainly glacial diamictites, and intercalated siltstone, mudstone, carbonaceous shale, chert and sandstone. Thickness of the Nantuo Formation varies from 50 to 100 m in the shelf and > 1500 m in the basin, respectively. The Doushantuo Formation is a fossil-rich (e.g. animal remains, multicellular algae and giant acritarchs) sequence of interbedded black shale and limestone, chert, phosphorite, silty dolomite and limestone, with 60 to 180 m thickness in the shelf to <100 m thickness in the basin. U-Pb zircon dates from volcanic ash beds within the Doushantuo Formation indicate that deposition occurred between 635 and 551 Ma (Condon et al., 2005). Two phosphorite beds in the Doushantuo Formation yielded Pb-Pb isochron ages of 576 ± 16 Ma for the upper part (Chen et al., 2004), and 599 ± 4 Ma for the lower part of the Upper Phosphorite unit (Barfod et al., 2002), respectively. The Dengying Formation rests above the Doushantuo Formation and is widely exposed in South China, and is overlain by Early Cambrian sequences. Lithology of the Dengying Formation mainly consists of thick dolomite and limestone in the shelf (> 800 m thick), and black shale and siliceous carbonate in the basin (< 150 m-thick). The dolomite of the Dengying Formation contains the tubular fossil Cloudina (Bengtson and Zhao, 1992).

4). Cambrian:

The Early Cambrian strata consist of the Niutitang Formation, Mingxinsi Formation, Jindingshan Formation and Qingxudong Formation in ascending order. The Zhalagou Formation and the Balang Formation are exposed in the southeast

Guizhou province, equivalent with the Mingxinsi Formation and the Jindingshan Formation occurred in the north Guizhou, respectively. The Niutitang Formation black shale is unconformably underlain by dolomite of the Dengying Formation. The Mingxinsi Formation is a suite of sandstone, siltstone and mudstone, and is overlain by the Jindingshan Formation siltstone and sandstone. Lithology of the Qingxudong Formation consists of dolomite and limestone with sandstone and shale interbeds. Fossils such as trilobites, sponges, ostracodes and megascopic algae occur in the Qingxudong Formation. The Middle Cambrian strata with abundant trilobite fossils include Gaotai Formation and Shilengshui Formation, consisting of dominant dolomite and a minor limestone and sandy shale. The Upper Cambrian Furong Formation consists of dolomite with rare fossils.

5). Ordovician:

Invertebrate fossils are common in the Ordovician strata, which consist of shallow facies sedimentary rocks and clastic components, with stable thickness. Carbonate rocks are dominant in the north of the study area, whereas sandstone, shale and carbonaceous shale are dominant in the southern part. Clay content increases gradually southwards.

6). Silurian:

The Silurian strata are only locally exposed in the Hunan and Guizhou province. Shell fossil-rich shale and sandstone are dominant, and locally occurs with interbedded Ca-rich sandstone, shale and carbonate rocks.

7). Devonian:

Except for the early interval of the Lower Devonian, all the Devonian strata are well exposed in the study area, generally consisting of carbonate and clastic rocks, with abundant foraminifera, brachiopoda, corals and trilobite fossils. Clay content increases northwards. Shallow facies carbonate and clastic rocks are interbedded with mudstone, chert and carbonate rocks of deep water facies.

8). Carboniferous:

Carboniferous strata are characterized by carbonate with intercalated chert. Fossils, including foraminifera, brachiopoda and corals, are abundant. Some sedimentary ore deposits are hosted in the Carboniferous strata in the Hunan and Guizhou provinces.

9). Permian:

The Lower Permian consists of carbonate rocks, and minor coal-bearing sandstone, shale and chert. Plant, brachiopoda and bivalve fossils are common. The Upper Permian is dominated by clastic rocks and limestone, with abundant coral and ammonite fossils.

10). Triassic:

Fossils are diversiform in Triassic strata, especially with abundant ammonite and bivalve fossils. The Lower Triassic is dominated by carbonate rocks. The Middle Triassic is mainly sandstone and mudstone. The Upper Triassic mainly consists of coal-bearing sandstone, conglomerate and mudstone.

11). Jurassic:

Both marine and terrestrial sediments were developed with plenty of animal and plant fossils. The Lower Jurassic consists of dark reddish mudstone, muddy shale and sandstone with plant, fish and ammonite fossils. The Middle Jurassic is dominated by thick dark greenish sandstone, mudstone and siltstone. Fossils are rare in the Middle Jurassic. The Upper Jurassic consists of greyish feldspar-quartz sandstone, calcareous mudstone with intercalated bitumen veins. Fossils such as *cf. Klukia brownian*a and *Lepidotes* are abundant.

12). Cretaceous:

Terrestrial sediments are dominant in the Cretaceous. Lithologies consist of conglomerate, sandstone and volcanics with abundant ammonite, chara and dinosaur footprint fossils.

13). Cenozoic:

The Cenozoic strata consist of conglomerate and sandy mudstone with locally exposed coal lines. Glacial and alluvial sediments are dominant in the Quaternary.

2.3 Paleogeographic reconstruction

2.3.1 Mesoproterozoic to Neoproterozoic (Pre-Sinian)

In the Mesoproterozoic, South China was largely covered by an extensive ocean (Fig. 2-3). The Upper Yangtze oldland was the largest one among several oldlands (micro-continents). A simple trench-are-basin system developed on the northern and western sides of the Upper Yangtze oldland. Near the ancient coast was marginal sea of back-arc basin type, and farther from the continent developed island arcs, beyond which was probably an open oceanic basin. A more complex trench-arc-basin system occurred on the southeastern side of the Upper Yangtze oldland. The South China oceanic plate subducted under the Upper Yangtze oldland, leading to the formation of roughly parallel island arcs and an interarc marine basin in between. The marginal sea between the Fanjingshan area and the Upper Yangtze oldland was a back-arc basin. The subduction of surrounding oceanic terrains towards the Upper Yangtze led to the diminution and southward retreat of the South China oceanic basin. At the same time, the Upper Yangtze oldland increased in its size through successive accretion and welding with the Lower Yangtze, leading to the formation of the integrated Yangtze Platform at about 1000 Ma (Fig. 2-4). A marginal sea to the south of the Yangtze oldland extended southwards and occupied the original site of the previous interarc seas. During this interval, the Yangtze oldland faced to an open ocean to the west and south. During the Middle and Late Proterozoic, successive migration of the trench-arc-basin system towards the ocean side and the accretion of the continental crust onto the Yangtze oldland were the basic patterns of paleogeographic development of South China. The general framework of the Yangtze Platform formed not earlier than 1000 Ma, but complete consolidation was accomplished at the end of the Jiangnan Movement at ~850 Ma (Wang et al., 1985).

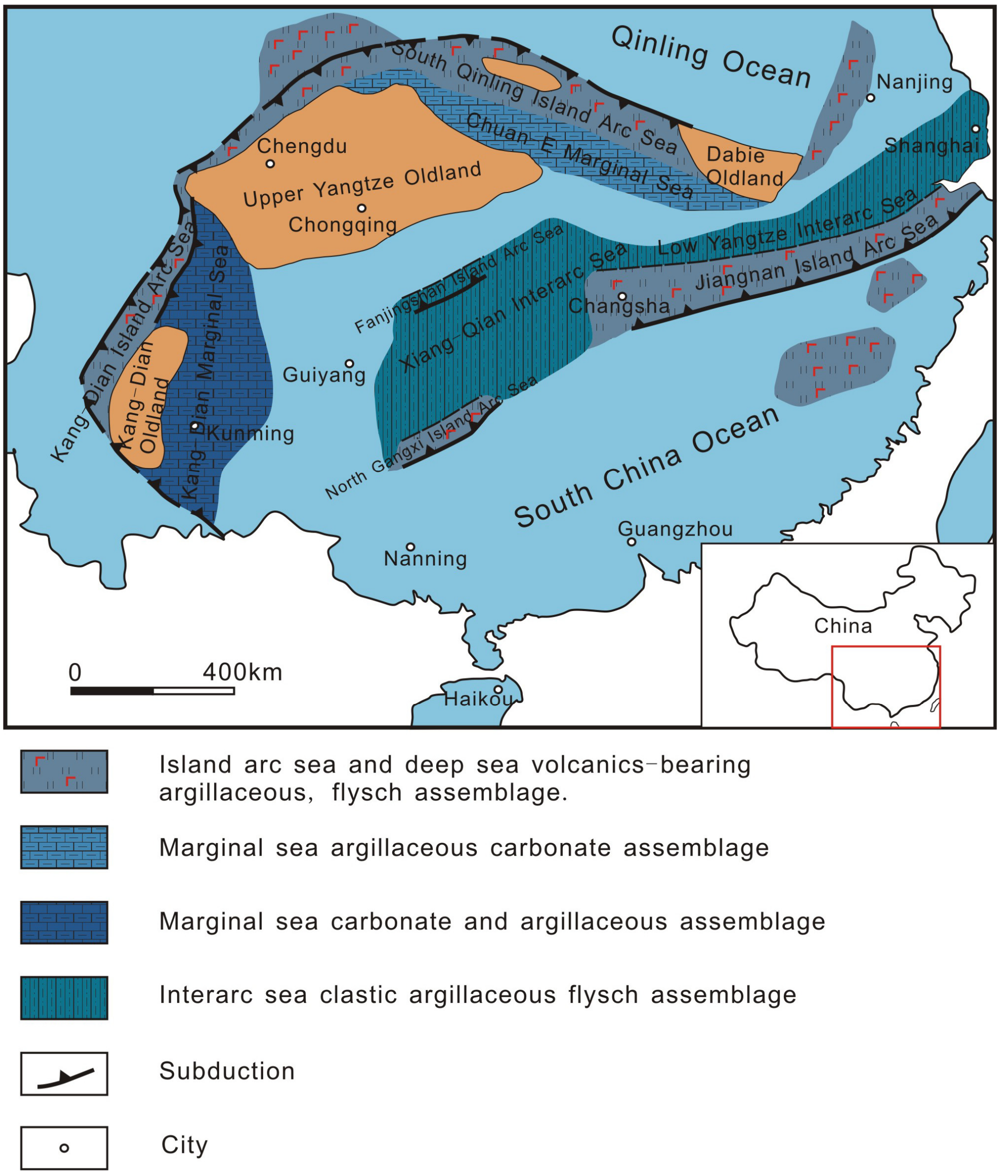

Fig. 2-3: Paleogeographic map of the Mesoproterozoic (prior to 1000 Ma) of South China (after Wang et al., 1985).

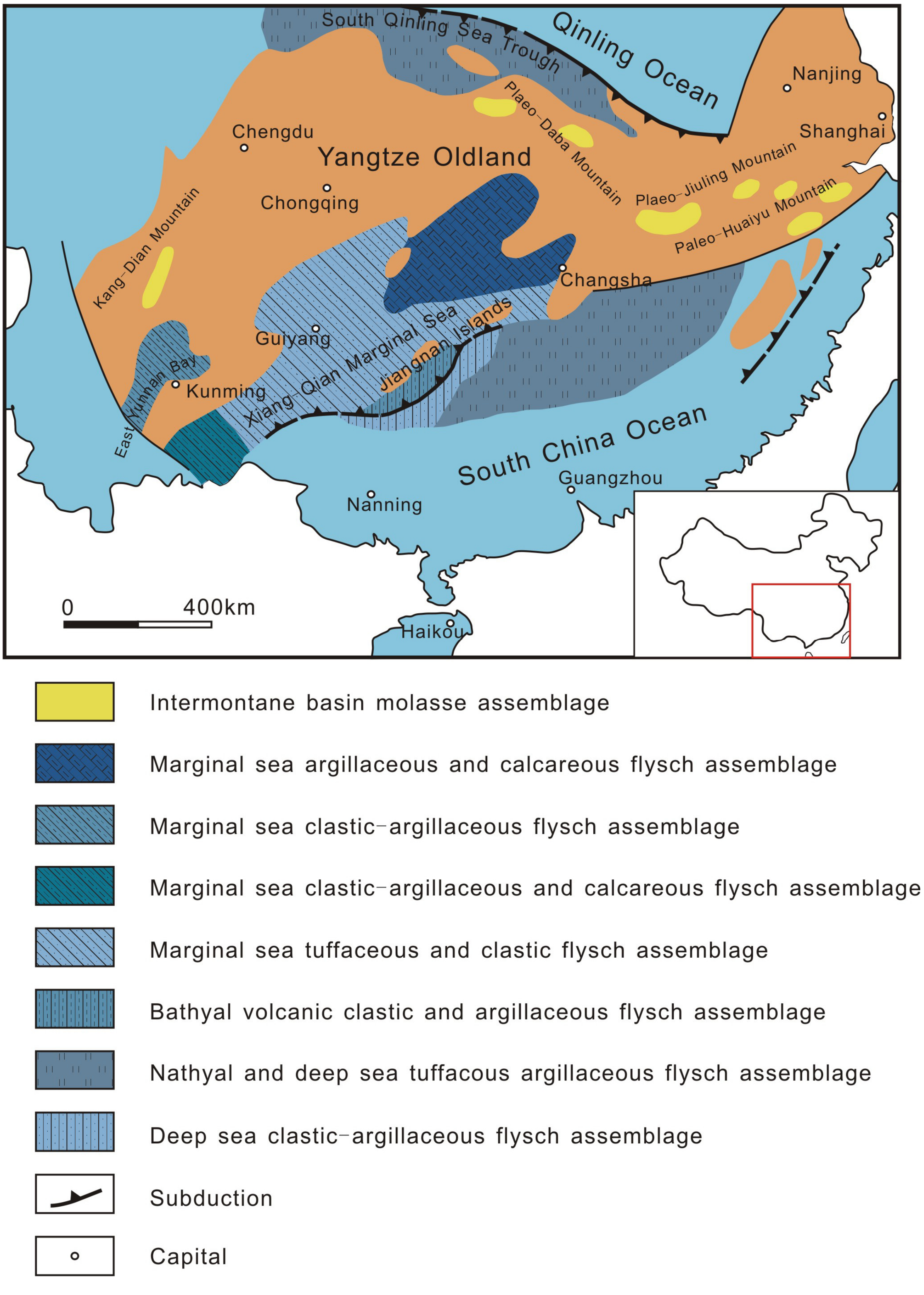

Fig. 2-4: Paleogeographic map of the Neoproterozoic (1000-850 Ma) of South China (after Wang et al., 1985).

2.3.2 Sinian (850 – 540 Ma).

The Sinian can be divided into Lower Sinian and Upper Sinian with appearance of tillite as boundary at the top of the Nantuo Formation. The Sinian was a significant interval in the crustal evolution history, during which the structural frame and paleogeographic configuration resulting by the Jinning Movement has defined the basic features for the later Sinian and Paleozoic evolution. At the beginning of the Sinian interval, North China, Yangtze and South Tibet (Gondwana) were three main oldlands, which were probably separated by open oceanic basins. Several glacial epochs occurred during this period and the biosphere has changed dramatically, characterized by the appearance of algae and metazoans.

After the Jinning Movement, the Yangtze oldland was located in the south of the Kunlun-Qinling Ocean, and continued to expand through accretion. To the northwest, the Songpan oldland probably formed by fragmentation of the Yangtze block, meanwhile the South China oceanic basin retreated to the east of the southeastern islands. In early stage of the Early Sinian, continental deposits were found at the margin of the Yangtze Platform. A NS-trending trough formed near the western margin in southern Sichuan and eastern Yunnan provinces, in which continental andesitic-mafic and andesitic-felsic volcanics and clastics were prevalent. In the late stage of the Early Sinian, the Yangtze Platform was again uplifted, and glaciation events occurred frequently, leading to a large amount of tillites which developed during this interval (Fig. 2-5). Tuffaceous clastics were dominant in the Lower Yangtze, and siliceous and argillaceous rocks developed in western Zhejiang province.

During the Late Sinian, the Yangtze Platform underwent widespread transgression, resulting in small islands scattered in the marginal sea. In addition, discontinuous submarine uplift occurred from central to northern Sichan province, and formed several restricted basins with evaporites during the Late Sinian interval.

To the north of Jiangnan islands, siliceous carbonates deposited in starved basins (Fig. 2-6).

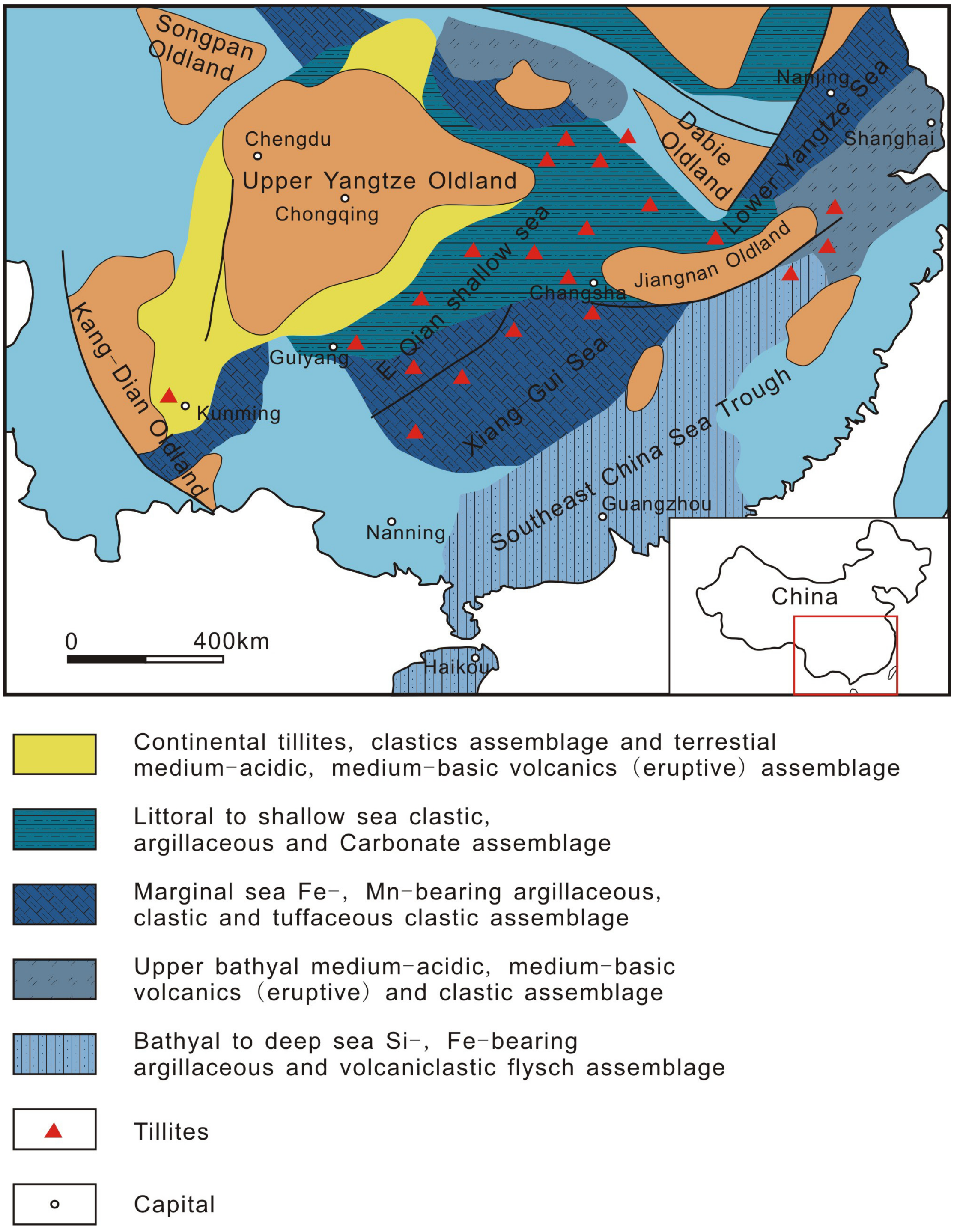

Fig. 2-5: Paleogeographic map of the Early Sinian (Nantuo Formation) of China (after Wang et al., 1985).

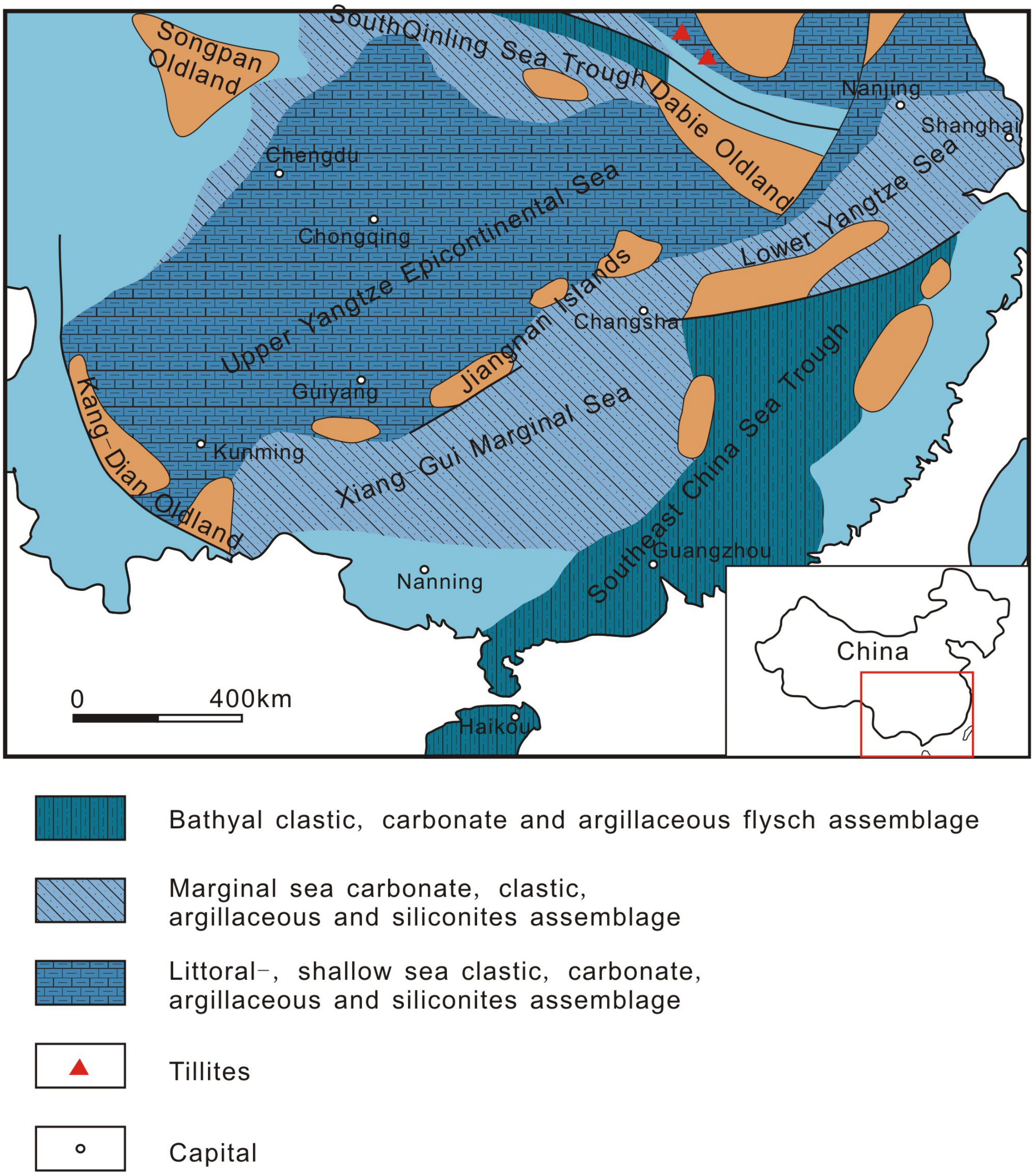

Fig. 2-6: Paleogeographic map of the Late Sinian (Doushantuo Formation) of China (after Wang et al., 1985).

2.3.3 Cambrian

The Cambrian paleogeographic pattern is essentially inherited from the Late Sinian. The Yangtze, Jiangnan and Southeast China regions constituted a complex and extensive terrain composed of epicontinental seas to marginal seas, with sea water getting generally deeper and deeper from northwest to southeast. An ideal section including different facies zones occurred southeastwards ranging from littoral-neritic, deeper shallow sea to bathyal facies, and farther to the southeast were the Zhe-Min islands and ancient Proto-Pacific oceanic basin. Marginal sea sediments are preserved along the northern margin of the Yangtze Platform. To the west of the Yangtze Platform, owing to later tectonic movements, it is very difficult to reconstruct the paleogeographical features during the Cambrian interval. In the whole region, topography was low in the Early Cambrian, while in the Middle and Late Cambrian it was elevated due to differential uplift, i.e. the Kang-Dian oldland. The uplifts caused a sharp contrast between the littoral to shallow seas and marginal seas, and led to marine current convection in marginal surroundings. A mixture of benthonic and pelagic trilobites flourished. Abundant magnesian carbonate deposits formed during this interval. The Southeast Sea troughs were deep and characterized by arenaceous to argillaceous turbidite sediments with a huge thickness. The South China biogeographic province in the Yangtze region was particularly evolved in the Austral-Asian biogeographic realm with many endemic genera and species, for example, trilobites, small shells, and the oldest archaeocyathid faunas (Wang et al., 1985).

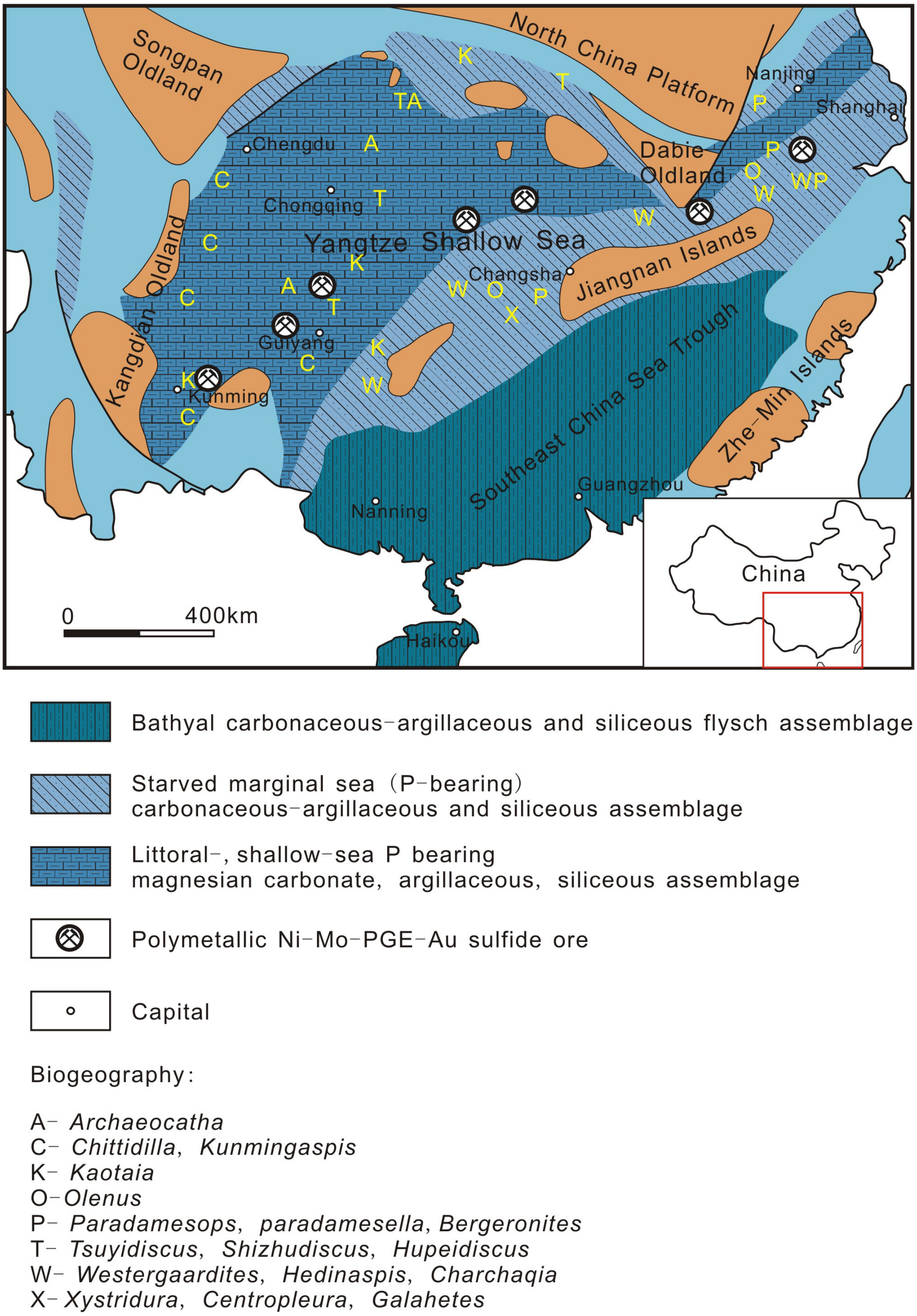

Fig. 2-7: Paleogeographic map and biogeography of the Early Cambrian of China (modified from Wang et al., 1985).

2.4 References

Barfod, G.H., Albarède, F., Knoll, A.H., Xiao, S.H., Telouk, P., Frei, R., Baker, J., 2002. New Lu-Hf and Pb-Pb age constraints on the earliest animal fossils. Earth and Planetary Science Letters 201, 203-212.

Bengtson, S., Zhao, Y., 1992. Predatorial borings in Late Precambrian mineralized exoskeletons. Science 257, 367-369.

Bureau of Geology and Mineral Exploration and Development of Guizhou Province, 1982. Ministry of Geological and Mineral Resources, Peoples`s Republic of China, Regional Geology of Guizhou Province. Beijing: Geological Press House, 1-665.

Chen, D.F., Dong, W.Q., Zhu, B.Q., Chen, X.P., 2004. Pb-Pb ages of Neoproterozoic Doushantuo phosphorites in South China: constraints on early metazoan evolution and glaciation events. Precambrian Research 132, 123-132.

Chen, L., 2006. Sedimentology and geochemistry of the Early Cambrian black rock series in the Hunan-Guizhou area, China. Ph.D thesis, 1-103 (in Chinese with English abstract).

Condon, D., Zhu, M.Y., Bowring, S., Wang, W., Yang, A.H., Jin, Y.G., 2005. U-Pb ages from the Neoproterozoic Doushantuo Formation, China. Science 308, 95-98.

Hou, Z.Q., Zaw, K., Pan, G.T., Mo, X.X., Xu, Q., Hu, Y.Z.Li, X.Z., 2007. Sanjiang Tethyan metallogenesis in SW China. Tectonic setting, metallogenic epochs and deposit types. Ore Geology Reviews 31, 48-87.

Liu, B.J., Xu, X.S., Pan, X.N., Huang, H.Q., Xu. Q., 1993. Sedimentary evolution of ancient continents and mineralization of South China. Beijing: Scinece Publishing House, 1-231 (in Chinese).

Seguin, M.K.Zhai, Y.J., 1992. Paleomagnetic Constraints on the Crustal Evolution of the Yangtze Block, Southeastern China. Tectonophysics 210, 59-76.

Wang, H.Z., Chu, X.C., Liu, B.P., Hou, F.F., Ma, L.F., (eds.), 1985. Atlas of the palaeogeography of China. Beijing: Cartographic Publishing House, 1-143.

Yokoyama, M., Liu, Y.Y., Halim, N.Otofuji, Y., 2001. Paleomagnetic study of Upper Jurassic rocks from the Sichuan basin: tectonic aspects for the collision between the Yangtze Block and the North China Block. Earth and Planetary Science Letters 193, 273-285.

CHAPTER THREE:

GEOLOGY OF GEOCHEMICAL PROFILES AND POLYMETALLIC Ni-Mo-PGE-Au SULFIDE DEPOSITS

The study area is one of the most important metalliferous regions in China, with Hg, Sb, Pb, Au and other mineral deposits. In recent years, this region has become known for Carlin-type gold (e.g. Cunningham et al., 1988; Peters et al., 2007; Su et al., 2008, 2009), barite (Wang and Li, 1991; Maynard and Okia, 1991; Xia et al., 2004; Goldberg et al., 2006; Yang et al., 2008), manganese (Fan et al., 1992), vanadium (Zhang et al., 1987; Liao et al., 1988), phosphorite (Bushinskii, 1966; Ye et al., 1989; Wang et al., 2004) and polymetallic Ni-Mo-PGE-Au mineralization (e.g. Fan et al., 1984; Mao et al., 2002; Jiang et al., 2006, 2007; Lehmann et al., 2003, 2007). Thus this region, including Guizhou and Hunan provinces, is an area containing mineral resources of many types. Many of these are hosted by the same Lower Cambrian black shale sequences (Chen et al., 1982) as the unusual polymetallic Ni-Mo-PGE-Au sulfide ore layer discussed in this work. The high-grade, but very thin polymetallic Ni-Mo-PGE-Au sulfide ore layer was initially discovered in Guizhou and Hunan in the 1970s, and was first described in the English literature by Fan (1983). Isolated and scattered occurrences of the sulfide ore layer were found within a 1600 km belt extending across several provinces in South China (Fig 1-2). The polymetallic Ni-Mo-PGE-Au sulfide ore layer occurs at approximately the same Neoproterozoic (Sinian)-Cambrian stratigraphic interval as beds of phosphorite, vanadium-rich black shale, stone coals, manganese and barite. The genesis of these types of deposits may have been related to paleo-oceanic anoxia, and the spatio-temporal relations among the various deposit types may serve as an exploration guide for similar deposits elsewhere. In this study, four polymetallic Ni-Mo-PGE-Au sulfide ore deposits, including Dazhuliushui and Maluhe in Guizhou province, and Sancha and Cili in Hunan province were investigated. Geological features of these deposits are described below.

3.1 Geological features of the polymetallic Ni-Mo-PGE-Au sulfide ore deposits

3.1.1 Dazhuliushui mine site

The Dazhuliushui Ni-Mo-PGE-Au deposit is located in the western part of the Songlin dome, about 26 kilometers from Zunyi city, Guizhou Province. From the dome center outwards, Late Proterozoic conglomerate of the Nantuo Formation, carbonaceous mudstone and dolomite of the Doushantuo Formation, dolomite of the Dengying Formation, and black shale of the Early Cambrian Niutitang Formation are exposed (Fig. 3-1). Thickness of the Niutitang Formation ranges from 30 to 50 m, and is overlain by carbonaceous siltstone and sandstone of the Early Cambrian Minxinsi Formation, dolostone of the Early Cambrian Qingxudong Formation, and Middle Ordovician dolomite and shale. The stratigraphic column of the Songlin dome is shown in Fig. 3-2. The Niutitang Formation consists of fine-grained, massive or laminated black shales with abundant fossils (e.g. *Tsunyidiscus sp*.). Framboidal and anhedral pyrite grains occur in the black shales (Fig. 3-9 B), and pyrite content decreases from the sulfide ore layer upwards. There are no magmatic rocks exposed in the area. Besides the Dazhuliushui polymetallic Ni-Mo-PGE-Au sulfide mine site, nearby Xiaozhuliushui, Huangjiawan, Zhongnancun and Xintugou are other mines which are located in the same stratigraphy and with similar mineralization style. The large east-north-, east-, north-northeast-, and noth-northwest-trending faults in the Songlin dome area are of post-Early Paleozoic age. However, small-scale synsedimentary fractures without hydrothermal infill are abundant (Mao et al., 2002).

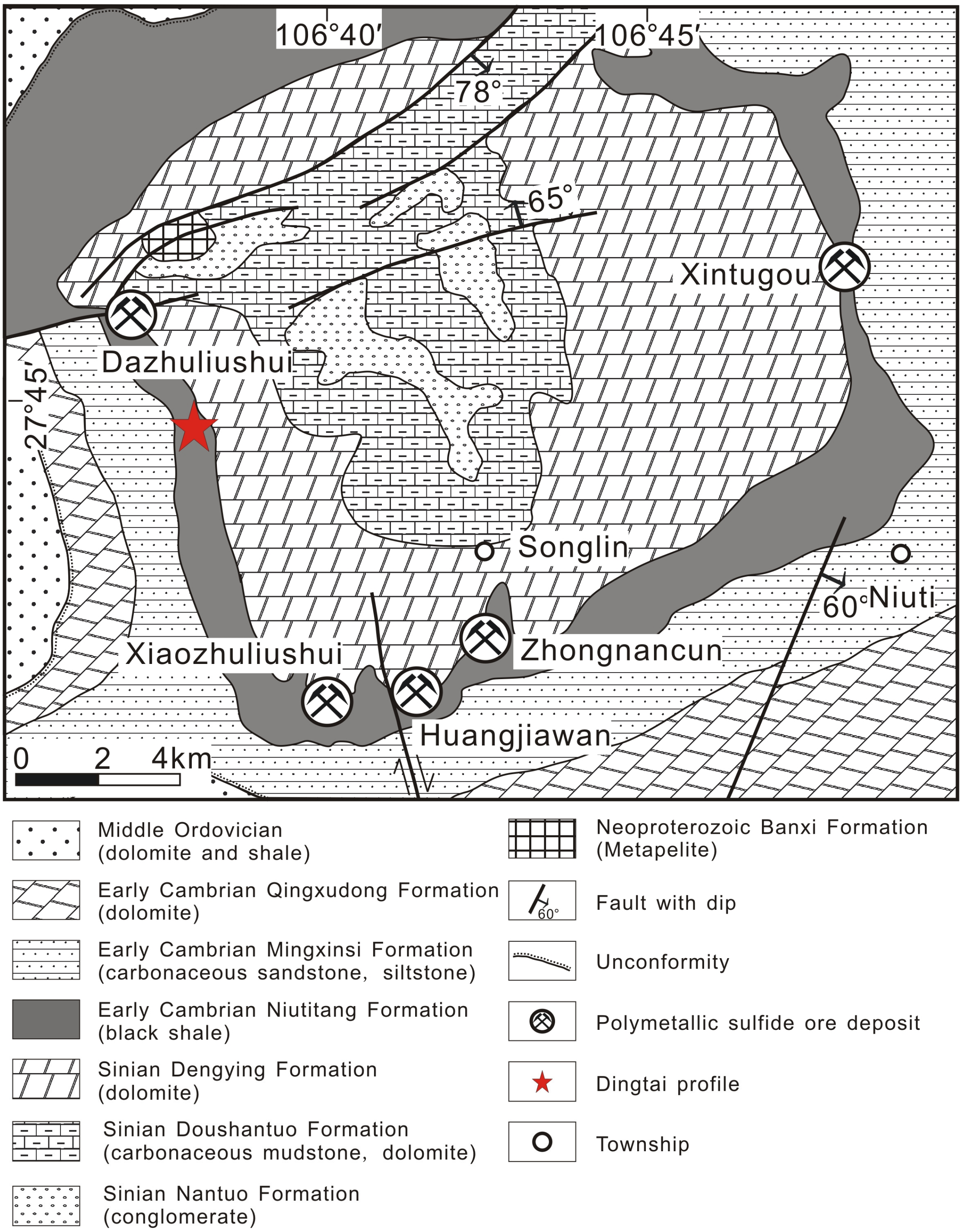

Fig. 3-1: Geological map of the Dazhuliushui mine district near Zunyi, Guizhou (after Mao et al., 2002).

Zeng (1998) investigated the Huangjiawan mine site and divided the ore-bearing Niutitang Formation into six lithological units form the bottom upwards, as follows:

1) A 0-0.3 m thick Fe-Mn oxide-rich weathering crust layer, which occurs as discontinuous lenses on the undulating paleosurface of the Neoproterozoic Dengying Formation dolomite.

2) An on average ~0.5 m thick brownish to black U-rich phosphorite intercalated with dolomite lenses. In some localities the thickness of phosphorite can reach up to several meters, and is then mined.

3) A 0.5–2.5 m organic carbon-rich hydromica claystone-shale intercalated with phosphorite nodules. Collophane contains 200 to 300 ppm U, and the concentration of Mo, Ni, V, Y and light REE in the claystone locally reaches economic grade.

4) A polymetallic Ni-Mo-PGE-Au sulfide ore layer, locally disrupted sulfide microlenses, and flat pebble-like conglomerates. The ore layer shows sharp boundaries with overlying and underlying units, and is continuous over several kilometer strike length with a thickness of 5-30 cm in the eastern part and 20-50 cm in the western part. The maximum thickness reaches up to 2 m.

5) A 0.5-2 m organic carbon-rich hydromica clastone-shale, known as the Mo-V-bearing stone coal layer, with contents up to 0.1 to 0.3% Mo, 0.05 to 0.2% Ni, and 0.05 to 0.9% V.

6) A carbonaceous hydromica claystone-shale with thickness of more than 100 m.

The Dazhuliushui and Huangjiawan polymetalllic sulfide mine sites are geographically near (Fig. 3-1), and have the same stratigraphic position. At the Dazhuliushui mine site, the thickness of the polymetallic sulfide ore layer is 0.02 – 0.08 m, with maximum of 0.39 m (Wang et al., 2006) (Fig. 3-9 C), which is thinner than that reported by Zeng (1998) for Huangjiawan, who gave a maximum thickness up to 2 m. However, field observation shows that the thickness of the two occurrences is similar, generally in the cm range. The reason may be because that Zeng (1998) described the thicker ore bed with a relatively low cut-off grade (as mineable width), which is not clarified in his literature. Consequently, some underlying and overlying black shales with low grade were also included.

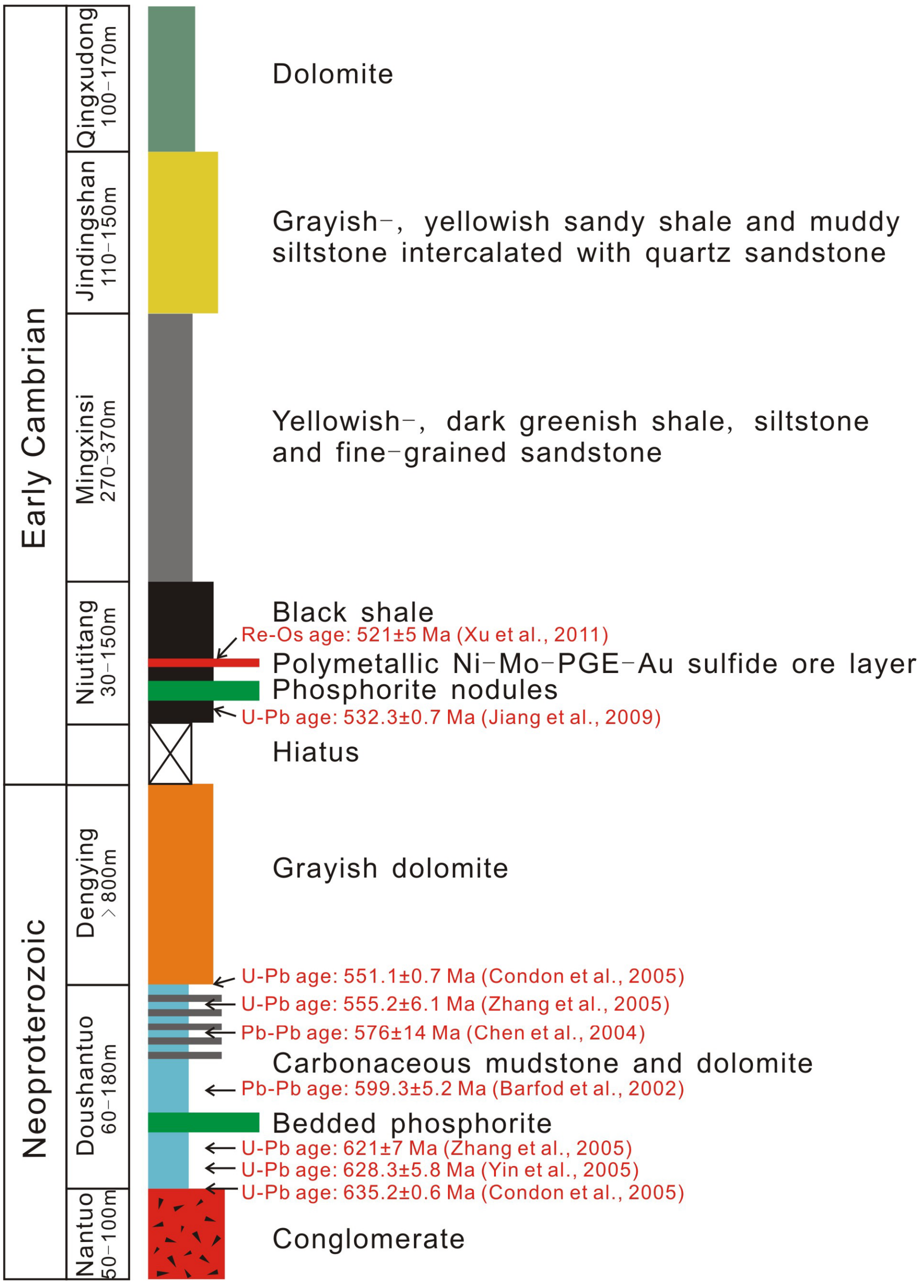

Fig. 3-2: Stratigraphic column showing the Neoproterozoic-Early Cambrian sequences of the slope facies sedimentary sequences of the Yangtze Platform. Radiometric ages are highlighted in red color. Thickness of each stratigraphic unit varies at different localities.

3.1.2 Maluhe mine site

The Maluhe district with the Maluhe, Shuidong and Dayuan Ni-Mo-PGE-Au deposits near Zhijin is 180 km southwest of the Dazhuliushui mine site. The Maluhe deposits are hosted in a broad anticlinal structure which exposes the Niutitang Formation, unconformably overlain by Carboniferous dolomite and dolomitic limestone, and underlain by dolomite of the Dengying Formation (Fig. 3-3). Thickness of the polymetallic sulfide ore layer is 2-3 cm. Ni and Mo contents of the sulfide ore are 1.29 - 8.04 % (2.84 % on average) and 2.42 – 6.42 % (4.10 % on average), respectively (Regional Geological Report, 1976*). Post-mineralization NE-trending faults are developed in the Maluhe district. The polymetallic ore layer is generally about 1 meter above the unconformable contact with dolomite of the Dengying Formation. However, karstic features resulted in a variable distance to the dolomite contact. For example, near the Maluhe district there is a local occurrence of a phosphorite bed between the Niutitang black shales and the Dengying dolomite. The thickness of the phosphorite bed reaches up to 20 m with low P_2O_5 grade. Carboniferous chert breccia can occasionally be found at the contact zone of phosphorite layer and Dengying dolomite (Fig. 3-9 D, E).

---

* Regional Geological Report of Bijie area, Guizhou province. 1976. Scale: 1/200000. Compiled by 108 Geological Team of Bureau of Geology and Mineral Exploration and Development of Guizhou Province.

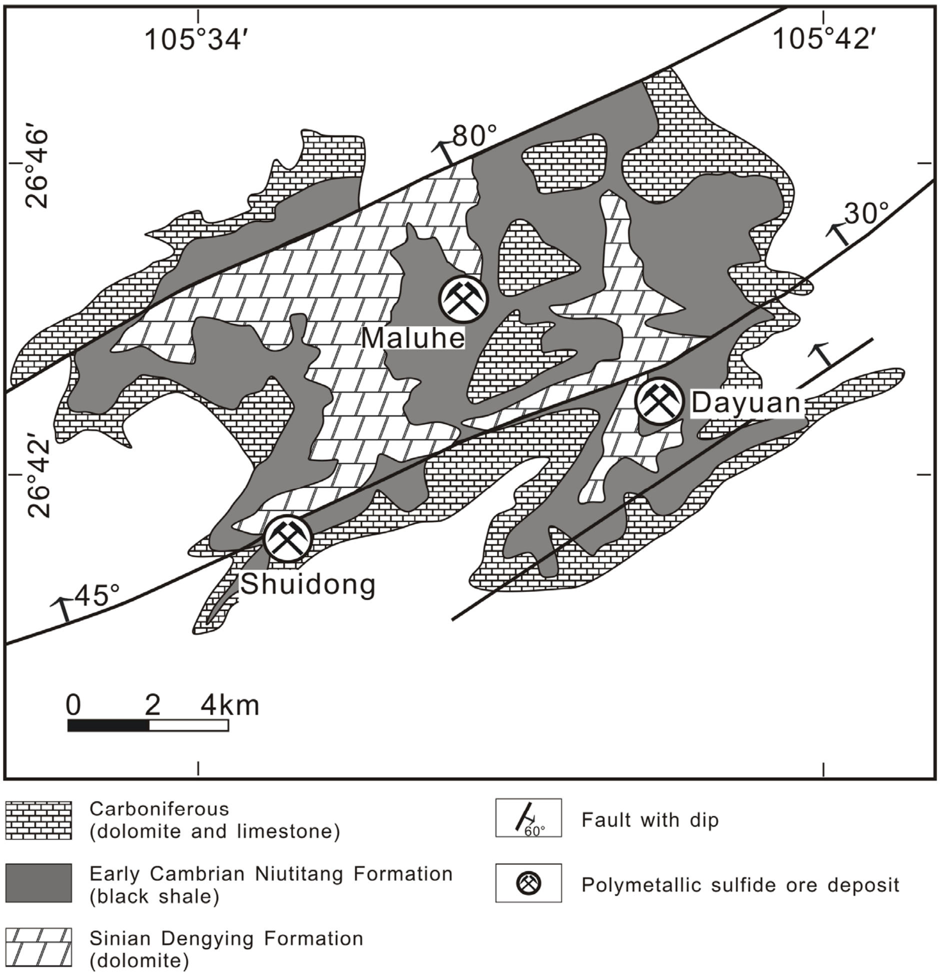

Fig. 3-3: Geological sketch map of the Maluhe mine district near Zhijin, Guizhou (modified from 1/200000 Mineral Resource Geological Map of Bijie area, Guizhou province. Compiled by 108 Geological Team of Bureau of Geology and Mineral Exploration and Development of Guizhou province).

3.1.3 Sancha mine site

The Sancha polymetallic Ni-Mo-PGE-Au district in Hunan province is ~380 km northeast of the Dazhuliushui mine site. The Sancha district includes a number of individual deposits, such as Sancha, Wangjiazhai, Ganziping, Chuanyanping, Houping, Langxi, Daping and Xiaoping, all of which are aligned in the limbs of the

Tianmenshan-Huangdong syncline. The axis of the synclinal structure is composed of Middle-Late Cambrian limestone and dolomite (Fig. 3-4). The sulfide ore layer in the Niutitang Formation is only 1 meter above the unconformable contact with the dolomite of the Dengying Formation. Phosphorite nodules and chert occur between the sulfide layer and the dolomite contact. The high grade polymetallic sulfide bed makes this ore layer a target for widespread small scale mining in the Sancha district (Fig. 3-9 F, G). From northeast to southwest in the Sancha district, occurrences of the polymetallic Ni-Mo-PGE-Au mineralization decrease gradually and grade into vanadium mineralization (i.e. Langxi V deposit) (Fig. 3-5).

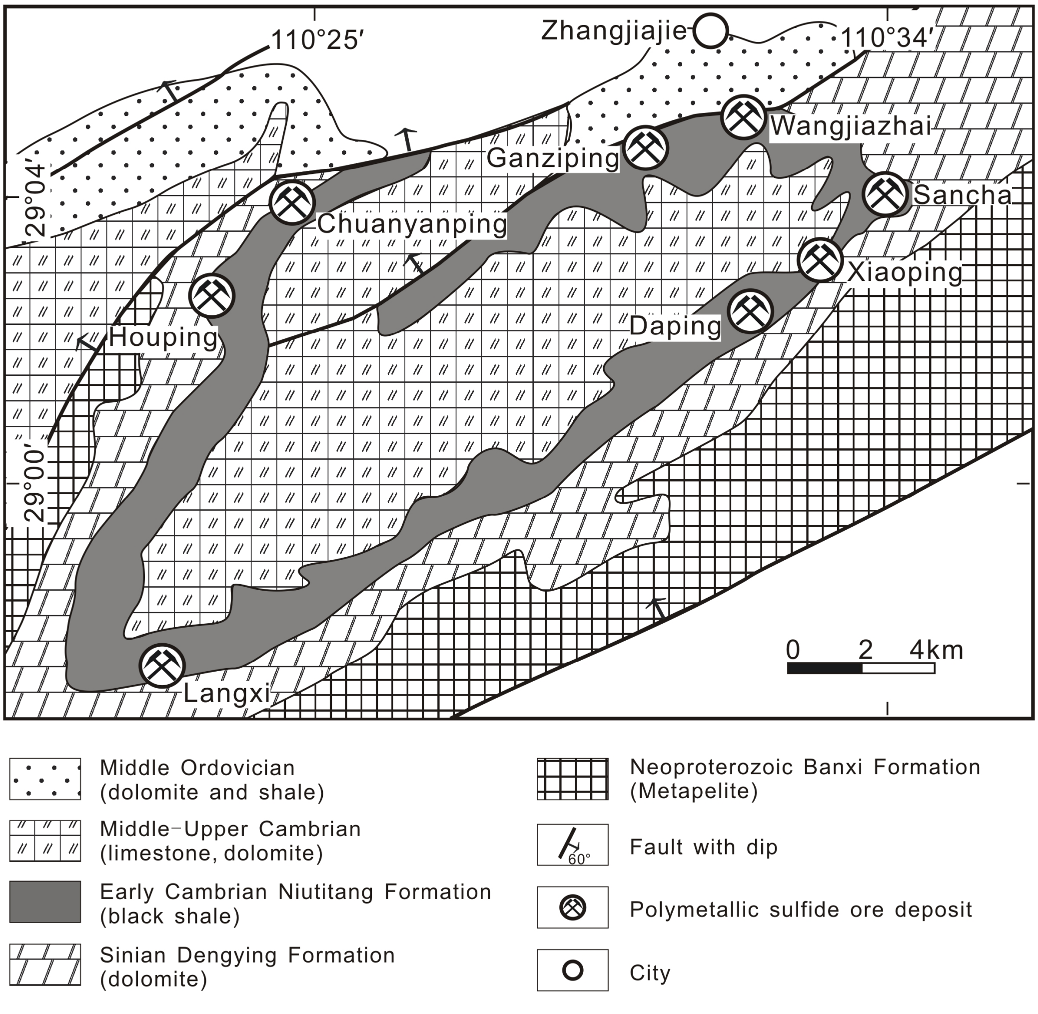

Fig. 3-4: Geological sketch map of the Sancha mine district near Zhangjiajie, Hunan (modified from Li et al., 2002). The Houping, Chuanyanping, Ganziping, Wangjiazhai, Sancha, Xiaoping and Daping are mined for Nickel and Molybdenum, whereas the Langxi is mined for vanadium.

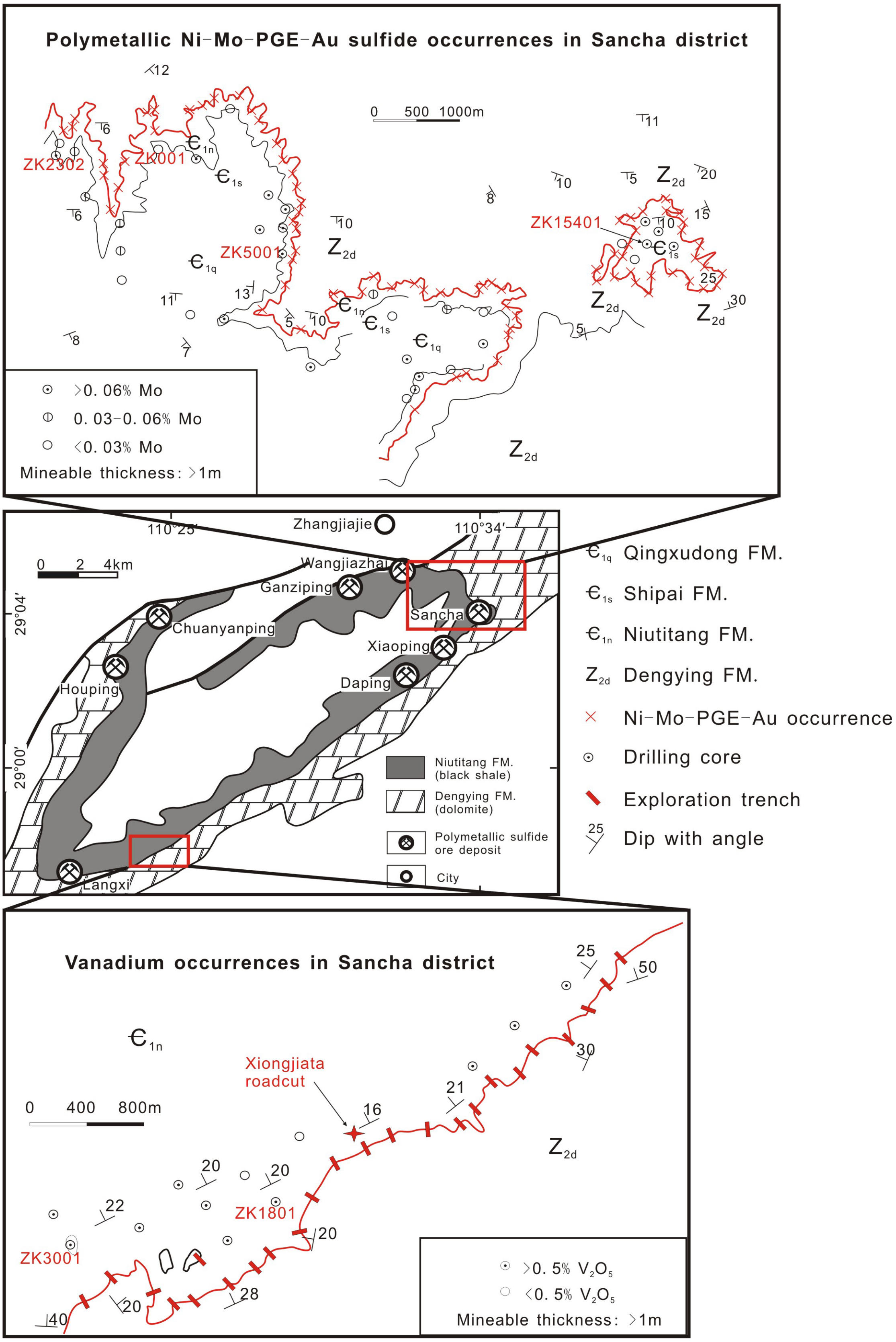

Fig. 3-5: Simplified geological map showing localities of drilling core and road-cut profiles. **Above:** red line indicates outcrop of the polymetallic Ni-Mo-PGE-Au sulfide ore layer, and red cross indicates active mine site of sulfide ore occurrence. **Below:** red line shows outcrop of vanadium bed.

3.1.4 Cili mine site

The Cili polymetallic Ni-Mo-PGE-Au sulfide deposit in Hunan province is ~70 km northeast of the Sancha mine site. As for the other known polymetallic Ni-Mo-PGE-Au mineralizations, the Cili ore deposit is hosted in the lowermost black shales of the Early Cambrian Niutitang Formation, which is underlain by the greyish dolomite of the Dengying Formation and overlain by the greyish-greenish shales with black shale interbeds of the Early Cambrian Balang Formation. From lowermost upwards, the Early Cambrian strata at the Cili mine site include Niutitang Formation, Balang Formation and Qingxudong Formation. The fossil-rich (*Arthricocephalus chauveaui, Changaspis sp., Pseudolancaslria sp., Balangia balangensis, Redlichia hupehensis, Yuehsienszella sp.,* and *Arlhricocephalus duyuensis*) Early Cambrian sedimentary rocks are overlain by Middle-Late Cambrian greyish shale and limestone (Regional Geology and Mineral Resource Report of Dayong Area, 1969[⊥]). The limbs of the synclinal structure are composed of Ordovician greenish limestone, dolomite and shale (Fig. 3-6). High angle NE-trending faults of post-Early Paleozoic age are widespread in the Cili district. The polymetallic sulfide ore layer in the Niutitang Formation is 0.5-3 m above the unconformity with the Dengying dolomite. Ni + Mo content of the polymetallic sulfide ore layer reaches up to 14 wt.%. Stone coal (combustible black shales) with high TOC content (up to 35 wt.%) is utilized as fuel by local people (Fig. 3-9 H). Nodular and massive phosphorite occurs between the sulfide layer and the Dengying dolomite contact. Thickness of the massive phosphorite bed varies from 0.3 to 0.5 m (maximum 1.35 m) with P_2O_5 grade of 10.6 – 33.4 wt.%, which makes this layer a target for widespread small-scale mining. The average Mo abundance of the phosphorite ranges from 0.28 to 0.50 wt.% (Regional Geology and Mineral Resource Report of Dayong Area, 1969[⊥]).

[⊥] Regional Geology and Mineral Resources Report of Dayong area, Hunan province. 1969. Scale: 1/200000. Compiled by the 5th Branch Team of Regional Geological Survey Bureau of Hunan province.

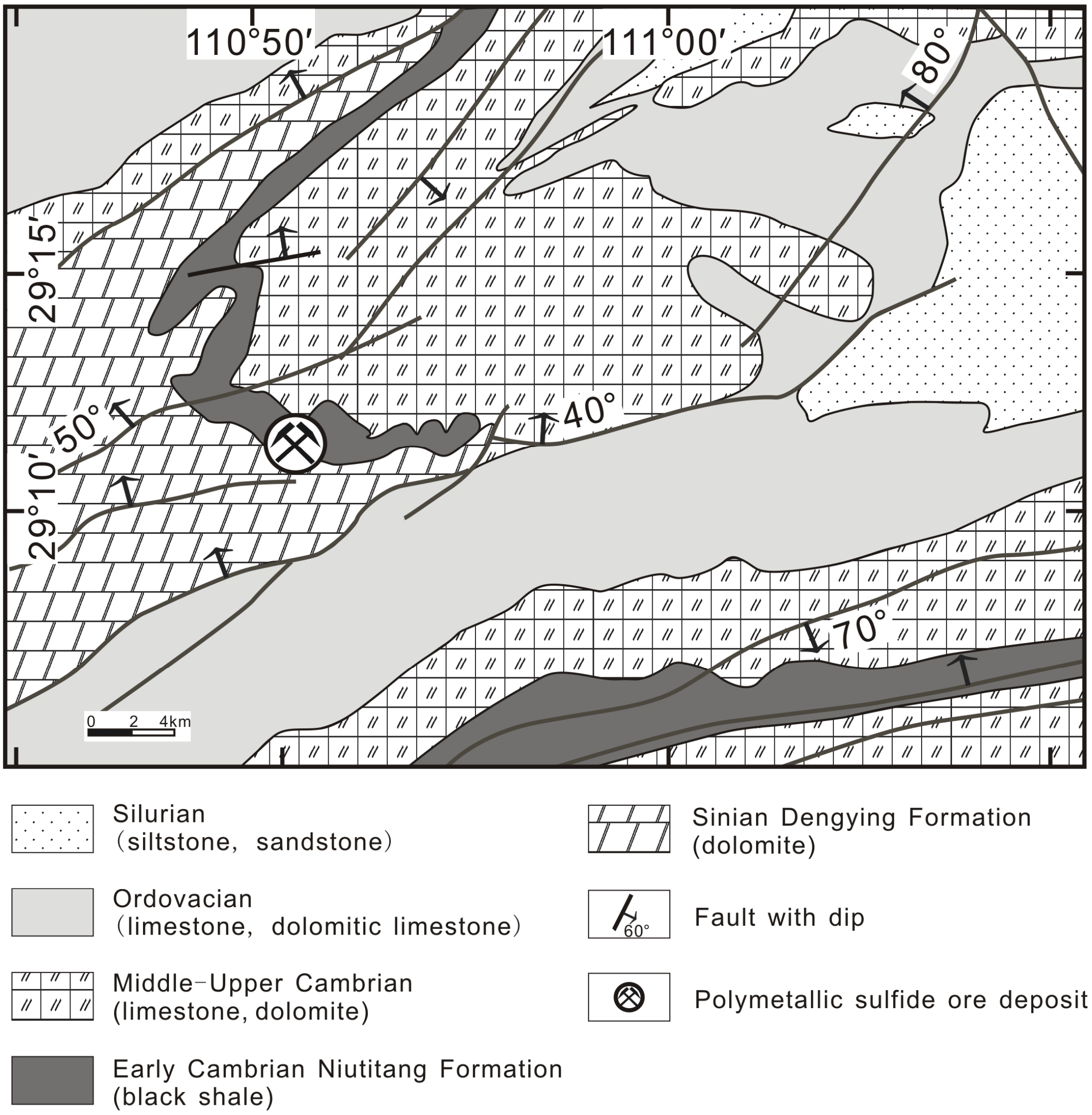

Fig. 3-6: Geological sketch map of the Cili polymetallic sulfide ore deposit in Hunan province [modified from 1/200000 Mineral Resource Geological Map of Dayong and Changde area, Hunan province. Compiled by the 5th Branch Team of Regional Geological Survey Bureau of Hunan province (present name: Bureau of Geology and Mineral Exploration and Development of Hunan Province)].

3.2 Geological features of the Dingtai profile

Investigation of high resolution geological profile has been applied widely to understand Earth evolution processes. The Dingtai profile is ~ 4 km southeast of the Dazhuiliushui mine site (Fig. 3-1), with geographic coordinates of N 27°42′48.9″ and E 106°38′58.2″. It is a well preserved profile consisting of the uppermost Sinian Dengying Formation, the Early Cambrian Niutitang Formation and the lowermost Early Cambrian Mingxisi Formation (Fig. 3-7). Due to the representative lithological components on the South margin of the Yangtze Platform, the Dingtai profile is an ideal place to investigate paleo-environment evolution during the PC/C interval.

According to recent sedimentological studies, the paleogeography of the Yangtze Platform from the Neoproterozoic to Early Cambrian can be divided into three zones from northwest to southeast: shallow-water settings of internal carbonate platform, transitional zones, and deep-water basins represented by black shales and cherts (Zhu et al., 2004). The Dingtai area is located on the internal carbonate platform, shelf of the southern Yangtze Platform, and connected to the deep-water basin during the Early Cambrian. The Dingtai profile is first time applied to investigate Early Cambrian paleo-environment evolution in South China. Except for the Dingtai profile, Shatan profile representing for a shallow carbonated platform setting, and Songtao, Sancha and Kunyang profiles representing for protected basinal sedimentary environments have been studied previously (see Fig. 6-2 in chapter six, Pan et al., 2004; Guo et al., 2007; Lehmann et al., 2007, Zhu et al., 2009). Because of strong weathering, the surface outcrops can be easily weathered and contaminated by detrital materials. Samples of the Dingtai profile were collected from unaltered outcrops by manual digging of channels and pits.

The Dingtai profile starts at the Dingying dolomite and ends at the Mingxisi greenish shales. Total thickness of the intermediate Niutitang Formation is 33 m. According to lithological investigation, Pi (2007) investigated a similar profile in the

Zhongnancun district (Fig. 3-1), which divided the Niutitang Formation into 10 units. In this study, however, based on field observation, only 5 stratigraphic units were distinguished because the minor differences between certain units are hard to detect by field observation. The lithology of the Dengying dolomite, 5 stratigraphic units of the black shale of the Niutitang Formation and the greenish shale of the Mingxisi Formation are described in ascending order as follows:

- **Dengying Formation dolomite:** Grayish massive dolomite with fracture zones. The contact zone with the black shales of the Niutitang Formation contains a thin weathering crust of detrital dolomite and black shale.
- **Unit 1:** Phosphorite layer. Thickness of unit 1 is 20 cm in the Dingtai profile. The phosphorite layer unconformably overlies dolomite of the Dengying Formation with a low angle (< 10°). Phosphorite occurs as nodules in variable size (1-10 cm) but is distributed regularly in this stratigraphic level. An equivalent unit containing small shelly fossils can reach up to decades of meters in thickness at Zhijin and Cili districts, where massive phosphorite mining is ongoing.
- **Unit 2:** Chert layer. The about 30 cm thick black chert intercalated with black shales. Small phosphorite nodules and organic debris are abundant in this unit.
- **Unit 3:** Polymetallic Ni-Mo-PGE-Au sulfide ore layer. This unit is only 4 cm thick, and consists of bitumen, pyrite, and silver-grey Mo and Ni sulfides. The polymetallic sulfide ore layer occurs as fine-grained laminated and intraformational polymictic pebble/clast units. The equivalent unit occurs in Hunan and Guizhou provinces of South China, making this layer a target for widespread small-scale mining.
- **Unit 4:** Black shale. Thickness of this unit is 10 m. Fossils, including sponge spicules and bivalved arthropods, have been found in the massive black shales.
- **Unit 5:** Silty black shale. The 21.3 m-thick silty black shale is overlain by the Mingxisi Formation greenish shales. Actually this unit has no distinct

boundary with the underlying unit black shale. Silty materials increase gradually upwards.

- **Mingxinsi Formation greenish shale:** This unit is dominant by greenish shale with thickness of 290 m. Fossils (eodiscid trilobite) are abundant in the Mingxinsi Formation (Steiner et al., 2001, 2007).

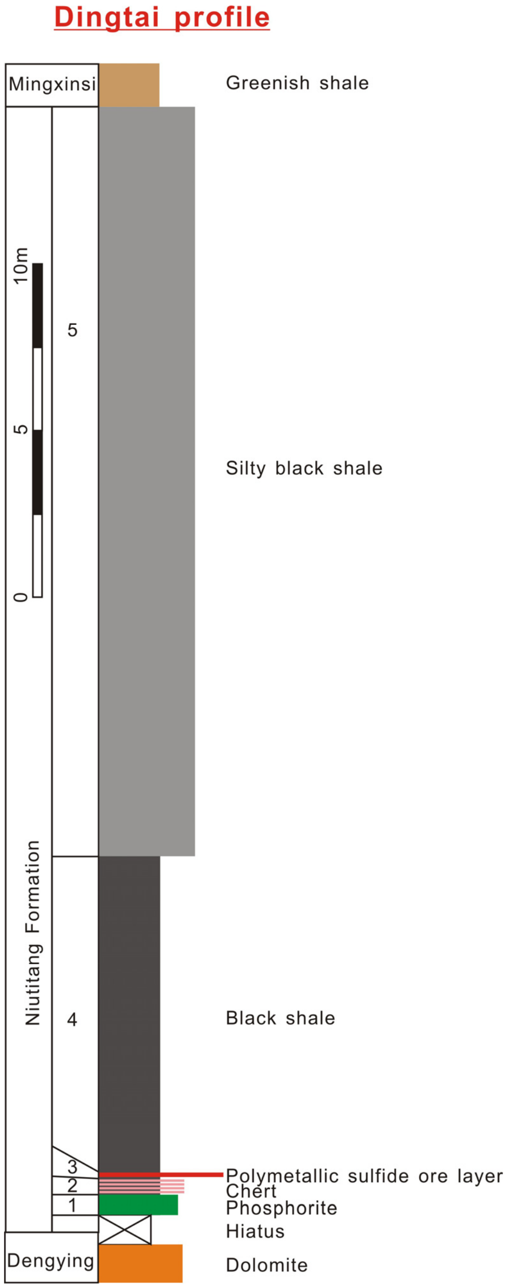

Fig. 3-7: Stratigraphic columns of the Dingtai profile near Zunyi, Guizhou province.

3.3 Petrology and Mineralogy

A total of 300 samples including dolomite, black shale, siltstone, sandstone, phosphorite, chert and polymetallic sulfide ore were collected from the four mine districts and the stratigraphic profile. They are carefully studied under the microscope. As described above, although some stratigraphic units may be absent in the profile and at some polymetallic mine sites, the correlation of different stratigraphic units at each mine site are strictly consistent. Petrology and mineralogy of the main rock types is described as follows:

Dolomite: The Dengying Formation dolomite is widespread exposed in the studied area. The greyish dolomite is massive, fine-grained, with anhedral to subhedral grain fabric (Fig. 3-9 A). Quartz occasionally occurs as clusters and veinlets.

Black shale: This is the dominant rock of the Niutitang Formation. The TOC and redox-sensitive metal contents (e.g. Mo, U and V) of the black shale sequence of the Niutitang Formation decrease from the lower part (up to 15 wt.% C and about 100 ppm Mo) upwards (3-9 wt.% C and about 10 ppm Mo) over a stratigraphic thickness of about 20-80 m (Steiner et al., 2001). The lower part of the Niutitang Formation is dominated by laminated black shales whereas, at the upper part, massive black shales are dominant (Fig. 3-9 C, D). At the lower part of the Niutitang Formation (Unit 4 equivalent), quartz and calcite occur as veinlets (Fig. 3-9B), which are scarcely observed at the upper part. Framboidal and anhedral pyrite grains occur in the black shales, and pyrite content decreases from the sulfide ore layer upwards. Laminated pyrite nodules at the lower part generally occur parallel with black shale stratification, indicating that pyrite is diagenetic (Fig. 3-8 B). Phosphorite nodules are common at the lowermost part of the Niutitang Formation. Bioclasts can be observed in phosphorus-rich debris (Fig 3-9 E, F).

Siltstone: The Mingxinsi and Jindingshan Formation consist of muddy, carbonaceous and siliceous siltstone, with greenish-yellowish color. The grain size of siltstone ranges from 0.004 to 0.06 mm. Quartz, feldspar, mica and debris are dominant minerals of siltstone. Clastic minerals take up to 70 vol.% of content. Pyrite is less than 1%.

Sandstone: Fine-grained sandstone is dominant at the upper part of the Mingxisi Formation and the lower part of Jindingshan Formation. It mainly consists of quartz, feldspar and siliceous debris. Pyrite content is less than 1%.

Stone coal (combustible black shales): In South China, the Early Cambrian is an important epoch of stone coal formation (sapropelic alginate). Stone coal is composed of organic matter and inorganic matters. Generally, the TOC content of stone coal is higher than black shale, reaching up to 35%. Self-ignition occasionally occurs due to high content of organic matter when a large volume of stone coal is accumulated (Fig. 3-8 H). Inorganic matter includes quartz, feldspar, calcite, clay minerals and pyrite. According to inorganic minerals, three types of stone coal can be distinguished: muddy stone coal, siliceous stone coal, and sandy stone coal.

Chert: At the lowermost part of the Niutitang Formation occurs a thin chert layer (average 0.4 m thick) with aphanitic siliceous matrix (70 vol.%), clay minerals (10 vol.%) and organic material (10 vol.%). Cherty breccias can be found at the contact zone of Dengying Formation dolomite and Niutitang Formation black shale (Fig. 3-8 E).

Phosphorite: The phosphorite layer occurs between the Dengying dolomite and the polymetallic sulfide ore layer. Thickness of the phosphorite layer is variable, ranging from several centimeters to decades of meters. Phosphorite occurs as nodules and massive ore. The phosphorite is mainly composed of clastic materials (70 vol.%) and matrix (30 vol.%). The clastic materials consist of organic debris and colloidal apatite, and the matrix is mainly fine-grained quartz, clay minerals, pyrite and limonite.

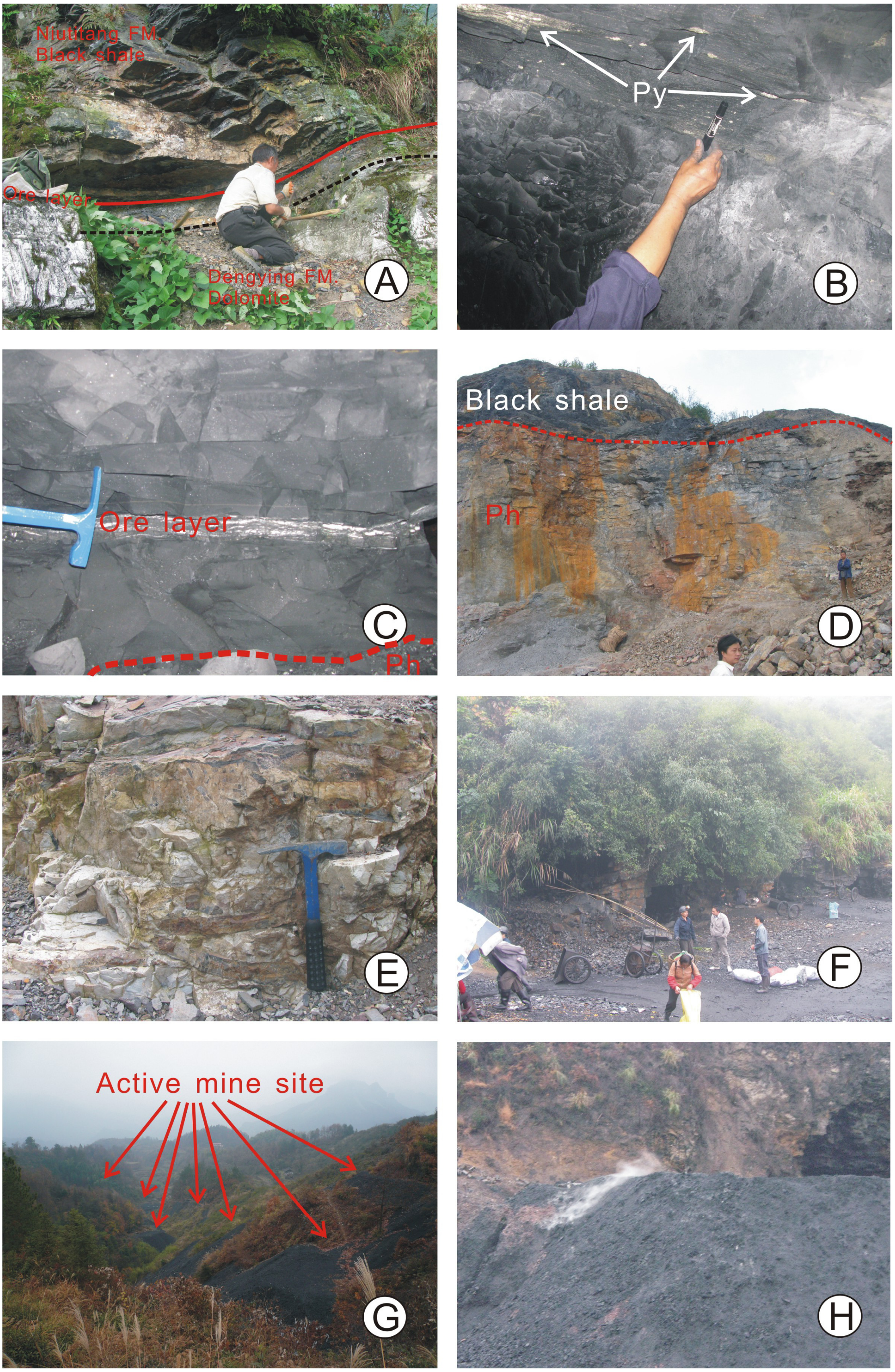
Niutitang FM.
Black shale
Ore layer
Dengying FM.
Dolomite
A
Py
B
Ore layer
Ph
C
Black shale
Ph
D
E
F
Active mine site
G
H

Fig. 3-8（continued）

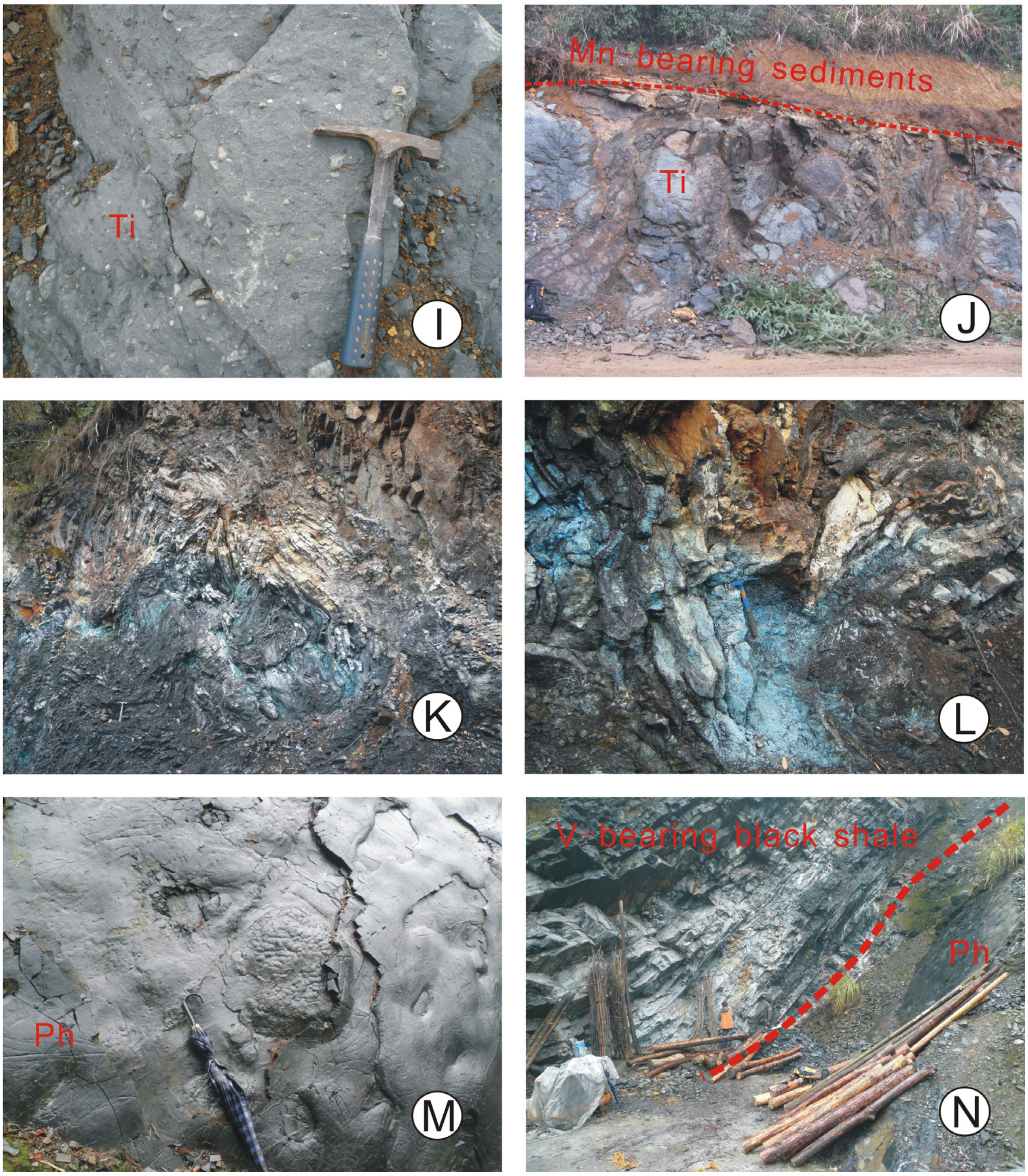

Fig. 3-8: Field photos of investigated polymetallic sulfide ore mine sites and profiles. **A:** The Ni-Mo-PGE-Au sulfide ore layer and PC/C boundary (black dashed line: contact to dolomite of Dengying Formation, photograph from Dingtai outcrop profile). **B:** Laminated pyrite nodules in the lower part of the black shale of the Niutitang Formation are generally parallel with the sedimentary stratification (photograph from Dazhuiliushui underground mine. **C:** The about 4 cm-thick sulfide ore layer showing a clear-cut boundary with the black shale host sequence (photograph from Dazhuliushui underground mine). **D:** Thick phosphorite layer overlain by Niutitang black shales (photograph from Zhijin phosphorite mine near the Maluhe district). **E:** Carbonaceous chert breccia in phosphorite and dolomite contact zone (photograph from Zhijin phosphorite mine near the Maluhe district). **F:** Small

scale mining caves for the polymetallic Ni-Mo-PGE-Au sulfide ore layer (photograph from Sancha district). **G:** An overview showing many active mine sites targeting for the polymetallic sulfide ore layer (photograph from Sancha district). **H:** Self-ignition of stone coal in tailings (photograph from Cili district). **I:** Nantuo Formation tillite (photograph from Xiongjiata vanadium deposit district, which is about 20 km southwest of the Sancha mine site). **J:** The Nantuo Formation tillite is overlain by Mn-bearing sediments (photograph from Xiongjiata vanadium deposit district). **K:** Strong corrugation in the chert, vanadium ore layer and black shales in Xiongjiata district (photograph from Xiongjiata vanadium deposit district). **L:** Malachite alteration in vanadium ore layer (photograph from Xiongjiata vanadium deposit district). **M:** Nodular phosphorite (photograph from Longbizui vanadium deposit, which is about 100 km southwest of the Sancha mine site). **N:** Chert and V-bearing black shale interbeds underlain by nodular phosphorite (photograph from Longbizui vanadium deposit). Abbreviations: Ti = tillite, Ph = phosphorite.

The Ni-Mo ore occurs within the lowermost few meters of the Niutitang Formation as both fine laminations and as a debris layer (Fig. 3-9 I, J), consisting largely of a MoSC phase (with the approximate composition of [$(Mo,Fe,Ni)(S,As)_2C_7$], pyrite, vaesite, bravoite, millerite, gersdorffite and jordisite, with minor arsenopyrite, chalcopyrite, covellite, sphalerite, tennantite, tiemannite, violarite and native Au (Fig. 3-9 , Conveney et al., 1994; Kao et al., 2001; Mao et al., 2002; Jiang et al., 2006). The amorphous MoSC phase (about 20 vol.%) is the only important Mo-carrier, in mm-sized ellipsoidal aggregates or fine laminations (Fig. 3-9). Rip-up clasts of MoSC phase aggregates are set in in-situ precipitated organic matter and Ni-bearing minerals (Fig. 3-9). Sapropel material (about 45 vol.%) occurs as matrix, and consists of organic matter, fine-grained illite, sericite, quartz, calcite, barite, and locally abundant apatite and collophane (Fig. 3-9 G, H). The organic matter is derived from in-situ sapropelized products of planktonic and benthic organisms, oncolite-like algal/bacterial remnants, and oil-derived migrabitumen, and has a high thermal maturity corresponding to the semi-anthracite to anthracite coalification stage (Kribek et al. 2007). Pyrite (about 25 vol.%) is intergrown with the MoSC phase in oncolite-like aggregates, and is cut by veinlets with nickel sulfides (about 5 vol.%, millerite, gersdorffite). Sedimentary features such as fine lamination and rip-up clasts and oncolites of pyrite and Ni-Mo sulfide ore indicate an origin as deeper-water hardground supplied with organic material from algal mats from a wave-agitated, shallow-water environment (Kribek et al., 2007).

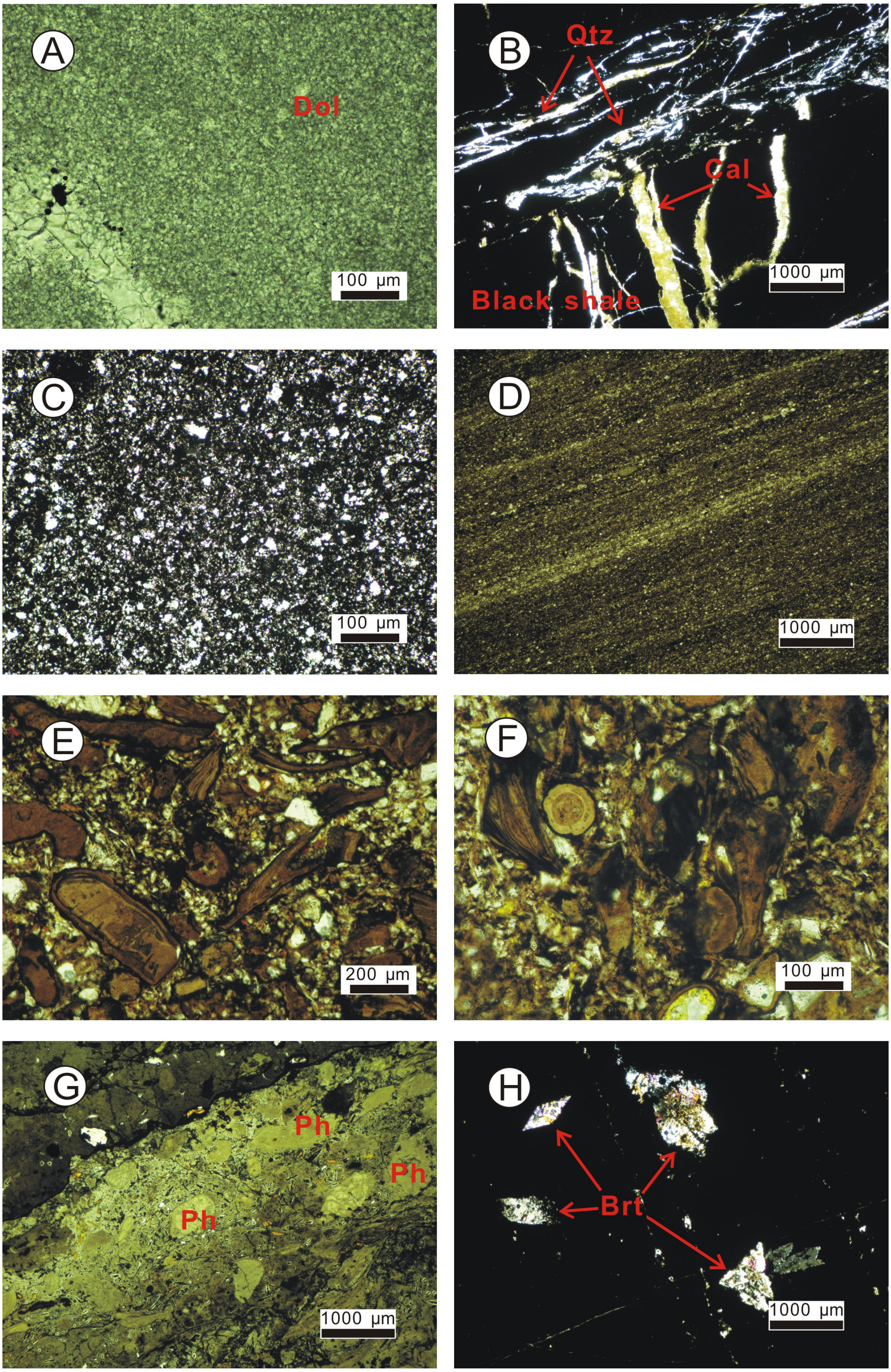
A
Dol
100 μm
B
Qtz
Cal
1000 μm
Black shale
C
100 μm
D
1000 μm
E
200 μm
F
100 μm
G
Ph
Ph
Ph
1000 μm
H
Brt
1000 μm

Fig. 3-9（continued）

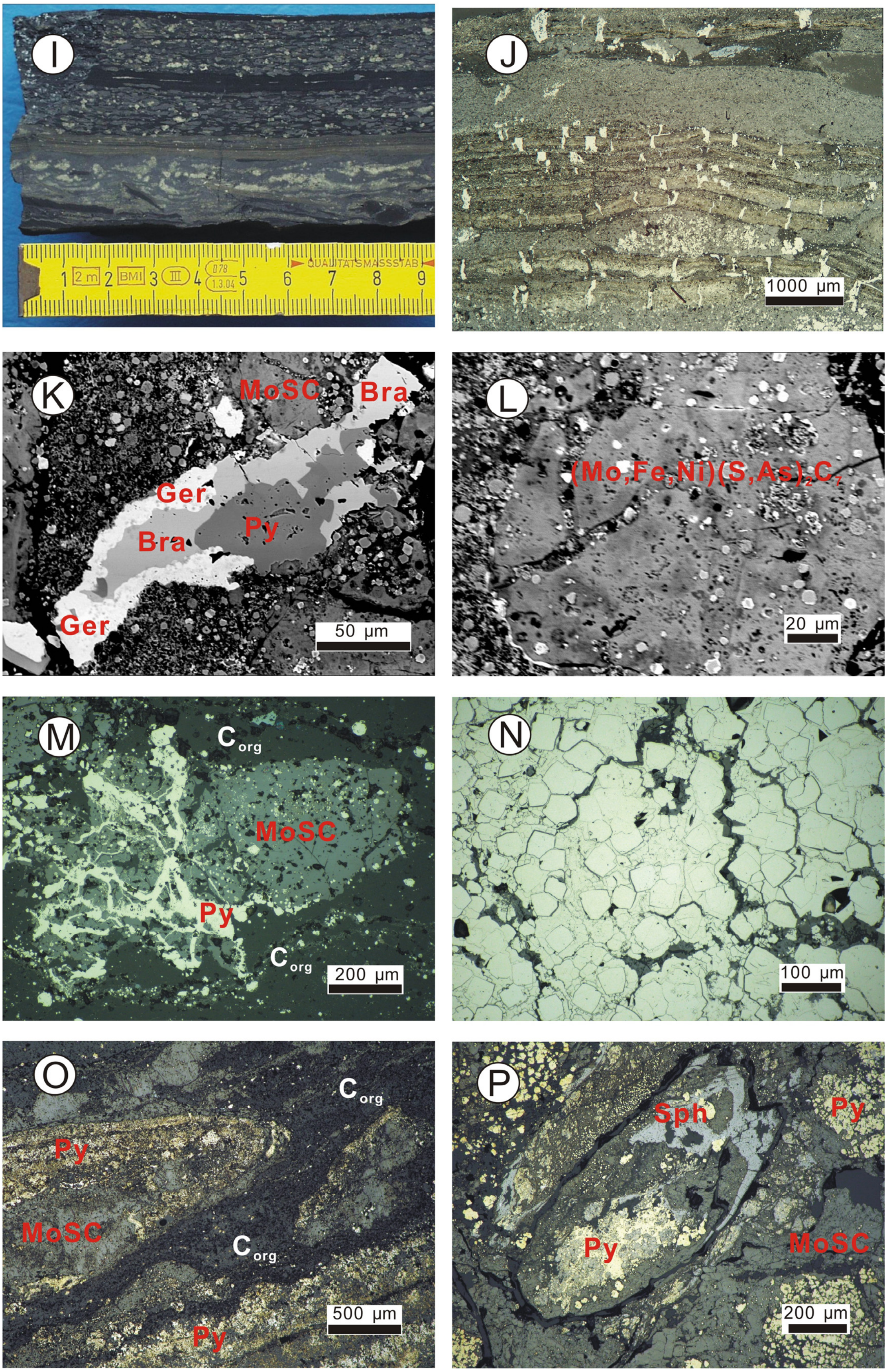

Fig. 3-9（continued）

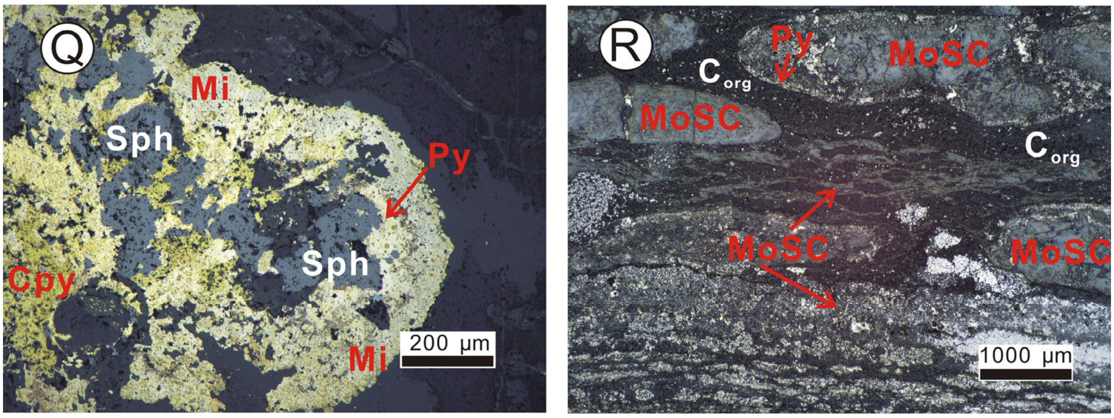

Fig. 3-9: Microphotographs of polished thin sections and hand specimen photographs of the polymetallic Ni-Mo-PGE-Au sulfide ores, black shales and dolomite. **A:** Fine-grained Dengying Formation dolomite (sample from Dingtai profile, transmitted light/crossed polars). **B:** Thin quartz and calcite veinlets in Niutitang Formation black shales (sample from Xiongjiata road-cut profile, transmitted/plane-polarized light). **C:** The Niutitang Formation non-mineralized black shales showing massive texture (sample from Dazhuliushui underground mine site, transmitted/plane-polarized light). **D:** The Niutitang Formation non-mineralized black shales showing laminated texture (transmitted/plane-polarized light). **E** and **F:** Microphotographic images showing abundant fossils in the lower part of the Niutitang Formation black shales (transmitted/plane-polarized light). **G:** Microphotographic image of phosphorus-rich material with bioclasts (sample from Dingtai profile, transmitted/plane-polarized light). **H:** Euhedral barite as gangue mineral in black shales (sample from Longbizui V deposit, transmitted light/crossed polars). **I:** Hand specimen of polymetallic sulfide ore showing thin thickness of the ore layer and laminated texture (sample from Huangjiawan underground mine, 10 km southeast of Dazhuliushui mine site). **J:** Microphotograph of the sulfide ore showing laminated texture and pyrite crystals (sample from Huangjiawan underground mine, reflected light/crossed polars). **K:** Backscattered electron (BSE) image of sulfide ore showing MoSC phase, bravoite and gersdorffite minerals (20 kV). **L:** BSE image of the MoSC phase (15 kv, 20 nA). **M:** Pyrite veinlets intergrown with MoSC phase surrounded by organic matters (samples from Sancha underground mine, reflected light/crossed polars). **N:** Euhedral pyrite crystals surrounded by recrystallized anhedral pyrite (Sample from Sancha underground mine, reflected light/crossed polars). **O:** Fine-grained pyrite in rim zones of colloidal MoSC phase nodules (samples from Sancha underground mine, reflected light/crossed polars). **P:** Framboidal pyrite and sphalerite intergrown with MoSC phase (samples from Cili underground mine, reflected light/crossed polars). **Q:** Sphalerite, chalcopyrite, milerite intergrown with anhedral pyrite (samples from Sancha underground mine, reflected light/crossed polars). **R:** Laminated and ellipsoidal MoSC phase with fine-grained pyrite intergrowths at

the rims, surrounded by sapropel matrix. Re-deposited aggregates showing rip-up clasts and in-situ precipitated organic matters (samples from Sancha underground mine, reflected light/crossed polars). **Abbreviations:** Bra = bravoite, Brt = barite, Cal = calcite, C_{org} = organic carbonaceous material, Cpy = chalcopyrite, Dol = dolomite, Ger = gersdorffite, Mi = millerite, Ph = phosphate, Py = pyrite, Qtz = quartz, Sph = sphalerite.

3.4 References

Barfod, G.H., Albarède, F., Knoll, A.H., Xiao, S.H., Telouk, P., Frei, R., Baker, J., 2002. New Lu-Hf and Pb-Pb age constraints on the earliest animal fossils. Earth and Planetary Science Letters 201, 203-212.

Bushinshi, G.I., 1966. Old phosphorites of Asia and their genesis (translated from Russian). Israel Program for Scientific Translations, Jerusalem, 266 p.

Chen, D.F., Dong, W.Q., Zhu, B.Q., Chen, X.P., 2004. Pb-Pb ages of Neoproterozoic Doushantuo phosphorites in South China: constraints on early metazoan evolution and glaciation events. Precambrian Research 132, 123-132.

Chen, N.S., Yang, X., Liu, D., Xiao, X., Fan, D.L., Wang, L., 1982. Lower Cambrian black argillaceous and arenaceous rock series in south China and its associated stratiform deposits. Mineral Deposits 1, 39-51 (in Chinese).

Condon, D., Zhu, M.Y., Bowring, S., Wang, W., Yang, A.H., Jin, Y.G., 2005. U-Pb ages from the neoproterozoic Doushantuo Formation, China. Science 308, 95-98.

Conveney Jr., R.M., Grauch, R.I., Murowchick, J.B., 1994. Metals, phosphate, and stone coal in the Proterozoic and Cambrian of China: The geolocial setting of precious metal-bearing Ni-Mo ore beds. Society of Economic Geologists Newsletter 18, 1 and 6-11.

Cunningham, C.G., Ashley, R.P., Chou, I.M., Huang, Z.S., Wan, C.Y., Li, W.K., 1988.

Newly discovered sedimentary rock-hosted disseminated gold deposits in the People`s Republic of China. Economic Geology 83, 1462-1467.

Fan, D., Yang, R.Y., Huang, Z.X., 1984. The Lower Cambrian black shales series and the iridium anomaly in south China. Developments in Geoscience, 27th International Geological Congress, Moscow. Beijing: Science Press, 215-225.

Fan, D.L., 1983. Polyelements in the Lower Cambrian black shale series in southern China, in Augustithis, S.S., ed., The significance of trace metals in solving petrogenetic problems and controversies. Theophrastus Publications, S.A., Athens, 447-474.

Fan, D.L., Liu, T.B., Ye, J., 1992. The process of formation of manganese carbonate deposits hosted in black shale series. Economic Geology 87, 1419-1429.

Goldberg, T., Mazumdar, A., Strauss, H., Shields, G., 2006. Insights from stable S and O isotopes into biogeochemical processes and genesis of Lower Cambrian barite-pyrite concretions of South China. Organic Geochemistry 37, 1278-1288.

Guo, Q.J., Shields, G.A., Liu, C.Q., Strauss, H., Zhu, M.Y., Pi, D.H., Goldberg, T., Yang, X.L., 2007. Trace element chemostratigraphy of two Ediacaran-Cambrian successions in South China: Implications for organosedimentary metal enrichment and silicification in the early Cambrian. Palaeogeography Palaeoclimatology Palaeoecology 254, 194-216.

Jiang, S.Y., Chen, Y.Q., Ling, H.F., Yang, J.H., Feng, H.Z., Ni, P., 2006. Trace- and rare-earth element geochemistry and Pb-Pb dating of black shales and intercalated Ni-Mo-PGE-Au sulfide ores in Lower Cambrian strata, Yangtze Platform, South China. Mineralium Deposita 41, 453-467.

Jiang, S.Y., Pi, D.H., Heubeck, C., Frimmel, H., Liu, Y.P., Deng, H.L., Ling, H.F., Yang, J.H., 2009. Early Cambrian ocean anoxia in South China. Nature 459, E5-E6.

Jiang, S.Y., Yang, J.H., Ling, H.F., Chen, Y.Q., Feng, H.Z., Zhao, K.D., Ni, P., 2007.

Extreme enrichment of polymetallic Ni-Mo-PGE-Au in lower Cambrian black shales of South China: An Os isotope and PGE geochemical investigation. Palaeogeography, Palaeoclimotology, Palaeoecology 254, 217-228.

Kao, L.S., Peacor, D.R., Coveney Jr., R.M., Zhao, G.M., Dungey, K.E., Curtis, M.D., Penner-Hahn, J.E., 2001. A C/MoS_2 mixed-layer phase (MoSC) occurring in metalliferous black shales from southern China, and new data on jordisite. American Mineralogist 86, 852-861.

Kribek, B., Sýkorová, I., Pasava, J., Machovic, V., 2007. Organic geochemistry and petrology of barren and Mo-Ni-PGE mineralized marine black shales of the Lower Cambrian Niutitang Formation (South China). International Journal of Coal Geology 72, 240-256.

Lehmann, B., Mao, J.W., Li, S.R., Zhang, G.D., 2003. Re-Os dating of polymetallic Ni-Mo-PGE-Au mineralization in lower Cambrian black shales of south China and its geological significance - A reply. Economic Geology 98, 663-665.

Lehmann, B., Nägler, T.F., Holland, H.D., Wille, M., Mao, J.W., Pan, J.Y., Ma, D.S., Dulski, P., 2007. Highly metalliferous carbonaceous shale and Early Cambrian seawater. Geology 35, 403-406.

Li, S.Y., Xiao, Q. Y., Shen, J.F., Sun, L., Liu, B., Yan, B.K., 2002. Source of Lower Cambrian platinum group elements in black shales in Hunan and Guizhou provinces, China and the Re-Os isotope dating. Science China (Series D) 32, 568-575 (in Chinese).

Liao, S.F., Wang, Y.G., Zhou, M.J., Wang, Q.S., 1988. Permian manganese ore deposits, Carbonaceous bauxite ore deposits, Sinian phosphorite deposits and related sedimentary facies in the Guizhou Province. Guidebook B2, International Association of Sedimentologists Symposium on Sedimentary Related to Mineral Deposits, Beijing, 20.

Mao, J.W., Lehmann, B., Du, A.D., Zhang, G.D., Ma, D.S., Wang, Y.T., Zeng, M.G., Kerrich, R., 2002. Re-Os dating of polymetallic Ni-Mo-PGE-Au mineralization in Lower Cambrian black shales of south China and its geologic significance. Economic Geology 97, 1051-1061.

Maynard, J.B., Okita, P.M., 1991. Bedded barite deposits in the United States, Canada, Germany, and China. Economic Geology 86, 364-376.

Pan, J.Y., Ma, D.S., Cao, S.L., 2004. Trace element geochemistry of the Lower Cambrian black rock series from northwestern Hunan, South China. Progress in Natural Science 85-91.

Peters, S.G., Huang, J.Z., Li, Z.P.Jing, C.G., 2007. Sedimentary rock-hosted Au deposits of the Dian-Qian-Gui area, Guizhou, and Yunnan Provinces, and Guangxi District, China. Ore Geology Reviews 31, 170-204.

Pi, D.H., 2007. Geochemistry investigation of the Early Cambrian black shales in Zunyi, Guizhou provence. Ph.D thesis, 1-121 (in Chinese with English abstract).

Steiner, M., Li, G.X., Qian, Y., Zhu, M.Y., Erdtmann, B.D., 2007. Neoproterozoic to early Cambrian small shelly fossil assemblages and a revised biostratigraphic correlation of the Yangtze Platform (China). Palaeogeography Palaeoclimatology Palaeoecology 254, 67-99.

Steiner, M., Wallis, E., Erdtmann, B.D., Zhao, Y.L., Yang, R.D., 2001. Submarine hydrothermal exhalative ore layers in black shales from South China and associated fossils: insights into a Lower Cambrian facies and bio-evolution. Palaeogeography Palaeoclimatology Palaeoecology 169, 165-191.

Su, W.C., Hu, R.Z., Xia, B., Xia, Y., Liu, Y.P., 2009. Calcite Sm-Nd isochron age of the Shuiyindong Carlin-type gold deposit, Guizhou, China. Chemical Geology 258, 269-274.

Su, W.C., Xia, B., Zhang, H.T., Zhang, X.C., Hu, R.Z., 2008. Visible gold in arsenian pyrite at the Shuiyindong Carlin-type gold deposit, Guizhou, China: Implications for the environment and processes of ore formation. Ore Geology Reviews 33,

667-679.

Wang, M., Sun, X.M., Ma, M.Y., 2004. Rare earth elements geochemistry and genesis of Xinhua large-size phosphorite deposit in western Guizhou. Mineral Deposits 23, 484-493 (in Chinese with English abstract).

Wang, S.H., Guo, W.L., Li, P.G. Zhong, C., 2006. Reconnaissance report of the Dazhuliushui Ni-Mo deposits in Songlin, Guizhou province. 106 Geological Team of Bureau of Geology and Mineral Exploration and Development of Guizhou Province, 1-29 (in Chinese).

Wang, Z.G., Li, G.Z., 1991. Barite and witherite deposits in Lower Cambrian shales of south China: Stratigraphic distribution and geochemical characterization. Economic Geology 86, 354-363.

Xia, F., Ma, D.S., Pan, J.Y., Sun, Z.X., Cao, S.L., Nie, W.M., Wu, K., 2004. Hydrothermal exhalative genesis of the Tianzhu and Yuping barite deposits in the Guizhou province: Evidence from Sr isotope. Science Bulletin 24, 2592-2595 (in Chinese).

Xu, L.G., Lehmann, B., Mao, J.W., Qu, W.J., Du, A.D., 2011. Re-Os age of polymetallic Ni-Mo-PGE-Au mineralization in Early Cambrian black shales of South China – A reassessment. Economic Geology, in press.

Yang, R.D., Wei, H.R., Bao, M., Wang, W., Wang, Q., Zhang, X.D., Liu, L., 2008. Discovery of hydrothermal venting community at the base of Cambrian barite in Guizhou Province, Western China: Implication for the Cambrian biological explosion. Progress in Natural Science 18, 65-70.

Ye., L.J., Chen, Q.Y., Zhao, D.X., 1989. Phosphorite in China. Beijing: Scientific Publishing House, 1-339 (in Chinese).

Yin, C.Y., Tang, F., Liu, Y.Q., Gao, L.Z., Liu, P.J., Xing, Y.S., Yang, Z.Q., Wan, Y.S., Wang, Z.Q., 2005. U-Pb zircon age from the base of the Ediacaran Doushantuo Formation in the Yangtze Gorges, South China: constraint on the age of Marinoan glaciation. Episodes 28, 48-49.

Zeng, M.G., 1998. Geological characteristics of the Huangjiawan Mo-Ni deposit and its development in the future. Guizhou Geology 15, 305-310 (in Chinese).

Zhang, A.Y., Wu. D.M., Guo, L.N., Wang, Y.L., 1987. The geochemical of Marine black shale formation and its metallogenic significance. Beijing: Scientific Publishing House, 1-240 (in Chinese).

Zhang, S.H., Jiang, G.Q., Zhang, J.M., Song, B., Kennedy, M.J., Christie-Blick, N., 2005. U-Pb sensitive high-resolution ion microprobe ages from the Doushantuo Formation in south China: Constraints on late Neoproterozoic glaciations. Geology 33, 473-476.

Zhu, M.Y., Zhang, J.M., Steiner, M., Yang, A.H., Li, G.X., Erdtmann, B.D., 2004. Sinian-Cambrian stratigraphic framework for shallow- to deep-water environments of the Yangtze Platform: An integrated approach. Progress in Natural Science (Special Issue 2004), 75-84.

Zhu, R.X., Li, X.H., Hou, X.G., Pan, Y.X., Wang, F., Deng, C.L., He, H.Y., 2009. SIMS U-Pb zircon age of a tuff layer in the Meishucun section, Yunnan, southwest China: Constraint on the age of the Precambrian-Cambrian boundary. Science in China Series D-Earth Sciences 52, 1385-1392.

CHAPTER FOUR:

Re-Os AGE OF POLYMETALLIC Ni-Mo-PGE-Au MINERALIZATION IN EARLY CAMBRIAN BLACK SHALES OF SOUTH CHINA — A REASSESSMENT

Xu Lingang[1*], Bernd Lehmann[1], Mao Jingwen[2], Qu Wenjun[3], Du Andao[3]

[1] *Mineral Resources, Technical University of Clausthal, 38678 Clausthal-Zellerfeld, Germany*

[2] *MLR Key Laboratory of Metallogeny and Mineral Assessment, Institute of Mineral Resources, China Academy of Geological Sciences, Beijing 100037, China*

[3] *National Research Center of Geoanalysis, Beijing 100037, China*

*Corresponding author: e-mail, lingang.xu@ tu-clausthal.de

Published in ***Economic Geology***, 2011, v. 106, p. 511-522.

4.1 Abstract

The Early Cambrian Niutitang Formation in South China consists of a black shale sequence with a synsedimentary organic carbon-rich polymetallic sulfide layer with extreme metal enrichment locally mined as Ni-Mo-PGE-Au ore. We report a new composite Re-Os isochron age of the sulfide ore layer of 521 ± 5 Ma (n = 14) from three mine sites (Dazhuliushui and Maluhe in the Guizhou, and Sancha in the Hunan province, respectively) several hundred kilometers apart. This age corresponds to the biostratigraphic Tommotian age, and is in agreement with recent interpolated Pb-Pb and SHRIMP zircon U-Pb ages from an underlying tuff unit. The initial $^{187}Os/^{188}Os$ value of the sulfide ore is 0.87 ± 0.07, which is equal to the initial $^{187}Os/^{188}Os$ ratio of ~0.80 of the black shale host rock, consistent with the seawater origin of the metals under depositional conditions of very low clastic input.

4.2 Introduction

The Precambrian/Cambrian (PC/C) transition represents a critical interval in Earth history characterized by global environmental and biological changes, such as major plate tectonic reconfiguration, ocean anoxia, mass extinction and accelerated diversification of metazoans (Brasier, 1992; Kaufman et al., 1993; Kirschvink et al., 1997; Shu et al., 2001). A possibly global ocean anoxia event is reflected by widespread black shale deposition in the Early Cambrian (Banerjee et al., 1997; Kimura and Watanabe, 2001; Schröder and Grotzinger, 2007). In South China, the transgressive Early Cambrian black shale sequence of the Niutitang Formation (and equivalent strata) occurs in a 1600 km-long belt that extends across the Yangtze Platform (Zhu et al., 2004), unconformably overlying dolomite of the Neoproterozoic Dengying Formation. The black shale sequence is enriched in a broad spectrum of redox-sensitive metals, i.e. Mo, Ni, Cr, V, PGE, Au, and U, typical of black shales in general (Vine and Tourtelot, 1970; Holland, 1979). However, an unusual organic carbon-, phosphate- and sulfide-rich layer is locally distributed in the lowermost part of the black shale sequence of South China (<10 m above the PC/C boundary). This sulfide-rich layer is only several centimeters thick, but it shows extreme metal enrichment (Table 4-1). Ni + Mo reach up to 14 wt.%, and platinum group element (PGE) + Au concentrations are around 1g/t (Fan et al., 1984; Coveney et al., 1994; Lehmann et al., 2007) which makes this layer a target for widespread small-scale mining in the Hunan and Guizhou provinces of South China. The minor elements Se, Re, Os, As, Hg, and Sb display $>10^4$-fold enrichment compared to average upper continental crust (Fan et al., 1984; Conveney et al., 1994; Lehmann et al. 2007). Determining a precise age and origin of the sulfide-rich black shale layer allows a better understanding of how this metal enrichment may or may not have been linked to global anoxia at the PC/C boundary.

The sulfide ore layer was repeatedly dated using the Re-Os method and yielded isochron ages of 560 ± 50 Ma (Horan et al., 1994), 542 ± 11 Ma (Li et al., 2002) and 541 ± 16 Ma (Mao et al., 2002). Pb-Pb dating of black shale and Ni-Mo-PGE-Au sulfide ores from the Niutitang Formation yielded an isochron age of 531 ± 24 Ma and 521 ± 54 Ma, respectively (Jiang et al., 2006). Recently, Jiang et al. (2009) reported a SHRIMP U-Pb zircon age of 532.3 ± 0.7 Ma for a volcanic ash bed a few meters beneath the sulfide ore layer near Zunyi, Guizhou province, suggesting that the mineralization age of the sulfide ore layer must be younger than 532 Ma, which is in contrast with the previously reported Re-Os ages.

We present new Re-Os isotope data from three mine sites in the Hunan and Guizhou provinces (Fig. 4-1), which are based on more samples and on a broader range of localities than in previous studies, and which both refine the mineralization age and further constrain the metal enrichment mechanism of the sulfide ore. Our findings confirm the claim by Jiang et al. (2009) that the sulfide ore layer does not mark the PC/C transition, but is about 20 Ma younger. Therefore, global correlations with the oceanic and biological evolution at the PC/C boundary are not possible. However, the sulfide ore layer documents a regional euxinic event on the Yangtze Platform during major plate reconfiguration in the Early Cambrian. This event produced a unique metallogenic footprint with spectacular metal enrichment.

Table 4-1: Major and trace elements for Ni-Mo-PGE-Au sulfide ore samples from Dazhuliushui, Sancha and Maluhe mine sites.

Deposit	Sample	SiO_2	TiO_2	Al_2O_3	FeS_2	MnO	MgO	CaO	Na_2O	K_2O	P_2O_5	Cl	F	MoS_2C_7	NiS	ZnS	AsS	Sum
		%	%	%	%	%	%	%	%	%	%	%	%	%	%	%	%	%
Dazhuliushui	DZLS-2	8.73	0.072	1.29	24.9	0.127	2.89	15.1	0.090	0.249	0.848	0.039	<0.05	18.6	9.68	0.516	1.39	84.6
	DZLS-5	7.88	0.067	1.35	32.1	0.087	3.29	9.75	0.110	0.181	1.11	0.049	<0.05	23.6	5.37	0.534	0.206	85.7
	DZLS-8	6.31	0.062	1.30	36.9	0.102	3.02	9.08	0.060	0.214	0.236	0.034	<0.05	16.0	9.26	0.656	1.18	84.4
	DZLS-11	7.22	0.052	0.88	31.4	0.126	2.76	15.8	0.070	0.180	1.80	0.033	<0.05	14.6	7.11	0.447	1.26	83.7
	DZLS-14	12.4	0.180	3.55	20.9	0.193	4.00	21.4	0.260	0.763	1.65	0.023	<0.05	9.24	4.71	0.656	0.605	80.6
	DZLS-17	11.1	0.110	1.93	24.4	0.131	1.61	18.2	0.210	0.377	0.433	0.034	<0.05	14.9	6.06	0.708	1.06	81.2
Sancha	SC-2	29.1	0.065	1.20	28.0	<0.001	0.310	3.51	0.040	0.395	1.98	0.032	<0.05	14.3	9.49	0.661	1.31	90.4
	SC-5	20.7	0.061	1.37	13.3	0.018	0.620	23.4	0.020	0.420	9.16	0.016	0.500	0.840	9.09	0.227	2.38	82.1
	SC-8	22.4	0.052	1.10	10.9	0.012	1.19	24.2	0.070	0.319	16.3	0.019	0.850	4.46	4.28	0.124	1.15	87.5
	SC-11	16.6	0.064	1.32	25.2	<0.001	0.310	12.1	0.060	0.463	5.48	0.041	0.160	16.7	4.61	0.575	0.360	84.1
	SC-14	21.7	0.041	0.89	33.6	0.002	0.270	7.53	0.040	0.301	3.85	0.027	<0.05	13.1	7.28	0.077	0.895	89.6
Maluhe	MLH-2	17.4	0.185	3.26	41.3	0.006	0.300	0.994	<0.01	0.939	0.638	0.033	<0.05	15.7	5.82	3.16	0.319	90.0
	MLH-5	13.1	0.093	1.71	47.0	0.008	0.200	0.816	<0.01	0.509	0.506	0.038	<0.05	18.0	5.59	3.92	0.186	91.7
	MLH-8	18.4	0.169	2.90	35.5	<0.001	0.290	2.75	<0.01	0.834	1.87	0.037	<0.05	16.8	6.30	2.69	0.256	88.8
	MLH-10	10.5	0.095	1.70	47.0	<0.001	0.170	1.05	<0.01	0.483	0.702	0.037	<0.05	17.0	6.57	4.36	0.138	89.8
	MLH-11	9.73	0.081	1.50	48.1	0.006	0.170	1.20	<0.01	0.405	0.804	0.033	<0.05	15.5	7.02	4.35	0.157	89.1
	MLH-12	17.1	0.225	3.96	42.2	<0.001	0.370	1.18	<0.01	1.15	0.776	0.034	<0.05	16.5	4.42	1.91	0.119	90.0

Deposit	Sample	As	Ba	Bi	Co	Cr	Cu	Mo	Ni	Pb	Rb	Sb	Sr	U	V	Y	Zn
		ppm	ppm	ppm	ppm	ppm	ppm	ppm	ppm	ppm	ppm	ppm	ppm	ppm	ppm	ppm	ppm
Dazhuliushui	DZLS-2	9750	391	19	273	53	2450	73100	62800	183	29	257	342	125	658	34.9	3460
	DZLS-5	1440	332	12	136	51	1680	92800	34800	74	17	104	341	318	724	28.9	3580
	DZLS-8	8250	680	22	220	55	2740	62800	60100	117	25	214	282	114	644	106	4400
	DZLS-11	8820	324	16	151	34	2330	57600	46100	182	25	251	528	255	486	24.9	3000
	DZLS-14	4240	520	14	116	51	1510	36400	30500	127	38	155	598	260	462	33.2	4400
	DZLS-17	7400	770	20	136	52	1900	58500	39300	141	27	224	478	133	655	28.6	4750
Sancha	SC-2	9190	374	19	172	68	2080	56400	61500	180	31	493	178	408	1680	28.9	4430
	SC-5	16700	33500	16	176	66	1310	3300	59000	67	23	313	943	396	913	79.2	1520
	SC-8	8100	21200	13	92	120	733	17500	27800	93	19	215	750	570	1210	27.7	829
	SC-11	2520	3280	7	111	149	1180	65900	29900	37	34	267	408	595	3780	117	3860
	SC-14	6270	7470	17	147	230	1620	51500	47200	125	29	365	304	359	3290	96.6	517
Maluhe	MLH-2	2240	518	20	254	64	1880	61600	37700	235	39	279	40	118	480	32.0	21200
	MLH-5	1310	1740	16	255	53	1970	70900	36300	156	36	263	41	112	423	148	26300
	MLH-8	1800	1150	14	296	66	1810	66100	40800	157	37	342	111	265	559	129	18000
	MLH-10	964	630	15	301	56	1830	66900	42600	62	33	216	30	109	329	307	29200
	MLH-11	1100	777	12	350	46	2050	61200	45500	90	27	222	37	137	258	313	29200
	MLH-12	836	734	10	206	86	1700	65000	28600	85	46	204	33	161	774	140	12800

All elements analyzed by X-ray fluorescence spectrometry (XRF). The normative MoSC abundances of the sulfide ores were calculated according to the approximate chemical formula of MoS_2C_7. The difference of about 10-20 wt.% to 100 % is the content of organic matter (C, N, H) which was not measured.

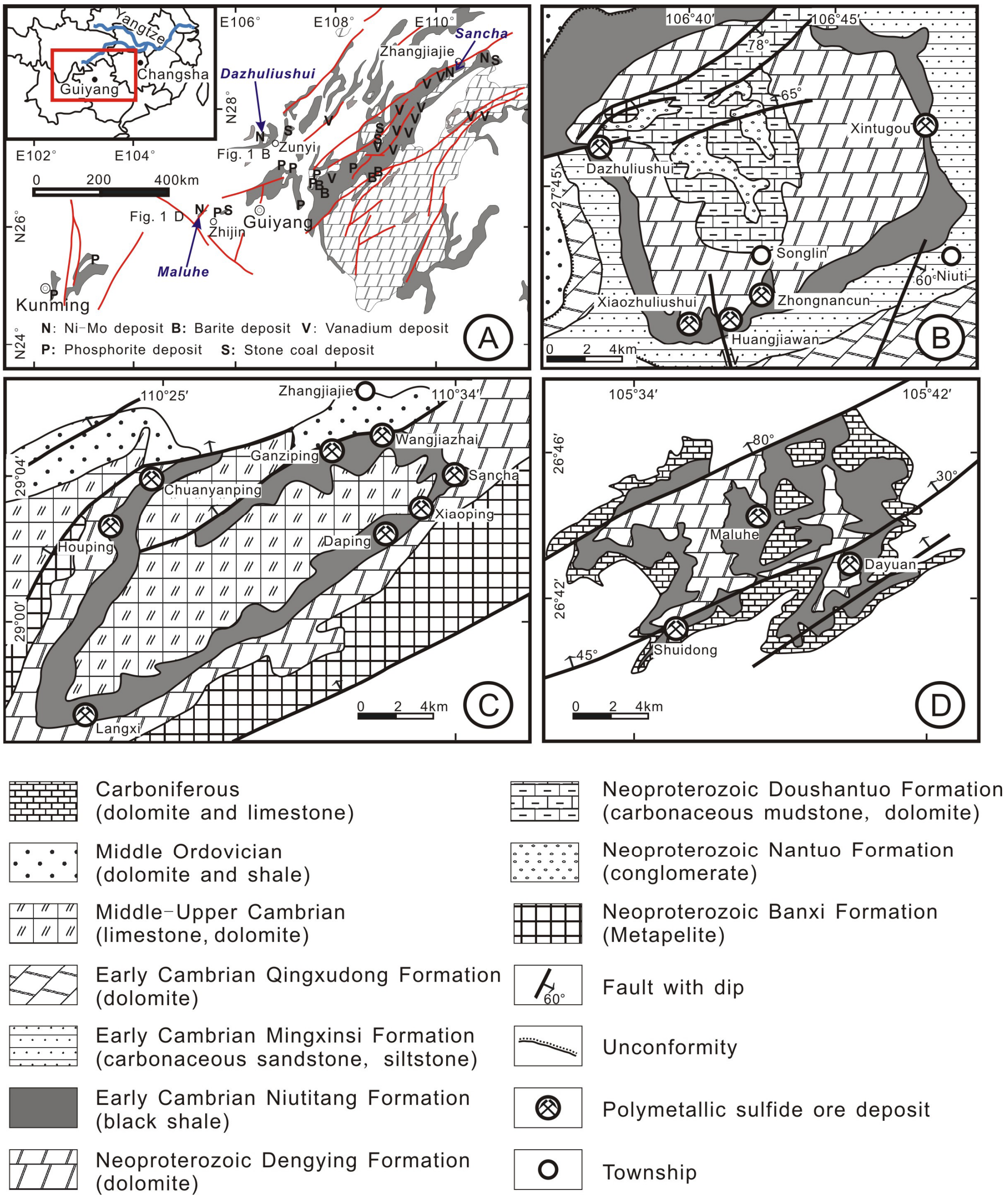

Fig. 4-1 A: Geological sketch map of South China showing the distribution of Early Cambrian black shale and related Ni-Mo-PGE-Au, barite, phosphorite, vanadium and stone coal mines and occurrences. **B:** Geological map of the Dazhuliushui mine district near Zunyi, Guizhou (after Mao et al., 2002). **C:** Geological sketch map of the Sancha mine district near Zhangjiajie, Hunan (modified from Li et al., 2002). **D:** Geological sketch map of the Maluhe mine district near Zhijin, Guizhou.

4.3 Previous Genetic Models

This peculiar polymetallic sulfide ore layer was discovered in the 1970s and the causes for metal enrichment are still much debated. Initial suggestions involved an extraterrestrial origin (Fan et al., 1984), soon disregarded due to the non-chondritic PGE distribution patterns (Coveney et al., 1992). The exceptional metal grades were then mostly ascribed to hydrothermal venting at the seafloor (Lott et al., 1999; Steiner et al., 2001; Jiang et al., 2006, 2007; Pasava et al., 2008, 2010a, b), with the interesting variant of hydrocarbon venting suggested by Emsbo et al. (2005). However, early sulfur isotope studies showed oscillatory zoning of sulfide aggregates with a large spread in delta S values over a range of about 50 per mil, interpreted as biologically mediated fractionation of seawater sulfate under sulfate-limiting conditions (Horan et al., 1994). The metal distribution pattern was interpreted by Mao et al. (2002) and Lehmann et al. (2003, 2007) as reflecting scavenging from average seawater at a very low clastic sedimentation rate. Mo isotope data confirm the seawater origin of the Mo enrichment (Lehmann et al., 2007). A further interpretation of the Mo isotope data by comparing Mo isotope data from Early Cambrian stratigraphic intervals in Oman and South China was given by Wille et al. (2008), who suggested that the Early Cambrian oceans were anoxic and that upwelling euxinic bottom waters may have been the cause of the extinction of the Ediacaran fauna. This interpretation was based on the assumption of synchroneity of the sample suites studied from Oman and South China which is, however, unlikely in the light of recent geochronological data (see discussion by Jiang et al., 2009; Wen et al., 2009; Wille et al., 2009, and below).

4.4 Geologic Setting

Neoproterozoic and Early Cambrian strata are well exposed on the Yangtze Platform of South China. Paleogeographic reconstruction reveals a depositional zonation from a shallow shelf facies of carbonate and phosphorite rocks in the northwest to a transitional and deep basinal facies of black shales and cherts in the southeast (Zhu et al., 2004). The Ni-Mo-PGE-Au sulfide ore layer occurs in the Early Cambrian Niutitang Formation along a narrow NE-striking belt of transitional and deep basinal facies. Sedimentary features such as fine laminations, rip-up clasts, and oncolites of pyrite and Ni-Mo sulfide ore indicate an origin as deeper-water hardground supplied with organic material from algal mats from a wave-agitated, shallow-water environment (Kribek et al., 2007).

The TOC and redox-sensitive metal contents of the black shale sequence of the Niutitang Formation decrease from the lower part (up to 15 wt.% C and about 100 ppm Mo) upwards (3-9 wt.% C and about 10 ppm Mo) over a stratigraphic thickness of about 20-80 m (Steiner et al., 2001). The Ni-Mo ore occurs within the lowermost few meters of the Niutitang Formation as both fine laminations and as a debris layer, consisting largely of a MoSC phase (with the approximate composition of $[(Mo,Fe,Ni)(S,As)_2C_7]$, pyrite, vaesite, bravoite, millerite, gersdorffite and jordisite, with minor arsenopyrite, chalcopyrite, covellite, sphalerite, tennantite, tiemannite, violarite and native Au (Conveney et al., 1994; Kao et al., 2001; Mao et al., 2002; Jiang et al., 2006). The amorphous MoSC phase (about 20 vol.%) is the only important Mo-carrier, with mm-sized ellipsoidal aggregates or fine laminations (Fig. 4-2). Sapropel material (about 45 vol.%) occurs as matrix, and consists of organic matter, fine-grained illite, sericite, quartz, calcite, barite, and locally abundant apatite and collophane. The organic matter is derived from in-situ sapropelized products of planktonic and benthic organisms, oncolite-like algal/bacterial organic remnants, and of oil-derived migrabitumen (Kribek et al., 2007), and has a high thermal maturity corresponding to the semi-anthracite to anthracite coalification stage (Kribek et al. 2007). Pyrite (about 25 vol.%) is intergrown with the MoSC phase in oncolite-like aggregates, and is cut by veinlets with nickel sulfides (about 5 vol.%, millerite, gersdorffite). It is important to note that the lower Niutiutang Formation not only hosts the polymetallic sulfide mineralization, but also hosts stratiform barite, phosphorite, vanadium and stone coal (combustible black shale) deposits (Fig. 4-1A).

The Niutitang Formation is unconformably underlain by up to 600-m thick dolomite of the Dengying Formation, containing the tubular fossil Cloudina (Bengtson and Zhao, 1992), and the fossil-rich (i.e. animal remains, multicellular algae and giant acritarchs) sequence of black shale, chert, phosphorite and dolomite of the Doushantuo Formation (up to 250 m) (Zhu et al., 2004). U-Pb zircon dates from volcanic ash beds within the Doushantuo Formation indicate that deposition occurred between 635 and 551 Ma (Condon et al., 2005). Two phosphorite beds in the Doushantuo Formation yielded Pb-Pb isochron ages of 576 ± 16 Ma for the upper part (Chen et al., 2004), and 599 ± 4 Ma for the lower part of the Upper Phosphorite unit (Barfod et al., 2002), respectively.

All Ni-Mo-PGE-Au deposits are hosted in the lowermost black shale section of the Niutitang Formation (Fig. 4-1). The Dazhuliushui Ni-Mo-PGE-Au deposit is located in the western part of the Songlin dome, about 26 km from Zunyi city, Guizhou province. From the dome center outwards, Late Proterozoic conglomerate of the Nantuo Formation, carbonaceous mudstone and dolomite of the Doushantuo Formation, dolomite of the Dengying Formation, and black shale of the Early Cambrian Niutitang Formation are exposed. The Niutitang Formation is overlain by carbonaceous siltstone and sandstone of the Early Cambrian Minxinsi Formation, dolostone of the Early Cambrian Qingxudong Formation, and Middle Ordovician dolomite and shale. The sulfide ore layer is 5-8 m above the dolomite contact (Fig. 4-3).

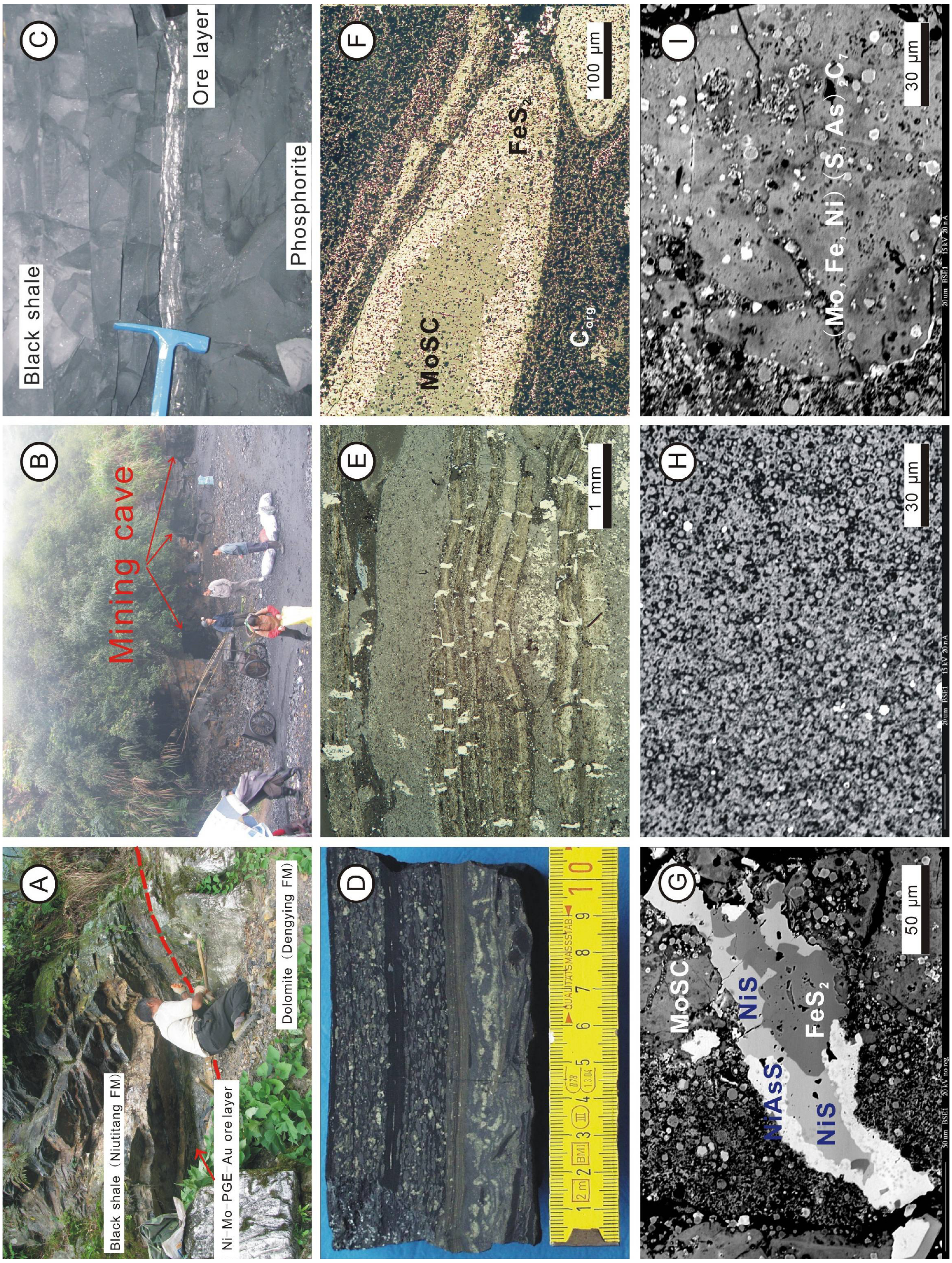

Fig. 4-2 A: Field photo of the Ni-Mo-PGE-Au sulfide ore layer and PC/C boundary (red dashed line: contact to dolomite of Dengying Formation). The location is ~4 km southeast of the Dazhuliushui mine site. **B:** Newly developed mining caves at the Sancha mine site, where samples were collected relatively near the surface. **C:** The 4 cm-thick sulfide ore layer showing a clear-cut boundary with the black shale host sequence (photograph from Dazhuliushui underground mine). **D:** The Ni-Mo-PGE-Au sulfide ore layer showing intraformational polymictic clast units with interlayers of black shale material.

Sulfide clasts in light color, sapropel matrix dark. **E:** Sedimentary features of lenticular, flattened, and fine-grained laminated textures with rip-up clasts and oncolites indicating redeposition of earlier formed sulfidic crusts/hardground a synsedimentary debris flow. **F:** Elongated aggregate of MoSC phase (light) intergrown in rim zones with fine-grained pyrite (bright) surrounded by sapropel matrix (dark). **G:** Back-scatter image of a nickel-rich veinlet within the MoSC phase in organic and phosphorus-rich debris. Note that Mo is fixed in sulfide-carbon aggregate, while Ni is (re)-precipitated in diagenetic cracks. **H:** Back-scatter image of phosphorus-rich material with organic features (phosphatized algal mat?). **I:** Back-scatter image of MoSC phase with the bulk composition of $[(Mo,Fe,Ni)(S,As)_2C_7]$ (unpublished electron microprobe data). The different grey shades reflect variable Mo content.

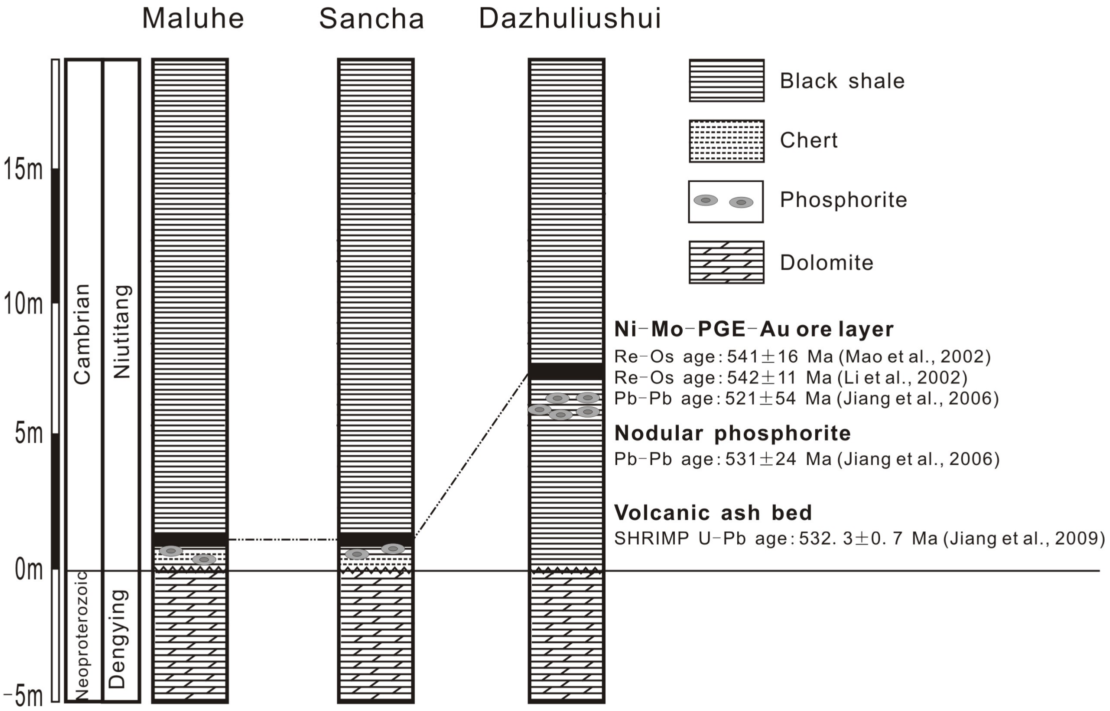

Fig. 4-3: Stratigraphic columns for the sampling sites at the Dazhuliushui, Sancha and Maluhe Ni-Mo-PGE-Au deposits.

The Sancha Ni-Mo-PGE-Au district is 380 km northeast of the Dazhuliushui mine site. The Sancha district includes a number of individual deposits, such as Sancha, Wangjiazhai, Ganziping, Chuanyanping, Houping, Langxi, Daping and Xiaoping, which are aligned along the limbs of the Tianmenshan-Huangdong syncline. The axis of the synclinal structure is composed of Middle-Late Cambrian limestone and dolomite. The sulfide ore layer in the Niutitang Formation is only 1 m above the unconformable dolomite of the Dengying Formation. Phosphorite nodules and chert occur between the sulfide layer and the dolomite contact.

The Maluhe district with the Maluhe, Shuidong and Dayuan Ni-Mo-PGE-Au deposits near Zhijin is 180 km southwest of the Dazhuliushui mine site. The Maluhe deposits are hosted in a broad anticlinal structure which exposes the Niutitang Formation, unconformably overlain by Carboniferous dolomite and dolomitic limestone, and underlain by dolomite of the Dengying Formation. The polymetallic ore layer is about 1 m above the unconformable contact with dolomite of the Dengying Formation.

4.5 Samples and Analytical Methods

A total of seventeen ore samples from the polymetallic sulfide layer were collected underground from the Dazhuliushui, Sancha and Maluhe mine sites. At each mine site, samples were collected at the same stratigraphic ore horizon but at different locations, up to hundreds of meters apart. The underground workings are focused on one sulfide-rich ore layer which is only 3-5 cm thick (Fig. 4-3). At the Sancha mine site, some samples were collected from newly developed shallow near-surface stopes. We took bulk ore samples of 0.5-1 kg, which were crushed, split and powdered with an agate shatter box. The samples were chemically characterized by X-ray fluorescence spectrometry (Table 4-1). The data in Table 4-1 are calculated as normative sulfide components for those major elements which are combined with sulfur, i.e. Fe, Mo, Ni, As. The normative MoSC phase composition of the sulfide ores ranges from 0.84 wt.% to 23.6 wt.% (mainly 14 – 20 wt.%) as calculated from the approximate chemical formula of MoS_2C_7 (Kao et al., 2001), which roughly corresponds to the modal abundance observed by reflected-light microscopy. The difference of the major element components to 100 % is around 10-20 wt.% which corresponds to the organic matter content (C, N, H) as measured in the sample set of Lehmann et al. (2007).

Re-Os isotope analyses were carried out at the Re-Os Laboratory of the National Research Center of Geoanalysis, Chinese Academy of Geological Sciences, in Beijing. Sample preparation, chemical separation and analytical procedure have been described in Du et al. (1995, 2001, 2004), Shirey and Walker (1995) and Markey et al. (1998). They are briefly summarized here.

HCl-HNO_3 digestion was used for sample dissolution. The sample (~100 mg) was loaded in a Carius tube (a thick-walled borosilicate glass ampoule) through a long thin-necked funnel. Enriched ^{190}Os and ^{185}Re spike solution (obtained from the Oak Ridge National Laboratory) and 3 ml 10 M HCl + 5 ml 16 M HNO_3 were added while the bottom part of the tube was frozen at -50 to -80°C in an ethanol-liquid nitrogen slush. The tube was sealed with an oxygen-propane torch. The tube was then placed in a stainless-steel jacket and heated for 24 h at 200°C. Upon cooling, the bottom part of the tube was kept frozen, the neck of the tube was broken, and the contents of the tube were poured into a distillation flask. The residue was washed out with 40 ml of deionized water.

Separation of osmium by distillation and separation of rhenium by extraction were performed following the analytical method of Du et al. (1995, 2001). OsO_4 was distilled at 105-110°C for 50 minutes and trapped in 10 ml of water, which was used for ICP-MS determination of the Os isotope ratio. The residual Re-bearing solution was saved in a 150 ml Teflon beaker for Re separation and was evaporated to near-dryness. 1 ml of water was added and then evaporated to near-dryness twice. 10 ml 5 M NaOH was added to the residue to obtain alkaline conditions, followed by Re extraction with 10 ml of acetone in a 120 ml Teflon separation funnel. The water phase was discarded. The acetone phase was washed with 2 ml 5 M NaOH for 2 minutes. Then the acetone phase was transferred to a 150 ml Teflon beaker that contained 2 ml of water. The solution was heated at ~50°C to dryness to erase acetone. Several drops of concentrated HNO_3 and 30 % H_2O_2 were added to dissolve Re and the solution was then evaporated to dryness and picked up in 2 % HNO_3 for ICP-MS determination of the Re isotope ratio. Cation-exchange resin was used to remove Na if the salinity of the Re-bearing solution was more than 1 mg/ml (Du et al., 2004).

A TJA X-series ICP-MS was used for Re and Os isotope determination. The analytical reliability was tested by analyses of the Certified Reference Material GBW04435 (HLP standard, Du et al., 2004). The molybdenite standard HLP is from a carbonatite vein-type Mo-Pb deposit in the Jinduicheng-Huanglongpu area of Shaanxi province, China. The average Re-Os age for HLP is 219.5 ± 3.5 Ma (95 % confidence), consistent with the certified value of 221 ± 5.6 Ma (Du et al., 2004). Average blanks for the Carius tube procedure are ~20 pg Re and ~1 pg Os. The analytical uncertainties for $^{187}Re/^{188}Os$ and $^{187}Os/^{188}Os$ are determined by error propagation of uncertainties in Re and Os mass spectrometer measurements, blank abundances and isotopic compositions, spike calibrations and reproducibility of standard Re and Os isotopic values. The Re-Os isotopic data for $^{187}Re/^{188}Os$ and $^{187}Os/^{188}Os$ are calculated with the decay constant of $\lambda^{187}Re = 1.666 \times 10^{-11}$ yr^{-1} with an absolute uncertainty of 0.017×10^{-11} (1 %) (Smoliar et al., 1996). The Isoplot package of Ludwig (2005) was used to calculate isochrons and the Re-Os age.

4.6 Results and Discussion

Re-Os abundances and isotopic data for the seventeen bulk ore samples are given in Table 4-2. Re, Os_{common} and ^{187}Os concentrations vary from 1532 to 16830 ppb, 41.22 to 97.51 ppb and 28.20 to 99.80 ppb, respectively. Re/Os_{common} ratios range from 77.4 to 262.4. ^{187}Re/^{188}Os and ^{187}Os/^{188}Os ratios range from 373.8 to 1268 and 4.111 to 11.92, respectively. Although the geographic distance of the three mine sites is several hundred kilometers apart (Fig. 4-1), the regression of 17 samples yields a Model 3 isochron age of 522 ± 15 Ma (2σ uncertainty, MSWD = 5.1, initial ^{187}Os/^{188}Os = 0.81 ± 0.23). This age is younger than the previous 6-point Re-Os isochron ages of 541 ± 16 Ma from the Huangjiawan mine (Mao et al., 2002) and 542 ± 11 Ma from the Sancha and Ganziping mines (Li et al., 2002). Most of the scatter in our data is attributable to three samples (DZLS-17, SC-11 and SC-14) that fall below the regression line. Omitting these three samples, the remaining 14 points define an isochron age of 521 ± 5 Ma (2σ uncertainty, MSWD = 0.95) with an initial ^{187}Os/^{188}Os = 0.87 ± 0.07 (Fig. 4-4). We interpret this age and initial ratio as the current best estimate for the polymetallic sulfide layer.

Several processes might explain the scatter in the Re-Os data. One possibility is primary heterogeneity in the source of Os. The Os ocean residence time is relatively short (~10 ka) which allows for rapid changes and local influences of the Os isotope ratio (Peucker-Ehrenbrink and Hannigan, 2000; Oxburgh, 2001). The deposition rate of the sulfidic sediments was estimated at about 10 ka/cm (Lehmann et al., 2007). Under conditions of restricted basins with relatively local Os sources from continental weathering, large variations in Os isotopic compositions are feasible over short time periods (McArthur et al., 2008; Pasava et al., 2010a). The locations of the five samples from the Sancha mine are from near-surface mining caves only several meters apart (Fig. 4-2B). Two samples (SC-11 and SC-14) have large scatter, while three samples (SC-2, SC-5 and SC-8) coincide with the isochron line. It is unlikely that the Os isotopic composition variations in the local water column only affected two samples, but not the other three samples. However, the nature of the samples as rip-up clasts and oncolites suggests a certain degree of redeposition of earlier formed sulfidic crusts. Therefore, it is likely that not all material is of exactly the same age and there may have been a limited amount of mixing between earlier formed sulfidic material and later formed sapropel in the final depositional environment.

Table 4-2
Re and Os isotope data for Ni-Mo-PGE-Au sulfide ore samples from Dazhuliushui, Sancha, Maluhe and Huangjiawan Mine sites (number in parentheses indicates analytical precision)

Deposit	Sample No.	Weight (g)	Re (ppb)	Os_{common} (ppb)	^{187}Os (ppb)	Re/Os_{common}	$^{187}Re/^{188}Os$	$^{187}Os/^{188}Os$	$(^{187/188}Os)t$
Dazhuliushui	DZLS-2	0.105	13364(96)	67.42(0.74)	81.00(0.63)	198.2	957.4(12.6)	9.23(0.11)	0.887
	DZLS-5	0.102	15330(151)	70.71(0.78)	91.79(0.61)	216.8	1047.2(15.5)	9.98(0.11)	0.848
	DZLS-8	0.106	12343(71)	74.69(0.44)	75.60(0.36)	165.3	798.2(6.5)	7.78(0.03)	0.821
	DZLS-11	0.106	10427(57)	64.29(0.42)	64.10(0.36)	162.2	783.4(6.7)	7.66(0.04)	0.833
	DZLS-14	0.108	8726(44)	50.86(0.31)	53.43(0.36)	171.6	828.8(6.5)	8.07(0.04)	0.849
	DZLS-17	0.042	10275(46)	54.92(0.57)	60.97(0.01)	187.1	903.7(10.2)	8.53(0.09)	0.654
Sancha	SC-2	0.101	13347(81)	90.34(0.64)	84.10(0.61)	147.7	713.6(6.7)	7.15(0.06)	0.930
	SC-5	0.104	4079(32)	52.71(0.42)	28.20(0.16)	77.4	373.8(4.2)	4.11(0.03)	0.852
	SC-8	0.105	5892(59)	41.22(0.28)	37.40(0.20)	142.9	690.5(8.4)	6.97(0.04)	0.954
	SC-11	0.100	14541(103)	84.13(0.71)	86.50(0.48)	172.8	833.8(7.5)	7.87(0.05)	0.596
	SC-14	0.103	16832(112)	97.51(0.58)	99.80(0.68)	172.6	834.9(9.2)	7.90(0.06)	0.624
Maluhe	MLH-2	0.100	9994(49)	48.29(0.44)	60.20(0.36)	207.0	1000(10)	9.57(0.08)	0.852
	MLH-5	0.101	11118(48)	50.06(0.33)	66.30(0.36)	222.1	1073(8)	10.18(0.05)	0.826
	MLH-8	0.100	15328(73)	58.40(0.34)	90.60(0.55)	262.5	1268(10)	11.92(0.06)	0.866
	MLH-12	0.102	12098(59)	49.29(0.34)	71.88(0.42)	245.4	1185(10)	11.21(0.07)	0.880
	MLH-10	0.103	12181(51)	53.85(0.37)	72.79(0.44)	226.2	1093(9)	10.39(0.07)	0.862
	MLH-11	0.105	11945(50)	55.87(0.48)	71.80(0.39)	213.8	1033(10)	9.88(0.08)	0.875
Huangjiawan	HJW-1-1	0.10103	10438(42)	133.92(0.54)*		-	731.2(4.2)	7.40(0.01)	1.02
	HJW-1-3	0.10079	10268(41)	124.35(0.50)*		-	813.3(4.6)	8.14(0.02)	1.05
	HJW-2-3	0.10060	12682(51)	162.14(0.65)*		-	736.5(4.2)	7.45(0.01)	1.03
	ZHL-7	0.10343	10901(44)	142.30(0.57)*		-	700.9(4.0)	7.03(0.01)	0.994
	ZHL-7-1	0.10055	12193(49)	156.76(0.63)*		-	726.3(4.1)	7.33(0.01)	1.01
	ZHL-7-2	0.10156	11358(45)	152.76(0.61)*		-	673.2(3.8)	6.88(0.01)	1.01
	ZHL-7-3	0.10021	10856(43)	142.05(0.57)*		-	705.9(4.0)	7.17(0.02)	0.917

Re-Os isotope data of Huangjiawan Ni-Mo-PGE-Au deposit from Mao et al. (2002) are cited for comparison. * is total Os.

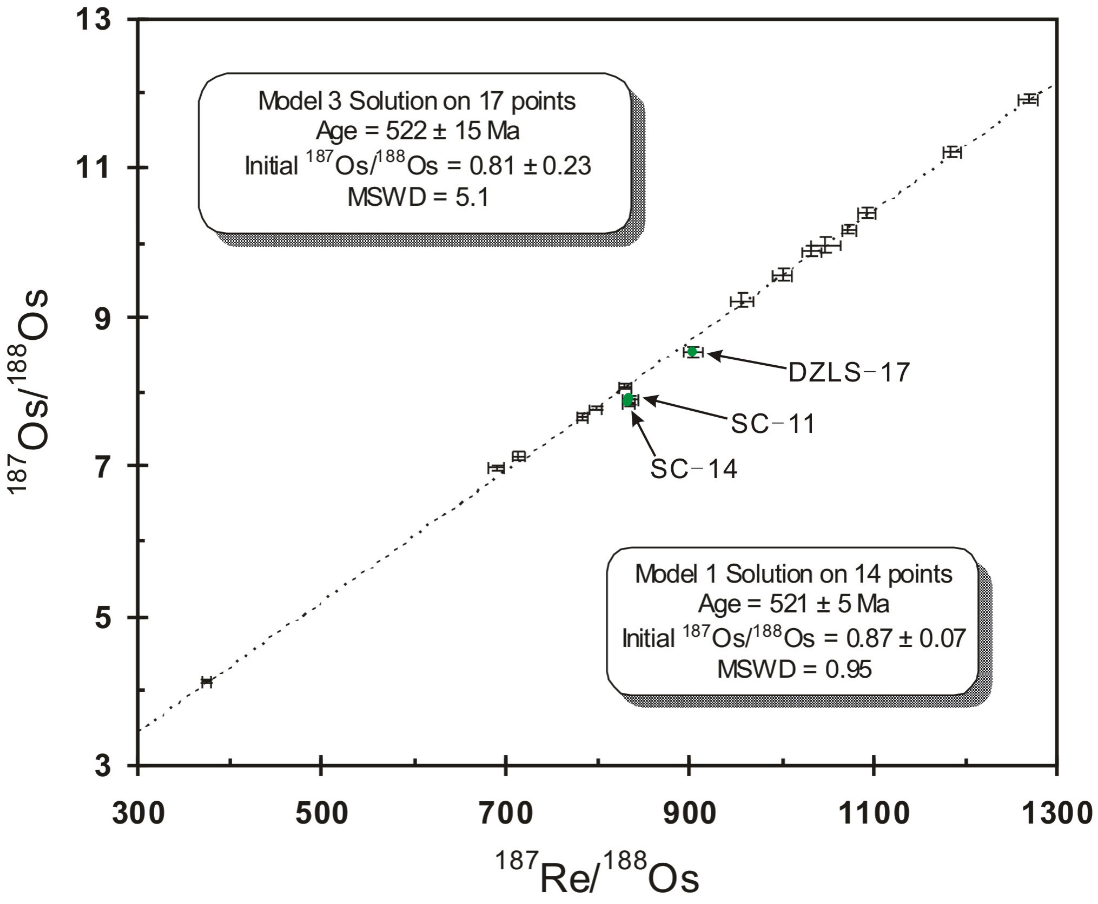

Fig. 4-4: Re-Os isochron diagram for Ni-Mo-PGE-Au sulfide ore samples from the Dazhuliushui, Sancha and Maluhe mine sites (amalgamated). ISOPLOT v.3.23 was used for isochron age calculation. The samples (n = 17) yield a model-3 isochron age of 522 ± 15 Ma (MSDW = 5.1). Three points excluded (green solid circle, SC-11, SC-14 and DZLS-17) yield a regression line with a model-1 isochron age of 521 ± 5 Ma (MSWD = 0.95), 2 sigma uncertainty range. Model 1 regression assumes that the assigned errors are the only reason for scatter whereas Model 3 regression treats the scatter as a combination of the assigned errors and variations in initial ^{187}Os/^{188}Os ratios. The Model 1 fit is used when the probability calculated by the program is reasonable high (> 15%); otherwise the Model 3 fit is used (Ludwig, 2005).

Scatter may also develop from overprint by post-depositional processes. Re loss after mineralization would drive samples to the left of the isochron line (e.g. Mathur et al., 1999). However, the samples SC-11 and SC-14 are located at the right side of the isochron and have the highest Re concentrations, suggesting that the scatter of these two samples was caused by Re enrichment, not Re loss. Hannah et al. (2001) suggested that remobilization of Re and Os on a small scale could be the result of weathering or variable interaction with ground water. By analyzing alteration phases from the surface of weathered black shale, Pierson-Wickmann et al. (2002) showed that Os liberated during alteration was partially reprecipitated in Fe oxides, with Os isotopic compositions very similar to those of the original rock, whereas Re was removed with the fluid phase. The results indicate that large amounts of Re can be lost during weathering processes. Peucker-Ehrenbrink and Hannigan (2000) found substantial mobility for both Re and Os during weathering. Although there are no observable textural or mineralogical differences between the Sancha samples that show scatter and the remaining sample set, the SC-11 and SC-14 samples were collected at near-surface localities (2-3 m to the surface) from newly developed caves. It is possible that meteoric water leached Re and Os from the overlying black shales and redeposited these elements at the polymetallic sulfide ore layer acting as a chemocline, and resulting in Re and Os abundances in the samples SC-11 and SC-14 that are slightly higher than in other samples (Table 4-2).

A further aspect which may explain scatter in the Os isotope data is the fact that part of the organic matter in the samples consists of migra-bitumen, i.e. former oil liberated during the thermal history of the black shale sequence (Kribek et al., 2007). Oil can transport several hundred ppb Re and up to 1 ppb Os in the asphaltene fraction (Selby et al., 2007), and typically has elevated amounts of vanadium. The two samples SC-11 and SC-14 have anomalously high vanadium contents of 3300 and 3800 ppm, respectively, which may indicate a contribution from oil.

It also appears that there is a significant effect of sample (aliquant) size on the accuracy and reproducibility of Re-Os data for molybdenite samples. Stein et al. (2001, 2003) and Selby and Creaser (2004) found that for some molybdenite samples, analysis of small sample aliquants may not yield accurate or reproducible Re-Os ages, whereas analysis of larger aliquants from the same mineral separate did yield reproducible Re-Os dates. This situation may apply to sample DZLS-17 with large scatter, for which the analyzed sample weight is 42 mg only, distinctly less than for the other samples with about 100 mg. Although the sample powder represents a split from a larger crushed and homogenized bulk-ore sample, the homogenization may not have been perfect.

Due to analytical problems in the early stage of Re-Os geochronology, i.e. incomplete equilibrium of spike and sample, Horan et al. (1994) were able to only obtain a relatively poorly defined Re-Os isochron age of 560 ± 50 Ma. In addition, Horan et al. (1994) measured ^{187}Os/^{186}Os ratios in their study, which typically are less precise than ^{187}Os/^{188}Os ratios. Two relatively precise Re-Os isochron ages of 541 ± 16 Ma and 542 ± 11 Ma were reported by Mao et al. (2002) and Li et al. (2002), respectively, using negative thermal ion mass spectrometry (NTIMS). The samples used in both surveys were from the same sulfide ore layer but from different mine sites in Hunan and Guizhou provinces (Huangjiawan for Mao et al., 2002, Sancha and Ganziping for Li et al., 2002). Although The NTIMS method has been widely used, recent studies indicate that ICP-MS determination of organic-rich samples is also accurate and effective (e.g. Pasava et al., 2010a). Generally, the reliability of Re-Os geochronology depends on sample quantity and quality (for example, integrity of Re-Os system and variance of Re/Os$_{\text{common}}$). Horan et al. (1994) and Li et al. (2002) obtained a relatively narrow range in Re and Os concentrations in their samples (with Re/Os ratios of 84.6 - 102.0 and 20.6 - 100.7, respectively), compared to Mao et al. (2002) and this study (Table 4-2). Our study involves a relatively large dataset (n = 17) and relatively wide variation range of Re/Os ratios (10.3 – 99.8), insuring that the age of 521 ± 5 Ma is reliable. The reliability of the age can also be shown by plotting the data for each individual mine site. The Re-Os isochron ages of the three localities studied are 520 ± 68 Ma, 493 ± 83 Ma and 526 ±29 Ma, respectively, with initial ^{187}Os/^{188}Os ratios of 0.82 ± 0.98, 1.11 ± 0.98, and 0.76 ± 0.54, respectively. These individual datasets with their relatively large age error are within error of the ages obtained by Mao et al. (2002) (Fig. 4-5).

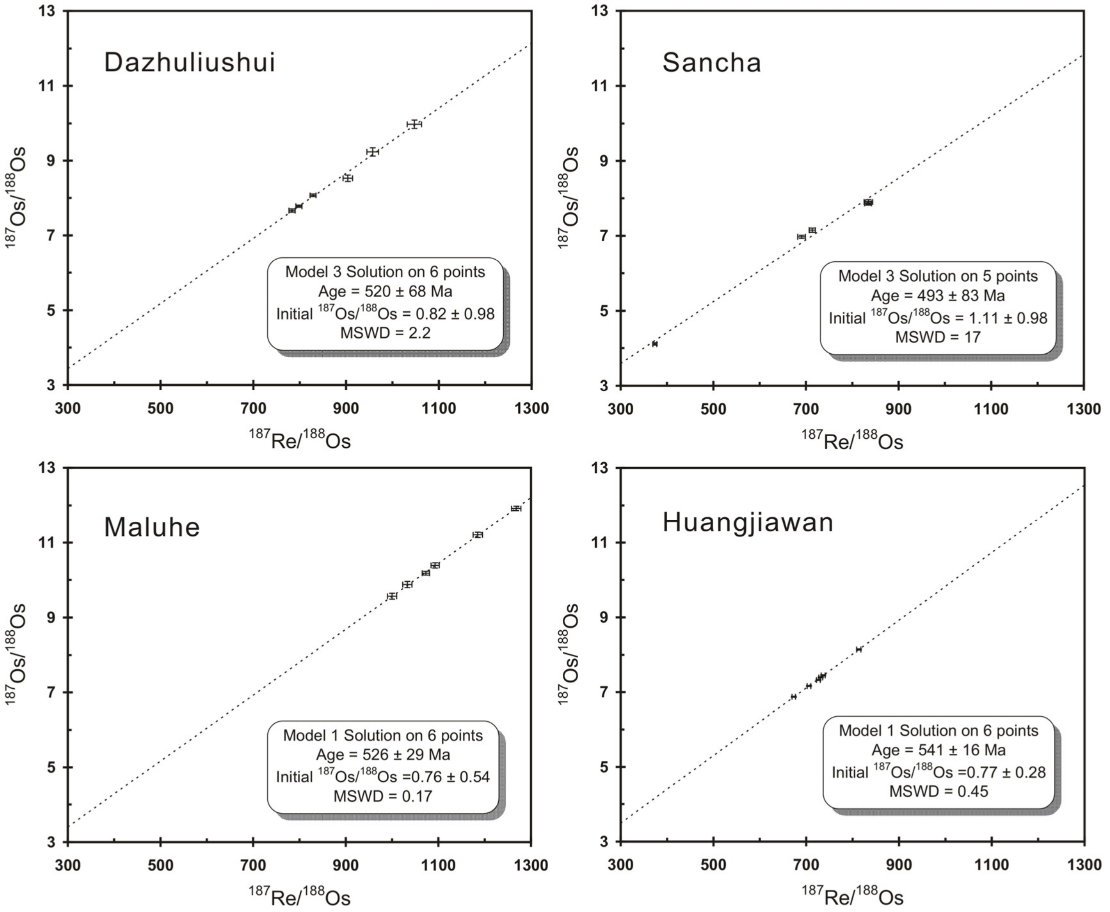

Fig. 4-5: Re-Os isochron diagrams for Ni-Mo-PGE-Au sulfide ore sample groups from the Dazhuliushui, Sancha and Maluhe mine sites. Re-Os isotope data of the Huangjiawan Ni-Mo-PGE-Au deposit from Mao et al. (2002) are plotted for comparison. The four Re-Os isochron ages overlap within their error ranges.

Our new Re-Os age of 521 ± 5 Ma of the sulfide ore layer is significantly younger than the previously reported Re-Os isochron ages, and does not correspond to the global PC/C boundary which has an age of 542 ± 1.0 Ma (Ogg et al., 2008). The new age is in agreement with Pb-Pb ages reported by Jiang et al. (2006), with 531 ± 24 Ma (n = 34, MSWD = 1.6) for black shales of the Niutitang Formation, and 521 ± 54 Ma (n =9, MSWD = 31) for the polymetallic sulfide bed, and with a 5-point Re-Os isochron age of 536 ± 11 Ma for black shales near Zunyi (Jiang et al., 2007). More recently, Jiang et al. (2009) provided a SHRIMP U-Pb zircon age of 532.3 ± 0.7 Ma for a volcanic ash bed within the Niutitang Formation below the sulfide ore layer which strongly suggests that the polymetallic mineralization must be younger than 532 Ma. These four ages and our result are also in agreement with the biostratigraphic age of the Niutitang Formation, which contains arthropods, sponges and small shelly fossils of Tommotian age (~530 Ma) (Steiner et al., 2001).

The Re-Os isotope system has been recognized as a possible geochemical tool not only for directly dating mineralization but also for tracing the source of metals. The Os isotope composition of seawater is controlled by continental weathering with ^{187}Os/^{188}Os >1.2 (Phanerozoic), hydrothermal input from seawater circulating through the oceanic crust with ^{187}Os/^{188}Os ~0.1 and contributions from cosmic dust with ^{187}Os/^{188}Os ~0.1 (Sharma et al., 1997). The seawater ^{187}Os/^{188}Os value varies through geological history. For example, the ratio of present-day seawater is 1.04 ± 0.04 (Sharma et al., 1997), but ranged from 0.15 to 0.8 and back to 0.6 over the Jurassic period (Cohen et al., 1999, 2004). The ^{187}Os/^{188}Os initial value of the sulfide ores in the Guizhou and Hunan provinces is 0.87 ± 0.07, which is equal to the ^{187}Os/^{188}Os ratio of 0.80 ± 0.04 of the shale host rock (Jiang et al., 2007). The overlap of the initial values of the sulfide ore bed and the black shale host rock suggest a common source for Os in both the sulfide layer and the black shale sequence, although Os is strongly enriched in the sulfide layer compared to the black shale sequence by about one to two orders of magnitude (black shale: 4.85 - 20.9 ppb Os; Jiang et al., 2007). We see no indication of a hydrothermal input of Os in the Niutitang Formation and its sulfide ore layer, although Jiang et al. (2003, 2007) argued that hydrothermal input may have affected both sulfide ore and the black shale host sequence. Field observation indicates that the Ni-Mo-PGE-Au sulfide ore layer has sharp boundaries with the black shale host rock and locally represents a debris layer of rip-up clasts and oncolites from a metal-rich hardground (Steiner et al., 2001; Kribek et al., 2007) (Fig. 4-2 C, D and E). No gradation can be observed between the sulfide ore layer and the black shale host rock. Further evidence is from bulk geochemical analysis, where abundances of Mo, Ni, U, V, Re, Os decrease sharply from the sulfide ore layer to the black shale (Mao et al., 2002; Lehmann et al., 2007). The metal content of the black shale host sequence is typical of black shales worldwide for which interelement relations indicate a seawater origin for many metals (Holland, 1979; Piper 1994). Singh et al. (1999) obtained an initial $^{187}Os/^{188}Os$ ratio of 1.18 ± 0.02 for the black shale in the Lesser Himalayas of India, with ^{187}Re-^{187}Os isochron ages of 554 ± 16 Ma and 552 ± 22 Ma, respectively. Jiang et al. (2007) considered this ratio to be representative of Early Cambrian seawater Os. However, this value is more elevated than for the Ni-Mo-PGE-Au sulfide layer, and is unlikely to be applicable to the South China situation because it is about 30 Ma older than the Niutitang Formation and geographically distant. Further Re-Os isotope data of black shale from the Niutitang Formation at high stratigraphic resolution would be needed to identify any secular variation in the Os isotope signature.

4.7 Conclusions

The 14-point isochron age of 521 ± 5 Ma is the currently most precise and accurate Re-Os age for the polymetalllic sulfide bed with Ni-Mo-PGE-Au mineralization in the Early Cambrian Niutitang Formation of South China. This age is ~20 Ma younger than in previous less comprehensive Re-Os studies, and is consistent both with the biostratigraphic Tommotian age, and with recent studies applying the Pb-Pb and SHRIMP U-Pb methods on over- and underlying rock units, respectively. It is particularly remarkable that all samples from the three localities plot on one isochron which strongly suggests that the polymetallic sulfide layer represents indeed one regionally distributed stratigraphic level.

The similar initial $^{187}Os/^{188}Os$ ratio of ~0.80 of the sulfide ore and black shale host rock indicates that osmium has a similar seawater origin. Osmium enrichment in the sulfide ore layer is likely from seawater scavenging, because leaching of (unexposed) ultramafic rocks or hydrothermal seafloor venting from a hidden mafic-ultramafic intrusion, as previously suggested, would be reflected in a much lower initial $^{187}Os/^{188}Os$ ratio. Both Os and other redox-sensitive metals in the sulfide ore are enriched by a factor of about 10^7 with respect to modern seawater. By analogy, the other redox-sensitive metals with a similar enrichment factor compared to seawater can also be attributed to scavenging from the water column. Such a process can efficiently enrich sediments in metals only at extremely low sedimentation rates, in line with the hardground situation of the depositional environment. The unusual sulfide ore layer attests to metal availability from seawater with a similar composition to the present-day oxic oceans, i.e. requires the presence of a large reservoir of deep oxic water in the Early Cambrian. The Early Cambrian polymetallic sulfide layer displays spectacular metal enrichment from seawater in an euxinic environment. The degree of metal enrichment is comparable to recent hydrogenetic deep-sea nodules/crusts which represent another spectacular case of metal scavenging from seawater, but in an oxic environment.

4.8 Acknowledgements

This research is funded by the Chinese Geological Survey Program (No. 1212010634001) and the Chinese Scholarship Council, as well as by Deutsche Forschungsgemeinschaft (LE578/32-1). We thank Dr. Zhang Ying from Institute of Geochemistry, Chinese Academy of Sciences, for assistance during the field work. We are grateful to Dr. Ryan Mathur and Dr. Judy Hannah for their thorough reviews, as well as for the editorial handling by Dr. K.D. Kelley and Dr. L.D. Meinert, that greatly improved the manuscript.

4.9 References

Banerjee, D.M., Schidlowski, M., Siebert, F., and Brasier, M.D., 1997, Geochemical changes across the Proterozoic-Cambrian transition in the Durmala phosphorite mine section, Mussoorie Hills, Garhwal Himalaya, India: Palaeogeography, Palaeoclimatology, Palaeoecology, v. 132, p. 183-194.

Barfod, G.H., Albarède, F., Knoll, A.H., Xiao, S.H., Telouk, P., Frei, R., and Baker, J., 2002, New Lu-Hf and Pb-Pb age constraints on the earliest animal fossils: Earth and Planetary Science Letters, v. 201, p. 203-212.

Bengtson, S., and Zhao, Y., 1992, Predatorial borings in Late Precambrian mineralized exoskeletons: Science, v. 257, p. 367-369.

Brasier, M., 1992, Background to the Cambrian explosion: Journal of the Geological Society of London, v. 149, p. 585-587.

Chen, D.F., Dong, W.Q., Zhu, B.Q., and Chen, X.P., 2004, Pb-Pb ages of Neoproterozoic Doushantuo phosphorites in South China: constraints on early metazoan evolution and glaciation events: Precambrian Research, v. 132, p. 123-132.

Cohen, A.S., 2004, The rhenium-osmium isotope system: applications to geochronological and palaeoenvironmental problems: Journal of the Geological Society, v. 161, p. 729-734.

Cohen, A.S., Coe, A.L., Bartlett, J.M., and Hawkesworth, C.J., 1999, Precise Re-Os ages of organic-rich mudrocks and the Os isotope composition of Jurassic seawater: Earth and Planetary Science Letters, v. 167, p. 159-173.

Condon, D., Zhu, M.Y., Bowring, S., Wang, W., Yang, A.H., and Jin, Y.G., 2005, U-Pb ages from the Neoproterozoic Doushantuo Formation, China: Science, v. 308, p. 95-98.

Conveney, R.M., Jr., Grauch, R.I., and Murowchick, J.B., 1994, Metals, phosphate, and stone coal in the Proterozoic and Cambrian of China: The geolocial setting of precious metal-bearing Ni-Mo ore beds: Society of Economic Geologists Newsletter, v. 18, p. 1, 6-11.

Coveney, R.M. Jr., Murowchick, J.B., Grauch, R.I., Glascock, M.D., and Denison, J.R., 1992, Gold and platinum in shales with evidence against extraterrestrial sources of metals: Chemical Geology, v. 99, p. 101-114.

Du, A.D., He, H.L., and Yin, N.W., 1995, A study of the rhenium-osmium geochronometry of molybdenites: Acta Geologica Sinica, v. 8, p. 171-181.

Du, A.D., Wang, S.X., Sun, D.Z., Zhao, D.M., and Liu, D.Y., 2001, Precise Re-Os dating of molybdenite using Carius tube, NTIMS and ICPMS. Proceedings SGA-SEG Joint Biennial Meeting, Krakow, Poland, p. 405-407.

Du, A.D., Wu, S.Q., Sun, D.Z., Wang, S.X., Qu, W.J., Markey, R., Stein, H., Morgan, J., and Malinovskiy, D., 2004, Preparation and certification of Re-Os dating reference materials: Molybdenites HLP and JDC: Geostandards and Geoanalytical Research, v. 28, p. 41-52.

Emsbo, P., Hofstra, A.H., Johnson, C.A., Koenig, A., Grauch, R., Zhang, X.C., Hu, R.Z., Su, W.C., Pi, D.H., 2005, Lower Cambrian metallogenesis of South China: Interplay between diverse basinal hydrothermal fluids and marine chemistry. In: Mao, J.W., Bierlein, F.P., eds., Mineral deposit research: Meeting the global challenge. Springer, Volume 1, pp. 115-118.

Fan, D., Yang, R.Y., and Huang, Z.X., 1984, The Lower Cambrian black shales series and the iridium anomaly in south China. Developments in Geoscience, 27th International Geological Congress, Moscow, Beijing Science Press, p. 215-225.

Hannah, J.L., Schersten, A., and Stein, H.J., 2001, Re-Os behavior in mafic magmas and terrestrial diagenetic: Extracting information from open system:

Geological Society of America, Abstracts with Programs, v. 33, p. A238.

Holland, H.D., 1979, Metals in black shales - a reassessment: Economic Geology, v. 74, p. 1676-1680.

Horan, M.F., Morgan, J.W., Grauch, R.I., Coveney, R.M., Jr., Murowchick, J.B., and Hulbert, L.J., 1994, Rhenium and osmium isotopes in black shales and Ni-Mo-PGE-rich sulfide layers, Yukon-Territory, Canada, and Hunan and Guizhou Provinces, China: Geochimica et Cosmochimica Acta, v. 58, p. 257-265.

Jiang, S.Y., Chen, Y.Q., Ling, H.F., Yang, J.H., Feng, H.Z., and Ni, P., 2006, Trace- and rare-earth element geochemistry and Pb-Pb dating of black shales and intercalated Ni-Mo-PGE-Au sulfide ores in Lower Cambrian strata, Yangtze Platform, South China: Mineralium Deposita, v. 41, p. 453-467.

Jiang, S.Y., J.H.Yang, Ling, H.F., Feng, H.Z., Chen, Y.Q., and Chen, J.H., 2003, Re-Os isotopes and PGE geochemistry of black shales and intercalated Ni-Mo polymetallic sulfide bed from the Lower Cambrian Niutitang Formation, South China: Progress in Natural Science, v. 13, p. 788-794.

Jiang, S.Y., Pi, D.H., Heubeck, C., Frimmel, H., Liu, Y.P., Deng, H.L., Ling, H.F., and Yang, J.H., 2009, Early Cambrian ocean anoxia in South China: Nature, v. 459, p. E5-E6.

Jiang, S.Y., Yang, J.H., Ling, H.F., Chen, Y.Q., Feng, H.Z., Zhao, K.D., and Ni, P., 2007, Extreme enrichment of polymetallic Ni-Mo-PGE-Au in lower Cambrian black shales of South China: an Os isotope and PGE geochemical investigation: Palaeogeography, Palaeoclimatology, Palaeoecology, v. 254, p. 217-228.

Kao, L.S., Peacor, D.R., Coveney, R.M., Zhao, G.M., Dungey, K.E., Curtis, M.D., and Penner-Hahn, J.E., 2001, A C/MoS_2 mixed-layer phase (MoSC) occurring in metalliferous black shales from southern China, and new data on jordisite:

American Mineralogist, v. 86, p. 852-861.

Kaufman, A.J., Jacobsen, S.B., and Knoll, A.H., 1993, The Vendian record of Sr and C-isotopic variations in seawater - Implications for tectonics and paleoclimate: Earth and Planetary Science Letters, v. 120, p. 409-430.

Kimura, H., and Watanabe, Y., 2001, Oceanic anoxia at the Precambrian-Cambrian boundary: Geology, v. 29, p. 995-998.

Kirschvink, J.L., Ripperdan, R.L., and Evans D.A., 1997, Evidence for a large-scale reorganization of Early Cambrian continental masses by inertial interchange true polar wander: Science, v. 277, p. 541-545.

Kribek, B., Sýkorová, I., Pasava, J., Machovic, V., 2007, Organic geochemistry and petrology of barren and Mo-Ni-PGE mineralized marine black shales of the Lower Cambrian Niutitang Formation (South China): International Journal of Coal Geology, v. 72, p. 240-256.

Lehmann, B., Mao, J.W., Li, S.R., Zhang, and Zeng, M.G., 2003, Re-Os dating of polymetallic Ni-Mo-PGE-Au mineralization in lower Cambrian black shales of south China and its geologic significance - a reply: Economic Geology, v. 98, p. 663-665.

Lehmann, B., Nägler, T.F., Holland, H.D., Wille, M., Mao, J.W., Pan, J.Y., Ma, D.S., and Dulski, P., 2007, Highly metalliferous carbonaceous shale and Early Cambrian seawater: Geology, v. 35, p. 403-406.

Li, S.Y., Q, Y.X., Shen, J.F., Sun, L., Liu, B., and Yan, B.K., 2002, Source of Lower Cambrian platinum group elements in black shales in Hunan and Guizhou provinces, China and the Re-Os isotope dating: Science China (Series D), v. 32, p. 568-575.

Lott, D.A., Coveney, R.M., Murowchick, J.B., and Grauch, R.I., 1999, Sedimentary exhalative nickel-molybdenum ores in south China: Economic Geology, v. 94, p. 1051-1066.

Ludwig, K., 2005, Isoplot/Ex version 3.23: a geochronogical toolkit for Microsoft Excel: Geochronology Center. Berkeley, California.

Mao, J.W., Lehmann, B., Du, A.D., Zhang, G.D., Ma, D.S., Wang, Y.T., Zeng, M.G., and Kerrich, R., 2002, Re-Os dating of polymetallic Ni-Mo-PGE-Au mineralization in lower Cambrian black shales of south China and its geologic significance: Economic Geology, v. 97, p. 1051-1061.

Markey, R., Stein, H., and Morgan, J., 1998, Highly precise Re-Os dating for molybdenite using alkaline fusion and NTIMS: Talanta, v. 45, p. 935-946.

Mathur, R., Ruiz, J. and Tornos, F., 1999, Age and sources of the ore at Tharsis and Rio Tinto, Iberian Pyrite Belt, from Re-Os isotopes: Mineralium Deposita, v. 34, p. 790-793.

McArthur, J., Algeo, T., van de Schootbrugge, B., Li, Q., and Howarth, R., 2008, Basinal restriction, black shales, Re-Os dating, and the Early Toarcian (Jurassic) oceanic anoxic event: Paleoceanography, v. 23, p. 4217, doi: 10.1029/2008PA001607.

Ogg, J.G., Ogg, G., and Gradstein, F.M., 2008, The concise geologic time scale. Cambridge University Press, p. 1-177

Oxburgh, R., 2001, Residence time of osmium in the oceans: G-cubed, Geochemistry Geophysics Geosystems, 2, 1018, doi: 10.1029/2000GC000104.

Pasava, J., Kríbek, B., Vymazalová, A., Sýkorová, I., Zák, K., and Orberger, B., 2008, Multiple sources of metals of mineralization in Lower Cambrian black shales of South China: evidence from geochemical and petrographic study: Resource Geology, v. 58, p. 25-42.

Pasava, J., Oszczepalski, S., and Du, A.D., 2010a, Re-Os age of non-mineralized black shale from the Kupferschiefer, Poland, and implications for metal enrichment: Mineralium Deposita, v. 45, p. 189-199.

Pasava, J., Frimmel, H., Taiyi, L., Koubová, M., Martínek, K., 2010b, Extreme PGE concentrations in Lower Cambrian acid tuff layer from the Kunyang phosphate deposit, Yunnan province, South China – Possible PGE source for Lower Cambrian Mo-Ni polyelement ore beds: Economic Geology, v. 105, p. 1047-1056.

Peucker-Ehrenbrink, B., and Hannigan, R.E., 2000, Effects of black shale weathering on the mobility of rhenium and platinum group elements: Geology, v. 28, p. 475-478.

Pierson-Wickmann, A.C., Reisberg, L., and France-Lanord, C., 2002, Behavior of Re and Os during low-temperature alteration: Results from Himalayan soils and altered black shales: Geochimica et Cosmochimica Acta, v. 66, p. 1539-1548.

Piper, D.Z., 1994, Seawater as the source of minor elements in black shales, phosphorites and other sedimentary rocks: Chemical Geology, v. 114, p. 95-114.

Schröder, S., and Grotzinger, J.P., 2007, Evidence for anoxia at the Ediacaran-Cambrian boundary: the record of redox-sensitive trace elements and rare earth elements in Oman: Journal of the Geological Society, v. 164, p. 175-187.

Selby, D., and Creaser, R.A, 2004, Macroscale NTIMS and microscale LA-MC-ICP-MS Re-Os isotopic analysis of molybdenite: Testing spatial restrictions for reliable Re-Os age determinations, and implications for the decoupling of Re and Os within molybdenite: Geochimica et Cosmochimica Acta, v. 68, p. 3897-3908.

Selby, D., Creaser, R.A., Fowler, M.G., 2007. Re-Os elemental and isotopic systematics of crude oil. Geochimica et Cosmochimica Acta, v. 71, p. 378-386.

Sharma, M., Papanastassiou, D.A., and Wasserburg, G.J., 1997, The concentration and isotopic composition of osmium in the oceans: Geochimica et Cosmochimica

Acta, v. 61, p. 3287-3299.

Shirey, S.B., and Walker, R.J., 1995, Carius tube digestion for low-blank rhenium-osmium analysis: Analytical Chemistry, v. 67, p. 2136-2141.

Shu, D.G., Morris, S.C., Han, J., Chen, L., Zhang, X.L., Zhang, Z.F., Liu, H.Q., Li, Y., and Liu, J.N., 2001, Primitive deuterostomes from the Chengjiang Lagerstatte (Lower Cambrian, China): Nature, v. 414, p. 419-424.

Singh, S.K., Trivedi, J.R., and Krishnaswami, S., 1999, Re-Os isotope systematics in black shales from the Lesser Himalaya: Their chronology and role in the Os-187/Os-188 evolution of seawater: Geochimica et Cosmochimica Acta, v. 63, p. 2381-2392.

Smoliar, M.I., Walker, R.J., and Morgan, J.W., 1996, Re-Os ages of group IIA, IIIA, IVA, and IVB iron meteorites: Science, v. 271, p. 1099-1102.

Stein, H., Scherstén, A., Hannah, J., and Markey, R., 2003, Subgrain-scale decoupling of Re and ^{187}Os and assessment of laser ablation ICP-MS spot dating in molybdenite: Geochimica et Cosmochimica Acta, v. 67, p. 3673-3686.

Stein, H.J., Markey, R.J., Morgan, J.W., Hannah, J.L., and Scherstén, A., 2001, The remarkable Re-Os chronometer in molybdenite: how and why it works: Terra Nova, v. 13, p. 479-486.

Steiner, M., Wallis, E., Erdtmann, B.D., Zhao, Y.L., and Yang, R.D., 2001, Submarine-hydrothermal exhalative ore layers in black shales from South China and associated fossils - insights into a Lower Cambrian facies and bio-evolution: Palaeogeography Palaeoclimatology Palaeoecology, v. 169, p. 165-191.

Vine, J.D., and Tourtelot, E.B., 1970, Geochemistry of black shale deposits - a summary report: Economic Geology, v. 65, p. 253-272.

Wen, H.J., Zhang, Y.X., Fan, H.F., and Hu, R.Z., 2009, Mo isotopes in the Lower Cambrian formation of southern China and its implication on paleo-ocean environment: Chinese Science Bulletin, v. 54, p. 4756-4762.

Wille, M., Nägler, T.F., Lehmann, B., Schröder, S., and Kramers, J.D., 2008, Hydrogen sulphide release to surface waters at the Precambrian/Cambrian boundary: Nature, v. 453, p. 767-769.

Wille, M., Nägler, T.F., Lehmann, B., Schröder, S., and Kramers, J.D., 2009, Early Cambrian ocean anoxia in South China - Reply: Nature, v. 459, p. E6.

Zhu, M.Y., Zhang, J.M., Steiner, M., Yang, A.H., Li, G.X., and Erdtmann, B.D., 2004, Sinian-Cambrian stratigraphic framework for shallow- to deep-water environments of the Yangtze Platform: an integrated approach: Progress in Natural Science (Special Issue 2004), p. 75-84.

CHAPTER FIVE：

Mo AND Mo STABLE ISOTOPE GEOCHEMISTRY: ISOTOPE SYSTEM, ANALYTICAL TECHNIQUE AND APPLICATIONS TO GEOLOGY

Xu Lingang [1, 2, *], Bernd Lehmann [1]

1 Mineral Resources, Technical University of Clausthal, 38678 Clausthal-Zellerfeld, Germany

2 MRL Key Laboratory of Metallogeny and Mineral Assessment, Institute of Mineral Resources, China Academy of Geological Sciences, Beijing 100037, China

* Corresponding author: email: lingang.xu@tu-clausthal.de

Published in ***Mineral Deposits*** (in Chinese with English abstract), 2011, v. 30, p. 1-22.

5.1 Abstract

Recently a number of transitional metal isotope systems have been investigated thanks to the advent of multi-collector inductively coupled plasma mass spectrometry (MC-ICP-MS). For example, the analytical uncertainty for Mo isotope measurement is less than ± 0.1‰ (2σ) using the element double spike method to calibrate mass fractionation during Mo purification and mass spectrometric analysis. Natural materials have maximum ~ 3‰ $\delta^{98/95}$Mo fractionation, which is related to redox processes. Under oxic conditions Mo coexists with Mn-oxyhydroxides as the stable oxyanion molybdate (MoO_4^{2-}) resulting in Mo-enriched Mn-Fe sediments characterized by light $\delta^{98/95}$Mo values. In contrast, in reducing H_2S-rich environments, Mo is efficiently removed from seawater. Dissolved molybdate (MoO_4^{2-}) is quantitatively transferred to thiomolybdate (MoS_4^{2-}) without isotopic fractionation. The isotopic composition in euxinic depositional settings therefore records $\delta^{98/95}$Mo values of contemporaneous seawater. Due to the redox-sensitive property, Mo isotope fractionation is a promising proxy for paleo-redox conditions of the Earth's oceanic system and atmosphere. As suggested already by Anbar (Reviews in Mineralogy and Geochemistry, v. 55, pp 429-454), geochemical application of the molybdenum isotope system has vigorously developed during the last years. We here provide an overview on the current state, including a review of the Mo geochemistry and its isotopic behavior, analytical technique, fractionation mechanism, natural reservoirs, and applications both as redox proxy and indicator of ore genesis.

Key words: Mo isotope, isotope fractionation, analytical technique, redox state, black shales

5.2 Transition metals and isotopes

The concept of “transition metal” (sometimes also called a transition element) was originally proposed by the Russian geochemist *Dmitri Ivanovich Mendeleev*, who classified all elements in the periodic table into two groups, one is elements from alkali metal to manganese group and the other is elements from copper group to halogens. The elements between the two groups (group IX, X and XI) were deduced having transitional characteristics. Although the term of transition metal has lost its original meanings, the name is still retained. In the past, the term of transition metal was referred to any element in the d-block of the period table, which includes groups III to XII on the periodic table. All elements in the d-block are metals. In modern terminology, the International Union of Pure and Applied Chemistry (IUPAC) defined that a transition metal is “an element whose atom has an incomplete d sub-shell, or which can give rise to cations with an incomplete d sub-shell”. Group XII elements are not transition metals in this definition.

Many elements in the transition metal family have a number of single-electrons in their electronic configuration, which are readily lost during chemical reaction processes. This characteristic makes most transition metals having variable valence states. For example, Molybdenum (Mo) and Vanadium (V) have several variably stable metal ions. Most of transition metals exist in the crust in oxidized and/or sulfidic states, whereas gold and silver are exceptional, which occur as native elements.

Transition metals are commonly having variable stable isotopes. In 1960s, first attempts of studying transition metal stable isotope systems in Earth sciences have been carried out by precursors (Murthy, 1962, 1963; Crouch et al., 1964; Wetherill, 1964). However, no great progresses were achieved due to the limitation of measurement technology. In recent years, transition metal (e.g. Cu, Zn, Fe and Mo) isotope geochemistry has made great progress thanks to the advent of analytical methods and the use of multiple-collector inductively coupled plasma mass spectrometry (MC-ICPMS), allowing measurement of elements difficult to ionize, for which traditional thermal ion mass spectrometry (TIMS) techniques are difficult to apply. The great innovation of analytical technology promotes understanding of non-traditional element (including transitional elements) isotope geochemistry rapidly. Besides traditional stable isotope systems (e.g. C, H, O, S and N), there are more than twenty non-traditional stable isotope systems reported up to 1996 (Fig. 5-1). Researches on traditional metal isotopes, especially Cu, Zn, Fe, Mo and Cr, are extremely flourishing in the past decade (Zhu et al., 2000; Jiang, 2003; Anbar, 2004; Schauble et al., 2004; Anbar et al., 2007; Asael et al., 2007; Moynier et al., 2007; Schoenberg et al., 2008; Fernandez et al., 2009). Transition metals such as Fe, Cu, Zn and Mo widely occur in almost all kinds of rocks, geological fluids and organisms, and broadly participate in diagenetic and mineralizing processes, and the biospheric cycle. Therefore, study of the geochemical behavior of the transitional metal isotope systems is thought an effective way of understanding geological and biological processes. Although initial attention focused on the potential applications of some non-traditional isotope systems as biosignatures, they are now emerging as powerful proxies for paleo-redox conditions of the Earth`s oceanic and atmospheric systems due to their multivalent and redox sensitive characteristics. Applications of transitional element isotopes to understand paleo-redox condition evolution, ore forming fluid origin and element circulation have gained rapid development (Anbar et al., 2000; Barling et al., 2001; Siebert et al., 2003, 2006; Arnold et al., 2004; Beard et al., 2004; Lehmann et al., 2007; Neubert et al., 2008).

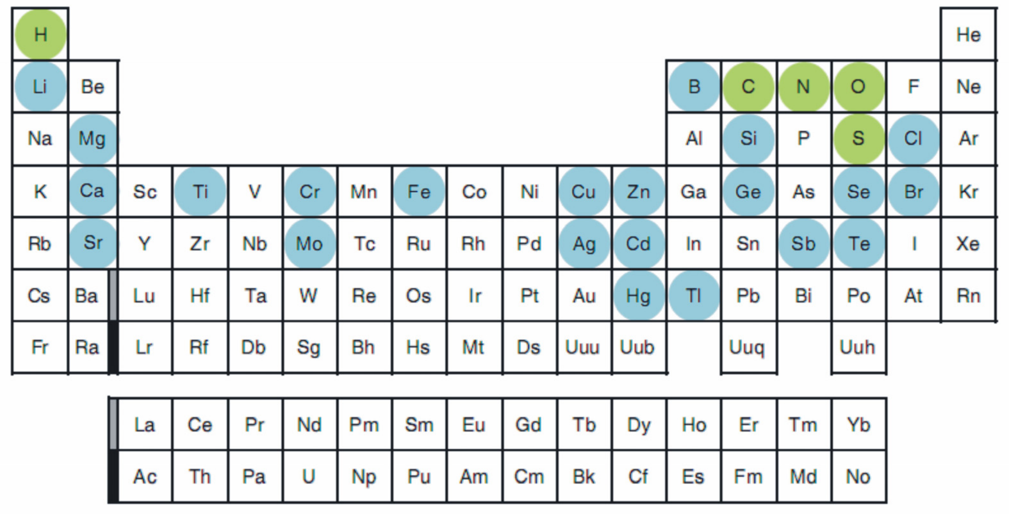

Fig. 5-1: Stable isotope systems used in geochemistry in the Periodic Table of the Elements (after Anbar et al., 2007). Traditional (green) and non-traditional (blue) systems are indicated.

Applications of Mo isotopes as proxies to trace paleocean redox evolution are particularly prosperous in recent years. There are several laboratories, such as the Arizona State University Anbarlab Laboratory in the United States, Isotope Geochemistry Laboratory of Bern University in Switzerland and University of Bristol isotope geochemistry laboratory in the United Kingdom, focusing on Mo stable isotope research, and more and more laboratories are joining in this realm. They have gained a large number of high-precision Mo isotopic data and have established a basic framework of the Mo isotope system, including analytical method, Mo isotope fractionation mechanism, isotopic natural reservoirs, and have accumulated some agreements in applications to paleoceanographic redox conditions reconstruction. However, researches on transition element isotopes, especially the Mo isotope system, are still in their infancy stage in China. This paper attempts to provide an overview on the current state, including a review of the Mo geochemistry and its isotopic behavior, analytical technique, fractionation mechanism, natural reservoirs and applications both as redox proxy and indicator of ore genesis, so as to promote the understanding of transition metal stable isotope systems.

5.3 Mo geochemistry

Molybdenum in the periodic table is located in the second transitional period and VIB group, with atomic number of 42, relative atomic mass of 95.94 and outer electronic structure of $4d^5 5s^1$. Because having empty d sub-shell which is easily forming compounds and high charge/radius ratio, Mo readily exists as stable compounds with a variety of ligands. Molybdenum does not occur as native element in nature, but occurs in variable oxidation states in minerals, ranging from Mo^{2-} to Mo^{6+}, the most stable states being Mo^{4+} and Mo^{6+}. Under oxic conditions Mo exists as stable oxyanion molybdate (MoO_4^{2-}) in solution, whereas under reducing conditions, Mo exists mostly as Mo^{4+} and Mo^{5+}. Although transition metals have some similar geochemical behaviors, each of them is distinguished from others. For example, Fe is a major component of the Earth, with abundance in the upper crust at 6.7 wt.% (Rudnick and Gao 2004), whereas Mo is a trace element with abundance in the upper crust of merely 1.5 ppm. However, it is noteworthy that Mo composition in the modern ocean is ~ 105 nmol/kg, significantly higher than other transitional trace metals (e.g. Cu upper crust abundance is 25 ppm compared to average composition in the oceans of 2.36 nmol/kg; Ni upper crust abundance is 44 ppm compared to average composition in oceans of 8.18 nmol/kg; V upper crust abundance is 107 ppm compared to average composition in oceans of 39.3 nmol/kg). The reason(s) for this differentiation is (are) closely related with the geochemical behaviors. Under the well oxygenated conditions that prevail over much of the Earth's surface, Mo is a highly soluble conservative element with low chemical reactivity, resulting in being the most concentrated of the dissolved trace metals in the ocean and having an exceptionally long residence time of ~ 0.8 Ma (Morford and Emerson, 1999), much higher than any other transition metal (e.g. residence time of Cu is 5 ka, Ni is 6 ka, and V is 50 ka, respectively). Mo in seawater has two main sources. About 90 % Mo is from riverine flux (average Mo content of river is 0.6 ppb), which makes clastic materials such as Mo-bearing rocks, minerals and particles into the seawater; the other ~ 10 % Mo is from low-temperature hydrothermal fluids at mid-ocean ridges (Siebert et al., 2003; Kendall et al., 2009). The two sources essentially form three major reservoirs of Mo in the marine system: seawater, lithogenic materials and authigenically precipitated Mo. With respect to paleo-oceanography, the paleoredox conditions vary between oxidizing and reducing. Tyson and Pearson (1991) and Tribovillard et al. (2006) suggested that the redox gradations can be classified into oxic, suboxic and anoxic. The anoxic conditions may be nonsulfidic or sulfidic depending on the existence of hydrogen sulfide within the water column. The latter condition is termed as euxinic. The anoxic condition with no free H_2S present can also be grouped into suboxic (Tyson and Pearson, 1991; Tribovillard et al., 2006). Under oxic conditions, oxygen concentration in bottom waters is > 2 ml O_2/l H_2O. Suboxic settings are characterized by low oxygen concentration (< 2 ml O_2/l H_2O) with no H_2S in the water column. Euxinic conditions are usually restricted to semi-enclosed basins such as the modern Black Sea and the Cariaco Trench. Oxygen concentration is extremely low (~ 0 ml O_2/l H_2O) and free H_2S is present in the water column under such conditions. As for all elements on the Earth, the distribution of Mo in the environment depends critically on its physical and chemical behaviors, including oxidation state. As a redox-sensitive element, Mo is present in different species according to the redox conditions. The surface seawater is oxic due to photosynthesis and interaction between atmosphere and seawater, where Mo exists mainly in the form of molybdate (MoO_4^{2-}). Mo is not concentrated by ordinary plankton nor is it readily absorbed by most types of natural particles, and it displays little affinity for the surfaces of clay minerals and $CaCO_3$ at marine pH values. However, Mo is readily absorbed onto Mn oxide and hydroxide, resulting in Mo enrichment under oxic conditions caused by Mn absorption mechanism (Goldberg et al., 1998; Erickson and Helz, 2000; Zheng et al., 2000; Tribovillard et al., 2006). Previous studies thought that Fe (oxyhydr)oxides adsorption of Mo is weak, however, through investigating Mo behaviors of variable Mo-, Fe-bearing minerals under different pH conditions and with different Mo/Fe ratios, Goldberg et al. (2009) suggested that Fe (oxyhydr)oxides can also readily adsorb Mo and preferential uptake the light Mo isotopes. This finding is important for better understanding global Mo cycling. In modern oceans, oxic sediments contain a large quantity of Mn and Fe (oxyhydr)oxides, resulting in very high Mo contents (up to 800 ppm) in Mn-Fe-rich sediments. In contrast, under reducing conditions, dissolved molybdate (MoO_4^{2-}) is transferred to thiomolybdate ($MoO_xS_{4-x}^{2-}$, x=0-3).The content of H_2S is a key factor of controlling the efficiency of this transformation process. For example, H_2S content under suboxic conditions is significantly lower than under euxinic conditions, resulting in an average Mo content in suboxic sediments (3-70 ppm) consistently lower than in euxinic sediments (40-150 ppm Mo on average) (Fig. 5-2). As a matter of fact, the Mo precipitation mechanisms related with the presence of H_2S in reducing environments are still not well understood until now. Through investigating Mo and sulfide contents of pore water in the Santa Barbara Basin sediments in America, Zheng et al. (2000) suggested that concentrations of pore water sulfide controlled the formation of authigenic Mo in marine sediments, and identified two chemocline thresholds: the two critical dissolved sulfide concentrations of 0.1 μM and 100 μM. When dissolved sulfide concentration is lower than 0.1 μM, there is no authigenic Mo formation. Authigenic Mo precipitates when the dissolved sulfide concentration is between 0.1 μM and 100 μM, probably by co-precipitation of a Mo-Fe-S phase. When sulfide concentration exceeds 100 μM, authigenic Mo will not precipitate with Fe, but then likely exists as Mo-S or as particle-bound Mo (e.g. MoS_4^{2-}). Through investigating the Mo composition at different water depth of the Black Sea, Emerson and Huested (1991) found that the Mo value is high (> 60 nmol/kg) in the surface water column, where oxic conditions prevail. With the water depth increasing, with less interaction between seawater and atmosphere, or no other sources of oxygen-bearing material, the water column at depth is transformed into a reducing environment. There is a redox chemocline at about 100 m depth, where the Mo content decreases sharply from ~ 40 mnol/kg to ~ 3 nmol/kg. The Mo content goes down to the lowest level at about 400 m, and keeps stable in deeper water columns. Neretin et al. (2001) reported that the H_2S content in the Black Sea is opposite to that of Mo. The content of H_2S increases with increasing seawater depth and the transformation is obvious at the oxic/suboxic boundary (Fig. 5-3). Helz et al.

(1996), Erickson and Helz (2000), Neubert et al. (2008) suggested that the geochemical character of Mo changes sharply in the H_2S-bearing water column of the Black Sea, which has been likened to a “geochemical switch” defined as Action Point of Switch (APS). In the Black Sea, the APS is 11 μM at about 400 m seawater depth, which is corresponding to the chemochine of suboxic and euxinic. The general finding by previous studies is that Mo enrichment occurs under two conditions: one is under oxic conditions related to Fe and Mn (oxyhydr)oxides absorption, the other is in H_2S-bearing euxinic sediments.

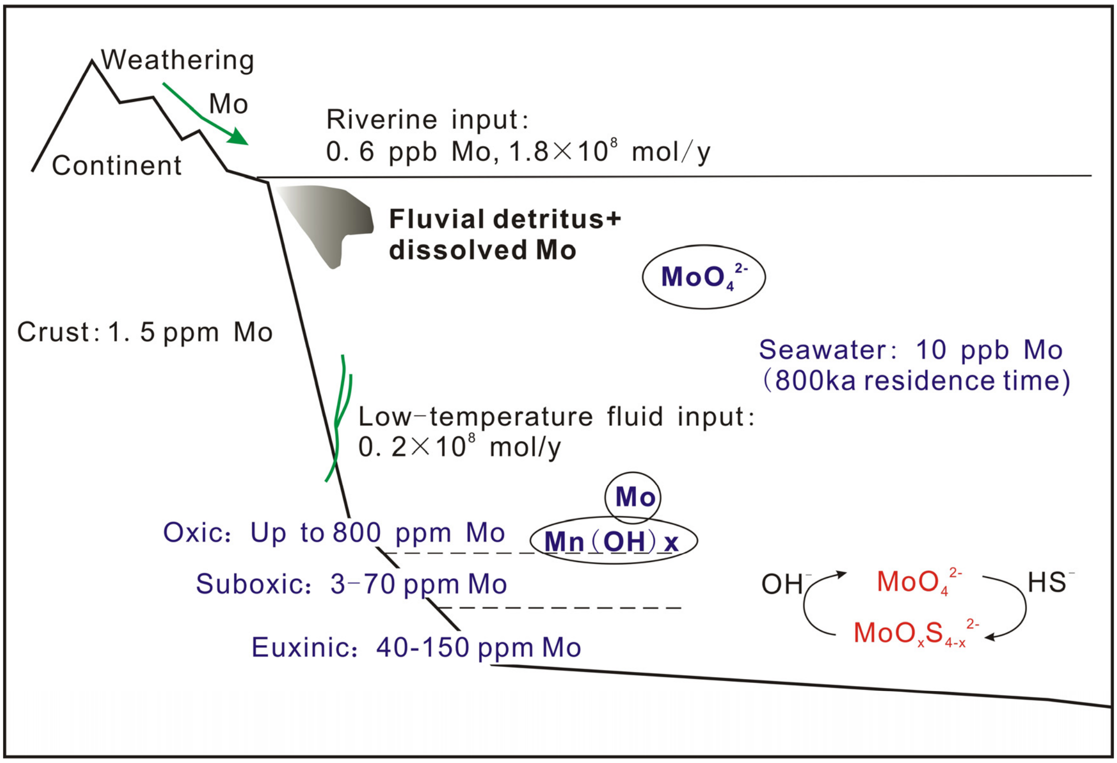

Fig. 5-2: Mo cycle in the modern ocean system. Mo in the modern ocean has two sources: continental weathering (90%) and low-temperature fluid input (10%), and forms three Mo-bearing sedimentary reservoirs in the oceans: oxic, suboxic and euxinic.

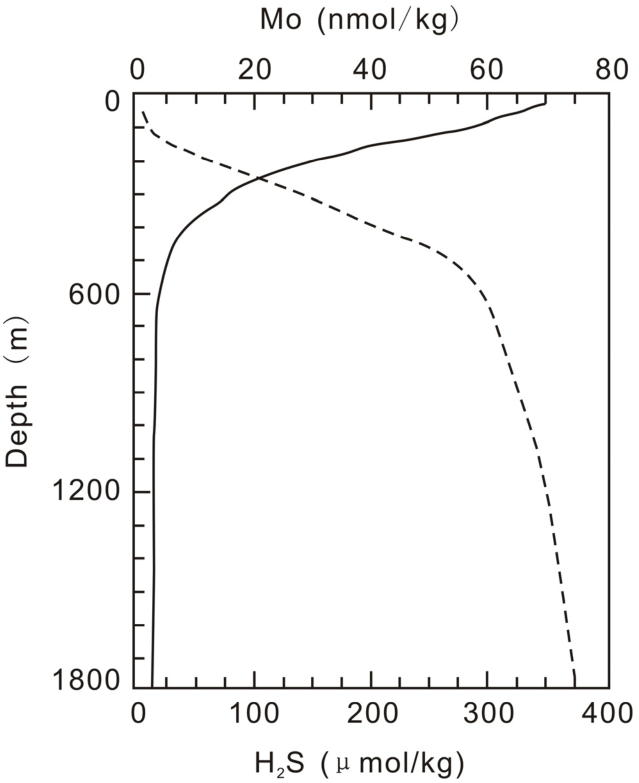

Fig. 5-3: Depth profiles of Mo (solid line) and H_2S (dashed line) in the Black Sea. Data sources: Emerson and Huested (1999); Neretin et al. (2001). The concentration of Mo falls sharply in the euxinic zone opposite to H_2S.

5.4 Mo isotope fractionation

There are seven stable isotopes of molybdenum in nature. The natural relative abundances range from 10% to 25%, covering a mass range of ~ 8% with ^{92}Mo (14.84%)，^{94}Mo (9.25%)，^{95}Mo (15.92%), ^{96}Mo (16.68%), ^{97}Mo (9.55%), ^{98}Mo (24.13%) and ^{100}Mo (9.63%) (Fig. 5-4). From an analyst's perspective, the seven Mo isotopes have a large mass spread, which can provide a number of options for isotope ratio determination. Previous studies have found that Mo isotope fractionation is significantly sensitive to redox conditions. And moreover, such fractionation is not sensitive to other physical and chemical factors (e.g. water column pH value, temperature, biological processes), which do not influence Mo isotope fractionation (Barling and Anbar, 2004; Nägler et al., 2004; Wasylenki et al., 2006). In addition, the advent of MC-ICP-MS technology makes possible to obtain high-precision Mo isotopic ratios (Anbar et al., 2001; Siebert et al., 2001). Due to the above discussed reasons, although the Mo isotope system attracted geologists` attention for only in recent years, applications of Mo stable isotope system to reconstructing paleo-oceanic redox conditions have shown unique advantages.

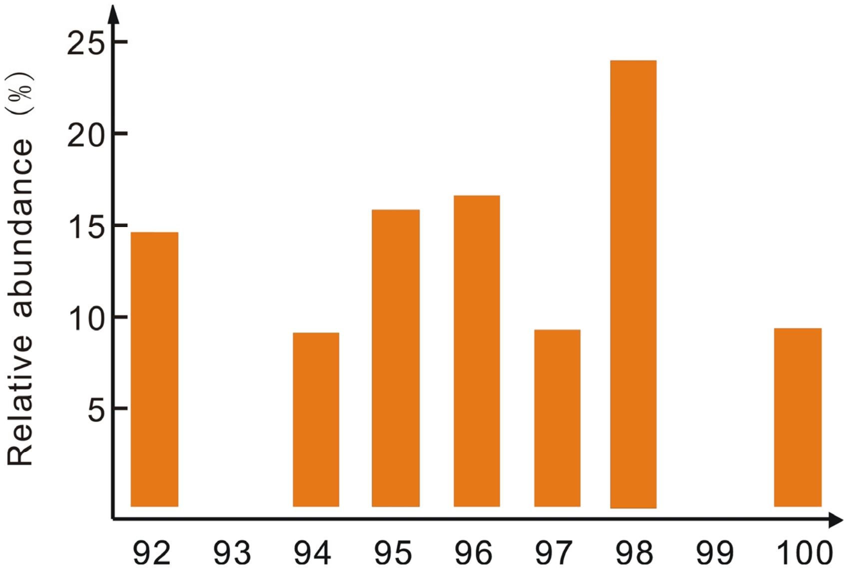

Fig. 5-4: The relative natural abundances of the stable Mo isotopes (after Moore et al., 1974).

5.4.1 Redox condition constraint on Mo isotope fractionation

Previous studies found that Mn oxyhydroxides are readily adsorbing Mo, which can lead to Mo isotope fractionation (Siebert et al., 2003; Arnold et al., 2004; Barling and Anbar 2004). Such fractionation is sensitive to the changes of overlying water column redox conditions. Conversely, changes of the Mo isotopes in sedimentary rocks may be indicative of coeval sedimentary conditions to some extent. In modern oceans, Mo adsorption onto oxide and hydroxide particles is obvious. The light Mo isotope is easily fractionated from solution, resulting in Fe-Mn nodules in the modern oceans which are rich in Mo content and characterized by light Mo isotopes (Barling et al., 2001; Siebert et al., 2003). This fractionation mechanism has also been proved experimentally (Barling and Anbar 2004; Wasylenki et al., 2006). The experiments indicated that adsorption on Mn oxyhydroxide was leading to light Mo enrichment, whereas the heavy Mo was kept in solution. They also found that pH and temperature had little influence on the Mo isotopic fractionation during adsorption processes. Barling and Anbar (2004) conducted an experimental investigation into the mass-dependent fractionation of Mo isotopes during adsorption onto Mn oxyhydroxide. Experimentally determined fractionation factors ($\alpha_{soln\text{-}MnOx}$) exhibit no systematic variation with different experimental pH condition. The mean ($\alpha_{soln\text{-}MnOx}$) for all experiments is 1.0018 ± 0.0005 (2 s.d). Wasylenki et al. (2006) conducted adsorption experiments to measure the effect of temperature on Mo isotopic fractionation and reveal little sensitivity to temperature.

Euxinic conditions can lead to enrichment of heavy Mo isotopes. However, the fractionation mechanism is still not well understood. Many scientists suggest that the Mo isotope fractionation under euxinic condition may relate to ligand exchange. Erickson and Helz (2000) investigated the state of Mo in different seawater depth in the Black Sea and suggested that under reducing conditions the existence of H_2S played an important role in processes of molybdate converting to thiomolybdate. Continued replacement occurred between H_2S and molybdate, leading to the formation of a series of thiomolybdates. Such processes ended with the formation of tetrathiomolybdate. In reducing solution, molybdate undergoes sulfidation in four steps that conserve Mo^{VI} and lead to formation of tetrathiomolybdate: $MoO_xS_{4-x}^{2-} + H_2S_{[aq]} \leftrightarrow MoO_{x-1}S_{5-x}^{2-} + H_2O(l)$, $1 \leq x \leq 4$. The above chemical reaction equation reaches equilibrium when the content of $H_2S_{[aq]}$ is above 11 μM, which is the so-called Action Point of Switch (APS). Above this level, molybdate is rapidly converted to oxythiomolybdates and removed from solution. Even though the content of $H_2S_{[aq]}$ may be continuously increasing with depth after reaching to the APS, the relative abundance of different thiomolybdate species below the APS is constant in the seawater column. Successful application of the above model to interpret the Mo isotopic changes with seawater depth in the Black Sea was carried out by Neubert et al. (2008), who found that below 400 m, where the seawater is under euxinic conditions, the water column is characterized by heavy Mo isotope composition (Fig. 5-5).

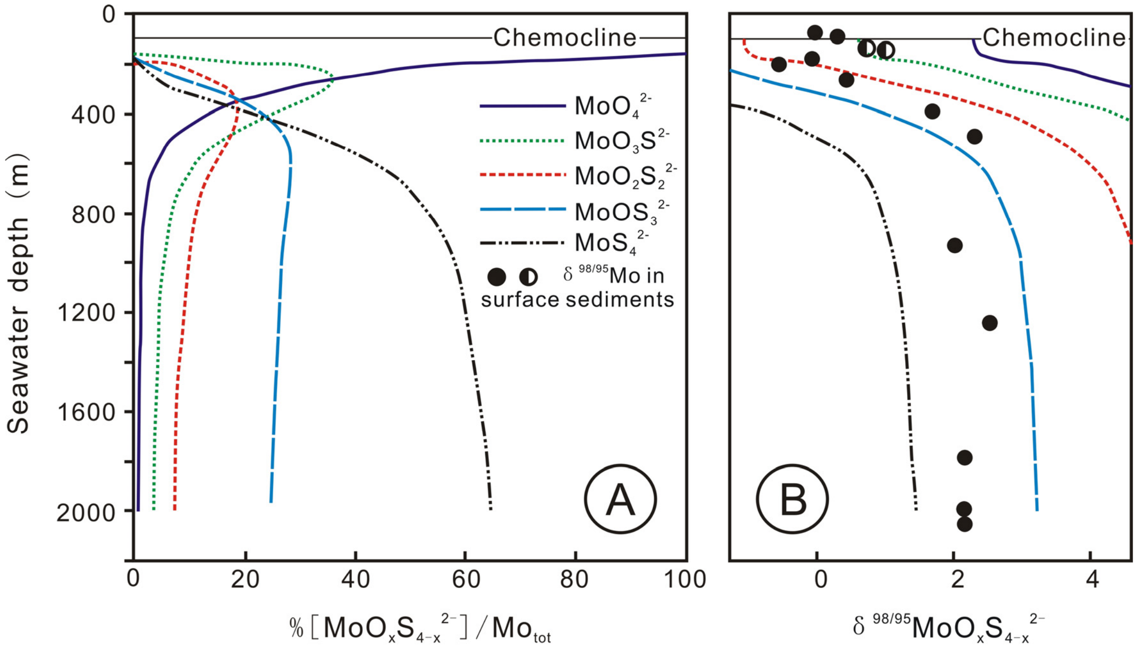

Fig. 5-5: Depth profile versus thiomolybdate species concentrations and $\delta^{98/95}$Mo values below the chemocline in the Black Sea (after Neubert et al., 2008). **A:** Graph shows depth profile of thiomolybdate species concentrations (Calculations are based on the model of Erickson and Helz, 2000 and Neretin et al., 2001). **B:** Graph shows depth profile of $\delta^{98/95}$Mo values of the respective species pools (Mo isotope fractionation between MoO_4^{2-},$MoO_2S_2^{2-}$ and MoS_4^{2-} is based on Tossell, 2005, MoO_3S^{2-} and $MoOS_3^{2-}$ are interpolated).

The Mo isotope fractionation under suboxic condition did not get much substantial attention in early studies (e.g. Arnold et al., 2004), and the thereby established the global Mesoproterozoic paleo-ocean redox model is questionable. In recent years, more and more studies emphasize the Mo isotopic fractionation processes under suboxic conditions (Poulson et al., 2006; Siebert 2006; Anbar and Gordon, 2008; Pearce et al., 2008; Scott et al., 2008; Gordon et al., 2009; Kendall et al., 2009). Although the Mo isotope fractionation mechanism under suboxic conditions is not yet clear, recent studies indicate that the Mo isotope fractionation efficiency under suboxic condition is somewhere in between oxic and euxinic conditions. The reason(s) for this phenomenon may be due to the lack of H_2S in water columns under suboxic conditions, which limits the conversion efficiency from MoO_4^{2-} to MoS_4^{2-}. There are a series of thiomolybdate species in pore waters ($MoO_{4-x}S_x^{2-}$), and the Mo isotope fractionation is thus influenced. The Mo isotopic values under suboxic conditions are normally in the range of oxic and euxinic conditions with $\delta^{98/95}$Mo values from -0.45‰ to 1.6‰ (Fig. 5-6).

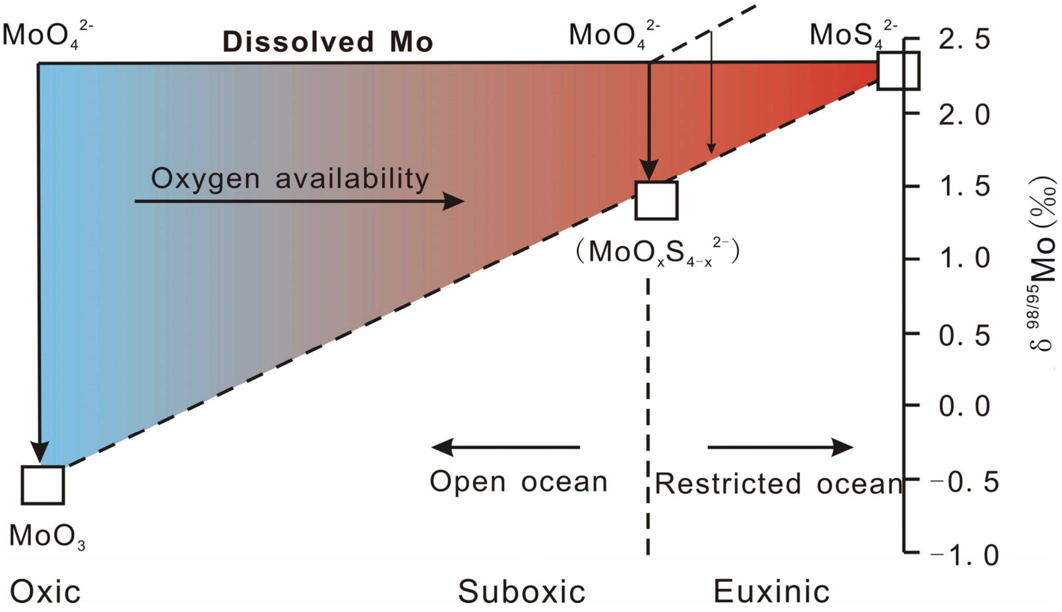

Fig. 5-6: Mo chemical behavior and Mo isotope compositions in different modern marine sediments (after Poulson et al., 2006)

5.4.2 Other factors which influence Mo isotope fractionation

In order to better understand the temperature influence to the Mo isotope fractionation, through quantum-mechanics theoretical calculation, Tossell (2005) predicted that equilibrium fractionation occurs between MoO_4^{2-} and MoO_3 in solution, followed by preferential adsorption of isotopically lighter MoO3, whereas heavy Mo isotope preferentially exists as MoO_4^{2-}. He predicted that temperature can influence the Mo isotope fractionation, the predicted soln-MnOx fractionation factor is 1.0019 at 0°C, but decreases sharply with increasing temperature to $\alpha = 1.0010$ at 25°C and 1.0006 at 100°C. However, Wasylenki et al. `s (2006) experiment indicated that the Mo isotopic fractionation is little sensitive to temperature, which is not in agreement with the theoretical calculations by Tossell (2005). Wasylenki et al. (2006) observed a fractionation factor of $\alpha = 1.0019 \pm 0.0001$ (2 s.d) at 1°C, and $\alpha = 1.0016 \pm 0.0001$ (2 s.d) at 50°C. This magnitude of fractionation is in good agreement with experimental work by Barling and Anbar (2004), who obtained a fractionation factor of 1.0018 ± 0.0005 (2 s.d) at 25°C. The experiments indicate that the influence of temperature to Mo isotope fractionation is weak. More studies of Mo isotope fractionation are still needed to know the reasons of deviation between theoretical calculation and experimental results.

Biological (including microbial) processes can lead to isotope fractionation for many elements, e.g. S, C, Si and Fe. Biological processes may influence the Mo isotope fractionation. Nägler et al. (2004) investigated the Mo isotope fractionation effects using the nitrogen-fixing marine cyanobacterium Trichodesmium sp.. The study indicated that biological processes can lead to Mo isotopic fractionation; however, such an effect is quite weak. Even though Trichodesmium sp. preferentially adsorbs light Mo isotope, the fractionation of $\delta^{98/95}$Mo is only -0.3 ‰.

5.5 Mo isotope analytical techniques

Since the early 1960s, precursors have tried to measure Mo isotope variations using thermal ion mass spectrometry (TIMS) (Murthy 1962, 1963; Crouch and Tuplin 1964). However, different studies have got very variable experimental results even when measuring the same materials. The main reason for these measurement uncertainties comes from analytical technique. The TIMS technique failed to correct Mo isotope fractionation that was produced during measurement, which resulted in large measuremental uncertainties. In some cases, the uncertainties caused by TIMS measurements were even larger than the actual natural isotope fractionation. Because of this reason, although TIMS-based studies on the Mo isotope system continued (e.g. Turnlund et al., 1993; Lu and Masuda, 1994; Wieser and DeLaeter, 2000, 2003; Yin et al., 2002), it is still not widely accepted. Only with the advent of MC-ICP-MS in the mid 1990s, studies focusing on the Mo isotope system are becoming vigorous. In recent years, applications of MC-ICP-MS technique to study Mo isotopes are widely accepted (e.g. Anbar et al., 2001; Siebert et al., 2001; Nakagawa et al., 2008). The MC-ICP-MS technique is generally preferred over TIMS because of the high ionization efficiency of Mo in the ICP source (permitting sample sizes < 1 μg), the elimination of blank contamination from Mo in TIMS filaments, and more rapid sample throughput (Halliday et al., 1995). Therefore, the MC-ICP-MS technique can get very accurate and precise analytical results for Mo isotopes and is preferred to TIMS.

5.5.1 Mo isotope definition

As the seven Mo stable isotopic natural abundances vary widely, the large number of Mo isotopes makes it possible to perform both analysis and data reporting in variable ways. It is common to analyze the relative abundances of as many isotopes as possible to confirm that the observed variations are mass dependent and not analytical artifacts. Such confirmation is particularly significant because the whole procedure of analysis must try to avoid isobaric interferences from other elements (e.g. Zr, Ru, $^{40}Ar^{55}Mn^+$ and $^{40}Ar^{56}Fe^+$). Similar to other transitional elements such as Fe, Cu and Zn, the Mo isotope data are generally reported using the conventional δ notation, which is expressed as follows:

$$\delta^{X/95}\mathrm{Mo} = \frac{(^{X}\mathrm{Mo}/^{95}\mathrm{Mo})_{\mathrm{sample}} - (^{X}\mathrm{Mo}/^{95}\mathrm{Mo})_{\mathrm{standard}}}{(^{X}\mathrm{Mo}/^{95}\mathrm{Mo})_{\mathrm{standard}}} \times 1000$$

Where x = 97 or 98, $\delta^{X/95}$Mo is presented as per mil. They are the two most popular definitions in recent studies. Anbar et al. (2001) and Barling et al. (2001) reported $\delta^{97/95}$Mo in their early studies, because ^{97}Mo and ^{95}Mo are the only Mo isotopes completely free of isobaric interferences from other elements. Siebert et al. (2001) established the ^{97}Mo-^{100}Mo double spike method to calibrate Mo isotope fractionation. Because ^{97}Mo is used in the elemental double spike procedure, they reported $\delta^{98/95}$ to express Mo isotope fractionation in their studies. Many recent ^{97}Mo-^{100}Mo double spike-based publications applied this definition (McManus et al., 2002; Siebert et al., 2003; Nägler et al., 2005; Neubert et al., 2008; Wille et al., 2008). No matter which definition, they can be converted to each other. The conversion is $\delta^{97/95}\mathrm{Mo}_{\mathrm{sample}}$(‰) ≈ $2/3\times\delta^{98/95}\mathrm{Mo}_{\mathrm{sample}}$(‰) (although this relationship is not exact for all fractionation laws, e.g. Criss 1999, Young et al. 2002). For better comparison, all data in this work are presented as $\delta^{98/95}$Mo.

5.5.2 Mo isotope standards

Up to now there is no uniform internationally-certified Mo isotope standard.

Different scientific groups have used different laboratorial standards. Therefore, comparing Mo isotope data from different laboratories needs special attention, because those data may be obtained based on different laboratory standards. At present, Johnson Mattey Company (JMC) ultra-pure molybdenum and Charleston ICP standard Mo solution are the two most popular Mo isotope standards used in different laboratories. Even though different laboratories applied the same JMC ultra-pure Mo standard (Mo content is up to 99.93%), the measurement method can also lead to different JMC Mo isotope data. For example, Barling et al. (2001) reported data relative to the Rochester JMC standard. This laboratory standard is similar to average crustal Mo and therefore is a convenient reference point. Siebert et al. (2003) used JMC ultra-pure Mo solution as standard in their studies, which is similar to the Rochester JMC standard applied by Barling et al. (2001), indicating that data from the two groups are comparable. Mean Ocean Mo (MOMO) standard is thought an ideal laboratorial standard, because data from different laboratories can be compared with reference to the mean Mo isotope composition of seawater (Siebert et al., 2003). However, MOMO is not a practical standard because the need for significant preconcentration of Mo from seawater creates a risk of contamination during sample handling or chromatographic isotope fractionation, because the Mo isotope composition of seawater is heavier than of most other materials (see below discussion) (Anbar, 2004). In order to know the comparability of data relative to different laboratorial standards, Zhang et al. (2008) attempted to compare different laboratorial standard solutions relative to *NIST SRM 3134 ICP* Mo standard and found that measurement results are basically consistent. Uncertainties of the measurements were better than 0.1 ‰ (Fig. 5-7). This means, although various laboratories applied different Mo isotope standards, data relative to different standards are essentially comparable. However, certification of an international reference standard for internationally laboratory comparison should be a high priority for the Mo stable isotope community.

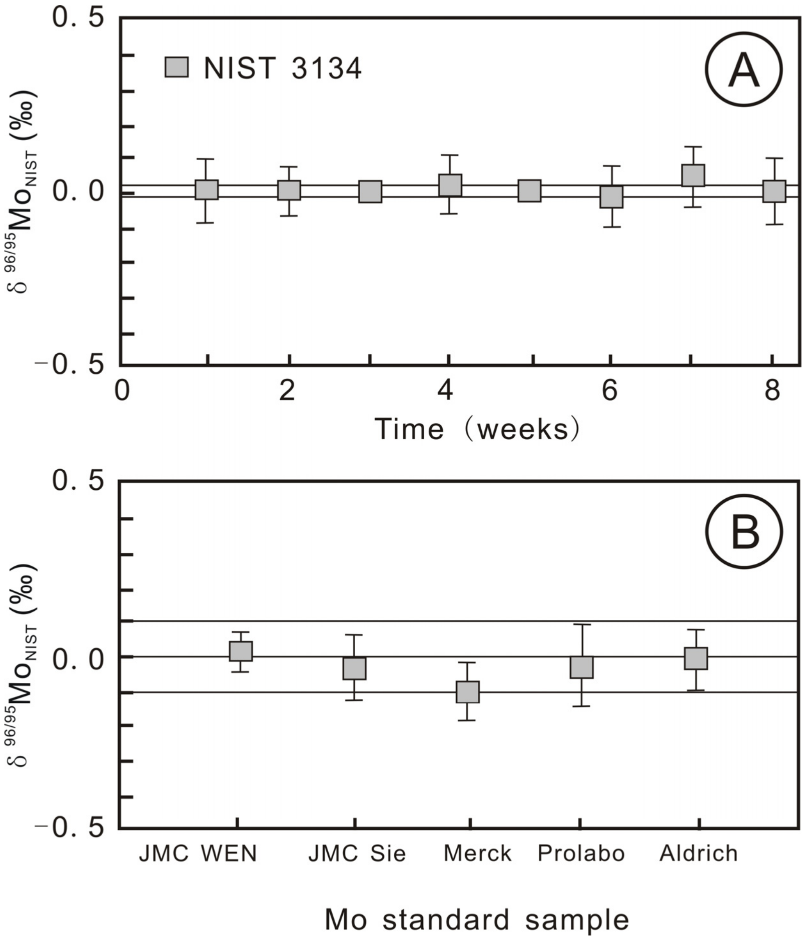

Fig. 5-7: A: Results of $\delta^{96/95}Mo_{NIST}$ values measured in eight weeks (after Zhang et al., 2008). **B:** Results of $\delta^{96/95}Mo_{NIST}$ values relative to the NIST SRM 3134 Mo standard.

5.5.3 Sample digestion and chemical separation

In order to obtain highly precise Mo isotope analytical results, a pretreatment procedure is necessary for most natural samples, in which generally Mo abundances range from 1 ppm (e.g. average curst) to ~ 100 ppm (e.g. black shales and marine Fe-Mn crusts and nodules). Actually, Mo composition in natural samples varies greatly. For example, the average Mo abundance in seawater is only ~ 10 ppb; whereas black shales formed under euxinic conditions usually contain n×10^2 ppm Mo

(Holland, 1979). Mo content of the Ni-Mo-PGE-Au polymetallic sulfide ore hosted by black shales in South China even reach up to n wt.% level (Steiner et al., 2001; Mao et al., 2002; Jiang et al., 2006). Before measurement, Mo abundances in natural samples need to be preconcentrated (or prediluted) to a measurable range. Normally Mo composition in n ~ n×10^2 ppm range is ideal for measurement. Purification is also essential for most natural samples. Measurements of Mo isotope fractionation may be influenced by isobaric interferences, especially elements or ion complexs with mass number between 94 and 97. For example, both Zr and Ru have three stable isotopes, including ^{92}Zr, ^{94}Zr, ^{96}Zr and ^{96}Ru, ^{98}Ru, ^{100}Ru, respectively, which have the same mass numbers with that of Mo isotopes (Fig. 5-8) (Wieser and DeLaeter, 2009). Potential polyatomic interferences at masses 95 and 96 from ^{55}Mn^{40}Ar$^+$ and ^{56}Fe^{40}Ar$^+$ in ICP-MS may also influence the measurement accuracy. Purification processes must meet three demands: (1) to make sure Mo composition in cleaning solution as low as possible, and most Mo comes into solution for measuring, which means, high Mo recovery; (2) to make sure chemical separation of isobaric elements is not conducing Mo isotope fractionation; (3) to make sure complete chemical separation of isobaric elements, which may influence the Mo isotopic fractionation during measurement.

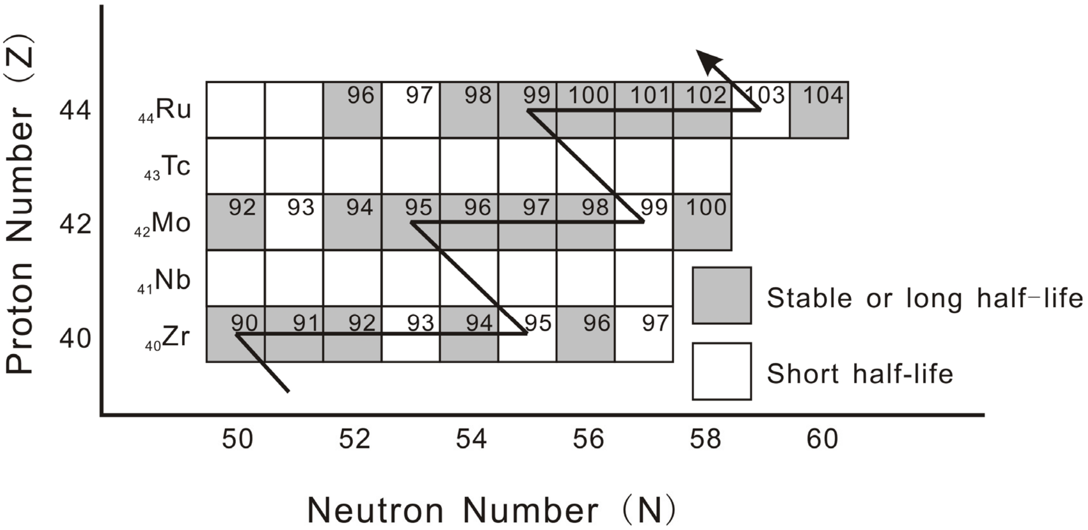

Fig. 5-8: A potential interference problem in the analysis of Mo isotopic composition caused by isobaric nuclides of Zr and Ru (after Wieser and DeLaeter 2009).

Ion Exchange Chromatography (IEC) is the traditional method for chemical purification. This method uses ion exchange resins to clean isobaric nuclides, which are potentially interferential. Currently the most popular used Mo isotope separation resins include Dowwx AG1, BioRad AG1-X8 anion resin and BioRad AG50W-X8 cation resin, Chelx100 resin and TSK-8HG resin. Because various laboratories applied different resins, procedures of the IEC used in those laboratories are slightly different (Barling et al., 2001; Siebert et al., 2001; Malinovsky et al., 2005; Pietrusxla et al., 2006).

Barling et al. (2001) and Siebert et al. (2001) used the anion and cation double resin columns method for chemical purification of Mo-bearing samples. This method includes several procedures. Firstly, powdered sample are ashed in a drying-cupboard at 800°C overnight to erase organic matter, and then dissolved with mixed HF and HNO_3 solution in Teflon bombs. Element spikes (see below) are added into solution, and then dried in a stink cupboard. Dissolution and dryness procedures can be repeated for several times to dissolve the sample completely. The sample is then finally dissolved in 6 M HCl. The two-column ion exchange separation technique is used for chemical purification. BioRad AG1-X8 anion resin and BioRad AG50W-X8 cation resin were successively loaded to clean isobaric nuclides. The BioRad AG1-X8 anion resin can separate Zr and substantial amounts of other cations (except for Fe) from Mo-bearing solution. Because Fe is a major element in most samples, the anion column does not separate Fe from Mo. In highly concentrated HCl solution, Fe exists as $FeCl_4^-$, which is residual in anion resin together with Mo. In order to erase Fe, the BioRad AG50W-X8 cation resin is employed. Sample is loaded and eluted in 1 M HCl. Mo (as anionic complexes) passes through the column, while cations and cationic complexes, such as Fe, are retained by the resin. Mo recovery from this column is quantitative.

Malinovsky et al. (2005) applied chelating resin Chelex-100 for sample purification, which improved Mo recovery rate from Fe ions. Aqua regia was used to dissolve ashed samples completely, and then dissolved into 0.3 M HNO_3 solution. 6

M HNO_3 and Milli-Q water were employed for resin cleaning. The reason for using 6 M HNO_3 for resin cleaning is that the final elution of Mo from the ion exchange resin was realized using 6 M NH_3 solution. Upload samples onto the chelating resin Chelex-100. 0.07 M HCl and 0.1 M HF solution were added successively in order to eluting matrix. Mo was then eluted from the column in 6 M NH_3 solution. The samples were dried down on a hot plate and re-dissolved in 0.3 M HNO_3 solution, which is ready for Mo isotopic analysis. The whole procedure of sample purification was done in a super-clean laboratory.

Pietruszka et al. (2006) improved the anion and cation two-column exchange resin technique. This technique is to dissolve and to dry the ashed samples repeatedly and then dissolved into 6 M HCl solution. HNO_3, Milli-Q water, and HCl were employed for resin cleaning. Upload samples onto the cleaned anion exchange resin to erase Zr and substantial amounts of other isobaric nuclides. Then, use mixed 0.1 M HF and 0.1 M HCl solution to elute the anion resin. Dry and re-dissolve the samples into 6 M HCl solution and then upload them into AG50W-X8 cation exchange resin, which is to erase Fe and other residual elements (e.g. U, Al, Ni, Mg and Zn). This technique is efficient for Mo recovery, for example, Pietruszka et al. (2006) applied this method for molybdenite Mo isotope analysis and obtained 97.7-99.5% Mo recovery. Nakagawa et al. (2008) developed a preconcentration technique using TSK-8HQ resin technique. The advantage of the TSK-8HQ resin technique is that Mo in seawater could be effectively separated from matrix elements such as alkali, alkaline earth, and other transitional metals. The common disadvantage of the preconcentration and purification methods mentioned above is that a large quantity of acid solution is employed for resin cleaning and isobaric nuclides elution. By step collecting eluted solution technique during eluting processes, Zhang et al. (2008) reduced the amount of acid solution used for resin cleaning and isobaric nuclides elution, which decreased contamination risk of low-Mo sample caused by acid solution. The Mo recovery rate of this technique is also satisfactory.

5.5.4 Mo isotope fractionation calibration

Two factors contribute to Mo isotope fractionation during analytical procedures: sample pretreatment and mass spectrometric analysis. Mo isotope fractionation conduced by sample pretreatment can be reduced by increasing Mo recovery rate. At present, Mo recovery rates of the purified samples applying above mentioned IEC techniques are better than 95%, which effectively reduce the problem of Mo isotope fractionation during sample pretreatment. For sample mass spectrometric analysis, the ionization effect when sample solutions pass through the analytical instrument can also conduce to Mo isotope fractionation. There are three most popular calibration techniques for Mo isotope fractionation conduced by sample mass spectrometric analysis. They are briefly summarized as follows:

Sample standard bracketing: This calibration method is based on the assumption that the analytical instrument has the same isotopic fractionation effect on both sample solutions and standard samples. In early studies (e.g. Murthy 1962, 1963; Crouch and Tulpin, 1964), the sample standard bracketing was used in TIMS techniques for Mo isotope fractionation calibration. However, it was realized that this method is questionable (Anbar, 2004). In TIMS technique, as a result of isotope enrichment during thermal evaporation and ionization, the isotope composition of an analyte increases during analysis. The time-course of this fractionation is highly sensitive to sample purity and operating conditions. Nevertheless, sample-standard comparison is more applicable in MC-ICP-MS technique, in which instrument mass fractionation is fundamentally in steady state. Applications of this method in MC-ICP-MS have been successful for some transitional metal isotopes (particularly Fe isotopes) (Zhu et al., 2004). However, unlike Fe, Mo is a trace constituent of most samples, which increases the risk of non-systematic changes in instrument mass fractionation, particularly arising from differences in matrices, between samples and standards. Thus, this calibration method is not widely accepted in MC-ICP-MS measurements.

Element spike: Barling et al. (2001) successfully employed Zr as the element spike for studying Mo isotope fractionations in geological materials. and precision of ± 0.25 ‰ (± 2σ) was reported in measurement of $\delta^{97/95}$Mo, with comparable results for other ratios. In this method, a different element with known isotopic composition is added to the sample, which is used for monitoring variations of instrumental mass fractionation. This method is reasonable for MC-ICP-MS analysis and based on the assumption that the relative isotopic fractionation behavior of different elements in ICP sources is more or less constant. The two most common used spikes are Ru and Zr in recent studies (Maréchal et al., 1999; Anbar et al., 2001).

Isotope double spike: Dietz et al. (1962) introduced this method which was applied to TIMS technique for isotopic fractionation calibration. Although sample pretreatment, double spike calibration and calculation of isotope fractionation are much more complex than sample standard bracketing and element spike methods, the isotope double spike method is thought the most rigorous for isotope fractionation calibration for its high precision. Samples are doped with a known quantity of spike Mo which consists of two isotopes in a known ratio. The double spike isotopes serve as an internal standard to monitor mass fractionation of the sample subsequent to spiking. The fundamental advantage over the element spike is that the spike isotopes follow exactly the same fractionation behavior as the isotopes of interest, therefore high precision measurement results can be obtained (Anbar, 2004). Siebert et al. (2001) successfully applied the double spike method in MC-ICP-MS. The precision of measured $\delta^{98/95}$Mo is ± 0.1‰ (± 2σ), using ^{97}Mo-^{100}Mo as double spike (Fig. 5-9). This calibration method has been employed to a range of natural materials (McManus et al., 2002; Siebert et al., 2003; Nägler et al., 2005; Neubert et al., 2008; Wille et al., 2008). Three reasons decide choosing masses ^{97}Mo and ^{100}Mo as double spike: (1) The relative abundance of ^{97}Mo and ^{100}Mo is low (9.55% and 9.63%, respectively). (2) There are no elemental isobaric interferences on mass 97. On mass 100, there is potential ^{100}Ru interference, however, which can easily be reduced using IEC method.

(3) Highly enriched ^{97}Mo and ^{100}Mo can be obtained, for example, from Oak Ridge National Laboratory (94.2% and 97.2 %, respectively) (Siebert et al., 2001). Because Siebert et al. (2001) use ^{97}Mo in their double spike procedure, $\delta^{98/95}$Mo is presented for isotope fractionation in their publications (Siebert et al., 2001; McManus et al., 2002; Siebert et al., 2003; Nägler et al., 2005; Neubert et al., 2008; Wille et al., 2008). The isotope double spike method is not only applied in MC-ICP-MS, but also in TIMS techniques. Wieser and de Laeter (2003) reported precision of better than ± 0.1‰/amu mass difference (± 2σ) using a ^{94}Mo-^{100}Mo double spike with the TIMS technique.

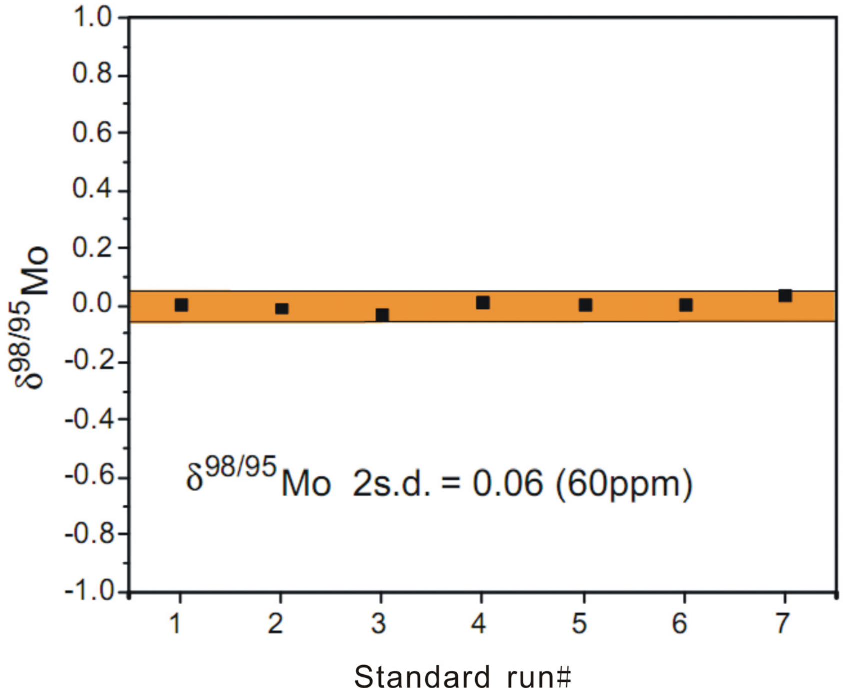

Fig. 5- 9: Plot of $\delta^{98/95}$Mo versus standard measurements within one session (after Siebert et al., 2001).

Because Mo isotope fractionation of natural materials is small ($\delta^{98/95}$Mo ~ 3‰, Poulson et al., 2006), analysis of Mo isotopes needs high precision. The isotope double spike method meets this demand compared with the sample standard bracketing and element spike methods. In addition, the isotope double spike can circumvent the need for high yield chemistry if the spike isotopes are added prior to Mo purification and extraction, thereby providing an internal reference point for isotope fractionation produced by the instrument as well as by the separation chemistry (Anbar, 2004). Considering the advantages of the isotope double spike method, it will have a bright future for studying geological samples.

5.6 Mo isotope reservoirs of natural materials

The currently available dataset for Mo isotopes is related with many aspects, including reservoirs, Mo sources and sinks of the ocean geochemical cycle. These works have drawn a framework of Mo isotope geochemistry. According to Mo geochemical cycling, the Mo isotope reservoirs of natural materials can be distinguished into three categories: igneous rocks, geological fluids and marine sediments. At present, Mo isotope data of igneous rocks are from basalts, granites and hydrothermal molybdenites. Mo-bearing geological fluids occur widely and can be classified into four groups: seawater, low-temperature hydrothermal fluids, suboxic porewaters, and lakes and rivers. In marine sediments, Mo is fixed mainly in Fe-Mn oxides, euxinic sediments, suboxic sediments, and clastic and pelagic sediments. Anbar (2004) summarized the Mo isotope reservoirs of natural materials. Fig. 5-10 gives an updated overview of principles of Mo distribution in different natural materials, including different types of rocks, minerals, geological fluids and sediments, as well as their isotopic characteristics.

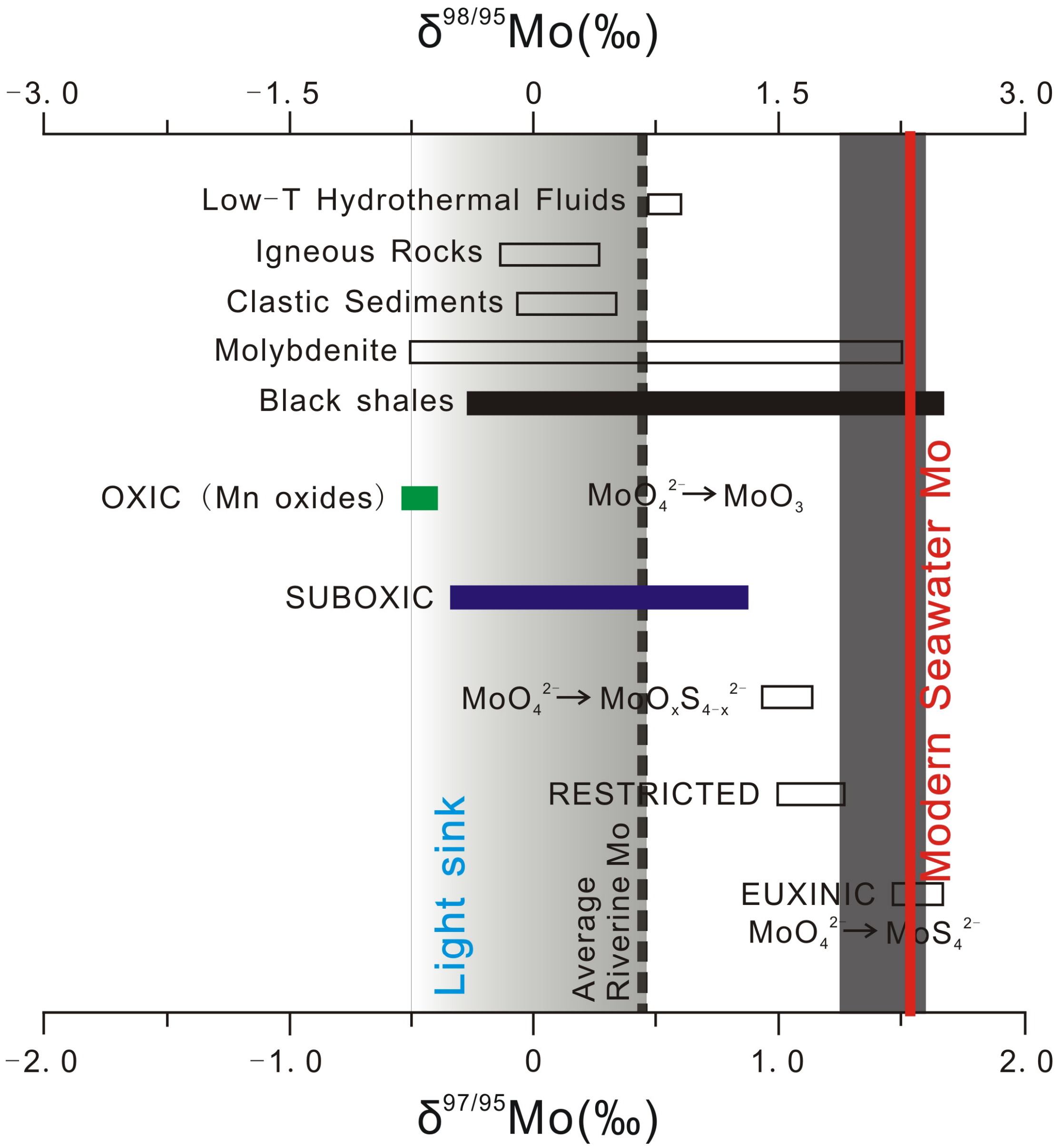

Fig. 5-10: Molybdenum isotope composition of present-day seawater sources and sinks (modified from Kendall et al., 2009). Data sources: Low-temperature fluids: McManus et al. (2002); igneous rocks, clastic sediments, molybdenites, black shales: Barling et al. (2001), Siebert et al. (2003, 2005), Arnold et al. (2004), Nägler et al. (2005), Kendall et al. (2006), Pietruszka et al. (2006), Malinovsky et al. (2007), Hannah et al. (2007), Mathur et al. (2010); Rivers: Archer and Vance (2008); Seawaters: Barling et al. (2001), Siebert et al. (2003); Mn oxides: Barling et al. (2001), Siebert et al. (2003); Suboxic sediments: Poulson et al. (2006), Siebert et al. (2006); Restricted basin sediments: Barling et al. (2001), Arnold et al. (2004), Nägler et al. (2005); Euxinic sediments: Barling et al. (2001), Arnold et al. (2004), Neubert et al. (2008).

5.6.1 Igneous rocks

Granites and basalts: The average Mo abundance in the Upper Continental Crust is 1.5 ppm, and granites have the highest Mo contents among magmatic rocks. In order to identify a background value of different types of rocks, Siebert et al. (2003) investigated Mo isotopes in granites of variable geological ages (Archean and Tertiary) and subduction-related basalts from Kamchatka. The reported $\delta^{98/95}$Mo values are similar, among which two granite samples have $\delta^{98/95}$Mo values of 0.10 ‰ and 0.14 ‰, respectively, and the $\delta^{98/95}$Mo values of seven basalt samples range from -0.09 ‰ to 0.25 ‰. Although the Mo isotope dataset of granite and basalt is small, the coherence of these samples from variable geological ages and localities suggests that Mo isotope fractionation during igneous processes is small.

Molybdenites: Hydrothermal molybdenite is the most common Mo-bearing minerals in nature with economic importance. Using the element spike method, Barling et al. (2001) investigated Mo isotopes of three different types of hydrothermal ore deposits from Australia, and reported $\delta^{98/95}$Mo values of -0.06 ± 0.05 ‰，0.14 ± 0.09 ‰ and -0.39 ± 0.04 ‰ (2σ), respectively. Wieser and de Laeter (2003) obtained $\delta^{98/95}$Mo values of molybdenite from West Australia and New South Wales ranging from -1.62 ‰ to 0.15 ‰. Malinovsky et al. (2005) reported three molybdenite Mo isotope values. Among them two molybdenites were from Chinese National Research Center of Geoanalysis, and another molybdenite was from Archean granite in North Sweden. The two molybdenites from China have been used as reference materials in studies of Re-Os dating (One is from a carbonate vein-type Mo-Pb deposit in the Jinduicheng-Huanglongpu area of Shaanxi, another is from Tuwu-Yandong porphyry Cu deposit in Xinjiang, China). The reported $\delta^{98/95}$Mo of three molybdenites are -0.30 ± 0.03 ‰, 0.16 ± 0.03 ‰ and 0.29 ± 0.03 ‰ (σ), respectively. Pietruszka et al. (2006) reported that $\delta^{98/95}$Mo values of different type of ore deposits ranging from -0.78 ‰ to 1.13 ‰. Hannah et al. (2007) investigated Mo isotopes in twenty molybdenite samples of variable ages from porphyry, skarn and vein type deposits, which represent a range of geological settings and cover a wide crystallization temperature from low (< 400°C) to high (> 600°C). The $\delta^{98/95}$Mo values range from -0.33 ‰ to 1.56 ‰. More recently, in an attempt to apply Mo isotopes in studying ore genesis, Mathur et al. (2010) reported Mo isotopes of molybdenites from different types of ore deposits, which were analyzed by two laboratories. The $\delta^{98/95}$Mo values are similar, ranging from -0.39 ‰ to 1.91 ‰. Judging from the available Mo isotope data of molybdenites, detectable Mo isotope variation is seen in molybdenites from hydrothermal ore deposits. Unfortunately, interpretation of these data is hampered by lack of a common standard for interlaboratory comparison. However, it is widely accepted that hydrothermal molybdenites have a large Mo isotope variation. The reason(s) of the isotope fractionation is still questionable, and may relate to hydrothermal fluid redox conditions and Rayleigh effects (Pietruszka et al., 2006; Hannah et al., 2007; Mathur et al., 2010).

5.6.2 Geological fluids

Seawater: Barling et al. (2001) reported a $\delta^{98/95}$Mo value of 2.22 ‰ for Pacific seawater. Siebert et al. (2003) investigated seawater samples from the Atlantic, Indian Ocean, Pacific and Labrador Sea, and obtained consistent $\delta^{98/95}$Mo values ranging from 2.3 ‰ to 2.5 ‰ (2.3 ± 0.1‰ on average, 2σ). The Mo abundances of different seawater samples are similar (~ 0.011 ppm), which is a result of the long residence time of Mo in seawater. Although seawater samples of two scientific groups were from different localities and different depths, the Mo isotopes are consistent, suggesting that no or weak $\delta^{98/95}$Mo fractionation in the oceans with location or depth. Another characteristic is that $\delta^{98/95}$Mo in the oceans is similar to the heaviest Mo of euxinic sediments and much heavier than in igneous rocks. Based on the uniform Mo abundances and Mo isotope compositions, Siebert et al. (2003) therefore recommended MOMO as the interlaboratorial standard for Mo isotope analysis.

Low-temperature hydrothermal fluids: About 10% Mo in the oceans is from low-temperature hydrothermal fluids. By investigating metal concentrations in submarine hot springs, Wheat et al. (2002) suggested that concentrations of Mo, together with other metals including Mn, Co, Ni, Zn and Cd in the spring waters are greater than in bottom seawater, whereas concentrations of Cu, U, V, Y and rare earth elements (excluding Ce) are less than in bottom seawater, indicating that the low-temperature hydrothermal fluids can bring oceanic crust-sourced Mo into seawater. The low-temperature hydrothermal fluids are found to be isotopically lighter than seawater, but heavier than igneous rocks, with average $\delta^{98/95}$Mo value of 0.8 ‰ (McManus et al., 2002).

Rivers and lakes: Rivers are the most important source of Mo in the oceans. About 90% Mo in oceans is from riverine fluxes. Early studies thought that Mo isotope compositions of rivers would be similar with crustal materials, such as granite, basalt and clastic rocks, which are characterized by light Mo isotopes (Barling et al., 2001; Siebert et al., 2003). However, Archer and Vance (2008) reported a broad range of Mo isotope composition of major rivers all over the world. Almost all samples were enriched in the heavy isotopes compared with continental rocks. The average $\delta^{98/95}$Mo value of rivers is 0.7 ‰, slightly lighter than low-temperature hydrothermal fluids (0.8 ‰, McManus et al., 2002). Mo isotope fractionation in lakes is limited by redox conditions of water columns. Dahl et al. (2010) investigated Mo isotope compositions in Cadagno Lake in Switzerland, which was classified into surface oxic zone, subsurface anoxic zone (suboxic condition) and deep sulfidic zone (euxinic condition) according to H_2S content in the water column. They found that Mo behaves conservatively in the oxic zone and non-conservatively in the sulfidic zone. Dissolved Mo in the surface oxic waters has a $\delta^{98/95}$Mo = 0.9 ± 0.1 ‰ (2σ), which matches that of the riverine input. In the deeper sulfidic waters, the dissolved Mo is $\delta^{98/95}$Mo = 1.8 ‰, significantly heavier than that of the surface oxic and subsurface anoxic waters. Porewater refers to the water filling the interstitial spaces in sediment; it is a major component in loose sediments and semi-cemented clastic sediments and marine sediments. Similarly, Mo isotope features of porewater are also depending on redox conditions, $\delta^{98/95}$Mo in suboxic porewaters is intermediate between igneous rocks and euxinic sediments and seawater. McManus et al. (2002) examined Mo isotope compositions in sediment porewaters from the Santa Monica basin, a well studied suboxic setting. $\delta^{98/95}$Mo immediately below the sediment/water interface is lighter than seawater, potentially reflecting release of light Mo associated to Mn oxides. Mo and Mn concentrations increase in fluids at the surface sediments. However, Mo concentration is progressively depleted at deeper depths (> 5 cm). In conjunction with this depletion, $\delta^{98/95}$Mo values are progressively heavier.

5.6.3 Marine sediments

Oxic sediments: Fe-Mn nodules are widely distributed in modern oceans. Mo is readily adsorbed to the Fe-Mn nodules, resulting in the Mo content of the modern oceanic Fe-Mn nodules which are very high (up to 800 ppm). Fe-Mn nodules were therefore becoming reasonable targets for isotope investigation at an early stage. Barling et al. (2001) reported $\delta^{98/95}$Mo values of -0.63 ± 0.1 ‰ and -0.95 ± 0.1 ‰, respectively, for Fe-Mn nodules from the Pacific and Atlantic oceans which are obviously characterized by light Mo isotopes. Siebert et al. (2003) investigated Fe-Mn nodule sedimentary profiles of the Atlantic and Pacific oceans, which span 60 million years of geological time. Similar to the data of Barling et al. (2001), $\delta^{98/95}$Mo values of nodules from two profiles range from -0.5 ‰ to -1.0 ‰, and from -0.6 ‰ to -0.7 ‰, respectively, suggesting for the last 60 million years Fe-Mn nodules have no variantion in Mo isotope composition. In addition, Fe-Mn nodules from the Pacific, Atlantic and Indian oceans have consistent $\delta^{98/95}$Mo values, ranging from -0.50 ‰ to -0.80 ‰. Siebert et al. (2003) also analyzed clastic and pelagic samples. Two clastic sedimentary samples are indistinguishable from igneous rocks and similar to Fe-Mo nodules in their Mo isotope compositions, with $\delta^{98/95}$Mo values of -0.3 ‰ and -0.5 ‰, respectively. Two pelagic clay samples have relatively light Mo isotope composition with $\delta^{98/95}$Mo values of 0.36 ‰ and 0.00 ‰, which may have inherited the Mo isotope features from original volcanic rocks.

Suboxic sediments: Suboxic conditions characterize water columns with a slight lack of oxygen (O_2 < 2 ml O_2/l H_2O and no free H_2S). Early studies on Mo isotopes did not pay enough attention to such conditions (e.g. Arnold et al., 2004), thus the established Mesoproterozoic global oceanic redox model based on two end-member (oxic and euxinic) is questionable (Ling et al., 2005). Actually, suboxic conditions exist widely in the whole Earth history. Understanding Mo isotope fractionation mechanism in suboxic conditions is a significant aspect in Mo stable isotope system application. Siebert et al. (2003) examined San Pedro Basin and Santa Monica Basin in America, and Chile margin suboxic sediments. The Mo isotopes presented a variable range, with $\delta^{98/95}$Mo values ranging from 0.52 ‰ to 1.62 ‰. Further study of continental margin sediments by Siebert et al. (2006) indicates that Mo isotope fractionation in suboxic conditions is more variable, with $\delta^{98/95}$Mo values ranging from -0.45 ‰ to 1.6 ‰, which is intermediate in between Fe-Mn oxic sediments ($\delta^{98/95}$Mo ~ -0.7 ‰) and modern seawater ($\delta^{98/95}$Mo ~ 2.3 ‰). In recent years, many studies focused on the Mo isotope fractionation under suboxic conditions (e.g. Siebert et al., 2006; Pearce et al., 2008; Scott et al., 2008; Gordon et al., 2009; Kendall et al., 2009). Gordon et al. (2009) compared two Devonian black shale sequences in America (Oatka Creek Formation and Geneseo Formation). Although the two sequences formed in the same time interval, detailed studies confirmed that they deposited under different conditions. The Oatka Creek Formation formed under euxinic conditions, whereas the Geneseo Formation formed under suboxic conditions. $\delta^{98/95}$Mo values of the Geneseo Formation black shales range from 0.85‰ to 1.32 ‰, significantly lighter than that of the Octka Creek Formation, with $\delta^{98/95}$Mo values of 1.32-1.96 ‰. Based on the modern oceanic mass-balance model, Scott et al. (2008) suggested that oxic, suboxic and euxinic sediments take up about 35%, 50% and 15% Mo, respectively, of the whole Mo budget. Since euxinic conditions include weakly euxinic and intermittently euxinic bottom waters as defined by Scott et al. (2008), the actual proportion of Mo being removed into strongly euxinic sediments is probably ~ 5%, and the proportion being removed into suboxic sediments reaches up to ~ 60% (Kendall et al., 2009).

Euxinic sediments: Euxinic conditions characterize water columns with extreme lack of oxygen and free H_2S. Black shales formed under such conditions are thought to faithfully record Mo isotope features of simultaneous seawaters, due to quantitative scavenging of Mo from the seawater column. The Black Sea and Cariaco Basin are the two largest euxinic basins at present, in which the sediment/water interface is overlain by H_2S-rich waters. For example, when the depth of seawater in the Black Sea exceeds ~ 100 m, H_2S content exceeds 100 μM, meanwhile, the concentration of Mo falls sharply in the euxinic zone opposite to H_2S (Fig. 5-3). The Mo content in oceanic euxinic sediments is 10-100 fold average continental crust. Mo isotope features in euxinic sediments are characterized by heavy Mo, similar to overlying seawater Mo. Barling et al. (2001) examined the two uppermost units in the Black Sea and Devonian black shales. The average $\delta^{98/95}$Mo values are 2.28 ± 0.11 ‰ and 1.53 ± 0.11 ‰, respectively. Arnold et al. (2004) comparatively investigated the modern Black Sea and Cariaco Basin euxinic sediments, and Mesoproterozoic Velkerri Formation (~ 1.4 Ga) and Wollogorang Formation (~ 1.7 Ga) black shales. The average $\delta^{98/95}$Mo values of the modern Black Sea and the Cariaco Basin sediments are 2.52 ± 0.07 ‰ and 1.79 ‰, respectively. In contrast, the average $\delta^{98/95}$Mo values of the Velkerri Formation and the Wollogorang Formation black shales are lighter than the modern euxinic sediments, with average $\delta^{98/95}$Mo values of 0.82 ‰ and 0.80 ‰, respectively. Thus they inferred that the degree of Mo isotope fractionation in seawater in the Mesoproterozoic was lower than present day. Lehmann et al. (2007) reported Mo isotope features of Early Cambrian black shales in South China. The black shale sequences extend about 1600 km along the Yangtze platform, and specially, locally host a Ni-Mo-PGE-Au polymetallic sulfide ore layer 1-10 m above the Precambrian/Cambrian transgressive contract (Fan et al., 1984; Mao et al., 2002; Jiang et al., 2006). Ni-Mo-PGE-Au sulfide ores hosted by euxinic black shales have average $\delta^{98/95}$Mo values of 1.09 ‰, interpreted to represent the Mo isotope value of the Early Cambrian seawater. Wille et al. (2008) further examined the Chinese Lower Cambrian black shales and synchroneous Ara Formation black shales in Oman. The average $\delta^{98/95}$Mo value of Ara Formation black shales is 1.15 ‰, similar with that of Chinese Lower Cambrian black shales. Wille et al. (2008) suggested a paleo-oceanic evolution model for the PC/C interval, favoring the upwelling of H_2S and euxinic bottom water, with the consequence of poisoning the Ediacaran fauna. Pearce et al. (2008) investigated the Toarcian global oceanic anoxic event (Jurassic, ~ 183 Ma) using Mo isotopes. According to the $\delta^{98/95}$Mo and Re/Mo proxies, they divided the Toarcian stage black shales from the Yorkshire region, United Kingdom, into four intervals. The $\delta^{98/95}$Mo values increase from old to young intervals, indicating the degree of global seawater anoxia increased during this period.

5.7 Applications of Mo isotopes

5.7.1 Reconstruction of paleo-oceanic redox conditions

The last 3.85 Ga of Earth history have experienced several global oxidation events (Holland, 2006). The oxygen concentration in atmosphere and hydrosphere has directly affected biosphere evolution, and element cycling and environmental change (Canfield et al., 2005; Holland, 2006; Anbar, 2008). Mo is a redox-sensitive element, due to this property, Mo and Mo isotopes have been widely used to reconstruct paleo-oceanic environments. Application of Mo isotopes is based on understanding Mo isotope fractionation mechanism (Barling et al., 2001; McManus et al., 2002;

Siebert et al., 2003). Under euxinic conditions, Mo isotope features in seawater are faithfully recorded in sediments, i.e. overlying seawater and simultaneous sediments have similar $\delta^{98/95}$Mo values (For example, the modern Black Sea and the Cariaco Basin sediments). This is the fundamental principle for using Mo isotopes as a proxy of paleo-ocean environments. Although the “deep anoxic basin” model for black shales is popular, when we study black shales more closely we find that they can form in a wide range of depositional environments. Black shales can form not only in euxinic conditions, but also under suboxic conditions (Werne et al., 2002; Williams et al., 2004). When using black shales Mo isotopes to reconstruct paleo-oceanic environments, it is necessary to confirm that the black shales formed under euxinic conditions, so as to avoid interferences of Mo isotope fractionation under suboxic or oxic conditions. In addition, even when there is H_2S in water columns (>100 μM), Mo scavenging in euxinic basins may not be quantitative if recharge from the open ocean is vigorous (Algeo and Lyons, 2006). Rapid recharge may lead to incomplete conversion from molybdate to thiomolybdate in a short period. Such mechanism likely explains the small but measurable Mo isotope offsets between seawater and sediments from the Cariaco Basin and Unit II of the Black Sea (Arnold et al., 2004).

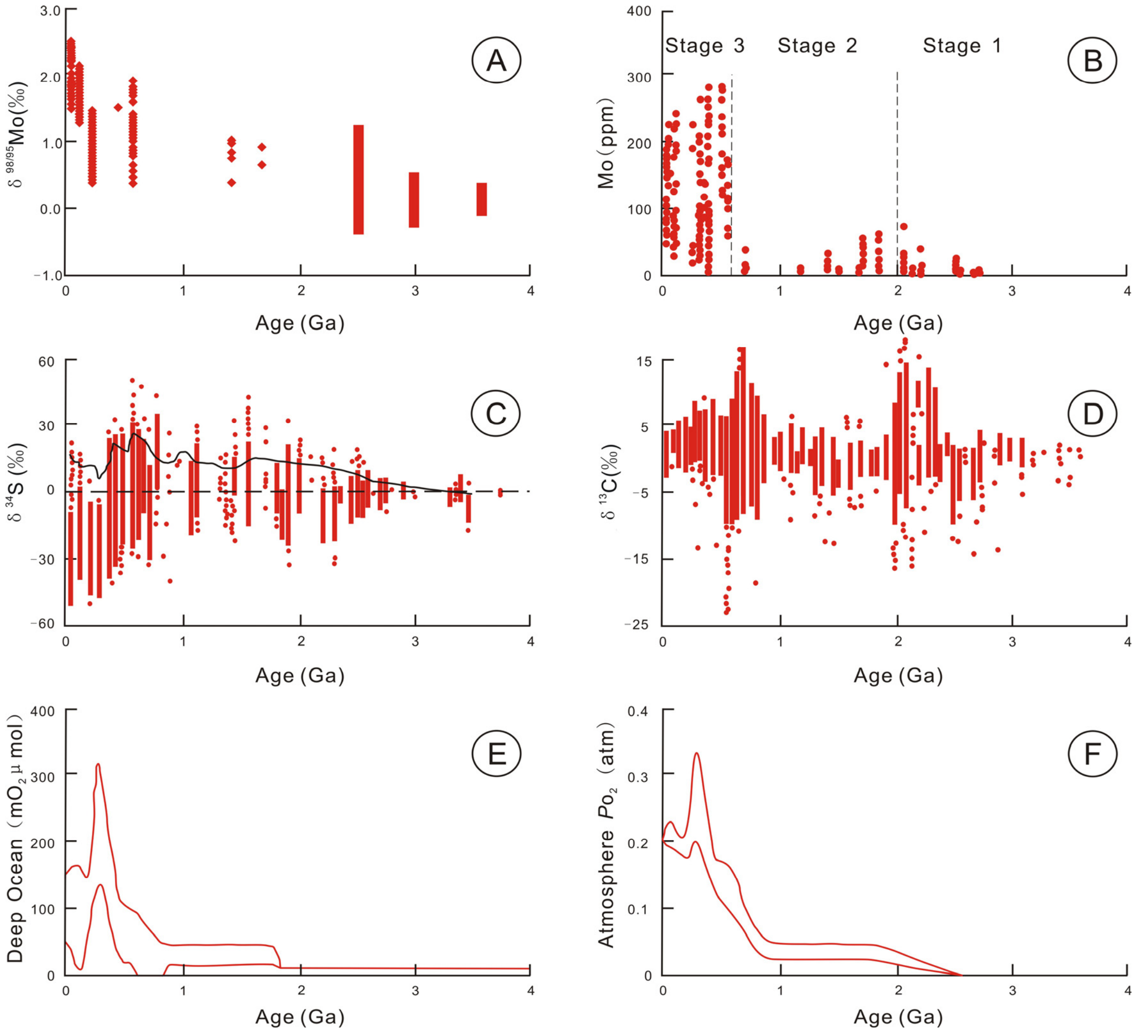

Fig. 5-11: Mo, S and C isotopic composition, Mo content, atmospheric and deep oceanic O_2 evolution through geological time. **A:** $\delta^{98/95}$Mo evolution of euxinic sediments through geological time. Data sources: Barling et al. (2001), Arnold et al. (2004), Lehmann et al. (2007), Wille et al. (2007, 2008), Pearce et al. (2008), Wen et al. (2010). Columns in the graph only indicate the range of $\delta^{98/95}$Mo values earlier than 2 Ga (Wen et al., 2010). **B:** Temporal trends in Mo enrichment in black shales (after Scott et al., 2008). Stage 1 recorded low delivery of sulfate and Mo to the ocean in the absence of appreciable oxidative continental weathering. Stage 2, post-Great Oxidation Event, increased oxidative weathering elevated the delivery of sulfate and Mo to the ocean. Stage 3 (<550 Ma), expanded oxidation with large quantity of Mo delivered into the oceans corresponding to rise in atmospheric oxygen. Black shale is apparently higher in Mo content. **C:** Isotopic composition of sedimentary sulfides through geological time (after Canfield, 2006). Columns in the graph indicating a large quantity of data are included. **D:** Carbon isotopic evolution of marine carbonate through geological time (Shields and Veizer, 2002). Columns in the graph indicating a large quantity of data are included. **E** and **F:** Estimated evolution of atmospheric PO_2 and the concentration of O_2 in the deep oceans (after Holland, 2006).

All the Mo isotope data cited in Fig. 5-11 are from euxinic black shales. In the early stage of the Earth (> 2.8 Ga), $\delta^{98/95}$Mo values of black shales are less than 0.59‰. The whole ocean was under reducing conditions. Mo in the oceans was all from rock debris, with no authigenic fixation (Siebert et al., 2005). In this stage, oxygen concentration in oceans and atmosphere was very low, and C and S isotope fractionations were not obvious (Fig. 5-11). From Neoarchean to Paleoproterozoic the Earth experienced great changes. The degree of Mo isotope fractionation increased in this stage. Wille et al. (2007) examined the Mo isotope composition of the Ghaap Formation (2.64 - 2.5 Ga) black shales. The $\delta^{98/95}$Mo values range from -0.27 ‰ to 1.34 ‰. In conjunction with Mo isotopes and Re/Os-REE data, Wille et al. (2007) suggested that oxygen concentration in hydrosphere and atmosphere increased during the 2.64 - 2.5 Ga interval. During the 2.5 – 1.8 Ga interval, oxygen concentration increased obviously, with the Great Oxidation Event (GOE, ~ 2.4 Ga) most notable. In this stage a large quantity of Mo was delivered to the oceans by weathering, and then largely fixed in widespread marine sedimentary manganese deposits (Holland, 2006). By analyzing $\delta^{97/95}$Mo in Mesoproterzoic-Neoproterozoic black shales from the McArthur Basin in Australia (~ 1.7 Ga and ~ 1.4 Ga), Arnold et al. (2004) found that the $\delta^{97/95}$Mo values were lighter than present day euxinic sediments and seawater, and thus inferred ocean euxinia expanded during this time, consistent with the hypothesis of Canfield (1998) and Anbar and Knoll (2002). H_2S concentrations increased during this stage, and allowed efficient Mo precipitation in the oceans. This is why the black shale Mo contents of this stage are higher than in former intervals (Fig. 5-11 B). The Precambrian/Cambrian transition represents a critical interval in Earth history that is characterized by changes of atmosphere, hydrosphere and biosphere, including extinction and accelerated diversification of metazoans, shift of global oceanic anoxia, and major plate tectonic reconfiguration and volcanism (Kaufman et al., 1993; Shu et al., 2001; Doblas et al., 2002; Schröder and Grotzinger, 2007). Mo isotopes of the Early Paleozoic black shales are characterized by heavy $\delta^{98/95}$Mo values. The $\delta^{98/95}$Mo fractionation between euxinic black shales and Fe-Mn oxides reaches up to 3.0 ‰. The average $\delta^{98/95}$Mo value of Early Cambrian black shale hosted Ni-Mo-PGE-Au polymetallic sulfide ores in South China is 1.09 ‰. In contrast, $\delta^{98/95}$Mo values of the host black shales have a large variation, with $\delta^{98/95}$Mo values ranging from 0.81 ‰ and 1.90 ‰. Nevertheless, both sulfide ore samples and the host black shales are characterized by relatively light $\delta^{98/95}$Mo compared to modern euxinic sediments (~ 2.3 ‰), suggesting that anoxic marine environments were more widespread during the Early Cambrian than today (Lehmann et al., 2007; Wille et al., 2008). The oxygen concentration in the Paleozoic atmosphere increased progressively, and reached a peak value in the Carboniferous. The Toarcian oceanic anoxic event (OAE) in Early Jurassic is one of the best documented Mesozoic OAEs. Pearce et al. (2008) divided this period into four intervals according to Mo isotope and other geochemical features. The $\delta^{98/95}$Mo values of interval II range from 0.81 ‰ to 1.58 ‰, obviously lighter than that of interval III (1.62 ‰ - 2.14 ‰) and interval IV (1.28 ‰ - 1.74 ‰). Considering that the interval II is corresponding to the Early Jurassic OAE, it is consistent with the theory that global scale anoxic environments produce relatively light $\delta^{98/95}$Mo values. Generally, from Early Cambrian to present day, the oceans become increasingly oxic. Accompanied with shrinks of anoxic environments, a large quantity of Mo precipitated in this stage (Fig. 5-11 B). Besides Mo, Mo/TOC has similar evolutionary trends (see Scott et al., 2008). Although available Mo isotope datasets are still small, applications to paleo-ocean redox condition reconstruction, as well as hydrosphere and atmosphere evolution have a bright future. In conjunction with other geochemical indicators, Mo isotopes will undoubtedly be a powerful proxy of paleo-environment reconstruction.

5.7.2 Mo isotope mass-balance for modern oceans

By investigating black shales from the Mesoproterozoic McArthur Basin, Arnold et al. (2004) established an oceanic Mo isotope mass-balance model. This model considered two Mo reservoirs in marine sediments: oxic and euxinic. However, many studies indicate that Mo isotope mass-balance is far more complex. Particularly, suboxic sediments should also be considered (Nägler et al., 2005; McManus et al., 2006; Poulson et al., 2006; Kendall et al., 2009) and Mo isotope patterns in rivers are not identical with igneous rocks (Archer and Vance, 2008). Based on recent progresses, Kendall et al. (2009) revised the Mo isotope mass-balance for the modern oceans, which is expressed as follows:

$$F_R\delta_R + F_{LTH}\delta_{LTH}=F_O\delta_O + F_{RED}\delta_{RED} + F_E\delta_E$$

Where F = Mo flux in mol/y, $\delta = \delta^{98/95}$Mo or $\delta^{97/95}$Mo. The left side of equation refers to two sources of Mo in oceans: rivers (R) and low-temperature hydrothermal fluids (LTH). The right side has three Mo reservoirs: oxic waters (O), reducing bottom waters, specifically suboxic and weakly or intermittently euxinic conditions, where $[H_2S]_{aq} < 11$ μM (RED), and strongly euxinic bottom waters, where $[H_2S]_{aq} > 11$ μM (E). This mass-balance equation is similar to that presented by McManus et al. (2006), who defined oxic basin, continental margin, and anoxic basin as primary sinks of Mo. However, the continental margin and anoxic basin sinks contain both the strongly euxinic sink where quantitative molybdate to thiomolybdate formation may occur in bottom water columns, and the reducing sink where Mo isotope fractionation is preserved in suboxic and weakly or intermittently euxinic sediments. The equation does not well distinguish these two Mo reservoirs.

Mo fluxes and isotopic compositions for major sources and sinks in the modern oceans are listed in Table 5-1. As discussed above, Mo in oceans has two sources: rivers and low-temperature hydrothermal fluids, which take up 90% and 10% Mo fluxes, respectively. Archer and Vance (2008) presented an isotopic analysis of Mo in a set of rivers all over the world that together account for 22% of the global riverine water discharge. The average δ_R ($\delta^{98/95}$Mo) value is 0.70 ‰, heavier than that of terrestrial materials (e.g. igneous rocks). MaManus et al. (2002) investigated low-temperature hydrothermal fluids Mo isotopes, and obtained δ_{LTH} ($\delta^{98/95}$Mo) of 0.80 ‰, similar with riverine Mo isotope values. Recent mass-balance modeling of the modern Mo marine budget suggests oxic, suboxic, and euxinic bottom waters may remove ~ 35%, 50%, and 15% of Mo ocean inputs, respectively (Scott et al., 2008). Considering that the euxinic estimate in the above study includes weakly euxinic and intermittently euxinic bottom waters, Kendall et al. (2009) suggested that the actual proportion of reducing bottom waters can reach up to 60%, which should also include weakly euxinic and intermittently euxinic bottom waters. Correspondingly, the proportion being removed into strongly euxinic sediments is probably ~ 5% of the oceanic Mo sink (Fig. 5-12). Previous studies indicated that the average $\delta^{98/95}$Mo value of Fe-Mn oxides in modern oceans is -0.70 ‰ and euxinic sediments have similar $\delta^{98/95}$Mo values as seawater (2.30 ‰). The $\delta^{98/95}$Mo values of suboxic sediments depend on the efficiency of MoO_4^{2-} converting to MoS_4^{2-}, with a wide $\delta^{98/95}$Mo range from -0.70 ‰ to 1.65 ‰ (Barling et al., 2001; Siebert et al., 2003; Arnold et al., 2004; Poulson et al., 2006; Neubert et al., 2008). Calculation using the above Mo isotope mass-balance equation obtains the average $\delta^{98/95}$Mo value of suboxic sediments of 1.40 ‰, which is in line with the data.

Table 5-1
Estimated Mo fluxes and isotopic compositions for major sources and sinks in the modern oceans (after Kendall et al., 2009).

	Flux（×10^8 mol/y）	$\delta^{98/95}$Mo (‰)
Source		
Rivers	1.8	0.7
Low-T hydrothermal fluids	0.2	0.8
Sink		
Oxic	0.7	-0.7
Suboxic	1.2	1.4
Euxinic	0.1	2.3

Data sources: Rivers: Martin and Meybeck (1979); Low-temperature hydrothermal fluids: Wheat et al. (2002); Oxic, suboxic, and euxinic: Scott et al. (2008).

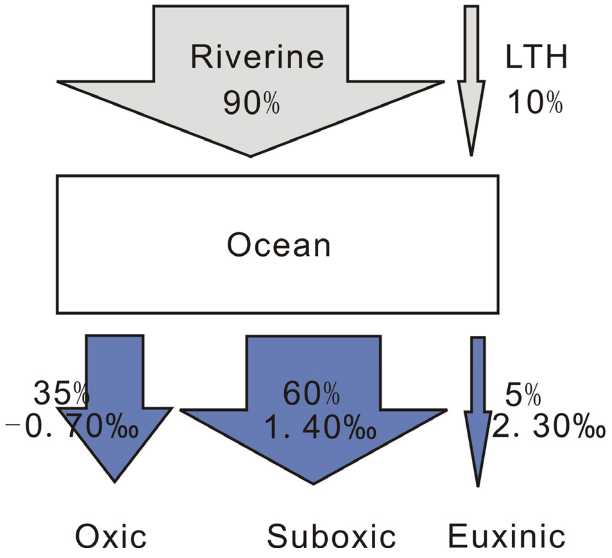

Fig. 5-12: Mo isotope mass-balance model for the modern ocean.

5.7.3 Mo isotope constraints on ore genesis

Applications of Mo isotopes to ore genesis are still tentative. Present studies are mostly focusing on Mo isotope features and fractionation mechanisms of different types of Mo-bearing hydrothermal ore deposits. Barling et al. (2001) reported three hydrothermal molybdenites $\delta^{98/95}$Mo of -0.06 ± 0.05 ‰, 0.14 ± 0.09 ‰ and -0.39 ± 0.04 ‰ (2σ). Malinovsky et al. (2005) analyzed three molybdenite samples, including two molybdenites that are used as reference materials in Re-Os dating in Chinese National Research Center of Geoanalysis (One is from a carbonate vein-type Mo-Pb deposit in the Jinduicheng-Huanglongpu area of Shaanxi, anther is from Tuwu-Yandong porphyry Cu deposit in Xinjiang, China), and one molybdenite from Archean granite in North Sweden. The $\delta^{98/95}$Mo values are -0.30 ± 0.03 ‰, 0.16 ± 0.03 ‰ and 0.29 ± 0.03 ‰ (σ), respectively. Pietruszka et al. (2006) reported that $\delta^{98/95}$Mo values of different type of ore deposits ranging from -0.78 ‰ to 1.13 ‰. Hannah et al. (2007) investigated Mo isotopes in twenty molybdenite samples of variable ages from porphyry, skarn and vein type deposits, representing a range of geological settings and covering a wide crystallization temperature from low (< 400°C) to high (> 600°C). The $\delta^{98/95}$Mo values range from -0.33 ‰ to 1.56 ‰.

Lehmann et al. (2007) investigated Mo isotopes of Ni-Mo-PGE-Au polymetallic sulfide ore deposits hosted by the lowermost Niutitang Formation black shales of the Early Cambrian. The average $\delta^{98/95}$Mo value of the polymetallic sulfide ore samples is 1.09 ‰, in the range of the host black shales with $\delta^{98/95}$Mo value ranging from 0.81 ‰ to 1.90 ‰. They proposed that the metals were derived from Early Cambrian euxinic seawater but not hydrothermal seafloor venting. This conclusion is in agreement with ore genesis model proposed by Mao et al. (2002), who employed Re-Os geochronology, and trace element and PGE geochemistry, and suggested that metals were scavenged form stagnant seawater.

Recognizing molybdenite Mo isotope features in different types of deposits is a fundamental principle for applying it to ore genesis studies. Mathur et al. (2010) investigated Mo isotopes of molybdenites from different types of ore deposits. In order to improve data precision, same samples were analyzed separately in two different laboratories. The $\delta^{98/95}$Mo values range from -0.39 ‰ to 1.91 ‰, which is by far the largest Mo isotopic variation in molybdenite observed from high-temperature ore deposits. The Mo isotope values vary as a function of the deposit type (Fig. 5-13), and the Re and Os concentrations of the samples. In general, molybdenites from porphyry copper deposits have the lightest values with an average $\delta^{98/95}$Mo of 0.11 ± 0.22 ‰; Average $\delta^{98/95}$Mo values of molybdenites form skarn deposits and Iron-Oxide Cu-Au deposits are 0.63 ± 0.29 ‰ and 0.96 ± 0.32 ‰, respectively. Although more Mo isotope data are still needed for accurately constraining Mo isotope features in different types of ore deposits, this study is undoubtedly offered a good beginning for applications of Mo isotope to ore genesis study. Considering Mo fractionation mechanisms in molybdenites, Hannah et al. (2007) suggested the variations could be related to the Rayleigh distillation effect during ore-forming processes in high temperature conditions, resulting in fractionation of Mo isotopes into different mineral phases. In addition, Mo isotope fractionation is directly related with redox conditions. That means Mo isotope fractionation would be recorded when redox conditions changed. Hydrothermal fluids of different types of ore deposits are distinct as evidenced by different types of alteration assemblages, therefore theoretically the Mo isotope pattern should be unique to each deposit type.

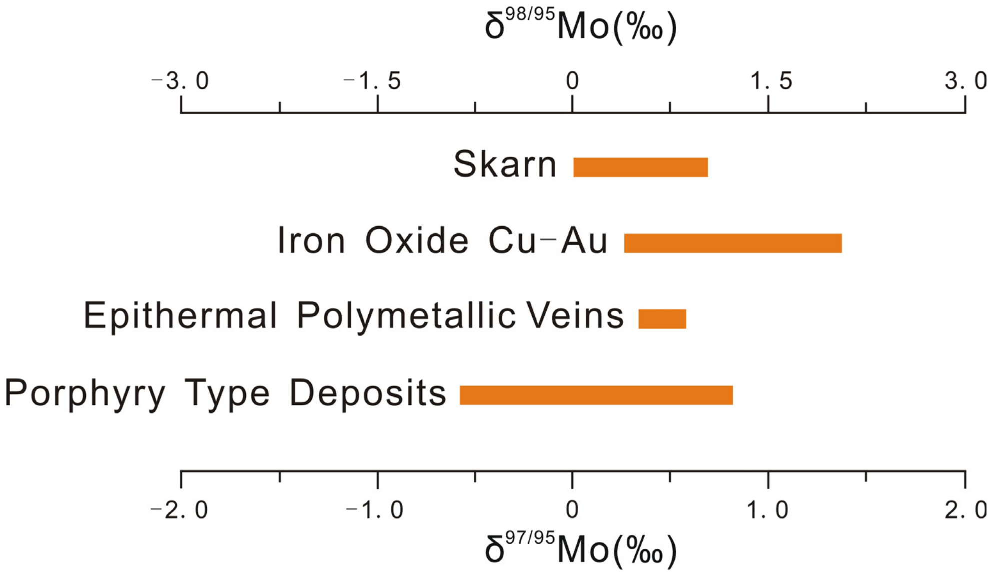

Fig. 5-13: Plot of the $\delta^{98/95}$Mo of molybdenite from different ore deposits (after Mathur et al., 2010).

Re-Os isotope geochronology is widely used in geosciences in recent years. In closed systems, Re-Os ages faithfully represent the geological ages of samples. However, the open-system behavior of the Re-Os isotope system has been debated in the literature. Re loss or redistribution caused by hydrothermal fluid overprint can result in big uncertainties between measured Re-Os ages and samples` true ages. By comparing different types of ore deposits Re-Os ages and Mo isotopes, Mathur et al. (2010) suggested that Re concentration and Mo isotope composition in molybdenites displayed a weak negative correlation. Compared to samples with reasonable ages, samples with unreasonable ages are generally characterized by low Re concentrations, and molybdenite with unreasonable Re-Os ages have a large variance in $\delta^{97/95}$Mo ratios compared to samples that produced reasonable ages (Fig. 5-14). Although further studies are still needed to clearly identify what most likely causes the variation in the Mo isotopic composition of molybdenites, the variation measured demonstrates the potential to use Mo isotopes to identify samples that yield unreasonable Re-Os ages and to identify ore-forming processes of different types of ore deposits.

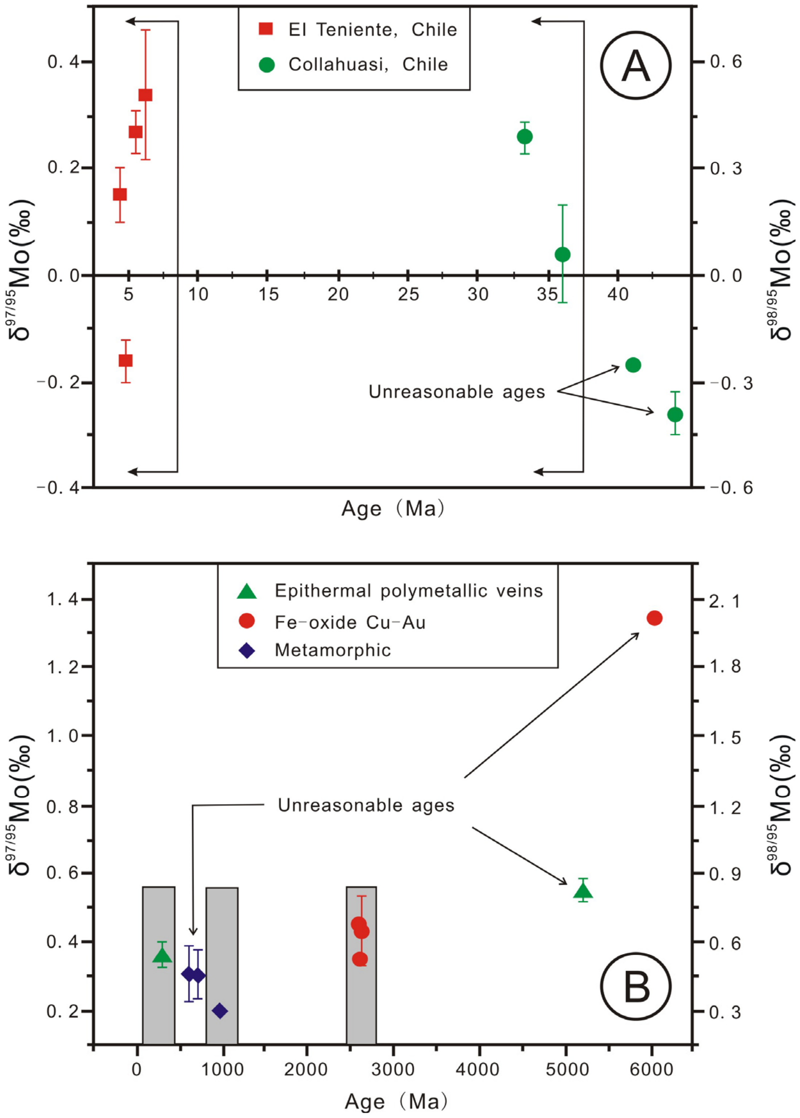

Fig. 5-14: Plots of molybdenite ages versus Mo isotope values. Lines with arrows and boxed ranges indicate geologically reasonable ages determined from host rock ages and known magmatic activity in the area. **A:** Porphyry Cu-Mo deposits; **B:** Results from Fe-oxide Cu-Au, epithermal polymetallic veins, and metamorphic deposits (after Mathur et al., 2010)

5.8 Potential applications of the Mo isotope system

The development of the MC-ICP-MS technique allows high precision Mo isotope analysis. Progresses in understanding Mo isotope fractionation mechanisms under variable geological settings have promoted applications to both identification of paleo-ocean environments and constraining ore genesis. The Mo isotope system is particularly suited and currently applied for investigations of global ocean paleoredox conditions. Undoubtedly more applications of the Mo isotope system to reconstruct paleography and paleoclimate will be prosperous. Based on the knowledge that variable ocean conditions (oxic, suboxic and euxinic) can be recorded by Mo isotopes in coeval sediments (e.g. black shales) and that global Mo isotope features of the open ocean are constant in certain geologic intervals, the Mo isotope system should also prove useful in local water column paleoredox reconstruction. Applications of Mo isotopes to local or regional scale water column condition reconstruction are under the premise of thorough understanding of global Mo isotope features of Earth history. When the global Mo isotope composition of seawater is constant, $\delta^{98/95}$Mo may monitor the extent of local redox conditions at the time of deposition. If euxinic black shales display distinct Mo isotope values with simultaneous seawaters, the local water column redox conditions may be different from that of global seawater, which may reflects restricted local basin settings. Mo isotopes might therefore become a powerful tool for understanding redox on a local or regional scale, the depositional conditions of sediments and will also help to understand the geochemical cycles of C and S (Anbar and Rouxel, 2007).

Mineral deposits are special products of geological events. Environmental changes, such as temperature, pressure, fluid pH and oxygen fugacity, may result in metal precipitation. Mo isotope fractionation has direct relations with redox changes, which therefore could be recorded by hydrothermal molybdenite. In addition, different types of ore deposits reflect distinct oxidation states, which is a theoretical foundation for using Mo isotopes to identify ore genesis.

The study of transitional metal isotopes by MC-ICP-MS techniques is a new development in recent years. Many studies are still in their infancy and available data are limited. The newly established theoretical framework of the Mo stable isotope system needs more studies to supplement and update the current models. It is foreseeable that in the near future, studies of transitional metal isotopes, especially the Mo isotope system, will gain in importance.

5.9 Acknowledgements

We benefited from discussions with many colleagues, principal among them are Thomas Nägler, Nadja Neubert, Daniel Hennig, Jasmi Hafiz Abdul Aziz, Alexander Cabral and Akwinga Victor Asaah. Reviews by two anonymous reviewers improved the manuscript. We are grateful to Prof. Jingwen Mao from Chinese Academy of Geological Sciences for his encouragement in writing this manuscript. Joint financial support was provided by the Chinese Geological Survey Program (No. 1212010634001) and the National Basic Research Program of China (No. 2007CB 411302) to Jingwen Mao, and the Chinese Scholarship Council.

5.10 References

Algeo T J, Lyons T W. 2006. Mo-total organic carbon covariation in modern anoxic marine environments: implications for analysis of paleoredox and paleohydrographic conditions. Paleoceanography, 21: PA 1016.

Anbar A D. 2008. Elements and evolution. Science, 322: 1481-1483.

Anbar A D, Knoll A H. 2002. Proterozoic ocean chemistry and evolution: a bioinorganic bridge? Science, 297: 1137-1142.

Anbar A D, Roe J E, Barling J, Nealson K H. 2000. Nonbiological Fractionation of iron isotopes. Science, 288: 126-128.

Anbar A D, Rouxel O. 2007. Metal Stable isotopes in paleoceanography. Annual Review of Earth and Planetary Sciences, 35: 717-746.

Anbar A D, Knab K A, Barling J. 2001. Precise determination of mass-dependent variations in the isotopic composition of molybdenum using MI-ICPMS. Analytical Chemistry, 73: 1425-1431.

Anbar A D. 2004. Molybdenum stable isotope: observation, interpretations and directions: Reviews in Mineralogy and Geochemistry, 55: 429-454.

Anbar A D, Gordon, G W. 2008. Redox renaissance. Geology, 36: 271-272.

Archer C, Vance D. 2008. The isotopic signature of the global riverine molybdenum flux and anoxia in the ancient oceans. Nature geoscience, 1: 597-600.

Arnold G L, Anbar A D, Barling J, Lyons T W. 2004. Molybdenum isotope evidence for widespread anoxia in mid-Proterozioc oceans. Science, 304: 87-90.

Asael D, Matthews A, Bar-Matthews M, Halicz L. 2007. Copper isotope fractionation in sedimentary copper mineralization. Chemical Geology, 243: 238-254.

Barling J, Anbar A D. 2004. Molybdenum isotope fractionation during adsorption by manganese oxides. Earth and Planetary Science Letters, 217: 315-329.

Barling J, Arnold G L, Anbar A D. 2001. Natural mass-dependent variations in the isotopic composition of molybdenum. Earth and Planetary Science Letters, 193: 447-457.

Beard B L, Johnson C M. 2004. Fe isotope variations in the modern and ancient earth and other planetary bodies. Reviews in Mineralogy and Geochemistry, 55:

319-357.

Canfield D E. 1998. A new model for Proterozoic ocean chemistry. Nature, 396: 450-453.

Canfield D E. 2005. The early history of atmospheric oxygen: Homage to Robert M Garrels. Annual Review of Earth and Planetary Sciences, 33: 1-36.

Criss R E. 1999. Priciples of stable isotope distribution. New York: Oxford University Press. 1-254.

Crouch A C, Tulpin T A. 1964. Isotopic composition and the atomic weight of naturally occurring molybdenum: a possible reflexion of the creation process. Nature, 202: 1282-1284.

Dahl T W, Anbar A D, Gordon G W, Rosing M T, Frei R, Canfield D E. 2010. The behavior of molybdenum and its isotopes across the chemocline and in the sediments of sulfidic Lake Cadagno, Switzerland. Geochimica et Cosmochimica Acta, 74: 144-163.

Dietz L A, Paghugki C F, Land G A. 1962. Internal standard technique for precise isotopic abundance measurements in themal ionization mass spectrometry. Analytical Chemistry, 34: 709-710.

Doblas M, Lopez-Ruiz J, Cebria J M, Youbi N, Degroote E. 2002. Mantle insulation beneath the West African craton during the Precamrian-Cambrian transition. Geology, 30: 839-842.

Emerson S R, Huested S S. 1999. Ocean anoxia and the concentrations of molybdenum and vanadium in seawater. Marine Chemistry, 34: 177-196.

Erickson B E, Helz G R. 2000. Molybdenum (VI) speciation in sulfidic waters: Stability and lability of thiomolybdates. Geochimica et Cosmochimica Acta, 64: 1149-1158.

Fan D L, Yang R Y, Huang Z X. 1984. The Lower Cambrian black shale series and the iridium anomaly in South China, in Contribution to the 27th International Geological Congress, Moscow: Beijing Science Press, 215-224.

Fernandez A, Borrok D M. 2009. Fractionation of Cu, Fe, and Zn isotopes during the oxidative weathering of sulfide-rich rocks. Chemical Geology, 264: 1-12.

Goldberg S, Su C, Forster H S. 1998. Sorption of Mo on oxides, clay minerals and soils. In: Jenne E A (Ed.) Adsorption of metals by geomedia. Academic Press: San Diego, Chapter 19.

Goldberg T, Archer C, Vance D, Poulton S W. 2009. Mo isotope fractionation during adsorption to Fe (oxyhydr)oxides: Geochimica et Cosmochimica Acta, in press, dio: 10.1016/j.gca.2009.08.004.

Gordon G W, Lyons T W, Arnold G L, Roe J, Sageman B B, Anbar A D. 2009. When do black shales tell molybdenum isotope tales? Geology, 37: 535-538.

Halliday A N, Lee D C, Christensen J N, Walder A J, Freedman P A, Jones C E, Hall C M, Yi W, Teagle D. 1995. Recent developments in inductively coupled plasma magnetic sector multiple collector mass spectrometry. International Journal of Mass Spectrometry and Ion Processes, 146: 21-33.

Hannah J L, Stein H J, Mieser M E, De Laeter J R, Varner M D. 2007. Molybdenum isotope variations in molybdenite: Vapor transprot and Rayleigh fractionation of Mo. Geology, 35: 703-706.

Helz G R, Miller C V, Charnock J M, Mosselmans J F W, Pattrick R A D, Garner C D, Vaughan D J. 1996. Mechanism of molybdenum removal from the sea and its concentration in black shale: EXAFS evidence. Geochimica et Cosmochimica Acta, 60: 3631-3642.

Holland, H.D., 1979. Metals in black shales: reassessment. Economic Geology 74: 1676-1680.

Holland H D. 2006. The oxygenation of the atmosphere and oceans. Philosophical Transactions of the Royal Society Bulletin, 361: 903-915.

Jiang S Y. 2003. Transition metal isotopes: analytical methods and geological applications. Earth Science Frontiers, 10: 269-278 (in Chinese with English abstract).

Jiang S Y, Chen Y Q, Ling H F, Yang J H, Feng H Z, Ni P. 2006. Trace- and rare-earth element geochemistry and Pb-Pb dating of black shales and intercalated Ni-Mo-PGE-Au sulfide ores in Lower Cambrian strata, Yangtze Platform, South China. Minerlium Deposita, 41: 453-467.

Kaufman A J, Jacobsen S B, Knoll A H. 1993. The Vendian record of Sr and C isotopic variations in seawater: Implications for tectonics and paleoclimate. Earth Planetary Science Letters, 120: 409-430.

Kendall B, Anbar A D, Gordon G, Arnold G L, Creaser R A. 2006. Constraining the redox state of the Proterozoic deep oceans using the Mo isotooe systematics of euxinic black shales. Geological Society of America Abstracts with Programs, 38: 56.

Kendall B, Creaser R A, Gordon G W, Anbar A D. 2009. Re-Os and Mo isotope systematics of black shales from the Middle Proterozoic Velkerri and Wollogorang Formations, McArthur Basin, northern Australia. Geochimica et Cosmochimica Acta, 73: 2559-2580.

Lehmann B, Nägler T F, Holland H D, Wille M, Mao J W, Pan J Y, Ma D S, Dulski P. 2007. Highly metalliferous carbonaceous shale and Early Cambrian seawater. Geology, 35: 403-406.

Ling H F, Gao J F, Zhao K D, Jiang S Y, Ma D S. 2005. Comment on “Molybdenum isotope evidence for widespread anoxia in Mid-Proterozoic oceans”. Science, 309: 1017C.

Lu Q, Masuda A. 1994. The isotopic composition and atomic-weight of molybdenum. International Journal of Mass Spectrometry and Ion Processes, 130: 65-72.

Malinovsky D, Hammardund D, Ilyashuk B, Martinsson O, Gelting J. 2007.

Variations in the isotopic composition of molybdenum in freshwater lake systems. Chemical Geology, 236: 181-198.

Malinovsky D, Rodushkin I, Baxter D C, Ingri J, Öhlander B. 2005. Molybdenum isotope ratio measurements on geological samples by MC-ICPMS. International Journal of Mass Spectrometry, 245: 94-107.

Mao J W, Lehmann B, Du A D, Zhang G D, Ma D S, Wang Y T, Zeng M G, Kerrich R. 2002. Re-Os dating of polymetallic Ni-Mo-PGE-Au Mineralization in Lower Cambrian black shales of South China and its geologic significance. Economic Geology, 97: 1051-1061.

Maréchal C N, Telouk P, Albarede F. 1999. Precise analysis of copper and zinc isotopic composition by plasma-source mass spectrometry. Chemical Geology, 156: 251-273.

Martin J M, Meybeck M. 1979. Elemental mass-balance of material carried by major world rivers. Marine Chemistry, 7: 173-206.

Mathur R, Brantley S, Anbar A, Munizaga F, Maksaev V, Newberry R, Vervoort J, Hart G. 2010. Variation of Mo isotopes from molybdenite in high-temperature hydrothermal ore deposits. Minerlium Deposita, 45: 43-50.

McManus J, Berelson W M, Severmann S, Poulson R L, Hammond D E, Kinkhammer G P, Holm C. 2006. Molybdenum and uranium geochemistry in continental margin sediments: Paleoproxy potential. Geochimica et Cosmochimia Acta, 70: 4643-4662.

McManus J, Nägler T F, Siebert C, Wheat C G, Hammond D E. 2002. Oceanic molybdenum isotope fractionation: Diagenesis and hydrothermal ridge-flank alteration. Geochemistry, Geophysics, Geosystems, 3 doi: 10.1029/2002GC000356.

Moore L J, Machlan L A, Shields W R, Garner E L. 1974. Internal normalization techniques for high accurate isotope dilution analyses. Application to molybdenum and nickel in standard reference materials. Geochimica et Cosmochimica Acta, 63: 1735-1750.

Morford J L, Emerson S. 1999. The geochemistry of redox sensitive trace metals in sediments. Geochimica et Cosmochimica Acta, 63: 1735-1750.

Moynier F, Blichert-Toft J, Telouk P, Luck J M, Albarede F. 2007. Comparative stable isotope geochemistry of Ni, Cu, Zn, and Fe in chondrites and iron meteorites. Geochimica et Cosmochimica Acta, 71: 4365-4379.

Murthy V R. 1962. Isotopic anomalies of molybdenum in some iron meteorites. Journal Geophysical Research, 67: 905-907.

Murthy V R. 1963. Elemental and isotopic abundances of molybdenum in some meteorites. Geochimica Cosmochimica Acta, 27: 1171-1178.

Nägler T F, Mills M M, Siebert C. 2004. Biological fraction of Mo isotopes during N-2 fixation by Trichodesmium. Geochimica et Cosmochimica Acta, 68: Supplement 1, A364.

Nägler T F, Siebert C, Lüschen H, Böttcher M E. 2005. Sedimentary Mo isotope record across the Holocene fresh-brackish water transition of the Black Sea. Chemical Geology, 219: 283-295.

Nakagawa Y, Firdaus M L, Norisuye K, Sohrin Y, Irisawa K, Hirata T. 2008. Precise isotopic analysis of Mo in seawater using Multiple Collector-Inductively Coupled Mass Spectrometry coupled with a chelating resin column preconcentration metrod. Analytical Chemistry, 80: 9213-9219.

Neretin L N, Volkov I I, Böttcher M E, Grinenko V A. 2001. A sulfur budget fot the Black Sea anoxic zone. Deep-Sea Rearch I, 48: 2569-2593.

Neubert N, Nägler T F, Böttcher M E. 2008. Sulfidity controls molybdenum isotope fractionation into euxinic sediments: Evidence from the modern Black sea. Geology, 36: 775-778.

Pearce C R, Cohen A S, Coe A L, Burton K W. 2008. Molybdenum isotope evidence for global ocean anoxia coupled with perturbations to the carbon cycle during the Early Jurassic. Geology, 36: 231-234.

Pietruszka A J, Walker R J, Candela P A. 2006. Determination of mass-dependent molybdenum isotopic variations by MC-ICP-MS: An evaluation of matrix effects. Chemical Geology, 225: 121-136.

Poulson R L, Siebert C, McManus J, Berelson W M. 2006. Authigenic molybdenum isotope signatures in marine sediments. Geology, 34: 617-620.

Rudnick R L, Gao S. 2004. Composition of the Continental Crust. In: Treatise on Geochemistry. Holland H D and Turekian K K (Editors), Elsevier, Amsterdam. 3: 1-64.

Schauble E, Rossman G R, Taylor H P. 2004. Theoretical estimates of equilibrium chromium isotope fractionations. Chemical Geology, 205: 99-114.

Schoenberg R, Zink S, Staubwasser M, Blanckenburg F. 2008. The stable Cr isotope inventory of solid Earth reservoirs determined by double spike MC-ICP-MS. Chemical Geology, 249: 294-306.

Schröder S, Grotzinger J P. 2007. Evidence for anoxia at the Ediacaran-Cambrian boundary: the record of redox-sensitive trace elements and rare earth elements in Oman. Geological Society of London, 64: 175-187.

Scott C, Lyons T W, Bekker A, Shen Y, Poulton S W, Chu X, Anbar A D. 2008. Tracing the stepwise oxygenation of the Proterozoic ocean. Nature, 452: 456-460.

Shields G, Veizer J. 2002. Precambrian marine carbonate isotope database: version 1.1. Geochemistry, Geophysics, Geosystems, 3: 12.

Shu D G, Morris S C, Han J, Chen L, Zhang X L, Liu H Q, Li Y, Liu J N. 2001. Primitive deuterostomes from the Chengjiang Lagerstätte (Lower Cambrian, China). Nature, 414: 419-424.

Siebert C, McManus J, Bice A, Poulson R, Berelson W M. 2006. Molybdenum isotope signatures in continental margin marine sediments. Earth and Planetary Science Letters, 241: 723-733.

Siebert C, Nägler T F, Kramers J D. 2001. Determination of molybdenum isotope fractionation by double-spike multicollector inductively coupled plasma mass spectrometry. Geochemistry, Geophysics, Geosystems, 2: doi: 10.1029/2000GC000124.

Siebert C, Nägler T F, Blanckenburg F, Kramers J D. 2003. Molybdenum isotope records as a potential new proxy for paleoceanography. Earth and Planetary Science Letters, 211: 159-171.

Siebert C, Kramers J D, Meisel T, Morel P, Nägler T F. 2005. PGE, Re-Os, and Mo isotope systematics in Archean and early Proterozoic sedimentary systems as proxies for redox conditions of the early Earth. Geochimica et Cosmochimica Acta, 69: 1787-1801.

Steiner M, Wallis E, Erdtmann B D, Zhao Y L, Yang R D. 2001. Sunmarine-hydrothermal exhalative ore layers in black shales from South China and associated fossils-Insights into Lower Cambrian facies and bio-evolution. Plaleogeography, Palaeochimatology, Palaeoecology, 169: 165-191.

Tossell J A. 2005. Calculation the partitioning of the isotopes of Mo between oxidic and sulfidic species in aqueous solution. Geochimica et Cosmochimica Acta, 69: 2981-2993.

Tribovillard N, Algeo T J, Lyons T, Riboulleau A. 2006. Trace metals as paleoredox and paleoproductivity proxies: An update. Chemical Geology, 232: 12-32.

Turnlund J R, Keyes W R, Peiffer G L. 1993. Isotope rations of molybdenum determined by thermal ionization mass spectrometry for stable isotope studies of molybdenum metabolism in humans. Analytical Chemistry, 65: 1717-1722.

Tyson R V, Pearson T H. 1991. Modern and ancient continental shelf anoxia: an overview. In Tyson R V, Pearson T H (Eds.), Modern and ancient continental shelf anoxia. Geological Society Special Pbulication, 58: 1-26.

Wasylenki L E, Anbar A D, Gorden G W. 2006. Temperature dependence of Mo isotope fraction during adsorption to δ-MnO2: Implications for the paleoredox proxy. Geochimica et Cosmochimica Acta, 70: Supplement 1, A691.

Wen H J, Zhang Y X, Fan H F, Hu R Z. 2010. Mo isotopes in the Lower Cambrian formation of southern China and its implications on paleo-ocean environment. Chinese Science Bulletin, 54: 4756-4762.

Werne J P, Sageman B B, Lyons T W, Hollander D J. 2002. An integrated assessment of a “type euxinic” deposit: evidence for multiple controls on black shale deposition in the Middle Devonian Oatka Creek Formation. American Journal of Science, 302: 110-143.

Wetherill G W. 1964. Isotopic composition and concentration of molybdenum in iron meteorites. Journal of Geophysics Research, 69: 4403-4408.

Wheat C G, Mottl M J, Rudnicki M. 2002. Trace element and REE composition of a low-temperature ridge-flank hydrothermal spring. Geochimica et Cosmochimica Acta, 66: 3693-3705.

Wieser M E, DeLaeter J R. 2000. Thermal ionization mass spectrometry of molybdenum isotopes. International Journal of Mass Spectrometry, 197: 253-261.

Wieser M E, DeLaeter J R. 2003. A preliminary study of isotope fractionation in molybdenites. International Journal of Mass Spectrometry, 225: 177-183.

Wieser M E, DeLaeter J R. 2009. Molybdenum isotope mass fractionation in iron meteorites. International Journal of Mass Spectrometry, 286: 98-103.

Wille M, Kramers J D, Nägler T F, Beukes N J, Schröder S, Meisel Th, Lacassie J P, Voegelin A R. 2007. Evidence for a gradual rise of oxygen between 2.6 and 2.5 Ga from Mo isotopes and Re-PGE signatures in shales. Geochimica

Cosmochimia Acta, 71: 2417-2435.

Wille M, Nägler T F, Lehmann B, Schröder S, Kramers J D. 2008. Hydrogen sulphide release to surface waters at the Precambrian/Cambrian boundary. Nature, 453: 767-769.

Williams G, Anbar A D, Lyons T W, Sageman B, Arnold G L. 2004. The redox state of Devonian oceans: Mo isotope evidence. Geological Society of America Abstracts with Programs, 36: 543.

Yin Q Z, Jacobsen S B, Yamashita K. 2002. Diverse supernova sources of pre-solar material inferred from molybdenum isotopes in meteorites. Nature, 415: 881-883.

Young E D, Galy A, Nagahara H. 2002. Kinetic and equilibrium mass-dependent isotope fractionation laws in nature and their geochemical and cosmochemical significance. Geochimica et Cosmochimica Acta, 66: 1095-1104.

Zhang Y X, Wen H J, Fan H F. 2008. Advances in the study of Mo stable isotope geochemistry. Acta Petrologic et Mineralogica, 27: 457-464 (in Chinese with English abstract).

Zheng Y, Anderson R F, van Geen A, Kuwabara J. 2000. Authigenic molybdenum formation in marine sediments: a link to pore water sulfide in the Santa Barbara Basin. Geochimica et Cosmochimica Acta, 64: 4165-4178.

Zhu X K, Guo Y, Williams R J P, O`Nions R K, Matthews A, Belshaw N S, Canters G W, Waal E C, Weser U, Burgess B K, Salvato B. 2002. Mass fractionation processes of transition metal isotopes. Earth and Planetary Science Letters, 200: 47-62.

Zhu X K, O`Nions R K Guo Y, Belshaw N S, Rickard D. 2000. Determination of natural Cu-isotope variation by plasma-source mass spectrometry: implications for use as geochemical tracers. Chemical Geology, 163: 139-149.

CHAPTER SIX:

Mo ISOTOPE AND TRACE ELEMENT PATTERNS OF EARLY CAMBRIAN BLACK SHALES IN SOUTH CHINA: MULTI-PROXY CONSTRAINTS ON THE PALEOENVIRONMENT

Xu Lingang[a,*], Bernd Lehmann[a], Mao Jingwen[b], Thomas F. Nägler[c], Nadja Neubert[c], Michael E. Böttcher[d]

[a] *Mineral Resources, Technical University of Clausthal, D-38678 Clausthal-Zellerfeld, Germany*

[b] *MLR Key Laboratory of Metallogeny and Mineral Assessment, Institute of Mineral Resources, Chinese Academy of Geological Sciences, 100037 Beijing, China*

[c] *Institute of Geological Sciences, University of Bern, CH-3012 Bern, Switzerland*

[d] *Leibniz Institute for Baltic Sea Research (IOW), Marine Geology Section, D-18119 Warnemünde, Germany*

Corresponding author: Email address: lingang.xu@tu-clausthal.de (Xu Lingang)

Submitted to ***Chemical Geology***

6.1 Abstract

The Precambrian/Cambrian boundary marks a critical interval in Earth history. Paleoenvironmental changes of the oceans have been suggested as a possible explanation for some significant events such as the marine biological evolution ("Cambrian explosion"). Here we report a remarkable variation range in trace element geochemical, iron speciation and molybdenum isotope signatures of black shales from the Early Cambrian Dingtai profile and three synsedimentary polymetallic Ni-Mo-PGE-Au sulfide ore deposits (Dazhuliushui and Maluhe in Guizhou province, and Sancha in Hunan province) on the Yangtze Platform, South China. Based on the (isotope) geochemical features, we classify the Dingtai profile into three intervals: Interval 1 (0-1 m) has extreme metal and TOC enrichment and heavy $\delta^{98/95}$Mo values. This unit has all features of a euxinic environment, and is then followed by interval 2 (1-11 m) with variable $\delta^{98/95}$Mo composition. Elevated contents of redox-sensitive elements and their ratios, and relatively high Fe_{HR}/Fe_T ratios (“reactive iron”) suggest ongoing euxinic conditions. The overlying interval 3 (11-33 m) reveals suboxic conditions with generally light $\delta^{98/95}$Mo values in the lowermost part and fluctuant $\delta^{98/95}$Mo values in the uppermost part, and relatively low redox-sensitive element contents. We propose a model of a partly closed ocean basin with periodic replenishment for the remarkable variability of $\delta^{98/95}$Mo values. Light $\delta^{98/95}$Mo values indicate restricted seawater circulation dominated by local continental input, periodically replenished by fresh seawater with heavy $\delta^{98/95}$Mo.

A global compilation of Mo isotope data from black shales indicates that the Mo isotopic variations have a consistent temporal trend, reflecting the oxygen evolution of the atmosphere and the oceans. Relatively light $\delta^{98/95}$Mo values of the Early Cambrian black shales compared to those of modern euxinic sediments are indicative of more widespread anoxic marine environments during the Early Cambrian.

Keywords: Molybdenum isotopes, Trace elements, Black shales, Paleoenvironment, Early Cambrian, South China

6.2 Introduction

Non-traditional stable isotopes (e.g. Mo and Fe) and iron speciation (e.g. degree of pyritization: DOP and highly reactive iron) have recently much contributed to the reconstruction of ancient marine redox conditions, together with conventional trace metal geochemistry (e.g. Mo, V and U) (e.g. Raiswell et al., 1988; Algeo and Maynard, 2004; Arnold et al., 2004; Rouxel et al., 2005; Pearce et al., 2008; Johnson et al., 2008; Voegelin et al., 2009 and many others). Molybdenum has attracted particular attention due to its low lithogenic background in marine sediments and relatively high authigenic abundance in reducing marine settings (e.g. Calvert and Pedersen, 1993; Crusius et al., 1996; Dean et al., 1999; Wilde et al., 2004; Nägler et al., 2005). Due to the long residence time (~ 800 kyr) compared to seawater overturn (Morford and Emerson, 1999), the Mo concentration in modern oceans is uniform, with an elevated concentration of ~ 10.5 µg/l (Morris 1975; Collier 1985). Mo isotope fractionation occurs during Mo removal from seawater to marine sediments under a wide range of environmental conditions and provides basic information on the paleo-redox conditions of the ocean-atmosphere systems (e.g. Barling et al., 2001; Siebert et al., 2003; Poulson et al., 2006; Neubert et al., 2008; Kendall et al., 2009; Wen et al., 2009). Under oxic conditions, Mo is adsorbed onto ferromanganese oxyhydroxides (Crusius et al., 1996). The adsorption process is mass-dependant and leads to light Mo isotope enrichment in the ferromanganese sediments with $\delta^{98/95}$Mo ~ -0.7 ‰ and complementary heavy Mo isotope enrichment in modern seawater with $\delta^{98/95}$Mo 2.3-2.5 ‰ (Barling et al., 2001; Siebert et al., 2003; Nakagawa et al., 2008). Under euxinic/sulfidic conditions, the bulk seawater Mo is quantitatively removed from the seawater column and the Mo isotope composition of euxinic sediments is then equal to coeval seawater (Nägler et al., 2005; Neubert et al., 2008). Isotopic analyses of modern seawater indicate a uniform Mo isotope composition of $\delta^{98/95}$Mo = 2.3 ± 0.2 ‰, which is similar to modern euxinic sediments (Barling et al., 2001; Siebert et al., 2003). The Mo isotopic composition of euxinic depositional settings therefore records $\delta^{98/95}$Mo values of contemporaneous seawater (Barling et al., 2001; Arnold et al., 2004; Lehmann et al., 2007; Pearce et al., 2008). Under anoxic or suboxic settings, where O_2 is scarce but H_2S is not abundant, Mo accumulates together with black shales and other organic-rich sediments, but the transfer from seawater to sediment is not quantitative. The Mo isotopic fractionation in such environments is intermediate between that in euxinic and oxic settings (Tossell, 2005; Poulson et al., 2006; Siebert et al., 2006; Anbar and Gordon, 2008).

Some trace elements including Mo, U, V, Cr, Ni and Co are enriched in reducing sediments and are highly sensitive to redox changes, making them and their ratios important proxies for paleoredox reconstruction (e.g. Vine and Tourtelot, 1970; Holland, 1979; Piper, 1994; Algeo and Maynard, 2004; Rimmer, 2004; Tribovillard et al., 2006, and many others). Both biotic and abiotic processes contribute to the removal of dissolved trace elements from the water column to sediments. Under oxic conditions, adsorption processes to insoluble oxyhydroxides are important, and some dissolved trace elements can become enriched along redox gradients from the oxic water column across the sediment-water interface to sediments. Abiotic processes are particularly efficient under euxinic conditions, where trace elements may be precipitated as sulfides or become adsorbed onto organic matter and insoluble oxyhydroxides (Tribovillard et al., 2006).

The Precambrian/Cambrian transition represents a critical interval in Earth history characterized by global environmental and biological changes, such as major plate tectonic reconfiguration, ocean anoxia, mass extinction and accelerated diversification of metazoans (Brasier, 1992; Kaufman et al., 1993; Kirschvink et al., 1997; Shu et al., 2001). A possibly global ocean anoxia event is seen in widespread Early Cambrian black shale deposition (Banerjee et al., 1997; Kimura and Watanabe, 2001; Schröder and Grotzinger, 2007). In South China, the transgressive Early Cambrian black shale sequence of the Niutitang Formation (and equivalent strata) occurs in an about 1600 km-long belt that extends across the Yangtze Platform (Zhu et al., 2004), unconformably overlying dolomite of the Neoproterozoic Dengying Formation. The black shale sequence is enriched in a broad spectrum of redox-sensitive metals, i.e. Mo, Ni, Cr, V, PGE, Au, and U, typical of black shales in general (Vine and Tourtelot, 1970; Holland, 1979). However, an unusual organic carbon-, phosphate- and sulfide-rich ore layer is locally distributed in the lowermost part of the black shale sequence of South China (<10 m above the Precambrian/Cambrian boundary), in which these metals are extremely enriched and locally reach ore grade and are mined for nickel, molybdenum, platinum-group elements and gold (Fan et al., 1984; Mao et al., 2002). This peculiar polymetallic sulfide ore layer, and its metal enrichment may be relevant to an understanding of the Early Cambrian ocean-atmosphere system. Previous work suggested a variety of mechanisms, ranging from an extraterrestrial origin (Fan et al., 1984), to hydrothermal venting at the seafloor (Lott et al., 1999; Steiner et al., 2001; Jiang et al., 2006, 2007; Pasava et al., 2008), to scavenging from average seawater at a very low clastic sedimentation rate (Mao et al., 2002; Lehmann et al., 2003, 2007).

We investigated black shales from the Early Cambrian Dingtai profile near Zunyi city, Guizhou province (33 m of stratigraphic thickness), and polymetallic Ni-Mo-PGE-Au sulfide ores and host black shales and phosphorite from the Dazhuliushui, Maluhe and Sancha polymetallic Ni-Mo-PGE-Au sulfide ore deposits from Guizhou and Hunan provinces. The joint application of Mo isotope, iron speciation and trace element geochemistry attempts to contribute to an understanding of the paleoenvironmental evolution of Early Cambrian seawater on the South China block, and its global implications.

6.3 Geological settings and studied profile

Neoproterozoic and Early Cambrian sedimentary rocks are widely exposed on the Yangtze Platform of South China. The sedimentary sequence represents a shelf environment characterized by repeated transgression-regression episodes on the Early Proterozoic-Archean Yangtze Platform (Qiu et al., 2000; Steiner et al., 2001) (Fig. 6-1). The Neoproterozoic Nantuo Formation is characterized by glacial diamictites with siltstone and sandstone interbeds, and is correlated with the 630 Ma Marinoan glaciation (Gradstein et al., 2004). The Doushantuo Formation overlies the diamictite of the Nantuo Formation, and consists of carbonaceous mudstone and dolomite, with interbedded phosphorite (Fig. 6-2). U-Pb zircon dates from volcanic ash beds within the Doushantuo Formation indicate that deposition occurred between 635 and 551 Ma (Condon et al., 2005). Two phosphorite beds in the Doushantuo Formation yielded Pb-Pb isochron ages of 576 ± 16 Ma for the upper part (Chen et al., 2004), and 599 ± 4 Ma for the lower part of the Upper Phosphorite unit (Barfod et al., 2002), respectively. Three zircon SHRIMP U-Pb ages of 628 ± 6 Ma, 621 ± 7 Ma, and 555 ± 6 Ma were reported for different volcanic ash interbeds, which constrain the age interval of the Doushantuo Formation (Yin et al., 2005; Zhang et al., 2005). Above the Doushantuo Formation rests the >1500 m-thick dolomite sequence of the Dengying Formation, followed by a stratigraphic hiatus. The Niutitang Formation and equivalent strata of black shales unconformably overlie the Dengying Formation. The Niutitang Formation is dominated by black shales but its lower part has a very variable lithology with important sedimentary phosphorite and barite units, and up to several tens of meters thick “stone coal” bed of algal origin (combustible shale). An organic- and sulfide-rich polymetallic ore layer is locally distributed in the lowermost part of the Niutitang Formation with a thickness of only 3 to 5 cm. The sulfide ore layer was dated using the Re-Os method and yielded isochron ages of 560 ± 50 Ma (Horan et al., 1994), 542 ± 11 Ma (Li et al., 2002) and 541 ± 16 Ma (Mao et al., 2002), respectively. Pb-Pb dating of black shale and Ni-Mo-PGE-Au sulfide ores from the

Niutitang Formation yielded an isochron age of 531 ± 24 Ma and 521 ± 54 Ma, respectively (Jiang et al., 2006). Jiang et al. (2009) reported a SHRIMP U-Pb zircon age of 532.3 ± 0.7 Ma for a volcanic ash bed a few meters below the sulfide ore layer near Zunyi, Guizhou province, suggesting that the mineralization age of the sulfide ore layer must be younger than 532 Ma. Recently, based on comprehensive sampling of the polymetalllic sulfide ores, Xu et al. (2011) reported a Re-Os age of 521 ± 5 Ma, which is consistent with the biostratigraphic Tommotian age. Chert and phosphorite beds occur below the sulfide ore layer, immediately above the Dengying dolomite. Phosphorite mostly occurs as discontinuous nodules, however, a locally thick massive phosphorite bed (reaching up to 20 meters) is also found, which is locally mined for phosphate ore (e.g. Zhijin phosphorite deposit, near the Maluhe polymetallic sulfide ore deposit, Guizhou province, or Kunyang phosphorite deposit near Kunming). The black shales and phosphorite nodules/beds of the Niutitang Formation contain abundant sponges, arthropods and other soft-bodied fossils of wide biological diversity reflecting the “Cambrian Explosion” (Brasier, 1992; Steiner et al., 2001, 2007). The Niutitang Formation is overlain by shale, siltstone and fine-grained sandstone (Mingxinsi Formation), sandy shale and muddy siltstone (Jindingshan Formation), and dolomite (Qingxudong Formation), in ascending order.

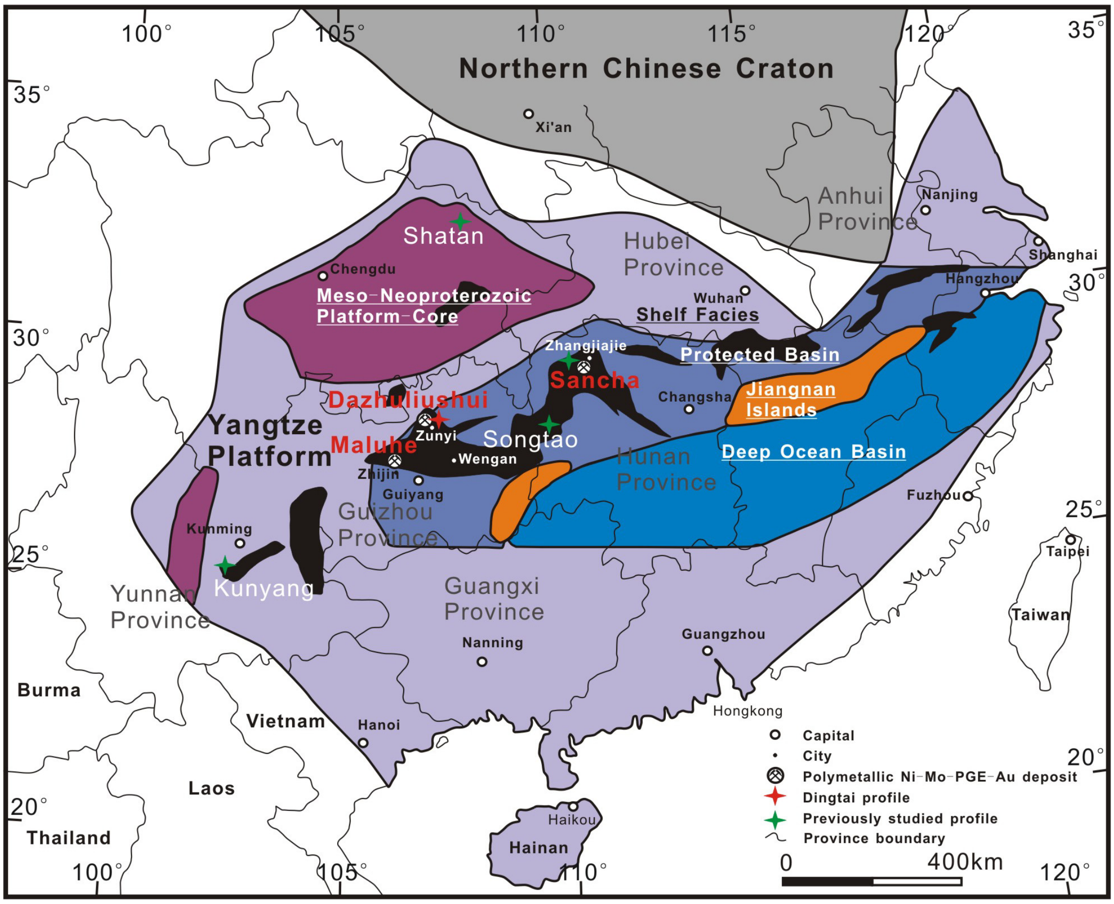

Fig. 6-1: Sketch map showing locations of the Dingtai profile and the Dazhuliushui, Maluhe and Sancha polymetallic Ni-Mo-PGE-Au sulfide ore deposits, and depositional environments during the Neoproterozoic-Cambrian interval (modified from Wallis, 2007). Black areas indicate the exposed Early Cambrian black shale sequence of the Niutitang Formation (and equivalent strata) in South China. Red cross-star is the Dingtai profile studied in this work, and green cross-stars are geolocial profiles studied previously (Pan et al., 2004; Guo et al., 2007, Zhu et al., 2009). Donation of colors: Lilac = Unspecified sedimentation, Blue = Protected basin, Ultramarine = Deep ocean basin, Orange = Positive area ((Jiangnan paleo-islands), Red = Positive area (Meso-Neoproterozoic Platform core).

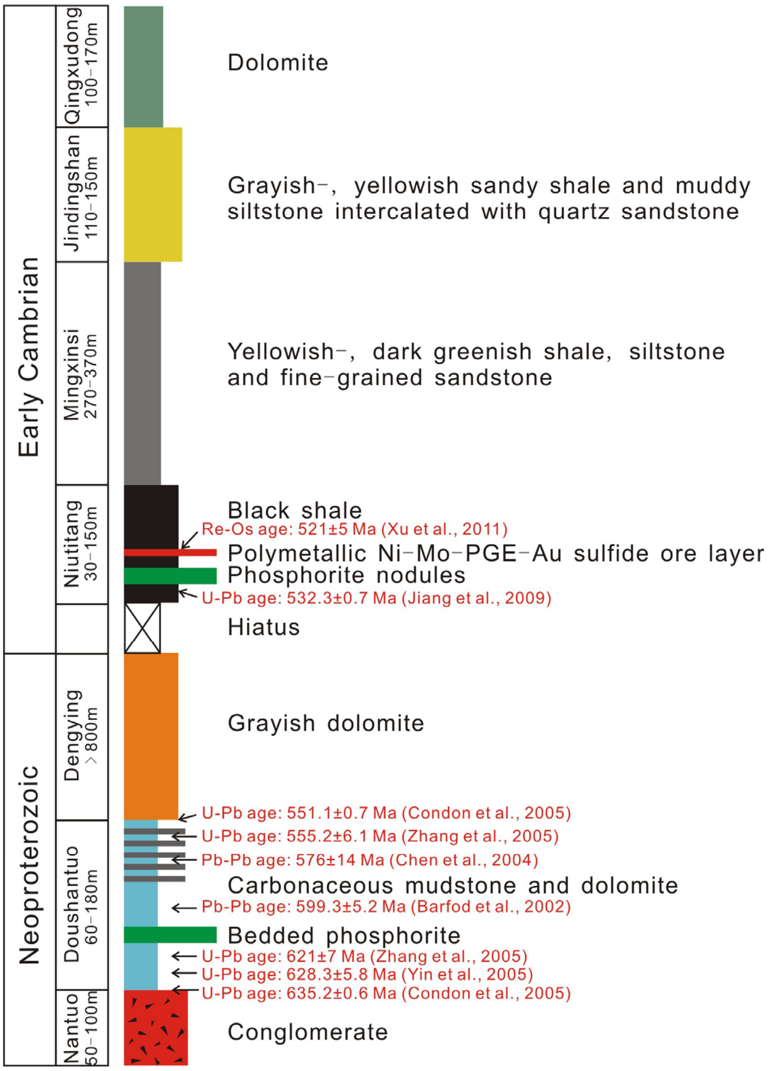

Fig. 6-2: Stratigraphic column showing the Neoproterozoic-Early Cambrian sedimentary sequences of South China. Radiometric ages are highlighted in red.

The Neoproterozoic-Cambrian paleogeographic reconstruction reveals a depositional zonation from a shallow shelf facies of carbonate and phosphorite rocks in the northwest to a protected and deep basinal facies of black shales and cherts in the southeast (Zhu et al., 2004; Wallis, 2007) (Fig. 6-1). The investigated Dingtai profile (N 27°42′48.9″, E 106°38′58.2″) and the three polymetallic Ni-Mo-PGE-Au sulfide ore deposits of Dazhuliushui (N 27°43′13.5″, E 106°38′44.3″) and Maluhe (N

26°44′40.0″, E 105°37′13.5″) in Guizhou province, and Sancha (N 29°04′26.6″, E 110°34′32.7″) in Hunan province, respectively, are all located in the protected basin but several hundred km apart (Fig. 6-1). Besides of the Dingtai profile studied in this paper, the Shatan profile representing a shallow carbonated platform setting, and Songtao, Sancha and Kunyang profiles representing protected basinal sedimentary environments have been studied previously (see Fig. 6-1, Pan et al., 2004; Guo et al., 2007; Lehmann et al., 2007, Zhu et al., 2009). The Dingtai profile is an outcrop profile which is ~4 km southeast of the Dazhuliushui mine site, spanning the upper part of the Dengying Formation, the Niutitang Formation and the lower part of the Mingxisi Formation. The stratigraphic thickness of the Niutitang Formation is 32.3 m in the Dingtai profile, and the polymetallic sulfide ore layer is only 0.5 m above the Neoproterozoic Dengying dolomite (Fig. 6-3 A). The Niutitang Formation can be divided into five lithological units from bottom upward:

Unit 1: A 20 cm-thick nodular phophorite-bearing black shale layer, unconformably overlying the Dengying dolomite. The low angle unconformity (<10°) is characterized by a thin layer of iron-manganese oxide-rich weathering crusts and lenses. The phosphorite nodules occur in variable size (1-10 cm of diameter). In some places (e.g. Zhijin, Cili and Kunyang) the thickness of this unit can reach up to decades of meters and is then mined for massive and nodular phosphate.

Unit 2: A 30 cm-thick black shale layer with black chert interbeds. Small phosphorite aggregates and organic debris are abundant in this unit (Fig. 6-3 B).

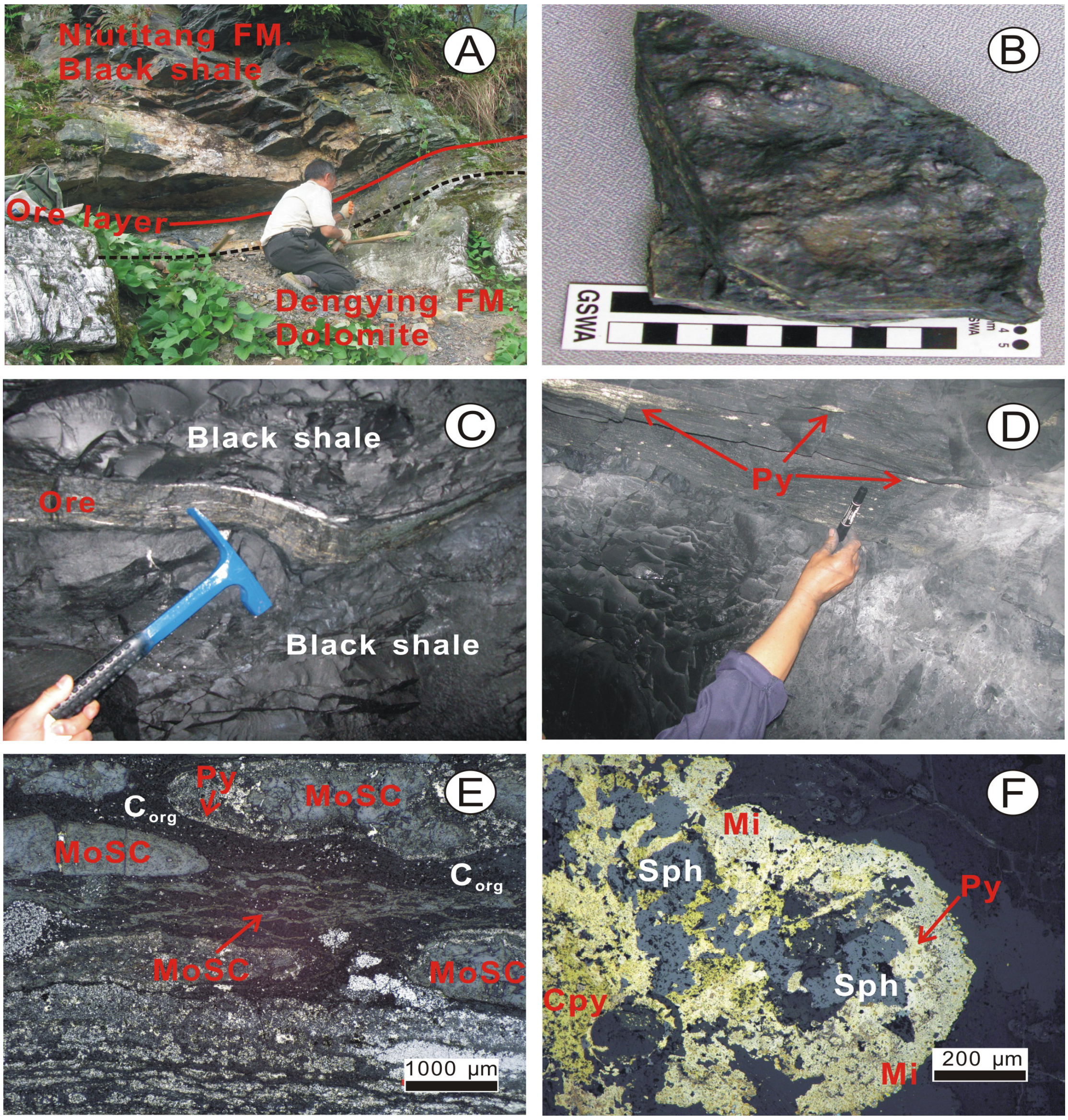

Fig. 6-3: Field photographs of the Dingtai profile in Guizhou province, and the polymetallic sulfide ore deposits, South China. **A:** Field photo of the Dingtai profile showing the polymetallic Ni-Mo-PGE-Au sulfide ore layer and PC/C boundary (black dashed line: contact to dolomite of Dengying Formation; red line: sulfide ore layer). The location is ~ 4 km southeast of the Dazhuliushui mine site. **B:** Black shale with phosphorite nodules from footwall of the polymetallic sulfide ore layer. **C:** The 5 cm-thick sulfide bed showing a clear-cut boundary with the black shale host sequence (Dazhuliushui underground mine) **D:** Laminated pyrites occurred in immediate black shales above the polymetallic sulfide ore layer (Dazhuliushui underground mine). **E:** Laminated and ellipsoidal MoSC phase with fine-grained pyrite rims surrounded by sapropel matrix. Re-deposited rip-up clasts in matrix of in-situ precipitated organic matter (Sancha underground mine). **F:** Sphalerite, chalcopyrite, millerite intergrown with anhedral pyrite (Sancha underground mine). Abbreviations: Cpy = chalcopyrite, C_{org} = organic matter, Mi = millerite, MoSC = Mo-Sulfur-Carbon phase aggregate, Py = pyrite, Sph = sphalerite.

Unit 3: A polymetallic Ni-Mo-PGE-Au sulfide ore layer with thickness of 4 cm (Fig. 6-3 C). Mo and Ni contents are extremely high, reaching up to 14 wt.% in total, and platinum group element (PGE) + Au concentrations are around 1 g/t. The minor elements Se, Re, Os, As, Hg, and Sb display $>10^4$-fold enrichment compared to average upper continental crust (Fan et al., 1984; Conveney et al., 1994; Lehmann et al. 2007). The Ni-Mo ore occurs both finely laminated and as a debris layer, and the sulfide components are lenticular, flattened and fine-grained laminated, consisting largely of a MoSC phase (with the approximate composition of $[(Mo,Fe,Ni)(S,As)_2C_7]$), pyrite, vaesite, bravoite, millerite gersdorffite and jordisite, with minor arsenopyrite, chalcopyrite, covellite, sphalerite, tennantite, tiemannite, violarite and native Au (Conveney et al., 1994; Kao et al., 2001; Mao et al., 2002; Jiang et al., 2006) (Fig. 6-3 F).

Unit 4: A 10 m-thick black shale sequence with abundant fossils, including sponge spicules and bivalved arthropods. At the bottom of this unit near the sulfide ore layer occurs abundant laminated pyrite (Fig. 6-3 D).

Unit 5: A 21.3 m-thick silty black shale layer without fossils, which is overlain by the greenish shales of the Mingxinsi Formation. No distinct boundary between Unit 4 and 5 can be discerned, and silty material increases gradually upwards.

6.4 Sampling and analytical methods

A total of 22 rock samples from the Dingtai profile and 10 bulk ore samples from three polymetallic Ni-Mo-PGE-Au mine sites were collected (Table 6-1). The three underground mine sites have a stratigraphic sequence similar to the Dingtai profile and the sample position can be correlated. Surface outcrops in South China are often affected by subtropical weathering and we took care to obtain fresh sample material (~ 1 kg per sample) for the Dingtai profile by manual digging of channels and pits. We determined the elemental and Mo isotope composition of the black shales and Ni-Mo-PGE-Au sulfide ores, as well as their iron speciation (degree of pyritization, DOP).

6.4.1 Trace and TOC analyses

Bulk powdered samples (finer than 200 mesh) were analyzed for trace elements using a Finnigan MAT ELEMENT high resolution inductively coupled plasma-mass spectrometer (ICP-MS), following the methods of Balaram et al. (1995) and Wu et al. (1996). The total organic carbon (TOC) contents were determined by a Leco infrared Carbon/Sulfur analyzer. Both trace elements and TOC analyses were carried out at the Chinese National Research Center of Geoanalysis in Beijing. In order to remove carbonate and calcium phosphate minerals, the powdered samples were leached with 2 N HCl, after which the residues were completely digested using a mixed HF and HNO_3 solution. After evaporation, samples were redissolved in 1 N HNO_3 for analysis. Errors for trace elements in this study are within ± 6%.

6.4.2 Mo purification and isotope analyses

The molybdenum stable isotope analyses were carried out using a Nu instruments MC-ICP-MS at the Isotope Laboratory of the University of Bern in Switzerland. The ^{97}Mo-^{100}Mo double spike technique was used to monitor and correct instrumental mass discrimination during Mo isotope measurements. The external standard reproducibility was 0.1 $\delta^{98/95}$Mo (2 σ).

Between 4.5 and 5.0 g of powered sample was oxidized at 800°C for 12 hours to remove organic matter and about 0.1 g was employed for Mo isotope measurement for each sample. Mo was purified using the separation procedure described in Siebert et al. (2001), Wille et al. (2008) and Voegelin et al. (2009). A minor modification was done to suit the Mo-rich ore samples. According to the previously determined Mo concentration, the approximate sample weight needed for measurement was calculated. The ore samples (up to wt.% Mo) were then pre-diluted to the ppm level to prevent lab contamination. To account for Mo isotope fractionation during column separation and to resolve instrumental mass bias, a calculated amount of ^{97}Mo-^{100}Mo double spike was added prior to dissolution and chemical purification. The ^{97}Mo-^{100}Mo double spike technique has several advantages: 1) low natural abundance of ^{97}Mo and ^{100}Mo, 2) no elemental isobaric interferences on ^{97}Mo, and ^{100}Mo is reducible from isobaric interferences of ^{100}Ru, and 3) highly enriched ^{97}Mo and ^{100}Mo can be obtained (Siebert et al., 2001).

Table 6-1

Mo isotope and geochemical data of the Dingtai profile, and the Dazhuliushui, Maluhe and Sancha polymetallic Ni-Mo-PGE-Au sulfide ore deposits, South China.

Sample	Depth (m)[‡]	Lithology	V ppm	Cr ppm	Co ppm	Ni ppm	Cu ppm	Zn ppm	Mo ppm	Pb ppm	U ppm	Fe_T wt.%	Al_2O_3 wt.%	MnO wt.%	TOC wt.%	Fe_{HR} wt.%	Fe_{HR}/Fe_T	DOP[$] %	$\delta^{98/95}Mo$ (‰) measured	$\delta^{98/95}Mo$ (‰) authigenic[#]	2σ[§]	Ni/Co	V/Cr	V/(V+Ni)	Mo/TOC ppm/wt.%
Dingtai profile																									
Interval 3																									
PM-27	32.3	Black shale	265	108	7.10	42.5	74.6	70.1	15.1	17.7	12.3	1.96	16.2	0.010	2.79	0.3	0.2		1.19	1.28	0.04	5.99	2.46	0.86	5.41
PM-24	29.3	Black shale	1010	122	8.39	92.9	59.5	162	24.4	8.75	11.0	2.40	15.7	0.010	3.33	0.8	0.3		0.26	0.27	0.03	11.1	8.26	0.92	7.34
PM-23	28.3	Black shale	385	112	7.34	60.7	35.6	80.0	27.6	22.7	17.0	1.37	15.5	0.009	4.09	0.4	0.3		0.39	0.41	0.06	8.27	3.45	0.86	6.74
PM-22	27.3	Black shale	248	104	11.5	74.5	37.8	124	26.1	25.2	13.2	1.57	14.8	0.006	4.25	0.4	0.3		1.53	1.59	0.07	6.48	2.39	0.77	6.14
PM-21	26.3	Black shale	1430	119	9.98	81.4	30.4	106	19.0	16.9	17.3	2.10	15.0	0.012	3.68	0.3	0.2		0.05	0.05	0.04	8.16	12.0	0.95	5.16
PM-20	25.3	Black shale	314	108	7.40	49.7	36.3	94.9	27.7	22.9	13.0	1.33	14.5	0.007	3.22	0.4	0.3		1.20	1.25	0.04	6.72	2.92	0.86	8.61
PM-19	23.8	Black shale	899	106	8.01	75.0	51.9	92.8	38.4	19.0	17.4	1.69	14.2	0.008	3.70	0.5	0.3		0.50	0.51	0.07	9.36	8.45	0.92	10.4
PM-18	22.3	Black shale	926	102	12.4	106	42.3	162	73.0	17.3	19.3	2.21	13.2	0.007	3.96	1.2	0.5		0.59	0.60	0.03	8.55	9.07	0.90	18.4
PM-17	20.8	Black shale	1060	119	36.2	202	74.8	210	24.8	19.2	17.9	2.29	14.7	0.014	3.77	0.6	0.3		0.31	0.32	0.08	5.58	8.93	0.84	6.58
PM-16	19.3	Black shale	2110	141	12.4	135	32.1	148	56.9	8.40	18.3	1.71	14.1	0.010	5.42	0.4	0.2		-0.35	-0.36	0.03	10.9	14.9	0.94	10.5
PM-15	17.8	Black shale	1410	116	8.36	104	37.3	158	49.9	11.4	18.8	1.45	13.6	0.009	4.42	0.4	0.3		-0.02	-0.02	0.05	12.4	12.2	0.93	11.3
PM-14	16.3	Black shale	756	105	11.0	88.6	112	269	26.5	18.9	15.7	1.45	14.9	0.006	3.16	0.3	0.2		-0.09	-0.10	0.05	8.05	7.17	0.90	8.40
PM-13	14.8	Black shale	1510	145	19.0	203	30.3	337	70.8	10.0	16.6	2.24	14.4	0.006	3.74	0.3	0.1		0.08	0.08	0.04	10.7	10.4	0.88	18.9
PM-12	13.3	Black shale	1240	122	3.11	36.5	16.8	83.9	13.9	12.5	9.35	1.21	15.1	0.005	3.93	0.3	0.2		0.00	0.00	0.05	11.7	10.2	0.97	3.54
PM-11	11.8	Black shale	980	111	3.44	65.8	16.9	35.3	86.4	20.2	17.2	0.51	12.6	0.003	7.06	0.1	0.3		-1.54	-1.56	0.04	19.1	8.79	0.94	12.2
Interval 2																									
PM-10	10.3	Black shale	1070	103	1.09	52.5	18.2	21.8	110	13.4	18.0	0.40	11.8	0.003	8.24	0.1	0.2		1.05	1.06	0.04	48.2	10.4	0.95	13.4
PM-9	8.8	Black shale	1750	110	4.29	215	24.9	99.5	394	13.1	23.3	1.25	11.7	0.003	6.85	0.8	0.6		1.07	1.07	0.03	50.1	15.9	0.89	57.5
PM-8	7.3	Black shale	1070	69.9	1.50	40.1	13.4	31.9	67.2	15.4	19.1	0.56	11.2	0.004	6.14	0.2	0.3		0.57	0.57	0.04	26.7	15.3	0.96	10.9
PM-7	5.8	Black shale	1160	96.3	3.24	120	21.6	86.8	374	20.2	26.9	1.23	12.5	0.004	6.56	0.7	0.6		0.67	0.67	0.03	37.0	12.0	0.91	57.0
PM-6	4.3	Black shale	4090	159	5.59	133	19.2	65.3	188	45.5	28.0	0.77	10.4	0.004	7.09	0.3	0.4		-0.14	-0.14	0.03	23.8	25.8	0.97	26.5
PM-5	2.8	Black shale	4400	1180	2.12	147	30.1	195	38.0	15.7	21.0	1.60	9.26	0.003	8.86	1.1	0.7		0.18	0.18	0.04	69.3	3.73	0.97	4.29
PM-4	1.3	Black shale	4270	2540	2.31	154	29.8	159	140	11.3	23.0	1.15	9.47	0.003	11.8	0.7	0.6		1.25	1.26	0.05	66.7	1.68	0.97	11.9

Table 6-1 (continued)

Sample	Depth (m)[‡]	Lithology	V ppm	Cr ppm	Co ppm	Ni ppm	Cu ppm	Zn ppm	Mo ppm	Pb ppm	U ppm	Fe_T wt.%	Al_2O_3 wt.%	MnO wt.%	TOC wt.%	Fe_{HR} wt.%	Fe_{HR}/Fe_T	DOP[$] %	$\delta^{98/95}$Mo (‰) measured	$\delta^{98/95}$Mo (‰) authigenic[#]	2 σ [§]	Ni/Co	V/Cr	V/(V+Ni)	Mo/TOC ppm/wt.%
Maluhe deposit																									
MLH-4	0.7	Black shale	310	116	32.1	301	69.0	330	142	47.2	54.9	4.27	14.2	0.048	8.14	3.4	0.8	97	1.70	1.71	0.05	9.38	2.67	0.51	17.4
MLH-5	0.5	Sulfide ore	423	53.0	255	36300	1970	26300	70900	156	112	11.6	1.29	0.008	n.d.	n.d.			1.38	1.38	0.02	142	7.98	0.01	n.d.
MLH-2	0.5	Sulfide ore	480	64.0	254	37700	1880	21200	61600	235	118	21.9	1.71	0.006	n.d.	n.d.			1.37	1.37	0.03	148	7.50	0.01	n.d.
MLH-6	0.3	Phosphorite	417	26.0	4.56	359	44.1	1411	117	3.09	517	0.30	1.80	0.002	4.11	0.2	0.8	93	1.57	1.57	0.03	78.7	16.0	0.54	28.5
Dazhuliushui deposit																									
DZLS-7	0.7	Black shale	409	93.0	22.5	332	71.4	66.9	65.2	15.3	30.6	4.35	12.1	0.072	6.74	1.0	0.2	82	0.89	0.90	0.02	14.8	4.40	0.55	9.67
DZLS-8	0.5	Sulfide ore	644	55.0	220	60100	2740	4400	62800	117	114	17.2	1.30	0.102	n.d.	n.d.			1.07	1.07	0.06	273	11.7	0.01	n.d.
DZLS-2	0.5	Sulfide ore	658	53.0	273	62700	2450	3460	73100	183	125	11.6	1.29	0.127	n.d.	n.d.			1.16	1.16	0.04	230	12.4	0.01	n.d.
DZLS-9	0.3	Black shale	320	85.1	18.5	249	52.8	306	90.6	15.4	24.5	3.00	11.6	0.053	8.65	1.8	0.6	93	1.58	1.59	0.03	13.5	3.76	0.56	10.5
Sancha deposit																									
SC-11	0.5	Sulfide ore	3780	149	111	29900	1180	3860	65900	37.0	595	11.8	1.31	<0.001	n.d.	n.d.		n.d.	1.19	1.19	0.02	269	25.4	0.11	n.d.
SC-2	0.5	Sulfide ore	1680	68.0	172	61500	2080	4430	56400	180	408	13.0	1.20	<0.002	n.d.	n.d.		n.d.	1.00	1.00	0.03	358	24.7	0.03	n.d.

[‡] level above the PC/C boundary. Level of samples from the three mine sites have been corrected to the Dingtai profile according to the lithological correlation.

[#] 'authigenic' refers to ratios corrected for detrital Mo based on Al contents.

[§] In run presision of analyses (2σ standard error). External reproducibility was ±0.1 ‰ (2 s.d.).

[$] DOP = Fe_P/Fe_{HR}. Fe_{HR} (highly reactive iron) is calculated as $Fe_{HR} = Fe_P + Fe_D$, where Fe_P refers to sulfur extracted by hot acidic $Cr(II)Cl_2$ solution and molar recalculation to Fe and Fe_D refers to Fe extracted with buffered Na dithionite solution.

n.d. = not determined.

The black shale sample with about 50 ng Mo was put in a Teflon beaker together with 6 M HCl to keep Mo in its highly soluble Mo^{6+} oxygenation state, and then heated to ~ 100°C on a heating stage overnight. The sample material was dried and dissolved with concentrated HF and HNO_3 (4:1) at ~ 100°C. Subsequently, organic and detrital material was separated from solution by centrifugation. The solution was transferred into another Teflon beaker. In order to completely leach Mo, the residue was again heated in 6 M HCl at ~ 100°C overnight, and then added to the second beaker. The aliquots were combined and dried on a hot plate. After evaporation, the material was taken up in pre-prepared HCl + H_2O_2 resolution (5 ml 4 M HCl and 0.3% H_2O_2) and loaded onto an anion exchange resin to wash out cations, followed by six-block stepwise loading onto anion exchange columns (Dowex^{TM} 1X8 resin, 200 - 400 mesh). Finally, the molybdate anion was eluted with 2 M HNO_3. For cleaning Fe and Zr from Mo solution, 6 ml 2 M HNO_3 is added to extract the Mo fraction, which is collected in a Teflon beaker and left to dry on a heating stage. A cation exchange column (Dowex 50WX8^{TM} resin, 200 - 400 mesh) was used to remove residual Fe. The dried Mo fraction is redissolved in 1 ml 0.5 M HCl and 0.1% H_2O_2 solution twice, and collected in a Teflon beaker. The remaining Mo is eluted with 4 ml 0.5 M HCl and 0.1% H_2O_2 solution and collected in the same beaker. Finally, the Mo-bearing solutions were dried and were measured as 0.5 M HNO_3 solution on a Nu Instruments MC-ICP-MS connected to an ESI Apex nebulizer. A measurement usually consists of 4 blocks with 10 cycles each. One standard and three black shale samples were analyzed alternately so as to monitor for drift in instrument sensitivity.

The molybdenum isotope data are reported as defined in previous studies as $\delta^{98/95}Mo_{sample}(‰) = [\ ^{98/95}Mo_{sample}/^{98/95}Mo_{standard}-1] \times 1000$. Throughout the text, sample Mo isotope data are reported as $\delta^{98/95}Mo$ relative to the Bern Laboratory standard solution (Johnson Matthews, 1000 µg/ml (± 0.3%) ICP standard solution) as in Siebert et al. (2003) and McManus et al. (2002).

6.4.3 Iron speciation determination

The iron speciation of both black shales and sulfide ores was determined in the Laboratories of the Geochemistry & Isotope Geochemistry Group at the Leibniz Institute for Baltic Sea Research (IOW) in Warnemünde, Germany. The pool of highly reactive iron (Fe_{HR}) is defined here as the sum of $Fe_P + Fe_D$, where Fe_P is the iron present as pyrite and Fe_D is the still reactive iron (mainly iron oxides and minor contributions from iron-bearing silicates) measured spectrophotometrically in extracts of sediment powders with buffered Na dithionite solution (Canfield, 1989). Sulfur bond to Fe_P was extracted by hot acidic $CrCl_2$ solution (Fossing and Jorgensen, 1989), measured spectrophotometrically according to Cline (1969), and recalculated to Fe considering the stoichiometry of pyrite (Böttcher et al., 2009; Hetzel et al., 2010). The degree of pyritization (DOP) is calculated as DOP = Fe_P/Fe_{HR}. Another redox indicator, Fe_{HR}/Fe_T ratio is also applied, where Fe_T represents the total iron in the sediment (e.g., Shen et al., 2003; Anderson and Raiswell, 2004; Grice et al., 2005).

6.5 Results

The geochemical and Mo isotopic data are presented in Table 6-1, and their stratigraphic trends are shown in Fig. 6-4 and 6-5. All the Mo isotope data used in this study is authigenic $\delta^{98/95}$Mo. The authigenic $\delta^{98/95}$Mo composition was derived by correction for the detrital contribution, assuming an average upper crustal Mo concentration of 1.1 ppm at 15.4 wt.% Al_2O_3 (Rudnick and Gao, 2004), and a corresponding Mo isotopic composition of 0.0 ‰. The detrital Mo concentration is calculated by $Mo_{det} = (Mo_{crust}/Al_{crust}) \times Al_{measured}$. The authigenic Mo concentration is then calculated by $Mo_{auth} = Mo_{tot} - Mo_{det}$, and its isotopic composition is defined by $\delta^{98/95}Mo_{auth} = [(\delta^{98/95}Mo_{tot} \times Mo_{tot} - \delta^{98/95}Mo_{det} \times Mo_{det})/Mo_{auth}]$. The detrital contributions are very minor only for the Mo-rich samples studied. The measured $\delta^{98/95}$Mo values of the samples vary from -1.54 to 1.70 ‰ with external 2 σ reproducibilities from 0.03 to 0.08 ‰. Based upon the $\delta^{98/95}$Mo, iron speciation and trace element data, we divide the Dingtai profile of the Early Cambrian Niutitang Formation into three geochemically distinct intervals (Fig. 6-4 and 6-5).

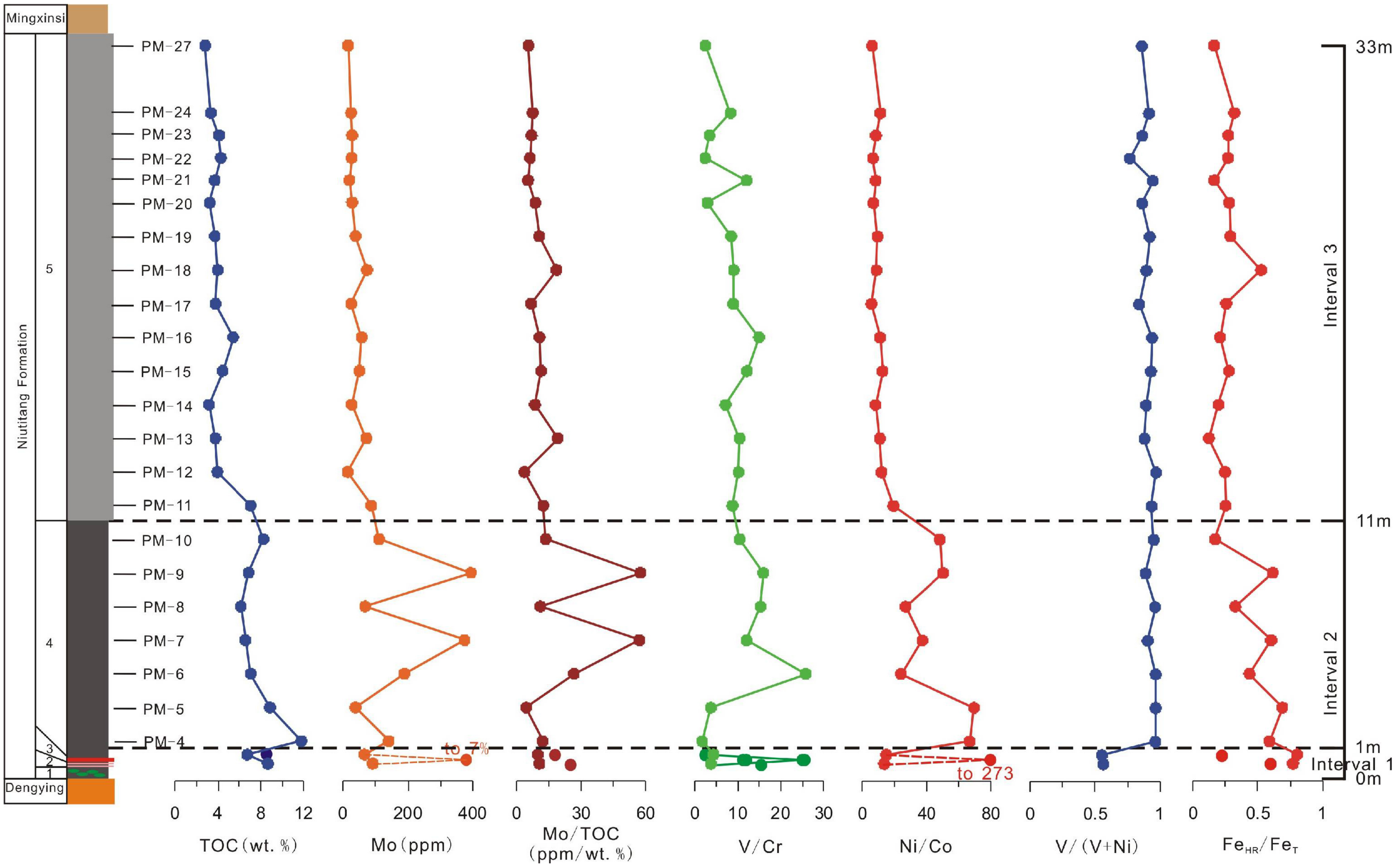
Mingxinsi
Niutitang Formation
5
4
3
2
1
Dengying
PM-27
PM-24
PM-23
PM-22
PM-21
PM-20
PM-19
PM-18
PM-17
PM-16
PM-15
PM-14
PM-13
PM-12
PM-11
PM-10
PM-9
PM-8
PM-7
PM-6
PM-5
PM-4
0 4 8 12
TOC (wt. %)
0 200 400
Mo (ppm)
to 7%
0 30 60
Mo/TOC (ppm/wt. %)
0 10 20 30
V/Cr
0 40 80
Ni/Co
to 273
0 0.5 1
V/(V+Ni)
0 0.5 1
Fe_{HR}/Fe_T
33m
11m
1m
0m
Interval 3
Interval 2
Interval 1

Fig. 6-4: Total organic carbon (TOC), [Mo], Mo/TOC, V/Cr, Ni/Co and V/(V+Ni) data from the Lower Cambrian Dingtai profile and the polymetallic sulfide ore deposits, South China. According to the lithology, the Dingtai profile has been classified into five lithological units. Orange shading represents dolomite; green ellipse represents phosphorite nodules; pink line represents chert interbeds; red shading represents polymetallic Ni-Mo-PGE-Au sulfide ore layer; black shading represents organic-rich black shales; gray shading represents silty black shales; and brown shading represents sandstone. The succession is divided into three intervals on the basis of their geochemical characteristics: 0 to 1 m (Interval 1), 1 to 11 m (Interval 2) and 11 to 32.3 m (Interval 3).

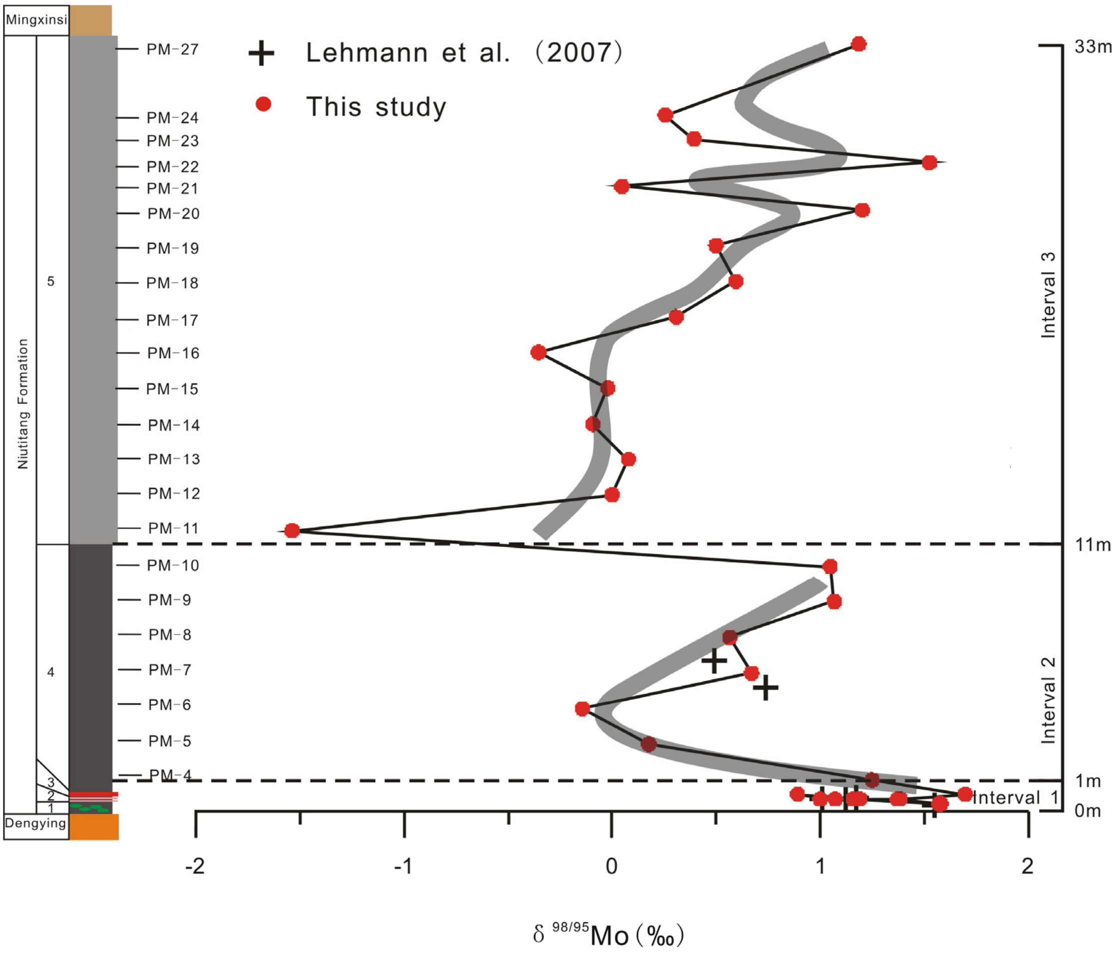

Fig. 6-5: $\delta^{98/95}$Mo values of black shales and polymetallic sulfide ores from the Dingtai profile and the polymetallic sulfide ore deposits. $\delta^{98/95}$Mo data from Lehmann et al. (2007) (black cross symbols) are also displayed for comparison. The external standard $\delta^{98/95}$Mo reproducibility was 0.1‰ (2σ). Division of stratigraphic units is same as in Fig. 6-4.

Interval 1 comprises the first 1 m on top of the Precambrian/Cambrian boundary marked by the unconformity above the dolomite of the Dengying Formation and is corresponding to units 1 to 3 in the Dingtai profile. This interval hosts phosphorite- and chert-bearing black shales and the polymetallic Ni-Mo-PGE-Au sulfide layer followed by the fossil-rich black shale sequence. The samples of interval 1 are from the three polymetallic sulfide ore deposits and consist of six polymetallic sulfide ores, three immediate host rocks (black shale) and one phosphorite sample. All samples are characterized by heavy$\delta^{98/95}$Mo values, high Fe_{HR}/Fe_T ratio, high TOC content and high abundances of redox-sensitive trace elements, such as Mo, V, Ni, Cr, Co and U. The mean $\delta^{98/95}$Mo value of polymetallic sulfide ores from the three stratigraphically equivalent mine sites is 1.20 ± 0.16 ‰ (1 σ, n = 6), slightly lighter than the average $\delta^{98/95}$Mo value of the host black shales of 1.40 ± 0.44 ‰ (1 σ, n = 3) and the underlying phosphorite of 1.57 ± 0.03 ‰ (Table 6-1). The results are consistent with previous findings (Lehmann et al. 2007), who reported $\delta^{98/95}$Mo = 1.06 ± 0.11‰ (n = 5) for the polymetallic sulfide ore from the Huangjiawan mine, which is about 12 km southeast of the Dazhuliushui mine site where we sampled. The three host black shales and one phosphorite are characterized by high DOP values varying from 82 to 97 % (mean: 91.3 ± 6.5 %), and elevated Fe_{HR}/Fe_T ratios varying from 0.2 to 0.8 (mean: 0.6 ± 0.3). TOC contents of the three black shale samples in interval 1 range from 6.74 to 8.65 wt.%, with an average of 7.85 ±0.99 wt.%. The sulfide ore is characterized by extremely high Ni and Mo contents with 4.80 ± 1.49 wt.% Ni and 6.51 ± 0.62 wt.% Mo (n = 6). The black shales from interval 1 are characterized by enrichment of redox-sensitive metals, such as 249 – 332 ppm Ni (mean: 294 ± 42 ppm, 1 σ) and 65.2 – 142 ppm Mo (mean: 99 ± 39 ppm, 1 σ), as well as 310 – 409 ppm V (mean: 346 ± 55 ppm, 1 σ), 85.1 – 116 ppm Cr (mean: 98.0 ± 17 ppm, 1 σ), 18.5 – 32.1 ppm Co (mean 24 ± 7 ppm, 1 σ) and 24.5 – 54.9 ppm U (mean: 37 ± 16 ppm, 1 σ). The Mo/TOC (ppm/wt.%) ratio of the black shales from interval 1 varies from 9.67 to 17.4, with an average of 12.5 ± 10.6. Due to the high Ni contents of the sulfide ores, their Ni/Co and V/(V+Ni) ratios are distinctly different from those of the black shales. Ni/Co and V/Cr ratios of the black shales from interval 1 vary from 9.38 to

14.8 (mean: 12.5 ± 2.81, 1 σ, n = 3) and from 2.67 to 4.40 (mean: 3.60 ± 0.88, 1 σ, n = 3), respectively. The three black shales from interval 1 have a consistent V/(V+Ni) ratio of 0.51 – 0.56 (mean: 0.54 ± 0.03, 1 σ), lower than in the overlying black shales from interval 2 and 3 (Table 6-1).

Interval 2 (1 to 11 m) corresponds to unit 4 of the Dingtai profile. Black shales from this interval are characterized by variable $\delta^{98/95}$Mo values, ranging from -0.14 to 1.26 ‰ (n = 7), with heavy $\delta^{98/95}$Mo composition of 1.26 ± 0.05 ‰ in the lowermost 1.3 m, followed by light/moderate $\delta^{98/95}$Mo composition ranging from -0.14 to 0.67 ‰ (n = 4) at 2.8 to 7.3 m, and then returning to heavy composition of 1.07 ± 0.03 ‰ and 1.06 ± 0.04 ‰ at 8.8 m and 10.3 m (Fig. 6-5). The Fe_T and Fe_{HR} contents vary from 0.40 to 1.25 wt.% (mean: 1.00 ± 0.43 wt.%, 1 σ, n = 7) and from 0.07 to 1.10 (mean: 0.55 ± 0.37 wt.%, 1 σ, n = 7), respectively, much lower than for the black shales from interval 1. The TOC contents of the black shales from interval 2 range from 6.14 to 11.8 wt.% (mean: 7.93 ± 1.94 wt.%, 1 σ, n = 7). Both Fe_T/Fe_{HR} ratios and TOC contents roughly decrease upwards. The V, Cr, Co, U, Ni and Mo contents of the black shales (n=7) from interval 2 are variable, with 1070 – 4400 ppm V (mean: 2550 ± 1620 ppm), 69.9 – 2540 ppm Cr (mean: 608 ± 942 ppm), 1.09 – 5.59 ppm Co (mean: 2.88 ± 1.61 ppm), 18.0 – 28.0 ppm U (mean: 22.8 ± 3.74 ppm), 40.1 – 215 ppm Ni (mean: 123 ± 60.5 ppm) and 38.0 – 394 ppm Mo (mean: 187 ± 143 ppm). The Mo/TOC (ppm/wt.%) ratios of the black shales (n=7) from interval 2 vary from 4.29 to 57.5, with an average of 25.9 ± 22.4. The Ni/Co, V/Cr and V/(V + Ni) ratios range from 23.8 to 69.3 (mean: 46.0 ± 18.0), from 1.68 to 25.8 (mean: 12.1 ± 8.10) and from 0.89 to 0.97 (mean: 0.95 ± 0.03), respectively.

Interval 3 (11 to 32.3 m) is represented by fifteen black shale samples corresponding to unit 5 of the Dingtai profile. This interval is characterized by variable $\delta^{98/95}$Mo values, relatively low TOC contents and low redox-sensitive metal concentrations. The black shale sample at 11.8 m displays an unusual light $\delta^{98/95}$Mo ratio of -1.56 ± 0.04 ‰. From 13.3 to 19.3 m, black shales are characterized by light $\delta^{98/95}$Mo values, ranging from -0.36 to 0.08 ‰ (mean: -0.08 ± 0.17 ‰, 1 σ, n = 5), followed by fluctuating Mo isotope compositions at 20.8 to 32.3 m, with $\delta^{98/95}$Mo values varying from 0.05 to 1.59 ‰ (mean: 0.67 ± 0.51 ‰, 1 σ, n = 9) (Fig. 6-5). The Fe_T and Fe_{HR} contents vary from 0.51 to 2.40 wt.% (mean: 1.70 ± 0.51 wt.%, 1 σ) and from 0.13 to 1.16 wt.% (mean: 0.44 ± 0.25 wt.%, 1 σ), respectively. Fe_{HR}/Fe_T ratios of the black shales from interval 3 range from 0.12 to 0.52 (mean: 0.26 ± 0.10, 1 σ), lower than the black shales from interval 1 and 2. Similarly, TOC contents are lower and vary from 2.79 to 7.06 wt.% (4.03 ± 1.04 wt.%). Black shales from interval 3 (n=15) are less enriched in redox-sensitive elements, with 248 – 2110 ppm V (mean: 970 ± 530 ppm), 102 – 145 ppm Cr (mean: 116 ± 12.8 ppm), 3.11 – 36.2 ppm Co (mean: 11.0 ± 7.96 ppm), 9.35 – 19.3 ppm U (mean: 15.6 ± 3.07 ppm), 36.5 – 203 ppm Ni (mean: 94.5 ± 50.9 ppm) and 13.9 – 86.4 ppm Mo (mean: 38.7 ± 23.1 ppm). The Mo/TOC (ppm/wt.%) ratios of the black shales from interval 3 vary from 3.54 to 18.9 (mean: 9.31 ± 4.52, 1 σ, n = 15), lower than in black shales from interval 1 and 2. Similarly, Ni/Co, V/Cr and V/(V + Ni) ratios (n=15) range from 5.58 to 19.1 (mean: 9.54 ± 3.41), from 2.39 to 15.0 (mean: 8.11 ± 3.82) and from 0.77 to 0.97 (mean: 0.90 ± 0.05), respectively.

6.6 Discussion

6.6.1 Mo isotope variations within the Dingtai profile and the polymetallic sulfide ore deposits

Molybdenum exists in modern seawater primarily as the soluble molybdate species MoO_4^{2-} which behaves conservatively with a long residence time of about 800,000 years (Morford and Emerson, 1999). The marine Mo inventory is dominated by riverine influx from oxidative weathering. Weathering and the transport of Mo into the oceans produces slight Mo isotope fractionation in such a way that the primary (igneous) crustal Mo isotope composition of $\delta^{98/95}$Mo of 0 ‰ is shifted to a range of heavier compositions with an average value of riverine $\delta^{98/95}$Mo of about 0.7 ‰ (Archer and Vance, 2008). The removal of molybdenum from seawater to sediments is accompanied by isotopic fractionation which is controlled by redox conditions (Barling et al., 2001; McManus et al., 2002; Siebert et al., 2003; Arnold et al., 2004). The largest isotope fractionation is observed under oxic conditions by preferential adsorption of light Mo on ferromanganese oxide surfaces with a fractionation factor $\Delta^{98/95}\mathrm{Mo}_{\mathrm{aqueous\text{-}solid}}$ of up to 3.0 ‰ (Barling et al., 2001; Goldberg et al., 2009), while euxinic conditions with $[H_2S]_{aq} > 11$ µM produce quantitative Mo removal (Helz et al., 1996) with no or very small isotopic fractionation (Siebert et al., 2003; Arnold et al., 2004; Nägler et al., submitted) so that sediments deposited under euxinic conditions and sufficiently high sulfide concentrations may directly reflect the coeval seawater Mo isotope composition. Under suboxic and anoxic conditions with $[H_2S]_{aq} < 11$ µM, Mo isotope fractionation is observed over a wide range, with $\delta^{98/95}$Mo from -0.5 to 1.6 ‰ in such sediments (Barling et al., 2001; Siebert et al., 2006). This broad range of isotope fractionation seems to depend on the balance between ferromanganese oxide adsorption processes and diagenetic suboxic/anoxic Mo fixation by processes of MoO_4^{2-} to MoS_4^{2-} conversion, which involve thiomolybdate intermediate complexes $MoO_xS_{4-x}^{2-}$ for which $\Delta^{98/95}\mathrm{Mo}_{\mathrm{aqueous\text{-}solid}}$ of about 0.7 ‰ has been observed (Poulson et al., 2006).

The black shale sequence of the Dingtai profile has a remarkably strong variability in $\delta^{98/95}$Mo isotope composition of -1.56 to 1.71 ‰ over a few meters of stratigraphic thickness only. Several mechanisms may contribute to this variability, including 1) oxic Mo isotope fractionation by adsorption to ferromanganese components and suboxic diagenetic processes, 2) influx of Mo from low-temperature hydrothermal systems in which Mo may have been fractionated by precipitation of hydrothermal Fe-Mn oxides (Ryb et al., 2009), and 3) influx of riverine Mo in restricted ocean basins not fully connected to the global ocean circulation.

Overprint by fractionated Mo from low-temperature hydrothermal systems onto sediments could result in wide variability of Mo isotope composition. However, microscopic observation gives no indications for hydrothermal overprint. Although stockworks of hydrothermal quartz veins have been identified in sulfide ores and below the black shales (Lott et al., 1999), $\delta^{98/95}$Mo values of the sulfide ores and their immediate black shale host rocks have consistently heavy values, heavier than available Mo isotope data of modern low-temperature hydrothermal fluids (McManus et al., 2002). Moreover, Re-Os geochronology of the sulfide ore and the host black shale reveals no post-depositional disturbances of the Re-Os system (Jiang et al., 2007; Xu et al., 2011), indicating that there was no post-depositional Mo enrichment, which would have affected the distribution of Re (Kendall et al., 2009). Therefore, a hydrothermal fluid-derived Mo contribution to the Mo isotopic variability of the Dingtai profile and the three sulfide ore deposits is unlikely.

Another process for the remarkable variability of $\delta^{98/95}$Mo composition in the black shales and the polymetallic sulfide ores could be continental input into restricted basins via riverine transport. Hannah et al. (2007) reported variable Mo isotopic compositions of molybdenite from a variety of settings and ages. Light $\delta^{98/95}$Mo values (~ 0‰) have been reported for igneous rocks and clastic sediments (Barling et al., 2001; Siebert et al., 2003, 2005). Major modern rivers have an average $\delta^{98/95}$Mo value of ~ 0.7 ‰, but with a wide range of isotopic compositions from 0.2 to 2.3 ‰ (Archer and Vance, 2008). The variability of $\delta^{98/95}$Mo composition of the Dingtai profile could result from a partly closed ocean basin with periodic replenishment. When the basin is freely connected to the open ocean, the Mo isotopic composition of the marine sediments would reflect the open ocean Mo signature. However, under euxinic conditions and in a restricted basin situation, Mo deposition may be so strong that the metal inventory of the basin becomes completely depleted in ocean-derived Mo, and Mo influx may become dominated by continental input. The Mo isotopic composition in euxinic sediments is then representing the continental input with light $\delta^{98/95}$Mo values, until replenishment by new seawater with heavy Mo restores the normal open-system situation. Evidence of a restricted basinal sedimentary environment comes from a geochemical comparison of geological profiles. The Mo contents of black shales from the Dingtai profile and the polymetallic sulfide layer are generally within the thousands to hundreds ppm range (Table 6-1), similar to black shales of the Jiumenchong Formation (Niutitang Formation equivalent) from the Songtao profile investigated by Guo et al. (2007), who argued that the Songtao profile represents a restricted basinal environment. In contrast, Mo contents of black shales from the Shatan profile of the Guojiaba Formation (Guo et al., 2007) and the Kunyang profile (own unpublished data) of the Meishucun Formation, both of which are Niutitang Formation equivalents, are <10 ppm, significantly lower than in the Dingtai profile, indicating that the Early Cambrian depositional environments on the Yangtze Platform were very variable, probably due to karstic paleotopography of the underlying dolomite of the Neoproterozoic Dengying Formation. The discontinuous occurrence of the polymetallic Ni-Mo-PGE-Au sulfide ore layer, reflecting locally extreme depositional environments (Xu et al., submitted), supports the restricted sedimentary basin model.

Some $\delta^{98/95}$Mo values of the polymetallic sulfide ores are slightly lighter than those of the host black shales. This can be interpreted as two-source model for the ore formation, which consisting of both euxinic in-situ precipitation and re-deposition of sulfide clasts under suboxic condition (Xu et al., submitted). Nevertheless, relatively consistent $\delta^{98/95}$Mo values of the polymetallic sulfide ores suggest that the Mo-aggregates formed under suboxic conditions represent only a small portion of the sulfide ore layer and re-deposition processes only occurred at a small scale. Alternatively, the moderate variation in Mo isotope composition in the sulfide mineralization could also derived from a moderate restricted basin situation, as indicated by sulfur isotope zoning in some sulfide aggregates (Horan et al., 1994).

6.6.2 Early Cambrian paleo-environmental reconstruction based on the Dingtai profile

The "deep anoxic basin" model for the formation of black shales has been popular for many years, However, black shales can form in a wide range of depositional conditions and Pan et al. (2004) and Goldberg et al. (2007) suggest that the Early Cambrian black shale sequence in South China developed in a shallow sea which progressively became more oxic. When looking into the Dingtai profile and the three polymetallic Ni-Mo-PGE-Au mine sites, three intervals of seawater redox conditions can be distinguished according to the patterns of Mo isotopes and redox-sensitive trace elements (Fig. 6-4 and 6-5).

In the interval 1 of the Dingtai profile which hosts the polymetallic Ni-Mo-PGE-Au sulfide ore layer, black shales are represented by heavy $\delta^{98/95}$Mo values (1.40 ± 0.44 ‰). The average $\delta^{98/95}$Mo value of 1.20 ± 0.16 ‰ of stratigraphically equivalent sulfide ores is generally consistent with data reported by Lehmann et al. (2007), who reported $\delta^{98/95}$Mo = 1.06 ± 0.16 ‰ of sulfide ore from Huangjiawan mine site, which is 12 km southeast of the Dazhuliushui mine site. Such heavy values are also observed in Early Cambrian euxinic sediments of the Ara Group in Oman (Wille et al., 2008). We infer that the redox conditions of the Early Cambrian seawater in South China during interval 1 were euxinic and that the Yangtze Platform was relatively well connected to the open ocean. The black shale sample with the heaviest $\delta^{98/95}$Mo value of 1.71 ± 0.05 ‰ would represent the Mo isotope composition closest to the coeval Early Cambrian global seawater. $\delta^{98/95}$Mo values of the polymetallic sulfide ores slightly lower than the immediate black shales indicate that Mo in the sulfide ores is either not solely formed by euxinic in-situ precipitation, but also by short-distance re-deposition of sulfide clasts formed under suboxic conditions (Kribek et al., 2007; Xu et al., submitted) or in a closed-basin situation (i.e. local continental input). The two-source model, i.e. open-ocean molybdenum plus local continental input, for the polymetallic sulfide ore is further supported by the textural observation of coexistence of both in-situ precipitated laminated ore and re-deposited rip-up clasts (Fig. 6-3 E).

Black shales from interval 2 and 3 are characterized by highly variable $\delta^{98/95}$Mo values. One reason may be the changing redox conditions. As discussed above, suboxic and anoxic conditions can lead to variable degree of Mo isotope fraction by the process of conversion from MoO_4^{2-} to MoS_4^{2-}. Such a process, however, would be minor compared to the effect caused by the formation of periodically restricted basins. The lowermost interval 2 is characterized by heavy $\delta^{98/95}$Mo values (1.26 ± 0.05 ‰), generally in the same range as in interval 1, indicating that the basin was relatively well connected to the open ocean. However, the sharp decrease in $\delta^{98/95}$Mo down to -0.14 ± 0.03 ‰ at 4.3 m is likely to reflect major Mo influx from continental material. After that episode, the restricted basins once again connected to the open ocean, leading to Mo components dominantly from the open sea. The heavy $\delta^{98/95}$Mo values in the uppermost interval 2 (1.07 ± 0.03 ‰ and 1.06 ± 0.04 ‰ at 8.8 m and 10.3 m, respectively) indicate that the water column during this period is still euxinc. The extremely light $\delta^{98/95}$Mo value of -1.54‰ at 11.8 m in the lowermost interval 3 is unusual, and may represent sample heterogeneity or another currently unknown process. The lower part of black shale interval 3 is generally characterized by light $\delta^{98/95}$Mo values, with fluctuant $\delta^{98/95}$Mo values upwards indicating that terrigenous Mo influx was dominant during the early period of interval 3. The periodical restricted basin-situation could be caused by transgressive or regressive processes in karstic districts. Although some black shales from the upper part of interval 3 are characterized by heavy $\delta^{98/95}$Mo values, they are generally lower than black shales from interval 1, consistent with the conclusion that the ocean redox conditions evolved towards more oxic from interval 1 to 3. Further evidence comes from the iron speciation data. Degree of pyritization (DOP) is commonly applied to evaluate paleodepositional redox conditions. The DOP is controlled by degree of sulfate reduction and pyrite formation in marine sediments. In contrast to the oxic bottom water, where pyrite is formed only during diagenesis when anoxic conditions develop in the sediments, under euxinic conditions pyrite can form both in the water column and in the sediments. Sediments deposited under euxinic conditions tend to have a relatively high concentration of iron that was originally reactive towards dissolved sulfide and is now almost entirely converted to pyrite. Therefore, DOP in euxinic conditions would be higher than in oxic or suboxic conditions. High DOP (> 75%) probably can be related to quantitative conversion of molybdate to thiomolybdate in bottom waters with $[H_2S]_{aq} > 11$ μM (Arnold et al., 2004). Values of DOP below a value of about 0.45 are characteristic for sediments deposited from oxic bottom water. The combined application of DOP and the ratio of highly reactive iron to total iron content (Fe_{HR}/Fe_T) have been proven effective indicators of euxinic depositional conditions for ancient black shales (Canfield et al., 1989, 1996; Raiswell and Canfield, 1998; Shen et al., 2002, 2003; Anderson and Raiswell, 2004; Arnold et al., 2004; Scott et al., 2008). A Fe_{HR}/Fe_T ratio above 0.4 is indicative for euxinic environments. The combined indicators of DOP > 0.75 and $Fe_{HR}/Fe_T > 0.4$ strongly indicate that the depositional environment is euxinic.

The black shales samples from interval 1 are characterized by high DOP values (91 ± 6 % on average) and high Fe_{HR}/Fe_T ratios (0.6 ± 0.3), suggesting that the Early Cambrian seawater in South China during interval 1 was indeed euxinic with elevated dissolved sulfide concentrations (Fig. 6-6). The Fe_{HR}/Fe_T ratio of black shales from interval 2 and 3 generally decreases upwards, indicating that the seawater became progressively more oxidized. However, most of the black shale samples from interval 2 have $Fe_{HR}/Fe_T > 0.4$ (except for 0.3 and 0.2 at 7.3 m and 10.3 m, respectively), indicating that the black shales from interval 2 deposited under largely euxinic conditions, but less euxinic than in interval 1. Black shales from interval 3 have $Fe_{HR}/Fe_T < 0.4$ (except for 0.52 at 22.3 m), consistent with suboxic conditions (Fig. 6-6). It should be noted, however, that Fe_{HR}/Fe_T ratios below 0.4 do not completely exclude sediment deposition in a euxinic environment but may also indicate changes in the sources or depositional setting (Andersson and Raiswell, 2004).

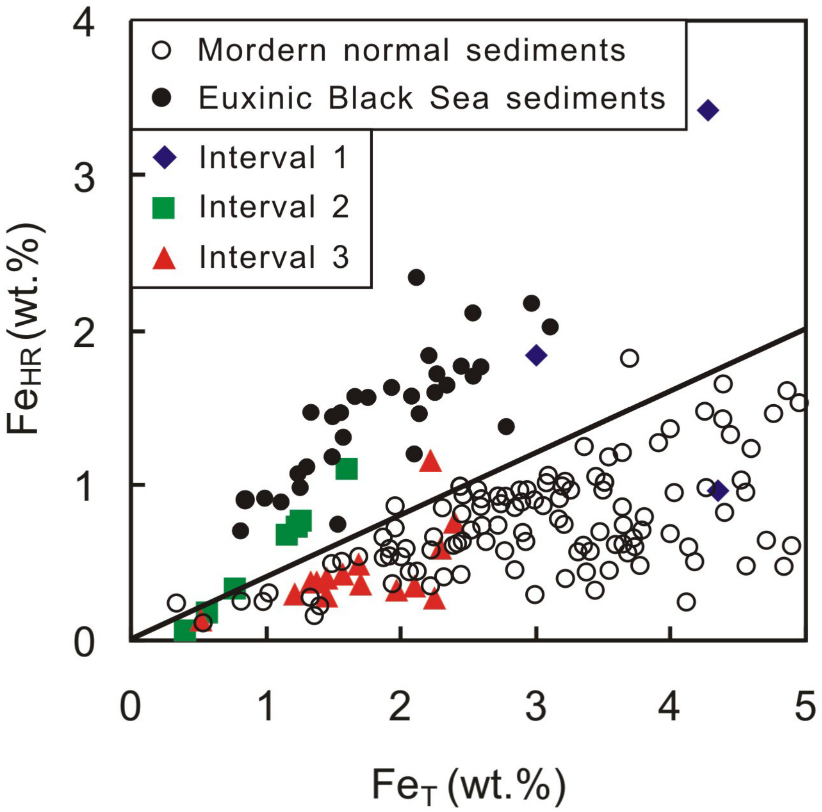

Fig. 6-6: Variations in the content of highly reactive Fe (Fe_{HR}) with total Fe (Fe_T) of black shales from the Dingtai profile and the polymetallic sulfide ore deposits. The reference lines (Fe_{HR}/Fe_T = 0.4) is according to Raiswell and Canfield (1998), indicating samples above the reference line are deposited under euxinic conditions. Fe_{HR}/Fe_T values below 0.4 are found in sediments below oxic bottom waters, where pyrite precipitates in the sediments. Data for modern marine sediments and euxinic Black Sea sediments for comparison are from Raiswell and Canfield (1998) and Shen et al. (2002), respectively.

Mo concentration may also be associated with adsorption to organic matter (Rimmer, 2004; Scott et al., 2008). A crossplot for Mo and TOC (Fig. 6-7 A) shows a combination of linear correlation and scatter for the Dingtai profile and the three mine sites. There is a good correlation of TOC and Mo content up to concentration levels of about 100 ppm Mo. Higher Mo contents do not correlate with TOC as these are then controlled by sulfide precipitation. The elevated average Mo/TOC (ppm/wt.%) ratio of intervals 1 and 2 is around 26, similar with that of the Cariaco Basin and the Black Sea sediments of 26 and 28, respectively, which are the two largest present-day euxinic basins (Lyons et al., 2003; Algeo and Lyons, 2006). In contrast, the average Mo/TOC (ppm/wt.%) ratio of interval 3 is around 9, indicating that the Mo content in the black shales from interval 3 was controlled by adsorption to TOC, and not by sulfide precipitation. The relatively low Mo concentrations and TOC values may reflect that accumulation were limited for both elements under suboxic conditions. A similar trend is seen in the U versus TOC plot (Fig. 6-7 B). U enrichment is minor in oxic-suboxic environments, where U is present mainly as soluble U^{6+} in the form of chemically unreactive uranyl carbonate complexes ($(UO_2(CO_3)^{4-})$. Under euxinic conditions, U is reduced to U^{4+} as the insoluble uranyl ion UO^{2+} or less soluble uranium fluoride complexes (Algeo and Lyons, 2006), leading to strong enrichment under reducing conditions. Execpt for a phosphorite sample with high U content (517 ppm) which is omitted in the U – TOC crossplot, because of the crystallochemical control of uranium by phosphorus minerals, Figure 7 B clearly shows that the contents of both components decrease from interval 1 and 2 to interval 3, suggesting that the redox conditions evolved from euxinic to suboxic.

Trace elements and their ratios, including Ni/Co, V/Cr and V/(V+Ni), have been widely used as indicators for paleoredox conditions (e.g. Dill, 1986; Hatch and Leventhal, 1992; Jones and Manning, 1994; Rimmer, 2004). Jones and Manning (1994) suggested that Ni/Co <5 indicates oxic conditions, 5–7 dysoxic, and >7 suboxic to anoxic conditions. For the V/Cr, ratios <2 indicates oxic conditions, 2–4.2 dysoxic conditions, and >4.2 suboxic to anoxic conditions. Hatch and Leventhal (1992) suggested that V/(V+Ni) ratios >0.84 are typical of euxinic, 0.54–0.84 anoxic, and 0.46–0.60 dysoxic conditions. Although the classification of redox conditions varies in the literature, the basic fact remains that Ni/Co, V/Cr and V/(V+Ni) ratios decrease with increasing oxygenation level in water columns. These trends are governed by geochemical properties of the redox-sensitive elements, i.e. the formation of insoluble sulfides (Ni, Co), or little soluble reduced species (V^{5+} to V^{4+} to V^{3+}, Cr^{6+} to Cr^{3+}). The three discrimination plots of Fig. 6-8 indicate the largely euxinic situation for the samples studied, with the black shale samples of interval 3 straddling the limit to suboxic conditions.

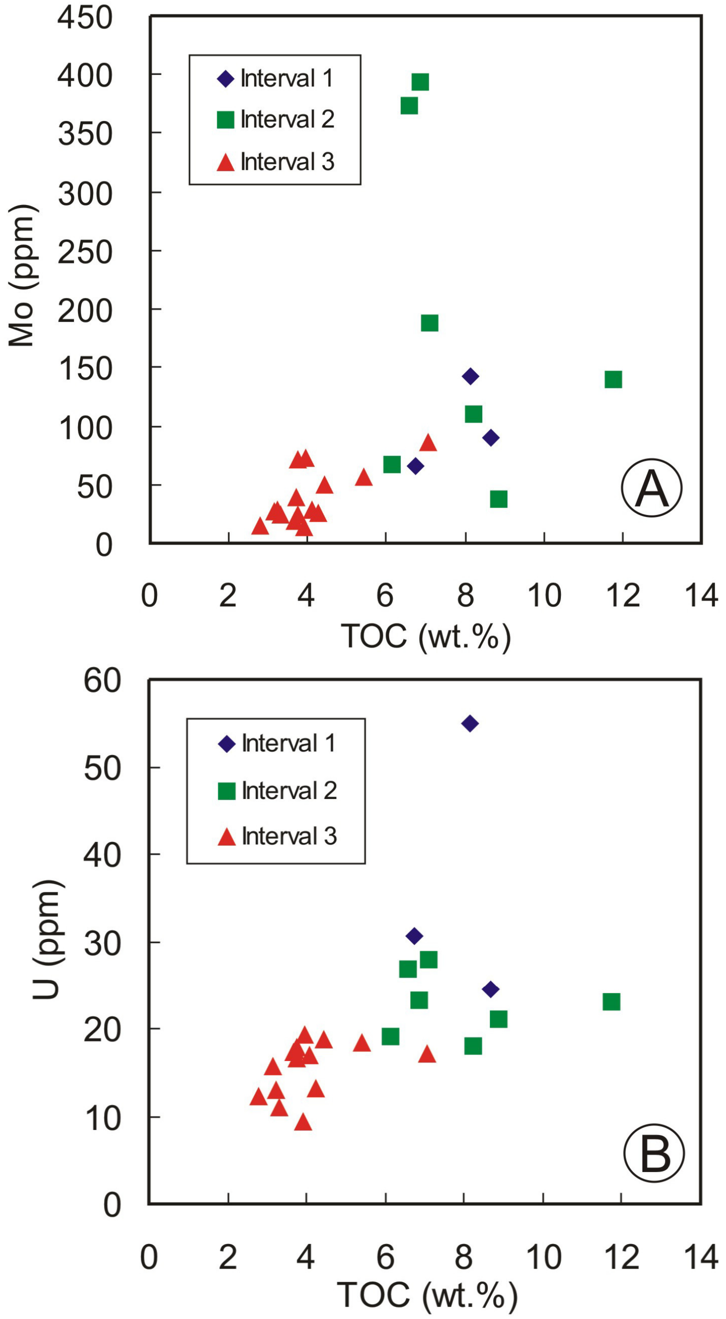

Fig. 6-7: Crossplots of [Mo] (ppm) and [U] (ppm) with total organic carbon (wt.%) showing decreasing contents from the interval 1 and 2 to interval 3.

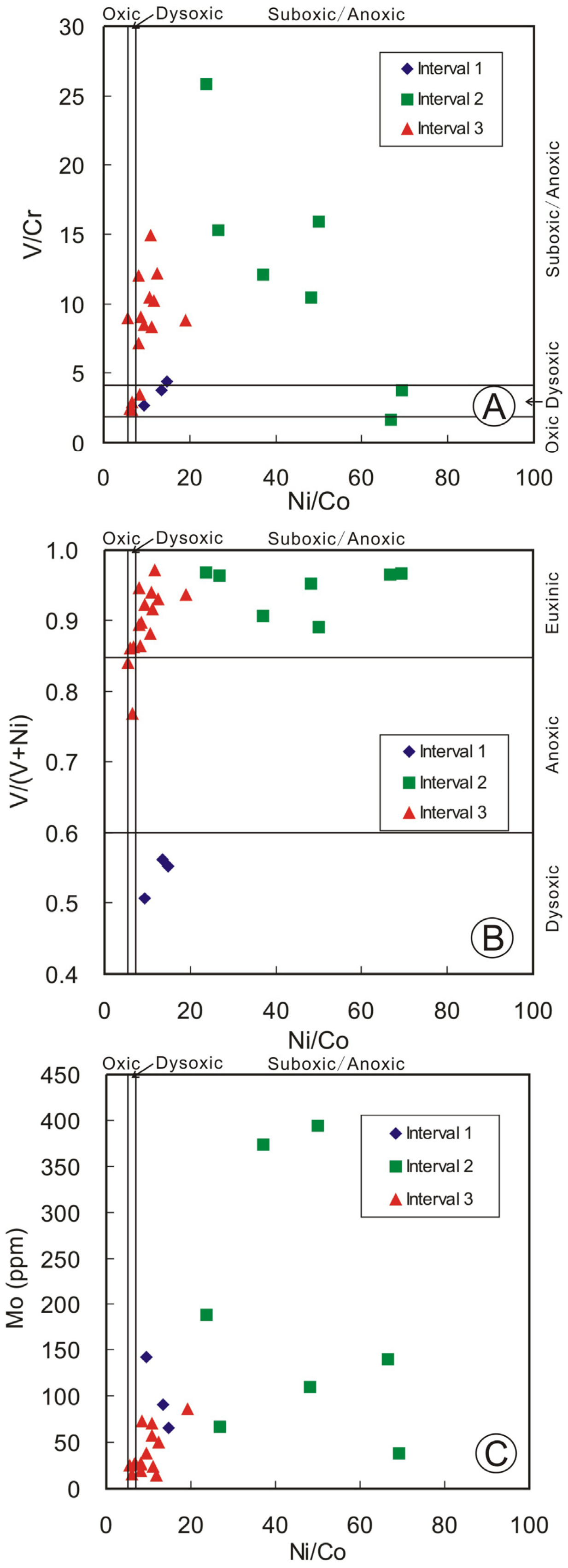

Fig. 6-8: Crossplots of trace element ratios used as paleoredox proxies. **A:** V/Cr vs. Ni/Co, **B:** V/(V+Ni) vs. Ni/Co, and **C:** Mo vs. Ni/Co.

6.6.3 Mo isotope implications for the oxidation state of the atmosphere

Mo isotope fractionation pattern have been used to reconstruct the oxidation state of the Earth's atmosphere and oceans (e.g. Siebert et al., 2005; Wille et al., 2007; Pearce et al., 2008; Wen et al., 2009; Kendall et al., 2010). Holland (2006) summarized the oxygenation state of the atmosphere and oceans, and classified Earth history into five stages. During stage 1 (>2.45 Ga) the atmosphere and oceans were largely or entirely anoxic. During stage 2 (2.45–1.85 Ga) atmospheric oxygen levels rose to 0.02 – 0.04 atm. Shallow oceans became mildly oxygenated, while the deep oceans continued to be anoxic. During stage 3 (1.85–0.85 Ga) the atmosphere and deep oceans were mildly oxygenated. Oxygenation levels continually rose during stage 4 (0.85-0.54 Ga), with oxygen in the atmosphere reaching up to 0.2 atm, and anoxic basins in deep oceans. Atmospheric oxygen levels during stage 5 (0.54 Ga–present) probably rose to a maximum during the Carboniferous. The shallow oceans are oxygenated, while the oxygenation state of the deep oceans fluctuates on geologically short periods. There are two main inputs of Mo into the oceans, i.e. chemical weathering of the continental crust (~90%) and low-temperature hydrothermal influx (~10%) (McManus et al., 2002). As discussed above, in euxinic environments, the interaction of Mo with H_2S results in particle reactive thiomolybdates when $[H_2S]_{aq}$ concentration exceeds ~ 11 μM, resulting in quantitative removal of Mo to euxinic sediments. In this case, no Mo fractionation between seawater and euxinic sediments occurs. In suboxic environments with $[H_2S]_{aq}$ concentration below 11 μM, Mo scavenging is incomplete, resulting in variable Mo fractionation within sediments. Therefore, the $\delta^{98/95}$Mo value of sediments cannot be heavier than that of coeval seawater. Mo components stored under euxinic conditions reflect coeval seawater and are useful as paleoredox indictor, whereas under suboxic conditions, the maximum $\delta^{98/95}$Mo values should reflect the lower limit of the Mo seawater isotopic signature.

Table 6-2

Mo isotopic composition of reducing sediments in Earth history

Age	Sample amount	Mo(ppm)$_{avg.}$	Mo$_{max}$	Mo$_{min}$	$\delta^{98/95}$Mo (‰)$_{avg.}$	2 σ	$\delta^{98/95}$Mo$_{max}$	$\delta^{98/95}$Mo$_{min}$	References
Phanerozoic									
Holocene[#]	11	41.1	67.7	25.8	1.94	0.04	2.46	0.36	Barling et al., 2001; Neubert et al., 2008
Juraasic	54	10.8	43.0	3.32	1.34	0.04	2.14	0.81	Pearce et al., 2008; Zhou et al., 2009
Devonian	15	92.5	394	1.00	1.44	0.09	1.96	0.85	Gordon et al., 2009; Zhou et al., 2009
Cambrian*	53	106	394	6.20	1.05	0.04	2.10	-0.47	Lehmann et al., 2007; Wille et al., 2008; Wen et al., 2009; this study
Proterozoic									
~1400 Ma	11	70.7	119	11.0	0.93	0.10	1.13	0.47	Arnold et al., 2004; Kendall et al., 2009
~1700 Ma	11	52.4	58.0	41.0	0.78	0.10	1.11	0.38	Arnold et al., 2004; Kendall et al., 2009
Archean									
2.45-2.15 Ga	14	1.10	3.72	0.16	0.04	0.18	0.61	-0.34	Siebert et al., 2005; Wille et al., 2007
2.64-2.5 Ga	53	2.59	8.32	0.27	0.58	0.05	1.72	-0.27	Wille et al., 2007
2.7 Ga	7	2.29	6.01	0.61	0.55	0.12	0.89	0.22	Siebert et al., 2005
3.25-3.12 Ga	24	1.62	3.21	0.75	0.20	0.08	0.70	-0.21	Siebert et al., 2005; Wille et al., 2007

* Extremely high Mo contents of Early Cambrian sulfide ore (Lehmann et al. (2007) and this study) are exclued for statistics.

[#] Mordern sediments below 400 m water depth from the Black Sea are cited as sediments deposited under euxinic conditions.

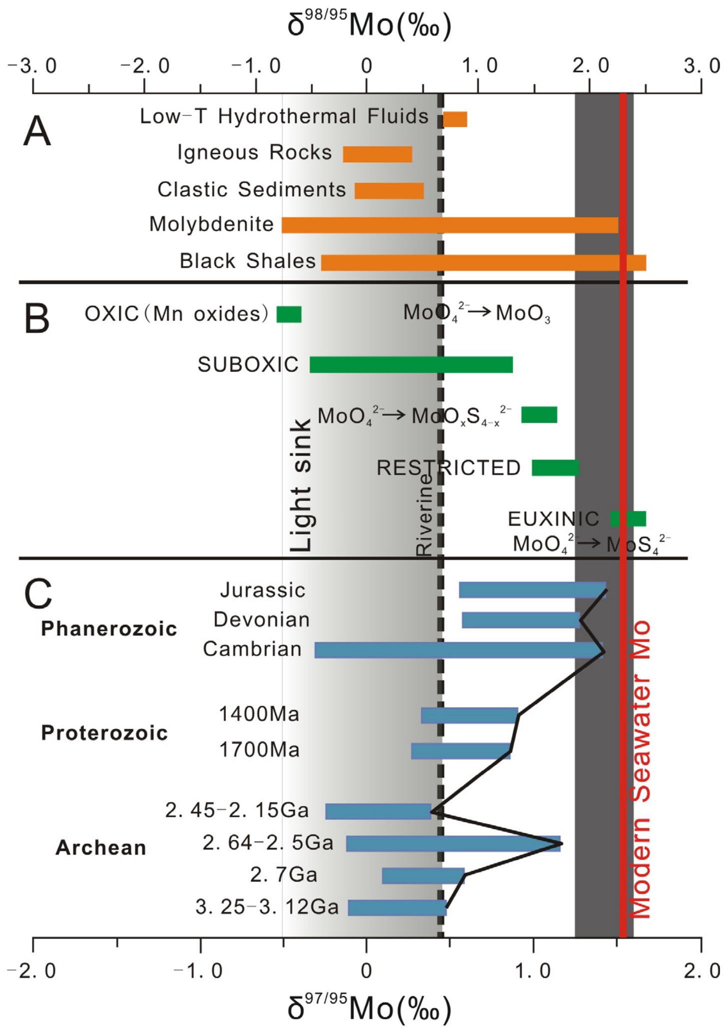

Fig. 6-9: Molybdenum isotope composition of present-day seawater, sources and sinks, and variations of reducing sediment in Earth history. Data sources: Low-temperature hydrothermal fluids: McManus et al. (2002); Igneous rocks, Clastic sediments, molybdenites and black shales: Barling et al. (2001), Siebert et al. (2003, 2005), Arnold et al. (2004), Nägler et al. (2005), Pietruszka et al. (2006), Malinovsky et al. (2007), Hannah et al. (2007), Pearce et al. (2008) and Kendall et al. (2009); Rivers: Archer and Vance (2008); Mn oxides: Barling et al. (2001) and Siebert et al. (2003); Suboxic sediments: Siebert et al. (2006); Restricted basin sediments: Barling et al. (2001), Arnold et al. (2004) and Nägler et al. (2005); Euxinic sediments: Barling et al. (2001), Arnold et al. (2004) and Neubert et al. (2008); Archean reducing sediments: 3.25 - 3.12 Ga: Siebert et al. (2005) and Wille et al. (2007); 2.7 Ga: Siebert et al. (2005); 2.64 - 2.5 Ga: Wille et al. (2007); 2.45 - 2.15 Ga: Siebert et al. (2005) and Wille et al. (2007); Proterozoic reducing sediments: ~ 1700 Ma: Arnold et al. (2004) and Kendall et al. (2009); ~ 1400 Ma: Arnold et al. (2004) and Kendall et al. (2009); Phanerozoic reducing sediments: Cambrian: Lehmann et al. (2007), Wille et al. (2008), Wen et al. (2009) and this study; Devonian: Zhou et al. (2009) and Gordon et al. (2009); Jurassic: Pearce et al. (2008) and Zhou et al. (2009).

Table 6-2 and Fig. 6-9 display a compilation of the available Mo isotope data of black shales from Archean to modern times. Siebert et al. (2005) reported $\delta^{98/95}$Mo values of black shales from the Fig Tree Group and Moodies Group (3.25 – 3.15 Ga), which are characterized by light Mo isotope values with a 0.59 ‰ maximum (0.16 ‰ on average). By contrast, the Belingwe Greenstone belt (2.7 Ga) black shale samples are relatively heavy, with a maximum $\delta^{98/95}$Mo value of 0.89 ‰ (0.55 ‰ on average) (Siebert et al., 2005). By joint application of PGE, Re-Os and Mo isotope data, Siebert et al (2005) concluded that first oxidizing conditions occurred at the late Archean. Further work was carried out by Wille et al. (2007), who reported Mo isotope characteristics of the Ghaap Group (2.64 – 2.5 Ga), Pretoria Group (2.45 – 2.15 Ga), and Fig Tree Group (3.23 Ga). Although variable $\delta^{98/95}$Mo values (from -0.2 to 1.75 ‰) were observed in the Ghaap Group, increased Mo abundances and isotopic fractionation in comparison to the continental crust indicate that during the 2.64–2.5 Ga interval the oxygenation level in the weathering and marine environments became high enough to mobilize Mo. This conclusion is in agreement with Anbar et al. (2007), who argued that a whiff of oxygen occurred before the Great Oxidation Event (GOE, 2.45 to 2.22 Ga). Compared to the generally anoxic conditions during the Archean, Mesoproterozoic black shales are characterized by relatively heavy $\delta^{98/95}$Mo values. Black shales from the Wollogorang Formation (~1700 Ma) and Velkerri Formation (~1400 Ma) have maximum $\delta^{98/95}$Mo values of 1.11 ‰ (0.78 ‰ on average) and 1.13 ‰ (0.93 ‰ on average), respectively (Arnold et al., 2004; Kendall et al., 2009). This magnitude is in between $\delta^{98/95}$Mo values of Archean and present-day euxinic sediments, indicating that the Middle Proterozoic seawater oxygenation level was slightly increased compared to the Archean, but still lower then present-day. During the Phanerozoic, atmospheric and hydrospheric conditions changed dramatically. Large amounts of Mo isotope data are available for the Early Cambrian, Devonian and Jurassic intervals. However, only a few and variable $\delta^{98/95}$Mo values have been observed for Ordovician, Silurian, Carboniferous, Permian and Triassic sediments (Zhou et al., 2009). The samples analyzed by Zhou et al. (2009) are largely clastic sediments, which formed under oxic or suboxic conditions, and therefore cannot represent coeval seawater Mo isotope composition. The $\delta^{98/95}$Mo values measured for the Early Cambrian black shales in this study and from Lehmann et al. (2007) are highly variable. However, euxinic condition of interval 1 of the Dingtai profile have been identified to represent the open ocean system, with the heaviest $\delta^{98/95}$Mo of 1.71 ‰ from black shale above the polymetallic sulfide ore layer. This Mo isotope ratio is higher than that of the Mesoproterozoic, but still lower than present-day seawater, indicating that the atmospheric oxygen level in the Early Cambrian was higher than in the Proterozoic, but lower than in the present-day atmosphere. Black shales in the euxinic Oatka Formation of Devonian age have small scatter of heavy $\delta^{98/95}$Mo values, with a maximum of 1.96 ‰ (1.71 ‰ on average) (Grodon et al., 2009). The Early Jurassic Whitby Mudstone Formation displays $\delta^{98/95}$Mo values of euxinic intervals which are consistently heavy, with a maximum of 2.14‰ (1.34‰ on average) (Pearce et al., 2008). Although the $\delta^{98/95}$Mo values of Phanerozoic black shales are fluctuant, all of them are characterized by relatively heavy Mo isotopes, although lower than present-day euxinic sediments (2.3 ‰).

6.7 Conclusions

1) From the results of a multi-proxy approach, combining Mo isotopes, iron speciation and redox-sensitive trace elements, we conclude that the depositional environment of the Early Cambrian black shale sequence on the Yangtze Platform was deposited under conditions of a periodically restricted basin. The lowermost black shale, including a synsedimentary polymetallic sulfide layer, represents euxinic depositional conditions in a mainly open ocean situation, followed by euxinic deposition in a periodically strongly restricted basin, grading upwards into an environment of suboxic marine deposition. The black shale sequence has an astonishingly wide variation in Mo isotope composition which results both from variable euxinic/suboxic depositional conditions, and, more importantly, from

continental Mo input during periods of a restricted basin situation.

2) The compilation of Mo isotope data on reducing sediments over Earth history indicates that the Mo stable isotope system is useful as a geochemical proxy to trace global redox change. Phanerozoic black shales document a dramatic increase in oxidative Mo isotope fractionation compared to the end-Archean and mid-Proterozoic and suggest significant expansion of marine suboxic/oxic sedimentation. The relatively low $\delta^{98/95}$Mo values of Early Cambrian euxinic black shales on the Yangtze Platform indicate more widespread euxinic marine environments during the Early Cambrian than present-day.

6.8 Acknowledgments

This research is jointly funded by Deutsche Forschungsgemeinschaft (LE578/32-1), Chinese Geological Survey Program (No. 1212010634001), National Basic Research Program of China (No. 2007CB411405) and Chinese Scholarship Council. We thank Dr. Zhang Ying from Institute of Geochemistry, Chinese Academy of Sciences, for assistance during the field work, and R. Rosenberg (IOW) for lab assistance.

6.9 References

Algeo, T.J., Lyons, T.W., 2006. Mo-total organic carbon covariation in modern anoxic marine environments: Implications for analysis of paleoredox and paleohydrographic conditions. Paleoceanography 21, PA1016.

Algeo, T.J., Maynard, J.B., 2004. Trace-element behavior and redox facies in core shales of Upper Pennsylvanian Kansas-type cyclothems. Chemical Geology 206,

289-318.

Anbar, A.D., Duan, Y., Lyons, T.W., Arnold, G.L., Kendall, B., Creaser, R.A., Kaufman, A.J., Gordon, G.W., Scott, C., Garvin, J., Buick, R., 2007. A whiff of oxygen before the Great Oxidation Event? Science 317, 1903-1906.

Anbar, A.D., Gordon, G.W., 2008. Redox renaissance. Geology 36, 271-272.

Anderson, T.F., Raiswell, R., 2004. Sources and mechanisms for the enrichment of highly reactive iron in euxinic Black Sea sediments. American Journal of Science 304, 203-233.

Archer C, Vance D, 2008. The isotopic signature of the global riverine molybdenum flux and anoxia in the ancient oceans. Nature Geoscience 1, 597-600.

Arnold, G.L., Anbar, A.D., Barling, J., Lyons, T.W., 2004. Molybdenum isotope evidence for widespread anoxia in mid-proterozoic oceans. Science 304, 87-90.

Balaram, V., Anjaiah, K.V., Reddy, M.R.P., 1995. Comparative study on the trace and rare earth element analysis of an Indian polymetallic nodule reference sample by inductively coupled plasma atomic emission spectrometry and inductively coupled plasma mass spectrometry. Analyst 120, 1401-1406.

Banerjee, D.M., Schidlowski, M., Siebert, F., Brasier, M.D., 1997. Geochemical changes across the Proterozoic-Cambrian transition in the Durmala phosphorite mine section, Mussoorie hills, Garhwal Himalaya, India. Palaeogeography Palaeoclimatology Palaeoecology 132, 183-194.

Barfod, G.H., Albarède, F., Knoll, A.H., Xiao, S.H., Telouk, P., Frei, R., Baker, J., 2002. New Lu-Hf and Pb-Pb age constraints on the earliest animal fossils. Earth and Planetary Science Letters 201, 203-212.

Barling, J., Arnold, G.L., Anbar, A.D., 2001. Natural mass-dependent variations in the isotopic composition of molybdenum. Earth and Planetary Science Letters 193, 447-457.

Böttcher, M.E., Hetzel, A., Brumsack, H.J., Schipper, A., 2006. Sulfur-iron-carbon geochemistry in sediments of the Demerara Rise. In Mosher, D.C., Erbacher, J., and Malone, M.J. (Eds.), Proc. ODP, Sci. Results, 207: College Station, TX (Ocean Drilling Program), 1–23.

Brasier, M.D., 1992. Background to the Cambrian Explosion. Journal of the Geological Society 149, 585-587.

Calvert, S.E., Pedersen, T.F., 1993. Geochemistry of recent oxic and anoxic marine sediments: implications for the geological record. Marine Geology 113, 67-88.

Canfield, D.E., 1989. Reactive iron in marine sediments. Geochimica et Cosmochimica Acta 53, 619-632.

Canfield, D.E., Lyons, T.W., Raiswell, R., 1996. A model for iron deposition to euxinic Black Sea sediments. American Journal of Science 296, 818-834.

Chen, D.F., Dong, W.Q., Zhu, B.Q., Chen, X.P., 2004. Pb-Pb ages of Neoproterozoic Doushantuo phosphorites in South China: constraints on early metazoan evolution and glaciation events. Precambrian Research 132, 123-132.

Cline, J.D., 1969. Spectrophotometric determination of hydrogen sulfide in natural waters. Limnol Oceanogr 14, 454-458.

Collier, R.W., 1985. Molybdenum in the Northeast Pacific-Ocean. Limnology and Oceanography 30, 1351-1354.

Condon, D., Zhu, M.Y., Bowring, S., Wang, W., Yang, A.H., Jin, Y.G., 2005. U-Pb ages from the Neoproterozoic Doushantuo Formation, China. Science 308, 95-98.

Conveney, R.M., Jr., Grauch, R.I., Murowchick, J.B., 1994. Metals, phosphate, and stone coal in the Proterozoic and Cambrian of China: The geolocial setting of precious metal-bearing Ni-Mo ore beds. Society of Economic Geologists Newsletter 18, 1, 6-11.

Crusius, J., Calvert, S., Pedersen, T., Sage, D., 1996. Rhenium and molybdenum enrichments in sediments as indicators of oxic, suboxic and sulfidic conditions of deposition. Earth and Planetary Science Letters 145, 65-78.

Dean, W.E., Piper, D.Z., Peterson, L.C., 1999. Molybdenum accumulation in Cariaco basin sediment over the past 24 k.y.: A record of water-column anoxia and climate. Geology 27, 507-510.

Dill, H., 1986. Metallogenesis of Early Paleozoic graptolite shales from the Graefenthal Horst (Northern Bavaria-Federal Republic of Germany). Economic Geology 81, 889-903.

Fan, D., Yang, R.Y., Huang, Z.X., 1984. The Lower Cambrian black shales series and the iridium anomaly in south China. Developments in Geoscience, 27th International Geological Congress, Moscow, Beijing Science Press, 215-225.

Fossing, H., Jørgensen, B.B., 1989. Measurement of bacterial sulfate reduction in sediments: Evaluation of a single-step chromium reduction method. Biogeochemistry 8, 205–222.

Goldberg, T., Archer, C., Vance, D., Poulton, S.W., 2009. Mo isotope fractionation during adsorption to Fe (oxyhydr)oxides. Geochimica et Cosmochimica Acta 73, 6502-6516.

Goldberg, T., Strauss, H., Guo, Q.J., Liu, C.Q., 2007. Reconstructing marine redox conditions for the early Cambrian Yangtze Platform: Evidence from biogenic sulphur and organic carbon isotopes. Palaeogeography Palaeoclimatology Palaeoecology 254, 175-193.

Gordon, G.W., Lyons, T.W., Arnold, G.L., Roe, J., Sageman, B.B., Anbar, A.D., 2009. When do black shales tell molybdenum isotope tales? Geology 37, 535-538.

Gradstein, F.M., Ogg, J.G., Smith, A.G., Bleeker, W., Lourens, L.J., 2004. A new geologic time scale, with special reference to Precambrian and Neogene.

Episodes 27, 83-100.

Grice, K., Cao, C., Love, G.D., Böttcher, M.E., Twitchett, R.J., Grosjean, E., Summons, R.E., Turgeon, S.C., Dunning, W., Jing, Y., 2005. Photic zone euxinia during the Permian-Triassic superanoxic event. Science 307, 706-709.

Guo, Q.J., Shields, G.A., Liu, C.Q., Strauss, H., Zhu, M.Y., Pi, D.H., Goldberg, T., Yang, X.L., 2007. Trace element chemostratigraphy of two Ediacaran-Cambrian successions in South China: Implications for organosedimentary metal enrichment and silicification in the early Cambrian. Palaeogeography Palaeoclimatology Palaeoecology 254, 194-216.

Hannah, J.L., Stein, H.J., Wieser, M.E., de Laeter, J.R., Varner, M.D., 2007. Molybdenum isotope variations in molybdenite: Vapor transport and Rayleigh fractionation of Mo. Geology 35, 703-706.

Hatch, J.R., Leventhal, J.S., 1992. Relationship between inferred redox potential of the depositional environment and geochemistry of the Upper Pennsylvanian (Missourian) stark shale member of the Dennis limestone, Wabaunsee country, Kansas, USA. Chemical Geology 99, 65-82.

Helz, G.R., Miller, C.V., Charnock, J.M., Mosselmans, J.F.W., Pattrick, R.A.D., Garner, C.D., Vaughan, D.J., 1996. Mechanism of molybdenum removal from the sea and its concentration in black shales: EXAFS evidence. Geochimica et Cosmochimica Acta 60, 3631-3642.

Hetzel, A., Böttcher, M.E., Wortmann, U.G., Brumsack, H.J., 2009. Paleo-redox conditions during OAE 2 reflected in Demerara Rise sediment geochemistry (ODP Leg 207). Palaeogeography, Palaeoclimatology, Palaeoecology 273, 302-328.

Holland, H.D., 1979. Metals in black shales: reassessment. Economic Geology 74, 1676-1680.

Holland, H.D., 2006. The oxygenation of the atmosphere and oceans. Philosophical

Transactions of the Royal Society B-Biological Sciences 361, 903-915.

Horan, M.F., Morgan, J.W., Grauch, R.I., Coveney, R.M., Murowchick, J.B., Hulbert, L.J., 1994. Rhenium and osmium isotopes in black shales and Ni-Mo-PGE-rich sulfide layers, Yukon-Territory, Canada, and Hunan and Guizhou provinces, China. Geochimica et Cosmochimica Acta 58, 257-265.

Jiang, S.Y., Chen, Y.Q., Ling, H.F., Yang, J.H., Feng, H.Z., Ni, P., 2006. Trace- and rare-earth element geochemistry and Pb-Pb dating of black shales and intercalated Ni-Mo-PGE-Au sulfide ores in Lower Cambrian strata, Yangtze Platform, South China. Mineralium Deposita 41, 453-467.

Jiang, S.Y., Pi, D.H., Heubeck, C., Frimmel, H., Liu, Y.P., Deng, H.L., Ling, H.F., Yang, J.H., 2009. Early Cambrian ocean anoxia in South China. Nature 459, E5-E6.

Jiang, S.Y., Yang, J.H., Ling, H.F., Chen, Y.Q., Feng, H.Z., Zhao, K.D., Ni, P., 2007. Extreme enrichment of polymetallic Ni-Mo-PGE-Au in lower Cambrian black shales of South China: An Os isotope and PGE geochernical investigation. Palaeogeography Palaeoclimatology Palaeoecology 254, 217-228.

Johnson, C.M., Beard, B.L., Roden, E.E., 2008. The iron isotope fingerprints of redox and biogeochemical cycling in the modern and ancient Earth. Annual Review of Earth and Planetary Sciences 36, 457-493.

Jones, B., Manning, D.A.C., 1994. Comparison of geochemical indexes used for the interpretation of palaeoredox conditions in ancient mudstones. Chemical Geology 111, 111-129.

Kao, L.S., Peacor, D.R., Coveney, R.M., Zhao, G.M., Dungey, K.E., Curtis, M.D., Penner-Hahn, J.E., 2001. A C/MoS_2 mixed-layer phase (MoSC) occurring in metalliferous black shales from southern China, and new data on jordisite. American Mineralogist 86, 852-861.

Kaufman, A.J., Jacobsen, S.B., Knoll, A.H., 1993. The Vendian record of Sr and

C-isotopic variations in seawater: implications for tectonics and paleoclimate. Earth and Planetary Science Letters 120, 409-430.

Kendall, B., Creaser, R.A., Gordon, G.W., Anbar, A.D., 2009. Re-Os and Mo isotope systematics of black shales from the Middle Proterozoic Velkerri and Wollogorang Formations, McArthur Basin, northern Australia. Geochimica et Cosmochimica Acta 73, 2534-2558.

Kendall, B., Reinhard, C.T., Lyons, T., Kaufman, A.J., Poulton, S., Anbar, A.D., 2010. Pervasive oxygenation along late Archaean ocean margins. Nature Geoscience 3, 647-652.

Kimura, H., Watanabe, Y., 2001. Oceanic anoxia at the Precambrian-Cambrian boundary. Geology 29, 995-998.

Kirschvink, J.L., Ripperdan, R.L., Evans, D.A., 1997. Evidence for a large-scale reorganization of early Cambrian continental masses by inertial interchange true polar wander. Science 277, 541-545.

Kribek, B., Sýkorová, I., Pasava, J., Machovic, V., 2007. Organic geochemistry and petrology of barren and Mo-Ni-PGE mineralized marine black shales of the Lower Cambrian Niutitang Formation (South China). International Journal of Coal Geology 72, 240-256.

Lehmann, B., Mao, J.W., Li, S.R., Zhang, G.D., 2003. Re-Os dating of polymetallic Ni-Mo-PGE-Au mineralization in lower Cambrian black shales of south China and its geological significance - A reply. Economic Geology 98, 663-665.

Lehmann, B., Nägler, T.F., Holland, H.D., Wille, M., Mao, J.W., Pan, J.Y., Ma, D.S., Dulski, P., 2007. Highly metalliferous carbonaceous shale and Early Cambrian seawater. Geology 35, 403-406.

Li, S.Y., Q, Y.X., Shen, J.F., Sun, L., Liu, B., Yan, B.K., 2002. Source of Lower Cambrian platinum group elements in black shales in Hunan and Guizhou provinces, China and the Re-Os isotope dating. Science China (Series D) 32,

568-575.

Lott, D.A., Coveney, R.M., Murowchick, J.B., Grauch, R.I., 1999. Sedimentary exhalative nickel-molybdenum ores in south China. Economic Geology 94, 1051-1066.

Lyons, T.W., Werne, J.P., Hollander, D.J., Murray, R.W., 2003. Contrasting sulfur geochemistry and Fe/Al and Mo/Al ratios across the last oxic-to-anoxic transition in the Cariaco Basin, Venezuela. Chemical Geology 195, 131-157.

Malinovsky, D., Hammarlund, D., Ilyashuk, B., Martinsson, O., Gelting, J., 2007. Variations in the isotopic composition of molybdenum in freshwater lake systems. Chemical Geology 236, 181-198.

Mao, J.W., Lehmann, B., Du, A.D., Zhang, G.D., Ma, D.S., Wang, Y.T., Zeng, M.G., Kerrich, R., 2002. Re-Os dating of polymetallic Ni-Mo-PGE-Au mineralization in lower Cambrian black shales of south China and its geologic significance. Economic Geology 97, 1051-1061.

McManus, J., Nägler, T.F., Siebert, C., Wheat, C.G., Hammond, D.E., 2002. Oceanic molybdenum isotope fractionation: Diagenesis and hydrothermal ridge-flank alteration. Geochemistry Geophysics Geosystems 3, doi: 10.1029/2002GC000356.

Morford, J.L., Emerson, S., 1999. The geochemistry of redox sensitive trace metals in sediments. Geochimica et Cosmochimica Acta 63, 1735-1750.

Morris, A.W., 1975. Dissolved Molybdenum and Vanadium in Northeast Atlantic Ocean. Deep-Sea Research 22, 49-54.

Nägler T.F., Neubert N., Böttcher M.E., Dellwig O., Schnetger B., 2011. Mo isotope fractionation in pelagic euxinia: Results from the modern Black and Baltic Seas. Chemical Geology, submitted.

Nägler, T.F., Siebert, C., Lüschen, H., Böttcher, M.E., 2005. Sedimentary Mo isotope record across the Holocene fresh-brackish water transition of the Black Sea.

Chemical Geology 219, 283-295.

Nakagawa Y., Firdaus M.L., Norisuye, K., Sohrin, Y., Irisawa, K, Hirata T., 2008. Precise isotopic analysis of Mo in seawter using multiple collector-industively coupled mass spectrometry coupled with a chelating resin column preconcentration method. Analytical Chemistry 80, 9213-9219.

Neubert, N., Nägler, T.F., Böttcher, M.E., 2008. Sulfidity controls molybdenum isotope fractionation into euxinic sediments: Evidence from the modern Black Sea. Geology 36, 775-778.

Pan, J.Y., Ma, D.S., Cao, S.L., 2004. Trace element geochemistry of the Lower Cambrian black rock series from northwestern Hunan, South China. Progress in Natural Science 14, 64-70.

Pasava, J., Kribek, B., Vymazalova, A., Sykorova, I., Zak, K., Orberger, B., 2008. Multiple sources of metals of mineralization in Lower Cambrian black shales of South China: Evidence from geochemical and petrographic study. Resource Geology 58, 25-42.

Pearce, C.R., Cohen, A.S., Coe, A.L., Burton, K.W., 2008. Molybdenum isotope evidence for global ocean anoxia coupled with perturbations to the carbon cycle during the early Jurassic. Geology 36, 231-234.

Pietruszka, A.J., Walker, R.J., Candela, P.A., 2006. Determination of mass-dependent molybdenum isotopic variations by MC-ICP-MS: An evaluation of matrix effects. Chemical Geology 225, 121-136.

Piper, D.Z., 1994. Seawater as the Source of Minor Elements in Black Shales, Phosphorites and Other Sedimentary-Rocks. Chemical Geology 114, 95-114.

Poulson, R.L., Siebert, C., McManus, J., Berelson, W.M., 2006. Authigenic molybdenum isotope signatures in marine sediments. Geology 34, 617-620.

Qiu, Y.M., Gao, S., 2000. First evidence of > 3.2 Ga continental crust in the Yangtze craton of South China and its implications for Archean crustal evolution and

Phanerozoic tectonics. Geology 28, 11-14.

Raiswell, R., Buckley, F., Berner, R.A., Anderson, T.F., 1988. Degree of pyritization of iron as a paleoenvironmental indicator of bottom-water oxygenation. Journal of Sedimentary Petrology 58, 812-819.

Raiswell, R., Canfield, D.E., 1998. Sources of iron for pyrite formation in marine sediments. American Journal of Science 298, 219-245.

Rimmer, S.M., 2004. Geochemical paleoredox indicators in Devonian-Mississippian black shales, central Appalachian basin (USA). Chemical Geology 206, 373-391.

Rouxel, O.J., Bekker, A., Edwards, K.J., 2005. Iron isotope constraints on the Archean and Paleoproterozoic ocean redox state. Science 307, 1088-1091.

Rudnick, R.L., Gao, S., 2004. Composition of the continental crust. In Rudnick, R.L., (ed.) Treatise in Geochemistry, Elsevier, Amsterdam 3, 1-64.

Ryb U., Erel Y., Matthews A., Avni Y., Gordon G.W., Anbar A.D., 2009. Large molybdenum isotope variations trace subsurface fluid migration along the Dead Sea transform. Geology 37, 463-466.

Schröder, S., Grotzinger, J.P., 2007. Evidence for anoxia at the Ediacaran-Cambrian boundary: the record of redox-sensitive trace elements and rare earth elements in Oman. Journal of the Geological Society 164, 175-187.

Scott, C., Lyons, T.W., Bekker, A., Shen, Y., Poulton, S.W., Chu, X., Anbar, A.D., 2008. Tracing the stepwise oxygenation of the Proterozoic ocean. Nature 452, 456-459.

Shen, Y.A., Canfield, D.E., Knoll, A.H., 2002. Middle proterozoic ocean chemistry: Evidence from the McArthur Basin, northern Australia. American Journal of Science 302, 81-109.

Shen Y.A., Knoll A.H., Walter, M.R., 2003. Evidence for low sulphate and anoxia in a mid-Proterozoic marine basin. Nature 423, 632-635.

Shu, D.G., Morris, S.C., Han, J., Chen, L., Zhang, X.L., Zhang, Z.F., Liu, H.Q., Li, Y., Liu, J.N., 2001. Primitive deuterostomes from the Chengjiang Lagerstatte (Lower Cambrian, China). Nature 414, 419-424.

Siebert, C., Kramers, J.D., Meisel, T., Morel, P., Nägler, T.F., 2005. PGE, Re-Os, and Mo isotope systematics in Archean and early Proterozoic sedimentary systems as proxies for redox conditions of the early Earth. Geochimica et Cosmochimica Acta 69, 1787-1801.

Siebert, C., McManus, J., Bice, A., Poulson, R., Berelson, W.M., 2006. Molybdenum isotope signatures in continental margin marine sediments. Earth and Planetary Science Letters 241, 723-733.

Siebert, C., Nägler, T.F., Kramers, J.D., 2001. Determination of molybdenum isotope fractionation by double-spike multicollector inductively coupled plasma mass spectrometry. Geochemistry Geophysics Geosystems 2, doi: 10.1029/2000GC000124.

Siebert, C., Nägler, T.F., von Blanckenburg, F., Kramers, J.D., 2003. Molybdenum isotope records as a potential new proxy for paleoceanography. Earth and Planetary Science Letters 211, 159-171.

Steiner, M., Li, G.X., Qian, Y., Zhu, M.Y., Erdtmann, B.D., 2007. Neoproterozoic to early Cambrian small shelly fossil assemblages and a revised biostratigraphic correlation of the Yangtze Platform (China). Palaeogeography Palaeoclimatology Palaeoecology 254, 67-99.

Steiner, M., Wallis, E., Erdtmann, B.D., Zhao, Y.L., Yang, R.D., 2001. Submarine-hydrothermal exhalative ore layers in black shales from South China and associated fossils - insights into a Lower Cambrian facies and bio-evolution. Palaeogeography Palaeoclimatology Palaeoecology 169, 165-191.

Tossell, J.A., 2005. Calculating the partitioning of the isotopes of Mo between oxidic and sulfidic species in aqueous solution. Geochimica et Cosmochimica Acta 69,

2981-2993.

Tribovillard, N., Algeo, T.J., Lyons, T., Riboulleau, A., 2006. Trace metals as paleoredox and paleoproductivity proxies: An update. Chemical Geology 232, 12-32.

Vine, J.D., Tourtelot, E.B., 1970. Geochemistry of Black Shale Deposits - a Summary Report. Economic Geology 65, 253-272.

Voegelin, A.R., Nägler, T.F., Samankassou, E., Villa, I.M., 2009. Molybdenum isotopic composition of modern and Carboniferous carbonates. Chemical Geology 265, 488-498.

Wallis, E., 2007. The climatic and environmental history of the South Chinese Yangtze platform during the Neoproterozoic and Early Cambrian: hydrothermally active and salinity stratified epicontinental basins a key for understanding the "Cambrian explosion"? Ph.D Thesis. Berlin. 1-227 (in Germany with English abstract).

Wen, H.J., Zhang, Y.X., Fan, H.F., Hu, R.Z., 2009. Mo isotopes in the Lower Cambrian formation of southern China and its implications on paleo-ocean environment. Chinese Science Bulletin 54, 4756-4762.

Wilde, P., Lyons, T.W., Quinby-Hunt, M.S., 2004. Organic carbon proxies in black shales: molybdenum. Chemical Geology 206, 167-176.

Wille, M., Kramers, J.D., Nägler, T.F., Beukes, N.J., Schroder, S., Meisel, T., Lacassie, J.P., Voegelin, A.R., 2007. Evidence for a gradual rise of oxygen between 2.6 and 2.5 Ga from Mo isotopes and Re-PGE signatures in shales. Geochimica et Cosmochimica Acta 71, 2417-2435.

Wille, M., Nägler, T.F., Lehmann, B., Schroder, S., Kramers, J.D., 2008. Hydrogen sulphide release to surface waters at the Precambrian/Cambrian boundary. Nature 453, 767-769.

Wu, S., Zhao, Y.H., Feng, X.B., Wittmeier, A., 1996. Application of inductively coupled plasma mass spectrometry for total metal determination in silicon-containing solid samples using the microwave-assisted nitric acid hydrofluoric acid hydrogen peroxide boric acid digestion system. Journal of Analytical Atomic Spectrometry 11, 287-296.

Xu, L.G., Lehmann, B., Mao, J.W., Qu, W.J., Du, A.D., 2011. Re-Os age of polymetallic Ni-Mo-PGE-Au mineralization in Early Cambrian black shales of South China – a reassessment. Economic Geology 106, 511-522.

Xu, L.G., Lehmann, B,. Mao, J.W., 2011. Seawater origin of polymetallic Ni-Mo-PGE-Au mineralization in Early Cambrian black shales of South China: evidence from Mo isotope, PGE, trace element and REE geochemistry. Ore Geology Reviews, submitted.

Yin, C.Y., Tang, F., Liu, Y.Q., Gao, L.Z., Liu, P.J., Xing, Y.S., Yang, Z.Q., Wan, Y.S., Wang, Z.Q., 2005. U-Pb zircon age from the base of the Ediacaran Doushantuo Formation in the Yangtze Gorges, South China: constraint on the age of Marinoan glaciation. Episodes 28, 48-49.

Zhang, S.H., Jiang, G.Q., Zhang, J.M., Song, B., Kennedy, M.J., Christie-Blick, N., 2005. U-Pb sensitive high-resolution ion microprobe ages from the Doushantuo Formation in south China: Constraints on late Neoproterozoic glaciations. Geology 33, 473-476.

Zhou, L., Gao, S., Chris, H., Corey, A., Xie, S.C., 2009. Preliminary Mo isotope data of Phanerozoic clastic sediments from the northern margin of the Yangtze block and its implication for paleoenvironmental conditions. Chinese Science Bulletin 54, 822-829.

Zhu, M.Y., Zhang, J.M., Steiner, M., Yang, A.H., Li, G.X., Erdtmann, B.D., 2004. Sinian-Cambrian stratigraphic framework for shallow- to deep-water environments of the Yangtze Platform: an integrated approach. Progress in Natural Science (Special Issue 2004), 75-84.

Zhu, R.X., Li, X.H., Hou, X.G., Pan, Y.X., Wang, F., Deng, C.L., He, H.Y., 2009. SIMS U-Pb zircon age of a tuff layer in the Meishucun section, Yunnan, southwest China: Constraint on the age of the Precambrian-Cambrian boundary. Science in China Series D-Earth Sciences 52, 1385-1392.

CHAPTER SEVEN:

SEAWATER ORIGIN OF POLYMETALLIC Ni-Mo-PGE-Au MINERALIZATIN IN EARLY CAMBRIAN BLACK SHALES OF SOUTH CHINA: EVIDENCE FROM Mo ISOTOPE, PGE, TRACE ELEMENT AND REE GEOCHEMISTRY

Xu Lingang[a],*, Bernd Lehmann[a], Mao Jingwen[b]

[a] *Mineral Resources, Technical University of Clausthal, 38678 Clausthal-Zellerfeld, Germany*

[b] *MLR Key Laboratory of Metallogeny and Mineral Assessment, Institute of Mineral Resources, Chinese Academy of Geological Sciences, Beijing 100037, China*

*Corresponding author: e-mail, lingang.xu@tu-clausthal.de

Submitted to ***Ore Geology Reviews***

7.1 Abstract

The Early Cambrian black shale sequence of the Niutitang Formation in South China hosts a synsedimentary organic carbon-rich polymetallic sulfide layer with extreme metal enrichment, locally mined as polymetallic Ni-Mo-PGE-Au sulfide ore. In combination with previously reported data, we present Mo isotope, platinum group element (PGE), and trace and rare-earth element (REE) data of the polymetallic sulfide ores and the host black shales from four mine sites (Dazhuliushui and Maluhe in Guizhou province, and Sancha and Cili in Hunan province, respectively), several hundred kilometers apart. The polymetallic sulfide ores have relatively consistent heavy $\delta^{98/95}$Mo values (from 0.94 to 1.38‰, with average of 1.13 ± 0.14‰, 1σ, n = 11) while the host black shale and phosphorite has variable $\delta^{98/95}$Mo values (0.81‰ to 1.70‰, with average of 1.28 ± 0.41‰, 1σ, n = 14). This variation is due to variable paleoenvironmental conditions from suboxic to euxinic, and partly closed-system fractionation in protected sedimentary basins. Both the polymetallic sulfides and the host black shales show PGE distribution patterns similar to present-day seawater, but different from hydrothermal fluids. The polymetallic sulfide bed has a generally consistent metal enrichment by a factor of 10^7 compared to present-day seawater, while the host black shales are largely controlled by terrigenous input. Ni- and Mo-based metal ratios reveal that both the polymetallic sulfide ores and the host black shales have ratios similar to present-day seawater. REE + Y patterns of the polymetallic sulfide bed are characterized by a remarkably positive Y anomaly, consistent with an origin of the REE budget dominantly from seawater. The Mo isotope, PGE, and trace and rare-earth element geochemistry suggest that metals in the polymetallic Ni-Mo-PGE-Au sulfide ore layer were scavenged from Early Cambrian seawater, by both in-situ precipitation and short distance re-deposition of sulfide clasts.

Keywords: Mo isotopes, PGE, REE, Polymetallic Ni-Mo-PGE-Au sulfide, Black shale, Early Cambrian, South China

7.2 Introduction

Black shale is a thinly laminated carbonaceous shale with elevated content in organic matter (5% or more carbon content) and sulfide (especially iron sulfide, usually pyrite), and commonly with unusual concentrations of certain trace elements (Neuendorf et al., 2005). Black shales occur in quite variable depositional geological settings and paleoenvironments since Archean times. In South China, the transgressive Early Cambrian black shale sequence of the Niutitang Formation (and equivalent strata) with abundant fossils (e.g. sponges, arthropods, phyto- and zooplankton, and bacterial colonies) occurs in an about 1600 km-long belt that extends across the Yunnan, Guizhou, Hunan, Jiangxi, Anhui and Jiangsu provinces on the Yangtze Platform (Fig. 7-1), unconformably overlying dolomite of the Neoproterozoic Dengying Formation (Zhu et al., 2004). The Early Cambrian black shale deposition is a reflection of a widespread ocean anoxia event during the Precambrian/Cambrian (PC/C) transition, which is a critical interval in Earth history characterized by global environmental and biological changes, such as major plate tectonic reconfiguration, ocean anoxia, mass extinction and accelerated diversification of metazoans (e.g. Brasier, 1992; Kaufman et al., 1993; Banerjee et al., 1997; Kirschvink et al., 1997; Kimura and Watanabe, 2001; Shu et al., 2001; Schröder and Grotzinger, 2007). The black shale sequence of the Niutitang Formation is enriched in a broad spectrum of redox-sensitive elements, i.e. Mo, Ni, Cr, V, PGE, Au, and U, typical of black shales in general (Vine and Tourtelot, 1970; Holland, 1979). Noticeably, an unusual polymetallic Ni-Mo-PGE-Au sulfide ore layer enriched in organic and phosphoritic materials is locally distributed in the lowermost part of the black shale sequence (generally <10 m above the PC/C boundary). Although the sulfide ore layer is only several centimeters thick, it shows extreme metal enrichment with Ni + Mo reaching up to 14 wt.%, and platinum group element (PGE) + Au concentrations around 1g/t (Fan et al., 1984; Coveney et al., 1994; Lehmann et al., 2007; Xu et al., 2011; this study), making this layer a target for widespread small-scale mining in the Hunan and Guizhou provinces. Besides the extreme enrichment in Ni, Mo, PGE and Au, the sulfide ore layer is also strongly enriched in Se, Re, Os, As, Hg, and Sb ($>10^4$ times average continental crust) (Fan et al., 1984; Conveney et al., 1994; Jiang et al., 2006; Lehmann et al. 2007).

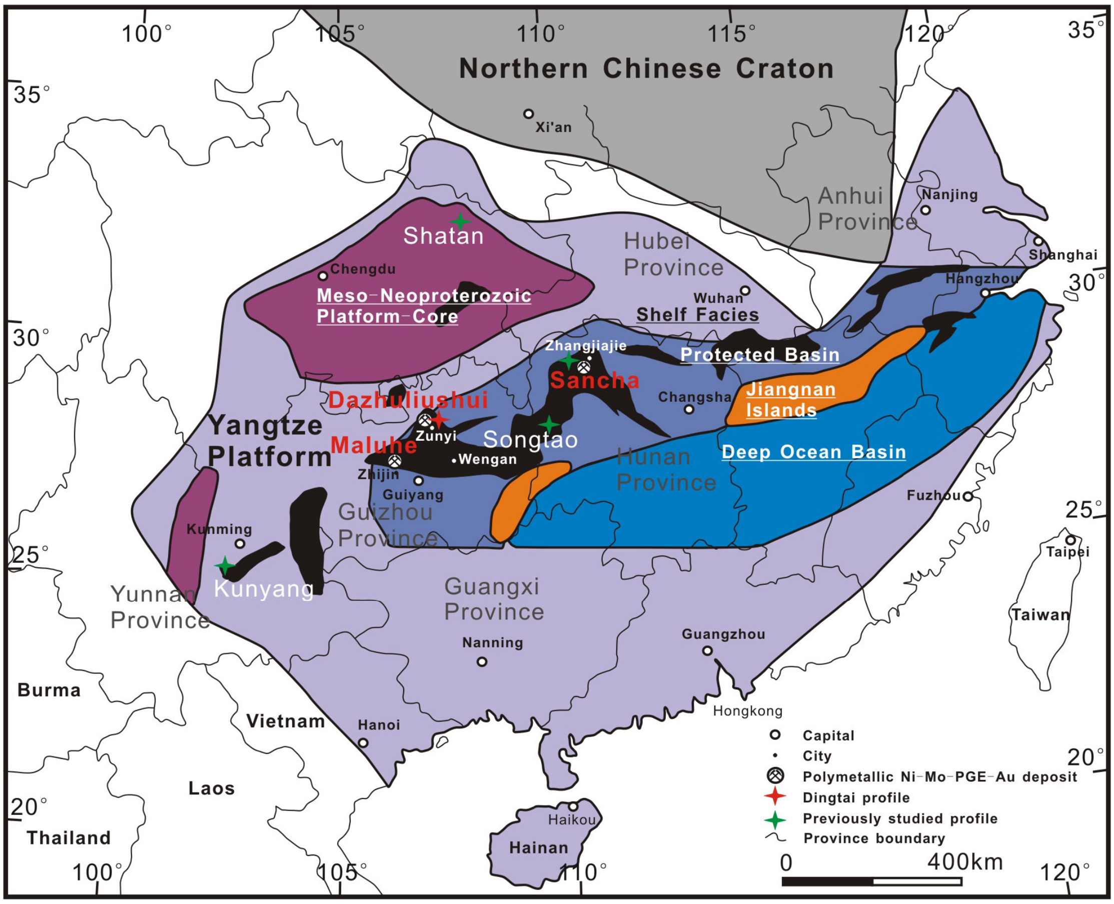

Fig. 7-1: Sketch map showing locations of the Dazhuliushui, Maluhe, Sancha and Cili polymetallic Ni-Mo-PGE-Au sulfide ore deposits, and depositional environments during the Neoproterozoic-Cambrian interval. Black areas indicate the exposed Early Cambrian black shale sequence of the Niutitang Formation (and equivalent strata) in South China (modified from Wallis, 2007).

Many petrological, mineralogical, chronological, paleontological and metallogenic studies on both sulfide ores and host black shales were done since the polymetallic sulfide ore layer was discovered in the 1970s (e.g. Fan et al., 1984; Coveney et al., 1992; Horan et al., 1994; Lott et al., 1999; Steiner et al., 2001; Kao et al., 2001; Mao et al., 2002; Lehmann et al., 2003, 2007; Jiang et al., 2006, 2007a, b, 2009; Pasava et al., 2008; Xu et al., 2011). However, the causes for metal enrichment are still much debated. Fan et al. (1994) suggested an extraterrestrial origin, which soon was disregarded due to the non-chondritic PGE distribution patterns (Coveney et al., 1992). The exceptional metal grades were then mostly ascribed to hydrothermal venting at the seafloor (Lott et al., 1999; Steiner et al., 2001; Jiang et al., 2006, 2007a, b, 2009). Pasava et al. (2008) suggested multiple sources of metals are related to the circulation of highly saline low temperature fluids which leached metals from underlying lithologies of the Doushantuo Formation, followed by discharge into seawater and scavenging of metals via co-precipitation with sulfides and formation of metal-organic complexes. However, early sulfur isotope studies showed oscillatory zoning of sulfide aggregates with a large spread in delta ^{34}S values over a range of about 50 per mil, interpreted as biologically mediated fractionation of seawater sulfate under sulfate-limiting conditions (Horan et al., 1994). By comparing chemical compositions of the present-day seawater, the host black shales and the polymetallic sulfide ores, Mao et al. (2002) and Lehmann et al. (2003, 2007) interpreted the metal distribution pattern as reflecting scavenging from average seawater at a very low clastic sedimentation rate. This interpretation is supported by the fact that the host black shales and the polymetallic sulfide ores have similar initial Os ratios (Xu et al., 2011). Lehmann et al. (2007) confirmed the seawater origin of the polymetallic sulfide ore deposits using Mo isotope data. A further interpretation of the Mo isotope data with global conclusions was attempted by Wille et al. (2008) by comparing Mo isotope data from Early Cambrian stratigraphic intervals in Oman and South China. This interpretation was based on the assumption of synchroneity of the sample suites studied from Oman and South China. However, recent studies indicate that the deposition of the black shales of the Niutitang Formation is about 20 Ma later than in

Oman (Amthor et al., 2003; Jiang et al., 2009; Wen et al., 2009; Wille et al., 2009; Xu et al., 2011).

In this study, Mo stable isotope, platinum group element (PGE), trace element and rare-earth element (REE) data are applied in order to discriminate in between the models of seawater scavenging or hydrothermal venting. We investigated the localities of Dazhuliushui and Maluhe in Guizhou province, and Sancha and Cili in Hunan province. Based on more samples and on a broader range of localities than in previous studies, we compare the polymetallic sulfide ores and the host black shales with typical syngenetic hydrothermal massive sulfide deposits (sedimentary-exhalative type and volcanogenic massive sulfide type) and modern active hydrothermal vent samples. In combination with previously reported data, we re-evaluate the available Mo isotope, PGE, trace element and REE data to constrain the causes for the spectacular metal enrichment in the Early Cambrian polymetallic Ni-Mo-PGE-Au sulfide ore layer on the Yangtze Platform.

7.3 Regional geology

Neoproterozoic and Early Cambrian sedimentary rocks are widely exposed on the Yangtze Platform of South China. The sedimentary sequence represents a sedimentary shelf environment characterized by repeated transgression-regression episodes on the Lower Proterozoic-Archean Yangtze craton (Qiu et al., 2000; Steiner et al., 2001). The Neoproterozoic Nantuo Formation, Doushantuo Formation and Dengying Formation are exposed in ascending order (Fig. 7-2). The Nantuo Formation is characterized by glacial diamictites with siltstone and sandstone interbeds, and is correlated with the 630 Ma Marinoan glaciation (Gradstein et al., 2004). The Doushantuo Formation overlies the diamictite of the Nantuo Formation, and consists of carbonaceous mudstone and dolomite, with interbedded phosphorite.

U-Pb zircon dates from volcanic ash beds within the Doushantuo Formation indicate that deposition occurred between 635 and 551 Ma (Condon et al., 2005). Two phosphorite beds in the Doushantuo Formation yielded Pb-Pb isochron ages of 576 ± 16 Ma for the upper part (Chen et al., 2004), and 599 ± 4 Ma for the lower part of the Upper Phosphorite unit (Barfod et al., 2002), respectively. Three zircon SHRIMP U-Pb ages of 628 ± 6 Ma, 621 ± 7 Ma, and 555 ± 6 Ma were reported for the distinctive volcanic ash interbeds, which constrain the age interval of the Doushantuo Formation (Yin et al., 2005; Zhang et al., 2005). Above the Doushantuo Formation rests the dolomite of the Dengying Formation, followed by a stratigraphic hiatus. The Dengying Formation reaches up to 600 m thickness and contains tubular Cloudina fossils (Bengtson and Zhao, 1992). The Niutitang Formation and equivalent sequences slightly unconformably overlie the Dengying Formation with a stratigraphic thickness of about 20-80 m. The Niutitang Formation is dominated by black shales but its lower part has a very variable lithology with important sedimentary phosphorite and barite units, and up to several tens of meters thick “stone coal” beds of algal origin (combustible shale). A marker bed of polymetallic Ni-Mo-PGE-Au sulfide ore is locally distributed in the lowermost part with a thickness of mostly only 3 to 5 cm. The sulfide ore layer was dated using the Re-Os method and yielded isochron ages of 560 ± 50 Ma (Horan et al., 1994), 542 ± 11 Ma (Li et al., 2002) and 541 ± 16 Ma (Mao et al., 2002), respectively. Pb-Pb dating of black shale and Ni-Mo-PGE-Au sulfide ores from the Niutitang Formation yielded an isochron age of 531 ± 24 Ma and 521 ± 54 Ma, respectively (Jiang et al., 2006). Jiang et al. (2009) reported a SHRIMP U-Pb zircon age of 532.3 ± 0.7 Ma for a volcanic ash bed a few meters beneath the sulfide ore layer near Zunyi, Guizhou province, suggesting that the mineralization age of the sulfide ore layer must be younger than 532 Ma. More recently, based on more representative and comprehensive sampling of polymetalllic sulfide ores, Xu et al. (2011) re-assessed a Re-Os age of 521 ± 5 Ma, which is consistent with the biostratigraphic Tommotian age. Chert and phosphorite beds occur below the sulfide ore layer, and immediately above the dolomite of the Dengying Formation. Phosphorite mostly occurs as discontinuous nodules, however, a locally thick massive phosphorite bed (reaching up to 20 meters) is also found, which is mined for phosphate ore (e.g. Zhijin phosphorite deposit, near the Maluhe polymetallic sulfide ore deposit, Guizhou province). The lower Niutitang Formation also locally hosts stratiform barite, vanadium and stone coal (combustible black shale) deposits. The black shales and phosphorite nodules/beds of the Niutitang Formation contain abundant sponges, arthropods and other soft-bodied fossils of wide biological diversity which mark the "Cambrian Explosion" (Brasier, 1992; Steiner et al., 2001, 2007). The Niutitang Formation is overlain by shale, siltstone and fine-grained sandstone (Mingxinsi Formation), sandy shale and muddy siltstone (Jindingshan Formation), and dolomite (Qingxudong Formation), in ascending order.

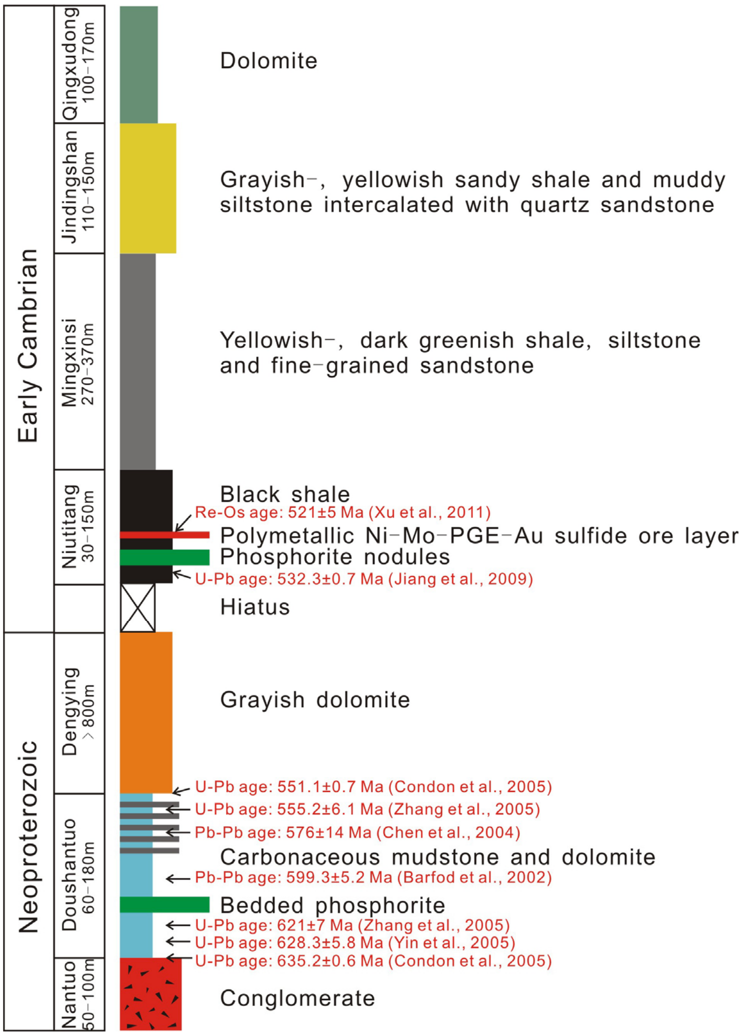

Fig. 7-2: Stratigraphic column showing the Neoproterozoic-Early Cambrian sedimentary sequences of the study area. Radiometric ages are highlighted with red color.

The Neoproterozoic-Cambrian paleogeographic reconstruction reveals a depositional zonation from a shallow shelf facies of carbonate and phosphorite rocks in the northwest to a protected and deep basinal facies of black shales and cherts in the southeast (Zhu et al., 2004; Wallis, 2007). The polymetallic Ni-Mo-PGE-Au sulfide ore layer occurs in the Early Cambrian Niutitang Formation along a narrow NE-striking belt of transitional and deep basinal facies. Geographic coordinates of the four investigated polymetallic Ni-Mo-PGE-Au sulfide ore deposits are: Dazhuliushui (N 27°43′13.5″, E 106°38′44.3″), Maluhe (N 26°44′40.0″, E 105°37′13.5″), Sancha (N 29°04′26.6″, E 110°34′32.7″) and Cili (N 29°11′10.0″, E 110°51′03.0″). They are all in areas of protected basins but several hundred km apart (Fig. 7-1).

7.4 Ore deposit geology

The Dazhuiliushui, Maluhe, Sancha and Cili polymetallic Ni-Mo-PGE-Au sulfide ore deposits are hosted in the lowermost black shale section of the Niutitang Formation (Fig. 7-3).

The Dazhuliushui Ni-Mo-PGE-Au deposit is located in the western part of the Songlin dome, about 26 km from Zunyi city, Guizhou province. From the dome center outwards, Neoproterozoic conglomerate of the Nantuo Formation, carbonaceous mudstone and dolomite of the Doushantuo Formation, dolomite of the Dengying Formation, and black shale of the Early Cambrian Niutitang Formation are exposed. The Niutitang Formation is overlain by carbonaceous siltstone and sandstone of the Early Cambrian Minxinsi Formation, dolostone of the Early Cambrian Qingxudong Formation, and Middle Ordovician dolomite and shale. NE-trending faults are dominant in the Songlin dome. The sulfide ore layer is 5-8 m above the Neoproterozoic dolomite contact. Besides the Dazhuliushui mine site, the nearby Xiaozhuliushui, Huangjiawan, Zhongnancun and Xintugou Ni-Mo-PGE-Au sulfide ore deposits are within the same stratigraphic interval (Fig. 7-3 A).

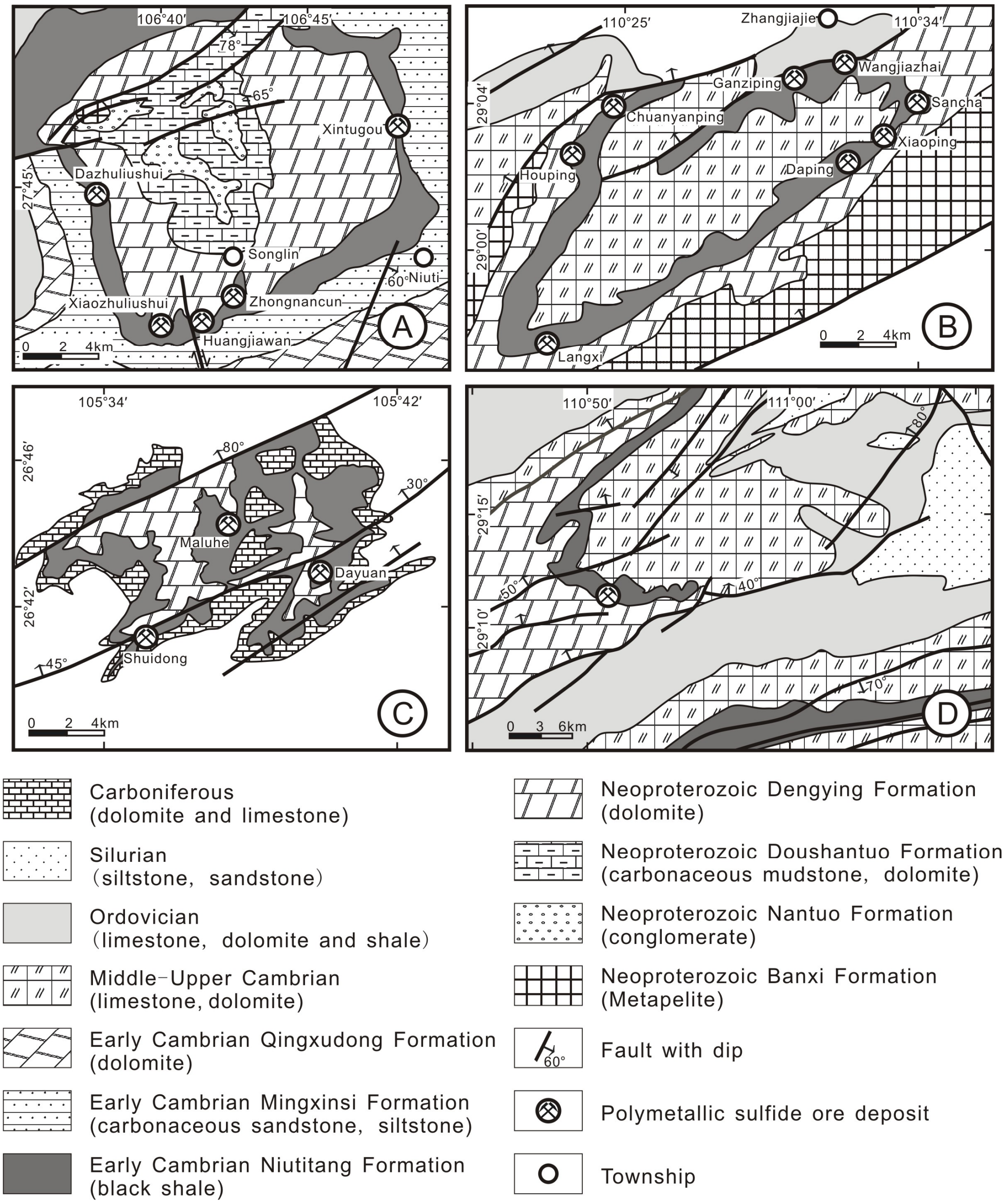

Fig. 7-3: Geological sketch maps of the study areas. **A:** Dazhuliushui mine district near Zunyi, Guizhou province (after Mao et al., 2002). **B:** Sancha mine district near Zhangjiajie, Hunan province (modified from Li et al., 2002). **C:** Maluhe mine district near Zhijin, Guizhou province. **D:** Cili mine district, Hunan province. The strata are mainly flat-lying with mild anticlinal folding/domal upwarp in the Zunji district (Songlin dome) and the Sancha mine district.

The Maluhe district with the Maluhe, Shuidong and Dayuan polymetallic sulfide ore deposits is located ~180 km southwest of the Dazhuliushui mine site near Zhijin County, Guizhou province. The Maluhe deposit is hosted in a broad anticlinal structure where exposes the Niutitang Formation, unconformably overlain by Carboniferous dolomite and dolomitic limestone, and underlain by dolomite of the Neoproterozoic Dengying Formation (Fig. 7-3 C). Post-mineralization NE-trending faults are developed in the Maluhe district. The polymetallic sulfide ore layer is about 1 m above the unconformable contact with dolomite of the Dengying Formation.

The Sancha Ni-Mo-PGE-Au district in Hunan province is ~380 km northeast of the Dazhuliushui mine site. The Sancha district includes a number of individual deposits, such as Sancha, Wangjiazhai, Ganziping, Chuanyanping, Houping, Langxi, Daping and Xiaoping, which are aligned along the limbs of the Tianmenshan-Huangdong syncline (Fig. 7-3 B). The axis of the synclinal structure is composed of Middle-Late Cambrian limestone and dolomite. The sulfide ore layer in the Niutitang Formation is only 1 m above the unconformity with the dolomite of the Neoproterozoic Dengying Formation. Phosphorite nodules and chert occur between the sulfide ore layer and the dolomite contact. From northeast to southwest in the Sancha district, the intensity of the polymetallic Ni-Mo-PGE-Au mineralization decreases gradually and grades into vanadium mineralization (not shown in Fig. 7-3 B, Xu et al. in preparation).

The Cili polymetallic Ni-Mo-PGE-Au sulfide deposit in Hunan province is ~70 km northeast of the Sancha mine site. As for the other known polymetallic Ni-Mo-PGE-Au mineralization occurrences, the Cili ore deposit is hosted in the lowermost black shales of the Early Cambrian Niutitang Formation, which is underlain by the grayish dolomite of the Dengying Formation and overlain by the grayish-greenish shales with black shale interbeds of the Early Cambrian Balang Formation and Qingxudong Formation. The fossil-rich (*Arthricocephalus chauveaui, Changaspis sp., Pseudolancaslria sp., Balangia balangensis, Redlichia hupehensis, Yuehsienszella sp.,* and *Arlhricocephalus duyuensis*) Early Cambrian sedimentary rocks are overlain by Middle-Late Cambrian grayish shale and limestone (Regional Geology and Mineral Resource Report, 1969). The limbs of the synclinal structure are composed of Ordovician greenish limestone, dolomite and shale (Fig. 7-3 D). NE-trending faults of post-Early Paleozoic age are widespread in the Cili district. The polymetallic sulfide ore layer is 0.5-3 m above the unconformity with the Dengying dolomite. Several m thick stone coal (combustible black shales) with high TOC content (reaching up to 35%) is utilized as fuel by local people. Nodular and massive phosphorite beds occur between the sulfide layer and the Dengying dolomite contact. The thickness of massive phosphorite beds varies from 0.3 to 0.5 m (maximum 1.35 m) with P_2O_5 grade of 10.6 – 33.4 wt.%, making this phosphorite a target for small-scale mining. The average Mo abundance of the phosphorite ranges from 0.28 to 0.50 wt.% (Regional Geology and Mineral Resource Report, 1969).

7.5 Lithology

Hand specimens of the host black shales are black, fine-grained, massive or laminated. Framboidal and anhedral pyrite grains occur in the black shales, and pyrite content decreases from the sulfide ore layer upwards. Nodular phosphorite locally occurs below the sulfide ore layer. The size of the phosphorite nodules is variable, ranging from several mm to about 1 meter, and is mostly in the cm range (Fig. 7-4 C). Bioclasts can be observed in phosphorus-rich debris (Fig. 7-4 D). The Ni-Mo ore occurs within the lowermost few meters of the Niutitang Formation as both fine laminations and as a debris layer (Fig. 7-4 E), consisting largely of a MoSC phase (with the approximate composition of $[(Mo,Fe,Ni)(S,As)_2C_7]$, pyrite, vaesite, bravoite, millerite, gersdorffite and jordisite, with minor arsenopyrite, chalcopyrite, covellite, sphalerite, tennantite, tiemannite, violarite and native Au (Fig. 7-4 G, Conveney et al., 1994; Kao et al., 2001; Mao et al., 2002; Jiang et al., 2006). The amorphous MoSC phase (about 20 vol.%) is the only important Mo-carrier, in mm-sized ellipsoidal aggregates or fine laminations (Fig. 7-4 E). Rip-up clasts of MoSC phase aggregates are set in in-situ precipitated organic matter and Ni-bearing minerals (Fig. 7-4 H). Sapropel material (about 45 vol.%) occurs as matrix, and consists of organic matter, fine-grained illite, sericite, quartz, calcite, barite, and locally abundant apatite and collophane. The organic matter is derived from in-situ sapropelized products of planktonic and benthic organisms, oncolite-like algal/bacterial remnants, and oil-derived migrabitumen, and has a high thermal maturity corresponding to the semi-anthracite to anthracite coalification stage (Kribek et al. 2007). Pyrite (about 25 vol.%) is intergrown with the MoSC phase in oncolite-like aggregates (Fig. 7-4 F), and is cut by veinlets with nickel sulfides (about 5 vol.%, millerite, gersdorffite). Sedimentary features such as fine lamination and rip-up clasts and oncolites of pyrite and Ni-Mo sulfide ore indicate an origin as deeper-water hardground supplied with organic material from algal mats from a wave-agitated, shallow-water environment (Kribek et al., 2007).

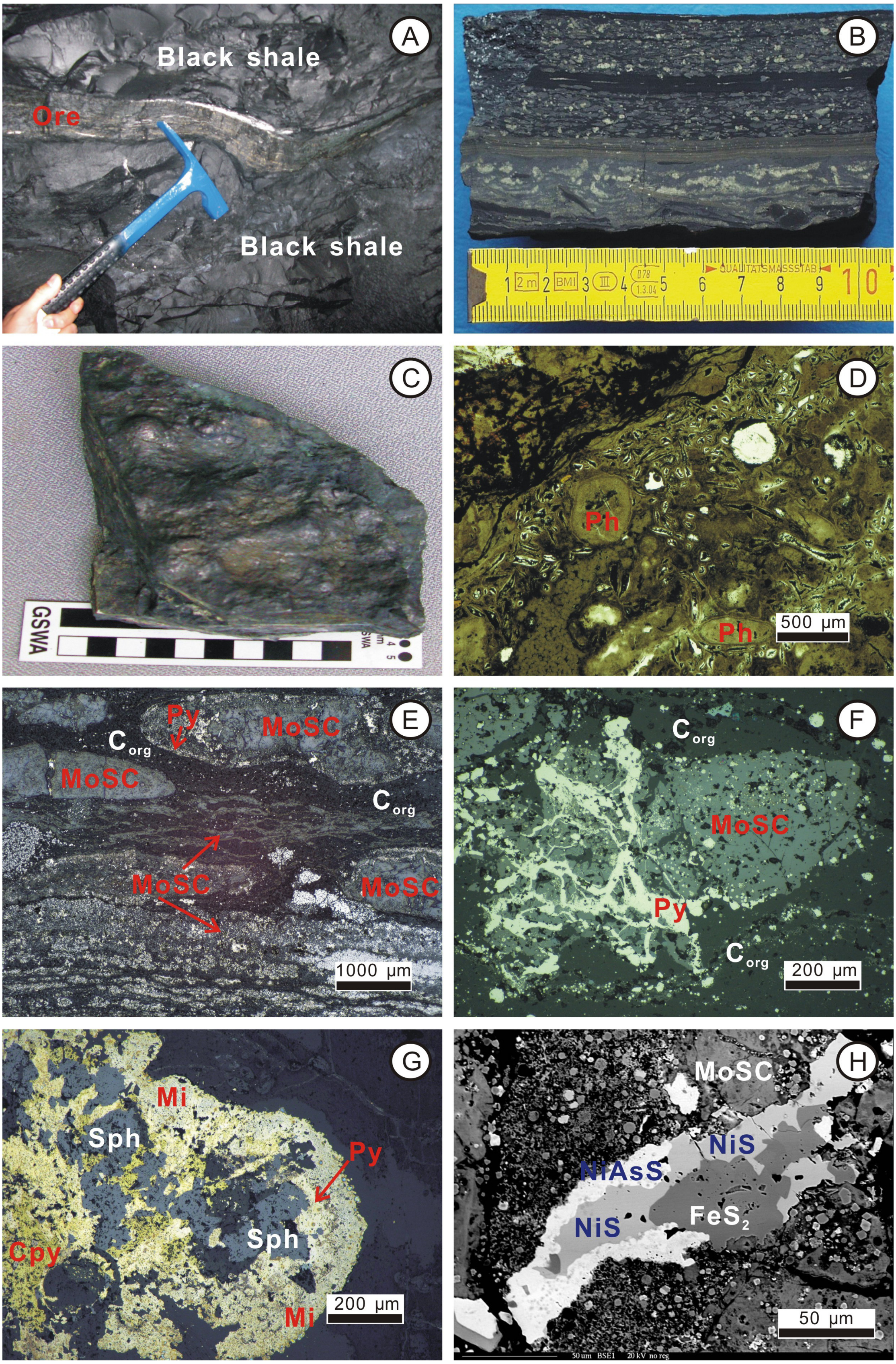

Fig. 7-4: Textures of the polymetallic Ni-Mo-PGE-Au sulfide layer. **A:** The 5 cm-thick sulfide bed showing a clear-cut boundary with the black shale host sequence (Dazhuliushui underground mine). **B:** Intraformational polymictic

clast units with interlayers of black shale material. Sulfide clasts in light color, sapropel matrix dark. **C:** Black shale with phosphorite nodules from footwall of the polymetallic sulfide ore layer (Sancha underground mine). **D:** Microphotograph of phosphorus-rich materical with bioclasts (Dazhuliushui underground mine). **E:** Laminated and ellipsoidal MoSC phase with fine-grained pyrite rims surrounded by sapropel matrix. Re-deposited rip-up clasts in matrix of in-situ precipitated organic matter (Sancha underground mine). **F:** Pyrite veinlets in MoSC phase in matrix of organic matter (Sancha underground mine). **G:** Sphalerite, chalcopyrite, millerite intergrown with anhedral pyrite (Sancha underground mine). **H:** Back-scatter electron image of a diagenetic nickel-rich veinlet in MoSC phase with bacterial (?) features. Abbreviations: Cpy = chalcopyrite, Ph = phosphate, Mi = millerite, C_{org} = organic matter, Py = pyrite, Sph = sphalerite.

7.6 Sampling and analytical techniques

A total of 26 polymetallic Ni-Mo-PGE-Au sulfide ore samples, 17 host black shale samples and 1 phosphorite sample were collected from the Dazhuliushui, Maluhe, Sancha and Cili mine sites. From this sample set, 6 sulfide ores, 3 host black shales and 1 phosphorite were measured for Mo isotope composition, and 17 sulfide ores were analyzed for PGE + Au concentrations. All samples were collected from underground mine sites to avoid weathering. Bulk samples (0.5-1 kg) were crushed, split and powdered (~200 mesh) with an agate shatter box.

7.6.1 Mo purification and isotope analyses

Between 4.5 and 5.0 g of powered sample was oxidized at 800°C for 12 hours to remove organic matter and about 0.1 g was employed for Mo isotope measurement for each sample. Mo was purified using the separation procedure described in Siebert et al. (2001), Wille et al. (2008) and Voegelin et al. (2009). A minor modification was done for the very Mo-rich ore samples. According to the previously determined Mo concentration, the approximate sample weight needed for measurement was calculated. The ore samples (up to several wt.% Mo) were then pre-diluted to the ppm level to prevent lab contamination. To account for Mo isotope fractionation during column separation and to resolve instrumental mass bias, a calculated amount of ^{97}Mo-^{100}Mo double spike was added prior to dissolution and chemical purification. The ^{97}Mo-^{100}Mo double spike technique has several advantages: 1) low natural abundance of ^{97}Mo and ^{100}Mo, 2) no elemental isobaric interferences on ^{97}Mo, and ^{100}Mo is reducible from isobaric interferences of ^{100}Ru, and 3) highly enriched ^{97}Mo and ^{100}Mo can be obtained (Siebert et al., 2001).

The black shale sample with about 50 ng Mo was put in a Teflon beaker together with 6 M HCl to keep Mo in its highly soluble Mo^{6+} oxygenation state, and then heated to ~100°C on a heating stage overnight. The sample material was dried and dissolved with concentrated HF and HNO_3 (4:1) at ~100°C. Subsequently, organic and detrital material was separated from solution by centrifugation. The solution was transferred into another Teflon beaker. In order to completely leach Mo, the residue was again heated in 6 M HCl at ~100°C overnight, and then added to the second beaker. The aliquots were combined and dried on a hot plate. After evaporation, the material was taken up in pre-prepared HCl + H_2O_2 resolution (5 ml 4 M HCl and 0.3% H_2O_2) and loaded onto an anion exchange resin to wash out cations, followed by six-block stepwise loading onto anion exchange columns (Dowex^{TM} 1X8 resin, 200 - 400 mesh). Finally, the molybdate anion was eluted with 2 M HNO_3. For cleaning Fe and Zr from Mo solution, 6 ml 2 M HNO_3 is added to extract the Mo fraction, which is collected in a Teflon beaker and left to dry on a heating stage. A cation exchange column (Dowex 50WX8^{TM} resin, 200 - 400 mesh) was used to remove residual Fe. The dried Mo fraction is redissolved in 1 ml 0.5 M HCl and 0.1% H_2O_2 solution twice, and collected in a Teflon beaker. The remaining Mo is eluted with 4 ml 0.5 M HCl and 0.1% H_2O_2 solution and collected in the same beaker. Finally, the Mo-bearing solutions are dried and measured in 0.5 M HNO_3 solution on a Nu Instruments MC-ICP-MS connected to an ESI Apex nebulizer. A measurement usually consists of 4 blocks with 10 cycles each. One standard and three black shale samples were analyzed alternately so as to monitor for drift in instrument sensitivity.

The molybdenum stable isotope analyses were carried out using a Nu instruments MC-ICP-MS at the Isotope Laboratory of the University of Bern in Switzerland. The molybdenum isotope data are reported as defined in previous studies as $\delta^{98/95}Mo_{sample}(‰) = [\,^{98/95}Mo_{sample}/^{98/95}Mo_{standard}-1] \times 1000$. Throughout the text, sample Mo isotope data are reported as $\delta^{98/95}Mo$ relative to the Bern Laboratory standard solution (Johnson Matthews, 1000 μg/ml (± 0.3%) ICP standard solution) as in Siebert et al. (2003) and McManus et al. (2002). The external standard reproducibility was 0.1 $\delta^{98/95}Mo$ (2 σ).

7.6.2 PGE geochemistry

The PGE + Au concentrations of the polymetallic sulfide ores were analyzed in the National Research Center of Geoanalysis in Beijing using NiS-fire assay pre-concentration followed by ICP-MS measurement. A sample aliquot of 30 g powder was mixed with sodium carbonate, sodium borate, borax, glass powder, nickel powder, iron powder, sulfur and wheat flour. The mixture was transferred into a fire-clay crucible with an appropriate amount of ^{190}Os spike solution and covered with a thin $Na_2B_4O_7$ layer. The crucible was fused at 1150°C for 1 h and dried under an infrared lamp. After cooling, the crucible was broken and the Ni-Fe button removed into a glass beaker containing 60 ml H_2O for a minimum of 10 h. To better dissolve the button, ~30 ml HCl was added into the beaker and heated at ~110°C, until the solution became clear and little residue remained. The solution was then filtered by a milli-pore filter membrane (diameter 25 mm, 0.45 mm). The residue was collected and washed 5 times with ~15 ml water. Subsequently, the residue and the filter membrane were transferred into a 7 ml Telflon beaker, and sealed together with 1 ml HCl + 1 ml H_2O_2. The beaker was then heated at ~110°C for 1.5 h. After cooling to room temperature, the beaker was opened and the solution was transferred and diluted with H_2O to 10 ml for ICP-MS analysis. The detection limit is 0.02 ng/g for Ru, 0.001 ng/g for Rh, 0.06 ng/g for Pd, 0.007 ng/g for Os, 0.01 ng/g for Ir and 0.03 ng/g for Pt.

7.6.3 Trace and rare earth element geochemistry

Bulk powdered samples were analyzed for trace element and rare earth element composition. Sulfide ore samples from Dazhuliushui, Maluhe and Sancha were analyzed by X-ray fluorescence spectrometry (XRF) on lithium-metaborate fused disks at the Federal Institute for Geosciences and Natural Resources in Hanover, Germany. Relative uncertainties of the XRF analyses were calculated according to the method of Rousseau (2001), with 10 - 30% for most trace elements. All samples from Cili and black shales from Dazhuliushui, Maluhe and Sancha were determined using a Finnigan MAT ELEMENT high resolution inductively coupled plasma-mass spectrometer (ICP-MS) at the Chinese National Research Center of Geoanalysis in Beijing, following the methods of Balaram et al. (1995) and Wu et al. (1996). Analytical reagent-grade HF and HNO_3 were used and purified prior to use by sub-boiling distillation. The PTFE bombs were cleaned for 1 h using 20 vol.% HNO_3 heated to 100°C. Around 100 mg of powdered sample was digested with 1 ml HF and 0.5 ml HNO_3 in screw top PTFE-lined stainless steel bombs at 190°C for 12 h. The solution was then drained and evaporated to dryness with 0.5 ml HNO_3. This procedure was repeated for twice. The final residue was re-dissolved by adding 8 ml 40 vol.% HNO_3. Subsequently, the bomb was resealed and heated in electric oven at 110°C for 3 h. After cooling to room temperature, the final solution was diluted to 100 ml by adding distilled de-ionized water. The reagent blanks were treated exactly following the same procedures as samples. Errors for trace and rare earth elements in this study are within ± 6% (1 σ).

7.7 Results

Mo isotope and abundance data of polymetallic Ni-Mo-PGE-Au sulfide ores, host black shales and a phosphorite from Maluhe, Dazhuliushui and Sancha are listed in Table 7-1, together with previously reported data by Lehmann et al. (2007). Mo concentrations of the polymetallic sulfide ores are high, ranging from 29000 to 73000 ppm, with average of 57800 ppm. The Mo isotope data are relatively consistent, ranging from 0.94 to 1.37‰ with an average value of 1.13 ± 0.14‰ (1 σ). In contrast, the host black shales and the phosphorite are characterized by relatively low Mo concentrations, varying from 12.0 to 293 ppm (average of 119 ppm). Their $\delta^{98/95}$Mo values are variable, ranging from 0.48 to 1.90‰ with an average value of 1.28 ± 0.41‰ (1 σ), slightly heavier than that of the sulfide ores but fully overlapping their compositional range.

Table 7-1

Mo isotope composition of the sulfide ores, host black shales and phosphorite from polymetallic Ni-Mo-PGE-Au sulfide mine sites on the Yangtze Platform, South China.

Sample	Lithology	Stratigraphic position (m)	Mo (ppm)	$\delta^{98/95}$Mo (‰)	2 σ
Maluhe					
MLH-4	black shale	0.2	142	1.70	0.05
MLH-5	sulfide ore	0	70900	1.38	0.02
MLH-2	sulfide ore	0	61600	1.37	0.03
MLH-6	phosphorite	-0.2	117	1.57	0.03
Dazhuliushui					
DZLS-7	black shale	0.2	65.2	0.89	0.02
DZLS-8	sulfide ore	0	62900	1.07	0.06
DZLS-2	sulfide ore	0	73000	1.16	0.04
DZLS-9	black shale	-0.2	90.6	1.58	0.03
Sancha					
SC-11	sulfide ore	0	65900	1.19	0.02
SC-2	sulfide ore	0	56400	1.00	0.03
Huangjiawan					
ZG-1	sulfide ore	0	42200	0.94	0.04
ZG-2	sulfide ore	0	54100	1.05	0.02
ZH-1	sulfide ore	0	29000	1.13	0.04
ZH-2	sulfide ore	0	71000	0.97	0.02
ZH-5	sulfide ore	0	48800	1.20	0.04
Ganziping					
ZG-3	black shale	-0.7	209	1.50	0.04
ZG-7	black shale	1.5	115	1.90	0.04
ZG-7	black shale	1.5	115	1.87	0.04
ZG-11	black shale	1.8	102	1.25	0.04
ZG-17	black shale	4.5	293	0.81	0.04
ZG-17	black shale	4.5	293	0.94	0.06
ZG-26	black shale	46.5	54.0	1.22	0.04
ZG-29	black shale	61	35.0	1.06	0.04
Yuanling					
L-60	black shale	0	22.0	1.10	0.04
L-66	black shale	6	12.0	0.48	0.04

Data of the Huangjiawan, Ganziping and Yuanling are from Lehmann et al. (2007). Location of each mine site is show in Fig.1 and Fig.3. Stratigraphic position is in meter relative to the polymetallic Ni-Mo-PGE-Au sulfide ore layer. $\delta^{98/95}$Mo values are relative to the Bern Laboratory standard as in MacManus et al. (2002) and Siebert et al. (2003). An assessment of the analytical uncertainty is the 2 σ external standard reproducibility of samples.

PGE concentrations in polymetallic Ni-Mo-PGE-Au sulfide ores and their host black shales from the Dazhuliushui, Maluhe and Sancha mine sites are presented in Table 7-2, which also includes some previously reported PGE + Au data from the polymetallic sulfide ore and the host black shales from Hunan and Guizhou provinces (Li and Gao, 2000; Mao et al., 2001; Wu et al., 2001; Luo et al., 2003; Lehmann et al. 2007). Reference data for PGE + Au concentrations of present-day seawater, massive sulfide ore from the Dajing Cu deposit (Sedex type), the Kuroko Cu-Pb-Zn deposits (VMS type), and the Roman Ruins and Satanic Mills (active black smokers) are also shown in Table 7-2. Average PGE concentrations in the polymetallic sulfide ores are 130 ppb Os, 9.59 ppb Ru, 3.71 ppb Ir, 12.9 ppb Rh, 315 ppb Pd and 310 ppb Pt. The host black shales have average 5.86 ppb Os, 6.76 ppb Ru, 1.13 ppb Ir, 1.04 ppb Rh, 20.0 ppb Pd and 37.8 ppb Pt. Au concentrations in the polymetallic sulfide ores vary from 70.0 to 553 ppb (average of 300 ± 153 ppb, 1 σ, n = 18), much higher than in the host black shales, ranging from 0.13 to 50.0 ppb (average of 8.21 ± 10.3ppb, 1 σ, n = 22). The Au/Pd ratio of the average sulfide ore is 0.97, in the same range with the average black shale (0.41) and present-day seawater (0.33), but remarkably lower than hydrothermal massive sulfides. Au/Pd ratios of massive sulfides form Kuroko deposits, and the Roman Ruins and the Satanic Mills vents are 139, 1495 and 20714, respectively. The Pt/Pd ratio of the average sulfide ore is 0.99, in the same range with that of average black shale (1.89) and present-day seawater (0.83). However, Pt/Pd ratios of the hydrothermal massive sulfide occurrences are variable, with 0.13, 0.57, 0.56 and 27.6 for the Dajing, Kuroko, Roman Ruins and Satanic Mills sulfides, respectively.

Table 7-2

PGE data of the polymetallic Ni-Mo-PGE-Au sulfide ores and the host black shales, compared to present-day seawater and hydrothermal sulfide deposits (ppb).

Sample	Lithology	Os	Ru	Rh	Pd	Ir	Pt	Au	Au/Pd	Pt/Pd	Ir/Ir*	Pt/Pt*	Data source
Dazhuliushui													
DZLS-2	sulfide ore	148	5.96	11.3	297	1.92	255			0.86	0.01	0.84	This study
DZLS-5	sulfide ore	163	8.02	11.8	284	2.34	253			0.89	0.01	0.86	
DZLS-8	sulfide ore	150	7.65	13.4	365	2.64	334			0.92	0.01	0.90	
DZLS-11	sulfide ore	128	5.28	9.92	275	1.95	235			0.85	0.01	0.84	
DZLS-14	sulfide ore	104	4.51	8.47	215	1.86	202			0.94	0.01	0.91	
DZLS-17	sulfide ore	116	8.07	10.6	229	2.11	237			1.03	0.01	0.98	
Maluhe													
MLH-2	sulfide ore	108	11.3	12.3	236	2.12	207			0.88	0.01	0.81	
MLH-5	sulfide ore	116	7.57	10.4	228	2.35	241			1.06	0.02	1.00	
MLH-8	sulfide ore	149	10.8	12.8	258	2.40	250			0.97	0.01	0.91	
MLH-10	sulfide ore	127	9.21	12.6	269	2.50	277			1.03	0.01	0.97	
MLH-11	sulfide ore	128	9.35	12.9	280	2.66	295			1.05	0.01	1.00	
MLH-12	sulfide ore	121	6.83	8.78	207	2.02	218			1.05	0.01	1.01	
Sancha													
SC-2	sulfide ore	174	11.1	15.6	401	2.81	382			0.95	0.01	0.93	
SC-5	sulfide ore	80.9	9.60	12.8	286	1.51	245			0.85	0.01	0.82	
SC-8	sulfide ore	78.6	4.52	5.79	164	1.06	145			0.88	0.01	0.87	
SC-11	sulfide ore	171	13.6	12.8	289	2.31	277			0.96	0.01	0.91	
SC-14	sulfide ore	197	12.6	15.6	369	3.05	407			1.10	0.01	1.06	
HJW-1-1	sulfide ore	134			347		406			1.17			Mao et al., 2002
HJW-1-3	sulfide ore	124			291		337			1.16			
HJW-2-3	sulfide ore	162			451		477			1.06			
ZHL-7	sulfide ore	142			446		460			1.03			
ZHL-7-1	sulfide ore	157			338		360			1.07			
ZHL-7-2	sulfide ore	153			403		386			0.96			
ZHL-7-3	sulfide ore	142			408		444			1.09			

Table 7-2（continued）

Sample	Lithology	Os	Ru	Rh	Pd	Ir	Pt	Au	Au/Pd	Pt/Pd	Ir/Ir*	Pt/Pt*	Data source
GZP5-2	sulfide ore	150	9.00	11.0	310	2.00	360	170	0.55	1.16	0.01	1.14	Li and Gao, 2000
GZP-6	sulfide ore	100	7.00	8.00	240	4.00	240	90.0	0.38	1.00	0.02	0.99	
DS14B1	sulfide ore	52.0	3.00	3.00	45.0	1.00	45.0	171	3.80	1.00	0.03	0.88	
DS14B2	sulfide ore	51.0	3.00	2.00	45.0	2.00	45.0			1.00	0.07	0.95	
T1-1	sulfide ore	160	8.00	12.0	380	1.00	380	260	0.68	1.00	0.004	1.00	
T4-3	sulfide ore	190	8.00	16.0	580	1.00	580	70.0	0.12	1.00	0.003	1.01	
T11-2	sulfide ore	110	6.00	11.0	270	1.00	270	160	0.59	1.00	0.01	0.97	
ZT05B4	sulfide ore	140	40.0	14.0	240	43.0	240	349	1.45	1.00	0.27	0.91	
ZXZ-C	sulfide ore	214	14.7	17.0	679	3.30	619	553	0.81	0.91	0.01	0.93	Luo et al., 2003
XZ3-3	sulfide ore	144	36.3	9.70	313	4.40	360	158	0.50	1.15	0.02	1.15	
ZN-10	sulfide ore	135	13.7	8.90	504	4.00	329	265	0.53	0.65	0.01	0.69	
ZH-1	sulfide ore	135	12.0	17.3	419	5.38	358	280	0.67	0.85	0.02	0.82	Lehmann et al., 2007
ZH-2	sulfide ore	109	8.92	16.4	412	4.03	347	360	0.87	0.84	0.02	0.82	
ZH-5	sulfide ore	127	5.78	16.7	421	4.07	337	282	0.67	0.80	0.02	0.78	
Z-6	sulfide ore	115	7.00	15.4	379	3.75	340	529	1.40	0.90	0.02	0.87	
Z-11	sulfide ore	130	9.63	16.7	421	3.58	349	432	1.03	0.83	0.01	0.80	
Z-12	sulfide ore	114	3.78	10.6	267	2.40	226	269	1.01	0.85	0.01	0.82	
ZG-1	sulfide ore	157	7.12	18.7	463	4.03	405	540	1.17	0.87	0.01	0.85	
ZG-2	sulfide ore	147	4.36	14.3	385	4.37	383	457	1.19	0.99	0.02	0.97	
GZP5-1	balck shale	4.00	1.00	6.00	100	<1	180	50.0	0.50	1.80		1.63	Li and Gao, 2000
DG08	balck shale	2.00	2.00	<1	<1	<1	4.00	6.00					
DG09	balck shale	<1	1.00	<1	2.00	<1	7.00	9.00	4.50	3.50			
DG10	balck shale	21.0	92.0	<1	10.0	3.00	16.0	6.00	0.60	1.60	0.37		
T5-1	balck shale	7.00	1.00	1.00	86.0	<1	46.0	17.0	0.20	0.53		0.58	
T20-4	balck shale	4.00	1.00	1.00	35.0	<1	25.0	10.0	0.29	0.71		0.72	
DZ-6	balck shale	2.00	<1	<1	40.0	<1	76.0	10.0	0.25	1.90			
DZ-13	balck shale	1.00	1.00	<1	22.0	1.00	110	10.0	0.45	5.00	0.03		

Table 7-2 （continued）

Sample	Lithology	Os	Ru	Rh	Pd	Ir	Pt	Au	Au/Pd	Pt/Pd	Ir/Ir*	Pt/Pt*	Data source
JH-12	black shale		1.80	0.20	5.30	0.50	17.0	5.00	0.94	3.21	0.08	3.13	Luo et al. 2003
ZY-1	black shale		1.90	0.30	20.0	0.60	18.0	17.8	0.89	0.90	0.05	0.96	
YX7	black shale		3.88	0.07	7.79	1.14	44.2	3.46	0.44	5.67	0.08	6.17	Wu et al. 2001
H5-2	black shale		5.27	2.31	5.74	0.92	22.4	1.17			0.12	1.64	
H5-1	black shale		2.57	1.93	1.98	1.35	21.6	2.08	1.05	10.9	0.22	2.43	
H27	black shale		1.80	0.28	3.22	0.74	17.2	1.74	0.54	5.33	0.13	4.42	
H19	black shale		0.93	0.24	4.51	2.12	13.3	4.80	1.06	2.95	0.41	2.73	
G45	black shale		3.06	0.35	3.84	1.22	17.8	1.88	0.49	4.63	0.20	3.79	
G22	black shale		2.39	0.29	3.88	0.45	17.0	1.16	0.30	4.37	0.08	3.77	
G18	black shale		6.88	0.23	2.81	0.76	19.3	3.29	1.17	6.87	0.13	5.79	
G14	black shale		1.80	0.52	9.37	0.71	41.0	0.77	0.08	4.38	0.05	4.02	
G12	black shale		3.14	0.19	1.60	0.26	11.8	0.13	0.08	7.39	0.07	5.59	
D8	black shale		4.31	1.98	48.5	1.75	67.0	10.9	0.22	1.38	0.05	1.33	
D7	black shale		3.16	0.83	6.62	1.53	40.6	8.47	1.28	6.13	0.12	4.55	
Average sulfide ore		134	9.81	12.1	328	3.78	315	300	0.97	0.97	0.02	0.92	
Average black shale		5.86	6.76	1.04	20.0	1.13	37.8	8.21	0.41	1.89	0.06	1.71	
Present-day seawater		0.000002	0.000005	0.00008	0.00006	0.0000001	0.00005	0.00002	0.33	0.83	0.003	0.14	Nozaki, 1997
Dajing (Sedex Cu)			11.7		21.9	1.74	2.82			0.13	0.17	0.07	Chu et al., 2002
Kuroko (VMS Cu-Pb-Zn)			0.41	0.49	1.37	0.07	0.78	191	139	0.57	0.09	0.26	Pan and Xie, 2001
Roman Ruins (black smoker)			1.80	3.50	9.90	0.80	5.50	14800	1495	0.56	0.14	0.25	Pasava et al., 2004
Satanic Mills (black smoker)			66.5	162	0.70	3.70	19.3	14500	20714	27.6	0.74	0.03	Pasava et al., 2004

Average sulfide ore and average black shale denote average values of the polymetallic sulfide ores (n = 43) and the host black shales (n = 22), respectively. Dajing (Sedex Cu) represents for average value of sulfides from the Dajiang polymetallic Cu deposit, North China (n = 4). Kuroko (VMS Cu-Pb-Zn) is average value of sulfides from the Kuroko deposit, Japan (n = 4). Roman Ruins and Satanic Mills represent for average values of sulfide mounds from hydrothermally active black smokers in the PACMANUS hydrothermal field, Papua New Guinea (n = 15 and 6, respectively).

Trace element and REE concentrations in polymetallic Ni-Mo-PGE-Au sulfide ores and in host black shales are shown in Table 7-3 and 7-4, respectively. Trace element concentrations in present-day seawater, selected syngenetic hydrothermal massive sulfides (including the Red Dog Sedex-type Zn-Pb-Ag sulfides and the Neves-Corvo VMS-type Cu-Sn sulfides) and a modern active hydrothermal vent (Hanging Garden vent) are also presented in Table 7-3 for comparison. Trace element enrichments in the polymetallic sulfide ores are generally higher than in the host black shales, except for Cr, Cs, Ga, Nb, Rb, Sc, Ta and Zr which are more enriched in the host black shales than in the polymetallic sulfide ores. REE + Y concentrations were normalized to chondrite (Anders and Grevesse, 1989). The REE + Y concentrations in present-day seawater, hydrothermal sulfides (including the Changba Sedex-type Zn-Pb sulfides and the Neves-Corvo VMS-type Cu-Sn sulfides) and a modern active hydrothermal vent (Hanging Garden vent) are also included in Table 7-4. The REE + Y pattern of the average polymetallic sulfide ore is generally similar to the average black shale. Both are characterized by slightly negative Eu anomaly and pronounced Y enrichment. ∑REE + Y in the polymetallic sulfide ores vary from 43.9 ppm to 1615 ppm (average of 369 ppm), higher than in the host black shales which range from 15.7 ppm to 270 ppm (average of 169 ppm). ∑REE + Y contents in polymetallic sulfide ores from the Dazhuliushui, Maluhe, Sancha and Cili sites are variable, ranging from 99.5 ppb to 409 ppb, from 90.2 ppb to 341 ppb, from 387 ppb to 980 ppb, and from 43.9 ppb to 1615 ppb, with an average of 267 ppb, 147 ppb, 618 ppb and 447 ppb, respectively. Y/Ho ratios of the polymetallic sulfide ores are high, ranging from 37.9 to 58.8 with an average of 49.6, consistent with present-day seawater of 47.2. In contrast, the host black shales are characterized by low Y/Ho ratios, ranging from 29.6 to 39.6 with an average of 32.6, similar to average continental crust. Average Y/Ho ratio of syngenetic hydrothermal massive sulfide from the Neves-Corvo deposits is 30.0.

Table 7-3

Trace elements of the polymetallic Ni-Mo-PGE-Au sulfide ores and the host black shales, compared to that of the present-day seawater, hydrothermal sulfides and active hydrothermal vents (ppm).

Sample	Lithology	Ba	Bi	Co	Cr	Cs	Cu	Ga	Hf	Mo	Nb	Ni	Pb	Rb	Sb	Sc	Sn	Sr	Ta	Th	U	V	W	Zn	Zr
Dazhuliushui																									
DZLS-2	sulfide ore	391	19.0	273	53.0	8.00	2450	3.00	11.0	73100	<5	62700	183	29.0	257	3.00	<4	342	<15	100	125	658	38.0	3460	30.0
DZLS-5	sulfide ore	332	12.0	136	51.0	5.00	1680	<2	<8	92800	<5	34800	74.0	17.0	104	4.00	<4	341	<12	108	318	724	20.0	3580	37.0
DZLS-8	sulfide ore	680	22.0	220	55.0	7.00	2740	3.00	<9	62800	<5	60100	117	25.0	214	<1	<4	282	<15	95.0	114	644	33.0	4400	25.0
DZLS-11	sulfide ore	324	16.0	151	34.0	4.00	2330	4.00	<8	57600	<5	46100	182	25.0	251	3.00	<4	528	<14	77.0	255	486	32.0	3000	37.0
DZLS-14	sulfide ore	520	14.0	116	51.0	5.00	1510	5.00	<8	36400	<4	30500	127	38.0	155	6.00	<5	598	<12	64.0	260	462	12.0	4400	59.0
DZLS-17	sulfide ore	770	20.0	136	52.0	7.00	1910	6.00	<8	58500	<5	39300	141	27.0	224	4.00	<4	478	<13	87.0	133	655	27.0	4750	43.0
Maluhe																									
MLH-2	sulfide ore	518	20.0	254	64.0	12.0	1880	19.0	11.0	61600	<5	37700	235	39.0	279	1.00	6.00	40.0	<13	83.0	118	480	20.0	21200	63.0
MLH-5	sulfide ore	1740	16.0	255	53.0	13.0	1970	16.0	<9	70900	<5	36300	156	36.0	263	2.00	6.00	41.0	<13	96.0	112	423	19.0	26300	34.0
MLH-8	sulfide ore	1150	14.0	296	66.0	11.0	1810	20.0	<8	66100	<5	40800	157	37.0	342	4.00	5.00	111	<13	87.0	265	559	24.0	18000	71.0
MLH-10	sulfide ore	630	15.0	301	56.0	14.0	1830	18.0	<9	66900	<5	42600	62.0	33.0	216	2.00	6.00	30.0	<14	96.0	109	329	16.0	29200	30.0
MLH-11	sulfide ore	777	12.0	350	46.0	13.0	2050	14.0	<9	61200	<5	45500	90.0	27.0	222	2.00	<3	37.0	<14	84.0	137	258	25.0	29200	46.0
MLH-12	sulfide ore	734	10.0	206	86.0	15.0	1700	17.0	<8	65000	<5	28600	85.0	46.0	204	4.00	<4	33.0	<12	90.0	161	774	14.0	12800	63.0
Sancha																									
SC-2	sulfide ore	374	19.0	172	68.0	<3	2080	9.00	<8	56400	<4	61500	180	31.0	493	1.00	<4	178	<15	82.0	408	1680	48.0	4430	27.0
SC-5	sulfide ore	33500	16.0	176	66.0	<4	1310	<2	<9	3300	<3	59000	67.0	23.0	313	4.00	<5	943	<15	24.0	396	913	33.0	1520	27.0
SC-8	sulfide ore	21200	13.0	92.0	120	<4	733	<2	<8	17500	<3	27800	93.0	19.0	215	3.00	<5	750	<11	35.0	570	1210	20.0	829	25.0
SC-11	sulfide ore	3280	7.00	111	149	6.00	1180	7.00	<8	65900	<5	29900	37.0	34.0	267	3.00	<4	408	<11	84.0	595	3780	27.0	3860	36.0
SC-14	sulfide ore	7460	17.0	147	230	8.00	1620	<2	<8	51500	<4	47200	125	29.0	365	2.00	<4	304	<14	76.0	359	3290	32.0	517	25.0
Cili																									
CL-Ore-1	sulfide ore	11500	1.20	26.2		2.30	439	5.40	0.90	>2000	1.80	8870	27.3	16.7	88.5	3.00	3.00	724	0.10	2.40	118	857	20.9	853	28.7
CL-Ore-2	sulfide ore	>50000	1.70	49.2		3.40	522	6.60	1.10	>2000	1.90	>10000	35.4	27.0	63.9	4.00	2.00	1270	0.40	2.30	54.1	803	23.3	765	34.3
CL-Ore-3	sulfide ore	6240	2.60	36.4		6.80	644	13.6	2.50	>2000	4.90	8900	35.4	60.1	96.5	7.00	4.00	884	0.40	6.20	153	1370	16.2	2310	95.4
CL-Ore-4	sulfide ore	>50000	0.20	5.60		1.40	95.3	2.80	0.80	929	1.30	912	4.20	14.3	11.5	3.00	<1	349	0.40	1.50	27.4	178	1.60	145	25.6
CL-Ore-5	sulfide ore	>50000	1.40	27.6		3.40	872	10.6	0.70	>2000	1.60	6550	38.2	24.6	199	2.00	3.00	1560	0.40	1.90	160	3390	25.6	3590	24.7
CL-Ore-6	sulfide ore	32700	2.40	52.0		8.30	509	10.5	0.40	>2000	1.80	>10000	69.8	22.6	297	3.00	6.00	733	<0.1	1.90	106	3400	57.2	4960	27.2
CL-Ore-7	sulfide ore	15100	5.10	66.0		12.4	896	9.80	0.80	>2000	3.00	>10000	94.1	17.7	582	4.00	11.0	1030	<0.1	2.70	1220	1260	170	4810	43.1
CL-Ore-8	sulfide ore	>50000	5.20	102		5.50	528	14.3	2.10	>2000	5.10	>10000	33.4	57.5	77.7	6.00	6.00	292	0.60	5.60	76.7	1460	10.7	3290	75.1
CL-2	sulfide ore	10700	1.90	41.9		10.4	433	15.0	2.20	>2000	11.0	>10000	37.3	64.2	105	9.00	5.00	674	0.50	7.40	193	2210	35.7	1740	87.8

Table 7-3（continued）

Sample	Lithology	Ba	Bi	Co	Cr	Cs	Cu	Ga	Hf	Mo	Nb	Ni	Pb	Rb	Sb	Sc	Sn	Sr	Ta	Th	U	V	W	Zn	Zr
Dazhuliushui																									
DZLS-1	black shale	1290	0.40	26.4	92.7	7.14	91.1	17.4	2.61	66.2	11.3	304	17.0	91.1	70.7	13.3	0.91	165	0.79	8.89	28.6	370	1.90	68.1	112
DZLS-3	black shale	356	<0.05	7.77	10.8	0.30	13.4	2.10	0.36	14.3	1.61	83.4	2.43	6.39	1.79	4.76	0.09	362	0.20	0.93	6.89	36.6	0.22	71.5	16.4
DZLS-4	black shale	1280	0.69	28.3	94.6	6.39	98.6	16.5	2.37	1178	10.4	1300	14.6	109	8.28	12.9	2.42	210	0.72	8.44	32.1	685	1.80	420	106
DZLS-6	black shale	1400	0.32	27.5	96.6	5.39	55.0	16.2	4.03	81.8	14.5	258	13.4	82.2	3.52	12.1	2.03	180	0.91	9.06	23.4	994	1.25	117	185
DZLS-7	black shale	1330	0.34	22.5	93.0	7.76	71.4	20.9	3.30	65.2	11.8	332	15.3	111	7.36	13.6	4.54	217	0.78	10.6	30.6	409	2.66	66.9	149
DZLS-9	black shale	1120	0.26	18.5	85.1	5.40	52.8	18.1	4.87	90.6	13.6	249	15.4	56.5	5.47	11.1	4.19	195	0.86	11.1	24.5	320	2.53	306	225
Maluhe																									
MLH-1	black shale	1230	0.50	28.9	102	17.9	64.2	21.1	3.82	133	13.2	245	54.5	112	5.01	14.3		116	0.86	12.0	49.2	265	1.92	253	170
MLH-3	black shale	1070	0.53	20.3	184	19.7	104	31.7	6.24	844	18.5	1180	18.0	88.8	14.8	11.7		50.3	1.12	12.9	34.5	3174	2.97	1650	304
MLH-4	black shale	985	0.51	32.1	116	17.4	69.0	21.6	3.82	142	14.1	301	47.2	108	4.21	14.8		96.7	0.85	12.9	54.9	310	2.51	330	184
MLH-7	black shale	1340	0.40	22.7	118	18.1	73.7	22.6	3.87	114	13.9	386	37.0	121	10.2	16.0		91.0	0.83	13.0	56.4	463	2.05	364	182
Cili																									
CL-3	black shale	4270	0.80	23.7		12.7	136	22.0	3.80	292	11.6	375	33.1	139	4.80	15.0	2.00	147	0.80	12.6	82.6	1120	12.2	202	145
CL-4	black shale	1900	0.80	23.0		14.6	141	20.7	4.20	278	11.3	427	32.3	146	4.30	15.0	3.00	57.5	0.80	12.6	61.8	1450	8.30	1420	141
CL-5	black shale	1400	0.80	22.8		14.8	139	20.4	4.00	282	11.5	415	29.7	144	3.40	14.0	3.00	43.7	0.90	13.0	63.3	1740	6.80	2483	145
CL-6	black shale	1190	1.00	22.2		14.0	147	18.4	3.30	366	11.0	476	35.9	128	2.30	14.0	3.00	89.3	0.80	11.4	57.8	1580	5.70	1116	127
CL-7	black shale	920	0.90	20.8		13.1	123	17.2	3.90	217	11.7	186	37.1	129	1.40	14.0	2.00	88.8	0.80	15.4	52.2	549	4.90	84.0	133
CL-8	black shale	838	0.70	20.1		12.0	115	15.9	3.50	83.1	10.8	102	35.6	116	1.50	13.0	2.00	65.7	0.90	13.1	37.5	299	4.10	42.0	127
CL-9	black shale	1100	0.70	23.3		14.4	103	17.4	4.20	61.6	12.0	73.9	30.4	132	1.00	13.0	2.00	58.2	0.90	14.7	34.8	258	4.20	39.0	138
Average sulfide ore		6850	10.9	146.1	76.5	7.91	1370	10.4	3.05	53800	3.60	36000	95.6	31.5	227	3.56	5.25	498	0.40	53.8	252	1240	30.8	7460	43.1
Average black shale		1350	0.60	23.0	99.2	11.8	93.9	18.8	3.66	253	11.9	394	27.6	107	8.83	13.1	2.40	131	0.81	11.3	43.0	825	3.88	531	152
Present-day Seawater (ppt)		15000	0.03	1.20	210	306	150	1.20	3.40	10000	5.00	480	2.70	120000	200	0.70	0.50	7800000	2.50	0.02	3200	2000	10.0	350	15.0
Red Dog (Sedex Zn-Pb-Ag)		1220		33.5	22.1	2.29	107	4.70	<0.1	15.3	<0.1	31.4	56500	2.55	264	<1		56.2	<0.1	0.20	1.99	12.7		214000	3.60
Neves-Corvo (VMS Cu-Sn)		90.7	101	142	25.0	2.34	86600	37.0	0.87	<5	4.34	20.0	333	17.7	335	16.4	276000	70.7	0.33	2.74	3.78	61.3	529	5830	16.5
Hanging Garden vents		>1.5		0.01		0.03	2.80						0.08	2.80				5.80		0.0000003				6.90	

Average sulfide ore and average black shale represent for average values of the polymetallic sulfide ores and the host black shales from Dazhuliushui, Maluhe, Sancha and Cili polymetallic Ni-Mo-PGE-Au sulfide mine sites (n = 26 and 17, respectively). Present-day seawater data are from Nozaki, 1997. Red Dog (Sedex Zn-Pb-Ag) denotes average value of Zn-Pb-Ag massive sulfides from the Red Dog district, Northern Alaska (n = 22, Slack et al., 2004). Neves-Corvo (VMS Cu-Sn) is average value of a semimassive/massive Cu-rich ore and a massive Cu-Sn-rich ore from the Neves-Corvo deposit, Portugal (Relvas et al., 2006). Hanging Garden vents represents for modern active hydrothermal vents at 21°N (Data from www.earthref.org).

Table 7-4

REE data of the polymetallic Ni-Mo-PGE-Au sulfide ores and the host black shales, compared to present-day seawater, hydrothermal sulfides and active hydrothermal vents (ppm).

Sample	Lithology	La	Ce	Pr	Nd	Sm	Eu	Gd	Tb	Dy	Y	Ho	Er	Tm	Yb	Lu	Y/Ho	∑REE
Dazhuliushui																		
DZLS-2	sulfide ore	14.1	22.5	3.32	14.9	3.46	1.18	3.64	0.52	3.21	28.9	0.64	1.67	0.20	1.14	0.16	45.2	99.5
DZLS-5	sulfide ore	58.7	85.1	12.1	50.0	10.1	3.31	10.2	1.45	8.73	79.2	1.68	4.26	0.50	2.65	0.34	47.3	328
DZLS-8	sulfide ore	25.3	35.4	4.13	17.2	3.78	1.26	3.68	0.57	3.45	27.7	0.67	1.80	0.23	1.24	0.17	41.2	126
DZLS-11	sulfide ore	75.8	92.3	13.5	57.3	11.3	4.14	12.7	1.77	10.6	117	2.21	5.69	0.66	3.32	0.44	53.1	409
DZLS-14	sulfide ore	56.7	90.6	12.6	58.1	12.6	4.49	13.0	1.77	10.3	96.6	2.08	5.04	0.57	2.96	0.39	46.4	368
DZLS-17	sulfide ore	79.1	96.3	10.2	35.8	4.85	1.70	4.05	0.55	3.45	32.0	0.68	1.77	0.22	1.14	0.16	47.0	272
Maluhe																		
MLH-2	sulfide ore	15.7	32.0	4.71	22.3	5.67	1.18	5.70	0.81	4.73	34.9	0.92	2.32	0.28	1.50	0.21	37.9	133
MLH-5	sulfide ore	7.76	20.9	3.53	18.1	4.62	1.03	4.64	0.67	3.78	28.9	0.72	1.83	0.21	1.06	0.15	40.1	97.9
MLH-8	sulfide ore	28.5	72.8	12.2	59.4	14.6	3.23	15.0	2.17	12.9	106	2.57	6.51	0.78	3.99	0.53	41.3	341
MLH-10	sulfide ore	9.21	21.0	3.20	15.8	3.88	0.86	4.05	0.56	3.29	24.9	0.63	1.52	0.18	0.96	0.12	39.6	90.2
MLH-11	sulfide ore	10.8	25.9	4.08	20.4	4.90	1.08	5.17	0.72	4.12	33.2	0.79	1.96	0.24	1.22	0.17	41.9	115
MLH-12	sulfide ore	12.2	23.4	3.58	16.9	4.04	0.88	4.12	0.60	3.48	28.6	0.72	1.83	0.23	1.37	0.18	39.5	102
Sancha																		
SC-2	sulfide ore	80.3	101	15.4	64.9	12.0	2.16	14.0	1.88	11.8	148	2.60	6.92	0.80	4.00	0.51	56.9	466
SC-5	sulfide ore	59.3	81.9	13.4	57.5	10.8	2.92	12.9	1.80	11.5	129	2.56	7.00	0.87	4.67	0.63	50.5	397
SC-8	sulfide ore	154	158	26.9	110	19.7	4.97	25.5	3.53	22.8	307	5.22	14.1	1.69	8.97	1.21	58.8	862
SC-11	sulfide ore	153	188	35.9	155	29.4	5.64	35.3	4.71	28.4	313	5.93	15.1	1.70	8.45	1.12	52.7	980
SC-14	sulfide ore	59.7	65.0	12.6	54.4	10.6	2.40	13.4	1.84	11.8	140	2.62	7.07	0.86	4.49	0.59	53.4	387
Cili																		
CL-Ore-1	sulfide ore	30.1	42.0	5.31	22.6	4.37	2.25	4.92	0.81	4.65	51.4	1.02	2.66	0.36	2.20	0.31	50.4	175
CL-Ore-2	sulfide ore	19.1	28.6	3.68	15.1	3.38	1.42	4.27	0.64	3.87	37.2	0.87	2.23	0.32	2.04	0.28	42.8	123
CL-Ore-3	sulfide ore	39.8	64.5	8.16	34.9	7.50	3.04	8.38	1.28	7.39	73.7	1.61	4.34	0.59	3.08	0.46	45.8	259
CL-Ore-4	sulfide ore	5.9	9.20	1.19	4.60	1.18	1.53	1.59	0.24	1.40	14.5	0.35	1.00	0.15	0.92	0.13	41.4	43.9
CL-Ore-5	sulfide ore	134	131	29.1	130	25.4	8.79	34.0	5.03	29.8	357	6.69	18.1	2.15	10.9	1.44	53.3	923
CL-Ore-6	sulfide ore	72.0	76.2	13.5	55.4	12.2	4.06	14.5	2.25	12.6	150	2.81	7.42	0.94	4.82	0.62	53.3	429
CL-Ore-7	sulfide ore	277	376	46.0	203	36.7	9.17	47.8	6.77	40.5	520	9.03	24.4	2.87	14.5	1.79	57.6	1615
CL-Ore-8	sulfide ore	20.3	31.8	4.14	16.7	3.92	1.56	3.68	0.53	2.91	25.0	0.67	1.86	0.28	1.68	0.26	37.3	115
CL-2	sulfide ore	51.7	88.5	11.0	46.3	9.55	2.86	10.3	1.61	9.19	93.2	2.03	5.53	0.73	4.20	0.60	45.9	337

Table 7-4（continued）

Sample	Lithology	La	Ce	Pr	Nd	Sm	Eu	Gd	Tb	Dy	Y	Ho	Er	Tm	Yb	Lu	Y/Ho	∑REE
Dazhuliushui																		
DZLS-1	black shale	23.6	40.0	4.88	16.8	3.04	1.05	3.49	0.46	3.03	19.5	0.60	1.92	0.27	2.03	0.30	32.5	121
DZLS-3	black shale	2.3	4.11	0.49	2.15	0.44	0.26	0.52	<0.05	0.46	4.36	0.11	0.26	<0.05	0.25	<0.05	39.6	15.7
DZLS-4	black shale	25.1	43.5	4.97	18.4	3.27	0.95	3.41	0.48	2.93	21.3	0.60	1.80	0.27	1.68	0.29	35.5	129
DZLS-6	black shale	25.0	44.5	5.87	21.9	4.28	1.00	4.23	0.64	3.75	26.8	0.77	2.27	0.34	2.13	0.33	34.8	144
DZLS-7	black shale	25.5	60.4	5.47	20.0	3.89	1.45	4.95	0.63	3.74	25.2	0.80	2.38	0.37	2.33	0.37	31.5	157
DZLS-9	black shale	20.1	34.3	4.27	15.8	3.11	1.18	3.91	0.49	2.88	18.6	0.61	1.86	0.29	1.91	0.32	30.5	110
Maluhe																		
MLH-1	black shale	29.8	79.3	6.87	26.2	5.66	1.68	6.82	0.90	5.34	34.4	1.11	3.13	0.45	2.92	0.45	31.0	205
MLH-3	black shale	33.1	50.1	3.85	12.3	2.13	0.93	2.86	0.36	2.35	20.6	0.55	1.86	0.33	2.30	0.38	37.5	134
MLH-4	black shale	31.2	75.7	7.06	25.9	5.27	1.50	6.26	0.84	5.00	32.3	1.02	3.07	0.45	2.89	0.46	31.7	199
MLH-7	black shale	34.7	83.6	6.95	25.2	4.83	1.58	5.72	0.74	4.32	27.7	0.89	2.74	0.43	2.76	0.44	31.1	203
Cili																		
CL-3	black shale	35.7	68.7	8.05	30.8	6.08	0.88	5.54	0.92	5.24	41.2	1.20	3.66	0.55	3.43	0.54	34.3	212
CL-4	black shale	33.5	63.9	7.63	28.7	5.56	0.94	4.96	0.86	4.97	36.3	1.09	3.16	0.48	3.14	0.49	33.3	196
CL-5	black shale	34.6	67.9	8.20	30.8	6.02	1.05	5.52	0.94	5.50	39.6	1.18	3.44	0.53	3.34	0.51	33.6	209
CL-6	black shale	33.4	63.0	7.47	28.9	5.40	1.03	5.12	0.85	4.80	36.1	1.07	3.10	0.47	3.09	0.47	33.7	194
CL-7	black shale	40.4	89.5	10.9	43.1	8.71	1.69	8.35	1.35	7.48	48.6	1.49	4.14	0.58	3.62	0.52	32.6	270
CL-8	black shale	30.7	61.5	7.04	26.7	4.90	0.89	4.40	0.74	4.33	28.5	0.96	2.72	0.43	2.91	0.44	29.7	177
CL-9	black shale	34.7	69.5	8.05	30.3	5.54	1.04	5.08	0.85	4.86	30.8	1.04	3.03	0.48	3.13	0.47	29.6	199
Average sulfide ore		59.6	79.2	12.1	52.2	10.4	2.97	12.2	1.73	10.4	115	2.24	5.92	0.71	3.75	0.50	46.9	369
Average black shale		29.0	58.8	6.35	23.8	4.60	1.12	4.77	0.75	4.18	28.9	0.89	2.62	0.42	2.58	0.42	32.6	169
Present-day Seawater (ppt)		5.60	0.70	0.70	3.30	0.57	0.17	0.90	0.17	1.10	17.0	0.36	1.20	0.20	1.20	0.23	47.2	33.4
Changba (Sedex Zn-Pb)		4.79	8.35	1.18	3.60	0.74	0.31	0.57	0.09	0.52		0.11	0.30	0.28	0.30	0.05		21.2
Neves-Corvo (VMS Cu-Sn)		18.1	34.4	3.20	14.2	3.48	1.10	2.89	0.46	2.33	12.0	0.40	1.09	0.14	0.88	0.11	30.0	94.9
Hanging Garden vents			0.002		0.0005	0.0001	0.0003	0.00009		0.00007			0.00004		0.00003			

Average sulfide ore and average black shale represent for average values of the polymetallic sulfide ores and the host black shales from Dazhuliushui, Maluhe, Sancha and Cili polymetallic Ni-Mo-PGE-Au sulfide mine sites (n = 26 and 17, respectively). Present-day seawater data are from Nozaki, 1997. Changba (Sedex Zn-Pb) denotes average value of Zn-Pb massive sulfides from the Changba deposit, China (n = 2, Ma et al., 2004). Neves-Corvo (VMS Cu-Sn) is average value of a semimassive/massive Cu-rich ore and a massive Cu-Sn-rich ore from the Neves-Corvo deposit, Portugal (Relvas et al., 2006). Hanging Garden vents are active hydrothermal vents at 21°N (Data from www.earthref.org).

7.8 Discussion

7.8.1 Mo isotope composition

The Mo stable isotope system has been successfully applied to both paleoenvironmental reconstructions (e.g. Barling et al., 2001; Siebert et al., 2003; Anbar and Rouxel, 2007 and references herein) and metallogenic studies (e.g. Lehmann et al., 2007; Mathur et al., 2010). The metal enrichment of the polymetallic Ni-Mo-PGE-Au sulfide ore has been debated since its discovery. Lehmann et al. (2007) reported a small scatter of the $\delta^{98/95}$Mo values of 1.06 ± 0.10‰ for five polymetallic sulfide ores from Huangjiawan, ~10 km southeast of the Dazhuliushui mine site (Fig. 7-3 A), and suggested that the consistently heavy Mo was scavenged from coeval euxinic seawater. Based upon the fact that some $\delta^{98/95}$Mo values of sulfide ores are slightly lighter than for the host black shales, Jiang et al. (2007b, 2008) questioned this interpretation and proposed that the polymetallic sulfide ores are not derived from euxinic seawater, but from hydrothermal fluids. In combination with the data from Lehmann et al. (2007), $\delta^{98/95}$Mo values versus Mo concentrations in both polymetallic sulfide ores and host black shales are presented in Fig. 7-5. The average $\delta^{98/95}$Mo value of the polymetallic sulfide ores (1.13 ± 0.14‰) is slightly lighter than the average value of the host black shales (1.28 ± 0.41‰).

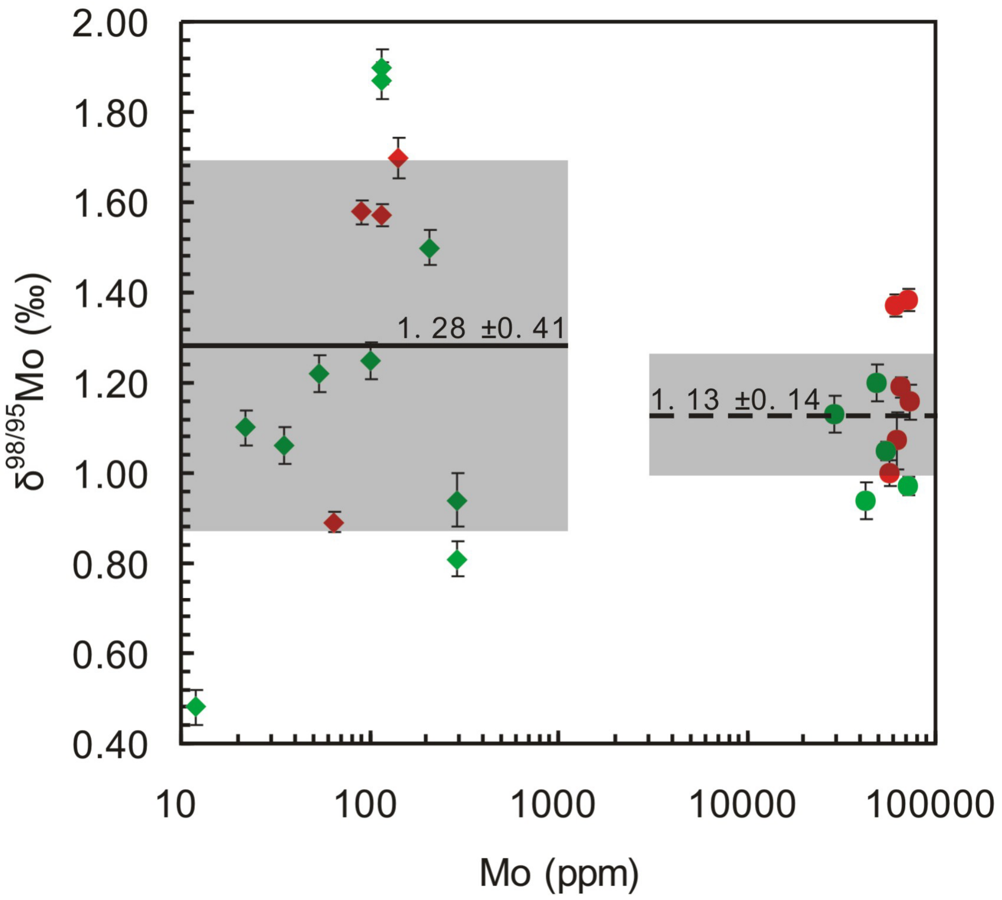

Fig. 7-5: Binary plot of Mo versus $\delta^{98/95}$Mo showing that polymetallic sulfide ores overlap with host black shales within 1 sigma variation range (grey shading). Diamond indicates black shale and solid circle indicates polymetallic sulfide ore samples. Solid and dashed black line represents average $\delta^{98/95}$Mo value of host black shales and polymetallic sulfide ores, respectively. Data are form Lehmann et al. (2007) (green) and this study (red).

If the assumption of Jiang et al. (2007b, 2008) is valid, that hydrothermal fluids only involved in the polymetallic sulfide ore but not in the host black shale, leading to $\delta^{98/95}$Mo values in sulfide ores slightly lower than in host black shales, two conclusions should be deduced: 1) the hanging wall black shales which were little or not influenced by hydrothermal fluids would be characterized by heavier Mo isotope composition, and 2) Mo concentrations in polymetallic sulfide ores would be inversely correlated with $\delta^{98/95}$Mo values. However, both deductions are not observed in this study. In fact, the $\delta^{98/95}$Mo values of the host black shales scatter strongly (Fig.

7-5), and some black shale samples above the polymetallic sulfide ore layer are characterized by relatively light $\delta^{98/95}$Mo (e.g. DZLS-7: 0.89 ± 0.02‰; ZG-17: 0.81 ± 0.04‰ and 0.94 ± 0.06‰ for duplicate measurement). The Mo isotope composition in sedimentary rocks can be affected by several factors, for instance, water column redox changes, local basin restriction, Mo recharge rate, and hydrothermal overprint. A black shale profile of the Early Cambrian Niutitang Formation proofed that $\delta^{98/95}$Mo values in black shales above the polymetallic sulfide ore layer are highly variable, ranging from -1.56 to 1.59‰ (Xu et al., in preparation), suggesting a partly closed basin situation with periodic replenishment. When the basins were freely connected to the open ocean, the Mo isotopic composition would reflect the open ocean Mo signature. When the ocean basins are restricted, Mo influx in such basins is dominated by continental input, and the Mo isotopic compositions of the sediments are thus representing terrigenous material with light $\delta^{98/95}$Mo values, but not the global coeval seawater, until replenishment by new seawater with heavy Mo signature restores the normal open-system situation.

MaManus et al. (2002) reported a relatively low $\delta^{98/95}$Mo of ~0.8‰ for a low-temperature ridge-flank hydrothermal system. Ryb et al. (2009) reported large (-0.9‰ to +3.5‰) $\delta^{98/95}$Mo variations occurred in Mo-enriched iron oxide veins located in the Dead Sea Rift valley, indicating that molybdenum isotope of hydrothermal systems is variable. If the Mo in the polymetallic sulfide ores was dominantly derived from hydrothermal fluids with light $\delta^{98/95}$Mo value, the higher the Mo content the closer the Mo isotope composition should be to hydrothermal fluids, i.e. have a light Mo isotope signature. That is, high-Mo polymetallic sulfide ore should be characterized by relatively light $\delta^{98/95}$Mo values. However, the negative correlation between Mo concentration and $\delta^{98/95}$Mo value in polymetallic sulfide ores is not observed (Fig. 7-6 A).

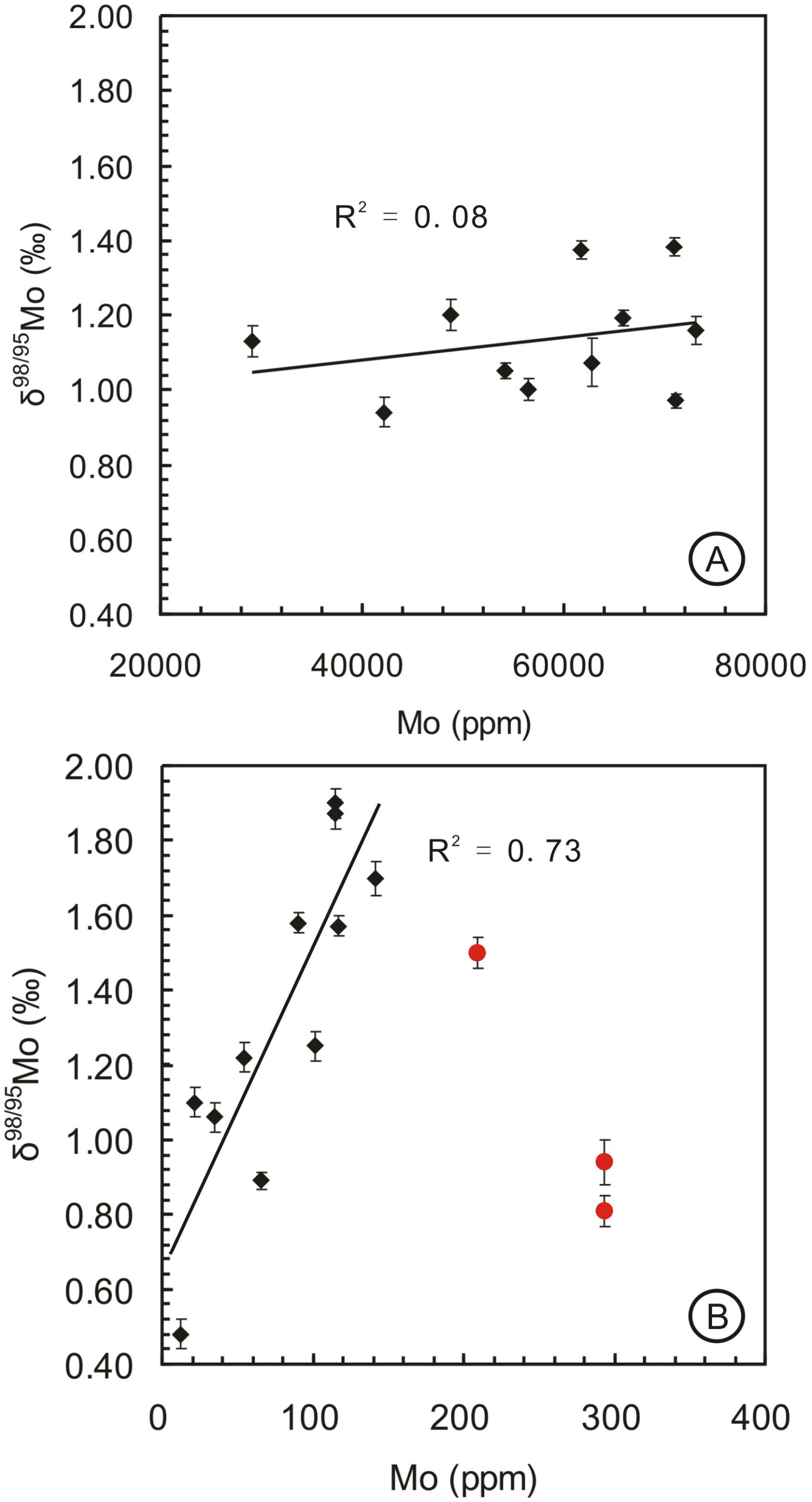

Fig. 7-6: A: Binary plot of $\delta^{98/95}$Mo and Mo concentration in polymetallic Ni-Mo-PGE-Au sulfide ores showing no correlation (R^2 = 0.08). **B:** Binary plot of $\delta^{98/95}$Mo and Mo concentration in host black shale showing a positive correlation for samples up to 150 ppm Mo. Three high-Mo black shale data (ZG-3 and ZG-17, duplicate measurement; red dots) do not follow the correlation trend.

By omitting two relatively high-Mo black shales (ZG-3 and ZG-17; duplicate measurement) of dataset by Lehmann et al. (2007), Jiang et al. (2008) suggested a positive correlation between Mo concentration and $\delta^{98/95}$Mo value for the host black shales. They interpreted a heavier authigenic euxinic-sourced seawater Mo mixed with a lighter Mo source of terrigenous materials in the black shales, and the two omitted black shales with relatively high Mo concentration (209 ppm and 293 ppm, respectively) may have been affected by hydrothermal fluid overprint. However, the interpretation for the omitted samples may be questionable because it is unlikely that hydrothermal fluids only affected the two black shales, but not others, considering the fact that there is a large stratigraphic distance between ZG-3 and ZG-17 (5.2 m) and low-Mo black shales are in between. More likely, the variation of Mo isotope composition is related to variable redox conditions. The positive correlation between Mo concentration and $\delta^{98/95}$Mo value (Fig. 7-6 B) may reflect that both authigenic seawater-sourced Mo and continental-sourced Mo contributed Mo to the black shales, and high-Mo samples (such as ZG-3 and ZG-17) may reflect changing redox conditions.

$\delta^{98/95}$Mo values of some polymetallic sulfide ores slightly lighter than those of the host black shales is not conflicting with the interpretation of the seawater scavenging model. Microscopic studies indicate that the polymetallic sulfide ore consists of in-situ precipitation and short distance re-deposition of sulfide aggregates (rip-up clasts from hardground). $\delta^{98/95}$Mo value in polymetallic sulfide ore is therefore a mixture of in-situ precipitated Mo and remobilized Mo. Regardless of the causes of re-deposition (for instance, tectonic event, storm activity), it is possible that the remobilized Mo deposited under relatively shallow and intermittent/suboxic conditions. $\delta^{98/95}$Mo formed under such conditions was lighter than that formed under euxinic conditions. Therefore, $\delta^{98/95}$Mo value of polymetallic sulfide ore is better explained as two component mixing model of a heavier in-situ precipitated Mo mixed with lighter re-deposited Mo.

7.8.2 PGE geochemistry

Layered igneous complexes are the most important economic sources of platinum-group elements (PGEs). A number of other geological progresses including marine sedimentation, sulfide magma fractionation and hydrothermal redistribution can also lead to PGE enrichment (e.g. Crocket et al., 1973; McCallum et al., 1976; Mernagh et al., 1994; Pan and Xie, 2001; Lightfoot and Keays, 2005; Naldrett et al., 2008). With respect to the black shale hosted polymetallic Ni-Mo-PGE-Au sulfide ore deposits of South China, PGE distribution patterns have been used for metallogenic interpretation (e.g. Li and Gao, 2000; Mao et al., 2001; Wu et al., 2001; Luo et al., 2003; Lehmann et al., 2003; Jiang et al., 2007a). According to the similarity of Pt/Pd and Au/Pd ratios between polymetallic sulfide ores and present-day seawater, distinctly different to hydrothermal sulfides, Lehmann et al. (2003) suggested a normal seawater scavenging model for metal enrichment in the polymetallic sulfide ores. However, Jiang et al. (2007a) argued that Pt/Pd ratios of modern Fe-Mn crusts, solely containing hydrogenous PGEs, are not similar to, but about 100-fold those of seawater. Subsequently, they suggested that similarity of Pt/Pd ratios in the polymetallic sulfide ores and in present-day seawater were not necessarily indicating genetic links between them. The argument of the very high Pt/Pd ratio in modern Mn-Fe crusts does not take into account that these crusts/nodules grow in an oxidative environment where selective Pt fixation is by oxidative scavenging. This situation is completely different from euxinic environments.

The polymetallic sulfide ore has a PGE +Au pattern roughly parallel with the host black shales, and both patterns are similar to present-day seawater, for instance, the negative Ir anomaly (Fig. 7-7). The similarity of PGE + Au patterns indicates that the polymetallic sulfide ore and the host black shales may have undergone the same geological processes. If hydrothermal fluids would have formed the sulfide ore but not the host black shales as proposed by Jiang et al. (2003, 2007a), PGE + Au patterns of the polymetallic sulfide ores would be different from the host black shales, but similar to hydrothermal massive sulfide ores. Crocket (1990) investigated hydrothermal deposits from the Juan de Fuca and Mid-Atlantic Ridges, where two massive Cu-Fe sulfide mounds from the central black smoker complex of the TAG hydrothermal area were characterized by very low Pd values (3.2-3.5 ppb), but rather high Au (up to 18,900 ppb) and slightly elevated Ir values (7.6 ppb). Pasava et al. (2007) reported extremely high Au/Pd ratios of ~1500 and ~20000 for modern active black smoker sites in the PACMANUS hydrothermal field (Roman Ruins and Satanic Mills, respectively). The Kuroko deposits are well documented VMS deposits. Au/Pd of the Kuroko sulfides is characterized by a high ratio around 139 (Pan and Xie, 2001). Due to the higher hydrothermal solubility of Au compared to the PGE under any rock-buffered conditions, hydrothermal Au deposits are much more common than hydrothermal PGE deposits (Crocket, 1990; Lehmann et al., 2003), in accordance with theoretical and experimental solubility data for PGE + Au (Wood et al., 1992; Pan and Wood, 1994; Gammons, 1996). Au concentrations of the polymetallic Ni-Mo-PGE-Au sulfide ores reported in the literature are very variable at the hundred ppb-level. Au/Pd ratios of the polymetallic sulfide ores are around 1, much lower than in hydrothermal massive sulfides (Fig. 7-8 A).

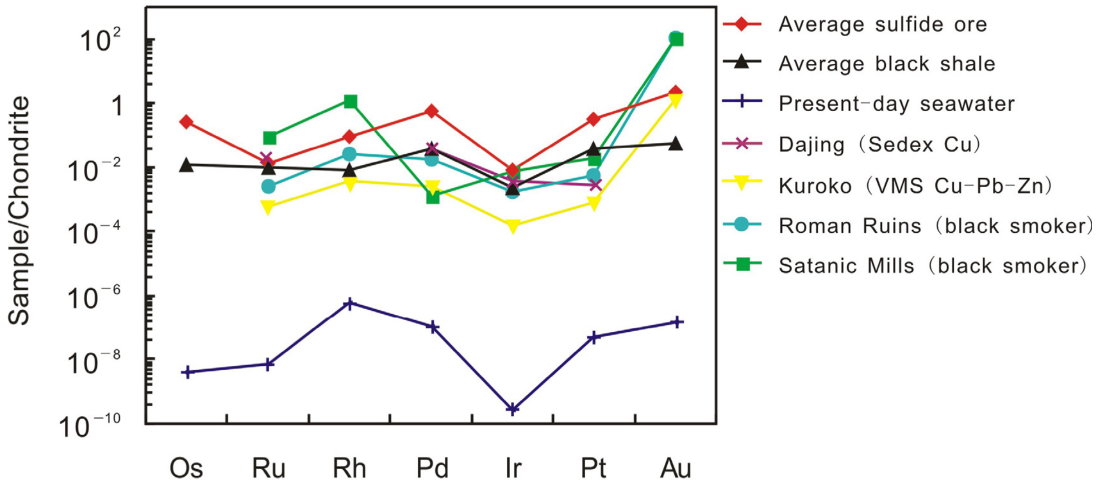

Fig. 7-7: Chondrite-normalized PGE + Au patterns of average polymetallic

Ni-Mo-PGE-Au sulfide ore and host black shale in South China, compared to present-day seawater (Nozaki, 1997), Dajing Sedex Cu sulfide deposit (Chu et al., 2002), Kuroko VMS sulfide deposits (Pan and Xie, 2001), Roman Ruins and Satanic Mills hydrothermal massive sulfide mounds (Pasava et al., 2004).

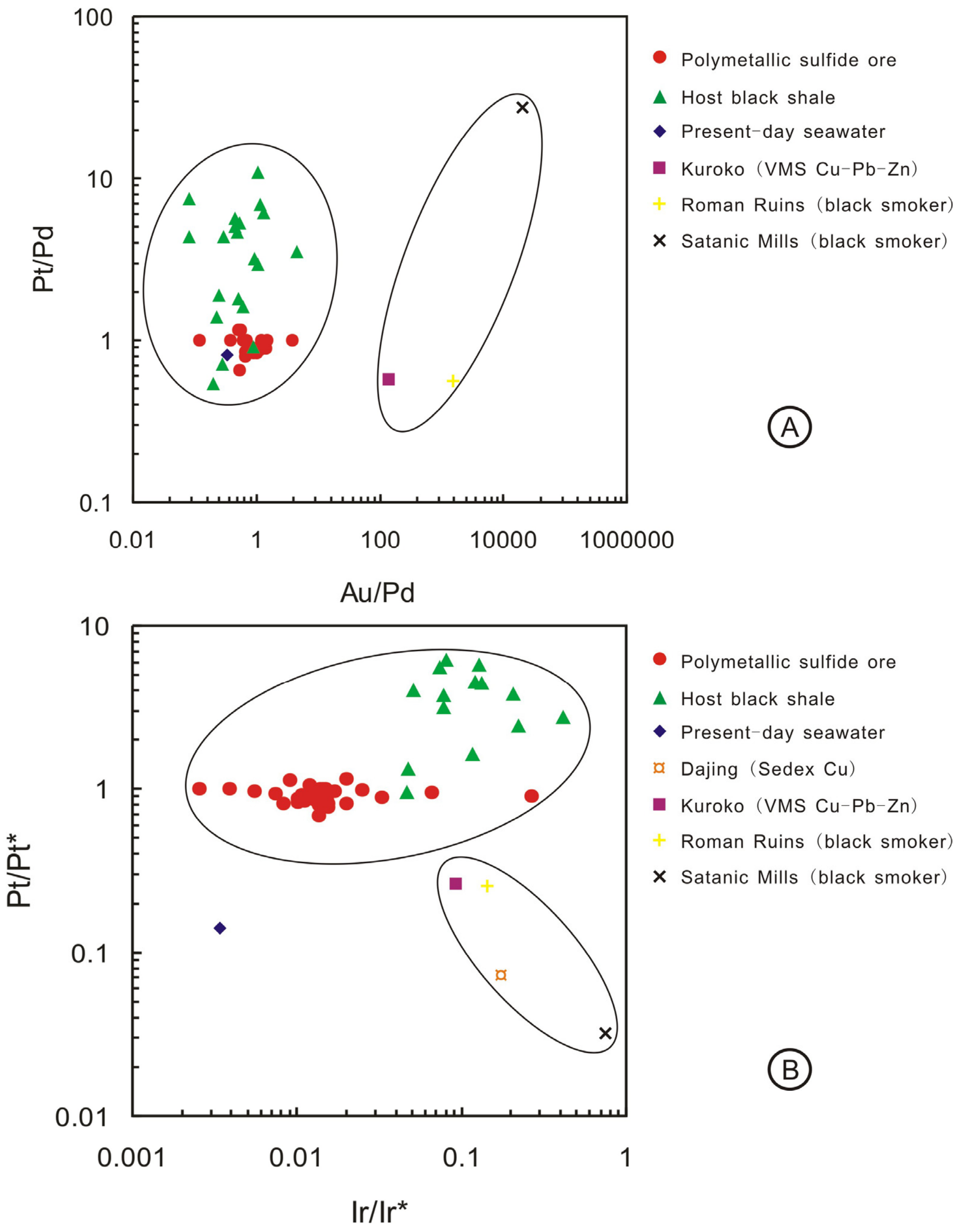

Fig. 7-8: Au/Pd vs. Pt/Pd **(A)** and Ir/Ir* vs. Pt/Pt* **(B)** binary plots of average polymetallic Ni-Mo-PGE-Au sulfide ore and average host black shale, compared to present-day seawater (Nozaki et al., 1997), Dajing Sedex Cu sulfide deposit (Chu et al., 2002), Kuroko VMS Cu-Pb-Zn sulfide deposit (Pan and Xie, 2001), Roman Ruins and Satanic Mills hydrothermal massive sulfide mounds (Pasava et al., 2004).

The Ir anomaly can also offer some hints on ore genesis. Pasava et al. (2004) reported relatively small fractionations between Pd and Ir in hydrothermal sulfides from modern active black smokers (Roman Ruins and Satanic Mills, with average Pd/Ir ratios of 12.4 and 0.19, respectively), close to data for modern hydrothermal vents reported by Crocket (1990) (Pd/Ir ratios of 0.42 to 0.46), and the Dajing Sedex Cu-polymetallic sulfides and the Kuroko VMS base metal sulfides (Pd/Ir ratios are 10.6 and 16.2, respectively, Pan and Xie, 2001; Chu et al., 2002). However, the polymetallic Ni-Mo-PGE-Au sulfide ores and present-day seawater are characterized by higher Pd/Ir ratios (72.9 and 396, respectively) compared to hydrothermal massive sulfides. By analogy with the Eu anomaly in chondrite-normalized REE patterns, we define Ir and Pt anomalies by $Ir/Ir^* = 2 \times Ir_N/(Pd_N + Pt_N)$ and $Pt/Pt^* = 2 \times Pt_N/(Rh_N + Pd_N)$, where Ir_N, Rh_N, Pd_N and Pt_N refer to chondrite-normalized values. The hydrothermal sulfides show high Ir/Ir* values (0.17, 0.09, 0.14 and 0.74 for Dajing, Kuroko, Roman Ruins and Satanic Mills sulfides, respectively). In contrast, the polymetallic sulfide ore is characterized by a very low average Ir/Ir* value of 0.02, remarkably lower than hydrothermal sulfides by about one order of magnitude. The Ir/Ir* value of the polymetallic sulfide ore is intermediate between hydrothermal sulfides and present-day seawater (Ir/Ir* is 0.003), and may mislead to the conclusion that the polymetallic sulfide ores represent a mix of high Ir/Ir* hydrothermal fluids and low Ir/Ir* seawater. However, this is not supported by the fact of average Ir/Ir* value in the host black shales (0.06) slightly larger than in the polymetallic sulfide ores (0.02). There is general agreement that the host black shales are not or at most weakly overprinted by hydrothermal fluids. If hydrothermal fluids were only involved during polymetallic sulfide ore mineralization but not during black shale formation, Ir/Ir* ratios in the polymetallic sulfide ores would be closer to hydrothermal sulfides than in the host black shales, which is, however, not observed. The reason why the Ir/Ir* value in present-day seawater is lower than in the polymetallic sulfide ore may be related to the very low solubility of Ir compared to Pd and Pt in seawater. Moreover, the Pt/Pt* value is obviously different between polymetallic sulfide ores and hydrothermal sulfides. Both polymetallic Ni-Mo-PGE-Au sulfide ores and host black shales are characterized by high Pt/Pt* values (0.95 and 1.71 on average, respectively), compared to low Pt/Pt* values of hydrothermal massive sulfides (0.07, 0.26, 0.25 and 0.03 for Dajing, Kuroku, Roman Ruins and Satanic Mills sulfides, respectively) (Fig. 7-8 B).

7.8.3 Trace element and REE geochemistry

Trace element geochemistry has been applied to constrain the genesis of the polymetallic Ni-Mo-PGE-Au sulfide deposits in South China (Mao et al., 2002; Jiang et al., 2006; Lehmann et al., 2003, 2007). Mao et al. (2002) and Lehmann et al. (2007) reported that the distributions of a suite of redox- and particle-reactive elements in the polymetallic sulfide ores and the host black shales are similar to that in seawater, and suggested a seawater scavenging model for metal enrichment in the polymetallic sulfide ore layer. Jiang et al. (2006) reported different distribution patterns between polymetallic sulfide ores and host black shales for some redox-sensitive elements (V, Ni, Mo, U and Mn), base metals (Cu, Zn, Pb), and Sr and Ba, and proposed that metals in the polymetallic sulfide ores were derived from hydrothermal vents. In order to clarify this controversy, we compared trace elements in polymetallic sulfide ores, host black shales, VMS-type, Sedex-type massive sulfides and modern hydrothermal vents to their concentration in present-day seawater (Fig. 7-9). The polymetallic sulfide ore displays a relatively constant enrichment factor between 10^6 and 10^8 for a suite of elements including PGE, Au, Mo, Ni, Cu, Zn, Sb, W, Pb, Sn, Y, Sb and rare earth elements. The black shale host sequence, however, has element patterns compared to present-day seawater with much scatter, indicating that the metals in the host black shales were not only of authigenic, but also of terrigenous origin. Low input of terrigenous material during the formation of the sulfide ore layer compared to the host black shales is supported by very low Zr, Ta, Sc, Rb, Nb, Ga, Cs, Cr and Hf concentrations in the sulfide ores (Table 7-2). The non-congruent pattern for element concentrations of present-day seawater and hydrothermal massive sulfides is in agreement with the fact that trace element concentration factors of hydrothermal massive sulfide ores are controlled by the composition of the hydrothermal fluids. Modern hydrothermal vents represent mixtures of hydrothermal fluid and seawater. The Hanging Garden hydrothermal vent at 21°N contains a suite of elements broadly enriched by a factor of 10^2 to 10^4 with respect to present-day seawater, indicating that mainly seawater feeds the hydrothermal vent (Fig. 7-9 E). The highly positive correlation of element enrichment factors between polymetallic Ni-Mo-PGE-Au sulfide ore and present-day seawater, but the variable relationship between hydrothermal sulfides and present-day seawater strongly supports the model that metals in the polymetallic Ni-Mo-PGE-Au sulfide ores were scavenged from normal seawater.

Hydrothermal Cu, Pb, Zn, Ag and Ba ore deposits are common, whereas hydrothermal Ni-Mo-PGE deposits have not been reported yet. Mo- and Ni-based trace element ratios of polymetallic Ni-Mo-PGE-Au sulfide ore, host black shales, present-day seawater and hydrothermal massive sulfide ores are listed in Table 7-5. The Mo- and Ni-based metal enrichment ratios for the sulfide ore, the black shale and present-day seawater are at the same order of magnitude, remarkably higher than those of the Red Dog Sedex Zn-Pb-Ag and Neves-Corvo MVS Cu-Sn massive sulfides. Although Mo and Ni concentrations for modern hydrothermal vent fluids are not reported, the Cu, Pb and Zn concentrations in the Hanging Garden hydrothermal vent are higher than any other elements, which invariably define low Mo- and Ni-based ratios. Similar Mo- and Ni-based ratios of the polymetallic sulfide ore and seawater indicate that there are close genetic links.

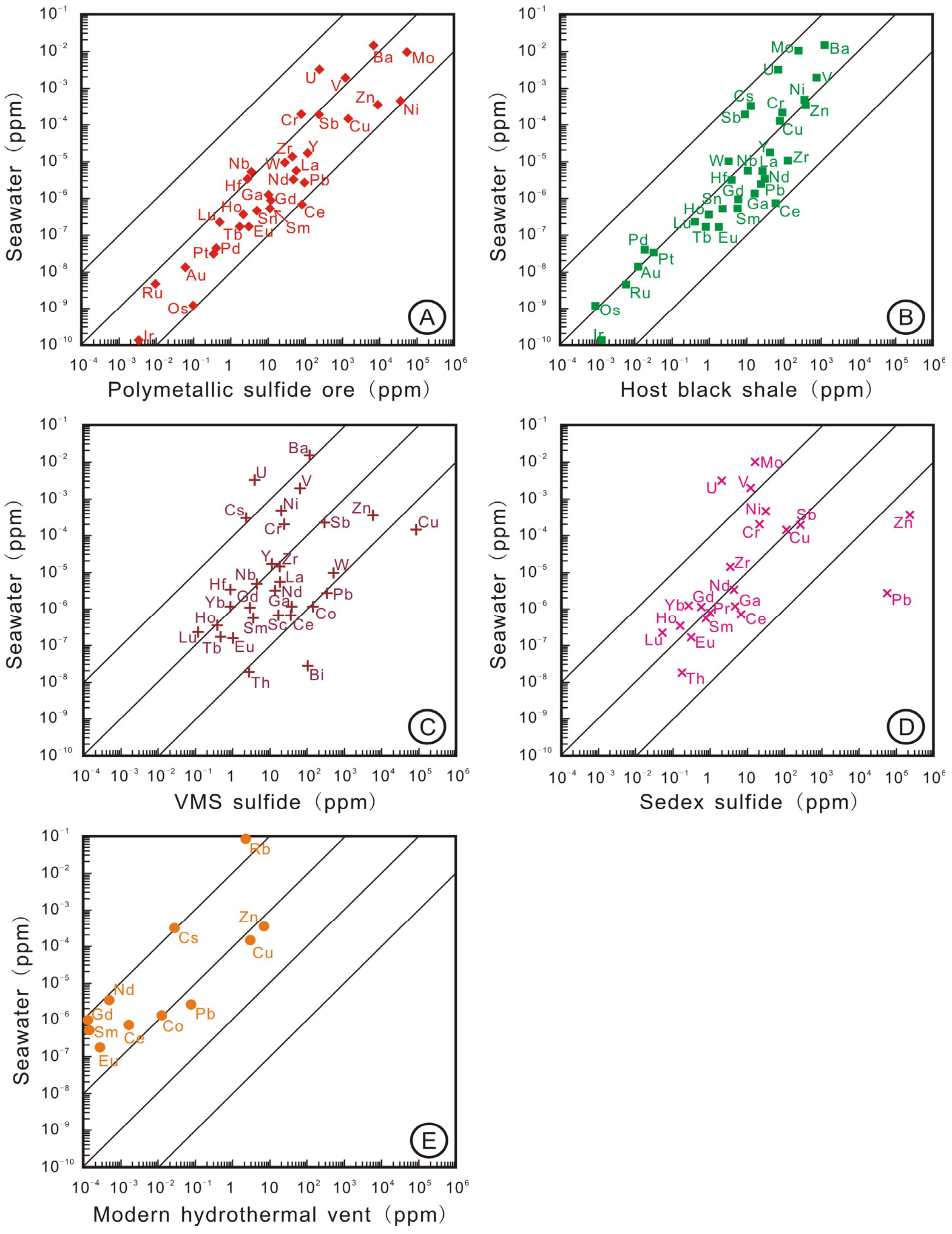

Fig. 7-9: Binary plots of average concentration of elements in different sample groups compared to present-day seawater. **A:** Average polymetallic Ni-Mo-PGE-Au sulfide ore vs. present-day seawater. **B:** Average host black shale vs. present-day seawater. **C:** VMS-type massive sulfide vs. present-day seawater. **D:** Sedex-type massive sulfide vs. present-day seawater. **E:** Modern hydrothermal vents vs. present-day seawater. Data are from Table 7-2, 7-3, 7-4, and references therein.

Table 7-5

Mo- and Ni-based ratios of average Pb, Cu and Zn abundances of polymetallic Ni-Mo-PGE-Au sulfide ores, black shales, present-day seawater and hydrothermal massive sulfides.

Metal ratios	Mo:Pb	Mo:Cu	Mo:Zn	Ni:Pb	Ni:Cu	Ni:Zn
Sulfide ore	563	39.2	7.21	376	26.2	4.83
Black shale	9.18	2.67	0.46	15.2	4.42	0.76
Present-day seawater	3704	66.7	28.6	178	3.20	1.37
Red Dog (Sedex Zn-Pb-Ag)	0.0003	0.1	0.00007	0.0006	0.29	0.0001
Neves-Corvo (VMS Cu-Sn)				0.06	0.0002	0.003

Data sources are same as in Table 7-3.

The geochemical behavior of the REE + Y has been the subject of extensive study over several decades towards a better understanding of a variety of petrological and mineralogical problems. For comparison, Fig. 7-10 shows chondrite-normalized REE + Y distribution patterns of average polymetallic Ni-Mo-PGE-Au sulfide ores, host black shales, hydrothermal massive sulfide ores and present-day seawater. ∑REE + Y contents of the average polymetallic sulfide ores and the host black shales are remarkably higher than those of hydrothermal massive sulfide ores. The REE + Y pattern of the polymetallic sulfide ore is generally concordant with the host black shale. Both show slight Eu depletion and pronounced Y enrichment, and a slight light REE enrichment with average chondrite-normalized La_N/Yb_N of 11.4 and 7.96, respectively. The seawater REE + Y distribution shows heavy REE enrichment and Ce depletion, which is, however, rarely found in marine authigenic rocks, due to post-depositional redistribution of REE.

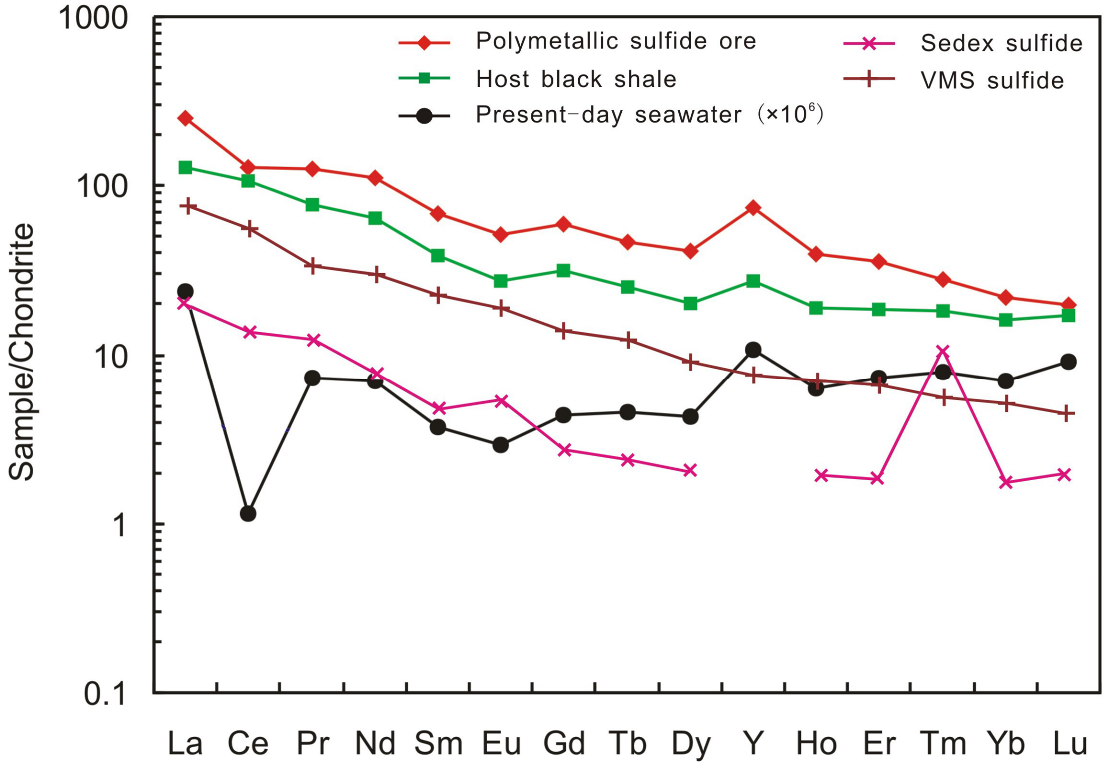

Fig. 7-10: Rare earth element distribution patterns of average polymetallic Ni-Mo-PGE-Au sulfide ore and average host black shale from the Dazhuliushui, Maluhe, Zijin and Cili mine sites, compared to present-day seawater (Nozaki, 1997), Changba Sedex Zn-Pb massive sulfides (Ma et al., 2004), and Neves-Corvo VMS Cu-Sn massive sulfides (Relvas et al., 2006).

In contrast to the weak negative Ce anomaly of the polymetallic sulfide ore, the REE + Y pattern of the host black shale does not show a Ce anomaly. The REE distribution pattern of modern seawater has a prominent negative Ce anomaly, in response to the oxidation of Ce^{3+} to Ce^{4+} and the precipitation of Ce^{4+} from solution as CeO_2, whereas upper continental crust has no Ce anomaly. The absence of the Ce anomaly in the host black shale indicates that they are dominated by terrigenous materials and/or a non-oxidizing seawater environment. Large negative Ce anomalies are observed in oxic water (such as modern seawater), whereas positive or no anomalies have been reported for samples from suboxic and euxinic conditions (e.g. De Baar et al., 1988; Chen et al., 2003; Jiang et al., 2006). It is likely that the weak depletion and absence of Ce for the polymetallic sulfide ore and the host black shale largely reflect globally reducing oceans. Ce depletions are common in hydrothermal sulfides. The hydrothermal massive sulfides from the Changba Sedex Pb-Zn deposit in China and the Neves-Corvo VMS Cu-Sn deposit in Portugal show slightly negative and absent Ce anomalies, respectively (Fig. 7-10), indicating that the behavior of Ce anomalies is variable in hydrothermal systems.

REE + Y patterns of both the polymetallic Ni-Mo-PGE-Au sulfide ores and the host black shales show a remarkable Y anomaly, similar to that in present-day seawater (Fig. 7-10). However, no positive Y anomaly is observed in the Neves-Corvo VMS Cu-Sn sulfides. Y and Ho are tightly coupled and display extremely coherent behavior in many geochemical processes, leading to invariable Y/Ho ratios of ~28 in natural igneous rocks and clastic sediments, and 44-74 in seawater (Bau, 1996). Although REE + Y patterns of both the polymetallic sulfides and the host black shales show a positive Y anomaly, Y/Ho ratios of the host black shales are distinctly lower than in the polymetallic sulfide ores (Fig. 7-11 A). All black shales are characterized by relatively low Y/Ho ratios, ranging from 29.6 to 39.6 with an average ratio of 33.1. The Y/Ho ratios are intermediate between igneous or clastic sedimentary rocks (~28) and seawater (~47.2), supporting the assumption that terrigenous materials and seawater have mixed during diagenesis. In contrast to the low Y/Ho ratios of the host black shales, the polymetallic sulfide ores have high Y/Ho ratios, ranging from 37.3 to 58.8 with an average of 46.9, similar to seawater with ~47.2, strongly supporting that the REE + Y budget of the polymetallic Ni-Mo-PGE-Au sulfide ores is dominated by coeval seawater. It is noteworthy that although the polymetallic sulfides have remarkably high Y/Ho ratios compared to the host black shales, the polymetallic sulfides from Maluhe and some from Cili are characterized by Y/Ho ratios of <44 (Fig. 7-11 B), indicating that a small percentage of terrigenous materials may have been involved in the sedimentation of the sulfide ore bed in the Maluhe and Cili districts. This is further evidenced by the weak positive correlation between the ∑REE + Y contents and Y/Ho ratios ($R^2 = 0.57$).

Relatively low ∑REE + Y contents for the Maluhe sulfides may have been caused by mixing of terrigenous materials with low REE content and seawater REE complexes. Nonetheless, relatively low Y/Ho ratios of the polymetallic sulfides from Maluhe and Cili are closer to authigenic sediments compared to the host black shales, suggesting involvement of only minor terrigenous material during the polymetallic sulfide ore formation, in agreement with stronger Y anomalies observed in polymetallic sulfide ores than in the host black shales (Fig. 7-10). Average Y/Ho ratio of hydrothermal sulfides from the Neves-Corvo VMS deposits is lower than in the polymetallic sulfide bed (Fig. 7-11). Hydrothermal fluids are aqueous but different with seawater of low-temperature aqueous solution. Fractionation of Y and Ho in hydrothermal systems can be related to different stabilities of Y and REE complexes under variable temperature conditions (Bau and Dulski, 1995).

7.8.4 A genetic model

There is a long standing debate about the origin of the polymetallic sulfide ore layer, with seawater scavenging and hydrothermal venting the most popular interpretations (Conveney et al., 1992, Lott et al., 1999; Steiner et al., 2001; Mao et al., 2002, Jiang et al., 2003, 2006, 2007a, b, 2009; Lehmann et al., 2007; Xu et al., 2011). Our study involves more samples and a broader geographic range than in previous studies. The geochemical features of the polymetallic sulfide ores and the host black shales in comparison with hydrothermal massive sulfides (samples from Sedex-, VMS-type deposits and modern active black smokers) are in favor of the model of scavenging from seawater. A sketch model of the depositional environment of the polymetallic sulfide ore layer is shown in Fig. 7-12.

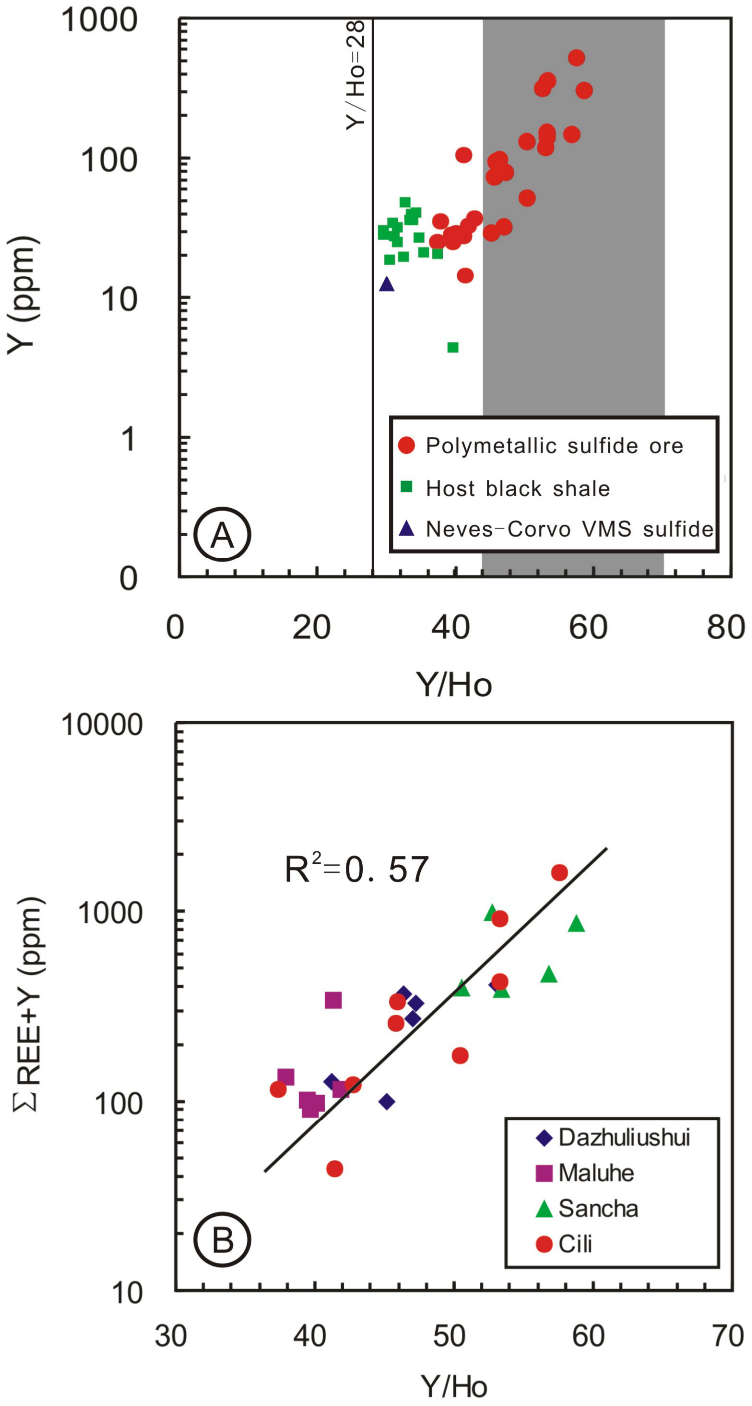

Fig. 7-11 A: Binary plot of Y/Ho ratio vs. Y concentration of the polymetallic sulfide ores and the host black shales, compared to Neves-Corvo VMS Cu-Sn sulfide deposit (Relvas et al., 2006). Grey shaded area indicates Y/Ho of 44-74 in seawater. **B:** Binary plot of Y/Ho ratio vs. ∑REE + Y concentration of the polymetallic sulfide ores from the Dazhuliushui, Maluhe, Sancha and Cili mine sites showing a positive correlation.

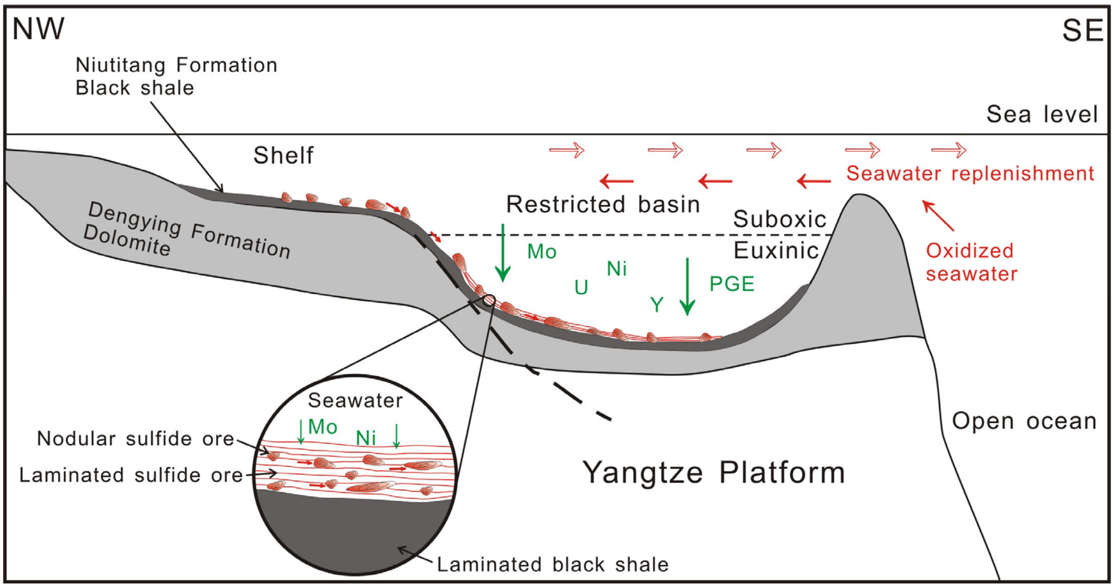

Fig. 7-12: Model of depositional environment of the polymetallic Ni-Mo-PGE-Au sulfide ore layer with both in-situ metal precipitation from seawater and short distance re-deposition of sulfide clasts from wave-agitated shelf to deeper parts of the restricted euxinic basin.

Although the four polymetallic Ni-Mo-PGE-Au sulfide ore deposits studied are several hundred kilometers apart, all of them are located in the transition belt from shallow shelf to deep basinal facies. The ore layer originated under conditions of low sedimentation rate in locally distributed restricted basins (Lehmann et al., 2007). $\delta^{98/95}$Mo values of the polymetallic sulfide ores are occasionally lower than those of the host black shales, consistent with the two-source model proposed in Fig. 7-12. The Mo-rich aggregates may have formed under variable suboxic to euxinic environments. Suboxic sediments are characterized by variable $\delta^{98/95}$Mo values, but lighter than euxinic sediments (Siebert et al., 2003, 2006; Scott et al., 2008). The Mo-aggregates with variable $\delta^{98/95}$Mo values were transported as rip-up clasts into deeper parts of restricted euxinic basins, and mixed with in-situ precipitated heavy $\delta^{98/95}$Mo sulfides. Although some $\delta^{98/95}$Mo values of the polymetallic sulfide ores are slightly lighter than those of the host black shales, relatively consistent values suggest that the Mo-aggregates formed under suboxic conditions represent only a small portion of the sulfide ore layer and re-deposition processes only occurred at a small scale. In contrast to the relatively consistent $\delta^{98/95}$Mo values in the polymetallic sulfide ores, variable $\delta^{98/95}$Mo values of the host black shales are caused by two reasons: input of terrrigeous materials and the suboxic depositional environment. Widespread suboxic conditions have been proven for the Early Cambrian in South China (Goldberg et al., 2007; Xu et al., in preparation). The sulfide ore in its present form represents a mixture of re-deposited rip-up clasts and in-situ precipitated laminated ore.

The distinctive difference in geochemical features of both the polymetallic sulfide ore and the host black shales compared with hydrothermal massive sulfides indicates that hydrothermal venting is not involved in the metal enrichment. PGE, trace- and rare-earth element geochemistry suggests that both the re-deposited aggregates and the in-situ deposited laminated ore were scavenged from seawater under restricted euxinic conditions. Polymetallic sulfides from the Maluhe mine site have a small percentage of terrigenous input. The seawater scavenging process occurred under conditions of low sedimentation rate and replenishment of restricted basins by upwelling oxidized seawater (Mao et al., 2002; Lehmann et al., 2007). In contrast to seawater-sourced nodular and laminated sulfides, the host black shales reflect mixing of terrigenous and seawater sources, and the terrigenous source may have been dominant.

7.9 Conclusions

The polymetallic Ni-Mo-PGE-Au sulfide ore layer on the Yangtze Platform provides a good theme for investigating both the Early Cambrian paleoceanic environment and mineralization. The Mo isotope signature supports a two-source model for the formation of the polymetallic sulfide ore layer. Re-deposited rip-up sulfidic aggregates with relatively light and variable $\delta^{98/95}$Mo values mixed with in-situ precipitated Mo with heavy values, resulting in $\delta^{98/95}$Mo values of the polymetallic sulfide ores that are occasionally lighter than those of the host black shales. Comparison among the polymetallic sulfide ores, the host black shales, the syngenetic hydrothermal massive sulfides (VMS-, Sedex-type and modern active black smoker sulfides) and present-day seawater reveals that the PGE ratios of the polymetallic sulfides are similar to present-day seawater, but different from hydrothermal massive sulfides. Element concentrations in the polymetallic sulfide ores are broadly consistent with present-day seawater with an enrichment factor of ~10^7, much different from hydrothermal sulfides with no correlation with seawater. Y-Ho fractionation of the polymetallic sulfide ores shows a pronounced positive Y anomaly, similar to that in present-day seawater, suggesting that the source of the REE in polymetallic sulfide ore was dominated by aqueous REE complexes. Overall, the Mo isotope, PGE, trace and rare-earth element geochemistry indicate that metal enrichment in the polymetallic Ni-Mo-PGE-Au sulfide ore layer was likely caused by seawater scavenging at low clastic sedimentation rate, whereas the host black shale formed by mixture of terrigenous materials and seawater-derived precipitations. Evidence for hydrothermal venting is not observed.

7.10 Acknowledgements

This research is jointly funded by the Chinese Geological Survey Program (No. 1212010634001), the National Basic Research Program of China (No. 2007CB411302) and the Chinese Scholarship Council, as well as by Deutsche Forschungsgemeinschaft (LE578/32-1). We thank Dr. Zhang Ying (from Institute of Geochemistry, CAS, China) and Mr. He Lingbang (from 405 Geological Team, Bureau of Geology and Mineral Exploration and Development of Hunan province, China), for assistance during field work. We are grateful to Prof. Thomas F. Nägler, Dr. Nadia Neubert and Andrea R. Voegelin for help with the Mo isotope analysis in Bern.

7.11 References

Amthor, J.E., Grotzinger, J.P., Schroder, S., Bowring, S.A., Ramezani, J., Martin, M.W., Matter, A., 2003. Extinction of Cloudina and Namacalathus at the Precambrian-Cambrian boundary in Oman. Geology 31, 431-434.

Anbar, A.D., Rouxel, O., 2007. Metal stable isotopes in paleoceanography. Annual Review of Earth and Planetary Sciences 35, 717-746.

Anders, E., Grevesse, N., 1989. Abundances of the elements: Meteoritic and solar. Geochimica et Cosmochimica Acta 53, 197-214.

Balaram, V., Anjaiah, K.V., Reddy, M.R.P., 1995. Comparative study on the trace and rare earth element analysis of an Indian polymetallic nodule reference sample by inductively coupled plasma atomic emission spectrometry and inductively coupled plasma mass spectrometry. Analyst 120, 1401-1406.

Banerjee, D.M., Schidlowski, M., Siebert, F., Brasier, M.D., 1997. Geochemical changes across the Proterozoic-Cambrian transition in the Durmala phosphorite mine section, Mussoorie hills, Garhwal Himalaya, India. Palaeogeography Palaeoclimatology Palaeoecology 132, 183-194.

Barfod, G.H., Albarède, F., Knoll, A.H., Xiao, S.H., Telouk, P., Frei, R., Baker, J., 2002. New Lu-Hf and Pb-Pb age constraints on the earliest animal fossils. Earth and Planetary Science Letters 201, 203-212.

Bau, M., 1996. Controls on the fractionation of isovalent trace elements in magmatic and aqueous systems: Evidence from Y/Ho, Zr/Hf, and lanthanide tetrad effect.

Contributions to Mineralogy and Petrology 123, 323-333.

Bau, M., Dulski, P., 1995. Comparative study of yttrium and rare-earth element behaviors in fluorine-rich hydrothermal fluids. Contributions to Mineralogy and Petrology 119, 213-223.

Bengtson, S., Zhao, Y., 1992. Predatorial borings in Late Precambrian mineralized exoskeletons. Science 257, 367-369.

Brasier, M.D., 1992. Background to the Cambrian Explosion. Journal of the Geological Society 149, 585-587.

Chen, D.F., Dong, W.Q., Qi, L., Chen, G.Q., Chen, X.P., 2003. Possible REE constraints on the depositional and diagenetic environment of Doushantuo Formation phosphorites containing the earliest metazoan fauna. Chemical Geology 201, 103-118.

Chen, D.F., Dong, W.Q., Zhu, B.Q., Chen, X.P., 2004. Pb-Pb ages of Neoproterozoic Doushantuo phosphorites in South China: constraints on early metazoan evolution and glaciation events. Precambrian Research 132, 123-132.

Chu, X.L., Sun, M., Zhou, M.F., 2002. PGE patterns of ores of Dajing Cu-polymetallic deposit in Linxi County, Inner Mongolia: Indicator to source of metallogenic elements. Chinese Science Bulletin 47, 1119-1124

Condon, D., Zhu, M.Y., Bowring, S., Wang, W., Yang, A.H., Jin, Y.G., 2005. U-Pb ages from the Neoproterozoic Doushantuo Formation, China. Science 308, 95-98.

Conveney, R.M., Jr., Grauch, R.I., Murowchick, J.B., 1994. Metals, phosphate, and stone coal in the Proterozoic and Cambrian of China: The geolocial setting of precious metal-bearing Ni-Mo ore beds. Society of Economic Geologists Newsletter 18, 1, 6-11.

Coveney, R.M. Jr., Murowchick, J.B., Grauch, R.I., Glascock, M.D., Denison, J.R., 1992. Gold and platinum in shales with evidence against extraterrestrial sources of metals. Chemical Geology 99, 101-114.

Crocket, J.H., 1990. Noble metals in Seafloor hydrothermal mineralization from the Juan de Fuca and Mid-Atlantic Ridges: a Fractionation of gold from platinum metals in hydrothermal fluids. Canadian Mineralogist 28, 639-648.

Crocket, J.H., Macdougall, J.D., Harriss, R.C., 1973. Gold, Palladium and Iridium in Marine Sediments. Geochimica et Cosmochimica Acta 37, 2547-2556.

De Baar, H.J.W., German, C.R., Elderfield, H., Van Gaans, P., 1988. Rare-earth element distributions in anoxic waters of the Cariaco Trench. Geochimica et Cosmochimica Acta 52, 1203-1219.

Fan, D., Yang, R.Y., Huang, Z.X., 1984. The Lower Cambrian black shales series and the iridium anomaly in south China. Developments in Geoscience, 27th International Geological Congress, Moscow, Beijing Science Press, 215-225.

Gammons, C.H., 1996. Experimental investigations of the hydrothermal geochemistry of platinum and palladium: Ⅴ. Equilibria between platinum metal, Pt(II), and Pt(IV) chloride complexes at 25 to 300°C. Geochimica et Cosmochimica Acta 60, 1683-1694.

Goldberg, T., Strauss, H., Guo, Q.J., Liu, C.Q., 2007. Reconstructing marine redox conditions for the early Cambrian Yangtze Platform: Evidence from biogenic sulfur and organic carbon isotopes. Palaeogeography Palaeoclimatology Palaeoecology 254, 175-193.

Gradstein, F.M., Ogg, J.G., Smith, A.G., Bleeker, W., Lourens, L.J., 2004. A new geologic time scale, with special reference to Precambrian and Neogene. Episodes 27, 83-100.

Holland, H.D., 1979. Metals in black shales: reassessment. Economic Geology 74, 1676-1680.

Horan, M.F., Morgan, J.W., Grauch, R.I., Coveney, R.M., Murowchick, J.B., Hulbert, L.J., 1994. Rhenium and osmium isotopes in black shales and Ni-Mo-PGE-rich sulfide layers, Yukon-Territory, Canada, and Hunan and Guizhou provinces, China. Geochimica et Cosmochimica Acta 58, 257-265.

Jiang, S.Y., Chen, Y.Q., Ling, H.F., Yang, J.H., Feng, H.Z., Ni, P., 2006. Trace- and rare-earth element geochemistry and Pb-Pb dating of black shales and intercalated Ni-Mo-PGE-Au sulfide ores in Lower Cambrian strata, Yangtze Platform, South China. Mineralium Deposita 41, 453-467.

Jiang, S.Y., Ling, H.F., Zhao, K.D., Zhu, M.Y., Yang, J.H., Chen, Y.Q., 2008. A discussion on Mo isotopic compositions of black shale and Ni-Mo sulfide bed in the Early Cambrian Niutitang Formation in South China. Acta Petrologica et Mineralogica 27, 341-345 (in Chincese with English abstract).

Jiang, S.Y., Pi, D.H., Heubeck, C., Frimmel, H., Liu, Y.P., Deng, H.L., Ling, H.F., Yang, J.H., 2009. Early Cambrian ocean anoxia in South China. Nature 459, E5-E6.

Jiang, S.Y., Yang, J.H., Ling, H.F., Chen, Y.Q., Feng, H.Z., Zhao, K.D., Ni, P., 2007a. Extreme enrichment of polymetallic Ni-Mo-PGE-Au in lower Cambrian black shales of South China: An Os isotope and PGE geochernical investigation. Palaeogeography Palaeoclimatology Palaeoecology 254, 217-228.

Jiang, S.Y., Zhao, K.D., Li, L., Ling, H.F., Zhu, M.Y., 2007b. Highly metalliferous carbonaceous shale and Early Cambrian seawater: Comment. Geology 35, e158.

Kao, L.S., Peacor, D.R., Coveney, R.M., Zhao, G.M., Dungey, K.E., Curtis, M.D., Penner-Hahn, J.E., 2001. A C/MoS_2 mixed-layer phase (MoSC) occurring in metalliferous black shales from southern China, and new data on jordisite. American Mineralogist 86, 852-861.

Kaufman, A.J., Jacobsen, S.B., Knoll, A.H., 1993. The Vendian Record of Sr and C-Isotopic Variations in Seawater: Implications for Tectonics and Paleoclimate. Earth and Planetary Science Letters 120, 409-430.

Kimura, H., Watanabe, Y., 2001. Oceanic anoxia at the Precambrian-Cambrian boundary. Geology 29, 995-998.

Kirschvink, J.L., Ripperdan, R.L., Evans, D.A., 1997. Evidence for a large-scale reorganization of Early Cambrian continental masses by inertial interchange true polar wander. Science 277, 541-545.

Kribek, B., Sýkorová, I., Pasava, J., Machovic, V., 2007. Organic geochemistry and petrology of barren and Mo-Ni-PGE mineralized marine black shales of the Lower Cambrian Niutitang Formation (South China). International Journal of Coal Geology 72, 240-256.

Lehmann, B., Mao, J.W., Li, S.R., Zhang, G.D., 2003. Re-Os dating of polymetallic Ni-Mo-PGE-Au mineralization in lower Cambrian black shales of south China and its geological significance - A reply. Economic Geology 98, 663-665.

Lehmann, B., Nägler, T.F., Holland, H.D., Wille, M., Mao, J.W., Pan, J.Y., Ma, D.S., Dulski, P., 2007. Highly metalliferous carbonaceous shale and Early Cambrian seawater. Geology 35, 403-406.

Li, S.R., Gao, Z.M., 2000. The source of noble metals in Early Cambrian black shales in Guizhou and Hunan provinces. Science in China (Series D) 30, 169-174 (in Chinese).

Li, S.Y., Xiao, Q. Y., Shen, J.F., Sun, L., Liu, B., Yan, B.K., 2002. Source of Lower Cambrian platinum group elements in black shales in Hunan and Guizhou provinces, China and the Re-Os isotope dating. Science China (Series D) 32, 568-575 (in Chinese).

Lightfoot, P.C., Keays, R.R., 2005. Siderophile and chalcophile metal variations in flood basalts from the Siberian trap, Noril'sk region: Implications for the origin of the Ni-Cu-PGE sulfide ores. Economic Geology 100, 439-462.

Lin, F.C., 2005. Geological and geochemical characteristics and genesis of supper-large-scale Sedex-type stratiform lead-zinc deposits in the Dadu River Valley on the western margin of the Yangtze Craton. Acta Geologica Sinica 79, 540-558 (in Chinese with English abstract).

Lott, D.A., Coveney, R.M., Murowchick, J.B., Grauch, R.I., 1999. Sedimentary exhalative nickel-molybdenum ores in South China. Economic Geology 94, 1051-1066.

Luo, T.Y., Zhang, H., Li, X.B., Zhu, D., 2003. Mineralization charcteristics of the multi-element-rich strata in the Niutitang Formation black shale series, Zunyi, Guizhou, China. Acta Mineralogica Sinica 23, 296-302 (in Chinese with English abstract).

Ma, G.L., Beaudoin, G., Qi, S.J., Li, Y., 2004. Geology and geochemistry of the Changba SEDEX Pb-Zn deposit, Qinling orogenic belt, China. Mineralium Deposita 39, 380-395.

Mao, J.W., Lehmann, B., Du, A.D., Zhang, G.D., Ma, D.S., Wang, Y.T., Zeng, M.G., Kerrich, R., 2002. Re-Os dating of polymetallic Ni-Mo-PGE-Au mineralization in lower Cambrian black shales of south China and its geologic significance. Economic Geology 97, 1051-1061.

Mao, J.W., Zhang, G.D., Du, A.D., Wang, Y,T., Zeng, M.G., 2001. Geology, geochemistry and Re-Os isotopic dating of the Huangjiawan Ni-Mo-PGE deposit, Zunyi, Guizhou province. Acta Geologica Sinica 75, 234-243 (in Chinese with English abstract).

Mathur, R., Brantley, S., Anbar, A., Munizaga, F., Maksaev, V., Newberry, R., Vervoort, J.Hart, G., 2010. Variation of Mo isotopes from molybdenite in high-temperature hydrothermal ore deposits. Mineralium Deposita 45, 43-50.

McCallum, M.E., Loucks, R.R., Carlson, R.R., Cooley, E.F., Doerge, T.A., 1976. Platinum metals associated with hydrothermal copper ores of the New Rambler mine, Medicine Bow Mountains, Wyoming. Economic Geology 71, 1429-1450.

McManus, J., Nägler, T.F., Siebert, C., Wheat, C.G., Hammond, D.E., 2002. Oceanic molybdenum isotope fractionation: Diagenesis and hydrothermal ridge-flank alteration. Geochemistry Geophysics Geosystems 3, doi: 10.1029/2002GC000356.

Mernagh, T.P., Heinrich, C.A., Leckie, J.F., Carville, D.P., Gilbert, D.J., Valenta, R.K., Wyborn, L.A.I., 1994. Chemistry of low-temperature hydrothermal gold, platinum, and palladium (± uranium) mineralization at Coronation Hill, northern Territory, Australia. Economic Geology 89, 1053-1073.

Naldrett, T., Kinnaird, J., Wilson, A., Chunnett, G., 2008. Concentration of PGE in the Earth`s crust with special references to the Bushveld Complex. Earth Science Frontiers 15, 264-297.

Neuendorf, K.K.E, Jackson, J.A., Mehl, J.P., 2005. Glossary of geology, 5th ed., American Geological Institute, Alexandria, Va.

Nozaki, Y., 1997. A fresh look at element distribution in the North Pacific. Eos (Transactions, American Geophysical Union). http://www.agu.org/pubs/eos-news/supplements/1995-2003/97025e-table.html

Pan, P., Wood, S.A., 1994. Solubility of Pt and Pd sulfides and Au metal in aqueous bisulfide solutions. Ⅱ. Results at 200°C to 350°C. Mineralium Deposita 29, 373-390.

Pan, Y.M., Xie, Q.L., 2001. Extreme fractionation of platinum group elements in volcanogenic massive sulfide deposits. Economic Geology 96, 645-651.

Pasava, J., Kribek, B., Vymazalova, A., Sykorova, I., Zak, K., Orberger, B., 2008. Multiple sources of metals of mineralization in Lower Cambrian black shales of South China: Evidence from geochemical and petrographic study. Resource Geology 58, 25-42.

Pasava, J., Vymazalova, A., Petersen, S., Herzig, P., 2004. PGE distribution in massive sulfides from the PACMANUS hydrothermal field, eastern Manus basin, Papua New Guinea: implications for PGE enrichment in some ancient volcanogenic massive sulfide deposits. Mineralium Deposita 39, 784-792.

Qiu, Y.M., Gao, S., 2000. First evidence of >3.2 Ga continental crust in the Yangtze craton of South China and its implications for Archean crustal evolution and Phanerozoic tectonics. Geology 28, 11-14.

Regional Geology and Mineral Resource Report, 1969. Dayong map sheet, Hunan province. Scale: 1/200000. Compiled by the 5th branch geological team of the Regional Geological Survey Bureau of Hunan province, China.

Relvas, J.M.R.S., Barriga, F.J.A.S., Ferreira, A., Noiva, P.C., Pacheco, N.Barriga, G., 2006. Hydrothermal alteration and mineralization in the Neves-Corvo volcanic-hosted massive sulfide deposit, Portugal. I. Geology, mineralogy, and geochemistry. Economic Geology 101, 753-790.

Rousseau, R.M., 2001. Detection limit and estimate of uncertainty on analytical XRF results. The Rigaku Journal 18, 33-47.

Ryb, U., Erel, Y., Matthews, A., Avni, Y., Gordon, G.W., Anbar, A.D., 2009. Large molybdenum isotope variations trace subsurface fluid migration along the Dead Sea transform. Geology 37, 463-466.

Schröder, S., Grotzinger, J.P., 2007. Evidence for anoxia at the Ediacaran-Cambrian boundary: the record of redox-sensitive trace elements and rare earth elements in Oman. Journal of the Geological Society 164, 175-187.

Scott, C., Lyons, T.W., Bekker, A., Shen, Y., Poulton, S.W., Chu, X., Anbar, A.D., 2008. Tracing the stepwise oxygenation of the Proterozoic ocean. Nature 452, 456-460.

Shu, D.G., Morris, S.C., Han, J., Chen, L., Zhang, X.L., Zhang, Z.F., Liu, H.Q., Li, Y., Liu, J.N., 2001. Primitive deuterostomes from the Chengjiang Lagerstatte (Lower Cambrian, China). Nature 414, 419-424.

Siebert, C., McManus, J., Bice, A., Poulson, R., Berelson, W.M., 2006. Molybdenum isotope signatures in continental margin marine sediments. Earth and Planetary Science Letters 241, 723-733.

Siebert, C., Nägler, T.F., Kramers, J.D., 2001. Determination of molybdenum isotope fractionation by double-spike multicollector inductively coupled plasma mass spectrometry. Geochemistry Geophysics Geosystems 2, doi: 10.1029/2000GC000124.

Siebert, C., Nägler, T.F., von Blanckenburg, F., Kramers, J.D., 2003. Molybdenum isotope records as a potential new proxy for paleoceanography. Earth and Planetary Science Letters 211, 159-171.

Slack, J.F., Kelley, K.D., Anderson, V.M., Clark, J.L., Ayuso, R.A., 2004. Multistage hydrothermal silicification mad Fe-Tl-As-Sb-Ge-REE enrichment in the Red Dog Zn-Pb-Ag district, northern Alaska: Geochemistry, origin, and exploration applications. Economic Geology 99, 1481-1508.

Steiner, M., Li, G.X., Qian, Y., Zhu, M.Y., Erdtmann, B.D., 2007. Neoproterozoic to early Cambrian small shelly fossil assemblages and a revised biostratigraphic correlation of the Yangtze Platform (China). Palaeogeography Palaeoclimatology Palaeoecology 254, 67-99.

Steiner, M., Wallis, E., Erdtmann, B.D., Zhao, Y.L., Yang, R.D., 2001. Submarine-hydrothermal exhalative ore layers in black shales from South China and associated fossils - insights into a Lower Cambrian facies and bio-evolution. Palaeogeography Palaeoclimatology Palaeoecology 169, 165-191.

Vine, J.D., Tourtelot, E.B., 1970. Geochemistry of black shale deposits: a summary report. Economic Geology 65, 253-272.

Voegelin, A.R., Nägler, T.F., Samankassou, E., Villa, I.M., 2009. Molybdenum isotopic composition of modern and Carboniferous carbonates. Chemical Geology 265, 488-498.

Wallis, E., 2007. The climatic and environmental history of the South Chinese Yangtze platform during the Neoproterozoic and Early Cambrian: hydrothermally active and salinity stratified epicontinental basins a key for understanding the "Cambrian explosion"? Ph.D Thesis. Berlin. 1-227 (in Germany with English abstract).

Wille, M., Nägler, T.F., Lehmann, B., Schroder, S., Kramers, J.D., 2008. Hydrogen sulphide release to surface waters at the Precambrian/Cambrian boundary. Nature 453, 767-769.

Wood, S.A., Mountain, B.W., Pan, P., 1992. The Aqueous geochemistry of platinum, palladium and gold: Recent experimental constraints and a reevaluation of theoretical predictions. Canadian Mineralogist 30, 955-982.

Wu, C.D., Shen, Y.P., Hou, Q.L., 2001. PGE geochemistry and enrichment factor of black shale series in west Hunan province. Natural Science Progress 11, 507-513 (in Chinese).

Wu, S., Zhao, Y.H., Feng, X.B., Wittmeier, A., 1996. Application of inductively coupled plasma mass spectrometry for total metal determination in silicon-containing solid samples using the microwave-assisted nitric acid hydrofluoric acid hydrogen peroxide boric acid digestion system. Journal of Analytical Atomic Spectrometry 11, 287-296.

Xu, L.G., Lehmann, B., Mao, J.W., Nägler, T.F., Neubert, N., Böttcher, M.E., 2011. Mo isotope and trace element patterns of Early Cambrian black shales in South China: constraints on the paleoenvironment and synsedimentary polymetallic Ni-Mo-PGE-Au mineralization. In preparation.

Xu, L.G., Lehmann, B., Mao, J.W., Qu, W.J., Du, A.D., 2011. Re-Os age of polymetallic Ni-Mo-PGE-Au mineralization in Early Cambrian black shales of South China – A reassessment. Economic Geology 105, 511-522.

Yin, C.Y., Tang, F., Liu, Y.Q., Gao, L.Z., Liu, P.J., Xing, Y.S., Yang, Z.Q., Wan, Y.S., Wang, Z.Q., 2005. U-Pb zircon age from the base of the Ediacaran Doushantuo Formation in the Yangtze Gorges, South China: constraint on the age of Marinoan glaciation. Episodes 28, 48-49.

Zhang, S.H., Jiang, G.Q., Zhang, J.M., Song, B., Kennedy, M.J., Christie-Blick, N., 2005. U-Pb sensitive high-resolution ion microprobe ages from the Doushantuo Formation in south China: Constraints on late Neoproterozoic glaciations. Geology 33, 473-476.

Zhu, M.Y., Zhang, J.M., Steiner, M., Yang, A.H., Li, G.X., Erdtmann, B.D., 2004. Sinian-Cambrian stratigraphic framework for shallow- to deep-water environments of the Yangtze Platform: an integrated approach. Progress in Natural Science (Special Issue 2004), 75-84.

CHAPTER EIGHT:

CONCLUSIONS, MODELS AND PERSPECTIVES

8.1 Conclusions

Based on detailed field work and lab experiments, this thesis presents new data on the black shales of the Early Cambrian Niutitang Formation in South China, and the locally distributed, polymetallic Ni-Mo-PGE-Au sulfide mineralization within the black shale sequence. In combination with data from the literature, the following conclusions are achieved:

(1) The new 14-point Re-Os isochron age of 521 ± 5 Ma is the currently most precise and accurate radiometric age for the polymetalllic Ni-Mo-PGE-Au mineralization in the Early Cambrian black shale sequence on the Yangtze Platform. This age is ~20 Ma younger than in earlier less comprehensive Re-Os studies, and is consistent both with the biostratigraphic Tommotian age, and with recent studies applying the Pb-Pb and SHRIMP U-Pb methods on over- and underlying rock units, respectively. A global correlation with the marine and biological evolution at the PC/C boundary, as previously suggested, is not possible. The initial $^{187}Os/^{188}Os$ ratio of the sulfide ore is 0.87 ± 0.07, which is equal to the initial $^{187}Os/^{188}Os$ ratio of ~0.80 of the black shale host rock, consistent with the seawater origin of the metals under depositional conditions of very low clastic input.

(2) A stratigraphic profile of the black shale sequence (Dingtai profile over 33 m of stratigraphic thickness) has been grouped into three paleoenvironmental intervals, based on Mo isotope features, Fe speciation and redox-sensitive geochemistry. Interval 1 (0-1 m) has all features of a euxinic environment, e.g. extreme metal and TOC enrichment and heavy $\delta^{98/95}Mo$ values, and is then followed by interval 2 (1-11 m) with variable $\delta^{98/95}Mo$ composition. Elevated contents of redox-sensitive elements and their ratios, and relatively high Fe_{HR}/Fe_T ratios ("reactive iron") suggest ongoing euxinic conditions. The overlying interval 3 (11-33 m) reveals suboxic conditions with generally light $\delta^{98/95}Mo$ values in the lowermost part and fluctuant $\delta^{98/95}Mo$ values in the uppermost part, and relatively low redox-sensitive element contents. The

black shale sequence has an astonishingly wide variation in Mo isotope composition which results both from variable euxinic/suboxic depositional conditions, and, more importantly, from continental Mo input during periods of a restricted basin situation.

(3) The polymetallic sulfide ores have relatively consistent heavy $\delta^{98/95}$Mo values (from 0.94 to 1.38‰, with an average of 1.13 ± 0.14‰, 1σ, n = 11) while the host black shale and phosphorite have variable $\delta^{98/95}$Mo values (0.81 to 1.70‰, with an average of 1.28 ± 0.41‰, 1σ, n = 14). This variation is due to variable paleoenvironmental conditions from suboxic to euxinic, and partly closed-system fractionation in protected sedimentary basins.

(4) Both the polymetallic sulfides and the host black shales show PGE distribution patterns similar to present-day seawater, but different from hydrothermal fluids. The polymetallic sulfide bed has a generally consistent metal enrichment by a factor of 10^7 compared to present-day seawater, while the host black shales are largely controlled by terrigenous input. Ni- and Mo-based metal ratios reveal that both the polymetallic sulfide ores and the host black shales have ratios similar to present-day seawater. REE + Y patterns of the polymetallic sulfide bed are characterized by a remarkably positive Y anomaly, consistent with an origin of the REE budget dominantly from seawater.

8.2 Models

8.2.1 Evolution model for the paleoenvironment during Early Cambrian

Molybdenum stable isotope fractionation is a promising proxy for paleo-redox conditions of the Earth's oceanic system and atmosphere. This thesis reports Mo isotope compositions of stratigraphically determined Early Cambrian black shales in South China. In combination with data from previous literature, we establish a primary framework of Mo isotope evolution during the Early Cambrian, and propose a model of partly closed ocean basins with periodic replenishment of fresh seawater for the Yangtze Platform. This model can explain the remarkable variability of $\delta^{98/95}$Mo values within a short stratigraphic interval of 33 m. Light $\delta^{98/95}$Mo values of the black shales around 0 permil represent for restricted basin conditions dominated by continental input of molybdenum, while heavy $\delta^{98/95}$Mo values define episodes of periodical replenishment by fresh seawater.

Several geochemical proxies indicate that the lowermost black shale of the Dingtai profile, including a synsedimentary polymetallic sulfide layer, represents euxinic depositional conditions in a mainly open ocean situation. During this interval, the basin is freely connected to the open ocean; the Mo isotope composition of the marine would reflect the open ocean Mo signature. The interval 1 is followed by euxinic deposition in a periodically strongly restricted basin during interval 2, grading upwards into an environment of suboxic marine deposition (interval 3). The black shale sequence has astonishingly wide variation in Mo isotope composition during interval 2 and 3 can be caused both by variable euxinic/suboxic deposition conditions and by continental Mo input during periods of a restricted basin situation. Under euxinic conditions and in a restricted basin situation, Mo deposition may be so strong that the metal inventory of the basin becames completely depleted in ocean-derived Mo, and Mo influx may became dominated by continental input. The Mo isotopic composition in euxinic sediments is then representing the continental input with light $\delta^{98/95}$Mo values, until replenishment by new seawater with heavy Mo restores the normal open-system situation. This model suggests a situation of restricted basins along the oceanic margin of the Yangtze Platform during the Early Cambrian. Major geological event (e.g. seawater transgression or plate reconfiguration) and the end-Proterozoic karst morphology likely controlled these restricted basins which periodically connected with the open ocean. Although variable euxinic/suboxic depositional condition is another possibility responsible for the wide variation in Mo isotope composition during interval 2 and 3, the process of periodical replenishment of a restricted basin situation would be dominant. In brief, the Early Cambrian marine black shale sedimentation in South China developed from euxinic to suboxic. The periodical replenishment model reveals that the sedimentary conditions during the Early Cambrian were not stable, but underwent from open to closed systems and back.

The Mo isotope composition of black shales formed under euxinic condition enable us to estimate the changes in the areal proportion of sediments. At the present-day, although the euxinic condition covering less than ~ 0.5% of the ocean floor, Mo precipitation into euxinic sediments account for ~ 25% of the Mo removal flux from seawater. A small decrease in the area of oxic sediments would therefore be accompanied by a large proportional increase in the area covered by euxinic sediments. At steady state, the periodic decreases in $\delta^{98/95}$Mo under euxinic conditions would have been consistent with an ~ tenfold increase world wide in the area of highly reducing sediment accumulation. Due to no available data on the extent of sediment accumulation that occurred under suboxic conditions, the above assumption is only considering oxic and euxinic accumulations. Actually, suboxic sedimentary environments once thought to be of negligible importance to the Mo elemental and isotope budgets. Changes of seawater Mo isotope owing to the contraction of oxic deposition could be partially countered by the expansion of suboxic deposition. Although little is known about the effect of suboxic sedimentation in the Early Cambrian oceans, the relatively low $\delta^{98/95}$Mo values of the interval 1 comparing to the present-day seawater (~ 2.3‰) is strongly indicative of more widespread euxinic marine environments during the Early Cambrian (Interval 1) than present-day (Fig. 8-1).

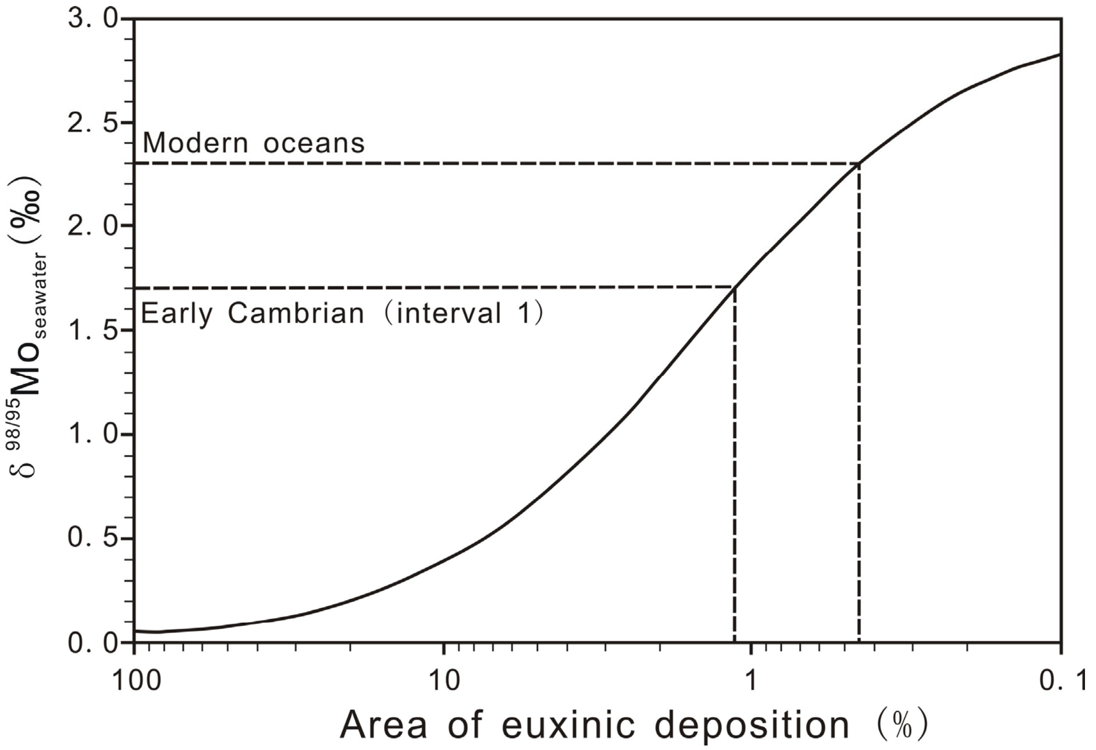

Fig. 8-1: Relatively light $\delta^{98/95}$Mo value of the Early Cambrian reducing sediments comparing to the Modern oceans indicating more widespread euxinic marine environments during the Early Cambrian than present-day.

8.2.2 Genetic model for the polymetallic Ni-Mo-PGE-Au mineralization

The origin of the metals extremely enriched in the polymetallic Ni-Mo-PGE-Au sulfide ore layer has been ascribed to seawater scavenging or hydrothermal venting. Samples from different mine sites yield one Re-Os isochron which strongly suggests that the polymetallic sulfide layer represents one regionally distributed stratigraphic level and formed by a uniform geological process. The initial ^{187}Os/^{188}Os ratio of the sulfide ore is 0.87 ± 0.07. Osmium enrichment in the sulfide ore layer is likely from seawater scavenging, because leaching of (unexposed) ultramafic rocks or hydrothermal seafloor venting from a hidden mafic-ultramafic intrusion would be reflected in a much lower initial ^{187}Os/^{188}Os ratio. Comparison of the polymetallic sulfide ores with the host black shales, syngenetic hydrothermal massive sulfides (VMS-, Sedex-type and modern active black smoker sulfides) and present-day seawater reveals that metal enrichment in the polymetallic Ni-Mo-PGE-Au sulfide ore layer was likely caused by seawater scavenging at low clastic sedimentation rate, whereas the host black shale formed by a mixture of terrigenous materials and seawater-derived precipitations. Evidence for hydrothermal venting is not observed.

Considering the Mo isotope investigation and micro-textural observation, we propose a two-source model for the spectacular metal enrichment in the polymetallic Ni-Mo-PGE-Au sulfide ore layer. $\delta^{98/95}$Mo values of the polymetallic sulfide ores are occasionally lower than those of the host black shales. This may have been caused by mixing of re-deposited Mo-rich aggregates formed under variable suboxic to euxinic environments and in-situ precipitated Mo. This proposition is supported by textural evidence of both laminated polymetallic sulfides and their rip-up clasts. Regardless of the causes of re-deposition (e.g. tectonic event, storm activity), it is possible that Mo deposited under relatively shallow and intermittent suboxic conditions. Suboxic sediments are characterized by variable $\delta^{98/95}$Mo values, but lighter than euxinic sediments. Although some $\delta^{98/95}$Mo values of the polymetallic sulfide ores are slightly lighter than those of the host black shales, relatively consistent values suggest that the Mo-aggregates formed under suboxic conditions represent only a small portion of the sulfide ore layer and re-deposition processes only occurred at a small scale. Alternatively, the moderate variation in Mo isotope composition in the sulfide mineralization could also derive from a moderate restricted basin situation, as indicated by sulfur isotope zoning in some sulfide aggregates. In contrast to the relatively consistent $\delta^{98/95}$Mo values in the polymetallic sulfide ores, strongly variable $\delta^{98/95}$Mo values of the host black shales are jointly caused by two reasons: input of terrrigeous materials with non-fractionated Mo, and the suboxic depositional environment, which have been proven widespread during the Early Cambrian in South China.

8.3 Perspective

The polymetallic Ni-Mo-PGE-Au sulfide mineralization and the black shale sequences on the Yangtze Platform provide a good topic for investigating both the Early Cambrian paleoceanic environment and ore formation. This thesis achieved some significant progress on both of them, which will surely benefit to futhre exploration and scientific study in this area. However, due to the complexity of the subject and time restrictions of this study, these scientific issues are far from the completely understood. Further studies should be done to help better understand atmosphere-hydrosphere-lithosphere interactions during the Early Cambrian and metallogenesis related to the black shales in South China.

Besides the polymetallic Ni-Mo-PGE-Au sulfide ore, the Early Cambrian black shale sequences also host stratiform barite, vanadium, phosphorite and stone coal deposits. We have finished field work and partly lab experiments on these deposits (see Appendix), however, no detailed investigation has been carried out yet. We noticed the metal zonation in the Sancha district, where from northeast to southwest, the intensity of the polymetallic Ni-Mo-PGE-Au mineralization decreases gradually and grades into vanadium mineralization. We infer that such zonation is a reflection of the regional redox gradient during sedimentary processes. Ongoing comparison between the polymetallic sulfide and vanadium mineralization may offer some evidence on this assumption.

Sedimentary phosphorite hosted in the Early Cambrian black shale sequence is the economically most important resource of the region, utilized as agricultural fertilizer. For example, the Kunyang phosphorite deposit in Yunnan province is the largest phosphorite mine in China. Stratigraphic correlations of the Kunyang phosphorite deposit have been well studied as it served as one of the three candidates for the Precambrian/Cambrian boundary Global Stratotype Section and Point (GSSP). The formation of the phosphorite deposits is related to suboxic to euxinic marine conditions. The paleoenvironmental comparison of different phosphorite deposits may reveal the cause of the variable thickness of the phosphorite beds and their relationship to redox conditions.

The Early Cambrian black shale hosted barite deposits on the Yangtze Platform are generally considered as related to seafloor hydrothermal venting, and they have been taken as evidence that the polymetallic sulfide ore is also of hydrothermal genesis. Do they really have genetic relations? Detailed geological and geochemical studies of the barite deposits may contribute to solve this argument.

In summary, the paleoenvironmental overview and integrated genetic understanding of Early Cambrian polymetallic sulfide, vanadium, phosphorite, barite and “stone coal” deposits on the Yangtze Platform is still in perspective.

APPENDIX

Table A12: Complete bulk rock geochemical data of V-bearing black shales from drilling core ZK3001 in Sancha district.

Table A13: Complete bulk rock geochemical data of V-bearing black shales from Xiongjiata roadcut profile.

Table A14: Complete bulk rock geochemical data of V-bearing black shales from drilling core ZK1801 in Sancha district.

Table A15: Complete bulk rock geochemical data of black shales from drilling core ZK001 in Sancha district.

Table A16: Complete bulk rock geochemical data of samples from Kunyang profile, Yunnan province.

Figure A1: Sample location in stratigraphic columns

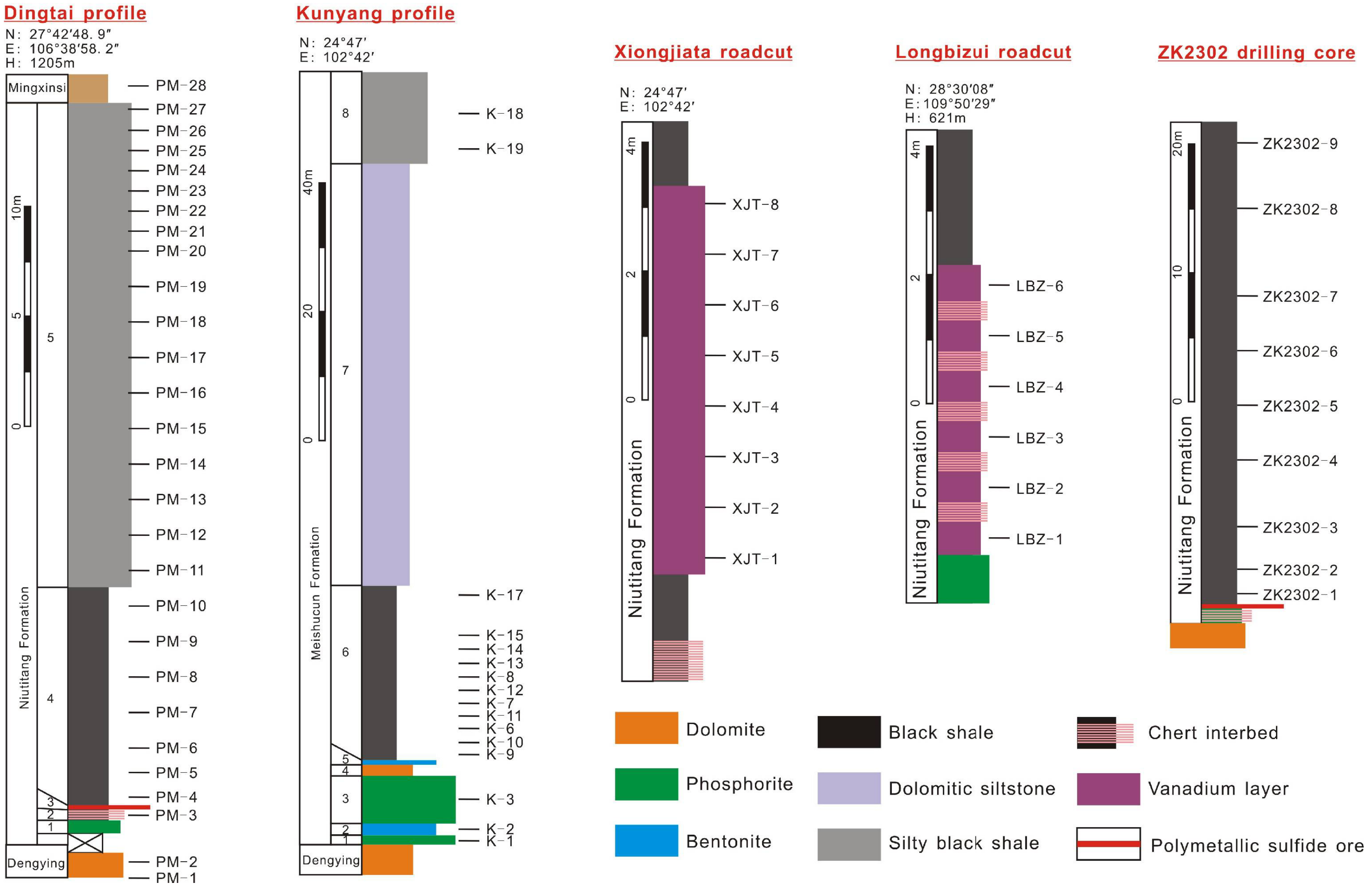

Figure A1（continued）

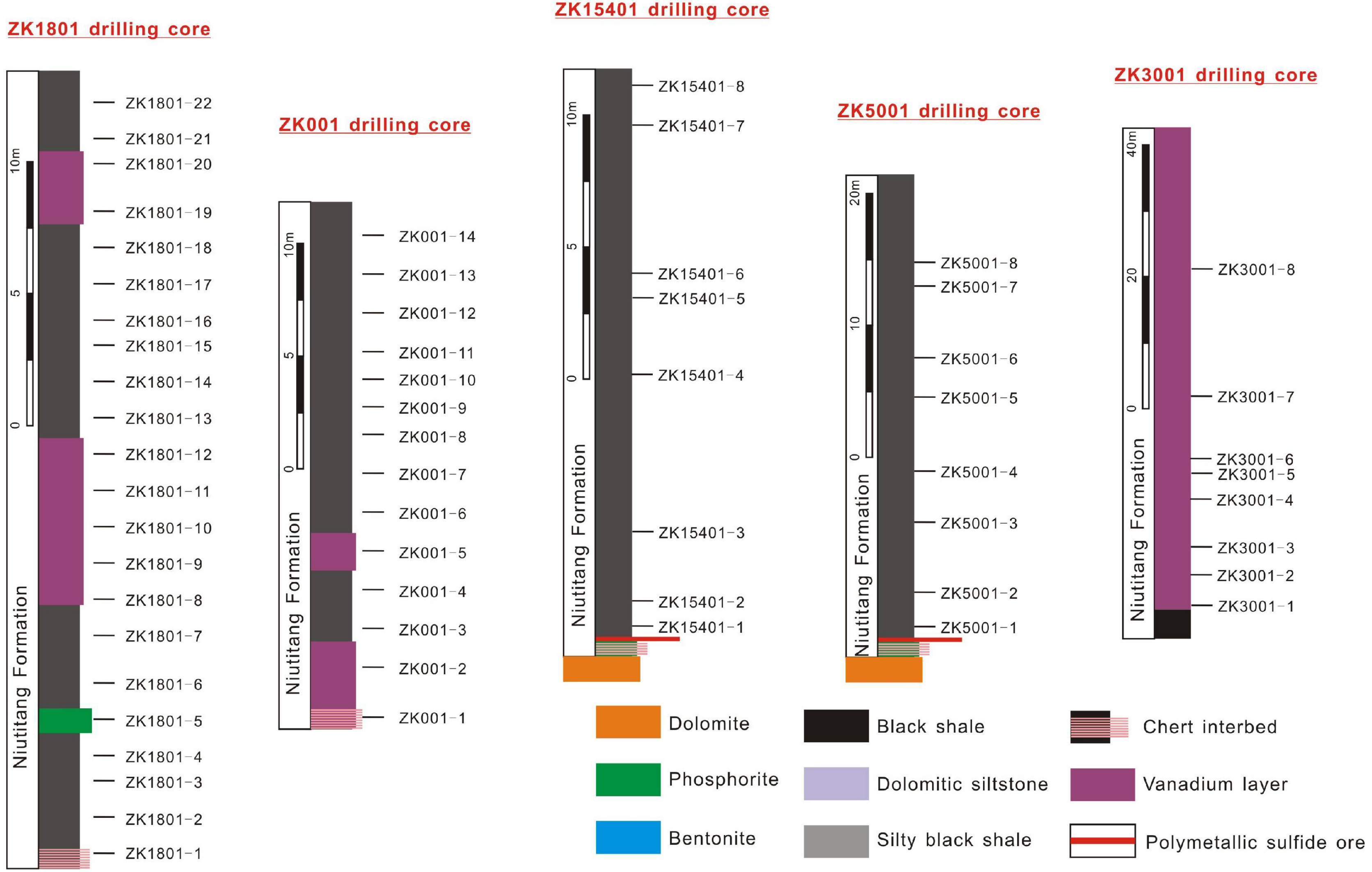

Table A1: Sample documentation in this thesis

Sample	Lithology	PTS	Major element	Trace element	REE	PGE	Mo isotope	DOP	Re-Os age
Dingtai outcrop profile (Latitude: 27°42′ 48.9″; Longitude: 106°38′ 58.2″; Altitude: 1205m)									
PM-1	Dolomite	√	√	√	√				
PM-2	Dolomite	√	√	√	√				
PM-3	Black shale	√	√	√	√				
PM-4	Black shale	√	√	√	√		√	√	
PM-5	Black shale		√	√	√		√	√	
PM-6	Black shale		√	√	√		√	√	
PM-7	Black shale	√	√	√	√		√	√	
PM-8	Black shale		√	√	√		√	√	
PM-9	Black shale		√	√	√		√	√	
PM-10	Black shale		√	√	√		√	√	
PM-11	Black shale	√	√	√	√		√	√	
PM-12	Black shale		√	√	√		√	√	
PM-13	Black shale		√	√	√		√	√	
PM-14	Black shale		√	√	√		√	√	
PM-15	Black shale		√	√	√		√	√	
PM-16	Black shale		√	√	√		√	√	
PM-17	Black shale	√	√	√	√		√	√	
PM-18	Black shale		√	√	√		√	√	
PM-19	Black shale		√	√	√		√	√	
PM-20	Black shale	√	√	√	√		√	√	
PM-21	Black shale		√	√	√		√	√	
PM-22	Black shale		√	√	√		√	√	
PM-23	Black shale		√	√	√		√	√	
PM-24	Black shale	√	√	√	√		√	√	
PM-25	Black shale		√	√	√				
PM-26	Black shale		√	√	√				
PM-27	Black shale		√	√	√		√	√	
PM-28	Shale	√	√	√	√				
PM-29	Shale		√	√	√				
PM-30	Shale		√	√	√				
Dazhuliushui underground (Latitude: 27°43′ 13.5″; Longitude: 106°38′ 44.3″; Altitude: 1200m)									
DZLS-1	Black shale	√	√	√	√				
DZLS-2	Sulfide ore		√	√	√	√	√		√
DZLS-3	Black shale	√	√	√	√				
DZLS-4	Black shale	√	√	√	√				
DZLS-5	Sulfide ore	√	√	√	√	√			√
DZLS-6	Black shale	√	√	√	√				
DZLS-7	Black shale		√	√	√		√	√	
DZLS-8	Sulfide ore		√	√	√	√	√		√
DZLS-9	Black shale		√	√	√		√	√	
DZLS-11	Sulfide ore	√	√	√	√	√			√
DZLS-14	Sulfide ore		√	√	√	√			√
DZLS-17	Sulfide ore	√	√	√	√	√			√
Maluhe underground (Latitude: 26°44′ 40.0″; Longitude: 105°37′ 13.5″; Altitude: 1402m)									
MLH-1	Black shale	√	√	√	√				
MLH-2	Sulfide ore	√	√	√	√	√	√		√
MLH-3	Black shale	√	√	√	√				
MLH-4	Black shale	√	√	√	√		√	√	
MLH-5	Sulfide ore	√	√	√	√	√	√		√
MLH-6	Phosphorite	√	√	√	√		√	√	
MLH-7	Black shale		√	√	√				
MLH-8	Sulfide ore		√	√	√	√			√
MLH-9	Black shale		√	√	√				
MLH-10	Sulfide ore	√	√	√	√	√			√
MLH-11	Sulfide ore	√	√	√	√	√			√
MLH-12	Sulfide ore		√	√	√	√			√

Table A1 (continued)

Sample	Lithology	PTS	Major element	Trace element	REE	PGE	Mo isotope	DOP	Re-Os age
Sancha underground (Latitude: 29°04′ 26.6″; Longitude: 110°34′ 32.7″; Altitude: 1861m)									
SC-2	Sulfide ore	√	√	√	√	√	√	√	√
SC-5	Sulfide ore	√	√	√	√	√			√
SC-8	Sulfide ore	√	√	√	√	√			√
SC-11	Sulfide ore	√	√	√	√	√	√	√	√
SC-14	Sulfide ore		√	√	√	√			√
Cili underground (Latitude: 29°11′ 10″; Longitude: 110°51′ 03″; Altitude: 624m)									
CL-1	Phosphorite	√	√	√	√				
CL-2	Sulfide ore	√	√	√	√				
CL-3	Black shale		√	√	√				
CL-4	Black shale		√	√	√				
CL-5	Black shale		√	√	√				
CL-6	Black shale		√	√	√				√
CL-7	Black shale		√	√	√				
CL-8	Black shale	√	√	√	√				
CL-9	Black shale		√	√	√				
CL-Ore-1	Sulfide ore		√	√	√				√
CL-Ore-2	Sulfide ore		√	√	√				√
CL-Ore-3	Sulfide ore		√	√	√				√
CL-Ore-4	Sulfide ore		√	√	√				√
CL-Ore-5	Sulfide ore		√	√	√				√
CL-Ore-6	Sulfide ore		√	√	√				√
CL-Ore-7	Sulfide ore		√	√	√				√
CL-Ore-8	Sulfide ore	√	√	√	√				√
Longbizui road-cut profile (Latitude: 28°30′ 08″; Longitude: 109°50′ 29″; Altitude: 621m)									
LBZ-1	Black shale	√	√	√	√				
LBZ-2	Black shale		√	√	√				
LBZ-3	Black shale		√	√	√				
LBZ-4	Black shale	√	√	√	√				
LBZ-5	Black shale		√	√	√				
LBZ-6	Black shale		√	√	√				
ZK2302 drilling core profile									
ZK2302-1	Black shale		√	√	√				
ZK2302-2	Black shale		√	√	√				√
ZK2302-3	Black shale		√	√	√				
ZK2302-4	Black shale		√	√	√				
ZK2302-5	Black shale		√	√	√				
ZK2302-6	Black shale		√	√	√				
ZK2302-7	Black shale		√	√	√				
ZK2302-8	Black shale		√	√	√				
ZK2302-9	Black shale		√	√	√				
ZK15401 drilling core profile									
ZK15401-1	Black shale		√	√	√				
ZK15401-2	Black shale		√	√	√				
ZK15401-3	Black shale		√	√	√				√
ZK15401-4	Black shale		√	√	√				
ZK15401-5	Black shale		√	√	√				
ZK15401-6	Black shale		√	√	√				
ZK15401-7	Black shale		√	√	√				
ZK15401-8	Black shale		√	√	√				
ZK5001 drilling core profile									
ZK5001-1	Black shale		√	√	√				
ZK5001-2	Black shale		√	√	√				
ZK5001-3	Black shale		√	√	√				√
ZK5001-4	Black shale		√	√	√				
ZK5001-5	Black shale		√	√	√				
ZK5001-6	Black shale		√	√	√				
ZK5001-7	Black shale		√	√	√				
ZK5001-8	Black shale		√	√	√				

Table A1 (continued)

Sample	Lithology	PTS	Major element	Trace element	REE	PGE	Mo isotope	DOP	Re-Os age
ZK3001 drilling core profile									
ZK3001-1	Black shale		√	√	√				
ZK3001-2	Black shale		√	√	√				
ZK3001-3	Black shale		√	√	√				
ZK3001-4	Black shale		√	√	√				
ZK3001-5	Black shale		√	√	√				
ZK3001-6	Black shale		√	√	√				√
ZK3001-7	Black shale		√	√	√				
ZK3001-8	Black shale		√	√	√				
Xiongjiata road-cut profile (Latitude: 28°56′ 56″; Longitude: 110°21′ 56″; Altitude: 451m)									
XJT-1	Black shale		√	√	√				
XJT-2	Black shale		√	√	√				√
XJT-3	Black shale	√	√	√	√				
XJT-4	Black shale		√	√	√				
XJT-5	Black shale	√	√	√	√				
XJT-6	Black shale		√	√	√				
XJT-7	Black shale		√	√	√				
XJT-8	Black shale		√	√	√				
ZK1801 drilling core profile									
ZK1801-1	Black shale		√	√	√				
ZK1801-2	Black shale		√	√	√				
ZK1801-3	Black shale		√	√	√				
ZK1801-4	Black shale		√	√	√				
ZK1801-5	Black shale		√	√	√				
ZK1801-6	Black shale		√	√	√				
ZK1801-7	Black shale		√	√	√				
ZK1801-8	Black shale		√	√	√				
ZK1801-9	Black shale		√	√	√				
ZK1801-10	Black shale		√	√	√				√
ZK1801-11	Black shale		√	√	√				
ZK1801-12	Black shale		√	√	√				
ZK1801-13	Black shale		√	√	√				
ZK1801-14	Black shale		√	√	√				
ZK1801-15	Black shale		√	√	√				
ZK1801-16	Black shale		√	√	√				
ZK1801-17	Black shale		√	√	√				
ZK1801-18	Black shale		√	√	√				
ZK1801-19	Black shale		√	√	√				
ZK1801-20	Black shale		√	√	√				
ZK1801-21	Black shale		√	√	√				
ZK1801-22	Black shale		√	√	√				
ZK001 drilling core profile									
ZK001-1	Black shale		√	√	√				
ZK001-2	Black shale		√	√	√				
ZK001-3	Black shale		√	√	√				
ZK001-4	Black shale		√	√	√				
ZK001-5	Black shale		√	√	√				
ZK001-6	Black shale		√	√	√				√
ZK001-7	Black shale		√	√	√				
ZK001-8	Black shale		√	√	√				
ZK001-9	Black shale		√	√	√				
ZK001-10	Black shale		√	√	√				
ZK001-11	Black shale		√	√	√				
ZK001-12	Black shale		√	√	√				
ZK001-13	Black shale		√	√	√				
ZK001-14	Black shale		√	√	√				

Table A1 (continued)

Sample	Lithology	PTS	Major element	Trace element	REE	PGE	Mo isotope	DOP	Re-Os age
Kunyang outcrop profile (Latitude: 24°47′; Longitude: 102°42′)									
K-2	Bentonite	√	√	√	√				
K-3	Phosphorite	√	√	√	√				
K-9	Black shale	√	√	√	√				
K-10	Black shale	√	√	√	√				
K-6	Black shale	√	√	√	√				
K-11	Black shale	√	√	√	√				
K-7	Black shale	√	√	√	√				
K-12	Black shale	√	√	√	√				
K-8	Black shale	√	√	√	√				
K-13	Black shale	√	√	√	√				
K-14	Black shale	√	√	√	√				
K-15	Black shale	√	√	√	√				
K-17	Black shale	√	√	√	√				
K-18	Black shale	√	√	√	√				
K-19	Black shale	√	√	√	√				

Note: PTS = polished thin section, PGE = platinum group element, DOP = degree of pyritization

Table A2: Mo isotope data

Sample	Depth (m)*	Lithology	$\delta^{98/95}$Mo (‰) measured	2 σ §
Dingtai Profile				
PM-27	32.3	Black shale	1.19	0.04
PM-24	29.3	Black shale	0.26	0.03
PM-23	28.3	Black shale	0.39	0.06
PM-22	27.3	Black shale	1.53	0.07
PM-21	26.3	Black shale	0.05	0.04
PM-20	25.3	Black shale	1.20	0.04
PM-19	23.8	Black shale	0.50	0.07
PM-18	22.3	Black shale	0.59	0.03
PM-17	20.8	Black shale	0.31	0.08
PM-16	19.3	Black shale	-0.35	0.03
PM-15	17.8	Black shale	-0.02	0.05
PM-14	16.3	Black shale	-0.09	0.05
PM-13	14.8	Black shale	0.08	0.04
PM-12	13.3	Black shale	0.00	0.05
PM-11	11.8	Black shale	-1.54	0.04
PM-10	10.3	Black shale	1.05	0.04
PM-9	8.8	Black shale	1.07	0.03
PM-8	7.3	Black shale	0.57	0.04
PM-7	5.8	Black shale	0.67	0.03
PM-6	4.3	Black shale	-0.14	0.03
PM-5	2.8	Black shale	0.18	0.04
PM-4	1.3	Black shale	1.25	0.05
Maluhe				
MLH-4	0.7	Black shale	1.70	0.05
MLH-5	0.5	Sulfide ore	1.38	0.02
MLH-2	0.5	Sulfide ore	1.37	0.03
MLH-6	0.3	Phosphorite	1.57	0.03
Dazhuliushui				
DZLS-7	0.7	Black shale	0.89	0.02
DZLS-8	0.5	Sulfide ore	1.07	0.06
DZLS-2	0.5	Sulfide ore	1.16	0.04
DZLS-9	0.3	Black shale	1.58	0.03
Sancha				
SC-11	0.5	Sulfide ore	1.19	0.02
SC-2	0.5	Sulfide ore	1.00	0.03

* Stratigraphic position is in meter relative to the polymetallic Ni-Mo-PGE-Au sulfide ore layer.

§ Mo isotope analyses were carried out at the stable isotope laboratory of university of Bern in Switzerland. An assessment of the analytical uncertainty is 2 σ external standard reproducibility of samples.

Table A3: PGE + Ag data

Sample	Lithology	Os ppb	Ru ppb	Rh ppb	Pd ppb	Ir ppb	Pt ppb	Ag ppm
Dazhuliushui								
DZLS-2	Sulfide ore	148	5.96	11.3	297	1.92	255	23.6
DZLS-5	Sulfide ore	163	8.02	11.8	284	2.34	253	27.5
DZLS-8	Sulfide ore	150	7.65	13.4	365	2.64	334	25.1
DZLS-11	Sulfide ore	128	5.28	9.92	275	1.95	235	26.0
DZLS-14	Sulfide ore	104	4.51	8.47	215	1.86	202	12.5
DZLS-17	Sulfide ore	116	8.07	10.6	229	2.11	237	15.5
Maluhe								
MLH-2	Sulfide ore	108	11.3	12.3	236	2.12	207	18.2
MLH-5	Sulfide ore	116	7.57	10.4	228	2.35	241	19.4
MLH-8	Sulfide ore	149	10.8	12.8	258	2.40	250	19.8
MLH-10	Sulfide ore	127	9.21	12.6	269	2.50	277	22.4
MLH-11	Sulfide ore	128	9.35	12.9	280	2.66	295	24.0
MLH-12	Sulfide ore	121	6.83	8.78	207	2.02	218	17.3
Sancha								
SC-2	Sulfide ore	174	11.1	15.6	401	2.81	382	30.6
SC-5	Sulfide ore	80.9	9.60	12.8	286	1.51	245	16.6
SC-8	Sulfide ore	78.6	4.52	5.79	164	1.06	145	14.1
SC-11	Sulfide ore	171	13.6	12.8	289	2.31	277	23.7
SC-14	Sulfide ore	197	12.6	15.6	369	3.05	407	17.0

Os, Ru, Rh, Pd, Ir, Pt were analysed by Inductively Coupled Plasma Mass Spectrometry (ICP-MS), and Ag was analysed by Atomic Absorption Spectrometry (AAS). Analyses were carried out at the National Research Center of Geoanylsis, China Academy of Geological Sciences.

Table A4: Re-Os isotope data

Sample	Lithology	Weight (g)	Re (ppb)	Os_{common} (ppb)	^{187}Os (ppb)	Re/Os_{common}	$^{187}Re/^{188}Os$	$^{187}Os/^{188}Os$	$(^{187/188}Os)t$
Dazhuliushui									
DZLS-2	Sulfide ore	0.105	13364(96)	67.42(0.74)	81.00(0.63)	198.2	957.4(12.6)	9.23(0.11)	0.887
DZLS-5	Sulfide ore	0.102	15330(151)	70.71(0.78)	91.79(0.61)	216.8	1047.2(15.5)	9.98(0.11)	0.848
DZLS-8	Sulfide ore	0.106	12343(71)	74.69(0.44)	75.60(0.36)	165.3	798.2(6.5)	7.78(0.03)	0.821
DZLS-11	Sulfide ore	0.106	10427(57)	64.29(0.42)	64.10(0.36)	162.2	783.4(6.7)	7.66(0.04)	0.833
DZLS-14	Sulfide ore	0.108	8726(44)	50.86(0.31)	53.43(0.36)	171.6	828.8(6.5)	8.07(0.04)	0.849
DZLS-17	Sulfide ore	0.042	10275(46)	54.92(0.57)	60.97(0.01)	187.1	903.7(10.2)	8.53(0.09)	0.654
Sancha									
SC-2	Sulfide ore	0.101	13347(81)	90.34(0.64)	84.10(0.61)	147.7	713.6(6.7)	7.15(0.06)	0.930
SC-5	Sulfide ore	0.104	4079(32)	52.71(0.42)	28.20(0.16)	77.4	373.8(4.2)	4.11(0.03)	0.852
SC-8	Sulfide ore	0.105	5892(59)	41.22(0.28)	37.40(0.20)	142.9	690.5(8.4)	6.97(0.04)	0.954
SC-11	Sulfide ore	0.100	14541(103)	84.13(0.71)	86.50(0.48)	172.8	833.8(7.5)	7.87(0.05)	0.596
SC-14	Sulfide ore	0.103	16832(112)	97.51(0.58)	99.80(0.68)	172.6	834.9(9.2)	7.90(0.06)	0.624
Maluhe									
MLH-2	Sulfide ore	0.100	9994(49)	48.29(0.44)	60.20(0.36)	207.0	1000(10)	9.57(0.08)	0.852
MLH-5	Sulfide ore	0.101	11118(48)	50.06(0.33)	66.30(0.36)	222.1	1073(8)	10.18(0.05)	0.826
MLH-8	Sulfide ore	0.100	15328(73)	58.40(0.34)	90.60(0.55)	262.5	1268(10)	11.92(0.06)	0.866
MLH-12	Sulfide ore	0.102	12098(59)	49.29(0.34)	71.88(0.42)	245.4	1185(10)	11.21(0.07)	0.880
MLH-10	Sulfide ore	0.103	12181(51)	53.85(0.37)	72.79(0.44)	226.2	1093(9)	10.39(0.07)	0.862
MLH-11	Sulfide ore	0.105	11945(50)	55.87(0.48)	71.80(0.39)	213.8	1033(10)	9.88(0.08)	0.875

Model age is calculated with an initial $^{187}Os/^{188}Os$ of 0.866 and an ^{187}Re decay constant of 1.666×10^{-11} yr^{-1} (Smoliar et al., 1996).

Number in parenthesis indicates analytical precision.

Analyses were carried out at the National Research Center of Geoanylsis, China Academy of Geological Sciences (CAGS).

Table A5: Analytical errors and detection limits of different analytical tecniques

XRF method (BGR Hanover)			ICP, ICP-MS methods (AcmeLabs in Canada)		
Components	**Analytical range**	**Uncertainty**	**Components**	**Detection limit**	**Upper limit**
SiO_2	40-100%	1%	**SiO_2**	0.01%	100%
TiO_2	0.1-1.5%	2%	**Al_2O_3**	0.01%	100%
Al_2O_3	0.2-2.0%	2%	**Fe_2O_3**	0.04%	100%
Fe_2O_3	0.2-25%	1%	**CaO**	0.01%	100%
MnO	0.001-0.15%	3%	**MgO**	0.01%	100%
MgO	0.01-3%	2%	**Na_2O**	0.01%	100%
CaO	0.01-5%	2%	**K_2O**	0.01%	100%
Na_2O	0.01-5%	2%	**MnO**	0.01%	100%
K_2O	0.05-5%	1%	**TiO_2**	0.01%	100%
P_2O_5	0.01-0.5%	3%	**P_2O_5**	0.01%	100%
As	up to 500 ppm	15%	**Cr_2O_3**	0.002%	100%
Ba	up to 2200 ppm	10%	**Ba**	5ppm	100%
Ce	up to 150 ppm	20%	**LOI**	0.10%	100%
Co	up to 20 ppm	20%	**C**	0.01%	100%
Cr	up to 60 ppm	25%	**S**	0.02%	100%
Cu	up to 60 ppm	20%	**Au**	0.5 ppb	100 ppb
Ga	up to 30 ppm	10%	**Ag**	0.1 ppm	100 ppm
La	up to 400 ppm	25%	**As**	1 ppm	10000 ppm
Nb	up to 30 ppm	15%	**Ba**	1 ppm	50000 ppm
Ni	up to 30 ppm	30%	**Be**	1 ppm	10000 ppm
Pb	up to 200 ppm	15%	**Bi**	0.1 ppm	2000 ppm
Rb	up to 200 ppm	5%	**Cd**	0.1 ppm	2000 ppm
Sc	up to 20 ppm	15%	**Co**	0.2 ppm	10000 ppm
Sr	up to 4000 ppm	5%	**Cs**	0.1 ppm	10000 ppm
Th	up to 50 ppm	30%	**Cu**	0.1 ppm	10000 ppm
U	up to 20 ppm	20%	**Ga**	0.5 ppm	10000 ppm
V	up to 200 ppm	15%	**Hf**	0.1 ppm	10000 ppm
Y	up to 25 ppm	25%	**Hg**	0.1 ppm	100 ppm
Zn	up to 150 ppm	10%	**Mo**	0.1 ppm	2000 ppm
Zr	up to 200 ppm	10%	**Nb**	0.1 ppm	50000 ppm
			Ni	0.1 ppm	10000 ppm
			Pb	0.1 ppm	10000 ppm
			Rb	0.1 ppm	10000 ppm
			Sb	0.1 ppm	2000 ppm
			Sc		10000 ppm
			Se	0.5 ppm	100 ppm
			Sn	1 ppm	10000 ppm
			Sr	0.5 ppm	50000 ppm
			Ta	0.1 ppm	50000 ppm
			Th	0.2 ppm	10000 ppm
			Tl	0.1 ppm	1000 ppm
			U	0.1 ppm	10000 ppm
			V	8 ppm	10000 ppm
			W	0.5 ppm	10000 ppm
			Y	0.1 ppm	50000 ppm
			Zn	1 ppm	10000 ppm
			Zr	0.1 ppm	50000 ppm
			La	0.1 ppm	50000 ppm
			Ce	0.1 ppm	50000 ppm
			Pr	0.02 ppm	10000 ppm
			Nd	0.3 ppm	10000 ppm
			Sm	0.05 ppm	10000 ppm
			Eu	0.02 ppm	10000 ppm
			Gd	0.05 ppm	10000 ppm
			Tb	0.01 ppm	10000 ppm
			Dy	0.05 ppm	10000 ppm
			Ho	0.02 ppm	10000 ppm
			Er	0.03 ppm	10000 ppm
			Tm	0.01 ppm	10000 ppm
			Yb	0.05 ppm	10000 ppm
			Lu	0.01 ppm	10000 ppm

Note: Highlighted elements digested by Aqua Regia

Table A6: Complete bulk rock geochemical data of the Dingtai profile

Sample	Level (m)	Lithology	SiO_2	Al_2O_3	TFe_2O_3	CaO	MgO	K_2O	Na_2O	TiO_2	MnO	P_2O_5	V_2O_5	Cr_2O_3	BaO	LOI	S	TOC	Sum
			%	%	%	%	%	%	%	%	%	%	%	%	%	%	%	%	%
			ICP-AES	ICP-AES	ICP-AES	ICP-AES	ICP-AES	ICP-AES	ICP-AES	ICP-AES	ICP-AES	ICP-AES	ICP-AES	ICP-AES	ICP-AES	ICP-AES	Leco	Leco	
PM-30	45.0	Shale	60.9	17.6	7.37	0.45	2.51	3.49	0.85	0.92	0.037	0.20			0.12	5.76	0.01	0.32	100.1
PM-29	38.0	Shale	60.5	17.7	7.52	0.11	2.28	3.58	0.80	0.90	0.050	0.20			0.13	5.95	0.01	0.25	99.7
PM-28	34.0	Shale	61.1	17.5	7.15	0.22	2.49	3.47	1.00	0.92	0.035	0.20			0.12	5.66	0.01	0.27	99.9
PM-27	32.3	Black shale	65.1	16.2	2.80	0.17	1.76	4.07	0.38	0.85	0.010	0.09			0.15	7.91	0.02	2.79	99.5
PM-26	31.3	Black shale	66.1	15.4	2.70	0.17	1.38	4.08	0.81	0.82	0.007	0.04			0.17	8.32	0.03	3.31	100.0
PM-25	30.3	Black shale	62.6	15.9	4.10	0.20	2.66	3.65	0.40	0.74	0.020	0.08	0.15		0.14	8.89	0.02	2.78	99.6
PM-24	29.3	Black shale	63.9	15.7	3.42	0.16	1.91	4.02	0.61	0.78	0.010	0.15	0.18		0.15	9.17	0.03	3.33	100.1
PM-23	28.3	Black shale	65.8	15.5	1.96	0.15	1.28	4.07	0.85	0.83	0.009	0.09			0.14	9.01	0.03	4.09	99.7
PM-22	27.3	Black shale	64.9	14.8	2.24	0.16	1.26	4.01	0.75	0.84	0.006	0.08			0.15	11.3	0.03	4.25	100.4
PM-21	26.3	Black shale	64.5	15.0	2.99	0.13	2.18	3.77	0.41	0.76	0.012	0.11	0.26		0.15	9.38	0.03	3.68	99.7
PM-20	25.3	Black shale	68.5	14.5	1.90	0.05	1.25	4.15	0.24	0.80	0.007	0.08			0.17	7.77	0.03	3.22	99.4
PM-19	23.8	Black shale	67.5	14.2	2.41	0.11	1.40	3.60	0.21	0.68	0.008	0.09	0.16		0.14	8.94	0.03	3.70	99.5
PM-18	22.3	Black shale	68.9	13.2	3.16	0.05	1.12	3.64	0.24	0.70	0.007	0.11	0.17		0.14	8.84	0.03	3.96	100.3
PM-17	20.8	Black shale	65.6	14.7	3.27	0.05	2.27	3.57	0.29	0.69	0.014	0.14	0.19		0.14	9.31	0.03	3.77	100.2
PM-16	19.3	Black shale	65.9	14.1	2.44	0.10	1.83	3.64	0.29	0.69	0.010	0.14	0.38		0.15	10.3	0.04	5.42	100.0
PM-15	17.8	Black shale	67.4	13.6	2.07	0.11	1.58	3.60	0.24	0.67	0.009	0.13	0.25		0.15	9.50	0.04	4.42	99.3
PM-14	16.3	Black shale	67.6	14.9	2.07	0.08	1.42	4.13	0.08	0.77	0.006	0.07	0.13		0.17	8.25	0.03	3.16	99.7
PM-13	14.8	Black shale	66.7	14.4	3.20	0.28	1.28	4.06	0.30	0.74	0.006	0.14	0.27		0.15	8.54	0.03	3.74	100.0
PM-12	13.3	Black shale	66.9	15.1	1.73	0.12	1.36	4.34	0.26	0.76	0.005	0.06	0.22		0.17	8.89	0.03	3.93	99.9
PM-11	11.8	Black shale	66.8	12.6	0.73	0.11	0.96	3.04	1.55	0.84	0.003	0.06	0.17		0.17	12.1	0.07	7.06	99.1
PM-10	10.3	Black shale	68.4	11.8	0.58	0.09	0.91	2.92	1.40	0.80	0.003	0.04	0.19		0.17	12.0	0.09	8.24	99.3
PM-9	8.8	Black shale	69.7	11.7	1.79	0.08	0.87	2.79	1.50	0.71	0.003	0.14	0.31		0.15	9.77	0.11	6.85	99.4
PM-8	7.3	Black shale	71.8	11.2	0.80	0.07	0.91	2.88	1.22	0.74	0.004	0.07	0.19		0.22	9.77	0.08	6.14	99.8
PM-7	5.8	Black shale	68.8	12.5	1.75	0.12	1.00	3.19	1.42	0.79	0.004	0.12	0.21		0.18	10.5	0.08	6.56	100.6
PM-6	4.3	Black shale	71.9	10.4	1.10	0.10	0.93	2.92	0.75	0.71	0.004	0.05	0.73		0.20	10.9	0.07	7.09	100.6
PM-5	2.8	Black shale	69.3	9.26	2.29	0.07	0.86	2.53	0.84	0.56	0.003	0.27	0.78	0.17	0.17	12.3	0.11	8.86	99.4
PM-4	1.3	Black shale	65.4	9.47	1.64	0.38	1.29	2.95	0.11	0.43	0.003	0.57	0.76	0.37	0.22	16.3	0.16	11.8	99.9
PM-3	0.5	Phosphorite	7.16	1.32	1.23	50.5	0.25	0.50	0.07	0.02	0.001	36.0	0.26	0.12		2.48	0.06	0.77	99.9
PM-2	-0.7	Dolomite	1.65	0.22	0.19	31.1	21.5	0.08	0.03	0.00	0.012	0.03				45.2	<0.005	0.04	100.0
PM-1	-0.3	Dolomite	0.82	0.13	0.17	30.7	21.4	0.04	0.03	0.00	0.017	0.04				46.3	<0.005	0.06	99.6

Table A6 (continued)

Sample	Li ppm ICP-MS	Ba ppm ICP-MS	Be ppm ICP-MS	Bi ppm ICP-MS	Cd ppm ICP-MS	Co ppm ICP-MS	Cr ppm ICP-MS	Cs ppm ICP-MS	Cu ppm ICP-MS	Ga ppm ICP-MS	Hf ppm ICP-MS	In ppm ICP-MS	Mo ppm ICP-MS	Nb ppm ICP-MS	Ni ppm ICP-MS
PM-30	28.9	4.11	2.76	0.31	1.83	10.2	105	1.94	76.1	20.1	4.22	0.20	17.6	180	87.7
PM-29	22.5	4.24	2.62	0.33	3.86	19.2	109	1.71	78.5	20.5	4.13	0.58	17.0	169	86.6
PM-28	25.2	3.65	2.46	0.27	3.52	7.21	104	18.0	66.1	19.1	4.28	0.21	16.8	175	82.5
PM-27	19.5	1168	3.47	0.56	0.93	7.10	108	7.32	74.6	21.5	4.22	<0.05	15.1	17.3	42.5
PM-26	8.41	7.34	2.41	0.62	14.3	9.83	98.4	3.74	26.3	20.0	3.99	2.19	16.2	169	70.2
PM-25	28.3	8.81	2.89	0.56	5.25	9.95	115	3.32	73.0	19.8	3.90	0.55	15.3	158	99.2
PM-24	14.6	1182	3.30	0.47	0.92	8.39	122	8.42	59.5	20.1	3.94	0.110	24.4	15.7	92.9
PM-23	8.96	1425	2.84	0.50	1.20	7.34	112	9.15	35.6	22.2	4.48	<0.05	27.6	18.0	60.7
PM-22	8.45	1339	3.07	0.50	1.53	11.5	104	9.03	37.8	21.1	4.18	<0.05	26.1	17.7	74.5
PM-21	18.1	1429	2.67	0.45	0.92	9.98	119	9.28	30.4	20.4	4.02	<0.05	19.0	15.7	81.4
PM-20	9.36	1550	2.44	0.46	1.03	7.40	108	9.62	36.3	21.3	4.21	<0.05	27.7	16.4	49.7
PM-19	15.2	1186	2.64	0.44	0.81	8.01	106	8.02	51.9	19.7	3.53	<0.05	38.4	14.0	75.0
PM-18	11.9	1464	2.80	0.50	1.59	12.4	102	8.14	42.3	20.9	3.62	0.100	73.0	15.0	106
PM-17	27.9	1323	3.37	0.53	1.12	36.2	119	8.92	74.8	21.8	4.05	<0.05	24.8	15.7	202
PM-16	21.0	1413	2.93	0.43	1.50	12.4	141	10.2	32.1	21.6	3.85	0.140	56.9	16.3	135
PM-15	21.6	1503	2.48	0.35	0.91	8.36	116	9.88	37.3	21.4	3.77	<0.05	49.9	16.0	104
PM-14	22.6	1587	3.03	0.41	0.46	11.0	105	11.5	112	22.7	4.24	<0.05	26.5	17.8	88.6
PM-13	25.0	1660	3.44	0.38	1.60	19.0	145	13.6	30.3	24.8	4.22	0.130	70.8	17.7	203
PM-12	13.8	1693	1.26	0.16	0.42	3.11	122	4.99	16.8	11.1	1.82	<0.05	13.9	7.29	36.5
PM-11	32.9	1911	2.55	0.34	0.87	3.44	111	7.61	16.9	19.5	5.10	<0.05	86.4	16.7	65.8
PM-10	47.0	1778	2.41	0.38	0.80	1.09	103	8.21	18.2	18.9	5.29	<0.05	110	16.5	52.5
PM-9	40.1	1571	2.59	0.31	3.34	4.29	110	9.36	24.9	17.0	4.54	<0.05	394	15.4	215
PM-8	11.0	1907	1.72	0.25	0.56	1.50	69.9	5.28	13.4	13.4	3.45	<0.05	67.2	12.0	40.1
PM-7	18.0	1884	2.34	0.50	2.93	3.24	96.3	9.50	21.6	19.1	4.86	<0.05	374	16.8	120
PM-6	17.3	2051	2.04	0.44	2.63	5.59	159	7.52	19.2	16.0	4.82	<0.05	188	13.9	133
PM-5	17.9	1850	2.03	0.28	0.70	2.12	1177	10.2	30.1	14.6	3.53	<0.05	38.0	11.5	147
PM-4	41.7	2439	3.59	0.63	1.31	2.31	2543	13.9	29.8	13.9	3.54	<0.05	140	11.9	154
PM-3	24.1	1.88	1.65	<0.05	2.58	5.70	789	1.84	40.8	10.2	0.47	1.54	1.15	12.9	64.0
PM-2	1.62	39.0	0.17	<0.05	<0.05	3.13	2.67	0.23	7.59	0.49	<0.05	<0.05	2.23	0.84	26.4
PM-1	1.59	<0.1	0.13	0.35	0.35	3.77	1.81	10.0	16.3	0.44	<0.05	0.15	0.76	2.84	30.7

Table A6 (continued)

Sample	Pb ppm ICP-MS	Rb ppm ICP-MS	Sb ppm ICP-MS	Sc ppm ICP-MS	Sn ppm ICP-MS	Sr ppm ICP-MS	Ta ppm ICP-MS	Th ppm ICP-MS	Tl ppm ICP-MS	U ppm ICP-MS	V ppm ICP-MS	W ppm ICP-MS	Zn ppm ICP-MS	Zr ppm ICP-MS
PM-30	9.71	80.0	2.28	15.1	<0.05	25.2	1.14	9.22	1.03	3.39	235	1.59	141	27.7
PM-29	11.8	67.8	1.04	13.4	<0.05	20.9	1.12	7.89	1.19	3.20	259	1.63	127	36.7
PM-28	9.64	61.1	1.29	12.4	<0.05	22.8	1.13	7.56	0.96	3.13	242	1.73	135	25.5
PM-27	17.7	90.0	48.8	13.2	2.56	14.7	1.17	8.67	1.42	12.3	265	1.99	70.1	184
PM-26	20.2	112	2.03	14.3	<0.05	27.5	1.14	10.1	1.79	15.1	346	1.88	111	23.0
PM-25	8.99	77.2	2.74	13.9	<0.05	22.3	1.10	9.61	1.69	14.8	822	1.87	135	43.2
PM-24	8.75	89.4	17.5	12.0	4.56	19.4	1.08	7.56	1.58	11.0	1014	1.98	162	165
PM-23	22.7	135	3.19	16.5	2.75	28.5	1.22	11.1	1.83	17.0	385	2.08	80.0	184
PM-22	25.2	112	2.00	11.4	2.22	24.1	1.24	8.39	1.68	13.2	248	2.11	124	183
PM-21	16.9	94.4	2.47	14.7	2.84	23.4	1.08	10.1	1.66	17.3	1434	1.89	106	165
PM-20	22.9	129	2.77	15.1	2.24	23.3	1.16	10.4	1.90	13.0	314	2.23	94.9	165
PM-19	19.0	106	5.76	12.4	3.94	15.4	0.98	8.28	1.80	17.4	899	1.81	92.8	148
PM-18	17.3	129	6.51	15.5	4.83	18.1	1.06	10.4	1.83	19.3	926	2.04	162	157
PM-17	19.2	80.0	387	14.3	4.18	21.5	1.15	9.56	1.96	17.9	1062	2.17	210	161
PM-16	8.40	101	4.03	14.7	3.78	23.0	1.09	9.72	2.21	18.3	2113	1.97	148	169
PM-15	11.4	135	6.38	16.9	2.92	18.6	1.07	9.89	1.98	18.8	1408	2.07	158	164
PM-14	18.9	123	3.31	14.7	4.52	28.7	1.28	10.3	2.27	15.7	756	2.15	269	180
PM-13	10.0	155	9.11	17.3	5.53	25.5	1.31	11.9	2.37	16.6	1514	2.23	337	182
PM-12	12.5	62.2	2.26	5.76	2.38	10.6	0.53	4.58	1.08	9.35	1237	1.15	83.9	74.2
PM-11	20.2	83.9	8.57	8.68	4.31	53.8	1.10	9.67	11.8	17.2	980	2.04	35.3	215
PM-10	13.4	97.8	9.74	11.2	3.81	33.7	1.10	10.3	1.98	18.0	1071	1.54	21.8	218
PM-9	13.1	109	9.02	12.9	3.02	42.5	1.01	10.4	4.26	23.3	1750	1.44	99.5	193
PM-8	15.4	85.6	7.29	11.6	0.93	29.3	0.81	8.72	1.83	19.1	1069	1.05	31.9	147
PM-7	20.2	101	17.8	12.5	4.19	39.7	1.14	10.6	3.53	26.9	1162	1.61	86.8	205
PM-6	45.5	96.7	15.6	11.6	3.07	26.8	1.10	10.6	3.60	28.0	4092	1.50	65.3	187
PM-5	15.7	107	10.1	10.6	4.34	28.9	0.82	8.39	2.08	21.0	4396	1.01	195	147
PM-4	11.3	117	8.83	9.97	4.16	38.0	1.02	8.33	2.84	23.0	4273	1.00	159	133
PM-3	5.08	20.0	1.84	5.91	<0.05	583	0.30	1.07	0.40	612	1437	0.75	68.5	434
PM-2	1.68	2.79	1.40	2.58	2.24	68.1	0.20	0.35	<0.05	1.67	3.43	0.40	7.56	4.35
PM-1	2.49	1.23	0.97	3.15	<0.05	157	0.42	0.52	<0.05	0.75	3.54	0.12	12.7	4.90

Table A6 (continued)

Sample	La ppm ICP-MS	Ce ppm ICP-MS	Pr ppm ICP-MS	Nd ppm ICP-MS	Sm ppm ICP-MS	Eu ppm ICP-MS	Gd ppm ICP-MS	Tb ppm ICP-MS	Dy ppm ICP-MS	Y ppm ICP-MS	Ho ppm ICP-MS	Er ppm ICP-MS	Tm ppm ICP-MS	Yb ppm ICP-MS	Lu ppm ICP-MS
PM-30	987	30.5	53.1	7.00	25.5	4.45	1.25	4.83	0.71	4.24	0.94	2.78	0.44	2.66	0.41
PM-29	1024	20.8	29.8	6.89	29.9	7.39	1.84	8.45	1.12	5.96	1.23	3.49	0.53	2.83	0.44
PM-28	893	20.8	34.5	5.54	21.4	4.11	1.09	4.35	0.68	4.06	0.82	2.61	0.40	2.51	0.38
PM-27	28.9	56.0	8.35	35.1	8.54	2.07	9.68	1.44	8.27	50.3	1.73	4.94	0.70	4.03	0.69
PM-26	1594	25.9	49.7	5.96	20.6	3.32	1.05	3.38	0.53	3.55	0.81	2.66	0.40	2.64	0.44
PM-25	1314	30.5	61.1	8.06	32.9	7.95	1.90	8.13	1.17	6.76	1.46	4.01	0.56	3.38	0.56
PM-24	27.6	49.7	6.57	24.2	4.45	1.30	5.59	0.78	4.75	36.2	1.05	3.10	0.44	2.70	0.47
PM-23	33.9	65.6	7.89	29.9	5.44	1.39	5.00	0.78	4.34	27.0	0.95	2.95	0.42	2.70	0.47
PM-22	27.3	54.5	6.72	23.0	4.05	1.10	3.78	0.57	3.29	21.5	0.74	2.40	0.38	2.37	0.37
PM-21	32.7	64.2	7.68	27.5	5.15	1.44	4.83	0.68	4.19	24.2	0.87	2.80	0.42	2.61	0.42
PM-20	33.7	66.7	8.89	35.3	7.27	1.99	7.72	1.09	5.74	29.9	1.12	3.11	0.45	2.84	0.46
PM-19	28.1	51.6	7.11	28.6	5.77	1.27	5.93	0.82	4.76	34.7	1.02	3.18	0.49	2.96	0.50
PM-18	30.5	58.7	7.52	29.0	6.16	1.31	6.60	0.95	5.54	44.3	1.25	3.67	0.53	3.33	0.54
PM-17	32.9	63.7	8.84	37.3	8.87	2.06	9.74	1.43	8.28	54.3	1.75	4.93	0.68	4.09	0.66
PM-16	30.1	58.9	7.52	28.8	5.53	1.50	6.00	0.82	4.72	29.5	1.05	3.13	0.46	2.86	0.50
PM-15	33.0	58.2	7.22	28.9	6.37	1.67	6.06	0.80	4.67	33.1	0.99	3.09	0.49	3.04	0.45
PM-14	39.4	75.0	10.6	45.4	10.1	2.43	9.19	1.24	7.11	41.0	1.47	4.35	0.62	4.05	0.69
PM-13	38.2	73.1	9.37	33.8	5.81	1.17	4.96	0.73	4.35	28.1	0.98	3.10	0.46	3.05	0.49
PM-12	13.7	27.1	3.48	13.5	2.74	0.44	2.41	0.32	2.04	13.9	0.44	1.27	0.20	1.21	0.20
PM-11	29.2	53.9	7.16	26.5	4.13	0.70	3.51	0.51	3.16	22.5	0.70	2.13	0.30	2.00	0.30
PM-10	30.7	60.0	7.68	27.5	4.70	0.89	4.15	0.66	4.17	26.7	0.87	2.67	0.39	2.38	0.35
PM-9	32.8	59.5	7.64	27.4	4.84	1.15	4.84	0.78	4.49	30.3	0.99	2.84	0.43	2.54	0.38
PM-8	32.8	57.3	7.39	25.9	4.47	0.95	4.60	0.64	4.35	32.4	0.94	2.59	0.35	2.13	0.30
PM-7	34.3	64.4	8.37	30.0	5.31	0.99	5.08	0.73	4.58	29.3	1.00	3.00	0.43	2.64	0.40
PM-6	33.1	56.9	7.85	28.1	5.21	0.95	4.63	0.71	4.63	31.7	1.04	2.94	0.42	2.59	0.39
PM-5	25.1	36.7	5.55	20.0	3.77	0.76	3.71	0.56	3.74	29.5	0.87	2.63	0.36	2.38	0.39
PM-4	35.3	44.0	8.72	34.8	7.02	1.29	8.77	1.39	9.78	108	2.39	7.22	1.02	6.03	0.96
PM-3	675	145	125	29.6	123	23.5	5.81	30.3	4.44	27.9	6.47	17.6	2.10	10.3	1.37
PM-2	2.79	2.47	0.49	2.04	0.36	<0.05	0.33	<0.05	0.23	2.9	<0.05	0.14	<0.05	<0.05	<0.05
PM-1	1124	2.14	4.19	0.75	3.02	0.71	0.37	0.75	0.10	0.6	0.13	0.33	<0.05	0.25	<0.05

Stratigraphic position is in meter relative to the polymetallic Ni-Mo-PGE-Au sulfide ore layer. Analyses were carried out at the National Research Center forGeoanalyis (NRCG), Chinese Academic of Geological Sciences in Beijing. Analyser: Han Huiming

Table A7: Complete bulk rock geochemical data of the polymetallic Ni-Mo-PGE-Au deposits

Sample	Lithology	SiO_2	TiO_2	Al_2O_3	TFe_2O_3	MnO	MgO	CaO	Na_2O	K_2O	P_2O_5	SO_3	Cl	F	LOI	S	TOC	Sum
		%	%	%	%	%	%	%	%	%	%	%	%	%	%	%	%	%
		XRF	XRF	XRF	XRF	XRF	XRF	XRF	XRF	XRF	XRF	XRF	XRF	XRF	XRF			XRF
		ICP	ICP	ICP	ICP	ICP	ICP	ICP	ICP	ICP	ICP				ICP	ICP		ICP
		ICP-AES	ICP-AES	ICP-AES	ICP-AES	ICP-AES	ICP-AES	ICP-AES	ICP-AES	ICP-AES	ICP-AES				ICP-AES	ICP-AES	Leco	ICP-AES
Dazhuliushui																		
DZLS-1	Black shale	52.5	0.54	12.7	8.26	0.05	2.87	4.23	1.08	3.27	0.15				13.4			99.4
DZLS-2	Sulfide ore	8.73	0.07	1.29	16.6	0.13	2.89	15.1	0.09	0.25	0.85	6.83	0.04	<0.05	25.9			93.3
DZLS-3	Black shale	5.03	0.05	1.10	0.52	0.06	0.79	50.6	0.30	0.18	0.04				41.3	0.32	1.12	100.0
DZLS-4	Black shale	51.5	0.51	12.2	6.41	0.07	3.46	5.43	1.04	3.06	0.18				15.4	4.00	7.12	99.8
DZLS-5	Sulfide ore	7.88	0.07	1.35	21.4	0.09	3.29	9.75	0.11	0.18	1.11	3.55	0.05	<0.05	31.7			94.1
DZLS-6	Black shale	57.7	0.68	12.4	4.45	0.03	2.23	3.42	2.00	2.98	0.22				12.9	2.52	8.02	99.3
DZLS-7	Black shale	52.6	0.51	12.1	6.22	0.07	3.40	5.80	1.07	3.00	0.15				15.3	3.46	6.74	100.6
DZLS-8	Sulfide ore	6.31	0.06	1.30	24.6	0.10	3.02	9.08	0.06	0.21	0.24	4.87	0.03	<0.05	30.8			94.0
DZLS-9	Black shale	57.3	0.64	11.6	4.29	0.05	2.83	3.92	2.32	2.27	0.21				14.2	2.33	8.65	99.9
DZLS-11	Sulfide ore	7.22	0.05	0.88	21.0	0.13	2.76	15.8	0.07	0.18	1.80	7.14	0.03	<0.05	26.4			94.6
DZLS-14	Sulfide ore	12.4	0.18	3.55	14.0	0.19	4.00	21.4	0.26	0.76	1.65	18.0	0.02	<0.05	12.5			96.5
DZLS-17	Sulfide ore	11.1	0.11	1.93	16.2	0.13	1.61	18.2	0.21	0.38	0.43	9.95	0.03	<0.05	23.7			94.9
Maluhe																		
MLH-1	Black shale	53.1	0.59	14.2	6.34	0.05	2.75	3.14	0.08	4.35	0.23				15.0	3.86	7.80	100.1
MLH-2	Sulfide ore	17.4	0.19	3.26	27.5	0.01	0.30	0.99	<0.01	0.94	0.64	1.29	0.03	<0.05	29.9			95.1
MLH-3	Black shale	56.7	0.88	15.7	4.06	0.03	2.11	1.82	0.12	4.97	0.34				11.7	2.66	6.37	99.3
MLH-4	Black shale	53.9	0.64	14.2	6.10	0.05	2.60	2.85	0.09	4.37	0.21				14.9	3.95	8.14	100.2
MLH-5	Sulfide ore	13.1	0.09	1.71	31.3	0.01	0.20	0.82	<0.01	0.51	0.51	1.00	0.04	<0.05	31.3			94.6
MLH-6	Phosphorite	19.0	0.09	1.80	0.43	0.00	0.16	41.6	0.18	0.58	30.2				5.44	0.51	4.11	99.9
MLH-7	Black shale	56.3	0.61	14.3	6.06	0.04	2.25	1.99	0.08	4.38	0.22				13.2	3.93	7.49	99.8
MLH-8	Sulfide ore	18.4	0.17	2.90	23.7	<0.001	0.29	2.75	<0.01	0.83	1.87	4.53	0.04	<0.05	26.3			94.9
MLH-9	Black shale	14.3	0.12	2.29	1.16	0.01	0.39	42.8	0.15	0.69	31.3				6.08	1.03	4.20	99.6
MLH-10	Sulfide ore	10.5	0.10	1.70	31.3	<0.001	0.17	1.05	<0.01	0.48	0.70	1.99	0.04	<0.05	32.4			94.8
MLH-11	Sulfide ore	9.73	0.08	1.50	32.1	0.01	0.17	1.20	<0.01	0.41	0.80	2.35	0.03	<0.05	32.4			94.8
MLH-12	Sulfide ore	17.1	0.23	3.96	28.1	<0.001	0.37	1.18	<0.01	1.15	0.78	1.14	0.03	<0.05	30.2			95.5

Table A7 (continued)

Sample	Ba	Bi	Co	Cr	Cs	Cu	Ga	Hf	Mo	Nb	Ni	Pb
	ppm	ppm	ppm	ppm	ppm	ppm	ppm	ppm	ppm	ppm	ppm	ppm
	ICP-MS	**ICP-MS**	**ICP-MS**	**ICP-MS**	**ICP-MS**	**ICP-MS**	**ICP-MS**	**ICP-MS**	**ICP-MS**	**ICP-MS**	**ICP-MS**	**ICP-MS**
	ICP-MS	**ICP-MS**	**ICP-MS**	**ICP-MS**	**ICP-MS**	**ICP-MS**	**ICP-MS**	**ICP-MS**	**ICP-MS**	**ICP-MS**	**ICP-MS**	**ICP-MS**
	ICP-MS	**ICP-MS**	**ICP-MS**	**ICP-MS**	**ICP-MS**	**ICP-MS**	**ICP-MS**	**ICP-MS**	**ICP-MS**	**ICP-MS**	**ICP-MS**	**ICP-MS**
Dazhuliushui												
DZLS-1	1291	0.40	26.4	92.7	7.14	91.1	17.4	2.61	66.2	11.3	304	17.0
DZLS-2	391	19.0	273	53.0	8.00	2448	3.00	11.0	73070	<5	62749	183
DZLS-3	356	<0.05	7.77	10.8	0.30	13.4	2.10	0.36	14.3	1.61	83.4	2.43
DZLS-4	1272	0.69	28.3	94.6	6.39	98.6	16.5	2.37	1178	10.4	1301	14.6
DZLS-5	332	12.0	136	51.0	5.00	1678	<2	<8	92828	<5	34830	74.0
DZLS-6	1403	0.32	27.5	96.6	5.39	55.0	16.2	4.03	81.8	14.5	258	13.4
DZLS-7	1331	0.34	22.5	93.0	7.76	71.4	20.9	3.30	65.2	11.8	332	15.3
DZLS-8	680	22.0	220	55.0	7.00	2739	3.00	<9	62828	<5	60067	117
DZLS-9	1121	0.26	18.5	85.1	5.40	52.8	18.1	4.87	90.6	13.6	249	15.4
DZLS-11	324	16.0	151	34.0	4.00	2334	4.00	<8	57604	<5	46068	182
DZLS-14	520	14.0	116	51.0	5.00	1513	5.00	<8	36364	<4	30527	127
DZLS-17	770	20.0	136	52.0	7.00	1906	6.00	<8	58499	<5	39303	141
Maluhe												
MLH-1	1227	0.50	28.9	102	17.9	64.2	21.1	3.82	133	13.2	245	54.5
MLH-2	518	20.0	254	64.0	12.0	1877	19.0	11.0	61625	<5	37719	235
MLH-3	1065	0.53	20.3	184	19.7	104	31.7	6.24	844	18.5	1176	18.0
MLH-4	985	0.51	32.1	116	17.4	69.0	21.6	3.82	142	14.1	301	47.2
MLH-5	1739	16.0	255	53.0	13.0	1972	16.0	<9	70864	<5	36256	156
MLH-6	402	0.08	4.56	26.0	2.22	44.1	7.14	0.96	117	2.65	359	3.09
MLH-7	1336	0.40	22.7	118	18.1	73.7	22.6	3.87	114	13.9	386	37.0
MLH-8	1154	14.0	296	66.0	11.0	1814	20.0	<8	66143	<5	40846	157
MLH-9	293	0.09	5.73	25.7	2.71	30.1	7.08	1.16	31.1	3.21	492	3.75
MLH-10	630	15.0	301	56.0	14.0	1827	18.0	<9	66885	<5	42623	62.0
MLH-11	777	12.0	350	46.0	13.0	2050	14.0	<9	61167	<5	45482	90.0
MLH-12	734	10.0	206	86.0	15.0	1701	17.0	<8	64942	<5	28642	85.0

Table A7 (continued)

	Rb	Sb	Sc	Sn	Sr	Ta	Th	U	V	W	Zn	Zr
	ppm	ppm	ppm	ppm	ppm	ppm	ppm	ppm	ppm	ppm	ppm	ppm
Sample	ICP-MS	ICP-MS	ICP-MS	ICP-MS	ICP-MS	ICP-MS	ICP-MS	ICP-MS	ICP-MS	ICP-MS	ICP-MS	ICP-MS
	ICP-MS	ICP-MS	ICP-MS	ICP-MS	ICP-MS	ICP-MS	ICP-MS	ICP-MS	ICP-MS	ICP-MS	ICP-MS	ICP-MS
	ICP-MS	ICP-MS	ICP-MS	ICP-MS	ICP-MS	ICP-MS	ICP-MS	ICP-MS	ICP-MS	ICP-MS	ICP-MS	ICP-MS
Dazhuliushui												
DZLS-1	91.1	70.7	13.3	0.91	165	0.79	8.89	28.6	370	1.90	68.1	112
DZLS-2	29.0	257	3.00	<4	342	<15	100	125	658	38.0	3455	30.0
DZLS-3	6.39	1.79	4.76	0.09	362	0.20	0.93	6.89	36.6	0.22	71.5	16.4
DZLS-4	109	8.28	12.9	2.42	210	0.72	8.44	32.1	685	1.80	420	106
DZLS-5	17.0	104	4.00	<4	341	<12	108	318	724	20.0	3578	37.0
DZLS-6	82.2	3.52	12.1	2.03	180	0.91	9.06	23.4	994	1.25	117	185
DZLS-7	111	7.36	13.6	4.54	217	0.78	10.6	30.6	409	2.66	66.9	149
DZLS-8	25.0	214	<1	<4	282	<15	95.0	114	644	33.0	4394	25.0
DZLS-9	56.5	5.47	11.1	4.19	195	0.86	11.1	24.5	320	2.53	306	225
DZLS-11	25.0	251	3.00	<4	528	<14	77.0	255	486	32.0	2993	37.0
DZLS-14	38.0	155	6.00	<5	598	<12	64.0	260	462	12.0	4399	59.0
DZLS-17	27.0	224	4.00	<4	478	<13	87.0	133	655	27.0	4745	43.0
Maluhe												
MLH-1	112	5.01	14.3		116	0.86	12.0	49.2	265	1.92	253	170
MLH-2	39.0	279	1.00	6.00	40.0	<13	83.0	118	480	20.0	21191	63.0
MLH-3	88.8	14.8	11.7		50.3	1.12	12.9	34.5	3174	2.97	1652	304
MLH-4	108	4.21	14.8		96.7	0.85	12.9	54.9	310	2.51	330	184
MLH-5	36.0	263	2.00	6.00	41.0	<13	96.0	112	423	19.0	26294	34.0
MLH-6	15.4	5.20	7.41		363	0.29	2.01	517	417	0.74	1411	33.8
MLH-7	121	10.2	16.0		91.0	0.83	13.0	56.4	463	2.05	364	182
MLH-8	37.0	342	4.00	5.00	111	<13	87.0	265	559	24.0	18034	71.0
MLH-9	19.6	5.55	8.55		387	0.30	2.34	552	447	0.92	466	42.9
MLH-10	33.0	216	2.00	6.00	30.0	<14	96.0	109	329	16.0	29220	30.0
MLH-11	27.0	222	2.00	<3	37.0	<14	84.0	137	258	25.0	29160	46.0
MLH-12	46.0	204	4.00	<4	33.0	<12	90.0	161	774	14.0	12813	63.0

Table A7 (continued)

Sample	La	Ce	Pr	Nd	Sm	Eu	Gd	Tb	Dy	Y	Ho	Er	Tm	Yb	Lu
	ppm	ppm	ppm	ppm	ppm	ppm	ppm	ppm	ppm	ppm	ppm	ppm	ppm	ppm	ppm
	ICP-MS	ICP-MS	ICP-MS	ICP-MS	ICP-MS	ICP-MS	ICP-MS	ICP-MS	ICP-MS	ICP-MS	ICP-MS	ICP-MS	ICP-MS	ICP-MS	ICP-MS
	ICP-MS	ICP-MS	ICP-MS	ICP-MS	ICP-MS	ICP-MS	ICP-MS	ICP-MS	ICP-MS	ICP-MS	ICP-MS	ICP-MS	ICP-MS	ICP-MS	ICP-MS
	ICP-MS	ICP-MS	ICP-MS	ICP-MS	ICP-MS	ICP-MS	ICP-MS	ICP-MS	ICP-MS	ICP-MS	ICP-MS	ICP-MS	ICP-MS	ICP-MS	ICP-MS
Dazhuliushui															
DZLS-1	23.6	40.0	4.88	16.8	3.04	1.05	3.49	0.46	3.03	19.5	0.60	1.92	0.27	2.03	0.30
DZLS-2	14.1	22.5	3.32	14.9	3.46	1.18	3.64	0.52	3.21	28.9	0.64	1.67	0.20	1.14	0.16
DZLS-3	2.31	4.11	0.49	2.15	0.44	0.26	0.52	<0.05	0.46	4.36	0.11	0.26	<0.05	0.25	<0.05
DZLS-4	25.1	43.5	4.97	18.4	3.27	0.95	3.41	0.48	2.93	21.3	0.60	1.80	0.27	1.68	0.29
DZLS-5	58.7	85.1	12.1	50.0	10.1	3.31	10.2	1.45	8.73	79.2	1.68	4.26	0.50	2.65	0.34
DZLS-6	25.0	44.5	5.87	21.9	4.28	1.00	4.23	0.64	3.75	26.8	0.77	2.27	0.34	2.13	0.33
DZLS-7	25.5	60.4	5.47	20.0	3.89	1.45	4.95	0.63	3.74	25.2	0.80	2.38	0.37	2.33	0.37
DZLS-8	25.3	35.4	4.13	17.2	3.78	1.26	3.68	0.57	3.45	27.7	0.67	1.80	0.23	1.24	0.17
DZLS-9	20.1	34.3	4.27	15.8	3.11	1.18	3.91	0.49	2.88	18.6	0.61	1.86	0.29	1.91	0.32
DZLS-11	75.8	92.3	13.5	57.3	11.3	4.14	12.7	1.77	10.6	117	2.21	5.69	0.66	3.32	0.44
DZLS-14	56.7	90.6	12.6	58.1	12.6	4.49	13.0	1.77	10.3	96.6	2.08	5.04	0.57	2.96	0.39
DZLS-17	79.1	96.3	10.2	35.8	4.85	1.70	4.05	0.55	3.45	32.0	0.68	1.77	0.22	1.14	0.16
Maluhe															
MLH-1	29.8	79.3	6.87	26.2	5.66	1.68	6.82	0.90	5.34	34.4	1.11	3.13	0.45	2.92	0.45
MLH-2	15.7	32.0	4.71	22.3	5.67	1.18	5.70	0.81	4.73	34.9	0.92	2.32	0.28	1.50	0.21
MLH-3	33.1	50.1	3.85	12.3	2.13	0.93	2.86	0.36	2.35	20.6	0.55	1.86	0.33	2.30	0.38
MLH-4	31.2	75.7	7.06	25.9	5.27	1.50	6.26	0.84	5.00	32.3	1.02	3.07	0.45	2.89	0.46
MLH-5	7.76	20.9	3.53	18.1	4.62	1.03	4.64	0.67	3.78	28.9	0.72	1.83	0.21	1.06	0.15
MLH-6	37.3	149	20.4	105	23.4	7.86	30.1	3.66	19.8	262	3.91	9.98	1.12	5.41	0.70
MLH-7	34.7	83.6	6.95	25.2	4.83	1.58	5.72	0.74	4.32	27.7	0.89	2.74	0.43	2.76	0.44
MLH-8	28.5	72.8	12.2	59.4	14.6	3.23	15.0	2.17	12.9	106	2.57	6.51	0.78	3.99	0.53
MLH-9	52.2	169	24.9	131	27.7	9.32	35.0	4.13	21.7	276	4.26	10.4	1.11	5.32	0.69
MLH-10	9.21	21.0	3.20	15.8	3.88	0.86	4.05	0.56	3.29	24.9	0.63	1.52	0.18	0.96	0.12
MLH-11	10.8	25.9	4.08	20.4	4.90	1.08	5.17	0.72	4.12	33.2	0.79	1.96	0.24	1.22	0.17
MLH-12	12.2	23.4	3.58	16.9	4.04	0.88	4.12	0.60	3.48	28.6	0.72	1.83	0.23	1.37	0.18

Table A7 (continued)

Sample	Lithology	SiO_2	TiO_2	Al_2O_3	TFe_2O_3	MnO	MgO	CaO	Na_2O	K_2O	P_2O_5	SO_3	Cl	F	LOI	S	TOC	Sum
		%	%	%	%	%	%	%	%	%	%	%	%	%	%	%	%	%
		XRF	XRF	XRF	XRF	XRF	XRF	XRF	XRF	XRF	XRF	XRF	XRF	XRF	XRF			XRF
		ICP	ICP	ICP	ICP	ICP	ICP	ICP	ICP	ICP	ICP				ICP	ICP		ICP
		ICP-AES	ICP-AES	ICP-AES	ICP-AES	ICP-AES	ICP-AES	ICP-AES	ICP-AES	ICP-AES	ICP-AES				ICP-AES	ICP-AES	Leco	ICP-AES
Sancha																		
SC-2	Sulfide ore	29.1	0.07	1.20	18.6	<0.001	0.31	3.51	0.04	0.40	1.98	0.15	0.03	<0.05	25.8			94.1
SC-5	Sulfide ore	20.7	0.06	1.37	8.87	0.02	0.62	23.4	0.02	0.42	9.16	13.3	0.02	0.50	7.31			95.9
SC-8	Sulfide ore	22.4	0.05	1.10	7.28	0.01	1.19	24.2	0.07	0.32	16.3	3.03	0.02	0.85	13.5			97.5
SC-11	Sulfide ore	16.6	0.06	1.32	16.8	<0.001	0.31	12.1	0.06	0.46	5.48	1.85	0.04	0.16	28.9			95.2
SC-14	Sulfide ore	21.7	0.04	0.89	22.4	0.00	0.27	7.5	0.04	0.30	3.85	0.88	0.03	<0.05	25.6			95.0
Cili																		
CL-Ore-1	Sulfide ore	25.6	0.08	1.72	5.37	0.07	1.46	28.6	0.01	0.53	0.67				23.9	6.75	6.33	90.6
CL-Ore-2	Sulfide ore	30.2	0.12	2.85	6.06	0.05	0.92	18.5	<0.01	0.88	0.28				17.6	9.20	7.00	84.1
CL-Ore-3	Sulfide ore	38.2	0.28	6.69	9.89	0.08	2.10	15.3	0.04	2.14	1.16				18.4	9.83	10.2	96.6
CL-Ore-4	Sulfide ore	58.1	0.07	1.82	1.09	0.02	0.96	16.3	<0.01	0.53	0.14				13.2	2.46	1.16	97.5
CL-Ore-5	Sulfide ore	15.6	0.09	2.32	4.02	<0.01	0.38	32.4	0.09	0.78	24.3				9.20	6.09	5.97	96.2
CL-Ore-6	Sulfide ore	28.3	0.09	2.21	12.1	<0.01	0.39	14.8	0.06	0.71	7.53				20.5	16.2	13.4	92.2
CL-Ore-7	Sulfide ore	7.97	0.09	1.94	17.5	0.01	0.23	8.91	0.10	0.60	6.52				34.4	24.8	29.4	82.2
CL-Ore-8	Sulfide ore	39.0	0.30	6.63	13.3	0.02	1.26	2.61	0.03	2.08	0.24				18.9	16.6	14.0	91.2
CL-1	Phosphorite	5.99	0.03	0.77	3.34	<0.01	0.34	43.8	0.11	0.28	32.4				8.20	5.08	5.78	98.1
CL-2	Sulfide ore	32.2	0.34	7.68	12.6	0.05	2.66	11.4	0.05	2.41	2.53				20.1	13.1	13.6	94.9
CL-3	Black shale	48.7	0.64	14.6	8.23	0.02	2.82	2.58	0.05	4.78	0.26				16.4	6.46	9.83	99.8
CL-4	Black shale	51.3	0.64	14.3	8.56	0.02	2.37	1.13	0.05	4.64	0.21				15.9	6.80	10.2	99.8
CL-5	Black shale	52.9	0.63	14.3	8.04	0.01	2.30	0.96	0.05	4.61	0.21				15.0	6.38	10.1	99.8
CL-6	Black shale	53.3	0.58	13.7	7.97	0.02	2.08	1.59	0.05	4.31	0.24				15.4	6.41	9.68	99.9
CL-7	Black shale	49.6	0.60	13.0	7.61	0.03	3.43	3.61	0.06	4.22	0.35				17.2	5.94	9.00	99.9
CL-8	Black shale	46.4	0.58	12.1	9.88	0.04	4.08	4.34	0.06	3.88	0.14				18.2	7.61	9.85	99.9
CL-9	Black shale	51.7	0.62	13.1	7.43	0.03	3.34	3.07	0.06	4.23	0.14				16.0	5.81	8.56	100.0

Table A7 (continued)

	Ba	Bi	Co	Cr	Cs	Cu	Ga	Hf	Mo	Nb	Ni	Pb
	ppm	ppm	ppm	ppm	ppm	ppm	ppm	ppm	ppm	ppm	ppm	ppm
Sample	**ICP-MS**	**ICP-MS**	**ICP-MS**	**ICP-MS**	**ICP-MS**	**ICP-MS**	**ICP-MS**	**ICP-MS**	**ICP-MS**	**ICP-MS**	**ICP-MS**	**ICP-MS**
	ICP-MS	**ICP-MS**	**ICP-MS**	**ICP-MS**	**ICP-MS**	**ICP-MS**	**ICP-MS**	**ICP-MS**	**ICP-MS**	**ICP-MS**	**ICP-MS**	**ICP-MS**
	ICP-MS	**ICP-MS**	**ICP-MS**	**ICP-MS**	**ICP-MS**	**ICP-MS**	**ICP-MS**	**ICP-MS**	**ICP-MS**	**ICP-MS**	**ICP-MS**	**ICP-MS**
Sancha												
SC-2	374	19.0	172	68.0	<3	2082	9.00	<8	56423	<4	61524	180
SC-5	33488	16.0	176	66.0	<4	1313	<2	<9	3303	<3	58952	67.0
SC-8	21176	13.0	92.0	120	<4	733	<2	<8	17535	<3	27756	93.0
SC-11	3276	7.00	111	149	6.00	1176	7.00	<8	65872	<5	29917	37.0
SC-14	7464	17.0	147	230	8.00	1617	<2	<8	51489	<4	47181	125
Cili												
CL-Ore-1	11463	1.20	26.2	61.6	2.30	439	5.40	0.90	>2000	1.80	8877.60	27.3
CL-Ore-2	>50000	1.70	49.2	61.6	3.40	522	6.60	1.10	>2000	1.90	>10000	35.4
CL-Ore-3	6236	2.60	36.4	109	6.80	644	13.6	2.50	>2000	4.90	8901.10	35.4
CL-Ore-4	>50000	0.20	5.60	13.7	1.40	95	2.80	0.80	928.50	1.30	911.60	4.20
CL-Ore-5	>50000	1.40	27.6	417	3.40	872	10.6	0.70	>2000	1.60	6551.60	38.2
CL-Ore-6	32703	2.40	52.0	239	8.30	509	10.5	0.40	>2000	1.80	>10000	69.8
CL-Ore-7	15144	5.10	66.0	116	12.4	896	9.80	0.80	>2000	3.00	>10000	94.1
CL-Ore-8	>50000	5.20	102	123	5.50	528	14.3	2.10	>2000	5.10	>10000	33.4
CL-1	7447	1.00	47.1	192	3.00	317	7.90	0.30	>2000	0.70	>10000	17.6
CL-2	10749	1.90	41.9	130	10.4	433	15.0	2.20	>2000	11.0	>10000	37.3
CL-3	4273	0.80	23.7	109	12.7	136	22.0	3.80	292	11.6	374.90	33.1
CL-4	1894	0.80	23.0	116	14.6	141	20.7	4.20	278	11.3	427.10	32.3
CL-5	1402	0.80	22.8	130	14.8	139	20.4	4.00	282	11.5	415.20	29.7
CL-6	1193	1.00	22.2	116	14.0	147	18.4	3.30	366	11.0	475.50	35.9
CL-7	920	0.90	20.8	88.9	13.1	123	17.2	3.90	217	11.7	186.00	37.1
CL-8	838	0.70	20.1	75.3	12.0	115	15.9	3.50	83.1	10.8	102.20	35.6
CL-9	1106	0.70	23.3	82.1	14.4	103	17.4	4.20	61.6	12.0	73.90	30.4

Table A7 (continued)

Sample	Rb	Sb	Sc	Sn	Sr	Ta	Th	U	V	W	Zn	Zr
	ppm	ppm	ppm	ppm	ppm	ppm	ppm	ppm	ppm	ppm	ppm	ppm
	ICP-MS	ICP-MS	ICP-MS	ICP-MS	ICP-MS	ICP-MS	ICP-MS	ICP-MS	ICP-MS	ICP-MS	ICP-MS	ICP-MS
	ICP-MS	ICP-MS	ICP-MS	ICP-MS	ICP-MS	ICP-MS	ICP-MS	ICP-MS	ICP-MS	ICP-MS	ICP-MS	ICP-MS
	ICP-MS	ICP-MS	ICP-MS	ICP-MS	ICP-MS	ICP-MS	ICP-MS	ICP-MS	ICP-MS	ICP-MS	ICP-MS	ICP-MS
Sancha												
SC-2	31.0	493	1.00	<4	178	<15	82.0	408	1678	48.0	4428	27.0
SC-5	23.0	313	4.00	<5	943	<15	24.0	396	913	33.0	1523	27.0
SC-8	19.0	215	3.00	<5	750	<11	35.0	570	1205	20.0	829	25.0
SC-11	34.0	267	3.00	<4	408	<11	84.0	595	3781	27.0	3855	36.0
SC-14	29.0	365	2.00	<4	304	<14	76.0	359	3286	32.0	517	25.0
Cili												
CL-Ore-1	16.7	88.5	3.00	3.00	724	0.10	2.40	118	857	20.9	853	28.7
CL-Ore-2	27.0	63.9	4.00	2.00	1272	0.40	2.30	54.1	803	23.3	765	34.3
CL-Ore-3	60.1	96.5	7.00	4.00	884	0.40	6.20	153	1366	16.2	2309	95.4
CL-Ore-4	14.3	11.5	3.00	<1	349	0.40	1.50	27.4	178	1.60	145	25.6
CL-Ore-5	24.6	199	2.00	3.00	1557	0.40	1.90	160	3384	25.6	3591	24.7
CL-Ore-6	22.6	297	3.00	6.00	733	<0.1	1.90	106	3391	57.2	4959	27.2
CL-Ore-7	17.7	582	4.00	11.0	1026	<0.1	2.70	1219	1259	170	4807	43.1
CL-Ore-8	57.5	77.7	6.00	6.00	292	0.60	5.60	76.7	1457	10.7	3289	75.1
CL-1	10.0	78.2	<1	3.00	562	<0.1	0.70	918	1948	8.60	3696	20.1
CL-2	64.2	105	9.00	5.00	674	0.50	7.40	193	2206	35.7	1742	87.8
CL-3	139	4.80	15.0	2.00	147	0.80	12.6	82.6	1116	12.2	202	145
CL-4	146	4.30	15.0	3.00	57.5	0.80	12.6	61.8	1452	8.30	1420	141
CL-5	144	3.40	14.0	3.00	43.7	0.90	13.0	63.3	1735	6.80	2483	145
CL-6	128	2.30	14.0	3.00	89.3	0.80	11.4	57.8	1576	5.70	1116	127
CL-7	129	1.40	14.0	2.00	88.8	0.80	15.4	52.2	549	4.90	84.0	133
CL-8	116	1.50	13.0	2.00	65.7	0.90	13.1	37.5	299	4.10	42.0	127
CL-9	132	1.00	13.0	2.00	58.2	0.90	14.7	34.8	258	4.20	39.0	138

Table A7 (continued)

	La	Ce	Pr	Nd	Sm	Eu	Gd	Tb	Dy	Y	Ho	Er	Tm	Yb	Lu
	ppm	ppm	ppm	ppm	ppm	ppm	ppm	ppm	ppm	ppm	ppm	ppm	ppm	ppm	ppm
Sample	**ICP-MS**	**ICP-MS**	**ICP-MS**	**ICP-MS**	**ICP-MS**	**ICP-MS**	**ICP-MS**	**ICP-MS**	**ICP-MS**	**ICP-MS**	**ICP-MS**	**ICP-MS**	**ICP-MS**	**ICP-MS**	**ICP-MS**
	ICP-MS	**ICP-MS**	**ICP-MS**	**ICP-MS**	**ICP-MS**	**ICP-MS**	**ICP-MS**	**ICP-MS**	**ICP-MS**	**ICP-MS**	**ICP-MS**	**ICP-MS**	**ICP-MS**	**ICP-MS**	**ICP-MS**
	ICP-MS	**ICP-MS**	**ICP-MS**	**ICP-MS**	**ICP-MS**	**ICP-MS**	**ICP-MS**	**ICP-MS**	**ICP-MS**	**ICP-MS**	**ICP-MS**	**ICP-MS**	**ICP-MS**	**ICP-MS**	**ICP-MS**
Sancha															
SC-2	80.3	101	15.4	64.9	12.0	2.16	14.0	1.88	11.8	148	2.60	6.92	0.80	4.00	0.51
SC-5	59.3	81.9	13.4	57.5	10.8	2.92	12.9	1.80	11.5	129	2.56	7.00	0.87	4.67	0.63
SC-8	154	158	26.9	110	19.7	4.97	25.5	3.53	22.8	307	5.22	14.1	1.69	8.97	1.21
SC-11	153	188	35.9	155	29.4	5.64	35.3	4.71	28.4	313	5.93	15.1	1.70	8.45	1.12
SC-14	59.7	65.0	12.6	54.4	10.6	2.40	13.4	1.84	11.8	140	2.62	7.07	0.86	4.49	0.59
Cili															
CL-Ore-1	30.1	42.0	5.31	22.6	4.37	2.25	4.92	0.81	4.65	51.4	1.02	2.66	0.36	2.20	0.31
CL-Ore-2	19.1	28.6	3.68	15.1	3.38	1.42	4.27	0.64	3.87	37.2	0.87	2.23	0.32	2.04	0.28
CL-Ore-3	39.8	64.5	8.16	34.9	7.50	3.04	8.38	1.28	7.39	73.7	1.61	4.34	0.59	3.08	0.46
CL-Ore-4	5.90	9.20	1.19	4.60	1.18	1.53	1.59	0.24	1.40	14.5	0.35	1.00	0.15	0.92	0.13
CL-Ore-5	134	131	29.1	130	25.4	8.79	34.0	5.03	29.8	357	6.69	18.1	2.15	10.9	1.44
CL-Ore-6	72.0	76.2	13.5	55.4	12.2	4.06	14.5	2.25	12.6	150	2.81	7.42	0.94	4.82	0.62
CL-Ore-7	277	376	46.0	203	36.7	9.17	47.8	6.77	40.5	520	9.03	24.4	2.87	14.5	1.79
CL-Ore-8	20.3	31.8	4.14	16.7	3.92	1.56	3.68	0.53	2.91	25.0	0.67	1.86	0.28	1.68	0.26
CL-1	107	86.9	19.2	83.8	15.1	4.43	20.3	2.94	17.9	274	4.36	12.0	1.45	7.64	1.02
CL-2	51.7	88.5	11.0	46.3	9.55	2.86	10.3	1.61	9.19	93.2	2.03	5.53	0.73	4.20	0.60
CL-3	35.7	68.7	8.05	30.8	6.08	0.88	5.54	0.92	5.24	41.2	1.20	3.66	0.55	3.43	0.54
CL-4	33.5	63.9	7.63	28.7	5.56	0.94	4.96	0.86	4.97	36.3	1.09	3.16	0.48	3.14	0.49
CL-5	34.6	67.9	8.20	30.8	6.02	1.05	5.52	0.94	5.50	39.6	1.18	3.44	0.53	3.34	0.51
CL-6	33.4	63.0	7.47	28.9	5.40	1.03	5.12	0.85	4.80	36.1	1.07	3.10	0.47	3.09	0.47
CL-7	40.4	89.5	10.9	43.1	8.71	1.69	8.35	1.35	7.48	48.6	1.49	4.14	0.58	3.62	0.52
CL-8	30.7	61.5	7.04	26.7	4.90	0.89	4.40	0.74	4.33	28.5	0.96	2.72	0.43	2.91	0.44
CL-9	34.7	69.5	8.05	30.3	5.54	1.04	5.08	0.85	4.86	30.8	1.04	3.03	0.48	3.13	0.47

Shading refers to alternative analytical laboratories. Data without background highlights are from BGR, Hanover; Data with bluish background highlights are from AcmeLab in Canada; Data with yellowish background highlights are from NRCG in China.

Table 8A: Complete bulk rock geochemical data of V-bearing black shales from Longbizui roadcut profile.

Sample	Level (m)	Lithology	SiO_2 % ICP	Al_2O_3 % ICP	Fe_2O_3 % ICP	MgO % ICP	CaO % ICP	Na_2O % ICP	K_2O % ICP	TiO_2 % ICP	P_2O_5 % ICP	MnO % ICP	Cr_2O_3 % ICP	TOC % Leco	TOT/C % Leco	TOT/S % Leco	LOI % ICP	Sum % ICP
LBZ-6	6.0	Black shale	58.5	11.4	4.60	1.14	0.81	1.68	2.75	0.58	0.20	0.01	0.05	11.0	8.75	3.97	15.2	97.0
LBZ-5	5.0	Black shale	67.1	8.69	3.28	0.77	0.44	1.12	2.06	0.45	0.16	<0.01	0.10	9.21	7.31	3.19	12.4	96.6
LBZ-4	4.0	Black shale	76.4	3.72	1.68	1.20	6.47	0.29	0.94	0.16	0.04	0.02	0.07	2.30	3.20	1.30	7.60	98.6
LBZ-3	3.0	Black shale	63.6	4.50	1.79	0.83	5.38	0.22	1.03	0.22	0.13	<0.01	0.16	10.6	12.8	2.05	19.9	97.8
LBZ-2	2.0	Black shale	54.2	9.42	3.89	1.44	5.41	1.57	2.07	0.39	0.17	<0.01	0.02	10.7	9.96	3.53	19.0	97.6
LBZ-1	1.0	Black shale	85.9	0.84	0.24	0.29	1.73	0.02	0.13	0.03	0.04	<0.01	0.01	5.71	6.75	0.70	9.10	98.4

Stratigraphic position is in meter relative to the phosphorite bed.

Table 9A: Complete bulk rock geochemical data of black shales from drilling core ZK2302 in Sancha district.

Sample		Lithology	SiO_2 % ICP	Al_2O_3 % ICP	Fe_2O_3 % ICP	MgO % ICP	CaO % ICP	Na_2O % ICP	K_2O % ICP	TiO_2 % ICP	P_2O_5 % ICP	MnO % ICP	Cr_2O_3 % ICP	TOC % Leco	TOT/C % Leco	TOT/S % Leco	LOI % ICP	Sum % ICP
ZK2302-9	40.0	Black shale	62.1	15.1	5.75	2.20	0.37	1.22	3.97	0.57	0.07	0.02	0.01	4.34	2.90	2.13	8.40	99.7
ZK2302-8	34.0	Black shale	60.5	16.7	5.79	2.50	0.52	1.30	4.58	0.64	0.08	0.03	0.01	3.14	2.10	1.47	6.90	99.5
ZK2302-7	26.0	Black shale	57.8	18.1	6.00	2.60	0.64	1.19	5.18	0.65	0.07	0.03	0.01	4.96	1.66	2.82	7.30	99.6
ZK2302-6	22.0	Black shale	55.4	14.8	7.30	2.54	2.06	1.05	4.49	0.65	0.10	0.03	0.01	5.94	2.86	5.21	11.2	99.6
ZK2302-5	17.0	Black shale	52.9	12.9	6.00	3.95	4.60	1.13	4.01	0.60	0.10	0.07	0.01	5.04	4.03	4.24	13.4	99.7
ZK2302-4	13.0	Black shale	57.4	13.1	6.72	2.00	1.32	0.84	4.18	0.58	0.13	0.02	0.01	8.51	5.63	5.11	13.3	99.7
ZK2302-3	7.0	Black shale	67.3	5.71	4.02	1.82	2.22	0.34	2.10	0.24	0.11	0.02	0.01	10.4	9.50	3.24	15.9	99.8
ZK2302-2	3.0	Black shale	64.9	6.43	3.44	2.30	3.21	0.09	2.44	0.26	0.14	0.03	0.01	10.0	9.94	2.81	16.4	99.7
ZK2302-1	1.0	Black shale	50.1	9.90	6.20	3.52	3.75	0.06	3.63	0.42	0.14	0.03	0.01	12.7	11.2	4.90	21.7	99.5

Stratigraphic position is in meter relative to the dolomite contact.

Table 10A: Complete bulk rock geochemical data of black shales from drilling core ZK15401 in Sancha district.

Sample		Lithology	SiO_2 % ICP	Al_2O_3 % ICP	Fe_2O_3 % ICP	MgO % ICP	CaO % ICP	Na_2O % ICP	K_2O % ICP	TiO_2 % ICP	P_2O_5 % ICP	MnO % ICP	Cr_2O_3 % ICP	TOC % Leco	TOT/C % Leco	TOT/S % Leco	LOI % ICP	Sum % ICP
ZK15401-8	24.0	Black shale	61.7	16.2	5.54	2.06	0.12	1.14	4.60	0.65	0.05	0.02	0.01	3.51	2.27	1.77	7.50	99.5
ZK15401-7	22.0	Black shale	59.2	16.5	6.15	2.64	0.18	1.28	4.52	0.65	0.09	0.04	0.01	3.56	2.38	1.29	8.30	99.5
ZK15401-6	16.0	Black shale	49.0	14.3	5.79	4.46	4.93	0.76	4.59	0.64	0.13	0.06	0.01	6.25	5.81	3.84	15.0	99.6
ZK15401-5	15.0	Black shale	52.3	14.1	7.45	2.85	2.72	0.98	4.48	0.69	0.10	0.04	0.01	7.8	5.83	4.97	13.9	99.6
ZK15401-4	12.0	Black shale	62.2	8.52	4.92	1.90	2.70	0.67	2.92	0.36	0.68	0.03	0.01	10.5	8.79	3.67	14.7	99.7
ZK15401-3	6.0	Black shale	72.7	5.59	2.84	1.44	1.98	0.39	1.98	0.23	0.43	0.02	0.01	8.44	7.63	2.20	12.1	99.8
ZK15401-2	2.0	Black shale	66.0	6.78	4.09	2.10	2.34	0.17	2.55	0.29	0.17	0.02	0.01	10.0	8.53	3.20	15.2	99.8
ZK15401-1	1.0	Black shale	60.0	10.4	4.37	2.77	2.79	0.05	3.69	0.42	0.23	0.02	0.02	7.81	6.84	3.23	14.7	99.5

Stratigraphic position is in meter relative to the dolomite contact.

Table 8A (continued)

Sample	Ag ppm ICP-MS	As ppm ICP-MS	Au ppm ICP-MS	Ba ppm ICP-MS	Be ppm ICP-MS	Bi ppm ICP-MS	Cd ppm ICP-MS	Co ppm ICP-MS	Cs ppm ICP-MS	Cu ppm ICP-MS	Ga ppm ICP-MS	Hf ppm ICP-MS	Hg ppm ICP-MS	Mo ppm ICP-MS	Nb ppm ICP-MS
LBZ-6	11.1	102	<0.5	10725	4.00	0.30	56.3	14.3	9.40	202	22.5	4.00	2.30	203	9.30
LBZ-5	17.1	132	<0.5	9827	3.00	0.40	191	11.5	7.60	426	22.1	2.90	4.91	86.3	7.00
LBZ-4	9.90	61.0	<0.5	9508	1.00	0.20	9.70	3.20	2.10	175	4.40	1.70	0.59	17.7	3.80
LBZ-3	10.6	38.3	<0.5	5525	3.00	0.40	45.5	5.20	6.50	158	13.5	1.70	1.09	75.4	5.60
LBZ-2	8.70	78.5	<0.5	18101	2.00	0.70	16.2	13.4	2.40	157	8.60	3.30	0.82	80.4	8.40
LBZ-1	0.90	8.80	0.80	11704	<1	<0.1	9.40	1.50	0.80	129	2.30	1.20	0.15	12.9	0.50

Table 9A (continued)

Sample	Ag ppm ICP-MS	As ppm ICP-MS	Au ppm ICP-MS	Ba ppm ICP-MS	Be ppm ICP-MS	Bi ppm ICP-MS	Cd ppm ICP-MS	Co ppm ICP-MS	Cs ppm ICP-MS	Cu ppm ICP-MS	Ga ppm ICP-MS	Hf ppm ICP-MS	Hg ppm ICP-MS	Mo ppm ICP-MS	Nb ppm ICP-MS
ZK2302-9	0.20	13.4	<0.5	2350	3.00	0.70	0.60	13.9	9.90	64.2	18.5	3.10	0.15	24.3	10.3
ZK2302-8	0.20	13.8	<0.5	3114	3.00	0.70	2.70	14.1	10.8	62.7	19.3	3.50	0.14	22.0	11.8
ZK2302-7	0.10	10.9	<0.5	2993	3.00	0.70	0.30	15.9	11.5	49.2	21.3	3.30	0.15	20.0	13.6
ZK2302-6	0.40	19.1	<0.5	1947	3.00	0.60	1.60	15.5	11.5	67.1	18.2	3.80	0.58	50.0	12.3
ZK2302-5	0.50	15.5	<0.5	1732	2.00	0.60	1.80	14.0	8.80	59.3	15.9	3.50	0.49	57.4	11.6
ZK2302-4	0.40	31.6	<0.5	1861	3.00	0.60	0.70	17.0	11.0	72.8	17.3	3.00	0.76	58.0	10.4
ZK2302-3	0.60	56.3	<0.5	826	1.00	0.40	3.80	16.5	3.60	88.5	7.70	1.50	1.86	101	4.70
ZK2302-2	0.80	62.8	<0.5	828	2.00	0.40	5.20	13.8	4.50	76.9	8.30	1.50	1.82	102	6.50
ZK2302-1	1.50	195	<0.5	1599	3.00	0.60	6.90	34.6	8.30	138	13.5	2.60	2.41	189	8.40

Table 10A (continued)

Sample	Ag ppm ICP-MS	As ppm ICP-MS	Au ppm ICP-MS	Ba ppm ICP-MS	Be ppm ICP-MS	Bi ppm ICP-MS	Cd ppm ICP-MS	Co ppm ICP-MS	Cs ppm ICP-MS	Cu ppm ICP-MS	Ga ppm ICP-MS	Hf ppm ICP-MS	Hg ppm ICP-MS	Mo ppm ICP-MS	Nb ppm ICP-MS
ZK15401-8	0.10	11.0	<0.5	2965	3.00	0.60	0.10	20.2	11.0	61.1	21.5	3.60	0.08	15.2	13.6
ZK15401-7	0.20	12.7	0.60	2673	4.00	0.90	0.50	19.8	9.80	54.1	21.5	4.00	0.13	30.6	16.7
ZK15401-6	0.40	17.0	<0.5	1803	3.00	0.60	1.40	18.2	12.7	62.1	18.9	3.30	0.36	21.8	12.0
ZK15401-5	0.50	23.6	<0.5	1804	3.00	1.00	2.20	27.1	10.4	66.4	18.3	3.50	0.46	58.6	12.6
ZK15401-4	0.50	42.3	<0.5	1504	2.00	0.50	0.90	17.6	5.50	109	12.1	2.40	0.56	144	7.00
ZK15401-3	0.40	40.0	<0.5	833	2.00	0.30	1.40	9.80	3.10	77.3	7.70	1.50	0.30	143	3.90
ZK15401-2	0.70	45.7	<0.5	1259	2.00	0.50	0.90	20.4	4.00	100	9.70	1.40	1.10	139	6.30
ZK15401-1	0.60	51.4	<0.5	2381	3.00	0.40	2.90	14.9	7.80	68.8	13.8	2.40	0.66	98.0	8.30

Table 8A (continued)

Sample	Ni ppm ICP-MS	Pb ppm ICP-MS	Rb ppm ICP-MS	Sb ppm ICP-MS	Se ppm ICP-MS	Sn ppm ICP-MS	Sr ppm ICP-MS	Ta ppm ICP-MS	Th ppm ICP-MS	Tl ppm ICP-MS	U ppm ICP-MS	V ppm ICP-MS	W ppm ICP-MS	Zn ppm ICP-MS	Zr ppm ICP-MS
LBZ-6	412	27.8	102	9.90	51.5	3.00	109	0.80	10.0	<0.1	65.8	8402	1.50	3017	135
LBZ-5	288	43.9	80.7	23.0	65.1	5.00	65.8	0.60	7.30	<0.1	36.8	7071	0.80	8100	104
LBZ-4	46.1	8.80	29.3	6.50	54.4	<1	991	0.40	3.00	0.10	10.9	944	<0.5	306	58.9
LBZ-3	288	31.4	45.6	9.40	30.1	1.00	292	0.30	4.50	<0.1	61.5	7396	0.90	2680	80.1
LBZ-2	269	24.4	57.4	14.1	46.6	1.00	301	0.90	8.50	0.20	40.3	1181	1.50	1057	118
LBZ-1	83.3	3.60	5.20	5.00	8.20	<1	258	0.30	0.50	<0.1	21.3	1509	<0.5	505	40.9

Table 9A (continued)

Sample	Ni ppm ICP-MS	Pb ppm ICP-MS	Rb ppm ICP-MS	Sb ppm ICP-MS	Se ppm ICP-MS	Sn ppm ICP-MS	Sr ppm ICP-MS	Ta ppm ICP-MS	Th ppm ICP-MS	Tl ppm ICP-MS	U ppm ICP-MS	V ppm ICP-MS	W ppm ICP-MS	Zn ppm ICP-MS	Zr ppm ICP-MS
ZK2302-9	53.9	30.1	140	0.20	1.20	3.00	62.0	0.80	14.0	0.10	8.90	118	1.60	66.0	100
ZK2302-8	81.2	22.1	150	0.30	2.10	3.00	98.6	0.80	15.1	0.20	8.40	175	1.80	209	116
ZK2302-7	50.8	22.9	165	0.20	1.20	3.00	117	0.90	15.4	0.20	9.70	114	1.70	47.0	116
ZK2302-6	144	24.0	137	0.30	10.5	3.00	145	0.90	13.3	0.50	20.6	419	1.70	86.0	130
ZK2302-5	126	20.0	119	0.30	8.10	2.00	132	0.80	11.8	0.50	17.4	264	1.60	77.0	117
ZK2302-4	109	23.9	131	0.30	5.70	2.00	92.2	0.80	11.7	0.30	31.6	160	2.20	38.0	99.8
ZK2302-3	102	21.5	53.6	1.70	9.50	<1	103	0.30	5.10	0.20	65.3	474	2.20	82.0	54.0
ZK2302-2	124	17.2	60.7	2.70	10.9	<1	147	0.40	5.50	0.40	59.9	705	1.90	189	57.4
ZK2302-1	143	29.3	99.0	4.00	24.8	2.00	129	0.60	9.40	0.60	121	789	2.80	200	96.8

Table 10A (continued)

Sample	Ni ppm ICP-MS	Pb ppm ICP-MS	Rb ppm ICP-MS	Sb ppm ICP-MS	Se ppm ICP-MS	Sn ppm ICP-MS	Sr ppm ICP-MS	Ta ppm ICP-MS	Th ppm ICP-MS	Tl ppm ICP-MS	U ppm ICP-MS	V ppm ICP-MS	W ppm ICP-MS	Zn ppm ICP-MS	Zr ppm ICP-MS
ZK15401-8	91.2	24.3	169	0.20	1.10	5.00	52.2	1.00	17.9	0.10	9.80	128	1.90	69.0	130
ZK15401-7	95.6	22.2	153	0.20	1.80	4.00	50.0	1.10	15.5	0.10	11.8	170	1.90	79.0	130
ZK15401-6	82.6	25.0	149	0.10	2.20	4.00	85.4	1.00	12.6	0.20	18.2	164	1.90	49.0	118
ZK15401-5	231	28.2	136	0.20	5.20	4.00	73.7	1.00	15.0	0.30	22.9	181	2.00	91.0	130
ZK15401-4	160	21.2	75.5	1.00	8.40	1.00	102	0.40	7.70	0.50	112	365	3.20	10.0	82.6
ZK15401-3	194	11.0	48.5	2.70	8.10	<1	71.3	0.30	4.40	0.30	79.4	553	1.90	43.0	49.6
ZK15401-2	80.3	23.7	62.0	0.80	8.70	<1	54.7	0.40	6.20	0.20	75.2	265	2.10	11.0	61.1
ZK15401-1	163	15.1	94.1	1.20	13.5	2.00	91.2	0.50	7.20	0.10	54.6	1161	3.00	108	86.8

Table 8A (continued)

Sample	La ppm ICP-MS	Ce ppm ICP-MS	Pr ppm ICP-MS	Nd ppm ICP-MS	Sm ppm ICP-MS	Eu ppm ICP-MS	Gd ppm ICP-MS	Tb ppm ICP-MS	Dy ppm ICP-MS	Y ppm ICP-MS	Ho ppm ICP-MS	Er ppm ICP-MS	Tm ppm ICP-MS	Yb ppm ICP-MS	Lu ppm ICP-MS
LBZ-6	36.1	51.4	8.47	34.1	6.93	1.71	8.08	1.31	8.08	74.2	1.87	5.58	0.81	4.81	0.74
LBZ-5	31.1	39.9	7.49	31.1	6.76	1.69	8.85	1.42	9.11	91.7	2.17	6.74	0.95	5.59	0.85
LBZ-4	17.5	16.5	3.87	15.9	3.24	1.56	4.32	0.72	4.56	47.5	1.14	3.41	0.48	2.81	0.44
LBZ-3	40.1	33.2	8.55	36.8	7.82	1.73	11.5	1.87	12.6	147	3.13	9.49	1.27	6.97	1.05
LBZ-2	30.9	46.1	7.86	32.1	7.48	1.79	9.37	1.66	10.5	79.5	2.44	7.32	1.04	6.25	0.93
LBZ-1	5.90	6.10	1.36	5.80	1.22	0.64	1.58	0.23	1.43	15.9	0.35	1.08	0.17	1.01	0.16

Analyses were carried out at Acmelabs in Canada except for TOC analysis (yellowish background) in NRCG in China. Bluish shading refers to inductively coupled plasma with extraction by Aqua Regia.

Table 9A (continued)

Sample	La ppm ICP-MS	Ce ppm ICP-MS	Pr ppm ICP-MS	Nd ppm ICP-MS	Sm ppm ICP-MS	Eu ppm ICP-MS	Gd ppm ICP-MS	Tb ppm ICP-MS	Dy ppm ICP-MS	Y ppm ICP-MS	Ho ppm ICP-MS	Er ppm ICP-MS	Tm ppm ICP-MS	Yb ppm ICP-MS	Lu ppm ICP-MS
ZK2302-9	30.0	58.1	6.54	23.7	3.80	0.72	2.89	0.51	2.84	16.1	0.60	1.76	0.27	1.74	0.27
ZK2302-8	33.9	66.0	7.74	29.8	5.47	1.02	4.54	0.75	4.02	21.6	0.81	2.25	0.34	2.30	0.34
ZK2302-7	36.6	71.2	8.37	30.5	5.33	1.00	4.33	0.72	3.93	21.5	0.80	2.21	0.35	2.30	0.34
ZK2302-6	32.9	64.0	7.44	27.4	4.79	0.93	4.04	0.68	3.72	22.1	0.80	2.35	0.36	2.42	0.35
ZK2302-5	27.3	55.4	6.44	23.9	4.51	0.90	3.85	0.67	3.84	21.8	0.78	2.29	0.35	2.21	0.34
ZK2302-4	30.7	58.6	6.81	25.9	4.81	0.97	4.41	0.75	4.06	24.4	0.85	2.37	0.38	2.40	0.37
ZK2302-3	13.8	28.5	3.03	12.0	2.29	0.48	2.21	0.39	2.25	16.8	0.50	1.50	0.23	1.50	0.24
ZK2302-2	16.0	31.9	3.55	13.8	2.76	0.58	2.67	0.46	2.65	21.3	0.61	1.82	0.27	1.83	0.27
ZK2302-1	23.6	47.9	5.36	20.9	4.00	0.80	3.71	0.65	3.56	25.9	0.83	2.48	0.38	2.48	0.38

Analyses were carried out at Acmelabs in Canada except for TOC analysis (yellowish background) in NRCG in China. Bluish shading refers to inductively coupled plasma with extraction by Aqua Regia.

Table 10A (continued)

Sample	La ppm ICP-MS	Ce ppm ICP-MS	Pr ppm ICP-MS	Nd ppm ICP-MS	Sm ppm ICP-MS	Eu ppm ICP-MS	Gd ppm ICP-MS	Tb ppm ICP-MS	Dy ppm ICP-MS	Y ppm ICP-MS	Ho ppm ICP-MS	Er ppm ICP-MS	Tm ppm ICP-MS	Yb ppm ICP-MS	Lu ppm ICP-MS
ZK15401-8	42.0	78.7	9.17	32.7	5.44	0.98	3.98	0.66	3.77	22.0	0.76	2.24	0.37	2.30	0.36
ZK15401-7	37.5	76.5	9.22	35.1	6.82	1.31	5.95	0.95	4.97	29.0	0.98	2.80	0.43	2.67	0.40
ZK15401-6	35.7	70.2	8.16	31.1	5.72	1.12	5.04	0.83	4.51	28.4	0.91	2.70	0.42	2.60	0.40
ZK15401-5	34.8	68.5	7.87	29.1	5.10	0.98	4.40	0.73	4.00	25.2	0.86	2.61	0.41	2.50	0.40
ZK15401-4	36.5	83.6	8.71	35.2	7.43	1.60	8.11	1.30	7.11	54.0	1.53	4.23	0.56	3.28	0.48
ZK15401-3	16.8	35.6	4.08	17.2	3.49	0.77	3.86	0.64	3.78	30.5	0.83	2.37	0.33	1.91	0.29
ZK15401-2	16.8	36.0	3.78	15.0	3.01	0.65	2.90	0.49	2.83	18.9	0.65	1.78	0.27	1.73	0.26
ZK15401-1	22.7	45.6	5.22	20.5	4.09	0.81	4.10	0.68	3.97	28.5	0.88	2.47	0.36	2.28	0.35

Analyses were carried out at Acmelabs in Canada except for TOC analysis (yellowish background) in NRCG in China. Bluish shading refers to inductively coupled plasma with extraction by Aqua Regia.

Table 11A: Complete bulk rock geochemical data of black shales from drilling core ZK5001 in Sancha district

Sample	Level (m)	Lithology	SiO_2 % ICP	Al_2O_3 % ICP	Fe_2O_3 % ICP	MgO % ICP	CaO % ICP	Na_2O % ICP	K_2O % ICP	TiO_2 % ICP	P_2O_5 % ICP	MnO % ICP	Cr_2O_3 % ICP	TOC % Leco	TOT/C % Leco	TOT/S % Leco	LOI % ICP	Sum % ICP
ZK5001-8	29.0	Black shale	60.8	17.1	5.05	2.05	0.21	1.15	4.98	0.69	0.11	0.02	0.01	5.44	2.11	2.44	7.40	99.5
ZK5001-7	27.0	Black shale	60.3	16.2	5.16	2.18	0.73	1.08	4.76	0.66	0.08	0.03	0.01	5.89	2.54	3.05	8.40	99.6
ZK5001-6	20.0	Black shale	50.2	15.2	6.25	3.88	3.83	1.02	4.80	0.66	0.14	0.07	0.01	6.01	4.91	4.16	13.3	99.3
ZK5001-5	18.0	Black shale	47.3	12.1	6.86	4.19	4.87	1.15	3.63	0.59	0.12	0.06	0.01	8.85	8.21	4.93	18.5	99.5
ZK5001-4	14.0	Black shale	51.5	11.4	7.71	3.35	3.63	0.98	3.51	0.56	0.09	0.05	0.01	8.93	7.42	5.55	16.7	99.6
ZK5001-3	10.0	Black shale	76.3	5.94	2.99	0.50	0.14	0.47	1.89	0.24	0.13	<0.01	0.01	9.2	8.04	2.26	11.1	99.7
ZK5001-2	4.0	Black shale	60.2	8.57	4.54	2.87	3.31	0.53	3.08	0.35	0.10	0.04	0.01	8.97	8.54	3.23	16.1	99.7
ZK5001-1	1.0	Black shale	58.9	7.70	4.65	3.05	3.76	0.57	2.77	0.33	0.13	0.03	0.01	11.4	11.4	3.53	17.7	99.6

Stratigraphic position is in meter relative to the polymetallic Ni-Mo-PGE-Au sulfide ore layer.

Table 12A: Complete bulk rock geochemical data of V-bearing black shales from drilling core ZK3001 in Sancha district

Sample	Level (m)	Lithology	SiO_2 % ICP	Al_2O_3 % ICP	Fe_2O_3 % ICP	MgO % ICP	CaO % ICP	Na_2O % ICP	K_2O % ICP	TiO_2 % ICP	P_2O_5 % ICP	MnO % ICP	Cr_2O_3 % ICP	TOC % Leco	TOT/C % Leco	TOT/S % Leco	LOI % ICP	Sum % ICP
ZK3001-8	55.0	Black shale	68.8	9.45	4.24	1.11	1.23	1.09	2.79	0.41	0.11	0.02	0.01	7.86	5.92	3.24	10.3	99.6
ZK3001-7	33.0	Black shale	65.4	8.34	4.91	0.54	1.67	1.01	3.05	0.41	0.23	0.01	0.01	7.80	9.42	4.08	13.7	99.3
ZK3001-6	23.0	Black shale	70.2	7.52	2.88	0.69	1.18	1.02	2.48	0.40	0.15	<0.01	0.01	10.4	8.97	2.42	12.5	99.1
ZK3001-5	21.0	Black shale	69.0	7.67	2.77	0.78	1.44	1.02	2.50	0.42	0.19	<0.01	0.02	10.2	9.32	2.47	13.2	99.0
ZK3001-4	17.0	Black shale	63.4	10.7	4.76	0.86	0.49	1.46	3.68	0.58	0.18	<0.01	0.02	10.1	8.42	4.03	12.7	98.8
ZK3001-3	10.0	Black shale	21.4	2.91	1.28	12.7	27.8	0.05	0.11	0.14	0.10	0.15	0.00	7.72	14.8	1.29	32.7	99.4
ZK3001-2	7.0	Black shale	69.7	6.98	2.61	0.98	0.37	0.61	2.37	0.36	0.14	<0.01	0.08	11.0	10.4	2.58	13.4	97.6
ZK3001-1	1.0	Black shale	61.3	8.12	3.40	1.01	0.86	0.05	3.81	0.38	0.15	<0.01	0.05	15.2	14.8	3.24	18.1	97.3

Stratigraphic position is in meter relative to the vanadium barren underlying black shale bed.

Table 13A: Complete bulk rock geochemical data of V-bearing black shales form Xiongjiata roadcut profile.

Sample	Level (m)	Lithology	SiO_2 % ICP	Al_2O_3 % ICP	Fe_2O_3 % ICP	MgO % ICP	CaO % ICP	Na_2O % ICP	K_2O % ICP	TiO_2 % ICP	P_2O_5 % ICP	MnO % ICP	Cr_2O_3 % ICP	TOC % Leco	TOT/C % Leco	TOT/S % Leco	LOI % ICP	Sum % ICP
XJT-8	7.2	Black shale	70.2	6.44	2.51	0.70	0.11	0.39	2.20	0.32	0.13	<0.01	0.03	12.3	12.4	2.30	15.1	98.2
XJT-7	6.5	Black shale	68.4	6.94	2.71	0.79	0.13	0.36	2.37	0.34	0.11	<0.01	0.04	12.6	12.6	2.76	15.5	97.8
XJT-6	5.9	Black shale	70.7	6.74	2.42	0.76	0.12	0.37	2.31	0.31	0.14	<0.01	0.05	12	10.7	2.25	14.1	98.0
XJT-5	5.2	Black shale	40.6	5.30	2.43	0.41	17.1	0.10	1.69	0.14	13.5	<0.01	0.11	11.9	11.1	2.80	16.0	97.4
XJT-4	4.6	Black shale	51.0	13.6	7.09	1.31	1.50	0.07	7.35	0.74	0.18	0.01	0.02	9.01	6.87	5.75	14.4	97.2
XJT-3	3.9	Black shale	57.5	13.1	6.30	1.03	1.33	0.07	7.33	0.62	0.11	0.03	0.02	6.12	4.26	4.00	10.0	97.4
XJT-2	3.3	Black shale	46.9	9.88	5.25	1.02	0.45	0.10	4.80	0.46	0.44	<0.01	0.08	23.4	22.5	4.92	27.5	96.9
XJT-1	2.6	Black shale	51.3	11.7	6.48	2.53	3.42	0.07	6.64	0.74	0.20	0.02	0.03	8.62	6.95	5.12	14.4	97.6

Stratigraphic position is in meter relative to the chert bed.

Table 11A (continued)

Sample	Ag ppm ICP-MS	As ppm ICP-MS	Au ppm ICP-MS	Ba ppm ICP-MS	Be ppm ICP-MS	Bi ppm ICP-MS	Cd ppm ICP-MS	Co ppm ICP-MS	Cs ppm ICP-MS	Cu ppm ICP-MS	Ga ppm ICP-MS	Hf ppm ICP-MS	Hg ppm ICP-MS	Mo ppm ICP-MS	Nb ppm ICP-MS
ZK5001-8	0.20	12.4	<0.5	2775	3.00	0.60	0.20	17.5	11.4	55.4	22.4	4.00	0.11	26.8	13.6
ZK5001-7	0.30	17.1	0.50	2502	4.00	0.60	0.40	16.6	11.9	55.4	21.2	3.90	0.15	31.6	12.6
ZK5001-6	0.40	14.4	0.80	4966	3.00	0.60	1.50	19.8	14.1	57.8	20.6	3.40	0.43	27.0	12.7
ZK5001-5	0.30	14.0	<0.5	2895	2.00	0.70	1.70	21.0	9.30	59.2	16.8	3.10	0.61	24.1	11.0
ZK5001-4	0.40	24.7	<0.5	2375	3.00	0.80	2.20	26.6	8.20	57.3	15.2	3.30	0.46	72.1	10.7
ZK5001-3	0.40	34.6	0.70	1041	1.00	0.30	1.00	15.2	3.40	72.3	8.60	1.40	0.21	123.9	4.70
ZK5001-2	0.80	45.5	<0.5	1227	2.00	0.40	1.90	21.7	5.70	81.1	11.9	2.20	0.64	99.0	6.60
ZK5001-1	1.30	59.9	<0.5	1276	2.00	0.50	4.10	26.6	5.10	102	11.4	2.10	0.80	157	7.10

Table 12A (continued)

Sample	Ag ppm ICP-MS	As ppm ICP-MS	Au ppm ICP-MS	Ba ppm ICP-MS	Be ppm ICP-MS	Bi ppm ICP-MS	Cd ppm ICP-MS	Co ppm ICP-MS	Cs ppm ICP-MS	Cu ppm ICP-MS	Ga ppm ICP-MS	Hf ppm ICP-MS	Hg ppm ICP-MS	Mo ppm ICP-MS	Nb ppm ICP-MS
ZK3001-8	0.30	16.0	<0.5	2833	2.00	0.40	0.90	14.2	4.80	63.4	11.5	2.40	0.07	30.7	11.4
ZK3001-7	1.80	76.9	<0.5	3950	2.00	0.30	2.40	11.5	2.70	69.9	8.60	2.60	0.19	180	6.90
ZK3001-6	1.20	55.6	<0.5	3346	1.00	0.20	4.90	7.90	3.00	49.0	10.3	2.30	0.11	210	5.60
ZK3001-5	2.50	60.9	<0.5	3222	2.00	0.20	19.4	8.80	3.50	89.8	10.7	2.90	0.25	123	6.40
ZK3001-4	2.80	72.3	<0.5	6145	2.00	0.20	13.7	14.7	3.70	77.9	15.3	3.70	0.23	111	8.50
ZK3001-3	2.00	32.9	<0.5	946	<1	<0.1	1.40	4.60	0.30	32.5	6.20	1.10	0.09	24.9	2.40
ZK3001-2	17.2	109	<0.5	4400	2.00	0.30	105	9.30	5.40	299	12.5	2.30	1.15	134	6.70
ZK3001-1	9.60	87.6	<0.5	18929	3.00	0.40	20.3	8.20	2.30	168	12.5	2.20	0.44	60.0	12.4

Table 13A (continued)

Sample	Ag ppm ICP-MS	As ppm ICP-MS	Au ppm ICP-MS	Ba ppm ICP-MS	Be ppm ICP-MS	Bi ppm ICP-MS	Cd ppm ICP-MS	Co ppm ICP-MS	Cs ppm ICP-MS	Cu ppm ICP-MS	Ga ppm ICP-MS	Hf ppm ICP-MS	Hg ppm ICP-MS	Mo ppm ICP-MS	Nb ppm ICP-MS
XJT-8	13.2	104	<0.5	4107	2.00	0.20	85.0	9.40	4.80	221	8.60	2.10	0.75	102	5.70
XJT-7	11.3	119	<0.5	4815	2.00	0.20	84.3	9.90	5.40	230	9.40	2.10	1.38	141	6.30
XJT-6	13.4	120	<0.5	4597	2.00	0.20	67.4	8.90	5.50	220	9.10	2.10	0.53	99.7	5.40
XJT-5	11.0	101	0.60	19629	2.00	0.10	30.5	4.00	2.50	201	4.70	0.80	0.35	18.0	3.00
XJT-4	5.60	102	<0.5	22938	3.00	0.20	46.8	13.2	3.60	68.9	18.0	3.20	0.19	13.5	14.9
XJT-3	3.30	58.5	0.80	21432	2.00	0.20	5.60	13.4	2.00	52.2	11.9	2.50	0.12	2.70	12.3
XJT-2	21.5	206	1.10	13540	4.00	0.90	82.6	26.2	7.40	454	14.5	2.60	0.82	370	9.50
XJT-1	5.60	88.4	<0.5	18440	2.00	0.20	4.70	13.0	2.20	73.1	10.9	3.70	0.28	10.0	13.3

Table 11A (continued)

Sample	Ni ppm ICP-MS	Pb ppm ICP-MS	Rb ppm ICP-MS	Sb ppm ICP-MS	Se ppm ICP-MS	Sn ppm ICP-MS	Sr ppm ICP-MS	Ta ppm ICP-MS	Th ppm ICP-MS	Tl ppm ICP-MS	U ppm ICP-MS	V ppm ICP-MS	W ppm ICP-MS	Zn ppm ICP-MS	Zr ppm ICP-MS
ZK5001-8	69.3	22.3	174	0.30	1.60	4.00	51.8	1.10	17.6	0.10	11.6	181	2.90	31.0	132
ZK5001-7	98.9	23.6	163	0.30	3.50	4.00	66.4	1.00	15.1	0.20	15.1	272	1.70	26.0	129
ZK5001-6	93.6	26.6	157	0.20	2.40	4.00	108	1.00	14.5	0.30	15.3	156	2.00	43.0	118
ZK5001-5	82.0	22.3	117	0.20	2.80	3.00	80.0	0.80	13.6	0.20	16.5	160	2.00	54.0	114
ZK5001-4	219	21.0	114	0.60	12.5	3.00	82.3	0.90	12.6	0.60	16.5	186	2.40	43.0	112
ZK5001-3	211	11.6	55.7	1.90	7.80	1.00	24.3	0.30	5.20	0.50	56.0	808	1.90	17.0	60.9
ZK5001-2	86.1	23.1	82.0	1.90	8.10	2.00	54.3	0.50	7.40	0.30	60.0	393	2.60	60.0	77.3
ZK5001-1	105	22.0	73.4	2.80	13.3	2.00	55.8	0.40	7.30	0.60	83.2	537	2.20	125	69.7

Table 12A (continued)

Sample	Ni ppm ICP-MS	Pb ppm ICP-MS	Rb ppm ICP-MS	Sb ppm ICP-MS	Se ppm ICP-MS	Sn ppm ICP-MS	Sr ppm ICP-MS	Ta ppm ICP-MS	Th ppm ICP-MS	Tl ppm ICP-MS	U ppm ICP-MS	V ppm ICP-MS	W ppm ICP-MS	Zn ppm ICP-MS	Zr ppm ICP-MS
ZK3001-8	36.2	13.8	77.9	1.30	3.20	2.00	80.5	0.50	9.10	0.10	15.4	121	2.00	9.00	88.4
ZK3001-7	269	20.0	68.4	7.40	16.7	<1	88.1	0.50	8.00	0.80	74.4	847	2.10	93.0	90.7
ZK3001-6	320	11.6	60.2	3.40	13.6	1.00	65.8	0.40	5.80	<0.1	46.0	2768	1.20	224.0	91.4
ZK3001-5	289	15.0	62.0	6.70	16.8	2.00	77.3	0.50	6.30	<0.1	66.3	2926	1.20	1129	102
ZK3001-4	242	16.3	84.4	6.20	24.2	3.00	63.9	0.70	9.40	0.20	48.0	2460	1.40	660	134
ZK3001-3	51.9	8.30	3.20	2.20	8.60	<1	1367	0.20	2.30	<0.1	29.2	500	0.70	60.0	41.1
ZK3001-2	317	44.5	71.0	23.4	86.7	2.00	43.2	0.50	6.70	<0.1	64.3	7858	1.20	5092	83.2
ZK3001-1	213	26.0	64.5	12.9	56.8	2.00	67.5	0.60	7.30	<0.1	42.6	2194	1.80	1181	88.3

Table 13A (continued)

Sample	Ni ppm ICP-MS	Pb ppm ICP-MS	Rb ppm ICP-MS	Sb ppm ICP-MS	Se ppm ICP-MS	Sn ppm ICP-MS	Sr ppm ICP-MS	Ta ppm ICP-MS	Th ppm ICP-MS	Tl ppm ICP-MS	U ppm ICP-MS	V ppm ICP-MS	W ppm ICP-MS	Zn ppm ICP-MS	Zr ppm ICP-MS
XJT-8	269	37.6	62.4	31.5	70.2	<1	28.9	0.40	5.40	<0.1	49.9	5619	0.90	3010	77.8
XJT-7	359	40.7	67.6	25.1	62.7	<1	40.9	0.40	6.10	<0.1	56.5	7105	1.60	3854	82.3
XJT-6	293	35.7	67.9	27.6	70.2	1.00	22.1	0.40	6.50	<0.1	44.4	6767	1.30	2975	79.7
XJT-5	84.5	14.5	36.8	17.9	73.0	<1	922	0.30	2.90	0.30	60.7	1192	0.70	504	34.9
XJT-4	94.1	13.8	107	4.00	26.2	1.00	127	0.90	11.0	0.60	33.6	599	3.30	363	111
XJT-3	95.6	9.20	102	4.20	17.7	2.00	83.4	0.90	10.1	0.50	8.30	165	2.20	1044	84.7
XJT-2	442	80.6	98.6	31.5	>100	<1	46.0	0.60	8.70	1.40	177	5859	4.20	3441	124
XJT-1	102	15.5	94.4	6.50	47.5	1.00	208	1.00	10.9	0.40	16.6	667	2.10	821	124

Table 11A (continued)

Sample	La ppm ICP-MS	Ce ppm ICP-MS	Pr ppm ICP-MS	Nd ppm ICP-MS	Sm ppm ICP-MS	Eu ppm ICP-MS	Gd ppm ICP-MS	Tb ppm ICP-MS	Dy ppm ICP-MS	Y ppm ICP-MS	Ho ppm ICP-MS	Er ppm ICP-MS	Tm ppm ICP-MS	Yb ppm ICP-MS	Lu ppm ICP-MS
ZK5001-8	39.5	78.5	9.36	34.9	6.70	1.22	5.57	0.85	4.52	25.8	0.89	2.60	0.41	2.60	0.39
ZK5001-7	36.8	70.9	8.32	31.1	5.67	1.12	4.93	0.78	4.36	25.3	0.86	2.53	0.40	2.51	0.39
ZK5001-6	38.2	72.6	8.30	31.5	5.83	1.19	5.07	0.82	4.53	26.8	0.93	2.73	0.42	2.55	0.40
ZK5001-5	31.6	63.3	7.22	27.2	5.03	1.00	4.41	0.72	3.97	25.3	0.86	2.55	0.39	2.49	0.38
ZK5001-4	28.8	54.4	6.24	22.6	4.43	0.89	4.33	0.71	4.01	25.8	0.84	2.56	0.39	2.38	0.37
ZK5001-3	16.3	32.3	3.79	15.6	3.58	0.86	4.78	0.78	4.40	36.8	0.99	2.92	0.41	2.43	0.37
ZK5001-2	19.5	38.3	4.20	15.8	3.10	0.65	2.79	0.49	2.87	20.5	0.65	1.94	0.31	1.92	0.31
ZK5001-1	18.4	36.5	4.16	15.8	3.21	0.68	3.00	0.50	2.74	19.9	0.62	1.87	0.28	1.72	0.28

Analyses were carried out at Acmelabs in Canada except for TOC analysis (yellowish background) in NRCG in China. Bluish shading refers to inductively coupled plasma with extraction by Aqua Regia.

Table 12A (continued)

Sample	La ppm ICP-MS	Ce ppm ICP-MS	Pr ppm ICP-MS	Nd ppm ICP-MS	Sm ppm ICP-MS	Eu ppm ICP-MS	Gd ppm ICP-MS	Tb ppm ICP-MS	Dy ppm ICP-MS	Y ppm ICP-MS	Ho ppm ICP-MS	Er ppm ICP-MS	Tm ppm ICP-MS	Yb ppm ICP-MS	Lu ppm ICP-MS
ZK3001-8	21.3	44.0	4.98	19.2	3.70	0.72	3.53	0.56	3.13	20.2	0.65	1.87	0.29	1.80	0.28
ZK3001-7	29.4	46.7	5.81	23.2	4.25	0.82	4.90	0.79	4.79	52.8	1.16	3.63	0.54	3.01	0.48
ZK3001-6	21.8	34.2	4.62	17.4	3.18	0.64	3.37	0.53	3.09	30.5	0.74	2.18	0.33	1.95	0.30
ZK3001-5	28.3	39.2	6.08	25.0	4.82	1.04	5.64	0.93	5.57	61.9	1.39	4.15	0.60	3.42	0.53
ZK3001-4	27.6	48.2	6.53	25.5	4.83	0.95	4.95	0.79	4.56	35.6	0.99	3.00	0.42	2.53	0.39
ZK3001-3	21.9	29.9	4.20	16.6	3.43	1.41	4.17	0.66	4.04	50.7	0.94	2.84	0.40	2.17	0.32
ZK3001-2	30.9	36.5	7.20	30.9	6.07	1.23	7.35	1.21	7.54	75.4	1.81	5.65	0.85	4.77	0.74
ZK3001-1	33.9	40.0	7.70	31.0	5.91	1.24	6.80	1.10	6.46	59.2	1.55	4.72	0.69	3.97	0.62

Analyses were carried out at Acmelabs in Canada except for TOC analysis (yellowish background) in NRCG in China. Bluish shading refers to inductively coupled plasma with extraction by Aqua Regia.

Table 13A (continued)

Sample	La ppm ICP-MS	Ce ppm ICP-MS	Pr ppm ICP-MS	Nd ppm ICP-MS	Sm ppm ICP-MS	Eu ppm ICP-MS	Gd ppm ICP-MS	Tb ppm ICP-MS	Dy ppm ICP-MS	Y ppm ICP-MS	Ho ppm ICP-MS	Er ppm ICP-MS	Tm ppm ICP-MS	Yb ppm ICP-MS	Lu ppm ICP-MS
XJT-8	21.2	26.9	4.72	17.9	3.16	0.67	3.65	0.65	4.43	40.5	1.04	3.35	0.49	3.11	0.46
XJT-7	21.4	26.9	4.76	19.8	3.81	0.83	4.72	0.81	5.32	53.4	1.31	4.27	0.64	3.90	0.59
XJT-6	19.6	25.3	4.21	16.1	3.01	0.66	3.51	0.63	4.04	41.1	1.01	3.33	0.49	3.02	0.47
XJT-5	62.4	51.1	13.9	61.5	12.9	4.27	17.1	2.56	15.5	174	3.57	10.6	1.38	7.71	1.09
XJT-4	58.3	78.3	12.4	50.9	9.47	1.95	10.89	1.60	8.37	67.2	1.81	5.11	0.68	3.89	0.57
XJT-3	32.1	40.2	6.28	22.8	3.46	0.62	2.99	0.46	2.69	20.7	0.59	1.81	0.29	1.74	0.27
XJT-2	83.6	93.6	21.3	96.7	19.1	4.19	24.7	3.80	23.5	253	5.88	17.9	2.45	14.3	2.16
XJT-1	37.6	53.3	8.41	33.0	5.99	1.21	6.13	0.97	5.63	50.6	1.31	3.92	0.59	3.54	0.54

Analyses were carried out at Acmelabs in Canada except for TOC analysis (yellowish background) in NRCG in China. Bluish shading refers to inductively coupled plasma with extraction by Aqua Regia.

Table 14A: Complete bulk rock geochemical data of V-bearing black shales from drilling core ZK1801 in Sancha district

Sample	Level (m)	Lithology	SiO$_2$	Al$_2$O$_3$	Fe$_2$O$_3$	MgO	CaO	Na$_2$O	K$_2$O	TiO$_2$	P$_2$O$_5$	MnO	Cr$_2$O$_3$	TOC	TOT/C	TOT/S	LOI	Sum
			%	%	%	%	%	%	%	%	%	%	%	%	%	%	%	%
			ICP	ICP	ICP	ICP	ICP	ICP	ICP	ICP	ICP	ICP	ICP	Leco	Leco	Leco	ICP	ICP
ZK1801-22	29.1	Black shale	49.7	8.73	6.09	2.67	9.58	1.03	3.08	0.48	0.16	0.06	0.02	9.17	8.91	3.33	17.4	99.0
ZK1801-21	27.9	Black shale	57.6	10.3	8.75	0.83	2.12	1.27	3.71	0.56	0.24	0.04	0.02	10.2	7.97	3.73	13.0	98.5
ZK1801-20	26.9	Black shale	58.6	10.9	6.89	0.91	1.68	1.32	3.92	0.59	0.48	0.04	0.03	10.1	7.93	3.47	12.9	98.4
ZK1801-19	25.4	Black shale	64.0	7.63	3.85	0.83	4.40	0.90	2.71	0.40	0.22	0.20	0.02	8.53	7.78	2.72	13.4	98.6
ZK1801-18	23.9	Black shale	70.0	2.44	2.30	0.51	9.32	0.19	0.94	0.12	0.07	0.05	0.01	7.11	8.50	1.15	13.5	99.5
ZK1801-17	22.5	Black shale	70.6	3.69	4.31	0.89	5.50	0.28	1.30	0.18	0.14	0.04	0.01	8.04	8.01	1.57	12.4	99.4
ZK1801-16	21.0	Black shale	63.1	6.16	6.20	2.66	2.40	0.39	2.17	0.30	0.19	0.03	0.01	10.9	9.46	2.95	15.4	99.1
ZK1801-15	19.9	Black shale	62.7	3.85	3.23	3.25	8.40	0.16	1.13	0.18	0.12	0.04	0.01	9.68	10.2	1.93	16.4	99.4
ZK1801-14	18.3	Black shale	70.0	3.24	3.49	1.10	7.11	0.23	1.21	0.15	0.09	0.04	0.01	8.01	8.55	1.48	12.7	99.4
ZK1801-13	16.7	Black shale	60.3	3.66	2.53	1.22	12.3	0.32	1.37	0.18	0.12	0.05	0.01	7.53	9.49	1.44	17.3	99.3
ZK1801-12	15.2	Black shale	63.0	7.81	6.44	0.93	1.63	0.74	2.90	0.40	0.14	0.04	0.03	11.2	9.83	2.57	14.4	98.4
ZK1801-11	13.8	Black shale	70.2	5.21	2.69	0.69	2.29	0.43	1.86	0.27	0.30	0.02	0.04	10.9	10.0	2.01	14.5	98.5
ZK1801-10	12.3	Black shale	70.8	4.53	4.48	0.67	1.29	0.32	1.60	0.23	0.18	0.03	0.03	11.4	10.4	1.82	14.1	98.4
ZK1801-9	10.8	Black shale	69.4	5.42	4.46	0.78	0.81	0.42	1.92	0.28	0.12	0.03	0.04	11.8	10.6	2.07	14.3	98.1
ZK1801-8	9.41	Black shale	68.8	5.79	3.38	0.91	1.63	0.44	2.11	0.28	0.13	0.02	0.05	11.0	10.7	2.19	14.6	98.2
ZK1801-7	7.80	Black shale	68.0	5.86	2.91	1.21	1.64	0.36	2.19	0.29	0.18	0.01	0.06	11.4	11.2	2.31	15.3	98.0
ZK1801-6	6.37	Black shale	65.0	5.45	3.55	1.52	3.02	0.28	2.13	0.27	0.80	0.02	0.08	11.3	11.7	2.32	16.0	98.1
ZK1801-5	4.88	Black shale	58.2	6.50	4.50	1.28	6.80	0.27	2.78	0.30	1.96	0.02	0.15	10.7	10.9	3.51	15.7	98.5
ZK1801-4	3.93	Black shale	46.1	5.46	3.58	5.53	11.3	0.07	2.46	0.19	1.31	0.04	0.07	8.62	11.8	2.12	22.1	98.1
ZK1801-3	2.43	Black shale	47.9	8.68	4.06	5.40	8.13	0.06	4.55	0.42	0.19	0.03	0.02	8.48	10.3	3.17	18.9	98.4
ZK1801-2	1.00	Black shale	53.8	5.47	6.54	3.97	6.18	0.06	2.69	0.27	0.15	0.04	0.02	11.1	12.3	2.52	19.5	98.6
ZK1801-1	0	Chert	62.3	5.71	6.09	2.84	4.96	0.04	3.11	0.31	0.32	0.04	0.02	5.71	6.04	2.39	12.4	98.2

Table 14A (continued)

Sample	Ag ppm ICP-MS	As ppm ICP-MS	Au ppm ICP-MS	Ba ppm ICP-MS	Be ppm ICP-MS	Bi ppm ICP-MS	Cd ppm ICP-MS	Co ppm ICP-MS	Cs ppm ICP-MS	Cu ppm ICP-MS	Ga ppm ICP-MS	Hf ppm ICP-MS	Hg ppm ICP-MS	Mo ppm ICP-MS	Nb ppm ICP-MS
ZK1801-22	2.20	70.3	<0.5	6290	2.00	0.20	4.50	12.4	2.60	55.0	11.0	3.50	0.17	113	7.60
ZK1801-21	2.60	91.6	0.80	8084	2.00	0.20	11.1	16.9	4.50	87.2	14.7	3.90	0.19	178	9.00
ZK1801-20	3.60	99.8	<0.5	7973	2.00	0.30	22.6	17.6	5.10	119	15.9	4.30	0.27	225	9.30
ZK1801-19	3.80	75.1	<0.5	5976	2.00	0.20	35.3	11.3	4.10	108	12.3	2.90	0.34	147	6.80
ZK1801-18	1.70	30.4	<0.5	2630	<1	<0.1	8.70	4.60	1.10	56.2	4.50	1.00	0.15	22.6	2.30
ZK1801-17	2.20	41.9	0.50	3918	<1	0.10	8.00	7.50	1.20	57.1	6.00	1.40	0.17	57.3	3.70
ZK1801-16	4.20	80.3	<0.5	5446	1.00	0.20	5.90	14.1	2.00	77.5	9.50	2.10	0.21	115	6.10
ZK1801-15	2.60	52.1	<0.5	2785	<1	0.10	6.50	7.70	1.00	81.1	7.50	1.20	0.22	55.6	3.80
ZK1801-14	2.00	40.1	<0.5	3548	<1	<0.1	4.50	6.20	1.20	53.0	5.50	1.20	0.12	39.6	3.30
ZK1801-13	2.10	38.0	<0.5	3296	<1	0.10	7.60	5.50	1.40	36.9	5.40	1.10	0.18	33.2	3.40
ZK1801-12	7.10	88.3	<0.5	5416	1.00	0.20	40.8	12.60	3.90	162	11.5	2.80	0.52	76.3	6.90
ZK1801-11	9.80	83.2	<0.5	3719	<1	0.20	63.7	7.30	3.40	185	8.90	2.00	0.69	70.8	5.20
ZK1801-10	7.90	87.6	<0.5	3095	<1	0.20	54.8	7.40	3.70	123	7.60	1.60	0.63	120	4.80
ZK1801-9	10.1	98.2	<0.5	3637	<1	0.20	84.4	8.70	3.70	164	9.50	1.70	0.86	110	5.00
ZK1801-8	13.9	121	<0.5	4555	2.00	0.20	87.0	7.70	3.80	295	8.00	2.00	0.96	75.5	4.90
ZK1801-7	14.5	118	<0.5	4733	1.00	0.20	93.7	7.90	4.20	293	8.40	1.90	0.84	103	5.50
ZK1801-6	17.0	121	<0.5	6486	2.00	0.30	92.4	7.40	3.80	293	8.80	1.80	0.73	80.8	5.00
ZK1801-5	21.0	127	<0.5	8207	2.00	0.30	39.8	7.30	4.30	322	9.00	2.00	0.70	33.9	5.90
ZK1801-4	9.90	75.9	<0.5	11280	2.00	0.20	24.2	4.30	2.70	155	8.40	1.50	0.46	26.4	6.60
ZK1801-3	2.80	64.0	<0.5	12024	2.00	0.20	2.00	8.70	1.70	51.8	9.80	1.90	0.14	9.90	9.20
ZK1801-2	5.20	82.0	<0.5	9092	1.00	0.30	3.70	10.3	1.60	80.6	8.70	1.70	0.22	67.0	5.70
ZK1801-1	8.40	64.9	0.50	12475	<1	0.20	12.2	8.20	1.40	86.4	5.30	1.60	0.57	22.9	6.20

Table 14A (continued)

Sample	Ni ppm ICP-MS	Pb ppm ICP-MS	Rb ppm ICP-MS	Sb ppm ICP-MS	Se ppm ICP-MS	Sn ppm ICP-MS	Sr ppm ICP-MS	Ta ppm ICP-MS	Th ppm ICP-MS	Tl ppm ICP-MS	U ppm ICP-MS	V ppm ICP-MS	W ppm ICP-MS	Zn ppm ICP-MS	Zr ppm ICP-MS
ZK1801-22	183	26.8	62.9	6.70	15.1	2.00	275	0.60	7.50	0.20	64.9	807	1.60	145	115
ZK1801-21	297	22.6	84.3	6.40	23.1	3.00	121	0.60	9.50	<0.1	65.8	2638	5.30	514	143
ZK1801-20	375	26.4	91.8	8.00	33.0	2.00	111	0.70	9.70	<0.1	76.8	3559	1.70	940	137
ZK1801-19	257	27.7	66.3	10.6	31.6	2.00	216	0.50	6.80	<0.1	57.5	3089	1.30	1607	104
ZK1801-18	68.6	16.7	20.6	6.60	8.70	<1	381	0.20	1.90	<0.1	21.1	802	0.90	550	31.2
ZK1801-17	123	13.9	27.7	7.20	11.5	1.00	242	0.20	2.80	0.10	41.4	663	4.20	477	46.1
ZK1801-16	254	18.8	43.6	9.90	24.8	1.00	116	0.40	5.60	0.20	96.0	938	1.80	247	80.4
ZK1801-15	103	23.3	22.6	12.3	11.9	<1	343	0.20	2.90	<0.1	47.0	702	2.20	377	48.5
ZK1801-14	100	17.0	24.0	8.30	10.5	1.00	354	0.20	2.70	<0.1	37.1	809	1.70	279	43.6
ZK1801-13	79.8	15.7	29.0	7.10	11.3	<1	425	0.20	2.90	<0.1	45.5	1073	0.90	431	45.5
ZK1801-12	187	37.6	73.9	13.4	34.9	3.00	89.6	0.50	7.00	<0.1	50.9	4018	4.10	2149	95.8
ZK1801-11	171	36.8	52.7	21.0	39.7	1.00	120	0.40	4.60	<0.1	42.0	3922	1.00	3232	66.4
ZK1801-10	216	32.0	48.3	12.9	43.9	1.00	93.3	0.30	4.00	<0.1	53.3	5682	1.10	3008	60.6
ZK1801-9	233	55.3	55.9	17.5	52.7	1.00	65.5	0.40	4.60	<0.1	50.2	5577	1.40	4428	66.8
ZK1801-8	176	54.8	51.3	26.9	70.7	2.00	97.7	0.40	5.10	<0.1	43.1	4437	1.10	4103	68.3
ZK1801-7	209	42.6	53.1	29.0	79.4	1.00	92.1	0.40	5.00	<0.1	49.2	4900	1.10	4298	66.2
ZK1801-6	165	49.9	50.2	32.7	77.1	2.00	147	0.40	5.00	<0.1	55.4	4198	1.10	2992	66.7
ZK1801-5	107	45.1	57.3	35.4	>100	1.00	326	0.50	5.50	<0.1	55.3	1988	0.80	1169	68.3
ZK1801-4	92.7	24.0	44.2	14.6	56.8	1.00	513	0.60	5.60	<0.1	35.9	1776	0.70	923	51.7
ZK1801-3	62.1	26.8	65.3	6.50	17.1	1.00	302	0.60	8.10	0.20	20.2	439	1.10	161	67.7
ZK1801-2	118	19.7	38.5	6.30	20.8	2.00	247	0.40	5.20	0.10	51.7	839	4.60	341	65.1
ZK1801-1	78.4	35.7	42.2	7.40	30.1	1.00	332	0.50	5.50	0.20	24.3	1395	3.40	478	59.8

Table 14A (continued)

Sample	La	Ce	Pr	Nd	Sm	Eu	Gd	Tb	Dy	Y	Ho	Er	Tm	Yb	Lu
	ppm	ppm	ppm	ppm	ppm	ppm	ppm	ppm	ppm	ppm	ppm	ppm	ppm	ppm	ppm
	ICP-MS	ICP-MS	ICP-MS	ICP-MS	ICP-MS	ICP-MS	ICP-MS	ICP-MS	ICP-MS	ICP-MS	ICP-MS	ICP-MS	ICP-MS	ICP-MS	ICP-MS
ZK1801-22	30.4	49.8	6.17	23.7	4.84	1.01	5.05	0.79	4.90	46.3	1.07	3.35	0.50	3.13	0.46
ZK1801-21	29.8	51.8	7.00	27.3	5.12	1.19	5.48	0.86	5.26	42.1	1.10	3.36	0.49	2.97	0.44
ZK1801-20	32.8	54.1	7.77	32.5	6.29	1.28	6.51	1.07	6.41	48.1	1.37	4.14	0.61	3.71	0.55
ZK1801-19	24.9	40.2	5.73	22.4	4.42	0.94	4.63	0.76	4.55	37.0	0.97	2.93	0.43	2.62	0.39
ZK1801-18	10.6	14.9	2.45	10.0	2.25	0.78	2.61	0.43	2.63	25.7	0.58	1.85	0.25	1.50	0.21
ZK1801-17	15.3	23.6	3.44	14.3	2.81	0.63	3.19	0.53	3.23	29.8	0.69	2.15	0.29	1.82	0.26
ZK1801-16	29.5	42.5	6.36	26.1	4.79	1.01	5.53	0.87	5.25	55.0	1.18	3.78	0.56	3.23	0.48
ZK1801-15	19.1	27.2	3.86	15.9	2.85	0.77	3.40	0.57	3.34	35.4	0.77	2.40	0.36	2.03	0.29
ZK1801-14	13.7	20.0	3.10	12.8	2.53	0.62	3.07	0.50	3.01	29.8	0.66	2.06	0.28	1.73	0.25
ZK1801-13	18.5	27.3	4.10	17.9	3.47	0.80	3.91	0.65	3.98	39.2	0.92	2.82	0.41	2.45	0.38
ZK1801-12	25.5	37.8	5.69	23.0	4.55	0.93	4.93	0.80	4.96	43.4	1.11	3.50	0.49	3.04	0.46
ZK1801-11	20.2	26.5	4.69	19.9	4.04	0.85	4.63	0.77	4.77	45.6	1.06	3.53	0.49	3.08	0.45
ZK1801-10	20.8	26.9	5.11	22.9	4.37	1.15	5.43	0.82	5.08	48.1	1.13	3.34	0.49	2.91	0.42
ZK1801-9	20.0	26.2	4.67	20.5	3.71	0.80	4.23	0.71	4.43	43.2	1.03	3.32	0.46	2.93	0.45
ZK1801-8	19.4	25.3	4.39	18.0	3.75	0.89	4.68	0.78	4.81	43.2	1.20	3.77	0.55	3.26	0.50
ZK1801-7	23.5	27.9	5.29	22.4	4.60	1.02	5.71	0.93	5.79	55.7	1.44	4.46	0.65	3.93	0.60
ZK1801-6	25.9	29.2	6.17	26.0	5.73	1.32	7.13	1.16	7.11	66.1	1.72	5.31	0.74	4.39	0.65
ZK1801-5	35.5	35.7	8.52	38.5	8.32	1.94	10.6	1.70	10.3	102	2.54	7.60	1.08	6.20	0.91
ZK1801-4	25.0	29.5	6.00	26.8	5.17	1.22	6.52	1.03	6.34	62.8	1.53	4.65	0.66	3.90	0.56
ZK1801-3	29.8	39.1	6.48	25.0	4.93	1.16	5.08	0.83	4.80	37.4	1.04	3.21	0.45	2.79	0.41
ZK1801-2	23.1	31.8	5.09	20.8	4.06	0.91	4.58	0.74	4.47	38.2	1.07	3.32	0.47	2.80	0.42
ZK1801-1	24.7	30.0	5.30	21.5	4.31	1.00	4.80	0.78	4.78	41.5	1.09	3.23	0.46	2.86	0.42

Stratigraphic position is in meter relative to the vanadium barren underlying black shale bed. Analyses were carried out at Acmelabs in Canada except for TOC analysis (yellowish background) in NRCG in China. Bluish shading refers to inductively coupled plasma with extraction by Aqua Regia.

Table 15A: Complete bulk rock geochemical data of black shales from drilling core ZK001 in Sancha district.

Sample	Level (m)	Lithology	SiO_2 % ICP	Al_2O_3 % ICP	Fe_2O_3 % ICP	MgO % ICP	CaO % ICP	Na_2O % ICP	K_2O % ICP	TiO_2 % ICP	P_2O_5 % ICP	MnO % ICP	Cr_2O_3 % ICP	TOC % Leco	TOT/C % Leco	TOT/S % Leco	LOI % ICP	Sum % ICP
ZK001-14	18.6	Black shale	49.4	6.83	3.92	2.58	13.9	0.92	2.24	0.35	0.15	0.05	0.01	7.15	8.89	2.47	18.9	99.2
ZK001-13	17.1	Black shale	56.7	8.08	5.00	3.80	5.62	1.05	2.72	0.42	0.14	0.06	0.01	8.7	8.61	2.95	15.5	99.2
ZK001-12	15.6	Black shale	59.5	8.93	5.09	2.51	3.34	1.12	3.13	0.47	0.15	0.04	0.02	9.05	7.63	3.23	14.5	98.9
ZK001-11	14.6	Black shale	58.2	8.23	4.48	2.41	5.46	1.03	2.87	0.44	0.14	0.04	0.01	8.87	8.45	3.09	15.7	99.0
ZK001-10	13.4	Black shale	64.6	7.81	4.42	0.69	3.01	1.02	2.84	0.42	0.16	0.02	0.02	9.69	8.71	2.74	13.8	98.9
ZK001-9	12.1	Black shale	66.2	7.41	3.52	1.00	3.05	0.90	2.71	0.41	0.16	0.02	0.03	9.15	8.35	2.54	13.4	98.8
ZK001-8	10.8	Black shale	51.0	8.90	5.29	5.11	6.69	0.93	2.68	0.49	0.17	0.07	0.01	9.36	8.80	3.46	17.5	98.9
ZK001-7	9.26	Black shale	48.2	9.01	4.98	1.31	11.7	1.11	3.39	0.48	0.25	0.04	0.02	8.19	8.78	3.05	18.1	98.6
ZK001-6	7.71	Black shale	54.2	9.15	5.71	1.46	5.10	1.00	3.56	0.48	0.33	0.03	0.02	11.2	10.0	3.58	17.5	98.5
ZK001-5	6.21	Black shale	65.2	7.46	4.20	0.88	2.04	0.74	2.87	0.38	0.77	0.02	0.06	10.9	9.32	2.61	13.6	98.3
ZK001-4	4.65	Black shale	43.3	4.35	4.65	1.62	19.3	0.29	1.82	0.21	0.41	0.05	0.02	8.91	11.7	2.02	23.0	99.0
ZK001-3	3.15	Black shale	60.9	5.24	4.84	2.76	4.77	0.32	2.18	0.26	0.19	0.04	0.01	11.3	11.2	2.58	17.4	99.0
ZK001-2	1.68	Black shale	70.5	5.75	3.43	0.92	1.52	0.33	2.23	0.29	0.13	0.02	0.06	9.45	8.55	2.09	12.8	97.9
ZK001-1	0	Chert	72.8	3.59	2.70	0.97	5.34	0.18	1.40	0.18	0.20	0.02	0.03	6.81	8.38	1.28	11.4	98.8

Table 15A (continued)

Sample	Ag ppm ICP-MS	As ppm ICP-MS	Au ppm ICP-MS	Ba ppm ICP-MS	Be ppm ICP-MS	Bi ppm ICP-MS	Cd ppm ICP-MS	Co ppm ICP-MS	Cs ppm ICP-MS	Cu ppm ICP-MS	Ga ppm ICP-MS	Hf ppm ICP-MS	Hg ppm ICP-MS	Mo ppm ICP-MS	Nb ppm ICP-MS
ZK001-14	1.10	36.9	<0.5	4750	2.00	0.10	3.80	10.0	2.30	46.6	8.70	2.70	0.12	87.6	6.20
ZK001-13	1.10	38.7	<0.5	5851	2.00	0.20	2.40	9.90	2.50	44.5	10.0	2.50	0.13	69.3	6.80
ZK001-12	1.70	51.7	<0.5	7333	3.00	0.20	8.90	12.0	3.60	57.9	12.9	3.50	0.17	91.4	8.00
ZK001-11	2.00	62.2	<0.5	5889	<1	0.20	9.10	10.5	3.20	67.9	10.8	2.50	0.20	136	6.50
ZK001-10	2.40	76.0	0.50	5682	1.00	0.20	17.2	11.3	3.50	97.9	10.9	2.70	0.22	188	6.60
ZK001-9	3.30	69.0	1.10	5837	1.00	0.20	23.0	9.60	3.30	115	10.0	2.60	0.22	140	6.70
ZK001-8	2.30	81.6	0.80	6391	1.00	0.20	5.70	12.9	2.70	69.0	11.9	3.20	0.24	137	8.10
ZK001-7	2.50	82.8	1.80	7726	1.00	0.20	8.40	14.6	4.00	68.7	12.3	3.60	0.22	170	7.70
ZK001-6	3.80	87.1	<0.5	7849	<1	0.20	18.6	15.5	4.30	101	12.6	3.40	0.32	209	8.10
ZK001-5	11.0	86.1	<0.5	5649	2.00	0.20	72.4	10.0	5.20	302	12.8	2.80	0.62	93.2	6.40
ZK001-4	3.50	44.9	<0.5	5548	1.00	0.10	11.0	8.70	1.70	91.1	6.90	1.20	0.28	63.2	4.30
ZK001-3	3.10	56.4	<0.5	6040	2.00	0.20	6.70	11.9	2.10	76.9	9.50	1.80	0.25	78.3	5.30
ZK001-2	11.4	100	<0.5	4583	1.00	0.20	105	7.60	4.50	296	9.40	1.90	1.02	99.3	5.20
ZK001-1	4.60	62.7	<0.5	3122	<1	0.10	29.4	12.6	2.80	97.0	5.20	1.20	0.36	82.7	3.50

Table 15A (continued)

Sample	Ni ppm ICP-MS	Pb ppm ICP-MS	Rb ppm ICP-MS	Sb ppm ICP-MS	Se ppm ICP-MS	Sn ppm ICP-MS	Sr ppm ICP-MS	Ta ppm ICP-MS	Th ppm ICP-MS	Tl ppm ICP-MS	U ppm ICP-MS	V ppm ICP-MS	W ppm ICP-MS	Zn ppm ICP-MS	Zr ppm ICP-MS
ZK001-14	114	15.6	48.4	3.40	7.60	2.00	321	0.40	6.20	<0.1	56.2	600	3.90	162	81.0
ZK001-13	100	27.4	55.1	3.50	8.60	2.00	203	0.50	6.70	0.10	52.1	320	1.70	87.0	91.0
ZK001-12	163	65.0	70.8	4.90	13.5	2.00	155	0.50	8.60	0.10	61.6	995	1.80	352	113
ZK001-11	202	20.7	62.2	5.40	14.8	2.00	181	0.50	6.30	0.10	72.4	1116	1.60	372	92.9
ZK001-10	317	19.9	65.9	7.20	20.2	2.00	118	0.50	6.40	<0.1	67.8	2231	2.40	765	96.7
ZK001-9	215	41.1	63.2	11.1	20.4	1.00	165	0.50	6.80	0.10	61.5	2311	1.20	1142	92.3
ZK001-8	210	34.8	56.6	7.00	17.0	2.00	305	0.50	7.70	0.10	65.5	1311	1.50	267	119
ZK001-7	256	32.9	74.9	5.90	22.6	2.00	329	0.60	8.40	0.20	72.2	2102	2.30	353	121
ZK001-6	383	26.9	75.5	10.0	34.7	2.00	175	0.60	8.10	<0.1	111	2489	3.40	738	119
ZK001-5	250	30.1	70.6	25.3	57.4	2.00	125	0.40	6.00	<0.1	48.1	3655	3.50	3298	91.2
ZK001-4	146	16.8	36.1	8.10	19.4	2.00	468	0.20	3.60	<0.1	49.9	1035	2.70	507	53.2
ZK001-3	173	67.8	42.0	8.30	19.3	1.00	185	0.30	4.60	<0.1	53.9	1092	1.50	441	68.8
ZK001-2	219	81.0	60.7	41.8	59.1	1.00	98.8	0.40	4.80	<0.1	43.1	4868	1.10	5339	67.7
ZK001-1	156	119	38.1	18.1	29.5	<1	265	0.20	3.10	<0.1	44.4	3835	1.00	1487	41.1

Table 15A (continued)

Sample	La ppm ICP-MS	Ce ppm ICP-MS	Pr ppm ICP-MS	Nd ppm ICP-MS	Sm ppm ICP-MS	Eu ppm ICP-MS	Gd ppm ICP-MS	Tb ppm ICP-MS	Dy ppm ICP-MS	Y ppm ICP-MS	Ho ppm ICP-MS	Er ppm ICP-MS	Tm ppm ICP-MS	Yb ppm ICP-MS	Lu ppm ICP-MS
ZK001-14	23.7	41.4	4.82	19.6	3.49	0.77	3.84	0.61	3.87	36.3	0.84	2.66	0.37	2.23	0.34
ZK001-13	24.0	43.1	4.93	18.7	3.54	0.72	3.44	0.57	3.38	30.7	0.73	2.27	0.32	2.08	0.30
ZK001-12	26.1	47.7	5.58	21.7	3.98	0.87	4.13	0.65	3.95	35.8	0.86	2.56	0.39	2.34	0.36
ZK001-11	26.0	44.0	5.20	21.4	3.84	0.83	3.94	0.63	3.86	37.6	0.86	2.76	0.40	2.42	0.36
ZK001-10	25.7	40.6	5.41	21.2	4.06	0.86	4.22	0.71	4.45	41.0	0.98	3.15	0.43	2.77	0.40
ZK001-9	27.6	39.8	5.88	25.4	4.48	0.99	5.18	0.83	5.24	51.5	1.19	3.66	0.52	3.14	0.46
ZK001-8	31.6	51.8	6.81	28.8	5.11	1.13	5.56	0.90	5.51	52.1	1.25	3.91	0.56	3.35	0.51
ZK001-7	29.0	48.7	6.51	26.1	5.12	1.15	5.11	0.85	5.21	43.2	1.12	3.46	0.50	3.13	0.47
ZK001-6	33.2	51.7	7.25	29.8	5.68	1.20	5.93	0.97	5.91	52.7	1.29	4.04	0.58	3.57	0.52
ZK001-5	28.4	38.1	6.95	30.1	5.97	1.36	6.99	1.15	7.07	67.7	1.58	4.97	0.72	4.27	0.65
ZK001-4	19.5	24.2	4.24	19.0	3.32	0.90	4.34	0.70	4.18	44.7	0.99	3.05	0.44	2.58	0.39
ZK001-3	22.3	33.6	5.11	21.3	4.01	0.92	4.76	0.74	4.51	44.4	1.04	3.20	0.43	2.56	0.37
ZK001-2	21.8	27.3	4.96	21.3	4.08	0.87	4.95	0.82	4.93	50.6	1.22	3.97	0.56	3.44	0.53
ZK001-1	19.7	22.2	4.24	17.6	3.56	0.88	4.24	0.67	4.20	42.5	0.98	3.19	0.44	2.61	0.41

Stratigraphic position is in meter relative to the vanadium barren underlying black shale bed. Analyses were carried out at Acmelabs in Canada except for TOC analysis (yellowish background) in NRCG in China. Bluish shading refers to inductively coupled plasma with extraction by Aqua Regia.

Table 16A: Complete bulk rock geochemical data of samples from Kunyang profile, Yunnan province.

Sample	Level (m)	Lithology	SiO_2 % XRF	TiO_2 % XRF	Al_2O_3 % XRF	TFe_2O_3 % XRF	MnO % XRF	MgO % XRF	CaO % XRF	Na_2O % XRF	K_2O % XRF	P_2O_5 % XRF	SO_3 % XRF	Cl % XRF	F % XRF	LOI % XRF	Sum % XRF
K-18	98.3	Black shale	35.6	0.39	6.54	3.58	0.17	10.7	15.3	0.02	2.11	0.54	0.85	0.02	0.09	23.9	99.8
K-19	95.3	Black shale	42.1	3.45	8.42	3.89	0.01	1.35	17.6	0.07	2.60	14.4	0.20	0.02	1.13	4.72	100.0
K-17	39.3	Black shale	60.1	0.66	12.6	4.44	0.05	5.29	3.51	0.06	3.82	0.44	0.78	0.02	0.06	7.89	99.8
K-15	20.3	Black shale	59.9	0.69	12.9	4.05	0.05	4.6	3.06	0.06	4.66	0.30	1.04	0.02	0.09	8.22	99.7
K-14	19.3	Black shale	57.9	0.69	12.4	4.12	0.05	4.94	4.04	0.06	4.52	0.48	1.16	0.02	0.12	9.28	99.8
K-13	18.3	Black shale	60.0	0.74	13.8	4.18	0.05	4.05	2.55	0.05	5.21	0.36	1.27	0.02	0.06	7.47	99.8
K-8	17.3	Black shale	63.0	0.71	13.4	3.59	0.04	3.43	1.83	0.06	5.24	0.28	0.94	0.01	0.11	7.26	99.8
K-12	16.8	Black shale	60.8	0.66	12.5	3.15	0.04	3.85	3.66	0.06	4.85	0.34	1.25	0.02	0.16	8.49	99.8
K-7	16.3	Black shale	58.3	0.64	12.5	2.85	0.05	4.24	4.46	0.06	4.80	0.49	1.06	0.02	0.16	10.1	99.7
K-11	15.8	Black shale	64.0	0.68	13.3	2.8	0.03	2.91	2.34	0.06	5.48	0.32	0.86	0.02	0.11	6.89	99.8
K-6	15.3	Black shale	48.3	0.53	10.4	3.01	0.10	6.54	9.31	0.04	4.06	0.71	1.70	0.02	0.18	15.0	99.8
K-10	14.8	Black shale	43.2	0.23	6.03	1.92	0.12	9.09	13.9	0.02	2.71	0.60	0.91	0.02	0.10	21.1	99.9
K-9	14.3	Black shale	66.1	0.31	12.6	4.17	0.01	1.79	1.19	0.03	6.14	0.29	1.22	0.01	0.16	5.80	99.9
K-3	8.0	Phosphorite	7.7	0.07	0.41	0.28	0.04	3.23	48.2	0.1	0.17	30.3	0.33	0.02	2.96	7.44	101.2
K-2	4.5	Bentonite	33.6	0.06	6.52	0.99	0.01	0.8	29.5	0.17	3.67	20.6	0.43	0.02	1.97	2.41	100.7

Table 16A (continued)

Sample	As ppm ICP-MS	Ba ppm ICP-MS	Bi ppm ICP-MS	Co ppm ICP-MS	Cd ppm ICP-MS	Cr ppm ICP-MS	Cs ppm ICP-MS	Cu ppm ICP-MS	Ga ppm ICP-MS	Hf ppm ICP-MS	Li ppm ICP-MS	Mo ppm ICP-MS	Nb ppm ICP-MS	Ni ppm ICP-MS
K-18	16.0	252	<4	6.00	0.24	31.0	<3	92.0	9.00	8.00	13.5	7.00	6.00	59.0
K-19	57.0	983	<4	8.00		234	18.0	19.0	10.0	8.00	6.89	21.0	62.0	15.0
K-17	10.0	455	<4	9.00	0.34	71.0	4.00	33.0	17.0	7.00	22.7	<3	10.0	31.0
K-15	20.0	562	<4	16.0	0.38	183	8.00	41.0	17.0	7.00	31.2	7.00	10.0	64.0
K-14	19.0	520	<4	10.0	0.17	116	7.00	28.0	16.0	<6	40.9	5.00	12.0	60.0
K-13	20.0	563	<4	14.0	0.88	131	8.00	33.0	18.0	<6	18.2	4.00	11.0	68.0
K-8	16.0	586	<4	14.0	0.17	77.0	8.00	32.0	18.0	<6	9.89	4.00	11.0	58.0
K-12	21.0	499	<4	9.00	0.21	144	10.0	32.0	16.0	<6	28.5	5.00	13.0	53.0
K-7	23.0	477	<4	9.00	0.17	365	8.00	38.0	19.0	9.00	31.1	7.00	12.0	58.0
K-11	26.0	562	<4	11.0	0.18	115	9.00	26.0	17.0	<6	46.1	5.00	10.0	55.0
K-6	32.0	389	<4	9.00	0.19	284	8.00	38.0	13.0	<6	49.7	7.00	9.00	62.0
K-10	15.0	210	<4	3.00	0.18	33.0	<3	16.0	7.00	<6	52.0	3.00	8.00	22.0
K-9	51.0	417	<4	7.00	0.18	61.0	5.00	20.0	19.0	<6	71.3	9.00	43.0	27.0
K-3	5.00	195	<5	<3	0.21	24.0	<4	10.0	<2	<7	38.1	<3	3.00	<3
K-2	12.0	359	<5	<3	0.37	6.00	<4	12.0	7.00	<7	38.6	<3	7.00	<3

Table 16A (continued)

Sample	Pb ppm ICP-MS	Rb ppm ICP-MS	Sb ppm ICP-MS	Sc ppm ICP-MS	Sn ppm ICP-MS	Sr ppm ICP-MS	Ta ppm ICP-MS	Th ppm ICP-MS	U ppm ICP-MS	V ppm ICP-MS	W ppm ICP-MS	Zn ppm ICP-MS	Zr ppm ICP-MS
K-18	6.00	59.0	<9	8.00	<4	103	5.00	14.0	8.00	42	<4	28.0	127
K-19	24.0	63.0	<10	16.0	<5	314	<5	42.0	84.0	201	<4	33.0	255
K-17	8.00	101	<7	12.0	4.00	62.0	5.00	21.0	4.00	97	<4	48.0	197
K-15	12.0	108	<7	12.0	<4	57.0	<4	18.0	13.0	649	<4	51.0	173
K-14	12.0	107	<7	12.0	<4	62.0	<4	20.0	10.0	255	<4	55.0	193
K-13	24.0	117	<7	14.0	<4	79.0	<4	20.0	13.0	392	<4	60.0	187
K-8	23.0	112	<7	12.0	<4	52.0	<4	18.0	11.0	164	<4	47.0	198
K-12	25.0	110	<7	12.0	<4	63.0	<4	19.0	14.0	254	<4	34.0	184
K-7	19.0	115	<7	12.0	<4	68.0	<4	19.0	14.0	657	<4	128	182
K-11	26.0	114	<7	12.0	<4	53.0	<4	17.0	13.0	252	<4	34.0	169
K-6	39.0	89.0	<8	11.0	<4	97.0	<4	19.0	18.0	379	<4	108	153
K-10	21.0	45.0	<8	6.00	<4	82.0	<4	13.0	10.0	146	<4	29.0	76.0
K-9	122	71.0	<6	5.00	<4	25.0	<4	25.0	12.0	271	<4	114	192
K-3	5.00	10.0	<13	<3	<5	575	<5	8.00	30.0	32	<5	6.0	210
K-2	15.0	33.0	<11	4.00	<5	725	<5	22.0	15.0	8	<4	11.0	84.0

Table 16A (continued)

Sample	La ppm ICP-MS	Ce ppm ICP-MS	Pr ppm ICP-MS	Nd ppm ICP-MS	Sm ppm ICP-MS	Eu ppm ICP-MS	Gd ppm ICP-MS	Tb ppm ICP-MS	Dy ppm ICP-MS	Y ppm ICP-MS	Ho ppm ICP-MS	Er ppm ICP-MS	Tm ppm ICP-MS	Yb ppm ICP-MS	Lu ppm ICP-MS
K-18	17.8	38.9	5.00	21.5	5.46	1.33	5.65	0.85	5.10	28.5	1.01	2.83	0.39	2.43	0.36
K-19	101	231	28.9	139	40.2	11.2	45.9	6.28	33.3	181	5.73	13.5	1.48	7.95	1.08
K-17	33.0	62.4	7.44	28.1	5.24	1.06	4.64	0.72	4.47	24.1	0.88	2.62	0.39	2.55	0.38
K-15	30.5	55.8	6.99	26.0	4.78	0.98	4.24	0.66	4.00	22.9	0.83	2.46	0.37	2.38	0.36
K-14	32.7	59.3	7.51	29.0	6.09	1.29	5.70	0.85	4.97	27.4	1.00	2.75	0.38	2.52	0.39
K-13	31.3	55.8	6.85	25.2	4.81	0.97	4.38	0.69	4.23	25.0	0.89	2.64	0.38	2.49	0.39
K-8	37.1	62.9	7.52	26.2	4.02	0.74	3.33	0.57	3.72	23.0	0.83	2.47	0.39	2.50	0.39
K-12	40.3	67.3	8.41	30.1	5.32	1.04	4.86	0.76	4.90	29.9	1.01	3.04	0.45	2.88	0.44
K-7	37.2	60.4	8.03	30.0	5.94	1.18	5.71	0.87	5.42	33.6	1.11	3.15	0.47	3.00	0.45
K-11	33.1	53.6	6.56	23.6	3.96	0.74	3.39	0.55	3.69	23.2	0.79	2.39	0.36	2.34	0.36
K-6	36.6	60.8	8.22	31.6	6.45	1.38	6.29	0.95	5.81	39.3	1.21	3.43	0.48	3.05	0.45
K-10	21.6	37.6	5.15	20.2	4.55	0.62	4.67	0.79	5.03	34.0	1.02	2.88	0.40	2.45	0.37
K-9	21.0	32.9	3.93	13.9	3.26	0.32	3.42	0.78	6.53	40.4	1.59	5.51	0.90	6.12	0.87
K-3	59.2	34.3	8.08	34.1	5.86	1.33	8.78	1.24	8.68	138	2.19	6.49	0.77	3.99	0.51
K-2	64.3	110	16.3	65.1	13.8	1.33	14.6	2.35	14.7	117	2.96	7.65	0.93	5.11	0.71

Stratigraphic position is in meter relative to the dolomite contact. Analyses were carried out at the BGR, Hannover.

Curriculum Vitae

Xu, Lingang

Mineral Resources, Technical University of Clausthal,
Adolph-Roemer-Str.2a, 38678, Clausthal-Zellerfeld, Germany.
Telephone: 0049-5323-722767
Cell phone: 0049-17620721232
Fax: 0049-5323-722511
E-mail: lingang.xu@tu-clausthal.de
Permanent e-mail: xulingang@sina.com

Personal information

Date of Birth: March 5. 1981
Place of Birth: Nei Mongol, China
Citizenship: Chinese
Gender: Male
Marital Status: Unmarried

University education

2007-present: Ph.D candidate. In Mineral Resource Unit, Technical University of Clausthal, Germany.
Thesis: Early Cambrian black shale and associated polymetallic Ni-Mo-PGE-Au mineralization, South China. (supervised by Prof. Bernd Lehmann & Prof. Mao Jingwen)

2007: M. Sc. In School of Earth Science and Resources, China University of Geosciences (Beijing). China.
Thesis: Geology, geochemistry and genesis of the Mengku iron deposit in Fuyun County, Xinjiang Province, NW China. (supervised by Prof. Mao Jingwen & Prof. Yang Fuquan)

2004: B. Sc. In College of Earth Science and Resources, Chang`an University, Xi`an, China.
Thesis: Granite contributions to the formation of the Wangfeng Au deposit, Xinjiang Province, NW China (supervised by Prof. Yan Haiqing)

Research interests

Transition elements stable isotope geochemistry

Atmosphere-surface interactions and sedimentary processes

Prophyry-skarn mineralization system

Hydrothermal ore deposits

Microanalytical techniques

Field exploration and mine development

Publications

Xu, L.G., Lehmann, B., Mao, J.W., Nägler, T.F., Neubert, N., Böttcher, M.E., 2011. Mo isotope and trace element patterns of Early Cambrian black shales in South China: constraints on the paleoenvironment. Submitted to Chemical Geology.

Xu, L.G., Lehmann, B., Mao, J.W., Qu, W.J., Du, A.D., 2011. Re-Os age of polymetallic Ni-Mo-PGE-Au mineralization in Early Cambrian balck shales of South China: a reassessment. Economic Geology 106, 511-522.

Xu, L.G., Lehmann, B., Mao, J.W., 2011. Seawater as origin of polymetallic Ni-Mo-PGE-Au mineralization in Early Cambrian black shales of South China: evidences from Mo isotope, PGE, trace element and REE geochemistry. Submitted to Ore Geology Reviews.

Xu, L.G., Lehmann, B., 2011. Mo and Mo stable isotope geochemistry: Isotope system, analytical technique and applications to geology. Mineral Deposits 30, 103-124 (in Chinese with English abstract).

Xu, L.G., Mao, J.W., Yang, F.Q., Hennig, D., Zheng, J.M., 2010. Geology, geochemistry and age constraints on the Mengku skarn iron deposit in Xinjiang Altai, NW China. Journal of Asian Earth Sciences 39, 423-440.

Xu, L.G., Yang, F.Q., Li, J.G., Cai, Y.B., Zheng, J.M., Huang, C.L., 2007. Geology and geochemistry of the Mengku iron deposit in Fuyun county, Xinjiang Uigur Autonomous. Acta Petrologica Sinica 23, 2653-2664 (in Chinese with English abstract).

Xu, L.G., Mao, J.W., Yang, F.Q., Ye, H.S., Zheng, J.M., Li, J.G., Cai, Y.B., Zha, X.L., Gao, J.J., 2007. Skarn mineral characteristics of the Mengku iron deposit in Xinjiang and their geological significance. Mineral Deposits 26, 455-463 (in Chinese with English abstract).

Xu, L.G., Yang, F.Q., Zheng, J.M., Gao, J.J., 2006. Mineralogy and geochemistry of the Mengku iron deposit in Xinjiang province. Mineral Deposits (supp.) 25, 329-332 (in Chinese).

Ye, H.S., Mao, J.W., Xu, L.G., Gao, J.J., Xie, G.Q., Li, X.Q., He, C.F., 2008. SHRIMP zircon U-Pb dating and geochemistry of the Taishanmiao Aluminous A-type granite in Western Henan province. Geological Review 54, 1-14 (in Chinese with English abstract).

Yang, F.Q., Mao, J.W., Chai, F.M., Liu, F., Zhou, G., Geng, X.X., Liu, G.R., Xu, L.G., 2008. Mineral deposits 27, 659-680 (in Chinese with English abstract).

Yang, F.Q., Mao, J.W., Xu, L.G., Zhang, Y., Liu, F., Huang, C.L., Zhou, G., Liu, G.R., Dai, J.Z., 2007. REE geochemistry of the Mengku iron deposit, Xinjiang, and its indication for iron mineralization. Acta Petrologica Sinica 23, 2443-2456 (in Chinese with English abstract).

Li, Y.C., Yang, F.Q., Zhao, C.S., Zhang, Y, Yan, S.H., Dai, J.Z., Xu, L.G., 2007. SHRIMP U-Pb zircon dating of the Beilekuduk pluton in Xinjiang and its geological implications. Acta Petrologica Sinica 23, 2483-2492 (in Chinese with English abstract).

Yang, F.Q., Mao, J.W., Zheng, J.M., Xu, L.G., Liu, D.Q., Zhao, C.S., Ye, H.S., 2006. Geology and metallogenic model of the Altay large metallogenic belt in Kazakhstan. Acta Geologica Sinica 80, 963-983 (in Chinese with English abstract).

Zheng, J.M., Chen, M.H., Xu, L.G., Gao, J.J., Hu, Y.Y., Liang, Z.H., 2006. Characteristics of structurally controlled skarn iron deposits and prospecting targets in Handan-Xingtai area. Mineral Deposits (supp.) 25, 115-118 (in Chinese).

Chen, L., Ye, H.S., Zheng, R.F., Xu, L.G., Gao, J.J., 2005. Characteristics of ore forming fluid of Dahu gold deposit, West Henan Province, China. In Zhao, C.S., Guo, B.J. (eds) Mineral Deposit Research: Meeting the Global Challenge. Beijing: China Land Publishing House 3, 186-189.

Memberships

2008-present: student member of SGA (Society for Geology Applied to Mineral Deposits)

2008-present: student member of SEG (Society of Economic Geologists)

Awards

Ph.D scholarship granted by the Chinese Scholarship Council (Dec. 2007-Nov. 2010)

Research assistant scholarship offered by the Mineral Resource Unit, Technical University of Clausthal (Dec. 2010-Jun. 2011).